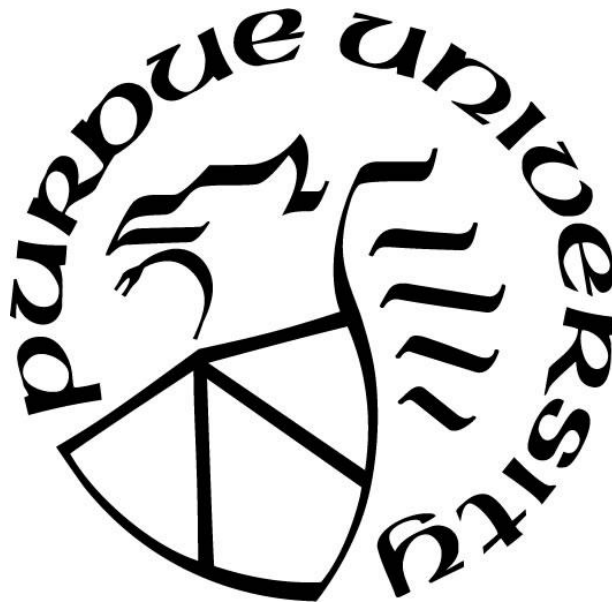# ON HEAT TRANSFER MECHANISMS IN SECONDARY COOLING OF CONTINUOUS CASTING OF STEEL SLAB

by

Haibo Ma

A Dissertation

Submitted to the Faculty of Purdue University

In Partial Fulfillment of the Requirements for the degree of

Doctor of Philosophy

School of Mechanical Engineering

West Lafayette, Indiana

August 2021

THE PURDUE UNIVERSITY GRADUATE SCHOOL
STATEMENT OF COMMITTEE APPROVAL

Dr. Chenn Q. Zhou Chair

School of Mechanical Engineering

Dr. Jay P. Gore

School of Mechanical Engineering

Dr. Jun Chen

School of Mechanical Engineering

Dr. Matthew John M. Krane

School of Materials Engineering

Approved by:

Dr. Nicole L. Key

Dedicated to my mother & father,
and Ziyue.

ACKNOWLEDGMENTS

was the best of times, it was the worst of times.". The fear of the global pandemic has entrapped us in our apartment for more than one year. Our life fills with frustration and social isolation. It is "love in the time of cholera.". Her encouragement and patience, not to mention her cooking skills, have enabled me to keep my head above the water. Her expectation has been and will always be the source to urge me to search for a better me.

My extended family has been supportive and encouraging. I would like to thank them for giving me a roof over my head when I grew up. My grandparents, uncles, aunts, and cousins were the source of love when I needed it the most. I also appreciate the friendship with my lifelong friends, Adam Liu, who cheered my success from the bottom of his heart every single time, and Bill Yuan, who named himself literally after Bill Gates and would like to collect the same amount of fortune in his life. I wish he is on the right track now. I would also like to thank Elizabeth Chen, a wonderful lady who enlightened me when I was drowning in grief, and the second woman I would like to call mom.

The Center for Innovation through Visualization and Simulation (CIVS) at Purdue University Northwest has been the second home for me in the past six years. I obtained all the resources required for this work at CIVS. I would like to thank all my present and past colleagues at CIVS for their support and great teamwork. Among them are Dr. Armin K. Silaen, Bin Wu, Dr. Tyamo Okosun, John Moreland, Nicholas Walla, Kyle Toth, Linda Robinson, Doreen M. Gonzalez-Gaboyan, Sandra Jacobs, Billie Cano, Ana Jovanovich, Dyan D. Murphy, Sonia B. Diaz, Felicia Armstrong, Charles A. Capek, Melissa C. Mollett, Guangwu Tang, Yuchao Chen, Xipeng Guo, Kaile Tang, Mingyi Liang, Matthew Moore, John Resa, Xiang Zhou, Saswot Thapa, Edwin A. Mosquera Salazar, Vitalis Ebuka Anisiuba, Luis Raygadas-Lara.

The Steel Manufacturing Simulation and Visualization Consortium (SMSVC) is also gratefully acknowledged for providing this project. I would like to express special thanks to all the present and past member companies and the project technical committee members for their guidance and support. I must also extend a special thank you to Dr. Sunday Abraham at SSAB Iowa. Through many critical discussions and with his valuable suggestions, this research has been considerably more impactful.

TABLE OF CONTENTS

LIST OF TABLES

LIST OF FIGURES

NOMENCLATURE

<u>Latin Symbols</u>

q''_{total}	total heat flux through mold walls, W/m^2
q''_{cond}	heat flux through conduction, W/m^2
q''_{conv}	heat flux through convection, W/m^2
q''_R	heat flux through radiation, W/m^2
L_{roll}	roll contact length, m
D	diameter, m
N	number
s_n	standard deviation
$\overline{D}$	mean diameter, m
s_g	geometric standard deviation
$\overline{D}_{ng}$	geometric number mean diameter, m
a_{norm}	norming constant of the 4P-H distribution
K_1	modified Bessel function of the third kind and first order
A_{norm}	normalization constant of the 3P-H distribution
a_{3PH}	parameter of the 3P-H distribution
a_{NT}	parameter of Nukiyama-Tanasawa distribution
b_{NT}	parameter of Nukiyama-Tanasawa distribution
q_{NT}	parameter of Nukiyama-Tanasawa distribution
p_{NT}	parameter of Nukiyama-Tanasawa distribution
X_{RR}	parameter of Rosin-Rammler distribution
q_{RR}	parameter of Rosin-Rammler distribution
Q	The fraction of the total volume contained in droplets of diameter less than D
a_{upper}	parameter of the upper-limit distribution
y_{upper}	parameter of the upper-limit distribution
k	turbulence kinetic energy, J/kg

u	velocity, m/s
d	diameter, m
t	time, s
C_D	drag coefficient
y_{dis}	droplet distortion, a value of 0 corresponds to no distortion, and 1 represents the maximum distortion.
r	radius, m
B_{coll}	impact parameter
b_{coll}	the distance from the center of one droplet to the relative velocity vector placed on the center of the other droplet
T	temperature, K
At	atomic weight, kg
h_{fg}	latent heat of vaporization, J/kg
P	pressure, Pa
c_p	specific heat, J/kg·K
g	gravitational acceleration, m/s^2
h, HTC	heat transfer coefficient, W/m^2·K
f_{roll}	fraction of heat flow per spray zone going to roll
L_{spray}	length of spray coverage, m
L_{roll}	length of roll contact, m
$L_{sp\,pitch}$	distance between adjacent sprays, m
q''_{roll}	heat loss from steel due to roll contacts, W/m^2
V_{ca}	casting speed, m/s
Q_w	spray water flux, L/m^2·s
a_{AM}	parameter of HTC correlation in GCM2D
b_{AM}	parameter of HTC correlation in GCM2D
c_{AM}	parameter of HTC correlation in GCM2D
d_{AM}	parameter of HTC correlation in GCM2D
e_{AM}	parameter of HTC correlation in GCM2D
f_{AM}	parameter of HTC correlation in GCM2D

g_{AM}	parameter of HTC correlation in GCM2D
h_{AM}	parameter of HTC correlation in GCM2D
P_{impact}	droplet impact pressure, Pa
Z_{mold}	mold length, m
h_{lat}	latent heat release, kJ/kg
L	latent heat of fusion, kJ/kg
f_{sol}	solid fraction in a control volume
T_{liq}	liquidous temperature, K
T_{sol}	solidus temperature, K
A	a user-defined number in the range of $0 \leq A \leq L$
B	some large number that is defined by users
S_{mass}	source term for the conservation of mass, kg/ m^3·s
S_{mom}	source term for the conservation of momentum, N/m^3
G_k	production of turbulence kinetic energy, kg/m·s^3
x	special coordinate, m
G_{ω}	generation of turbulence dissipation rate, kg/m^3·s^2
S	modulus of the mean rate-of-strain tensor, 1/s
R_{ω}	parameter of the k-ω SST model
R_k	parameter of the k-ω SST model
F_1	blending function of the k-ω SST model
$y_{k\omega}$	distance to the next surface in the k-ω SST model, m
$CD_{k\omega}$	cross-diffusion term in the k-ω SST model
R_{β}	parameter of the k-ω SST model
a_t	parameter of the k-ω SST model
F_2	blending function of the k-ω SST model
Y_i	mass fraction of the ith species
$D_{i,m}$	mass diffusion coefficient of the ith species, m^2/s
$D_{T,i}$	thermal diffusion coefficient of the ith species, m^2/s
$M_{w,i}$	molecular weight of the ith species, g/mol
X_i	molar fraction of the ith species

E	total energy, J
J_i	diffusion flux of the ith species, 1/m²·s
h_i	sensible enthalpy of the ith species, J/kg
S_R	mass source term due to radiation, W/m³
a_{abs}	absorption coefficient, 1/m
n_R	refractive index
k_{wave}	wave number
C_{dc}	discharge coefficient
m	mass, kg
Y_d	mass fraction of droplet
w	width of spray region, m
F_{a-l}	momentum source term due to surface tension, N/m³
n	surface normal
$RStd$	radius standard deviation
RSO	radius-surface orthogonality
A_i	facet area in i^{th} control volume, m²
S_{trsn}	mass source term due to the VOF-to-DPM transition, kg/s
V	volume, m³
B_0	child droplet size constant
B_1	breakup time constant
$P(n)$	possibility of collision
n	number of collisions
b_{offset}	offset of the trajectories of colliding droplets
b_c	critical offset
H_{sheet}	liquid sheet height, m
H_π	liquid sheet height at $\Psi = \pi$, m
Δy	distance from the solid centroid to the face centroid, m
G	incident radiation, W/m²
I	radiation intensity, W/sr
k_c	mass transfer coefficient, m/s

B_m	Spalding number
R_{uni}	universal gas constant, 8.314J/mol·K
A_{mushy}	crystal constant
F_μ	switching function in the Enthalpy-Porosity method
f_{st}	critical solid fraction
K_{per}	permeability, m^2
C_{cool}	cooling rate, °C/s
STD	standard deviation
ΔT_{sup}	superheat, K
L_{ML}	metallurgical length, m

Greek Symbols

θ_{roll}	roll contact angle, degree
α_{lh}	arbitrary parameter of the log-hyperbolic distribution
β_{lh}	arbitrary parameter of the log-hyperbolic distribution
δ_{lh}	arbitrary parameter of the log-hyperbolic distribution
ξ_{lh}	arbitrary parameter of the log-hyperbolic distribution
θ	parameter of the 3P-H distribution
μ_0	parameter of the 3P-H distribution
x_{3PH}	parameter of the 3P-H distribution
μ_{3PH}	parameter of the 3P-H distribution
δ_{upper}	parameter of the upper-limit distribution
ε	turbulence dissipation rate, m^2/s^3
ω	specific dissipation rate, 1/s
ρ	density, kg/m^3
σ	surface tension, N/m
μ	viscosity, N·s/m^2
γ	a random number between 0 and 1
β_s	surface thermal parameter
λ	thermal conductivity, W/m·K

ε_{st}	steel surface emissivity
σ_{SB}	Stefan-Boltzmann constant, 5.67×10^{-8} W/m$^2 \cdot$K^4
α_{cal}	machine-dependent calibration factor
θ_{slab}	the slab surface angle from horizontal, degree
α	parameter of the k-ω SST model
α_{∞}	parameter of the k-ω SST model
α^*	parameter of the k-ω SST model
$\alpha_{\infty,1}$	parameter of the k-ω SST model
$\alpha_{\infty,2}$	parameter of the k-ω SST model
σ_k	turbulent Prandtl numbers for k
σ_{ω}	turbulent Prandtl numbers for ω
β_k	parameter of the k-ω SST model
β_{ω}	parameter of the k-ω SST model
α_0	constant of the k-ω SST model
α_{∞}^*	constant of the k-ω SST model
α_0^*	constant of the k-ω SST model
$\beta_{i,1}$	constant of the k-ω SST model
$\beta_{i,2}$	constant of the k-ω SST model
β_{∞}^*	constant of the k-ω SST model
$\sigma_{\omega,1}$	constant of the k-ω SST model
$\sigma_{\omega,2}$	constant of the k-ω SST model
κ	constant of the k-ω SST model
$\sigma_{k,1}$	constant of the k-ω SST model
$\sigma_{k,2}$	constant of the k-ω SST model
η	wave amplitude of disturbances
ω_{wave}	complex growth rate
Ω	maximum growth rate of wavy disturbances
Λ	dominance wavelength of wavy disturbances, m
t_{sht}	sheet thickness, m
ρ_r	ratio of air density and liquid density

ν_l	liquid kinematic viscosity, m^2/s
α_{sp}	spray angle, degree
β_{spread}	spread angle, degree
α_a	volume fraction of air
α_l	volume fraction of water
κ_a	curvature of the interface
Ψ	the exit angle, degree
ϕ	the impinge angle, degree
ζ	wall jet model parameter
ε_{eff}	heat transfer effectiveness
Ω_{sol}	solid angle, square degree
λ_{PDAS}	primary dendrite arm spacing, m
λ_{SDAS}	secondary dendrite arm spacing, m
δ_{st}	shell thickness, m
ε_{th}	thermal strain
α_{th}	thermal linear expansion coefficient, 1/K
δ_{ovlp}	spray overlapping length, m
η_{sp}	spray overlapping length, m

Subscripts

$cond$	conduction
$conv$	convection
R	radiation
i	i^{th} value
$norm$	normal
lh	log-hyperbolic
$3PH$	three-parameter log-hyperbolic
NT	Nukiyama-Tanasawa
RR	Rosin-Rammler
max	maximum

a	air
d	droplet
D	drag
dis	distortion
$coll$	collision
1	the larger droplet prior to collision
2	the smaller droplet prior to collision
B	boiling
PA	pure adhesion
PR	pure rebounding
N	Nukiyama
v	vapor
c	critical
sur	surface
LF	Leidenfrost
st	steel
SB	Stefan-Boltzmann
W	water
cs	casting
cal	calibration
m	mold
liq	liquid
sol	solid
cen	centroid
mom	momentum
k	turbulence kinetic energy
abs	absorption
∞	free stream condition
t	turbulent
tra	translation

rot	rotation
b	breakup
noz	nozzle
ax	axial
ra	radial
L	ligament
sht	sheet
r	relative
Ω	parameter corresponds to the maximum growth rate
inj	injection
$a-l$	air-to-water
g	gravity
$trsn$	transition
cro	cross
int	interaction
$cell$	control volume
par	partial
v	vapor
sat	saturation
nrg	energy
lat	latent heat
in	in
o	out
$curr$	current
$prev$	previous
pse	pseudo
op	operating
uni	universal
por	porous
per	permeability

PDAS	primary dendrite arm spacing
SDAS	secondary dendrite arm spacing
p	porous
vert	vertical
avg	average
th	thermal
ter	terminal
ovlp	overlapping
sen	sensible
lat	latent
sp	spray
sup	superheat
ML	metallurgical length

Superscripts

$''$	flux
a	subscript for mean diameter
b	subscript for mean diameter
$-$	mean value
$\rightarrow$	vector
$'$	instantaneous value
0	reference

Dimensionless Numbers

Re	Reynolds number
Nu	Nusselt number
We	Weber number
Oh	Ohnesorge number
Pe	Peclet number
Sc_t	turbulent Schmidt number

Le	Lewis number
Pr	Prandtl number
Br	Brinkman number
Ta	Taylor number
Da	Darcy number

ABSTRACT

Secondary cooling during continuous casting is a delicate process because the cooling rate of water spray directly affects the slab surface and internal quality. Undercooling may lead to slab surface bulging or even breakout, whereas overcooling can cause deformation and crack of slabs due to excessive thermal residual stresses and strains. Any slab which does not meet the required quality will be downgraded or scrapped and remelted. In order to remain competitive and continuously produce high-quality and high-strength steel at the maximum production rate, the secondary cooling process must be carefully designed and controlled. Efficient and uniform heat removal without deforming or crack the slab is a significant challenge during secondary cooling. In the meantime, the on-site thermal measurement techniques are limited due to the harsh environment. In contrast, experimental measurements are only valid for the tested conditions, and the measurement process is not only labor-intensive, but the result might be inapplicable when changes in the process occur. On the other hand, the high-performance computing (HPC)-powered computational fluid dynamics (CFD) approach has become a powerful tool to gain insights into complex fluid flow and heat transfer problems. Yet, few successful numerical models for heat transfer phenomena during secondary cooling have been reported, primarily due to complex phenomena.

Therefore, the current study has proposed two three-dimensional continuum numerical models and a three-step coupling procedure for the transport of mass, momentum, and energy during the secondary cooling process. The first numerical model features the simulation of water spray impingement heat and mass transfer on the surface of a moving slab considering atomization, droplet dispersion, droplet-air interaction, droplet-droplet interaction, droplet-wall impingement, the effect of vapor film, and droplet boiling. The model has been validated against five benchmark experiments in terms of droplet size prior to impingement, droplet impingement pressure, and heat transfer coefficient (HTC) on the slab surface. The validated model has been applied to a series of numerical simulations to investigate the effects of spray nozzle type, spray flow rate, standoff distance, spray direction, casting speed, nozzle-to-nozzle distance, row-to-row distance, arrangement of nozzles, roll and roll pitch, spray angle, spray water temperature, slab surface temperature, and spray cooling on the narrow face. Furthermore, the simulation results have been

used to generate a mathematically simple HTC correlation, expressed as a function of nine essential operating parameters. A graphic user interface (GUI) has been developed to facilitate the application of correlations. The calculated two-dimensional HTC distribution is stored in the universal comma-separated values (csv) format, and it can be directly applied as a boundary condition to on-site off-line/on-line solidification calculation at steel mills. The proposed numerical model and the generic methodology for HTC correlations should benefit the steel industry by expediting the development process of HTC correlations, achieving real-time dynamic spray cooling control, supporting nozzle selection, troubleshooting malfunctioning nozzles, and can further improve the accuracy of the existing casting control systems.

In the second numerical model, the volume-averaged Enthalpy-Porosity method has been extended to include the slurry effect at low solid fractions through a switching function. With the HTC distribution on the slab surface as the thermal boundary condition, the model has been used to investigate the fluid flow, heat transfer, and solidification inside a slab during the secondary cooling process. The model has been validated against the analytical solution for a stationary thin solidifying body and the simulation for a moving thin solidifying body. The effects of secondary dendrite arm spacing, critical solid fraction, crystal constant, switching function constant, cooling rate, rolls, nozzle-to-nozzle distance, and arrangement of nozzles have been evaluated using the validated model. In addition, the solidification model has been coupled with the predictions from the HTC correlations, and the results have demonstrated the availability of the correlations other than on-site continuous casting control. Moreover, the model, along with the three-step coupling procedure, has been applied to simulate the initial solidification process in continuous casting, where a sufficient cooling rate is required to maintain a proper solidification rate. Otherwise, bulging or breakout might occur. The prediction is in good agreement with the measured shell thickness, which was obtained from a breakout incident. With the help of HPC, such comprehensive simulations will continue to serve as a powerful tool for troubleshooting and optimization.

1. INTRODUCTION

1.1 Research significance

Steel is the most versatile material, and it plays a significant role in our daily activities. The steel industry is crucial to the national economy and security. The steel industry consumes around 7.9% of the total energy used in the entire U.S. manufacturing sector [1]. Approximately 98% of 92.4 million short tons of crude steel produced in the U.S. were produced via the continuous casting process, where liquid steel is solidified by water-cooled mold and water sprays to form semi-finished slabs or billets. Secondary cooling is a delicate process because the cooling rate of water spray directly affects the slab surface and internal quality. Any slab which does not meet the required quality will be downgraded or scrapped, and remelted. With over 5% of produced steel ending up rejected and reprocessed as scrap [2], inefficiencies and production faults represent enormous energy and financial burden. An electric arc furnace (EAF) based facility consumes 1.5MMBtu electricity per short ton of tapped steel on average [3], which indicates that each ton of lost production has a high direct energy cost besides other losses such as additional material consumptions. In addition, re-melting of steel can result in delays of critical projects for the public, which can also include a significant increase in cost.

However, due to the complexity of the process, our knowledge of the interplay between the physical, chemical, and metallurgical phenomena occurring during casting is incomplete. Therefore, the application of high-performance computing (HPC) to systematic parametric studies of heat transfer and solidification process during continuous casting, especially water spray cooling stage where most of the defects occur, can enhance our understanding of the process, resulting in cost savings in the steel industry and expand the application of steel products. A reduction of 1% in the product rejection rate from 5% for the entire U.S. steel industry is equivalent to $52 million/year in cost savings due to energy waste from reprocessing rejected products. The current study results also have the potential of improving the internal quality of existing products, and hence, their performance in the field. For example, the weld properties of line pipe steel can be impacted by the internal quality, particularly centerline segregation. According to the Pipeline and Hazardous Materials Administration's data from 1986 to 2013, there were nearly 8000 pipeline

failure incidents (nearly 300 per year on average), resulting in more than 500 deaths, more than 2300 injuries, and nearly $7 billion in damage. About 17% of the failures were attributed to weld/material/equipment [4]. Hence, improvement to the internal quality of line pipe products will reduce the risk of pipeline failures and improve public safety and environmental protection.

In addition, one of the new trends to improve yield and energy efficiency in continuous casting is to employ real-time online dynamic casting control systems, which are designed to consistently produce high equality steel products with the help of real-time temperature measurements and dynamic adjustment of spray cooling rate. The major challenge is to obtain an accurate Heat Transfer Coefficient (HTC) on the surface of the steel product as a boundary condition for on-site real-time heat transfer and solidification calculations. Tremendous effort has been devoted to experimentally developing HTC correlations to predict the spray cooling rate. However, these correlations are limited to a handful of operating conditions. Not only the development process is labor-intense, but also the correlation might fail to predict correct HTC when changes in the process occur. Therefore, knowledge and understandings of the heat transfer phenomena during the secondary cooling process in continuous casting of steel are critical for controlling and optimizing the process.

1.2   Process description

Continuous casting is an efficient way to produce large volumes of semi-finished steel products. This process has been getting increasingly popular since it was introduced in the 1950s, and it makes more than 90% of the steel in the world today [5]. Figure 1-1 illustrates the essential components at a typical continuous casting facility, and they are: ladle furnace, tundish, mold, waters spray nozzles, rolls, and oxygen torches [6].

As shown in Figure 1-2, during the operation, the molten steel is tapped into the ladle furnace and undergoes any necessary ladle treatment, such as alloying and degassing. After the ladle treatments, the refined molten steel is transferred from the ladle furnace to the continuous caster through a tundish, which serves as a reservoir to maintain the liquid steel level during the ladle exchanges. The empty ladle sitting in a slot on a rotating turret is switched to the "off-cast" position while another ladle is rotated to the "on-cast" position to feed the tundish. From the tundish, the hot

molten steel is drained into the top section of the caster machine, which is known as the mold, through the submerged entry nozzle (SEN). The mold is made of copper and is cooled by water flowing in the channels that are embedded in the mold walls. The depth of the mold is usually determined by the casting speed and the cooling rate in the mold during the design stage, while the width of the mold can be adjusted during the operation based on the width of the casting products.

Once the molten steel enters the mold, it solidifies into a thin sold shell against the water-cooled mold walls. This is referred to as the primary cooling process. The newly-formed thin shell, together with the molten steel core enclosed, is withdrawn from the mold by rolls located below the mold and enters the secondary cooling region at a constant casting speed. The semi-solidified steel slab is further cooled down in the secondary cooling region by multiple water sprays until it completely solidifies. In the meantime, a series of rolls gradually turn the slab to the horizontal direction. Finally, the solid steel slab is cut into segments with preferable length by oxygen torches and sent to the later processes.
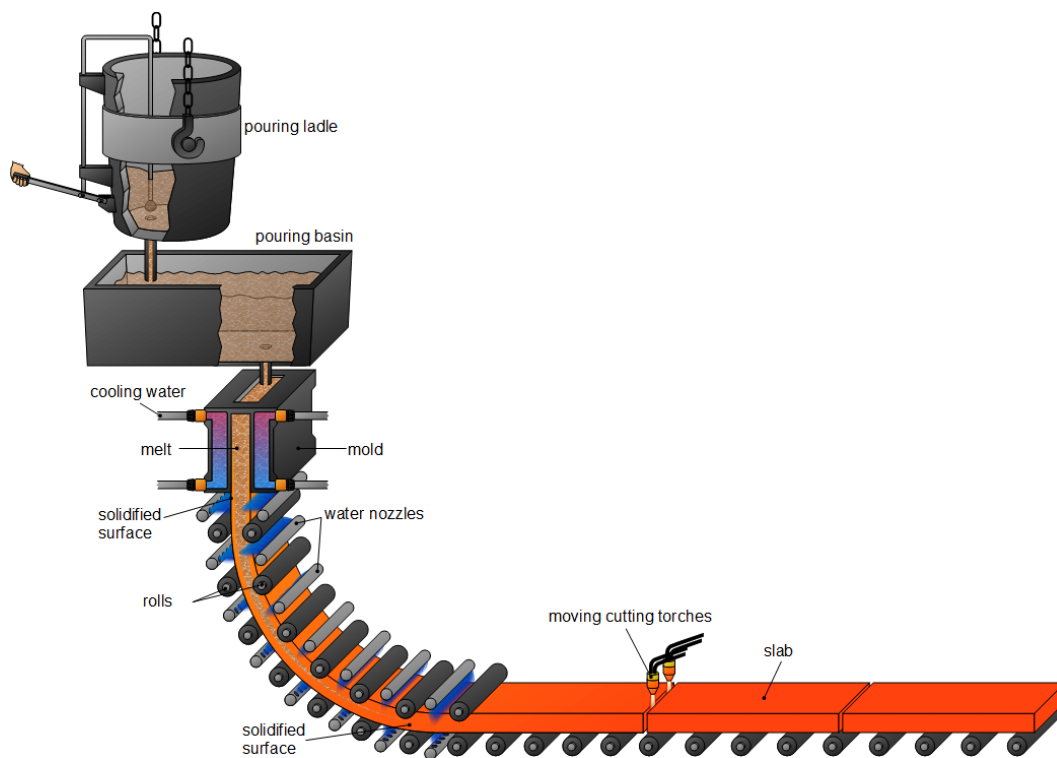
Figure 1-1. Illustration of the continuous casting process [6].
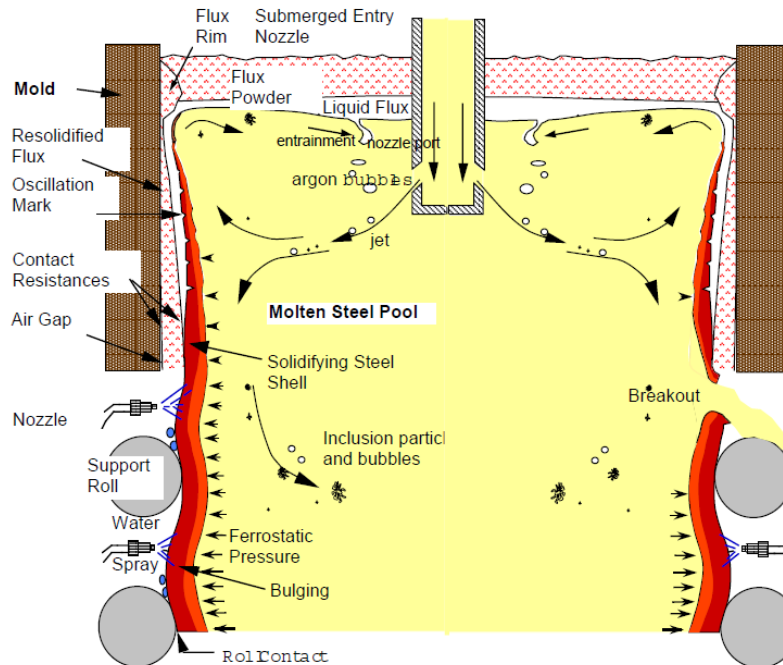
Figure 1-2. Cross-section view of the continuous casting process during the initial solidification stage [7].

Figure 1-3 summarizes the heat transfer mechanisms in the secondary cooling region. Inside the steel slab, heat is transferred through convection (molten steel to the solidified shell) and conduction (within the solidified shell). During this process, molten steel releases latent heat and transfers into the solid. Therefore, shell thickness continues to increase. On the surface of the solidified shell, however, heat is dissipated through all three heat transfer mechanisms, i.e., conduction (solidified shell to roll, solidified shell to vapor, solidified shell to droplets, and vapor to droplets), convection (solidified shell to air, roll to air, droplets to air), and radiation (solidified shell to the environment, and roll to the environment). Among the heat transfer processes, the heat transfer from the solidified shell to roll and to droplets through the vapor is crucial to produce high-quality steel slabs, as improper heat transfer will result in significant residual thermal stresses and strains, which could lead to deformation and crack of steel slabs.
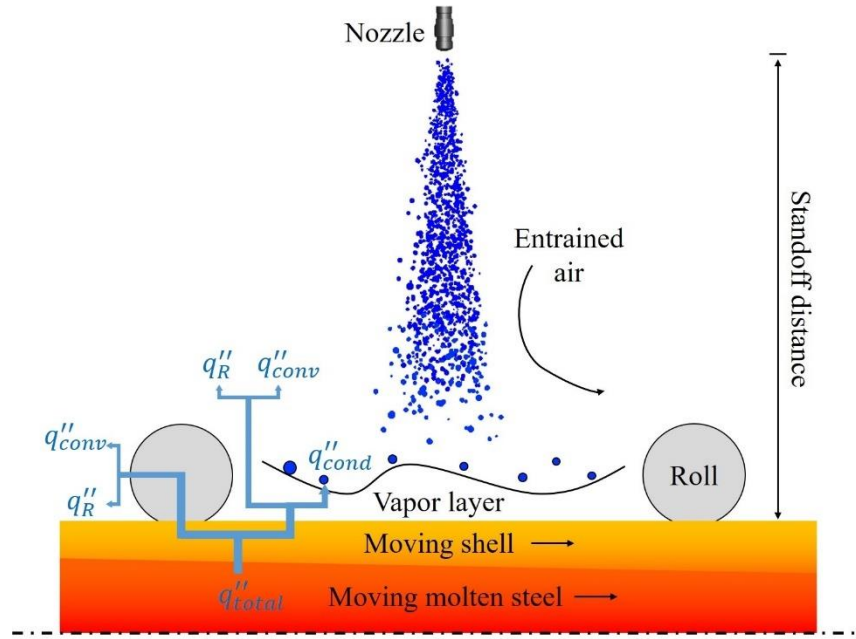
Figure 1-3. Summary of the heat transfer mechanisms in the secondary cooling region.

In the process of spray, both the single fluid hydraulic nozzle and the two-fluid air-mist nozzle have been widely adopted by the steel industry. Figure 1-4 shows two examples of these nozzles. The hydraulic nozzles have been utilized for continuous casting since the continuous casting technology emerged. There is the only kind of fluid, water in continuous casting, injected through the hydraulic nozzles as opposed to the other type. The flow passage inside the nozzle is relatively short, and the internal structure of the nozzle is also simple. The V-cut groove at the nozzle tip forces the fluid to form a thin liquid sheet upon injection. Such liquid sheet will further breakup into fine droplets during the atomization process before the spray impinges on the slab surface. This type of nozzle requires less power to operate, and the spray system is also relatively easy to install. On the contrary, the two-fluid nozzle shown in Figure 1-4 (b) requires longer fluid passage and considerable pumping power. The reason is that the two perpendicularly injected fluids, usually air and water in continuous casting, can better mix up in the long fluid passage, and the intense two-phase interaction will promote the breakup of water before the atomization process. This pre-atomization breakup will eventually lead to much finer droplets, which are beneficial to heat transfer due to the large surface-to-volume ratio, thereby higher heat transfer rate. The uniform droplet size distribution and the high transfer rate provided by the two-fluid nozzles counterbalance

the additional investment compared to that of the single-fluid nozzles. Therefore, an increasing number of continuous casting machines have been equipped with two-fluid nozzles.

(a)   (b)

Figure 1-4. (a) Lechler high-pressure flat fan series 602 [8], (b) Lechler two-fluid MasterCooler SMART [9].

Figure 1-5 illustrates the roll-contact heat transfer mechanism. Rolls in the secondary cooling region of continuous casting serve two purposes: to move the solidified shell and support the shell against the enclosed molten steel. Rolls are rotated by motors at the casting speed so that the solidified shell can be constantly withdrawn from the mold, achieving continuous production. To ensure rolls can move the solidified shell, they must be carefully aligned before production. Some steel manufacturers have already started to develop real-time alignment systems to dynamically change the roll alignment based on the casting operation conditions, such as steel grades, superheat, casting speed, etc. Nevertheless, the proper roll alignment requires sufficient contact between rolls and the solidified shell. The alignment can be measured either by the contact angle, θ_{roll}, or the contact length, L_{roll}. A 7° contact angle is recommended by Meng and Thomas [7]. 10-20% of the roll diameter [10, 11], or 20mm [12], is also considered as acceptable contact length by other researchers. Because of the contact, rolls constantly absorb heat from the moving solidified shell through heat conduction. A portion of the absorbed heat increases the temperature of rolls, and the rest dissipates into the surroundings through convection and radiation. It is also worth mentioning that because rolls rotate during the heat transfer, they experience periodical heating and cooling during operation. Rolls absorb heat at the contact surface with the solidified shell and gradually lose the heat to the surroundings while rotating until returning to the contact point. This periodical

39

thermal loading significantly affects the life span of rolls. Thus, the roll-contact heat transfer is of great interest to steel manufacturers.
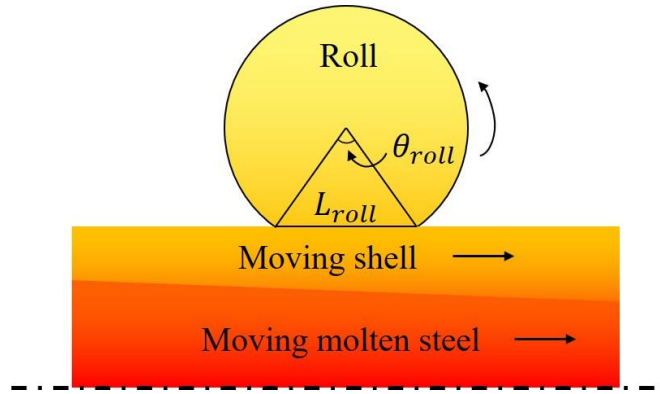
Figure 1-5. Cross-section view of the roll-contact heat transfer mechanism.

1.3   Literature review

1.3.1   Heat transfer on the steel slab surface

Rapid jet cooling of hot surfaces has become an efficient way to provide a high heat transfer rate in many industrial applications. The high cooling rate is achieved through either forced convection or the combination of forced convection and boiling by injecting liquid or gaseous flow at a certain distance against a hot surface. The jet impingement heat transfer applications include cooling of semi-solidified moving slabs in continuous casting, runout table in hot mill process, blades in gas turbines, electronic components, combustion engine walls, nuclear power plants, and many other industrial processes. The typical impinging jet cooling process consists of two distinct regions: free jet region and impingement heat transfer region. In the free jet region, cooling fluid issued from a nozzle forms a free submerged jet with an undisturbed potential core in the middle surrounded by a high-gradient shear layer, where the cooling fluid and the surrounding medium undergo extensive momentum and energy transfer. As the jet approaches the hot surface, it loses the axial velocity component at the stagnation point and turns to a wall jet that moves laterally parallel to the surface. In this region, cooling fluid absorbs heat from the hot surface while moving outward, and the boiling regime gradually develops from single-phase forced convection to nucleate boiling, transition boiling, and eventually, film boiling with the increase of wall superheat [13].

Several critical parameters affect the performance of jet impingement cooling, such as nozzle type, including the exit opening shape and the number of phases passing through, cooling fluid type and flow rate, jet orientation, surface temperature, and roughness, jet-to-surface distance, and jet-to-jet spacing [14-17]. Compared to single jet cooling, a low-temperature surface that only involves forced convection, multiple jets impinging on a high-temperature surface are much more complex due to the interactions between the adjacent jets and the phase change involved. Two unique jet-to-jet interactions were observed that do not occur in single jet applications [18]. The first is the interaction prior to jet impingement due to the expansion of shear layers laterally, forming a pair of circulations in the space between the two jets. Such phenomenon occurs predominantly in confined cooling space with closely spaced nozzles. The second is the interaction due to the collision of the wall-parallel flows after jet impingement, resulting in forming the secondary stagnation point and potentially the fountain effect [16]. While the single jet configuration has been well studied, the design and optimization of the multi-jet system for cooling high-temperature surfaces remain challenging. One example is secondary cooling in the continuous casting of steel.

In the secondary cooling region, the solid shell is subjected to significant temperature changes on its surfaces due to spray cooling. Such temperature differences can lead to complex phase transformation and residual thermal stress buildup inside the steel slab. Efficiently and uniformly heat removal without crack or deforming slabs during the secondary cooling process is of great importance, as both undercooling and overcooling significantly affect the slab quality and the smooth operation of the process [11]. The spray parameters must be carefully selected to provide sufficient and uniform heat transfer across the cooling surface because insufficient cooling will lead to breakout where molten steel breaks the thin shell and bursts out. In contrast, excess cooling will result in cracks and other defects due to significant residual thermal stresses and strains [19]. Knowledge and understandings of the jet impingement on a moving high-temperature surface (>1000 °C) and the subsequent heat transfer are essential to produce high quality and high strength steel, especial during the initial solidification stage where the shell thickness is thin and the temperature of the solidified surface is high.

Heat transfer by water spray

Flow structure of an impinging jet

Figure 1-6 illustrates the typical flow structure of an impinging jet. First, a liquid or gaseous flow is discharged from a nozzle or opening into a gaseous atmosphere. The velocity profile of the discharged flow depends on the upstream condition. The injected flow has a parabolic velocity profile for the flow issued from a circular orifice or opening. In contrast, the flow delivered from a slot opening by the kinetic energy of the flow will develop a relatively flat velocity profile. Thus, a round jet has an axisymmetric flow profile, whereas a slot jet has a two-dimensional flow profile.
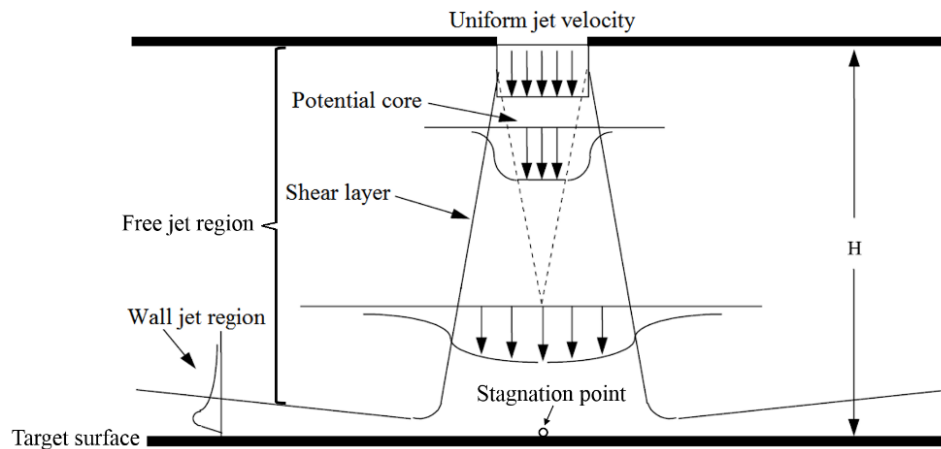
Figure 1-6. The flow regions of an impinging jet [20].

Upon injection, although the released bulk fluid disintegrates and transforms into discrete tiny droplets through the rapid atomization process, the overall flow structure is comparable to that of a continuous stream. Immediately after injection, the jet widens laterally and changes momentum with the surrounding gas through a shear layer, where the velocity gradient is the highest. As some of the surrounding gas is displaced by the jet, additional fluid is entrained in the jet due to mass conservation, increasing the total mass flow of the jet. At the core of the jet, the velocity profile of the flow is unaffected by the momentum transfer across the shear layer. However, this core region decays in the jet axial direction and can even disappear if the nozzle is placed sufficiently far away from the target surface. The velocity profile across the jet eventually flattens beyond the potential core region, resembling a Gaussian distribution [20]. Similar to the pipe flow, the Viskanta referred to the region with the potential core as the "developing zone" as opposed to the "fully developed zone" where the potential core disappears [21].

Once the jet impinges on the rigid target surface, it loses axial velocity while building up a higher static pressure and turns to wall jet flow. The impingement point is referred to as the stagnation point. The turning flow near the stagnation point experiences high normal and shear stresses, leading to variation of the local flow structure [20]. The height of the stagnation region is estimated to be 1.2 nozzle diameters for round nozzles [22], and 13% of the nozzle-to-surface height [23] for slot nozzles.

After impingement, the flow splits into several wall jets at the stagnation point. In the wall jet region, the flow moves laterally outward parallel to the target surface. The name of the wall jet implies that the turning flow from impingement behaves as if it were injected from the stagnation point. As the wall jet moves outward, the boundary layer develops within the flow. The height of the wall jet varies along the moving direction. The minimum height occurs within 0.75-3 diameters from the stagnation point [20]. After which, the wall jet entrains the surrounding flows and grows in thickness. The overall average flow velocity of the wall jet decreases as the thickness increases, but the velocity of the core region increases due to the non-slip condition at the wall and the conservation of momentum across the thickness of the wall jet. As the wall jet progresses on the wall, the average velocity of the wall jet continues to decrease until the wall jet disappears or interrupts by other flow structures.

Droplet formation from the disintegration of a jet

In the process of spray, the jet issued from the nozzle disintegrates when the surface tension forces are overcome and transforms into numerous tiny droplets. Accurate knowledge of the droplet size distribution is a prerequisite for the fundamental analysis of heat and mass transfer [24]. Lord Rayleigh identified and mathematically analyzed the aerodynamic instability that eventually leads to breakup of the jet in the late 19th century [25]. The jet instability and the two consequent breakup processes, i.e., primary breakup and secondary breakup, have been substantially investigated since then. Later Weber extended the jet instability theory to include viscous liquids [26], and Ohnesorge proposed the Ohnesorge number to characterize different jet breakup mechanisms [27]. Numerically, the Eulerian-Eulerian approach has become popular in modeling the jet formation and breakup [28- 31]. However, this approach can be time-consuming and numerically challenging

due to the strong coupling between the liquid jet and the surrounding air. In addition, the initial condition of the jet at the nozzle exit is unknown without the simulation of flow inside the nozzle in advance. It is recommended if detailed structure and distribution of droplets are required [30]. As an alternative, the Eulerian-Lagrangian approach has been adopted by many researchers when the domain of interest is located farther downstream. This approach ignores the primary and secondary breakups by defining the initial spray characteristics at the breakup length where the liquid jet has completely broken into droplets [32]. The most used model of such an approach is the Linear Instability Sheet Spray (LISA) model developed by Reitz et al. based on the Kelvin-Helmholtz stability analysis [33]. The LISA model assumes the jet as a two-dimensional viscous incompressible liquid sheet created upon exiting the nozzle, and the droplet distribution satisfies the Rosin-Rammler distribution at the breakup length. Then, droplets are treated as discrete phases and tracked simultaneously in the Lagrangian frame by solving Newton's law of motion. This model has been implemented in many spray-related applications, validated thoroughly, and has gained popularity in many spray-related industrial applications [34-36].

Droplet size and velocity distribution

Owing to the heterogeneous nature of the atomization process, droplets generated from jet disintegration vary widely in diameter. In most practical applications, droplet size ranges from a few micrometers up to a few hundred micrometers [37]. Accurate knowledge of the droplet size distribution is a prerequisite for the fundamental analysis of heat and mass transfer [24]. It is mathematically convenient to represent the droplet size distribution in a spray by a continuous function, together with an arbitrarily defined representative diameter and some measure of deviation from this mean diameter. Table 1-1 shows some of the most well-recognized representative diameters.

Table 1-1. Most well-recognized representative diameters [37].

Name	Definition
$D_{0.1}$	Drop diameter such that 10% of total droplets is in smaller diameter
$D_{0.5}$	Drop diameter such that 50% of the total liquid volume is in the smaller diameter, also known as the Mass Median Diameter (MMD)
$D_{0.632}$	Drop diameter such that 63.2% of the total liquid volume is in smaller diameter
$D_{0.9}$	Drop diameter such that 90% of the total liquid volume is in smaller diameter
$D_{0.999}$	Drop diameter such that 99.9% of the total liquid volume is in smaller diameter
D_{peak}	The peak of droplet size-frequency curve

The mean diameter is another well-known diameter. The mean diameter is convenient to work with in many calculations and mathematical derivations, but it is different from the representative diameter in nature. Mugele and Evans generalized and standardized the concept of mean diameter in 1951 [24]. Eq. (1) shows the general form of mean diameter. The sum of $a + b$ is the order of the mean diameter.

$$D_{ab} = \left[\frac{\sum N_i D_i^a}{\sum N_i D_i^b} \right]^{1/(a-b)}$$ (1)

Where N_i is the number of droplets in size range i and D_i is the middle diameter of the size range i. It is worth mentioning that no single mean diameter is superior to another, and no single universal mean diameter can completely define the droplet size distribution in any spray.

Table 1-2. Definition and applications of some well-recognized mean diameters [37, 24].

a	b	$a + b$	Name	Definition	Applications
1	0	1	Arithmetic mean	$D_{10} = \dfrac{\sum N_i D_i}{\sum N_i}$	Comparisons
2	0	2	Surface mean	$D_{20} = \sqrt{\dfrac{\sum N_i D_i^2}{\sum N_i D_i}}$	Surface area controlling
3	0	3	Volume mean	$D_{30} = \sqrt{\dfrac{\sum N_i D_i^3}{\sum N_i}}$	Volume controlling
3	2	5	Sauter mean	$D_{32} = \dfrac{\sum N_i D_i^3}{\sum N_i D_i^2}$	Mass transfer
4	3	7	De Brouckere mean	$D_{43} = \dfrac{\sum N_i D_i^4}{\sum N_i D_i^3}$	Combustion equilibrium

The continuous frequency distribution curves have more benefits over the discrete histograms in terms of representing the droplet size distribution. A frequency distribution curve can be uniquely determined by a continuous function with only a few parameters. This is convenient for smoothing the results when only a limited number of measured data is available and extrapolating droplet sizes out of the measurement range. Some of the well-known droplet size distribution functions are summarized in Table 1-3. The four-parameter log-hyperbolic equation and the Nukitama-Tanasawa equation are best known for their high accuracy and flexibility among all the size distribution functions. However, both equations have drawbacks. The four-parameter log-hyperbolic equation is very sensitive to even minor changes and could suffer from numerical stability problems [38-40]. It is only recommended if detailed information about the size variation is required throughout the spray [38]. The Nukitama-Tanasawa equation, on the other hand, requires simultaneous optimization of the four parameters [37]. It is only feasible when the multivariable regression analysis can be carried out by computer software.

Thus, relatively simple two-parameter equations are more popular among the engineering community. The most widely used simple distribution function is the Rosin-Rammler equation,

also known as the Weibull distribution [41]. The two constants in the equation are the representative diameter of some kind, X, and the spread number, q. The spread number provides the spread of droplet size about the representative diameter. An ideal spray that produces a uniform size of the droplet has a spread number of infinite. For most of the sprays, the spread number is somewhere between 1.5 to 4 [37]. Another essential feature of the Rosin-Rammler equation is that it can only be used for single-peaked size distributions, owing to the nature of its mathematical expression. Nevertheless, the Rosin-Rammler equation will continue to maintain its popularity due to its simplicity. j

Table 1-3. Well-known droplet size distribution functions [37-40].

Distribution function (parameters)	Definition
Normal $(s_n, \bar{D})$	$f(D) = \dfrac{1}{\sqrt{2\pi s_n}} \exp\left[-\dfrac{1}{2s_n^2}(D - \bar{D})^2\right]$
Log-normal $(s_g, \bar{D}_{ng})$	$f(D) = \dfrac{1}{\sqrt{2\pi D s_g}} \exp\left[-\dfrac{1}{2s_g^2}\left(InD - In\bar{D}_{ng}^2\right)^2\right]$
Four-parameter log-hyperbolic $(\alpha_{lh}, \beta_{lh}, \delta_{lh}, \xi_{lh})$	$f(D) = a_{norm} exp[-\alpha_{lh}\sqrt{\delta_{lh}^2 + (x - \xi_{lh})^2} + \beta_{lh}(x - \xi_{lh})]$
Three-parameter log-hyperbolic $(a_{3PH}, \theta_{3PH}, \mu_{3PH})$	$f(D)$ $= A_{norm} exp[-\dfrac{a_{3PH}}{a^2 cos^2\theta_{3PH} - sin^2\theta_{3PH}}$ $\times \sqrt{(a_{3PH}^2 cos^2\theta_{3PH} - sin^2\theta_{3PH}) + (x_{3PH} + \mu_0 - \mu_{3PH})^2}$ $- \dfrac{(a_{3PH}^2 + 1)sin\theta_{3PH}cos\theta_{3PH}}{a_{3PH}^2 cos^2\theta_{3PH} - sin^2\theta_{3PH}}(x_{3PH} + \mu_0 - \mu_{3PH})]$
Nukiyama-Tanasawa $(a_{NT}, b_{NT}, q_{NT}, p_{NT})$	$f(D) = a_{NT}D^{p_{NT}} \exp[-(b_{NT}D)^{q_{NT}}]$
Rosin-Rammler (X_{RR}, q_{RR})	$1 - Q = \exp\left[-\left(\dfrac{D}{X_{RR}}\right)^{q_{RR}}\right]$
Modified Rosin-Rammler (X_{RR}, q_{RR})	$1 - Q = \exp\left[-\left(\dfrac{\ln D}{\ln X_{RR}}\right)^{q_{RR}}\right]$
Upper-limit $(\delta_{upper}, a_{upper}, D_{max})$	$\dfrac{dQ}{dy_{upper}} = \delta_{upper} \exp(\dfrac{-\delta_{upper}^2 y_{upper}^2}{\sqrt{\pi}})$

Note:

- *In four-parameter log-hyperbolic function,*

$a_{norm} = \dfrac{\sqrt{\alpha_{lh}^2 - \beta_{lh}^2}}{2\alpha_{lh}\delta_{lh}K_1(\delta\sqrt{\alpha_{lh}^2 - \beta_{lh}^2})}$

- *In three-parameter log-hyperbolic function,*

$$A_{norm} = -\frac{\sqrt{a_{3PH}^2-(a_{3PH}^2+1)^2 sin^2\theta_{3PH}cos^2\theta_{3PH}}}{2a_{3PH}\sqrt{a_{3PH}^2 cos^2\theta_{3PH}-sin^2\theta_{3PH}}\,K\left(\sqrt{\frac{a_{3PH}^2-(a_{3PH}^2+1)^2 sin^2\theta_{3PH}cos^2\theta_{3PH}}{a_{3PH}^2 cos^2\theta_{3PH}-sin^2\theta_{3PH}}}\right)}$$

$$\mu_0 = -\frac{(a_{3PH}^2+1)sin\theta_{3PH}cos\theta_{3PH}}{\sqrt{\frac{a_{3PH}^2-(a_{3PH}^2+1)^2 sin^2\theta_{3PH}cos^2\theta_{3PH}}{a_{3PH}^2 cos^2\theta_{3PH}-sin^2\theta_{3PH}}}}$$

- *In the upper-limit function,*

$$y_{upper} = \ln\frac{a_{upper}D}{D_{max}-D}$$

Constants in the aforementioned size distribution functions are determined through data fitting, and several measurement techniques can be used to characterize droplet size. Table 1-4 summarizes some of the most used droplet size measurement techniques. These techniques rely on optical methods and have no influence on spray during the measurement.

Table 1-4. Droplet size measurement techniques.

Technique	Equipment	Application	Comments
Imaging			
Photography	Light Camera Computer	Coarse sprays	Suffer from errors from blurring, depth of field variations, and improper sample.
Holography			
Non-imaging			
Laser diffraction	Transmitter Receiver Computer	1.2-1800μm size range Two-fluid sprays Hydraulic sprays Flat sprays	Measure a large number of drops simultaneously. Suffer from errors from multiple scattering.
Optical array probes	Light Photo-diode array Computer	100-12400μm size range Large capacity nozzles	Only measure one individual droplet. But can also measure velocity in addition to size.
Phase Doppler Particle Analyzer	Transmitter Receiver Signal processor Computer	0.5-10000μm size range	

The optical imaging technique can provide spatial information by sampling over a finite volume, but the result is sensitive to the droplet number density and is unsuitable for dense sprays. The laser diffraction technique, however, can be used to measure dense sprays from out-of-focus images. The technique is based on measuring the scattered light intensity by the droplets as they pass through the sampling area. This techniques has several variations, including Interferometric Particle Imaging (IPI) [42, 43], Interferometric Laser Imaging for Droplet Sizing (ILIDS) [44, 45], Global Phase Doppler (GPD) [46, 47]. Optical array probes and Phase Doppler Particle Analyzer (PDPA) is also widely used, but both techniques can only provide measurement at an individual point. A large number of measurements at different spatial points are required to resolve the spatial variations in a spray. Although the measurement process is time-consuming, both techniques can also be incorporated with velocity measurement instruments to yield velocity information simultaneously.

Droplet velocity is another essential characteristic of a spray. It directly affects the subsequent impingement outcome, which then determines the droplet-wall heat transfer. There are different ways to measure droplet velocities, such as Particle Image Velocimetry (PIV) [48-50] and Laser Doppler Velocimetry (LDV) [51-53]. One advantage of the PIV technique is that it can produce a two-dimensional or even three-dimensional velocity vector field, whereas LDV only measures velocity at a point. Zhang et al. evaluated both techniques very recently [54]. They measured the droplet velocity in an air-mist spray with both techniques and concluded that the LDV technique performs much better than the PIV technique in the vicinity of the nozzle tip. To improve the accuracy and minimize the measurement efforts, they proposed a new technique, which combines both PIV and LDV. The labor-intense LDV measurement is recommended for the near nozzle tip region, while the PIV technique can further resolve the velocity field downstream.

As both droplet size and velocity are required in many measurements, a technique that can measure both parameters is desired. PDPA is one of the techniques that can provide droplet size and velocity information at the same time. The underlying principle of PDPA is based on light-scattering interferometry, and no calibration is required [55-57]. According to Husted et al., who compared the PIV and the PDPA techniques on two high-pressure water mist nozzles, both techniques have trouble achieving reliable results close to the nozzle tip where the spray is dense [58]. Further

downstream, where velocities of different sizes of the droplet are similar, PIV outperforms PDPA. Another disadvantage of PDPA is that it can only be applied to steady-state sprays, and the measurement volume must be optimized prior to the measurement. Another promising technique is the Digital in-line Holography (DIH). The DIH technique records the interference between a plane reference wave and the wave reflected from the object. The resulting hologram is digitally stored and can be reconstructed via the solution of the diffraction integral equations [59]. This technique is drawing more attention due to several advantages, including (1) droplet size and shape can be measured at its in-focus location, (2) three-dimensional velocity vector field can be obtained from two or more measurements, and (3) non-spherical droplet can also be accounted [60]. The DIH technique faces some challenges as well. For example, the results may also include out-of-focus noises, and the overlapping droplets in the field of view are difficult to separate. Guildenbecher et al. combined some of the previous solutions and proposed a hybrid method [61]. Figure 1-7 shows the impact of a single droplet on a thin film. The hybrid DIH method accurately captures the liquid crown and the secondary droplets after the impingement. The complex 3-D representation of droplet size and velocity has demonstrated the capability of the DIH technique for providing great detail for in-depth analysis.
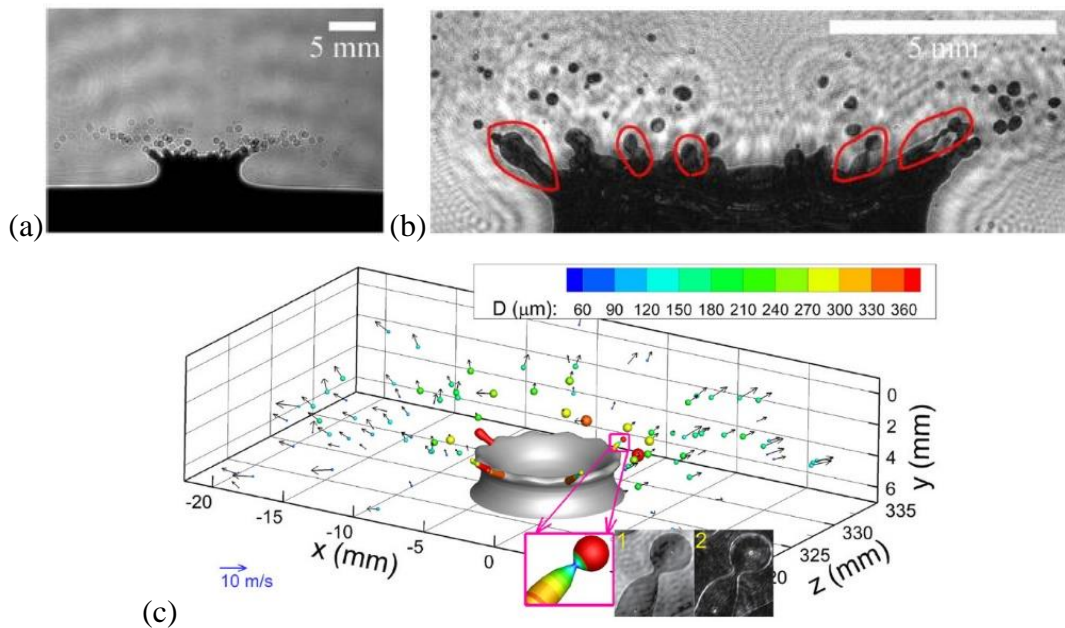
Figure 1-7. Secondary breakup of a single droplet impinging on a thin film: (a) hologram, (b) reconstructed image, and (c) 3-D representation of the crown and the secondary droplets [60].

Turbulent impinging jet and modeling

It is well-recognized that turbulence significantly promotes heat and mass transfer. Therefore, most industrial impinging jet applications involve turbulent flow downstream of the jet due to the entrainment effect or the injection device before the jet forms. The behavior of an impinging jet can be characterized by Reynolds number, in which the characteristic length can be evaluated by the exit diameter of a round orifice or twice of the orifice width of a slot injector [20]. The transition of the flow regime occurs at 1000<Re<3000 [21]. At Re>3000, the flow is believed to be fully turbulent. For a typical single-fluid flat-fan nozzle with a spray angle of 90°, the jet enters the fully turbulent state when the exit velocity is greater than:

$$|\vec{u}_{exit}| = \frac{\text{Re}\mu_w}{\rho_w 2w_{noz}} = \frac{3000 \times 100.2 \times 10^{-5}}{998.2 \times 2 \times 1.9 \times 10^{-3}} = 0.792 m/s \qquad (2)$$

Where water material properties are evaluated at room temperature.

The minimum velocity shown in Eq. (2) is equivalent to a spray flow rate of 0.457L/min, which is comparable to, if not lower than, the lowest flow rate that is typically used in the secondary cooling process. Thus, the prediction of turbulence has been one of the significant challenges for modeling the impinging jet heat and mass transfer process. Comprehensive reviews on the numerical flow and heat transfer under impinging jets can be found elsewhere [62-64].

The direct numerical simulation (DNS) method is the most accurate numerical method in which the Navier-Stokes equations are numerically solved without any additional turbulence model. The whole range of spatial and temporal scales of the turbulence is resolved in each control volume. As a result, the length scale of the control volume must be smaller than the turbulent length scale, which is in the microscopic scale. Consequently, the number of the total control volume and the computational cost of DNS is exceptionally high. For high Reynolds number applications such as impinging jets during industrial processes, it is impractical to apply this method due to the limitation of the computational resources. However, this method has been served as a valuable tool in fundamental research for model development and model validation. A more practical method to solve the Navier-Stokes equations for industrial applications is the Large Eddy Simulation

(LES), in which small-scale information is removed from the numerical simulation by filtering the conservation equations. The effect of the removed small-scale turbulent eddies is modeled through sub-grid scale models. Successful predictions for impinging jets using the LES method can be found elsewhere [65-68]. However, similar to the DNS method, the LES method also requires high spatial and temporal resolutions to capture the formation and propagation of turbulent eddies.

In comparison, two-equation turbulence models such as the standard k-ε model [69] have gained popularity because of simplicity and lower computational cost. However, the k-ε model was derived based on the assumption that the flow is fully turbulent. Thus, it gives relatively accurate predictions in the free-jet region where Reynolds number is high, but it fails to predict the stagnation location and the wall jet flow, where the viscous effect is comparable to the turbulent effect [20, 70]. Variations of the standard k-ε model, such as the renormalization group (RNG) k-ε model [71] and the realizable k-ε model [72] have been derived to remedy this situation. The RNG k-ε model incorporates an additional term in the ε equation to improve the accuracy for predicting swirling flows and low-Reynolds number flows, whereas the realizable k-ε model contains the modified ε equation, which was derived from an exact equation for the transport of the mean-square vorticity fluctuation. Both the RNG k-ε model and the realizable k-ε model have shown substantial improvements over the standard k-ε model in situations where the swirling flow occurs. Yet, the RNG k-ε model was found to overpredict the spreading rate for jets [73, 74]. Similarly, the standard k-ω model derived by Wilcox [74] to account for low-Reynolds number effects, compressibility, and shear flow spreading was found to overpredict the heat transfer by up to 18% [75]. Another drawback of the standard k-ω model is its sensitivity to the upstream condition. Menter blended the standard k-ω model with the standard k-ε model through a blending function and derived one of the most accurate hybrid turbulence models [76]. The shear stress transport (SST) k-ω model developed by Menter transforms to the standard k-ε model in the far-field and returns to the standard k-ω model in the near-wall region where turbulent shear stress becomes more important.

Zuckerman and Lior summarized the performance of different turbulent models regarding the prediction of Nu number and the correspondingly computational cost. They concluded that all the k-ε model, the k-ω model, the algebraic stress model (ASM), and the Reynolds stress model (RSM) give relatively large errors compared to the experimental measurements. When considering both

the accuracy and the computational cost, the SST k-ω model and the v^2-f model are recommended [20]. Similar conclusions can also be found in the study conducted by Hofmann et al. [63], who assessed 13 widely used RANS turbulence models for predicting the flow structure and heat transfer of impinging jets. The SST k-ω model is the only model that can accurately predict the laminar-turbulent transition, while other models are only recommended for predicting heat transfer in the turbulent wall jet region.

Droplet breakup and collision

The mechanisms of droplet breakup and collision are essential to numerical simulations. Strictly speaking, droplet breakup and collision mechanisms are only necessary when the simulation takes the Lagrangian approach. In this approach, droplets are treated as discrete points traveling through a continuous gas/liquid phase. Owing to the nature of the point mass assumption, droplets in numerical simulations will not deform and break up or collide and coalesce as those will in the physical world. Thus, breakup and collision models are prerequisites for simulations involved with droplets/bubbles. These models usually define one or a few critical conditions, and such conditions are repeatedly tested during numerical iterations. Once the conditions are satisfied, the program updates the diameter, velocity, and the number of droplet/bubble accordingly. In other words, the Lagrangian approach neglects the breakup/coalescence process and only considers the outcomes from such a process. This underlines the importance of the breakup/collision models, as they significantly determine the accuracy of the numerical simulations.

It should be noted that there appears to be no general definition of which effect dominants the spray process between breakup and collision, as both processes can generate smaller droplets. Historically, extensive studies have been devoted to the droplet breakup process. One reason for such a trend is that most heat and mass transfer processes are influenced by the vaporization rate, which is strongly dependent on the liquid breakup process. The surface-to-volume ratio increases after the breakup, and the high surface-to-volume ratio significantly promotes the heat and mass transfer process.

Indeed, the investigation of droplet breakup dates back to the beginning of the twentieth century. Lane [77] and Hinze [78] suggested various mechanisms of breakup, and the outcomes of breakup

are also different. Researches on droplet breakup in the air can be divided into two categories: steady acceleration and sudden exposure. Large free-falling droplets in still air are the best example of steady acceleration. In this situation, the droplet gradually elongates in the direction that is perpendicular to the falling direction, and at a critical velocity, it is blown out into a form of a hollow bag attached to a circular rim [37, 77]. The rim, which contains more than 70% of the total mass, breaks up into several larger droplets. In the second scenario where a droplet suddenly exposes to an airstream, which usually blows in the transverse direction with respect to the moving direction of the droplet, the droplet deforms into a saucer shape and then into a thin sheet, which further breaks into finer droplets [37]. Although the exact mechanism of the secondary atomization is not well understood, it is believed that the phenomena can be characterized by the Weber number and the Ohnesorge number [79]:

$$\text{We} = \frac{\rho_a u_d^2 d_d}{\sigma_d} \tag{3}$$

$$\text{Oh} = \frac{\mu_d}{\sqrt{\rho_d \sigma_{a-d} d_d}} \tag{4}$$

Based on the two critical numbers, sometimes Weber number alone, researchers have identified several breakup regimes. Reitz et al. have categorized the droplet breakup process into three regimes: (1) bag breakup regime [80], (2) shear or boundary-layer stripping breakup [81], and (3) catastrophic breakup [82]. However, they also cast considerable doubt on the validity of the shear or boundary-layer stripping breakup theories [83]. The previous two theories attribute the breakup to either a boundary layer separation driven by the gas shear at the liquid interface or the formation and breaking of capillary surface waves. Both theories imply that droplet Reynolds number should play an essential role in determining the rate of droplet breakup. Reitz and colleagues experimentally proved that droplet breakup in this regime depends primarily on the droplet Weber number instead of the droplet Reynolds number. They also suggested a term for this regime, which is "sheet thinning and deformation" [83]. Unfortunately, no critical values of Weber number are given for each regime. Krzeczkowski [84] suggested the following four breakup regimes:

Table 1-5. Droplet breakup regime and the corresponding Weber number [84].

Breakup regime	Weber number
Bag breakup	We = 13.5
Bag-jet breakup	We = 36
Transition breakup	We = 48.1
Sheer-stripping breakup	We = 162

Pilch and Erdman [85] reviewed data on acceleration-induced fragmentation of liquid droplet from the literature and suggested the following five distinct breakup regimes:

Table 1-6. Droplet breakup regime and the corresponding Weber number [85].

Breakup regime	Weber number	Illustration
Vibrational breakup	We ≤ 12	
Bag breakup	12 < We ≤ 50	
Bag-stamen breakup	50 < We ≤ 100	
Sheet stripping breakup	100 < We ≤ 350	
Catastrophic breakup	We > 350	

Pilch and Erdman also correlated the total breakup time with Weber number from the literature. The total breakup time defines when the droplet and all its shattered child droplets undergo no further breakup. The correlations are summarized in Table 1-7.

Table 1-7. Breakup time and the corresponding Weber number by Pilch and Erdman [85].

Breakup time	Weber number
$t_{bu} = 6(\text{We} - 12)^{-0.25}$	$12 \leq \text{We} \leq 18$
$t_{bu} = 2.45(\text{We} - 12)^{0.25}$	$18 \leq \text{We} \leq 45$
$t_{bu} = 14.1(\text{We} - 12)^{0.25}$	$45 \leq \text{We} \leq 351$
$t_{bu} = 0.766(\text{We} - 12)^{0.25}$	$351 \leq \text{We} \leq 2670$
$t_{bu} = 5.5$	$\text{We} \geq 2670$

Hsiang and Faeth [79] experimentally study the droplet deformation properties induced by both shock wave and steady disturbances and extended their previous work [86, 87] to help resolve issues related to the breakup by general disturbances. They compiled their measurements with data reported by literature and created a breakup regime map, as shown in Figure 1-16. The regime map shows that the deformation and breakup are functions of the Weber number and the Ohnesorge number. The map is in excellent agreement with the regimes identified by Hinze [78] and Krzeczkowski [84]. One unique feature of this map is the transitions to the non-oscillatory and oscillatory deformation regimes. These transitions were not reported before, but they are essential as they define the onset of the bag breakup behavior. Figure 1-8 also suggests that the Weber number remains constant for the small Ohnesorge number (<0.1), and it progressively increases with the increase of the Ohnesorge number (0.1-10). However, it remains an open question whether or not a droplet still undergoes deformation and breakup at a large Ohnesorge number (>1000).
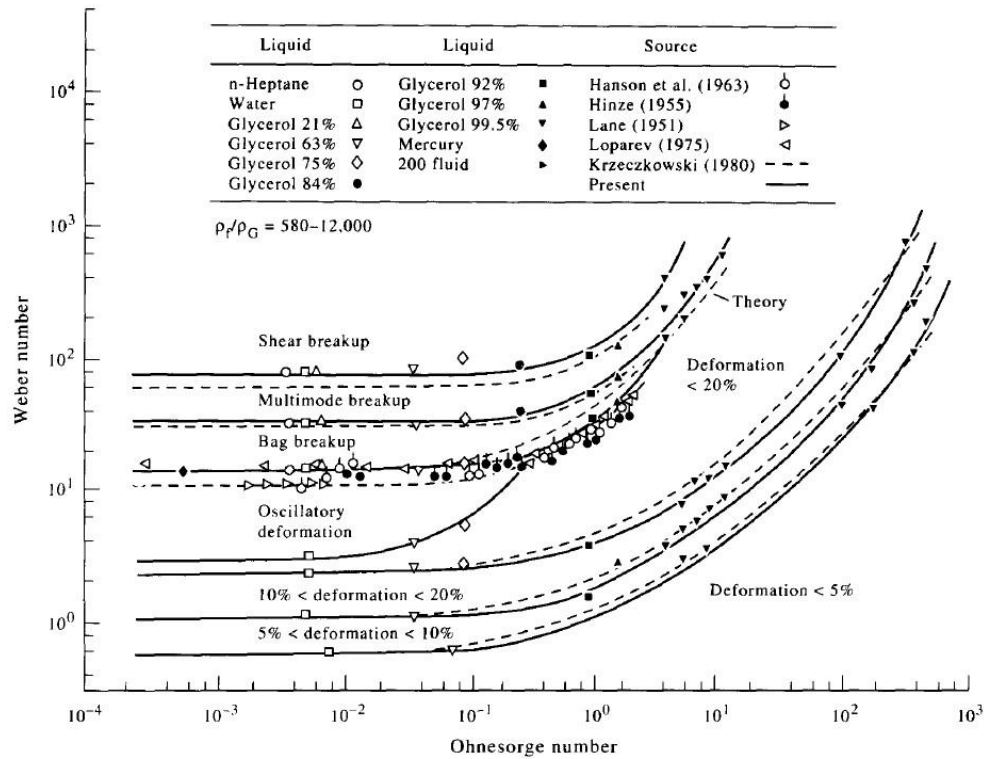
Figure 1-8. Droplet deformation and breakup regime map by Hsiang and Faeth [79].

Wierzba [88] examined previous research on droplet breakup and found discrepancies in critical Weber numbers. Previous research defines the Weber number as the Weber number corresponds to the beginning of the bag breakup. The result is that the critical Weber number from the literature is scattered over a wide range, between 2.2 and 99.6, as shown in Table 1-8. Wierzba provided three reasons for such discrepancies. First, the experimental method is not consistent throughout the literature. There are at least six different methods in Table 1-8. Besides, the experiment conditions also vary. The critical Weber numbers tend to be larger in steady acceleration experiments than from the sudden exposure experiments. Second, it is found that these experiments used different liquids, and the effect of liquid viscosity was not taken into consideration. The last reason is the droplet size. The initial droplet size also varies over a broad range from 300μm to 5600μm. To avoid any confusion in the future, the author suggested a different definition of the critical Weber number, which corresponds to completing the bag breakup. With the new definition, the author conducted a small horizontal wind tunnel test and found the critical Weber number is between 13.7 and 14.07 [88].

Table 1-8. Critical Weber number from previous literature by Wierzba [88].

Reference	Critical Weber number	Experiment
Lenard (1904)	We = 5.8	Freefall
Merrington and Richardson (1947)	15.4 ≤ We ≤ 29.8	Freefall
Lane (1951)	We = 10.8	Vertical wind tunnels
Volynskii (1948)	11 ≤ We ≤ 15.8	Horizontal wind tunnels
Buhman (1954)	2.2 ≤ We ≤ 3.6	Horizontal wind tunnels
Hinze (1955)	We = 13	Horizontal wind tunnels
Krzeczkowski (1980)	11 ≤ We ≤ 38	Horizontal wind tunnels
Nichiporenko et al. (1982)	10.9 ≤ We ≤ 17.7	Horizontal wind tunnels
Wierzba (1985)	We = 14	Horizontal wind tunnels
Isshiki (1959)	9.26 ≤ We ≤ 29	Suction orifices
Haas (1964)	We = 11.2	Suction orifices
Naida et al. (1973)	8.4 ≤ We ≤ 12.1	Suction orifices
Yoshida (1985)	10 ≤ We ≤ 48	Suction orifices
Hanson et al. (1963)	7.2 ≤ We ≤ 47.6	Horizontal shock tubes
Simpkins (1971)	We = 13	Horizontal shock tubes
Gelfand et al. (1972)	12 ≤ We ≤ 16	Horizontal shock tubes
Simpkins and Bales (1972)	We = 14	Horizontal shock tubes
Gelfand et al. (1973)	10 ≤ We ≤ 50	Horizontal shock tubes
Gelfand et al. (1974)	We = 10	Horizontal shock tubes
Reichman and Temkin (1974)	We = 7	Horizontal shock tubes
Korsunov and Tishin (1971)	15 ≤ We ≤ 32	Convergent nozzles
Lopariev (1975)	14.6 ≤ We ≤ 99.6	Venturi scrubbers
Caveny and Gany (1979)	20 ≤ We ≤ 30	Convergent nozzles
Borisov et al. (1986)	40 ≤ We ≤ 60	Horizontal shock tubes

Omidvar and Khaleghi [89] utilized the analytical approach to determine the critical Weber number in turbulent flows. Their analysis is based on the Taylor Analogy Breakup (TAB) model, and the authors also proposed a hybrid time scale to combine the turbulent time scale and the

breakup time scale. The results indicate that the critical Weber number decreases from 12 as predicted by Pilch and Erdman [85] to 2 with the increase of turbulent intensity.

Other than the critical Weber number, the drag coefficient is also subject to change during the breakup process. As soon as the droplet deforms by its surrounding aerodynamic pressures, the pressure distribution around the droplet also changes, as shown in Figure 1-9. Either a new state of equilibrium between the aerodynamic pressures and the internal forces due to surface tension and viscosity is established after the change, or further deformation follows and eventually leads to the breakup.
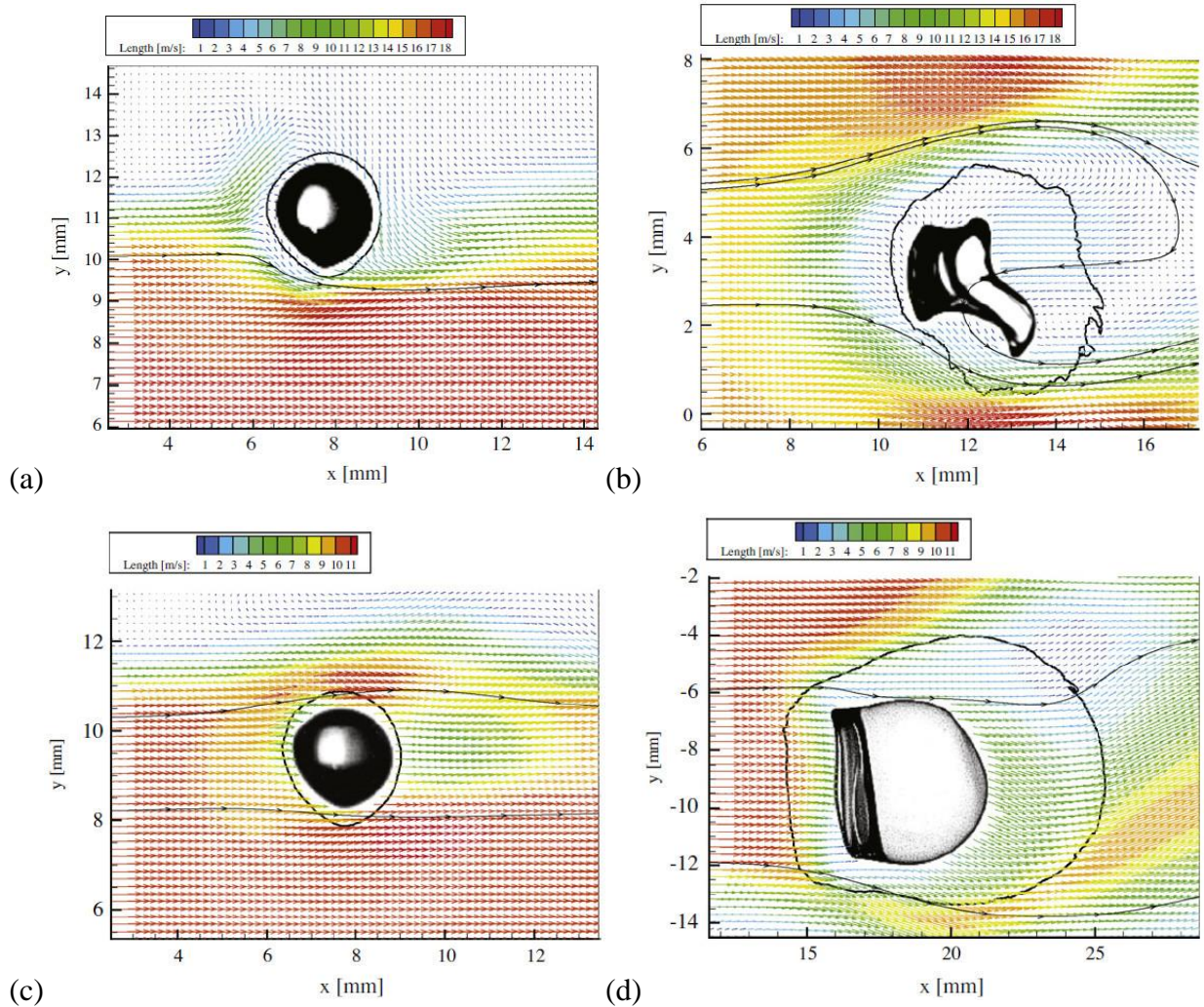
Figure 1-9. Instantaneous average velocity fields: (a) $t = 0s$ in sheet-thinning breakup, (b) $t = 15ms$ in sheet-thinning breakup, (c) $t = 0s$ in bag breakup, and (d) $t = 11ms$ in bag breakup [90].

Liu et al. proposed the Dynamic Drag and Breakup (DDB) model to incorporate the effect of droplet deformation into the drag law of a rigid sphere [91]. The drag coefficient for a rigid spherical object is defined as follows:

$$C_{D,sphere} = \begin{cases} \dfrac{24}{Re_d}(1 + \dfrac{1}{6}Re_d^{2/3}) & Re_d \leq 1000 \\ 0.424 & Re_d > 1000 \end{cases} \tag{5}$$

Liu et al. assume the drop drag coefficient linearly varies between that of a sphere and a disk, and it can be related to the magnitude of the droplet deformation with:

$$C_D = C_{D,sphere}(1 + 2.632y_{dis}) \tag{6}$$

Where y_{dis} is the droplet distortion, a value of 0 corresponds to no distortion, and 1 represents the maximum distortion.

Previous experimental observations have led to the development of various analytical models. The most famous and classic one is the Taylor Analogy Breakup (TAB) model. The TAB model is based upon Taylor's analogy between an oscillating and distorting droplet and a spring-mass system, as illustrated in Figure 1-10. With this analogy, the forces acting upon the droplet can be converted to internal and external forces on the spring-mass system, as summarized in Table 1-9. The distortion and oscillation of the droplet can be obtained at any given time by solving the differential equation for a damped and forced oscillator. The size of the child droplets after the breakup is determined by energy conservation, whereas the velocity direction of the child droplets is set to be perpendicular to that of the parent droplet. Detailed derivation can be found elsewhere [92, 93]. The TAB model applies to many engineering sprays where both spray velocity and the Weber number are relatively low.
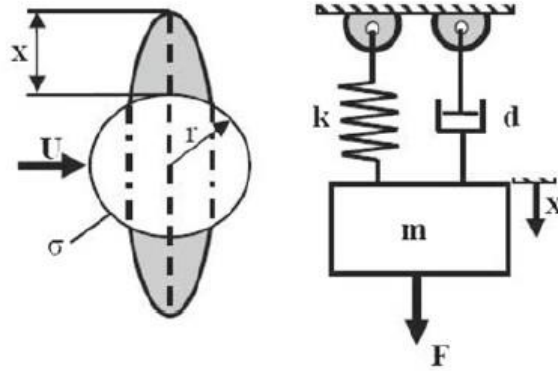
Figure 1-10. Schematic illustration of Taylor's analogy breakup model [89].

Table 1-9. Analogy of forces in the TAB model.

Oscillating and distorting droplet	Spring mass system
Surface tension force	Restoring force
Drag force	External force
Viscosity force	Damping force

For applications where the Weber number is greater than 100, the WAVE model is more applicable. The WAVE model was proposed by Reitz and Bracco [94, 95], and it is recommended for high-speed sprays. Reitz considers the atomization process as the injection of a series of "blobs" with a size equal to the nozzle exit diameter. The breakup time and the resulting droplet size are related to the fast-growing Kelvin-Helmholtz instability derived from the jet stability analysis. This method can successfully predict breakup in various regimes and has been extensively applied to fuel injection analysis in engines [94, 96]. Other breakup models are also available for numerical simulations. These models include Kelvin-Helmholtz Rayleigh-Taylor (KHRT) model [97, 98], the Stochastic Secondary Droplet (SSD) model [99], the Enhanced Taylor Analogy Breakup (ETAB) model [100], the Droplet Deformation Breakup model [101], and the Unified Spray Breakup (USB) model [102]. Detailed information can be found elsewhere [103].

Droplet collision and coalescence also received considerable attention over the past decades. Many experiments have been conducted to address the dynamics and outcomes of droplet collision [104-115]. The primary objectives of the experimental studies are to identify the collision outcomes and to define characteristic parameters which distinguish between different collision outcomes. It

should be noted that most of the experiments and their corresponding analytical models are based on binary droplet systems. In general, there are four possible outcomes from the collision of two droplets: bouncing, coalescence, reflexive separation, and stretching separation, as illustrated in Figure 1-11.

Bouncing	Coalescence	Reflexive separation	Stretching separation
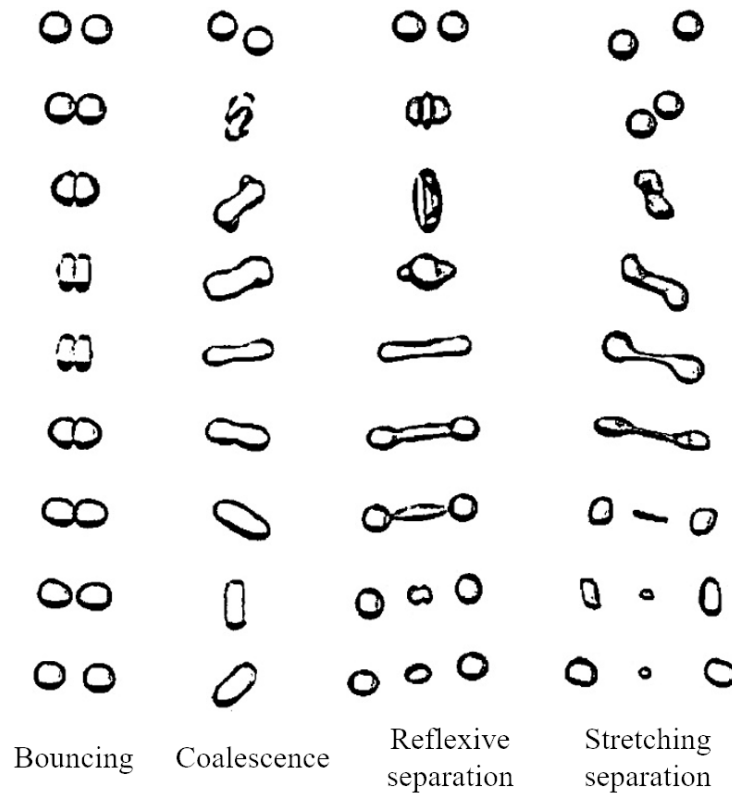
Figure 1-11. Illustration of binary droplet collision outcomes [116].

In the bouncing collision, two droplets collide and deform without merging. The intervening gas film prevents the contact of droplet surfaces. In the coalescence collision, two droplets permanently combine into one single droplet. And the separation collisions are when two droplets temporarily combine into one single droplet and later separate into a string or several smaller droplets [117]. Ashgriz and Poo experimentally documented the possible collision outcomes of two water droplets in low Weber numbers (1-100), as shown in Figure 1-12. Their experimental study proves that the Reynolds number plays a minor role in determining the outcomes of collision. Instead, the Weber number and the impact parameter govern the collision process. From the observations, Ashgriz and Poo concluded that the onset of the reflexive separation occurs. The

kinetic energy is larger than 75% of the surface energy, and the stretching separation is the result of the competition between the kinetic energy and the surface energy.
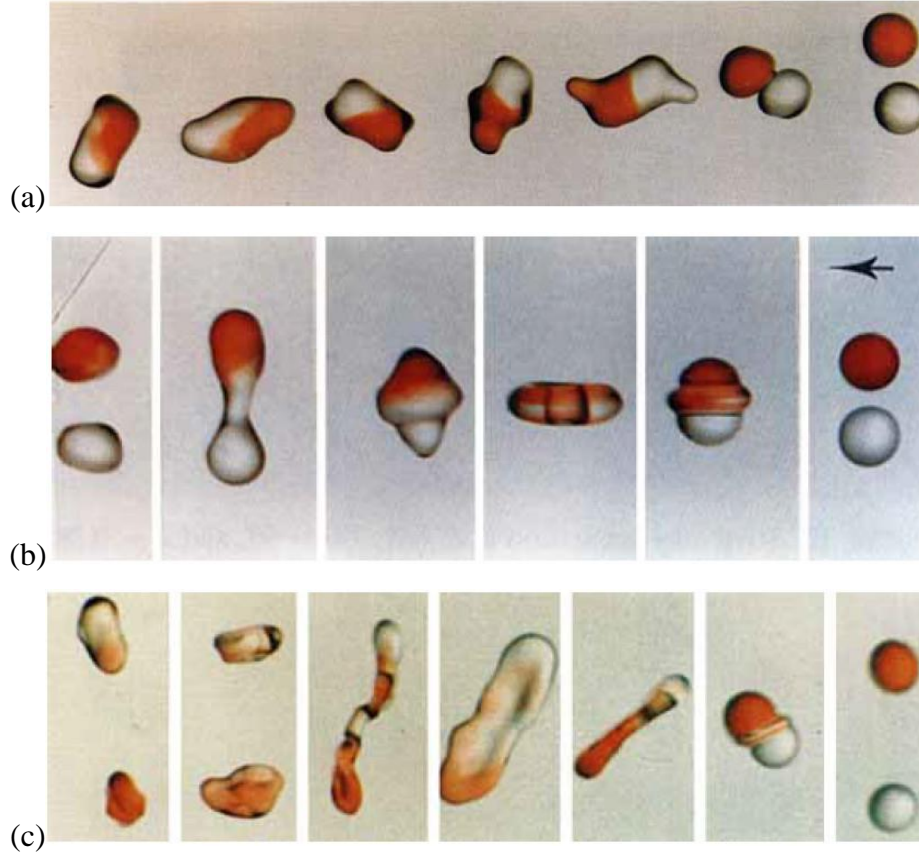
Figure 1-12. Photographic proof of collision outcomes by Ashgriz and Poo: (a) coalescence, (b) reflexive separation, and (c) stretching separation [117].

The dominant effect of the two governing parameters, i.e., the Weber number and the impact parameter, has also been confirmed by other researchers. The Weber number, also referred to as the collision Weber number, is defined as follows:

$$We_{coll} = \frac{\rho_d (u_1 - u_2)^2 (r_1 + r_2)}{\sigma_d} \tag{7}$$

The impact parameter, on the other hand, has two different definitions. The first definition is proposed by Ashgriz and Poo and is schematically illustrated in Figure 1-13. The impact parameter showing in Eq. (8) represents the ratio of the distance from the center of one droplet to the relative

velocity vector placed on the center of the other droplet [117]. By definition, the collision between the two droplets is the head-on collision when $B_{coll} = 0$ and the two droplets barely graze each other when $B_{coll} = 1$.

$$B_{coll} = \frac{2b_{coll}}{d_1 + d_2} \qquad (8)$$
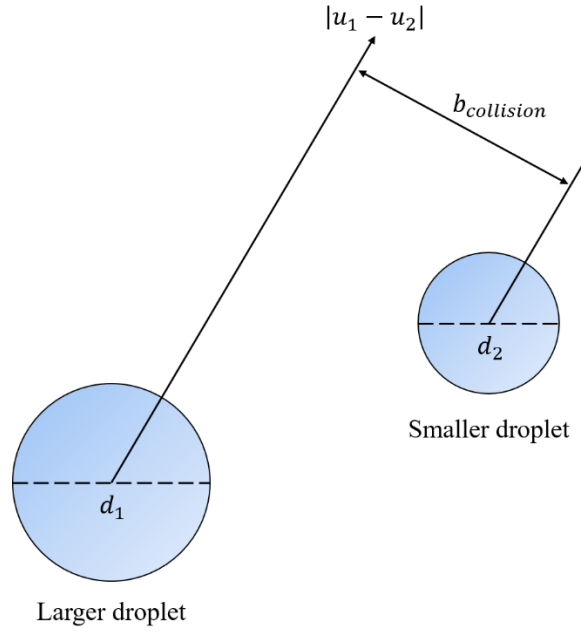
Figure 1-13. Geometric definition of the impact parameter.

The second definition is based on O'Rourke's probability collision theory [118]. O'Rourke assumes the collision between droplets is a random event. Instead of checking whether or not the two droplets are within a collision volume, which is centered at the larger droplet with the radius of $r_1 + r_2$, the method computes the possibility of the smaller droplet being within the collision volume. Therefore, the distance, b_{coll}, in Eq. (8) is modified as follows:

$$b_{coll} = (r_1 + r_2)\sqrt{\gamma} \qquad (9)$$

Where γ is a random number between 0 and 1, suggesting the collision is a stochastic process.

Figure 1-14 shows the collision regime maps as a function of the impact parameter and the collision Weber number. The O'Rourke model is most applicable for low-Weber-number collisions where bouncing and coalescence are the most likely outcomes. The Ashgriz-Poo model predicts somewhat intense collision between two droplets, as droplets are more likely to undergo separation collisions. It is worth mentioning that no one model is superior to the other. Both models have been applied to various applications and generated reasonable results [94, 116].
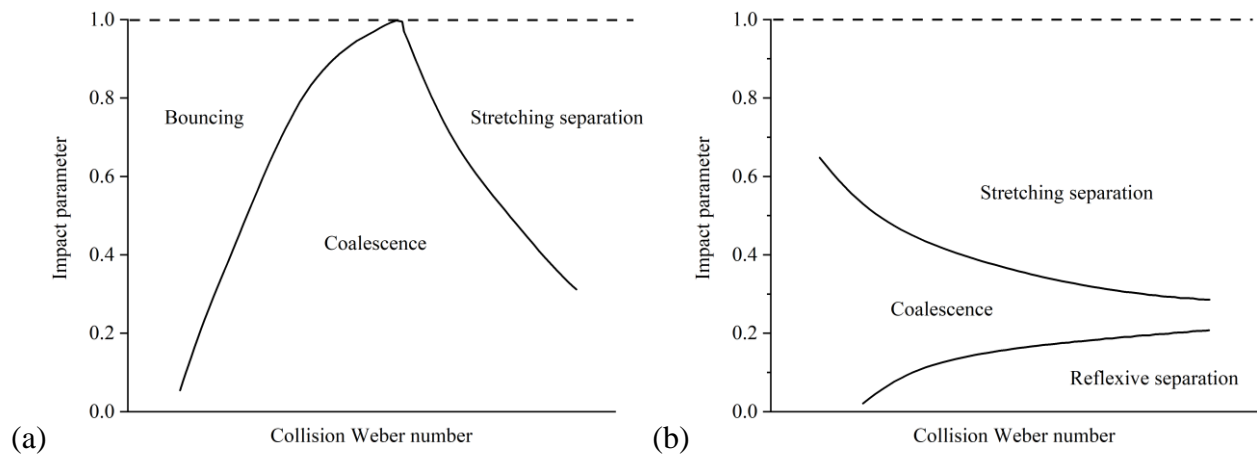
Figure 1-14. Collision regime maps: (a) O'Rourke [118], and (b) Ashgriz and Poo [117].

Droplet-wall impingement heat transfer

Once droplets impinge on the rigid slab surface, the possible outcomes of the impingement include deposit, reflection, spread, splashing, breakup, and many others, depending on the surface properties such as wettability and roughness and the Weber number of the droplet prior to the impingement. Rioboo et al. have summarized six possible outcomes when a droplet impinges on drywall [119], as shown in Figure 1-15. In the deposition scenario, the droplet deforms after impingement and stays on the surface without rebound or breakup. As the droplet, initial velocity increases in the prompt splash, the spreading droplet ejects smaller droplets outward from the contact region with the surface. Under similar conditions but with smaller surface tension, a corona is observed upon impingement, and it eventually breaks into smaller droplets from the spreading lamella. In the receding breakup scenario where the surface is non-wettable due to the increased advancing and receding angles, the receding motion of the lamella is sufficiently low, and the shrinking lamella is left on the surface until it breaks into smaller droplets. Suppose the surface

and the remaining kinetic energy in the spreading lamella is sufficiently high. In that case, the kinetic energy will squeeze the liquid upward and eject one or a few droplets at the top of the rebound liquid, as shown in the partial rebound scenario, or the entire liquid completely rebounds from the surface if the kinetic energy further increases. The desired outcome of an impingement dramatically varies in different applications. In internal combustion engines, droplets are expected to rebound from the engine wall to ensure minimal stick and complete evaporation, whereas secondary cooling droplets should remain in contact with the slab surface to promote heat transfer.

	Deposition
	Prompt splash
	Corona splash
	Receding breakup
	Partial rebound
	Complete rebound
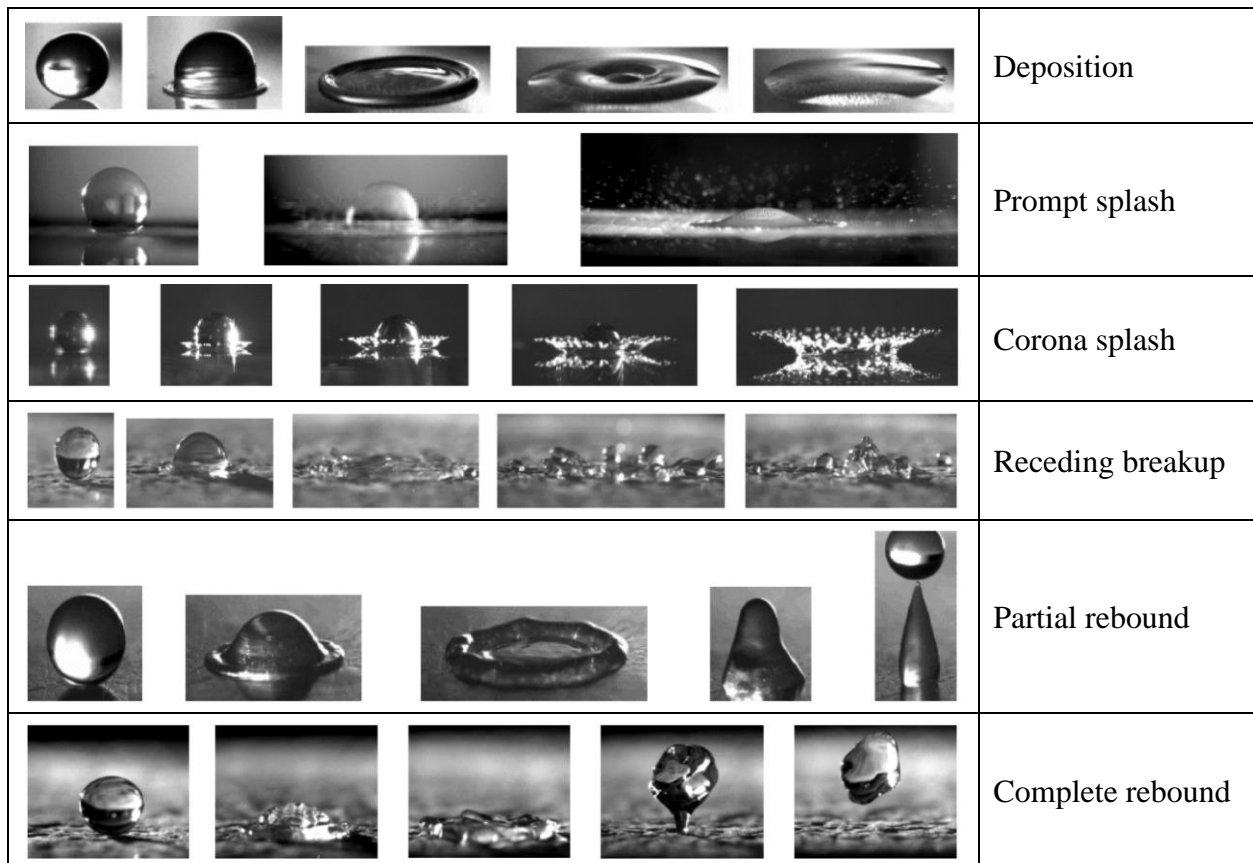
Figure 1-15. Possible outcomes of a droplet impinging on a dry surface (experiment conducted by Rioboo et al. [119], image reproduced based on the review of Yarin [120]).

Researchers have attempted to summarize the possible impingement outcomes of a droplet in impingement maps, which only depend on surface temperature and the impingement Weber number [36, 121-127]. The significant challenges of developing such impingement maps are classifying the impingement regimes and identifying each regime's criteria. For example, Figure 1-16 compares the regime map developed by Grover and Assanis [124], developed by Bai and

Gosman [125]. Grover and Assanis identified three impingement regimes which are stick, rebound, and splash. The stick and rebound regimes are distinguished at the boiling temperature, while the splash regime is in the upper region of the map and is bounded by a critical Weber number, reflecting the minimum inertia to initiate the breakup, as shown in Figure 1-16 (a). In contrast, Bai and Gosman further refined the regime map and identified several breakup regimes, as shown in Figure 1-16 (b). Bai and Gosman acknowledged the difference between the wetted ($T_{sur} < T_{PA}$) and non-wetted surface ($T_{sur} > T_{LF}$), as well as the transition region in between. At certain surface temperatures, the impingement outcome is further divided into several sub-regimes according to the critical Weber numbers, which vary in different applications and are still an active area of research [125,129-136]. But it is also evident that each impingement regime map and its transition criteria between regimes are not applicable for every operating condition. Any impingement regime map applied in the numerical model must be carefully chosen and calibrated to predict realistic outcomes. The reason is that some of the existing maps are restricted to the impact of a single droplet or a handful of droplets onto a pre-defined drywall or wetted wall [128].
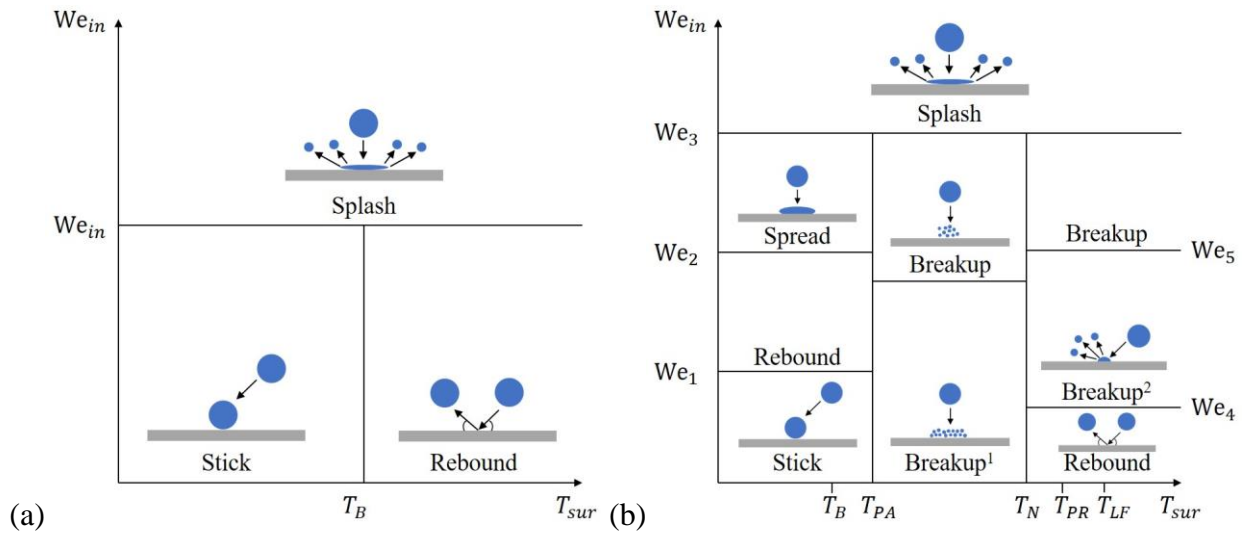
Figure 1-16. Comparison of droplet-wall impingement regime maps developed by: (a) Grover and Assanis [124] and (b) Bai and Gosman [125] (images reproduced based on the work of Mahulkar et al. [128] and Lee and Ryu [129]. Breakup[1] represents the boiling induced breakup, and Breakup[2] stands for the breakup associated with rebound.).

The numerical droplet-wall impingement models can be categorized into two groups: the Eulerian-based Volume-Of-Fraction (VOF) model and the Lagrangian-based Discrete Phase Model (DPM).

The VOF model is most useful when detailed droplet-wall interactions, including the impingement outcome, especially under the wetted surface condition and the droplet morphology during the impingement process, are desired. The key to successful modeling is to correctly predict both the internal and external forces governing the impingement process. The principle forces include inertial, surface tension, viscous force, and adhesion [128]. Comprehensive reviews on droplet-wall modeling can be found elsewhere [120, 129]. In addition, the VOF model can also be used to develop more advanced impingement maps. Mahulkar et al. reported a numerical study on developing impingement regime maps for single-component and multi-component heavy hydrocarbon droplets [128]. The VOF model was coupled with the geo-reconstruct scheme in their research work, and the conservation equations were solved in high-resolution meshes to obtain a sharp liquid-vapor interface. Their simulations have revealed two new types of splash regimes that were never reported before. Other improvements to the impingement maps were also made based on their research. However, the VOF based simulations are somewhat limited by their relatively high computational costs and have been mainly used for the scenario where only one or a few droplets present. On the other hand, the DPM-based simulations are more suitable for studying the impingement behaviors by dense sprays. The saved computational resources for modeling the droplet deformation can be devoted to the simulation of much more critical phenomena such as droplet-droplet interaction, droplet reflection, and droplet-wall heat transfer. For instance, Naber and Reitz developed the well-known wall-jet model based on the DPM method for internal combustion engine applications [36]. Although the model only includes three basic impingement regimes: stick, reflect, and wall jet, it has been rigorously validated against various studies [122, 123].

Another essential aspect of droplet impingement is heat transfer. The evaluation of the heat flux between droplets and the hot surface is of great interest to both academia and industry. Experimentally, the heat flux through the surface can be measured through either steady-state or transient methods [137]. The sample is heated up to the target temperature in the steady-state method and maintained at that temperature while cooling by the liquid. The calculations of the wall heat flux involved are straightforward, but multiple experiments must measure the heat flux at different temperatures. On the other hand, in the transient method, only one experiment is necessary to obtain the cooling curve for a specific operating condition. Once the sample is heated

up to the target temperature, the heating source is removed, and liquid spray is applied to cool down the sample to the desired temperature. The wall heat flux is computed from the embedded thermocouples using the inversed heat conduction method. This method is relatively complex, but it is closer to the industrial conditions and has been used extensively for most research studies [138, 139].

In the meantime, the exact heat transfer mechanisms for the drop-wall impingement heat transfer process are still not fully understood. Many researchers assume that once a droplet reaches the vicinity of the hot surface, a thin vapor film immediately forms above the surface, and heat must go through the vapor film from the surface to the droplet [140, 141]. However, this kind of theory tends to underestimate the intensity of heat transfer. Other researchers consider an extra contact-spread process before vapor film forms due to boiling. This assumption suggests that droplet deforms upon impingement and contact with the surface for a short period of time, during which the droplet absorbs heat from the surface [142]. This model was approved to match experimental results satisfactorily and extended from a single droplet to the whole spray [137]. However, only limited numerical models for the impingement heat and mass transfer between droplets and high-temperature surfaces have been reported, mainly owing to the complex phenomena involved. Further advances in the drop-wall impingement heat transfer will require the development of new experimental techniques to reveal the fundamental mechanisms of this process and the more efficient and comprehensive numerical models to optimize spray cooling in industrial applications.

Leidenfrost effect

In the spray cooling process, the desire to obtain high-strength steel with uniform material properties is requiring increased control over heat removal rates. One of the challenges that inhibit rapid uniform spray cooling during continuous casting is the Leidenfrost effect. Figure 1-17 shows the famous Nukiyama boiling curve. The curve illustrates that the amount of heat transferred from the hot solid surface to the liquid droplet is highly dependent on the wall superheat, which is the difference between the wall temperature and the saturation temperature of the liquid droplet. The curve also exhibits four distinct heat transfer regimes, i.e., single-phase convection (A-B), nucleate boiling (B-C), transition boiling (C-D), and film boiling (D-E). In the single-phase convection region, when the temperature excess is still low, heat from the solid surface is conducted through

the liquid-gas interface to the liquid droplet, and the motion of the fluid near the heating surface is due to convection only. This region is characterized by low heat flux and single-phase heat transfer. At point B, a vapor bubble starts to form on the heating surface. As the temperature excess gradually increases (from point B to point C), bubbles grow in number and size and move upwards through the liquid droplet. The rising of vapor bubbles greatly enhances the convection, thus drastically increasing the heat transfer rate. At point C, the upper limit of the nucleate boiling region, nucleate boiling is fully developed, and the corresponding heat flux at point C is known as Critical Heat Flux (CHF). Beyond point C, non-continuous vapor bubbles start to merge from vapor film beneath the liquid droplet. The high thermal resistance of the vapor film leads to a sharp decrease in the heat flux. This marks the initiation of the transition boiling region. Heat flux continues to drop in this region as the existing liquid columns connecting the heating surface the liquid droplet gradually disappear. This region is named as "transition region" because the vapor film between the solid surface and the liquid droplet is unstable and it breaks up frequently. This process continues till point D, where the heat flux reaches its minimum value. Point D is referred to as the Leidenfrost point. It is the lowest temperature at which a stable vapor layer can form on the hot solid surface and completely separate the liquid droplet from the heating surface. Beyond the Leidenfrost point, a stable vapor blanket hovers above the solid surface, and further heat transfer from the heating surface to the liquid droplet must go through the vapor layer in the form of conduction and radiation. This region is also known as the film boiling region. The phenomenon in which a liquid droplet produces an insulating vapor layer that keeps the liquid from rapid boiling is termed the Leidenforst effect. It is named after the German doctor Johann Gottlob Leidenfrost, who described this phenomenon in 1751.
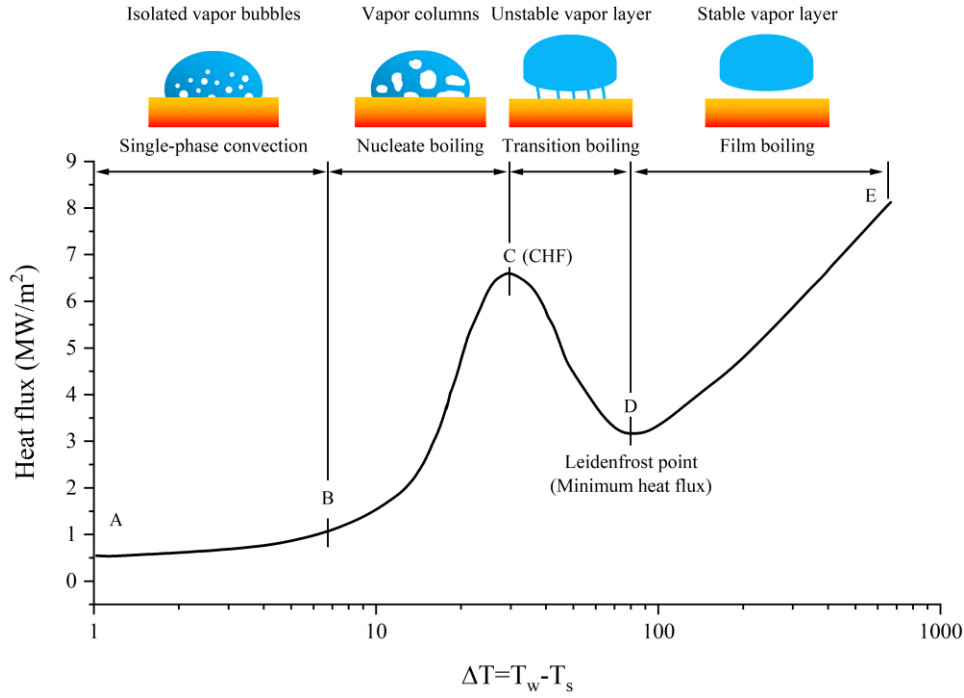
Figure 1-17. Nukiyama boiling curve.

It is evident that the solid surface temperature should be high enough to maintain the film boiling, at least 100 degrees above the saturation temperature of the liquid droplet. Such conditions can be easily satisfied in continuous casting. The typical temperature of the newly solidified steel shell at the mold exit is around 1500°C, and the saturation temperature of liquid water is 100°C at one atmosphere. It is evident that the spray cooling process in continuous casting is always associated with the Leidenfrost effect. Consequently, accurate knowledge of the Leidenfrost temperature is necessary if enhanced cooling and uniform temperature are desired. Unfortunately, the Leidenfrost temperature varies significantly for different materials. Table 1-10 shows the Leidenfrost temperature for stainless steel summarized by Bernardin and Mudawar [143].

Table 1-10. Leidenfrost temperature for stainless steel from Bernardin and Mudawar [143].

Leidenfrost temperature (°C)	Reference
302	Tamura and Tanasawa (1959)
285	Gottfried (1962)
320	Godleski and Bell (1966)
280	Gottfried et al. (1966)
305	Patel and Bell (1966)
282	Emmerson (1975)
280-310	Xiong and Yuen (1991)

Raudensky and Horsky [144] experimentally measured the Leidenfrost temperature of an austenite steel plate, which was cooled by three sizes of air-mist nozzles from 1250°C. The spray nozzle was placed on a moving trolly to mimic the moving effect in continuous casting. The spray water pressure was also varied while maintaining that of air to investigate the effect of water pressure. The measured Leidenfrost temperature is shown in Figure 1-18. It can be seen that the Leidenfrost temperature is sensitive to both nozzle size and water pressure. The value of the Leidenfrost temperature varies from 600°C to 1200°C, which is a significant increase compared to the stainless steel shown in Table 1-10.

As a matter of fact, Bernardin and Mudawar also summarized some of the most influential parameters in determining the Leidenfrost temperature, including the size of liquid mass, method of liquid deposition, liquid subcooling, solid thermal properties, surface conditions, and environmental pressure, along with several Leidenfrost Point (LFP) models [143].

A more recent study by Hnizdil et al. [145] has proposed several different correlations for determining the Leidenfrost temperature in the application of continuous casting of steel. The authors experimentally measured the heat flux through an austenite steel plate which was cooled from 1250°C to 100°C by an upward facing moving flat-fan nozzle. Both air-mist and hydraulic nozzles were considered in this study. All the testing conditions were carefully selected based on the typical operating conditions during the secondary cooling process. At the end of the study, the

authors presented ten correlations for the Leidenfrost temperature, using different combinations of operating parameters. The correlation between spray water density, mean droplet velocity and Sauter mean diameter is recommended for predicting the Leidenfrost temperature in the secondary cooling process through a residual analysis.
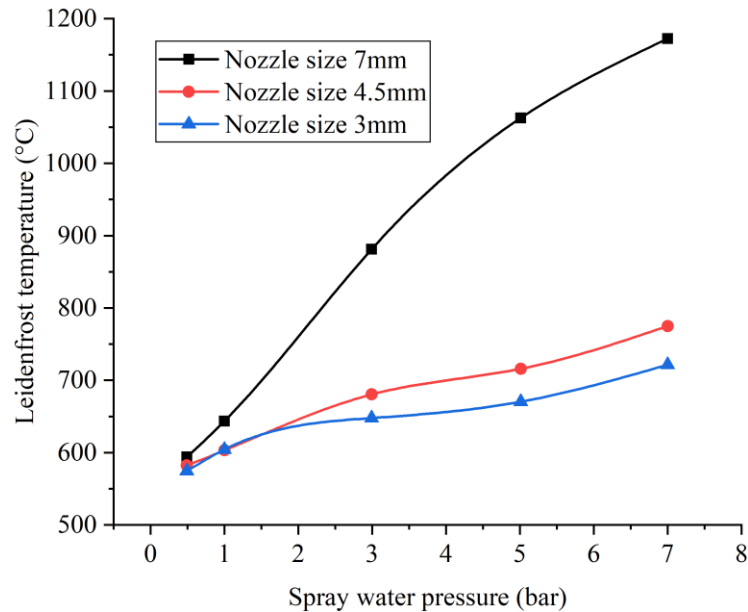
Figure 1-18. Leidenfrost temperature as a function of spray water pressure for three sizes of air-mist nozzle [144].

Table 1-11 summarizes the aforementioned correlations for predicting the Leidenfrost temperature, along with other similar correlations. However, if conditions permit, the Leidenfrost temperature should be determined by experiments. Its value can be interpreted from the turning point of either droplet lifetime on the heating surface or heat flux, or surface temperature.

Table 1-11. Correlations for predicting the Leidenfrost temperature.

Correlation	Reference
$T_{LF} = 351Q_w^{0.111}u_d^{0.174}D_{32}^{0.006}$	[145]
$T_{LF} = T_d + \dfrac{0.844T_c\left\{1 - \exp\left[-0.016\left(\dfrac{\left(\dfrac{\rho_w}{At}\right)^{1.33}}{\sigma}\right)^{0.5}\right]\right\} - T_d}{\exp(3.006 \times 10^6 \beta_{sur})\, erfc(1758\sqrt{\beta_{sur}})}$	[146]
$T_{LF} = 162.0 + 24.3u_d^{0.64}$	[147]
$T_{LF} = 536.8Q_w^{0.116}$	[148]
$T_{LF} = 1400We_d^{0.13}$	[149]
$T_{LF} = T_{LF,1atm} + 7.024 + 123log_{10}\left(\dfrac{P}{P_{1atm}}\right) + 36log_{10}\left(\dfrac{P}{P_{1atm}}\right)^2$	[150]
$T_{LF} = T_{sat} + 0.127\dfrac{\rho_v h_{fg}}{k_v}\left[\dfrac{g(\rho_d - \rho_v)}{\rho_v + \rho_d}\right]^{\frac{2}{3}}$ $\left[\dfrac{\sigma_d}{g(\rho_v - \rho_d)}\right]^{1/2}\left[\dfrac{\mu_v}{g(\rho_v - \rho_d)}\right]^{1/3}$	[151]

Note:

- Q_w is the spray water density, kg/m²·s.
- $\beta_{sur} = \dfrac{1}{k_{sur}\rho_{sur}C_{p,sur}}$
- At is the atomic weight of surface material.

HTC correlation and casting control

Many efforts have also devoted to developing heat transfer and solidification models for the whole continuous caster to incorporate with the off-line or on-line control system to improve the steel quality and reduce the cost [152-154]. The principal objective of the control system is to constantly predict the degree of solidification, or the thickness of the solid shell, at any point in the secondary cooling region to allow caster machines to flexibly operate while maintaining important parameters within desired ranges [152]. The prediction is achieved by solving the energy

conservation equation within the semi-solidified steel slab with the surface cooling condition defined in Eq. (10) as the boundary condition. The predicted solid thickness and the metallurgical length (complete solidification) must be maintained within the designed range. Once the prediction deviates from the desired value, the system immediately reacts and dynamically adjusts either casting speed or spray water flow rate. Figure 1-19 illustrates the basic control scheme of such a system.

$$q''_{total} = q''_{cond} + q''_{conv} + q''_R = \text{HTC}\left(T_{sur} - T_{spray}\right) + q''_R \tag{10}$$

As mentioned in the previous sections, the primary goal of continuous casting is to completely freeze the molten steel before the oxygen torches cutting the slab into pieces, i.e., to maintain a proper metallurgical length. Because the direct measurement of the metallurgical length is impractical, the standard method is to solve the energy equation for the entire steel strand, and the point where the steel temperature is below the solidus temperature is the metallurgical length. Thus, one of the critical components in a control system is the heat transfer solver. The equation itself is straightforward and can be found in any heat transfer textbook. The significant challenges are boundary conditions and the dimension of the computational domain.
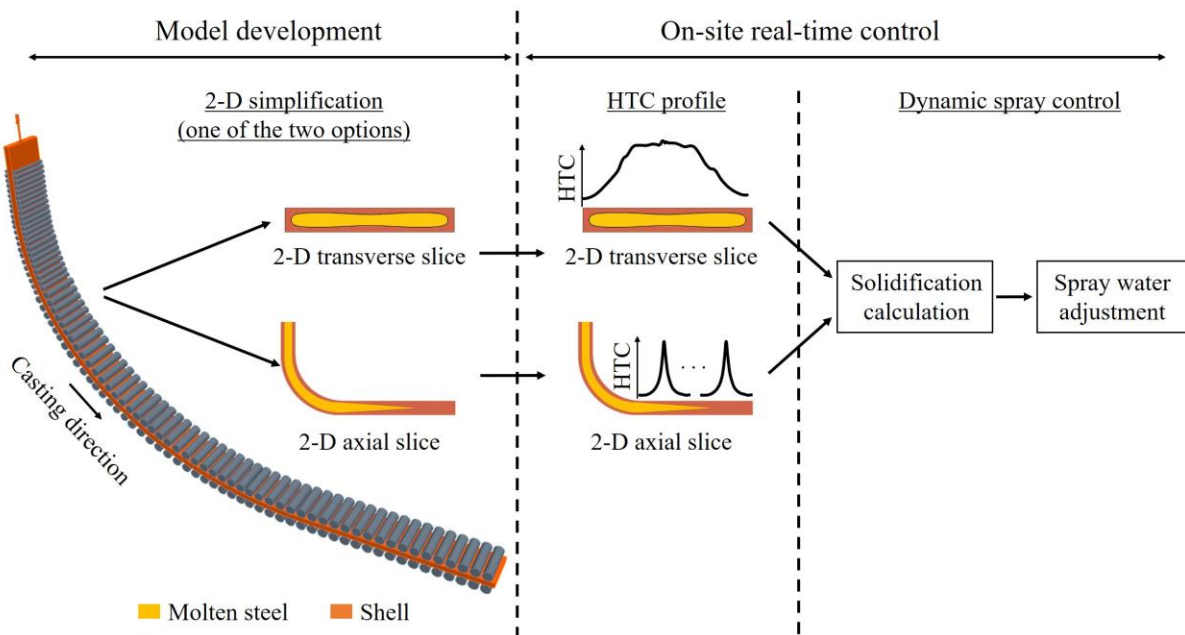
Figure 1-19. Illustration of the scheme of a typical spray cooling control system.

The heat transfer boundary conditions are complicated by the nature of the continuous caster design. Figure 1-20 illustrates the four heat transfer mechanisms in the spray cooling region: roll contact heat transfer, spray water impinging heat transfer, convection, and radiation. It is also essential to know that these four heat transfer boundary conditions periodically occur along the casting direction due to alternating rolls and spray nozzles. The most practical technique to resolve the periodic boundary condition problem is to manually divide the boundary surface into many small patches and assign only one type of boundary condition in terms of heat flux or heat transfer coefficient to each patch [7, 10, 11, 155-163]. Table 1-12 summarizes the most widely used thermal boundary conditions for heat balance calculation in spray cooling region from literature.
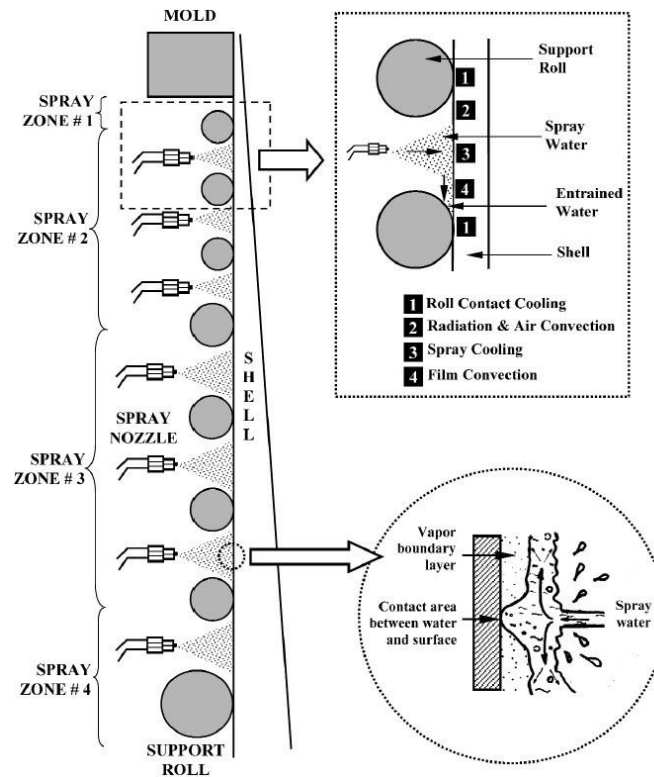
Figure 1-20. Schematic illustration of heat transfer mechanisms in spray cooling region [19].

Table 1-12. Summary of thermal boundary conditions for heat balance calculation in spray cooling region from literature.

Boundary condition	Reference
Radiation	
$h_R = \varepsilon_{st}\sigma_{SB}(T_{sur}^2 + T_{evn}^2)(T_{sur} + T_{evn})$	[7, 10, 11]
Convection	
$h_{conv} = 8.7$ (constant)	[7]
$h_{conv} = 0.84(T_{sur} - T_{evn})^{1/3}$	[10, 11]
Roll contact cooling	
$h_{roll} = f_{roll}\left[\dfrac{(h_R + h_{conv} + h_{spray})L_{spray}}{L_{roll}(1 - f_{roll})} + \dfrac{(h_R + h_{conv})(L_{spray\,pitch} - L_{spray} - L_{roll})}{L_{roll}(1 - f_{roll})}\right]$	[7]
$q''_{roll} = 11513.7T_{sur}^{0.76}V_{ca}^{-0.2}(2\theta_{roll})^{-0.16}$	[11]
$h_{roll} = 700$ (constant)	[164]
Spray cooling	
$h_{sp} = 0.3925Q_w^{0.55}(1 - 0.0075T_{sp})$	[7, 165-167]
$h_{sp} = \dfrac{1570Q_w^{0.55}(1 - 0.0075T_{sp})(1 - 0.15cos\theta_{slab})}{\alpha_{cal}}$	[10, 11, 164]
$h_{sp} = a_{AM}Q_w^{b_{AM}}P_w^{c_{AM}}T_{sur}^{d_{AM}} + e_{AM}T_{sur}^{f_{AM}}\exp\left(-g_{AM}T_{sur}^{h_{AM}}\right)$	[153]
$h_{sp} = h_0\exp\left[A_{sp}(t - t_0)\right]$	[159]
$h_{sp} = 141300Q_w^{0.566}u_d^{0.639}(T_{sur} - T_w)^{-0.539}$ (high flow rates)	[168]
$h_{sp} = 63.25Q_w^{0.264}D_{32}^{-0.062}(T_{sur} - T_w)^{0.691}$ (low flow rates)	[168]
$h_{sp} = 1.9N_d^{0.65}D_{32}^{1.1}u_d^{1.1}$	[169]
$h_{sp} = 118.03(\rho_d Q_w)^{0.277}\bar{u}_d^{0.554}$	[170]
$h_{sp} = 379930Q_w^{0.318}D_{30}^{-0.024}u_d^{0.33}T_{sur}^{-0.895}$	[171]
$h_{sp} = 38.448P_{impact}^{0.454}Q_w^{0.132}$	[172]
Integrated heat transfer coefficient (including all heat transfer mechanisms)	
$h_{spray} = 2950.190T_{sur}^{-0.235}Q_w^{0.805}$	[173]

Note:

- $\varepsilon_{st} = \frac{0.85}{1+\exp{(42.68-0.02682 T_{sur})^{0.0115}}}$ [174].

- f_{roll}: fraction of heat flow per spray zone going to roll, a value of 0.05 is recommended [7].

- L_{spray}: length of spray coverage.

- L_{roll}: length of roll contact.

- $L_{spray\,pitch}$: distance between adjacent sprays.

- V_{ca}: casting speed.

- θ_{roll}: angle of the roller contact.

- θ_{slab}: the slab surface angle from horizontal.

- α_{cal}: machine-dependent calibration factor, a value of 4 is recommended [165].

- $a_{AM}, b_{AM}, c_{AM}, d_{AM}, e_{AM}, f_{AM}, g_{AM}, h_{AM}$ are experimentally determined but not given in the literature.

- h_0: initial heat transfer coefficient.

- A_{spray}: exponent coefficient depending on the nature of cooling conditions of cooling sub-region [159].

- t_0: initial time of cooling sub-region.

- N_d: droplet number.

- P_{impact}: droplet impact pressure.

In the meantime, it remains challenging to acquire accurate HTC values under different operating conditions. It is well known that HTC is a localized parameter, and its value varies throughout the secondary cooling region [19]. HTC is sensitive to both nozzle configurations and casting operating conditions. Some of the most recognized parameters that affect HTC include nozzle type, spray water flow rate, spray angle, standoff distance, steel surface temperature, spray direction, and nozzle-to-nozzle distance. In practice, researchers have correlated HTC with the most critical operating parameters such as casting speed and spray water flow rate through small-scale hot plate experiments [153, 165, 173, 175, 176]. The most well-recognized correlation was developed by Nozaki [165] and is shown in Table 1-12. This equation takes both spray water flux and spray water temperature into account since both parameters are essential to the spray cooling process, and they are relatively convenient to obtain through on-site measurements. Nozaki also acknowledges the differences between caster machines by adding a machine-depend calibration

parameter, α_{cal}. With the knowledge of specific nozzle arrangement, this coefficient can be easily tuned. Due to its simplicity and flexibility, this correlation has been extensively used since the 1970s. Some of the latest HTC correlations are either a variation of Nozaki's correlation [7, 10, 11, 164, 166, 167] or an extension of this formula [153].

On the other hand, other essential casting parameters such as steel surface temperature, casting speed, and nozzle-to-nozzle distance are not included in Eq. (2). For example, steel surface temperature has been proven to affect droplet impingement heat transfer and local Leidenfrost temperature (Bernardin and Mudawar, 1999). Casting speed can alter the droplet residence time on the steel surface, increasing or decreasing the amount of energy transferred. Moreover, heat transfer is noticeably increased under the overlapping spray area in the short nozzle-to-nozzle distance. Thus, it is necessary to develop more comprehensive and general HTC correlations to include these phenomena. In addition, it is worth mentioning that the existing correlations were specially developed for a limited number of nozzles and operation conditions. Each casting condition requires at least one experiment to uniquely determine the coefficients in the correlation, and the correlation might be inapplicable when changes in the casting process occur.

The second challenge for the energy balance calculation is the dimension of the computational domain. Ideally, a three-dimensional view of the temperature distribution inside the whole steel strand from the mold exit down to the cut-off point is preferred. However, a three-dimensional steady-state/transient heat transfer calculation coupled with different alternating boundary conditions would require days even weeks of computational time. Such computational expensive calculation is not suitable for "instantaneous" control during the process. That is why most of the existing spray control systems are built on two-dimensional heat transfer assumptions. There are two classic two-dimensional assumptions throughout the literature search, and they are illustrated in Figure 1-21.

(a)

(b)
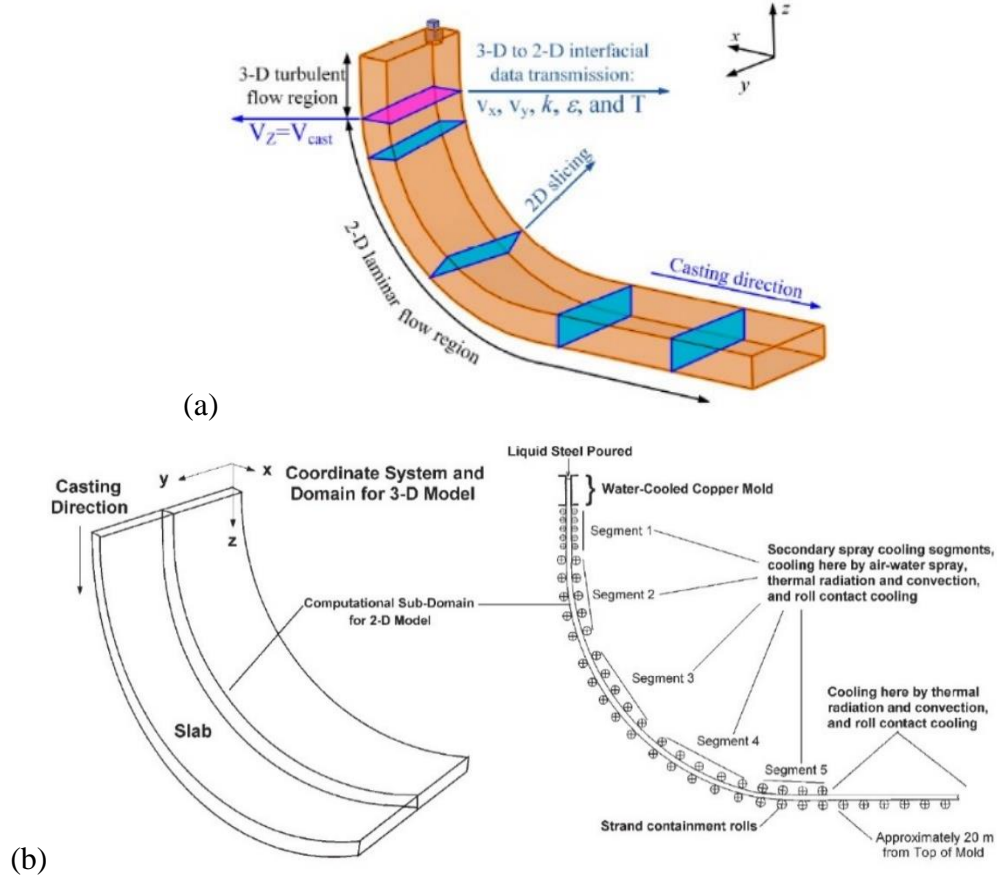
Figure 1-21. Two classic types of two-dimensional representation of secondary cooling region:
(a) transverse slices [173], and (b) axial slices [10].

The first kind is to assume that the entire secondary cooling region consists of hundreds of transverse slices, as shown in Figure 1-21 (a). The basis of such assumption is that the axial heat conduction is negligible in the steel strand, as indicated by the large Peclet number. The Peclet number at a typical continuous caster can be calculated from the following expression [7]:

$$\mathrm{Pe} = \frac{V_{ca} Z_m \rho_{st} c_{p,st}}{\lambda_{st}} = \frac{0.0167 \times 0.81 \times 7400 \times 670}{30} = 2236 \tag{11}$$

At such a large Peclet number, the dependency of the flow upon downstream locations is diminished, and the heat transfer is reasonable to be treated as two-dimensional. Such treatment can be found in many applications [7, 156, 157, 173, 177].

The second kind slices the steel strand along the axial direction or casting direction, instead of the transverse direction, as shown in Figure 1-21 (b). Depending on the need for resolution, the number of slices can range from a few dozens to a few hundred. The advantage of this treatment is that each slice contains the information of shell evolution along the casting direction, whereas the other method can only show the "global" trend when all of the slices are correctly ordered and presented simultaneously. However, the drawback of the treatment is that every single slice requires alternating boundary conditions, unlike the other one in which boundary conditions of each slice are much simpler to define.

Nevertheless, regardless of the two-dimensional treatment method, once the dimension of the steel product is known, an in-house program can automatically divide the three-dimensional strand into two-dimensional slices based on the predefined spacing between slices. Then, the two-dimensional heat equation is solved for each slice with its boundary conditions. After the calculation, the results of all of the slices can be colored by the desired parameter, usually temperature, and displayed in a graphic user interface, as shown in Figure 1-22. The values at locations between slices are obtained from interpolation during post-processing. Users are able to directly interact with the output window to check parameters of interest, such as shell thickness, metallurgical length, slab temperature, and many others. In the off-line system, the calculated information will not be directly used to adjust operating parameters. Instead, it is often used as a virtual simulator for training purposes or a tool for developing cooling strategies and new caster design. In the on-line system, such information is frequently updated (in seconds) and is used to adjust the spray water flow rate based on the difference between the calculated value and the expected value. In addition, the heat transfer solver has to be integrated with sensors and controllers in order to achieve real-time control. The control scheme of CONONLINE shown in Figure 1-23 demonstrates the complexity of the on-line spray cooling control systems. In general, the heat transfer and solidification solver in these control systems are very mature now. The major challenge for the steel industry to achieve smart manufacturing is to develop "smart" sensors, and it will remain challenging in the foreseeable future.

(a)

(b)

Figure 1-22. Two examples of casting control system: (a) BrCCM [162], and (b) GCM2D [153].

Figure 1-23. Closed-loop diagram of CONONLINE system [154].

Heat transfer by roll contact

During the continuous casting process, rolls are primarily used to move the slab in the casting direction and compress the slab to minimize the centerline segregation. The heat transfer between rolls and slab has received little attention since most of the superheat and latent heat are removed by water spray cooling in the secondary cooling region. Many research has focused on roll misalignment [178, 179] and roll wear [180]. However, it is well recognized that rolls are experiencing wear in continuous casting and thermal fatigue, and high-temperature corrosion [181, 182]. Investigations of the influence of rolls on heat transfer in the secondary cooling region is pivotal to expand the rolls' lifespan further.

Previous research tends to simplify the heat transfer by roll contact by treating it as merely one of the thermal boundary conditions for solidification calculation instead of the research goal. The assumption made was that a roll contacts with slab through a flat contact surface, and either the heat transfer coefficient or the heat flux through that surface is constant. The heat transfer coefficient or the heat flux can be calibrated based on the specific casting machine [7, 10, 11, 164]. As for the degree of contact, it can be evaluated from either the contact angle, θ_{roll}, where 7° is recommended by Meng and Thomas [7], or the contact length, L_{roll}, which is equivalent to 10-20% of the roll diameter [10, 11]. Under such assumptions, researchers were able to obtain the shell thickness and the slab surface temperature during solidification, and the results have shown good agreements with the measurements [7, 10, 11].

More recently, Xia and Schiefermuller conducted a comprehensive study on the influence of rolls on heat transfer in continuous casting [12]. To overcome the harsh environment, they employed a guide tube installed through the spray chamber and extended close to the slab surface between rolls, in which a thermocouple was inserted to record the temperature. From the temperature drops, they were able to identify the roll contact length, which is about 20mm regardless of the roll diameter. Later, the measured contact length and roll surface temperature were input into a mathematical model to predict solidification, phase transformation, and shrinkage. With the help of the mathematic model and a heat balance calculation, the heat removal by roll contact was determined to be 10% of the total energy extracted from the secondary cooling process, which corresponds to a cooling rate of 50°C-80°C per roll, a much lower rate than it was believed [19].

Bolender and Cappel took another approach to study the heat transfer by roll contact. The effort was made to address the well-known surface defect issue related to non-uniform cooling in the secondary cooling region. Unfortunately, the existing water/air spray cooling method cannot meet the desired cooling requirement, especially for micro-alloyed carbon steel. As a result, a helical roll was developed to replace the spray cooling system. Figure 1-24 shows the internal structure of the helical roll. The new roll consists of a rigid core and a spiral water channel through which cooling water flows. This new design significantly increases the amount of energy transferred to rolls to a point where spray cooling is nonessential. Therefore, this continuous casting process is termed "dry casting", implying no water is involved in the cooling process. The cooling rate of the dry casting operation was closely related to the diameter and the wall thickness of the roll, as shown in Figure 1-25. Large roll diameter and small wall thickness are beneficial to the heat transfer process. However, a minimum 15mm wall thickness was required when considering the construction limitations.
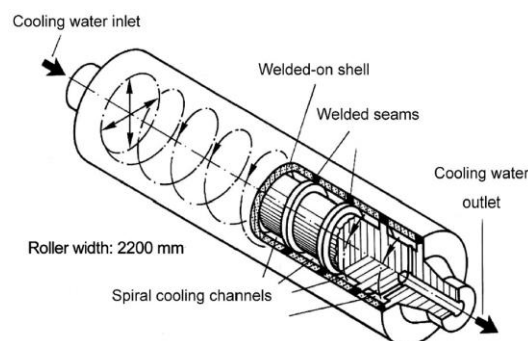
Figure 1-24. Illustration of the helical roll with internal cooling [183].
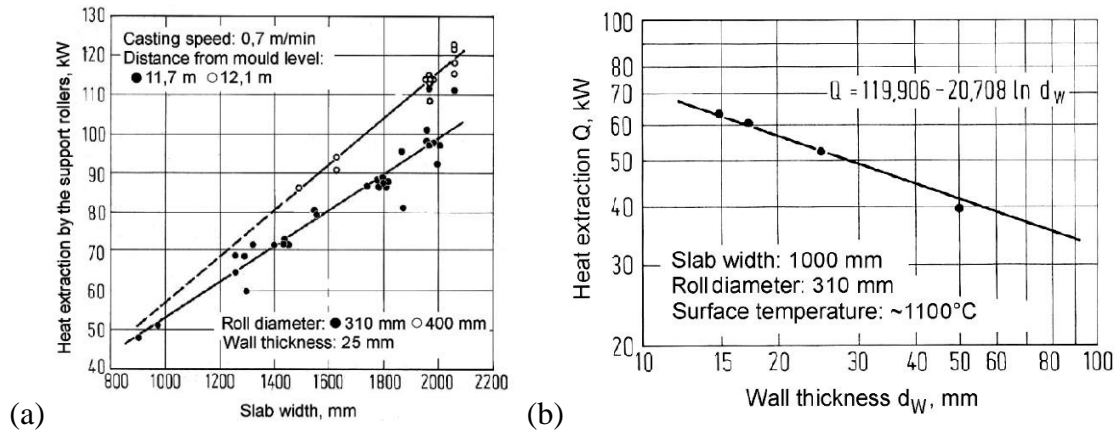
Figure 1-25. Heat transfer rate influenced by: (a) roll diameter, and (b) roll wall thickness [183].

1.3.2 Solidification

Upon entering the secondary cooling section, the solidified steel shell acts as a container to support the remaining liquid while they are withdrawn from the mold by rollers installed below the mold at the casting speed [184]. Based on a breakout shell measurement and the numerical simulations conducted by Thomas et al., the solidified shell can grow up to 20mm-25mm at the mold exit on both narrow face and broad face [185]. Once the semi-solidified slab enters the secondary cooling section, liquid steel enclosed by the solid shell continues to lose heat and solidify due to the direct and intense spray cooling onto the slab surface. As a result, the solid shell gradually grows from both narrow face and broad face towards its center throughout the whole secondary cooling process until it solidifies.

It is critical to understand the solidification process during the continuous casting of steel since the solidification of steel is closely related to the quality of the final product. To cast a slab that is free of cracks and has minimal macro-segregation is challenging. Direct observation and measurement of the solidification process are almost impossible due to the high casting temperature and the movement of the semi-liquid steel inside the solid shell. One exception for direct measurement of the solid shell is when a breakout occurs during the continuous casting. Once the molten steel bursts through the shell after the breakout occurs, the remaining hollow solidified shell can provide great insights into the solidification process, such as the shell thickness at different locations, the oscillation mark depth and width, and inclusion entrainment [184]. Such valuable information can be not only used for process control but also benefit numerical simulations.

The numerical study on the solidification of molten steel during continuous casting has been developed for a couple of decades. Thomas et al. has studied the flow and the initial solidification stage of molten steel inside the mold since the early 90s, and his group has developed a FORTRAN program, CON1D, to model the 1-D heat transfer and solidification in the mold and spray region. The model is carefully validated and has generated some meaningful results since early 2000 [7, 152]. However, even though the existing solidification models predict reasonable slab temperature and shell profile, the assumptions made in the models, such as 2-D heat conduction with the slab, the flow condition in the mold is one-way coupled with the solidification process, the dynamic spray cooling process is simplified as a single heat transfer correlation applied on the slab surface, sometimes oversimplify the characteristics of the continuous casting process. A 3-D dynamic comprehensive solidification model coupled with the flow condition in the mold and the spray cooling is still unavailable.

The biggest obstacle in developing a 3-D solidification model coupled with the fluid flow is to find a way to bridge physical phenomena on different scales. Figure 1-26 illustrates the solidification process of liquid metal on different length scales. On the macroscopic scale, molten steel freezes into a chunk of the slab during the solidification process. The interface between the molten steel and the solidified shell appears continuous and smooth, as depicted in Figure 1-2. However, the interface becomes uneven and may be discontinued on the microscopic scale. In the order of the micrometer, the solidified shell is a cluster of dendrites (also known as crystals). Figure 1-27 (a) and (b) show columnar dendrites in 2-D and 3-D space, respectively. On the microscopic scale, the solidification process is equivalent to the formation and growth of dendrites. Figure 1-28 schematically illustrates the dendritic growth process. The wall on the left side of the image is a representation of the water-cooled mold wall. The space right to the wall is initially filled with molten steel, and a temperature gradient is established between the molten steel and the cold wall. When the molten steel contacts the wall, it freezes against the wall due to the heat loss to the wall and forms an array of dendrites. These columnar dendrites continue to grow from the wall into the rest of the molten steel at a certain speed. Dendrites grow like trees, with primary trunks and secondary branches on the side. The spacing between the primary trunks is termed the primary dendrite arm spacing and is labeled λ_1 in Figure 1-28. The spacing between the secondary branches is called the secondary arm spacing and is labeled λ_2 in Figure 1-28. The columnar

dendrites tend to grow in one preferred direction, which is the direction of the temperature gradient. As the columnar dendrites grow further into the molten steel, the convection effect of the molten steel becomes significant. The tip of the dendrites may be washed away by the strong movement of the bulk flow. In addition, because the steel alloys solidify over a temperature range (between the liquidus and solidus temperature), the nucleation can also occur far away from the wall. Dendrites that grow from this mechanism are called equiaxed dendrites. This type of dendrites has no preferred growth direction, as the constrain from the wall no longer exists. The equiaxed dendrites usually present between the columnar dendrites and the molten steel, forming a thin mushy region.
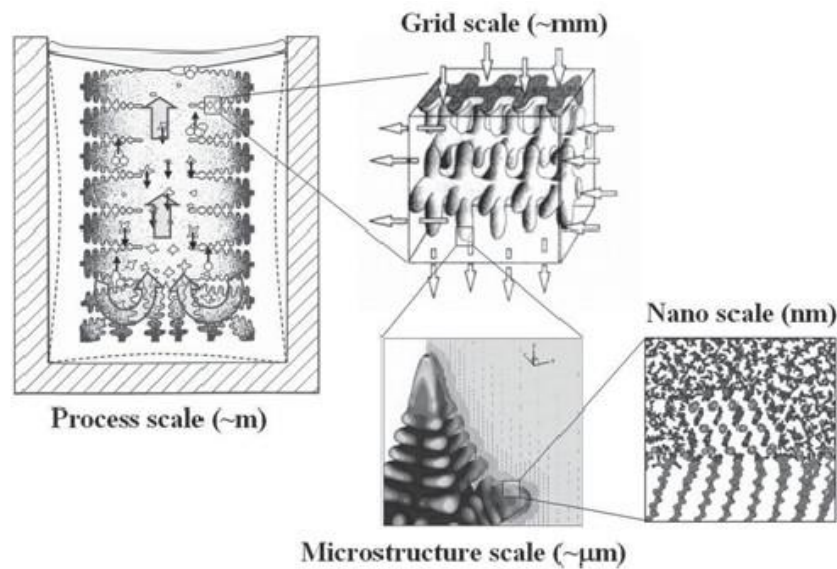
Figure 1-26. Solidification process on different length scales [186].
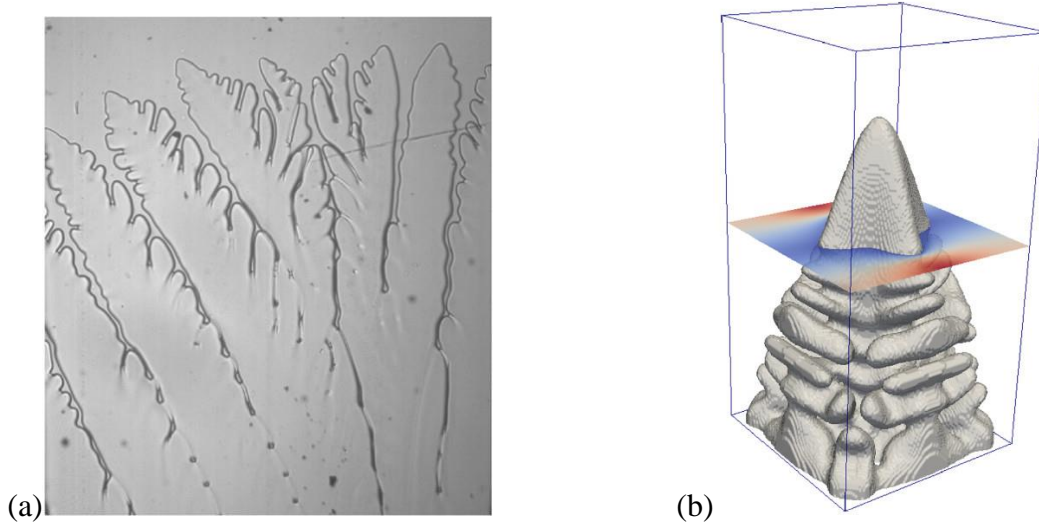
Figure 1-27. Dendrite morphology: (a) a group of columnar dendrites from a 2-D scan (the width of the image is around 1700μm) [187], and (b) a columnar dendrite in 3-D space (200μm by 100μm by 100μm) [188].
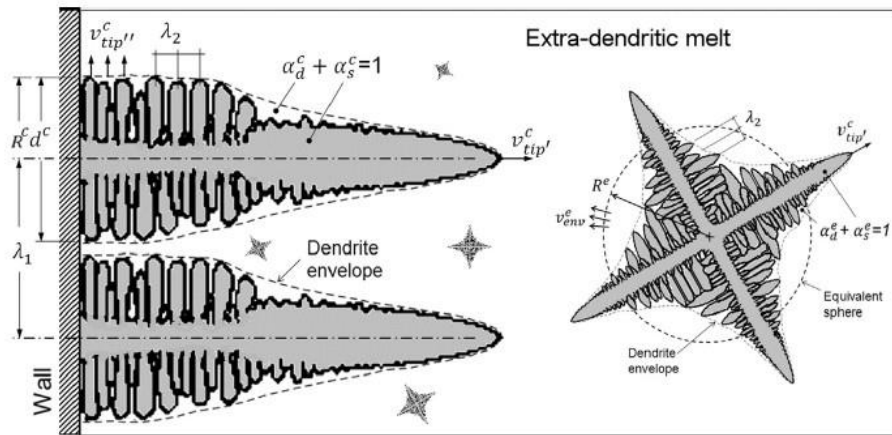
Figure 1-28. Schematic illustration of dendritic mixture [189].

Numerical simulations of the microstructural evolution during the solidification process have been made possible with the advent of high-performance computers. Phase Field (PF) and Cellular Automation (CA) are the most successful mathematical approaches. In the PF method, the diffuse nature of the solid-liquid interface is substituted by the evolution of a phase-field, ϕ. The value of the phase-field varies continuously from zero in the liquid to unity in the solid over a finite thickness. Solving the equation of the phase-field, together with another equation for free energy, one can obtain the evolution of both heat and the solute without tracking the solid-liquid interface

dynamically [190]. Figure 1-27 (b) is an example of the phase-field simulations. The CA method is much more abstract than the PF method. In the CA method, each cell in the computational domain is in one of the three possible states: solid, liquid, and solidi-liquid mixture. The state of a cell is updated at each discrete step and can only be influenced by the state of the neighboring cells [191]. The method was initially proposed by John von Neumann and Stanislaw Ulam to solve the problem of self-replicating systems in the 1940s [192]. The PF method is more robust between the two approaches than the CA method in a hexagonal dendrite growth simulation [193]. The CA method is somewhat mesh-dependent and is comparable to the PF method only when the hexagonal type of mesh is available. In fact, the PF method does receive more attention in microstructural evolution simulations [188, 194-196].

The aforementioned simulations, along with numerous similar simulations, are essential for understanding the phenomena associated with the solidification process, but it is impractical to resolve the complicated boundary of dendrites in a macroscale simulation. A more realistic approach is to neglect the complicated dendritic geometry and average the microscopic phenomena such as mass transfer, solute partitioning, latent heat release, and momentum exchange over a volume [186]. The interfacial solidification and melting phenomena on the local microscale can be incorporated into the global macroscale simulation. Several volume-averaging methods have been reported, and some of them are summarized in [186].

Among the existing volume-averaging methods, the mixture solidification model, also known as the Enthalpy-Porosity method, is the most popular model for continuous casing simulations and has produced meaningful results [197-199]. The Enthalpy-Porosity method was proposed by Voller et al. in 1985 to resolve the "moving liquid-solid interface" issue and the "zero velocity in solid region" issue [200-204]. The method is significant both mathematically and practically. The engineering field can be used to model phase change phenomena, such as solidification and melting. In the field of mathematics, it solved the time-dependent moving interface problem. The Enthalpy-Porosity method is illustrated in Figure 1-29. The figure shows a small section of a larger computational domain. The section is oriented so that the liquid-solid interface is in the middle of the figure. To better understand the numerical approach, the physical-based dendritic sketch is overlaid with a uniform mesh. The mesh is fixed in space during the solidification simulation,

89

which saves the computational effort to track the moving interface dynamically. This technique is also named the "fixed grid" method [203]. A close-up view shows that the complicated dendritic geometry in the physical world is neglected in the numerical simulation, and only two effects from the dendrite growth are included, namely the latent heat release and the resistance on the molten flow.
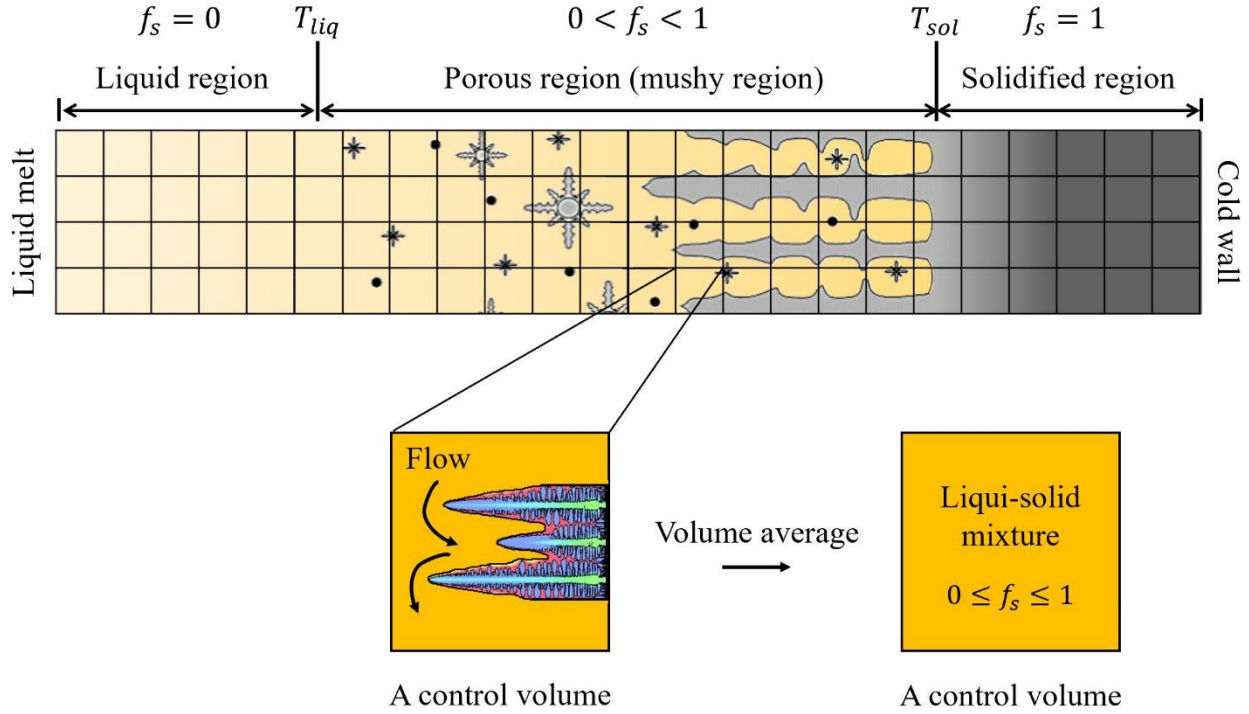
Figure 1-29. Schematic illustration of the Enthalpy-Porosity method.

The latent heat release is calculated on the cell basis. At each iteration, velocity and temperature of each cell centroid are solved (assume it is the finite volume method, other types of numerical methods need to derive their governing equations, but the concept still holds), and then the following step function is employed:

$$
h_{lat} = \begin{bmatrix} L & T_{liq} \leq T \\ L(1 - f_{sol}) & T_{sol} < T < T_{liq} \\ 0 & T \leq T_{sol} \end{bmatrix} \tag{12}
$$

Where L is the latent heat of fusion and f_{sol} is the solid fraction in a control volume, which accounts for space in a cell occupied by dendrites. As Eq. (12) indicates, the existence of dendrites is only determined by the centroid temperature, and it is compared with two critical pre-determined temperatures, the liquidus temperature T_{liq} and the solidus temperature T_{sol}. These two critical temperatures divide the computational domain into three regions: pure liquid region ($T_{liq} < T$), pure solid region ($T < T_{sol}$) and the mushy region ($T_{sol} < T < T_{liq}$), as shown in Figure 1-29. No special attention is required in both the pure liquid region and pure solid region, as the material in both regions only has one phase. The typical energy conservation equation is sufficient to deal with the heat transfer in such regions. In the mushy region, however, both liquid phase and solid phase present in a control volume. The product of $L(1 - f_{sol}) < L$ suggests that the latent heat release in these volumes is incomplete and more liquid phase can transfer to solid phase if the centroid temperature continues to decrease. A latent heat source term is added to the energy conservation equation at the end of each iteration to represent the phase transformation.

The treatment of velocities of cell centroids in the solid region and the mushy region is more complicated than the latent heat release. Eq. (12) only affects temperature and has no impact on velocities. Without additional constraints, "solid" in the solid region and the mushy region will not hold together as it is supposed to be in the physical world. According to the observations, in reality, flow velocities should reduce from that in the liquid region to specific smaller values in the mushy region and become zero in the solid region. In other words, special rules must be applied to the momentum equation in those two regions. The most straightforward approach is to overwrite the velocity in the solid region and set it to zero [205]. This method is also called the switch-off technique [202]. It follows the previous latent heat release calculation. Once the enthalpy distribution is known, the corresponding region is also defined. Then, velocities of centroids are set to zero when the following condition is satisfied:

$$u_{cen} = 0, \quad h_{lat} \leq A \tag{13}$$

Where A is a user-defined number, and it takes the value in the range $0 \leq A \leq L$. The parameter A can be understood as the cut-off line between the zero-velocity cells and the nonzero-velocity

ones. It is not entirely an arbitrary number. Since the value of A is determined based on the latent heat, the parameter A can be treated as one of the isothermal lines. A value of $A = L$ indicates that the switch-off function takes effect immediately at the liquid-mushy region interface where ($T = T_{liq}$), whereas a value of $A = L$ indicates that the flow velocity is not set to zero until the cell is determined in the solid region where ($T \leq T_{sol}$).

The second method is to vary viscosity in order to slow down the molten flow [206]. It is more subtle compared to the previous method. Similarly, this approach relies on the calculated temperature field. Viscosities instead of velocities are modified based on the following function:

$$\mu_{cen} = \mu_{liq} + B(L - h_{lat}) \tag{14}$$

Where B is some large number that is defined by users. As the value of h_{latent} changes between 0 and L, the value of $\mu_{centroid}$ increases from μ_{liq} in the liquid region to a large number in the solid region. Such large viscosity may not exist in the real world, but it resembles the sluggish effect in the mushy region and the static behavior in the solid region as if an infinitely large resistance was imposed on the flow.

The last technique assumes that both the mushy region and the solid region are permeable porous mediums where the flow can still flow through but at the sacrifice of losing pressure [201-203]. This concept is borrowed from Darcy's law, in which the flow velocity is proportional to the pressure gradient. The method transfers the pressure gradient term in Darcy's law into the following source term for the momentum equation:

$$S_{cen} = B(L - h_{lat}) \tag{15}$$

Similar to the viscosity approach, the source term arises significantly as the molten flow enters the mushy region and completely stops the flow in the solid region.

Voller compared all five aforementioned velocity correction techniques and one improved non-linear Darcy source term in a test problem. The problem describes the solidification process through convection and conduction in a square cavity, which is maintained insulated on both top and bottom surfaces. The cavity contains a liquid initially at a uniform temperature. At time zero, the left surface temperature is reduced to a lower value, and a temperature gradient establishes. Natural convection is also included via the Boussinesq approximation. The simulation results are presented in Figure 1-30. The solid fraction in the switch-off $A = L/2$ is chosen as a normalizing factor. The variable viscosity technique tends to overpredict the solidification regardless of the discretization method. Voller explained that the viscosity of a cell centroid is evaluated from its neighboring cells, and it is likely that the high viscosities in the solid region are carried into the liquid region. The linear Darcy source term produces similar results as the switch-off $A = L$. Both techniques cut off the velocity further upstream in the liquid region, and the predicted solid regions are much thicker than the baseline case (switch-off $A = L/2$). The nonlinear Darcy source term deaccelerates the rate of increase in the source term. Thus, it yields a thinner solid region. No significant difference is observed between the baseline and the switch-off $A = 0$ at the initial solidification stage ($t < 1000s$). However, such behavior only exists when the mushy region is relatively thin compared to the other two regions. Overall, the Darcy source term method is recommended among all of the aforementioned methods, and it has become a standard method for the later macroscopic casting simulations [207-212].
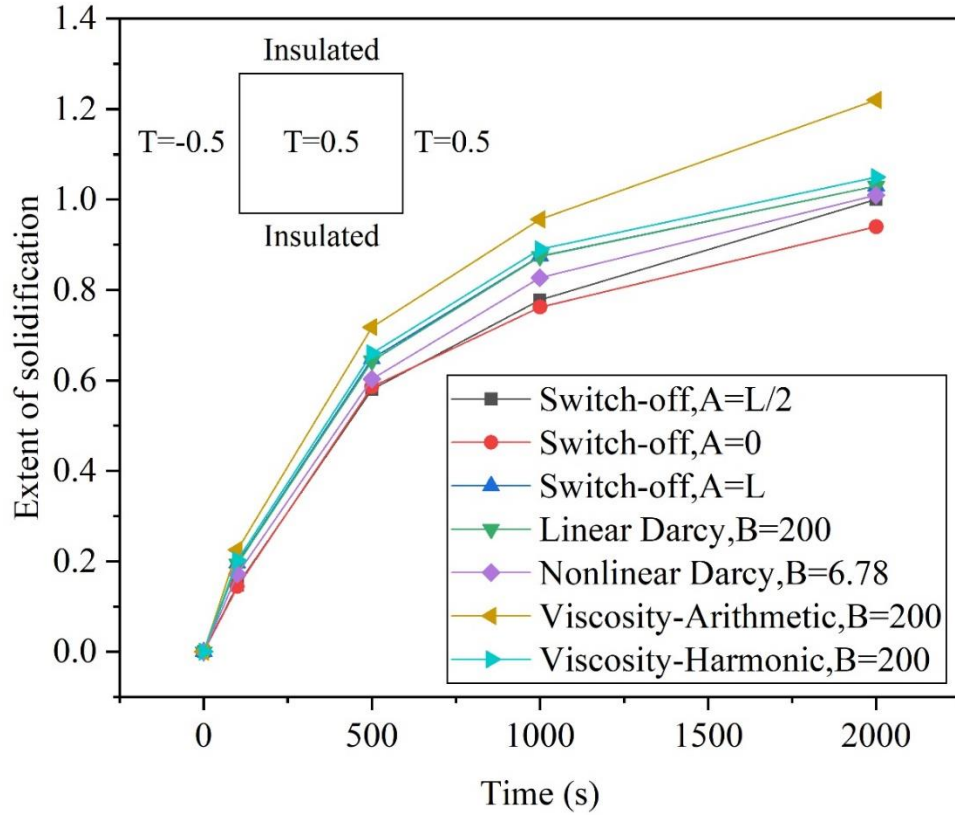
Figure 1-30. The extent of solidification by different velocity correction techniques [202].

1.4 Research motivation and objectives

In order to remain competitive and continuously produce high-quality and high-strength steel at the maximum production rate, the spray parameters must be carefully selected to provide sufficient and uniform heat transfer across the cooling surface because insufficient cooling will lead to breakout where molten steel breaks the thin shell and bursts out. In contrast, excessive cooling will result in cracks and other defects due to significant residual thermal stresses and strains. Yet, few successful numerical simulations combining fluid flow in the mold, spray cooling, and thermal-mechanical behavior of solidifying shell during continuous casting process have been reported, mainly owing to complicated physical phenomena involved.

Therefore, the current study aims to:

(1) Develop high-fidelity three-dimensional numerical models and provide the fundamental perspectives for the heat transfer processes in secondary cooling of continuous casting of steel slab

and foundation for future stress and macrosegregation models. The two numerical models consider atomization, droplet dispersion, droplet-air interaction, droplet-wall impingement, the effect of vapor film, droplet-wall impingement heat transfer, droplet boiling, roll contact heat transfer, molten steel solidification, and steel slab movement.

(2) Perform parametric studies to investigate the effect of important configuration and operating parameters on the heat transfer process to provide guidance for the casting machine design and process optimization.

(3) Develop an efficient method to convert the high-fidelity simulations into mathematically simple correlations of HTC, which can be used as a boundary condition for on-site off-line/on-line solidification calculation and further improve the accuracy of the existing casting control systems.

2. METHODOLOGY

Figure 2-1 summarizes the numerical models of heat transfer in secondary cooling of continuous casting of steel slab. The heat transfer processes inside the steel slab and on the slab surface are evaluated separately to gain computational efficiency. However, the simulations in the two regions are connected by sharing a mutual interface, which is the slab surface. The heat transfer simulation on the slab surface is conducted first to obtain the heat transfer coefficient profile on the interface. The simulation in this region includes the atomization of water droplets, droplet dispersion, droplet-air interaction, droplet-wall impingement, the effect of vapor film, droplet-wall impingement heat transfer, droplet boiling, roll contact heat transfer, steel slab movement, and radiation. Following the first simulation, a second simulation is performed for the entire slab region to study the effect of molten steel solidification and heat conduction through the solidified shell. The heat transfer coefficient profile on the slab surface obtained from the first simulation is used as the thermal boundary condition for the spray cooling affected area. Thus, the influence of spray is integrated into the second simulation. The two simulations are one-way coupled due to the significant difference in time scale.
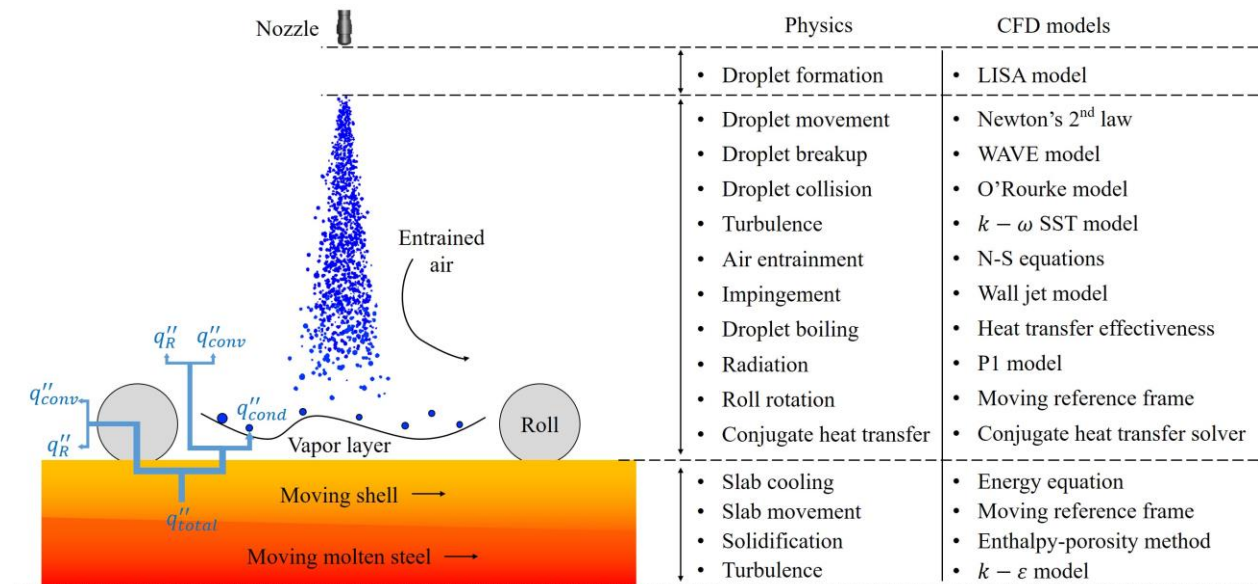
Figure 2-1. Summary of numerical models of heat transfer in secondary cooling of the continuous casting process.

2.1　Heat transfer on steel slab surface in secondary cooling region

The Eulerian-Lagrangian approach is applied due to its low computational cost compared to the Eulerian-Eulerian approach. Air entrainment due to the high-speed water spray, heat conduction in the solidified shell, and heat conduction in the rolls are modeled in the Eulerian frame, while water droplets are treated as discrete phases and tracked in the Lagrangian frame.

2.1.1　Assumptions

In deriving the model, the following assumptions are made:

(1) The whole secondary cooling region is assumed to consist of several sections that have the same spray cooling and rolling conditions, such as spray standoff distance, spray flow rate, roll diameter, and roll spacing. Therefore, the cooling condition by each water spray is identical and can be represented by the simulation of a single spray.

(2) The surrounding gaseous phase is considered a single-phase multi-component mixture of 77wt% nitrogen and 23wt% oxygen. The properties of the mixture are calculated using the mass-weighted average. The gas mixture is assumed to be an incompressible and isotropic gas.

(3) The jet impingement heat transfer is assumed to be conducted in quiescent air under one standard atmospheric pressure.

(4) At the normal casting speed of 1m/min, it takes 6s for the steel slab to pass a spray that spans about 100mm in the casting direction, but it only takes 0.01s for droplets traveling at 13m/s to reach the steel surface which is placed 130mm below the nozzle tip. Due to the drastic difference in time scale, it is numerically convenient and efficient to exclude the solidification process from the current simulations.

(5) During the normal casting operation, the average thickness of the solidified shell is between 25mm to 30mm at the mold exit, and the growth rate of the shell was estimated between 0.1mm/s

97

and 0.4mm/s [213]. Thus, a 30mm-thick slab is thick enough to include the temperature gradient within the solidified shell but thin enough to exclude the solidification within the steel slab.

(6) The cooling water is assumed to be 100% H_2O, and its initial properties are evaluated at the temperature on the injection plane under one atmospheric pressure. Liquid droplets generated from atomization are assumed to be spherical and rigid throughout their lifetime.

(7) Because the curve of the steel slab in the vicinity of one spray is negligible, the solidified shell is treated as a smooth and flat moving plate in the current studies. The moving velocity of the plate equals the casting speed. This assumption also excludes oscillation marks and any defects on the slab surface.

(8) The current model is developed based on the normal casting operation where transient features such as the startup of the casting process were not considered in the model. The solidified shell is assumed to feed into the secondary cooling region from the mold continuously. Thus, the simulations are conducted in steady-state.

2.1.2 Governing equations

Eulerian phase (air, roll, slab)

The Reynolds-averaged Navier-Stokes equations for mass, momentum, energy and species transport are solved for the gas mixture, and only the energy equation is solved for the steel plate and rolls.

Mass conservation

The equation for conservation of mass of an incompressible and isotropic Newtonian fluid can be written as follows:

$$\frac{\partial \rho_a}{\partial t} + \nabla \cdot (\rho_a \vec{u}_a) = S_{mass} \qquad (16)$$

Where ρ_a and u_a are the density and the velocity of the air mixture, respectively. The properties of the mixture can be found by using the mass-weighted average. S_{mass} is the source term added to the continuous phase from the discrete phase due to droplet vaporization and is defined in Eq. (145) in the two-way coupling section.

Momentum conservation

The conservation of momentum of the gaseous phase is described by the following equation:

$$\frac{\partial}{\partial t}(\rho_a \vec{u}_a) + \nabla \cdot (\rho_a \vec{u}_a \vec{u}_a) = -\nabla P + \mu_a \nabla^2 \vec{u}_a + \rho_a \vec{g} + S_{mom} \tag{17}$$

Where P, μ_a, and g are the static pressure, the dynamic viscosity, and the gravitational acceleration, respectively. S_{mom} is the external source term corresponding to the momentum exchange between air and droplets. At the end of each droplet time step, the effect of momentum exchange is incorporated in the subsequent continuous phase calculation through S_{mom}. The definition of S_{mom} is shown in Eq.(146) in the two-way coupling section.

Turbulence model

The surrounding air is entrained into the spray as a result of mass conservation. The entrained air moves together with the spray and impinges on the slab surface. After the impingement, both the airflow and the droplets lose the axial velocity, turn into wall jets, and accelerate in the radial direction parallel to the surface. The Reynolds number of air moving at 13m/s on a 200mm flat plate at 20°C room temperature is:

$$\text{Re}_a = \frac{\rho_a |\vec{u}_a| L}{\mu_a} = \frac{1.2 \times 13 \times 0.2}{1.813 \times 10^{-5}} = 1.72 \times 10^5 > 10^5 \tag{18}$$

As indicated in Eq. (18), the flow becomes unstable and turbulent. Therefore, an accurate turbulent model is necessary to predict correct flow separation at the stagnation point and the acceleration of the wall jets.

Hofmann et al. [214] and Zuckerman et al. [20] examined the performance of the most widely spread Reynolds-averaged Navier-Stokes turbulence models and have found that even with high-resolution grids, the k-ε model, k-ω model, Reynolds stress model, and Algebraic stress model, all failed to predict accurate heat transfer on the surface. The only model which is able to give an agreeable prediction in impinging jet flows while balancing the computational cost is the k-ω SST model.

Therefore, Menter's Shear Stress Transport (SST) model is chosen for turbulence modeling due to its high accuracy in predicting the jet impinging heat transfer without sacrificing too much computational power [20, 76]. The SST model takes advantages of both the k-ε model and the k-ω model and combines both of them to produce better predictions in turbulence.

$$\frac{\partial}{\partial t}(\rho_a k) + \nabla \cdot (\rho_a k \vec{u}_a) = \nabla \cdot \left[\left(\mu_a + \frac{\mu_t}{\sigma_k} \right) \nabla k \right] + G_k - \rho_a \beta_k k \omega \qquad (19)$$

$$\frac{\partial}{\partial t}(\rho_a \omega) + \nabla \cdot (\rho_a \omega \vec{u}_a) = \nabla \cdot \left[\left(\mu_a + \frac{\mu_t}{\sigma_\omega} \right) \nabla \omega \right] + G_\omega - \rho_a \beta_\omega \omega^2 \qquad (20)$$

Where k is the turbulence kinetic energy, ω is the turbulence dissipation rate, μ_t is the turbulent viscosity and is defined in Eq. (37), G_k is the generation of turbulence kinetic energy due to mean velocity gradients are defined in Eq. (22), G_ω is the generation of turbulence dissipation rate is defined in Eq.(24), σ_k and σ_ω are the turbulent Prandtl numbers and are defined in Eq. (33) and Eq. (34), respectively. β_k and β_ω are model coefficients and are defined in Eq. (35) and Eq. (36), respectively.

From Eq. (19), the production of turbulence kinetic energy can be defined as follows:

$$G_k = -\rho_a \overline{u_i' u_j'} \frac{\partial u_j}{x_i} \qquad (21)$$

To evaluate G_k in a manner consistent with the Boussinesq approximation, Eq. (21) can be written as follows:

$$G_k = \mu_t S^2 \tag{22}$$

Where S is the modulus of the mean rate-of-strain tensor and is defined as follows:

$$S = \left| \frac{1}{2} (\nabla \vec{u}_a + \nabla \vec{u}_a^T) \right| \tag{23}$$

The generation of turbulence dissipation rate is evaluated by:

$$G_\omega = \frac{\rho_a \alpha \alpha^*}{\mu_t} G_k \tag{24}$$

Where α and α^* are the model coefficients and can be evaluated as follows:

$$\alpha = \frac{\alpha_\infty}{\alpha^*} \left(\frac{\alpha_0 + \mathrm{Re}_t / R_\omega}{1 + \mathrm{Re}_t / R_\omega} \right) \tag{25}$$

$$\alpha^* = \alpha_\infty^* \left(\frac{\alpha_0^* + \mathrm{Re}_t / R_k}{1 + \mathrm{Re}_t / R_k} \right) \tag{26}$$

Where, α_0, α_∞^*, α_0^*, R_ω, and R_k are the model coefficients and are given in Table 2-1, and Re_t is defined as follows:

$$Re_t = \frac{\rho_a k}{\mu_a \omega} \tag{27}$$

α_∞ in Eq. (25) is defined as follows:

$$\alpha_\infty = F_1 \alpha_{\infty,1} + (1 - F_1) \alpha_{\infty,2} \tag{28}$$

$$\alpha_{\infty,1} = \frac{\beta_{i,1}}{\beta_\infty^*} - \frac{\kappa^2}{\sigma_{\omega,1} \sqrt{\beta_\infty^*}} \tag{29}$$

$$\alpha_{\infty,2} = \frac{\beta_{i,2}}{\beta_\infty^*} - \frac{\kappa^2}{\sigma_{\omega,2}\sqrt{\beta_\infty^*}} \tag{30}$$

Where $\beta_{i,1}$, $\beta_{i,2}$, β_∞^*, κ, $\sigma_{\omega,1}$, and $\sigma_{\omega,2}$ are the model coefficients and are given in Table 2-1. F_1 in Eq. (28) is the blending function that switches between the k-ε model in the bulk region to the k-ω model in the vicinity of the impingement surface. It takes advantage of both models and retains the accuracy while saving computational resources. The blending function is defined as follows:

$$F_1 = \left[\left\{\min\left(\max\left(\frac{\sqrt{k}}{0.09\omega y_{k\omega}}, \frac{500\mu_a}{\rho_a y_{k\omega}^2 \omega}\right), \frac{4\rho_a k}{\sigma_{\omega,2} CD_{k\omega} y_{k\omega}^2}\right)\right\}^4\right] \tag{31}$$

$$CD_{k\omega} = \max\left(2\rho_a \frac{1}{\sigma_{\omega,2}} \frac{1}{\omega} \nabla k \cdot \nabla\omega, 10^{-10}\right) \tag{32}$$

Where $y_{k\omega}$ in Eq. (31) is the distance to the next surface.

The turbulent Prandtl numbers for k and ω in Eq. (19) and (20) are defined as follows, respectively:

$$\sigma_k = \frac{1}{F_1/\sigma_{k,1} + (1 - F_1)\sigma_{k,2}} \tag{33}$$

$$\sigma_\omega = \frac{1}{F_1/\sigma_{\omega,1} + (1 - F_1)\sigma_{\omega,2}} \tag{34}$$

Where $\sigma_{k,1}$, $\sigma_{k,2}$, $\sigma_{\omega,1}$, and $\sigma_{\omega,2}$ are the model coefficients and are given in Table 2-1.

β_k and β_ω in Eq. (19) and Eq. (20) are defined as follows:

$$\beta_k = \beta_\infty^* \left[\frac{4/15 + \left(\mathrm{Re}_t/R_\beta\right)^4}{1 + \left(\mathrm{Re}_t/R_\beta\right)^4}\right] \tag{35}$$

$$\beta_\omega = F_1 \beta_{i,1} + (1 - F_1)\beta_{i,2} \tag{36}$$

Where β_∞^*, $\beta_{i,1}$, $\beta_{i,2}$, and R_β are the model coefficients and are given in Table 2-1. Re_t is given in Eq. (27).

To account for the transport of the turbulent shear stress in situations where the onset of flow separation from the smooth surface becomes important, the turbulent viscosity in Eq. (19), (20), (22), and (24) can be evaluated from the following expression:

$$\mu_t = \frac{\rho_a k}{\omega} \frac{1}{\max\left(\frac{1}{\alpha^*}, \frac{SF_2}{a_t\omega}\right)}$$

(37)

Where α^* is the model coefficient and is defined in Eq. (26), S is the modulus of the mean rate-of-strain tensor and is defined in Eq. (23), a_1 is the model coefficient and is given in Table 2-1, F_2 is another blending function and is defined as follows:

$$F_2 = \tanh\left[\left(\max\left(\frac{2\sqrt{k}}{\beta_k \omega y_{k\omega}}, \frac{500\mu_a}{\rho_a y_{k\omega}^2 \omega}\right)\right)^2\right]$$

(38)

Where β_k is a model coefficient and is defined in Eq. (35)

The model constants in the turbulence model are summarized in Table 2-1.

Table 2-1. k-ω SST model constants [215].

Coefficient	Value	Coefficient	Value	Coefficient	Value
α_0	0.11	$\beta_{i,1}$	0.075	κ	0.41
R_ω	2.95	$\beta_{i,2}$	0.0828	$\sigma_{k,1}$	1.176
α_∞^*	1	β_∞^*	0.09	$\sigma_{k,2}$	1
α_0^*	0.024	$\sigma_{\omega,1}$	2	R_β	8
R_k	6	$\sigma_{\omega,2}$	1.168	a_t	0.31

Species transport

During the spray cooling, liquid droplets change phase to water vapor due to diffusion and boiling. The generated water vapor mixes with the surrounding gaseous phase. The gas mixture at any given location within the computational domain consists of three species, which are nitrogen, oxygen, and water vapor. The properties of the mixture can be found by using the mass-weighted average. The local mass fraction of the ith species in turbulent flows can be found by solving the following convection-diffusion equation:

$$\frac{\partial}{\partial t}(\rho_a Y_i) + \nabla \cdot (\rho_a \vec{u}_a Y_i) = \nabla \cdot \left[\left(\rho_a D_{i,m} + \frac{\mu_t}{\text{Sc}_t} \right) \nabla Y_i + D_{T,i} \frac{\nabla T}{T} \right] \tag{39}$$

Where Y_i is the mass fraction of the ith species, $D_{i,m}$ is the mass diffusion coefficient of the ith species in the mixture, Sc_t is the turbulent Schmidt number, $D_{T,i}$ is the thermal diffusion coefficient of the ith species, and T is the local temperature.

Although the mixture composition changes during the spray cooling process, the mass fractions of oxygen and water vapor are much smaller than that of nitrogen. It is reasonable to assume that the surrounding gas mixture is diluted by oxygen and water vapor. The mass diffusion coefficients for oxygen and water vapor in air at one atmospheric pressure are set to 0.176cm^2/s and 0.282cm^2/s, respectively [216]. Using the binary mass diffusion coefficient, the mass diffusion coefficient of the ith species in the mixture can be calculated as follows:

$$D_{i,m} = \frac{1 - \chi_i}{\sum_{j,j \neq i} \frac{\chi_i}{D_{i,j}}} \tag{40}$$

Where χ_i is the mole fraction of the ith species, $D_{i,j}$ is the binary mass diffusion coefficient.

Sc_t in Eq. (39) represents the ratio of turbulent momentum diffusivity and turbulent mass diffusivity. The value of Sc_t is widely distributed in the range of 0.2-1.3 in various CFD applications. For the simulation of jet flows, a value between 0.7-0.9 is recommended to ensure

correct predictions [217, 218]. Even though $Sc_t = 0.9$ yields better prediction on concentration in jet flows, Yimer et al. suggests that 0.7 is much more suitable when considering the consistency with the prediction of the velocity field [217]. Therefore, $Sc_t = 0.7$ is applied to the current study.

The effect of thermal diffusion is as important as the mass diffusivity during the spray cooling process. The importance of thermal diffusion can be seen from the Lewis number. Using the nominal values for air at 300K and one atmospheric pressure, the Lewis number can is found to be:

$$\text{Le} = \frac{\lambda_a}{\rho_a c_{p,a} D_{i,m}} = \frac{0.02514}{1.2 \times 1000 \times 0.176 \times 10^{-4}} = 1.19 > 1 \tag{41}$$

Eq. (41) indicates a comparable thermal gradient on the slab surface to that of the mass. The following empirical correlation based on the kinetic theory is applied to the current study to compute the thermal diffusion coefficient in Eq. (39) [219]:

$$D_{T,i} = -2.59 \times 10^{-7} T^{0.659} \left(\frac{M_{w,i}^{0.511} X_i}{\sum_{i=1}^{N} M_{w,i}^{0.511} X_i} - Y_i \right) \left(\frac{\sum_{i=1}^{N} M_{w,i}^{0.511} X_i}{\sum_{i=1}^{N} M_{w,i}^{0.489} X_i} \right) \tag{42}$$

Where T is the local temperature, $M_{w,i}$ is the molecular weight of the ith species, X_i is the molar fraction of the ith species, and Y_i is the mass fraction of the ith species.

Energy conservation

The energy conservation equation for the gas phase can be written in the following form:

$$\frac{\partial}{\partial t}(\rho_a E_a) + \nabla \cdot [\vec{u}_a(\rho_a E_a + P)] = \nabla \cdot \left(\lambda_{eff} \nabla T_a + \sum_{i=1}^{N} h_i \vec{J}_i \right) + S_{nrg} + S_R \tag{43}$$

Where E_a is the total energy and is defined in Eq. (47), λ_{eff} is the effective conductivity and is defined in Eq. (46), h_i is enthalpy of the ith species and is defined in Eq.(45), S_{nrg} is the source

term added to the continuous phase from the discrete phase due to droplet vaporization and is defined in Eq. (147) in the two-way coupling section. S_R is the source term due to radiation and is defined in Eq. (49). J_i is the diffusion flux of the ith species and is defined as follows:

$$J_i = -\left(\rho_a D_{i,m} + \frac{\mu_t}{\text{Sc}_t}\right)\nabla Y_i - D_{T,i}\frac{\nabla T}{T} \tag{44}$$

Where the definitions of the parameters in Eq. (44) can be found in the species transport section.

h_i shown in Eq. (43) represents the sensible enthalpy of the ith species and can be found from the following definition:

$$h_i = \int_{T_{ref}}^{T} c_{p,i}dT \tag{45}$$

Where $c_{p,i}$ is the specific heat of the ith species and T_{ref} is the reference temperature and is set to 300K in the current study.

The effect of turbulence on energy transfer was taken into account through the effective conductivity, λ_{eff}, shown in Eq. (43). The effective conductivity is defined as follows:

$$\lambda_{eff} = \lambda_a + \frac{c_p \mu_t}{\text{Pr}_t} \tag{46}$$

Where λ_a and c_p are the thermal conductivity and specific heat of the gas phase and can be found from mass-weighted mixing law, respectively. μ_t is the turbulent viscosity and is defined in Eq. (37). Pr_t is the turbulent Prandtl number and is defined as the ratio of the momentum eddy diffusivity and the heat transfer eddy diffusivity. This term has been experimentally determined for different types of flows. In turbulent boundary layer flows, an average value of 0.85 is recommended [74, 220-222].

The total energy shown in Eq. (43) is defined as follows:

$$E_a = h_a - \frac{P}{\rho_a} + \frac{|\vec{u}_a|^2}{2} \tag{47}$$

Where h_a is the sensible enthalpy for air and can be found from the following definition:

$$h_a = \sum_{i=1}^{N} h_i Y_i \tag{48}$$

The source term due to radiation shown in Eq. (43) is modeled by the P1 model due to its computational efficiency. The P1 model defines the source term due to radiation as follows [223]:

$$S_R = a_{abs}G - 4a_{abs}n_R^2\sigma_{SB}T^4 \tag{49}$$

Where a_{abs} is the absorption coefficient, n_R is the refractive index, σ_{SB} is the Stefan-Boltzmann constant, T is the temperature, G is the incident radiation and is defined as follows:

$$G = \int_{\Omega_{sol}=4\pi} I d\Omega_{sol} \tag{50}$$

Where I is the radiation intensity, Ω_{sol} is the solid angle.

The viscous dissipation term is dropped from Eq. (43) as viscous heating is negligible in the continuous casting process. The typical surface temperature of the steel slab in the secondary cooling region ranges from 1000-1500°C. Assuming a steel slab with an average surface temperature of 1250°C is cooled by water spray. The entrained air flows at 5m/s in the vicinity of the surface. The Brinkman number for this application is:

$$\text{Br} = \frac{\mu_a |\vec{u}_a|^2}{\lambda_a (T_{sur} - T_{bulk})} = \frac{1.813 \times 10^{-5} \times 5^2}{0.02514 \times (1250 - 20)} = 1.466 \times 10^{-5} < 1 \tag{51}$$

Eq. (51) suggests that the heat production by viscous dissipation is negligible compared to the heat transported by molecular conduction. Thus, the viscous dissipation term is excluded from the energy conservation equation applied to the current study.

Both rolls and the solidified shell are treated as rigid bodies in the simulations. During the secondary cooling process, roll, regardless of driver roll or support roll, rotates around its center, while solidified shell moves in the casting direction. However, owing to the fact that only a symmetric sectioned continuous casting machine is simulated in the current study, the movement of the solidified shell and the rotation of rolls can be modeled by converting the motion of the rigid bodies to that of the reference frames. Figure 2-2 illustrates the relations between the stationary reference frame, fixed on the ground, and the moving reference frames. Because the curvature of the solidified shell is neglected, the motion in the casting direction is equivalent to linear motion.
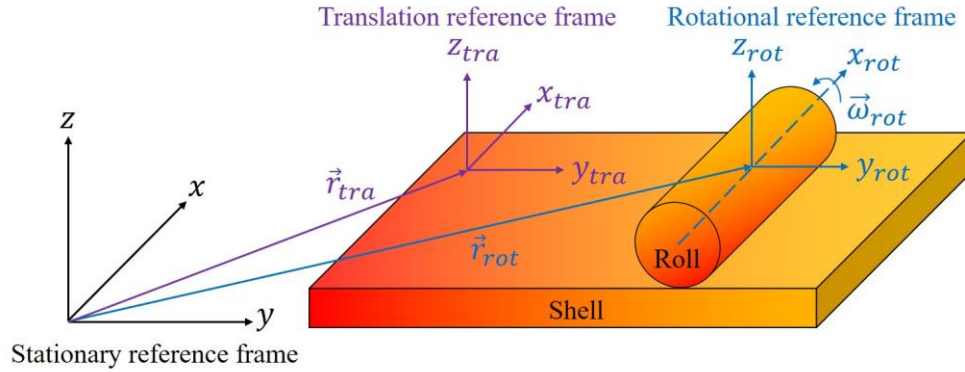
Figure 2-2.Illustration of the translation and the rotational reference frames (not to scale).

The relative velocity of the translation reference frame and the rotational reference frame to the stationary reference frame are defined as follows, respectively:

$$\vec{u}_r = \vec{u}_{tra} \tag{52}$$

$$\vec{u}_r = \vec{\omega}_{rot} \times \vec{r} \tag{53}$$

Where $\vec{u}_{tra}$ is the translational velocity of the translation reference frame and is equal to the casting speed. $\vec{r}$ is the position vector from the origin of the rotational reference frame to the given point in the roll. $\vec{\omega}_{rot}$ is the angular velocity of the rotational reference frame, and its magnitude can be computed from the following equation:

$$|\vec{\omega}_{rot}| = \frac{|\vec{u}_{cs}|}{r_{roll}} \tag{54}$$

Where $\vec{u}_{cs}$ is the casting speed and r_{roll} is the roll diameter.

The relative velocities defined in Eq. (52) and Eq. (53) are considered in the energy conservation equation for rolls and solidified shell by:

$$\frac{\partial}{\partial t}(\rho_a h_{sol}) + \nabla \cdot (\rho_{sol}\vec{u}_r h_{sol}) = \nabla \cdot (\lambda_{sol}\nabla T_{sol}) \tag{55}$$

Where $\rho_{sol}, h_{sol}, \lambda_{sol}\ T_{sol}$ are the density, enthalpy, thermal conductivity, and local temperature of the solid region, respectively.

Lagrangian phase (droplet)

Liquid droplet upon injection is treated as discrete phase and is tracked in the Lagrangian frame till the end of its lifetime, i.e., complete evaporation or escape from the computational domain. The trajectory of a droplet is computed by integrating Newton's second law over a small time step. The transient tracking treatment is used to improve numerical efficiency and stability, as many droplets are introduced in the domain, and there are intense droplet-droplet interactions in the spray region. Due to the significant difference in droplet formation mechanism, two different models are used to predict droplets generated from hydraulic nozzles and air-mist nozzles. However, the rest of the models is identical for droplets issued from both types of nozzles.

Droplet formation from a hydraulic nozzle

Physically, droplets are formed through two sequential breakup processes, i.e., the breakup of liquid sheet and the breakup of ligaments due to aerodynamic instabilities [37], regardless of nozzle type. The two breakup processes are collectively referred to as the primary breakup instead of the secondary breakup, where droplets formed from the primary breakup process further break up into smaller droplets due to aerodynamic instabilities or droplet-droplet collisions. Historically, the breakup process of sprays issued from hydraulic nozzles was well-studied, and there are substantial theories and correlations available for predicting the resulting droplet size and the length of the primary breakup region. This research has been rigorously validated in the past few decades [25-27, 33-36]. To balance the accuracy and efficiency of the numerical simulations, the current study utilizes the LISA model to predict droplet formation from hydraulic nozzles without modeling the internal flow inside the nozzle and the primary breakup process.

Figure 2-3 illustrates the droplet formation simulation strategy for hydraulic nozzles. The LISA model assumes the liquid jet issued from a fan-shape nozzle as a two-dimensional viscous incompressible sheet moving through a quiescent inviscid incompressible gas medium, which becomes unstable due to the growth infinitesimal sinuous wavy disturbance and breaks into ligaments [33]. The spectrum of infinitesimal wavy disturbances takes the following form [94]:

$$\eta = \eta_0 \exp(ik_{wave}x + \omega_{wave}t) \tag{56}$$

Where η_0 is the initial wave amplitude, k_{wave} is the wave number, ω_{wave} is the complex growth rate, t is time. Among the spectrum of wavelengths involved, one would be found to have the maximum growth rate, Ω, and would result in a dominance wavelength, Λ, which eventually leads to the breakup of the sheet. The dominant wavelength and its growth rate can be found by maximizing the following expression as a function of k_{wave} based on the analysis of the Kelvin-Helmholtz stability:

$$\Omega = \frac{1}{\tanh(0.5k_{wave}t_{sht}) + \rho_r} \left\{ -2\nu_{lid}k_{wave}^2\tanh(0.5k_{wave}t_{sht}) \right.$$

$$\left. + \sqrt{\begin{array}{l} 4\nu_{lid}^2 k_{wave}^4 \tanh^2(0.5k_{wave}t_{sht}) - \rho_r^2 k_{wave}^2 u_{total}^2 - \\ [\tanh(0.5k_{wave}t_{sht}) + \rho_r]\left[-\rho_r k_{wave}^2 u_{total}^2 + \dfrac{\sigma k_{wave}^3}{\rho_{lid}} \right] \end{array}} \right\} \quad (57)$$

Where t_{sht} is the thickness of the sheet and can be evaluated from Eq. (60), ρ_r is the ratio of air density and liquid density, ν_{lid} is the liquid kinematic viscosity, ρ_{lid} is the liquid density, σ is the air-to-liquid surface tension, u_{total} is the total velocity. The liquid properties can be found in that of water. The total velocity depends on the water flow rate through the nozzle and the internal structure of the nozzle. The precise measurement would be impractical. Alternatively, the total velocity can be evaluated from the following equation proposed by Han et al. [224]:

$$|\vec{u}_{total}| = C_{dc}\sqrt{\frac{2\Delta P}{\rho_{lid}}} \quad (58)$$

Where C_{dc} is the discharge coefficient, ΔP is the pressure difference, ρ_{lid} is the liquid density. The discharge coefficient is a function of nozzle design and injection pressure. It is the ratio of the actual volumetric flow rate and the ideal volumetric flow rate through the nozzle. The upper limit of C_{dc} is unity from conservation of energy. On the other hand, the lower limit varies from 0.5 to 0.9 for different nozzle designs [225-228]. A value of 0.7 is usually recommended as the lower limit for flat-fan nozzles. Another physical limit for C_{dc} is the non-negative condition. When water is injected from a flat-fan nozzle, the size of the water sheet must not be larger than that of the nozzle exit. Assuming the shape of the sheet at the nozzle orifice is rectangular, and the area of the flat-fan nozzle is equivalent to that of a circle, then the following condition must be met during the atomization:

$$\pi t_{sht}(d_{noz} - t_{sht}) \leq \frac{\pi d_{noz}^2}{4} \quad (59)$$

Where d_{noz} is the equivalent nozzle diameter. The term on the left-hand side can be related to the mass flow rate through the nozzle by:

$$\frac{\dot{m}_{lid}}{\rho_{lid}|\vec{u}_{ax}|} = \pi t_{sht}(d_{noz} - t_{sht}) \leq \frac{\pi d_{noz}^2}{4} \tag{60}$$

Where $\dot{m}_l$ is the mass flow rate through the nozzle, u_{ax} is the axial velocity of water, and it is related to the total velocity defined in Eq. (58) by:

$$\vec{u}_{ax} = \vec{u}_{total}\cos\frac{\alpha_{spray}}{2} \tag{61}$$

Where α_{spray} is the spray angle. The constraint for C_{dc} can be derived by combining Eq. (58), Eq. (60), and Eq. (61):

$$C_{dc} \geq \frac{4\dot{m}_{lid}}{\pi d_{noz}^2 \rho_{lid}\cos\frac{\alpha_{spray}}{2}}\sqrt{\frac{\rho_{lid}}{2\Delta P}} \tag{62}$$

Therefore, the following expression is used to determine C_{dc} with the consideration of all the aforementioned constraints [224]:

$$C_{dc} = \max\left[0.7, \frac{4\dot{m}_{lid}}{\pi d_{noz}^2 \rho_{lid}\cos\frac{\alpha_{spray}}{2}}\sqrt{\frac{\rho_{lid}}{2\Delta P}}\right] \tag{63}$$

Once C_{dc} is determined, $\vec{u}_{total}$ and $\vec{u}_{ax}$ can also be determined from Eq. (58) and Eq. (61). Similarly, the radial velocity of the water sheet at the nozzle orifice can be computed from the following equation:

$$\vec{u}_{ra} = \vec{u}_{total}\sin\frac{\alpha_{spray}}{2} \tag{64}$$

The water sheet is assumed to break up into ligaments at the breakup length due to the disturbance with the maximum growth rate, which can be expressed as follows:

$$\eta_\Omega = \eta_0 \exp(\Omega t) \tag{65}$$

The time for the sheet to break up after injection can be derived by rearranging Eq. (65):

$$t = \frac{1}{\Omega} \ln\left(\frac{\eta_\Omega}{\eta_0}\right) \tag{66}$$

Where the term $\ln\left(\frac{\eta_\Omega}{\eta_0}\right)$ is usually referred to as the sheet constant. Weber recommended a value of 12 for liquid jets [26]. Dombrowski and Hooper affirmed Weber's finding through various fan nozzles with different types of liquid over a range of Weber numbers from 2 to 200 [229]. The current study also adopts the value of 12 for the sheet constant due to similar Weber numbers.

The breakup length of the sheet can be computed by assuming that the sheet is moving at the total velocity within the breakup length and there is no momentum loss before breakup:

$$L_b = \frac{|\vec{u}_{total}|}{\Omega} \ln\left(\frac{\eta_\Omega}{\eta_0}\right) \tag{67}$$

Ligaments are assumed to form immediately after the breakup of the sheet at half-wavelength intervals. Ligaments are also treated as cylindrical shapes with a diameter of:

$$d_L = \sqrt{\frac{8t_{sht}}{k_{wave,\Omega}}} \tag{68}$$

Where $k_{wave,\Omega}$ is the wave number corresponding to the maximum growth rate, and it is defined as follows:

113

$$k_{wave,\Omega} = \frac{2\pi}{\Lambda}$$

(69)

At the breakup length, the droplet formation process completes. Owning to the fact that L_b is negligible compared to the spray distance, and the droplet size distribution at the breakup length has been well studied, the process of sheet formation and breakup, ligament formation and breakup, and droplet formation are excluded from the current study to grain the overall computational efficiency. As illustrated in Figure 2-3 (a) and (b), the spray nozzle and the region from the nozzle orifice to the breakup length are not simulated in the current study. Instead, a group of droplets is directly introduced into the domain at the inlet plane for all the simulations.
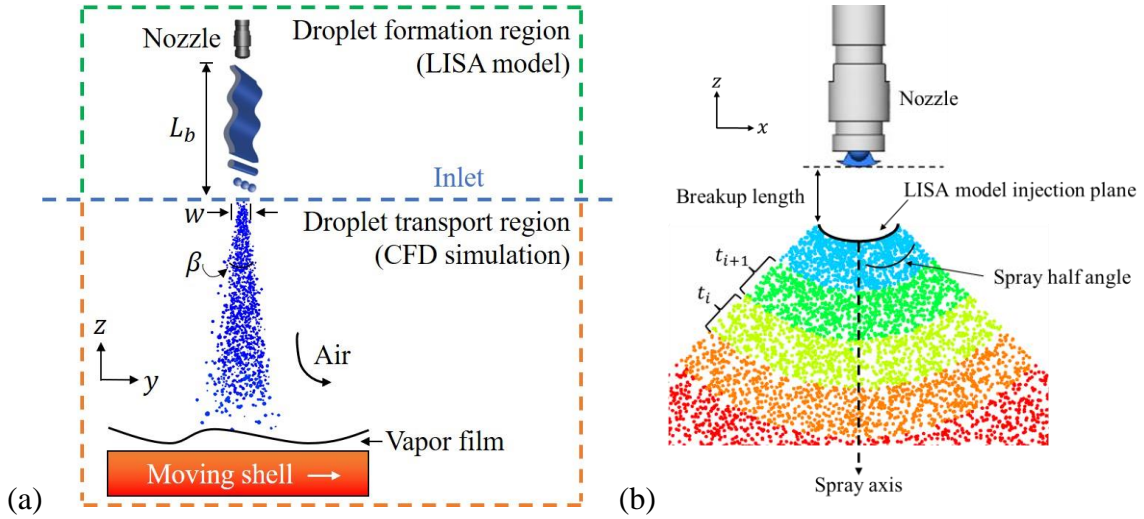
Figure 2-3. Illustration of the droplet formation simulation strategy and the injection location for hydraulic nozzles: (a) side view, and (b) front view.

At the breakup length, droplet size distribution is assumed to satisfy Rosin-Rammler distribution with a spread number of 3.5 [230]. The mass fraction of droplet and the mean diameter of the distribution is determined by:

$$Y_d = \exp\left[-\left(\frac{d_d}{d_0}\right)^{3.5}\right]$$

(70)

$$d_0 = 1.88d_L(1 + 3\text{Oh})^{1/6}$$

(71)

114

The dimension of the injection plane at the breakup length can be found from the geometric relations shown in Figure 2-4 (a) and (b). It is assumed that the jet expands linearly in both the x and y directions within the breakup length. Therefore, the dimensions of the droplet injection plane at the breakup length can be expressed as:

$$L_{inj} = 2L_b tan \frac{\alpha_{spray}}{2} + L_{noz} \tag{72}$$

$$w_{inj} = 2L_b tan \frac{\beta_{spread}}{2} + w_{noz} \tag{73}$$

Where L_0 and w_0 are the length and width of nozzle exit, respectively. α is the spray angle, and it expands along the x direction. β is the spread angle and is measured along the y direction. At the beginning of each droplet time step, a group of droplets satisfying Rosin-Rammler distribution are randomly injected into the computational domain from the injection plane that is confined by spray characteristics, as shown in Figure 2-4 (b).
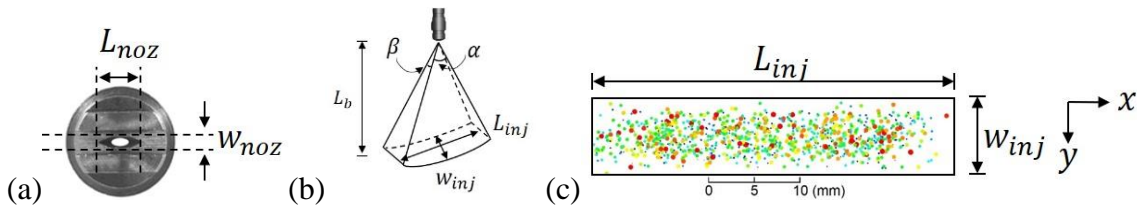
Figure 2-4. Droplet formation calculation: (a) dimensions of nozzle exit, (b) geometric relations between droplet formation location and jet characteristics, and (c) top view of droplet distribution at the injection location.

Droplet formation from an air-mist nozzle

Two-fluid nozzles have many advantages over single-fluid hydraulic nozzles, such as high flexibility in terms of steel grades and slab sizes, high heat transfer rate, and much fewer nozzle clogging issues. Due to these desired features, an increasing number of modern continuous casting machines have been equipped with two-fluid nozzles, mostly air-mist nozzles. The secondary fluid, air in air-mist nozzles, accelerates the breakup of the water sheet through intense two-phase interactions. Air is introduced to the liquid flow inside the nozzle so that the two-phase interactions can reach a much higher level. The primary feature of air-mist nozzles is the length mixing

chamber compared to the short fluid passage of hydraulic nozzles. The primary breakup process is believed to be the same, but the breakup length is drastically reduced for air-mist nozzles. Because of the intricate two-phase flow interaction and many external and internal forces involved, theoretical models and empirical correlations of the breakup length and the droplet size distribution after the primary breakup process have yet to be available.

Without such information, the aforementioned simulation strategy for hydraulic nozzles is no longer suitable for air-mist nozzles. One alternative is to employ the Volume-Of-Fluid (VOF) method to numerically track the two-phase interfaces throughout the primary breakup process. This approach, however, would require significant fine mesh cells around the interfaces of the two fluids. Besides, the time step size of the simulation must be at least comparable to the breakup time scale. Otherwise, the simulation might diverge very quickly. These limitations substantially increase the computational time, which counterbalances the gained accuracy of the interface predictions.

Recently years, a growing number of researchers have started to look into ways to couple the VOF and Discrete Phase Model (DPM) together [231, 232]. Hence, the primary breakup process, which includes small structures such as thin liquid sheet and ligaments, can be resolved by the VOF model, and the droplets from the primary breakup process, which are almost spherical, can be transitioned to the DPM model and tracked in the Lagrangian frame with much lower computational cost.
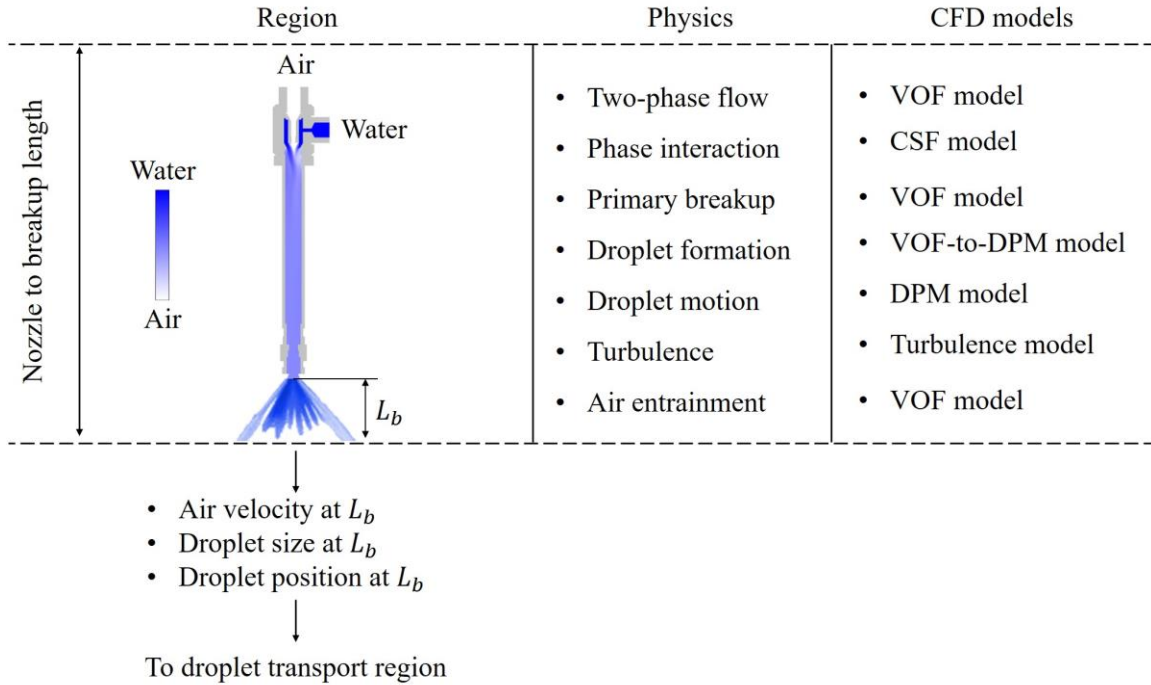
Figure 2-5. Simulation strategy and models for air-mist nozzles.

Figure 2-5 shows the application of the coupled model in the secondary cooling process. The computational domain includes the entire section of the nozzle and a region below the nozzle orifice for the primary breakup process to develop. Air and water are pumped into the nozzle through two perpendicular inlets. The two fluids are guided to a lengthy mixing chamber to undergo two-phase interactions. Liquid water mixed with high-velocity air forms a thin sheet at the nozzle orifice and later breaks up into numerous ligaments, further breaking into near-spherical droplets. The VOF model simulates the phenomena described above. The current study adopts the transient VOF simulation to resolve the intricate two-phase interactions.

The VOF model is designed for two or more immiscible fluids where the position and shape of the interface between the fluids are of interest. In the VOF model, different fluids share the same set of conservation equations for mass, momentum, and energy. Because the fluids are immiscible to one another, the volume occupied by one fluid can not be shared by others. Thus, different fluids can be represented by a single variable, the volume fraction. The volume fraction of one fluid is the ratio of the fluid and the cell volume. In each control volume, the sum of the volume fractions must be unity. For air-water two-phase simulation, the sum of the volume fractions is:

117

$$\alpha_a + \alpha_l = 1 \tag{74}$$

Where α_a and α_l are the volume fraction of air and water, respectively. The volume fractions can be found by solving the following continuity equations for each phase:

$$\frac{\partial}{\partial t}(\alpha_a \rho_a) + \nabla \cdot (\alpha_a \rho_a \vec{u}) = S_{trsn,a} \tag{75}$$

$$\frac{\partial}{\partial t}(\alpha_l \rho_l) + \nabla \cdot (\alpha_l \rho_l \vec{u}) = S_{trsn,l} \tag{76}$$

Where ρ_a and ρ_l are densities of air and water, respectively. S_{trsn} is the mass source term and is defined in Eq. (89) and Eq. (90) for air and water, respectively. u is the velocity of fluid. Because the two phases share a single set of momentum and energy conservation equations, both phases have the same velocity and temperature. The velocity can be found by solving the following momentum equation for both phases:

$$\frac{\partial}{\partial t}(\rho \vec{u}) + \nabla \cdot (\rho \vec{u} \vec{u}) = -\nabla P + \nabla[\mu(\nabla \vec{u} + \nabla \vec{u}^T)] + \rho \vec{g} + F_{a-l} \tag{77}$$

Where ρ is the density of the two-phase mixture in each control volume, and it is defined as follows:

$$\rho = \alpha_a \rho_a + (1 - \alpha_a)\rho_l \tag{78}$$

F_{a-l} defined in Eq. (77) is the source term due to the surface tension along the air-water interface. The following continuum surface force (CSF) model is adopted to compute this term [233]:

$$F_{a-l} = \frac{\sigma_{a-l} \rho \kappa_a \nabla \alpha_a}{0.5(\rho_a + \rho_l)} \tag{79}$$

Where σ_{a-l} is the surface tension between air and water, and it is constant along the interface. ρ is the density of the two-phase mixture in each control volume, and it can be evaluated from Eq. (78). κ_a is the curvature of the interface, and it is defined in terms of the divergence of the unite normal:

$$\kappa_a = \nabla \cdot \frac{n}{|n|} \tag{80}$$

Where n is the surface normal, and it is defined as the gradient of the volume fraction of air:

$$n = \nabla \alpha_a \tag{81}$$

The energy equation for both air and water is defined as follows:

$$\frac{\partial}{\partial t}(\rho E) + \nabla \cdot [\vec{u}(\rho E + P)] = \nabla \cdot \left(\lambda_{eff} \nabla T \right) \tag{82}$$

Where E is the total energy, P is the pressure, λ_{eff} is the effective conductivity and is defined in Eq. (46), T is the temperature. E and T are calculated from the following mass-averaged method:

$$E = \frac{\alpha_a \rho_a E_a + \alpha_l \rho_l E_l}{\alpha_a \rho_a + \alpha_l \rho_l} \tag{83}$$

$$T = \frac{\alpha_a \rho_a T_a + \alpha_l \rho_l T_l}{\alpha_a \rho_a + \alpha_l \rho_l} \tag{84}$$

Where E_a and E_l are the total energy for air and water, respectively. T_a and T are the temperature for air and water, respectively.

Once the ligament breakup and the droplet formation process concludes at the breakup length, any liquid lump satisfying three transition criteria will be removed from the VOF simulation and converted to a particle parcel in the Lagrangian frame. Figure 2-6 illustrates the three transition criteria. These criteria are examined at the end of each VOF time step. A designated solver will

identify the broken liquid ligaments, referred to as lumps [234], and classify the lumps by one size criterion and two geometric criteria.
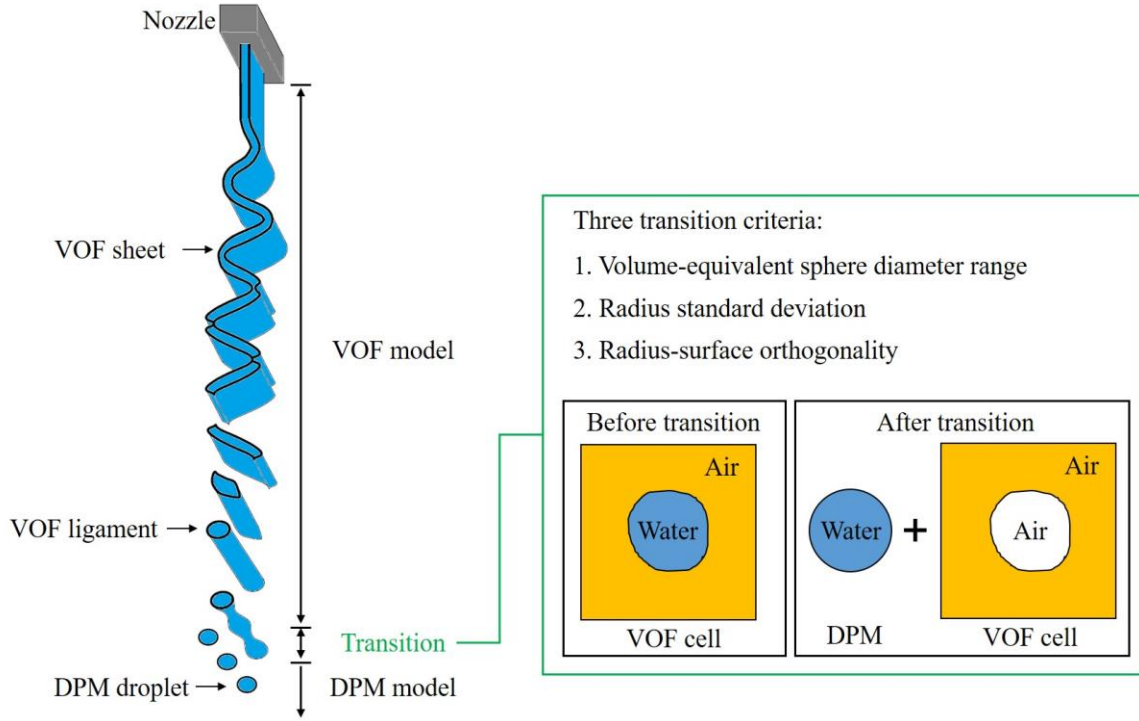
Figure 2-6. Transition criteria from the VOF model to the DPM model.

The volume-equivalent sphere diameter range sets the minimum and maximum diameters for a volume-equivalent sphere. Liquid ligament with the volume-equivalent sphere diameter inside this range will be converted to DPM droplet:

$$d_{min} \leq d_{lump} \leq d_{max} \qquad (85)$$

Where d_{min} and d_{max} should be determined based on droplet size distribution obtained from experiments for specific nozzle types and operating conditions.

The two geometric criteria are the radius standard deviation and the radius-surface orthogonality. Figure 2-7 shows the derivation of the two criteria. The radius standard deviation, $RStd$, measures

the distance between the lump center of gravity and the facet center of the lump interface in each control volume:

$$RStd = \frac{\sqrt{\frac{1}{N}\sum_{i=1}^{N}(r_i - r_g)^2}}{\frac{1}{N}\sum_{i=1}^{N} r_i} \tag{86}$$

Where r_g is the lump center of gravity and can be found by using the following definition:

$$r_g = \frac{\sum_{i=1}^{N} m_i r_i}{\sum_{i=1}^{N} m_i} \tag{87}$$

Where m_i is the lump mass in i^{th} control volume.

The denominator in Eq. (86) represents the average radius of the liquid lump. By normalizing the standard deviation over the average radius, the value of $RStd$ is scaled to a number between 0 and 1. A value of 0 represents a perfect sphere. An increasing $RStd$ indicates more deviations of the liquid lump to a perfect sphere.

Another geometric criterion is the radius-surface orthogonality, RSO, which computes the facet area-weighted average degree between the facet unit normal and the vector from the lump center of gravity to the facet center:

$$RSO = \frac{\sum_{i=1}^{N} A_i \frac{\vec{n}_i \cdot \vec{r}_i}{|\vec{r}_i|}}{\sum_{i=1}^{N} A_i} \tag{88}$$

Where A_i is the facet area in i^{th} control volume, $\vec{n}_i$ is the facet unit normal in i^{th} control volume, $\vec{r}_i$ is the vector from the lump center of gravity to the facet center i^{th} control volume. The scaled RSO also ranges from 0 to 1, and a value of 0 represents a perfect sphere.
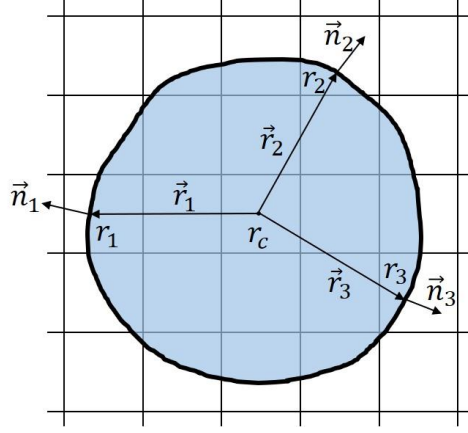
Figure 2-7. A cross-section view of a liquid lump overlapping on control volumes.

A value of 0.5 is recommended for both $RStd$ and RSO as the upper limit for most spray-related simulations [234, 235]. A liquid lump that meets all three transition criteria at the end of each VOF time step will be converted to DPM particles. As shown in Figure 2-6, the mass of the liquid lump that is marked for transition is deleted from the liquid phase through a mass source term:

$$S_{trsn,l} = \frac{\rho_l V_l}{\Delta t} \tag{89}$$

Where V_l is the liquid lump that satisfies transition criteria and will be converted to DPM particles.

On the other hand, because the DPM model is built on the "point mass" assumption, the generated DPM particle after transition does not impose volume displacement in the control volume where the liquid lump is deleted. To avoid incorrect solutions after the transition, another mass source term is added to the continuity equation of the gas phase to force the volume conservation in the control volume. The mass source term is derived by assuming a volume of gas with the same volume as the liquid lump fills in the "void" that is occupied by the liquid lump before the transition:

$$S_{trsn,a} = \frac{\rho_a V_a}{\Delta t} \tag{90}$$

Where V_a is the volume of the gas, and it is forced to equal to V_l in order to maintain the volume conservation before and after the transition.

122

After the transition, a DPM particle or a group of DPM particles will be injected from the corresponding control volumes where the liquid lump is deleted. The number of DPM particles created from the liquid lump depends on the relative size between the lump and the control volume. If the lump is smaller than the control volume, a single DPM particle will be placed in the same control volume after the transition. If the lump spans several control volumes before the transition, then the lump will be converted to as many DPM particles as the number of control volumes occupied by the lump. The magnitude and direction of the lump velocity at the cell centroid is assigned to the DPM particle to ensure consistency of the spray.

Droplet motion

The unsteady stochastic tracking method is used to predict the trajectories of droplets throughout their lifetime. As soon as droplets are injected into the computational domain, either from the LISA model in the simulation of hydraulic nozzles or from the VOF-to-DPM transition in the simulation of air-mist nozzles, they are subject to multiple external forces such as gravitational force, drag force, buoyancy force, and many others. Studies have shown that gravitational force and drag force are the only dominant forces in most jet cooling-related applications [236]. Thus, by neglecting other forces, the motion of a droplet can be solved based on Newton's second law:

$$\frac{d\vec{u}_d}{dt} = \frac{3\mu_d C_D \mathrm{Re}_D}{4\rho_d d_d^2}(\vec{u}_a - \vec{u}_d) + \frac{\vec{g}(\rho_d - \rho_a)}{\rho_d} \tag{91}$$

Where $\vec{u}_a$ is the instantaneous velocity of the gas phase, μ_d is the dynamic viscosity, ρ_d and ρ_a are the density of droplet and air, respectively. d_d is the diameter, Re_D is the Reynolds number used to determine the drag coefficient and is defined as follows:

$$\mathrm{Re}_D = \frac{\rho_a d_d |\vec{u}_a - \vec{u}_d|}{\mu_a} \tag{92}$$

Where ρ_a and μ_a are the density and the dynamic viscosity of the gas phase.

The two terms on the right-hand side of Eq. (91) represent the drag force and the gravitational force due to the relative movement between the droplet and the surrounding gas mixture. The drag coefficient, C_D, is calculated from a piecewise function for the spherical droplet [91]:

$$C_D = \begin{cases} 0.424 & \text{Re}_d > 1000 \\ \dfrac{24}{\text{Re}_d}\left(1 + \dfrac{1}{6}\text{Re}_d^{2/3}\right) & \text{Re}_d \leq 1000 \end{cases} \tag{93}$$

The effect of turbulence in the continuous phases on the dispersion of droplets is simulated by considering the fluctuating gas phase velocity. The instantaneous velocity in Eq. (91) and Eq. (92) is the sum of the mean velocity and the fluctuation velocity of the gas phase:

$$\vec{u}_a = \vec{\bar{u}}_a + \vec{u}'_a \tag{94}$$

Where $\vec{\bar{u}}_a$ is the mean gas velocity and $\vec{u}'_a$ is the fluctuating gas phase velocity.

The eddy lifetime model is used to predict the fluctuating gas phase velocity [237]. The model assumes the turbulence in the continuous phase is isotropic and satisfies a Gaussian distribution. The standard deviation of the Gaussian distribution is related to the turbulence kinetic energy by:

$$\sigma_{std} = \sqrt{\frac{2k}{3}} \tag{95}$$

Then, the fluctuating gas phase velocity can be calculated through a random sampling process:

$$\vec{u}'_a = \gamma \sigma_{std} \tag{96}$$

Where γ is a normally distributed random number.

During each droplet time step, droplets are assumed to interact with the turbulence eddies in the continuous phase over a time interval. The interaction between a droplet and eddies should be one of the following scenarios:

(1) The relative velocity between the droplet and the gas phase is small enough so that the droplet remains within the eddy during the whole eddy lifetime, t_{edd} [215]:

$$t_{edd} = \frac{10}{3\omega}$$
(97)

Where ω is the specific dissipation rate in the k-ω model.

(2) The relative velocity between the droplet and the gas phase is sufficient to allow the droplet to cross the eddy in a transit time, t_{cro} [237]:

$$t_{cro} = -t_{rex} \ln\left(1 - \frac{L_{edd}}{t_{rex}|\vec{u}_a - \vec{u}_d|}\right)$$
(98)

Where t_{rex} is the droplet relaxation time and is defined as follows [238]:

$$t_{rex} = \frac{4\rho_d d_d}{3\rho_a C_D |\vec{u}_a - \vec{u}_d|}$$
(99)

L_{edd} shown in Eq. (98) is the eddy length scale and is evaluated from the following equation:

$$L_{edd} = t_{edd}|\vec{u}_a'|$$
(100)

Where t_{edd} is the eddy lifetime and is defined in Eq. (97). $\vec{u}_a'$ is the fluctuating gas velocity and is computed from Eq. (96).

The interaction time between a droplet and eddies should be the smaller of t_{cro} and t_{cro}:

$$t_{int} = \min(t_{cro}, t_{cro}) \tag{101}$$

The droplet is assumed to interact with eddies over the interaction time. Once this time is reached, a new normally distributed random number will be obtained to reevaluate the fluctuating gas velocity using Eq. (96).

Droplet breakup

When traveling through the gas phase, droplets are subject to breakup, collision, and evaporation. Droplet breakup occurs when surface tension force is overcome by external forces. Droplet breakup prediction is crucial for the subsequent droplet-steel impingement heat transfer, as droplet number and size undergo significant changes during this event. The simulation of the exact breakup process requires an accurate droplet surface tracking model and a force balance model. However, the exact shape of droplets before and after the breakup is not the primary interest of the current study compared to other parameters such as the number of droplets generated and their corresponding velocities and droplet diameters. Hence, the WAVE model is incorporated in the current study to predict the rate of droplet radius change and the radius of the newly-formed droplets [94]. The model assumes that breakup time and the resulting droplet size are related to the fastest-growing Kelvin-Helmholtz instability. The radius of the newly-formed droplets is proportional to the wavelength of the fastest-growing unstable surface wave on the parent droplet:

$$r_{child} = B_0 \Lambda \tag{102}$$

Where B_0 is a model constant, and a value of 0.61 is recommended [94]. Λ is the wavelength of the fastest growing wave, which leads to the breakup of droplets and is defined in Eq. (106).

The breakup rate of parent droplets is defined as follows:

$$\frac{dr_{parent}}{dt} = -\frac{r_{parent} - r_{child}}{t_b} \tag{103}$$

Where t_b is the breakup time over which parent droplets are allowed to breakup:

126

$$t_b = \frac{3.726 B_1 r_{parent}}{\Lambda \Omega} \tag{104}$$

Where B_1 is the breakup time constant, and a value of 1.73 is recommended [91]. Ω is the maximum growth rate of the fastest-growing wave. Ω and Λ can be found by maximizing Eq. (57) based on the analysis of the Kelvin-Helmholtz stability. Alternatively, they can be found by the following correlations:

$$\Omega \sqrt{\frac{\rho_d d_{parent}^3}{\sigma_d}} = \frac{0.34 + 0.38 We_{child}^{1.5}}{(1 + Oh)(1 + 1.4 Ta^{0.6})} \tag{105}$$

$$\frac{\Lambda}{d_{parent}} = 9.02 \frac{(1 + 0.45 Oh^{0.5})(1 + 0.4 Ta^{0.7})}{(1 + 0.87 We_{child}^{1.67})^{0.6}} \tag{106}$$

Where We_{child} is the Weber number of the child droplets and is defined as follows:

$$We_{child} = \frac{\rho_d d_{child} |\vec{u}_{child}|^2}{\sigma_d} \tag{107}$$

Oh and Ta shown in Eq. (105) and Eq. (106) are the Ohnesorge number and the Taylor number, which are defined as follows:

$$Oh = \frac{\sqrt{We_{parent}}}{Re_{parent}} \tag{108}$$

$$Ta = Oh \sqrt{We_{child}} \tag{109}$$

Where We_{parent} and Re_{parent} are the Weber number and the Reynolds number of parent droplets, which are defined as follows:

$$We_{parent} = \frac{\rho_d d_{parent} |\vec{u}_{parent}|^2}{\sigma_d} \tag{110}$$

$$\text{Re}_{parent} = \frac{\rho_d d_{parent} |\vec{u}_{parent}|}{\mu_d} \tag{111}$$

During the breakup, mass is accumulated from the parent drop until the shed mass is equal to 5% of the initial parcel mass. At this time, a new parcel is created with a radius given by Eq. (102). The new parcel is given the same properties as the parent parcel except for radius and velocity. The new parcel is given a component of velocity randomly selected in the plane orthogonal to the direction vector of the parent parcel, and the momentum of the parent parcel is adjusted so that momentum is conserved. The velocity magnitude of the new parcel is the same as the parent parcel.

Droplet collision

The droplet coalescence model is based on the O'Rourke method [118]. The method is a stochastic estimate of collisions. Two droplets must present at the same cell in order to be considered for coalescence. When this condition is satisfied, rather than calculating whether or not the trajectories of two droplets intersect, the algorithm calculates the probability of the smaller droplet being within the collision volume centered at, the larger droplet. The collision volume is defined as a cylinder with a circular area of $\pi(r_1 + r_2)^2$ and a length of $(\vec{u}_1 - \vec{u}_2)\Delta t$. The subscript 1 donates to the larger droplet and the subscript 2 represents the smaller droplet. If the smaller droplet is somewhere within the collision volume, the two droplets are subject to a collision. Depending on the offset of the larger droplet center and the trajectory of the smaller droplet, there are two possible collision outcomes, namely coalescence, and bouncing. The possibility of collision between the two droplets are:

$$P(n) = e^{-\bar{n}} \frac{\bar{n}^n}{n!} \tag{112}$$

$$\bar{n} = \frac{n_2 \pi (r_1 + r_2)^2 (\vec{u}_1 - \vec{u}_2)\Delta t}{V_{cell}} \tag{113}$$

Where n is the number of collisions, $\bar{n}$ is the mean expected number, V_{cell} is the control volume where the smaller droplet presents.

The outcome of a collision depends on the offset of the trajectory of the smaller droplet to the larger droplet. The offset is a function of the center distance between the two droplets and a random number, which resembles the randomness of collisions:

$$b_{offset} = (r_1 + r_2)\sqrt{\gamma} \tag{114}$$

Where γ is a random number between 0 and 1.

The calculated offset is compared with a critical value defined as follows:

$$b_c = (r_1 + r_2)\sqrt{min\left\{1.0, \frac{2.4}{We}\left[\left(\frac{r_1}{r_2}\right)^3 - 2.4\left(\frac{r_1}{r_2}\right)^2 + 2.7\left(\frac{r_1}{r_2}\right)\right]\right\}} \tag{115}$$

If $b_{offset} < b_c$, the two droplets are considered to coalesce. Otherwise, the two bounce off from each other. After the collision, the magnitude and direction of droplet velocities are computed from the conservation of kinetic energy and momentum.

Droplet-wall impingement heat transfer

The Droplets-wall impingement heat transfer model predicts the impingement outcome and the heat and mass transfer between droplets and the hot surface. It is worth mentioning that the slab temperature is higher than the Leidenfrost temperature throughout the entire continuous casting process [239]. At high surface temperature, liquid droplets boil immediately after impingement and form a thin vapor film above the surface. Later heat transfer between the incoming droplets and the surface must go through the vapor film [137]. The wall-jet model is used to estimate the outcomes of jet impingement under such conditions. There are three possible outcomes: stick, reflect, and wall-jet based on the previous research [36], as illustrated in Figure 2-8.
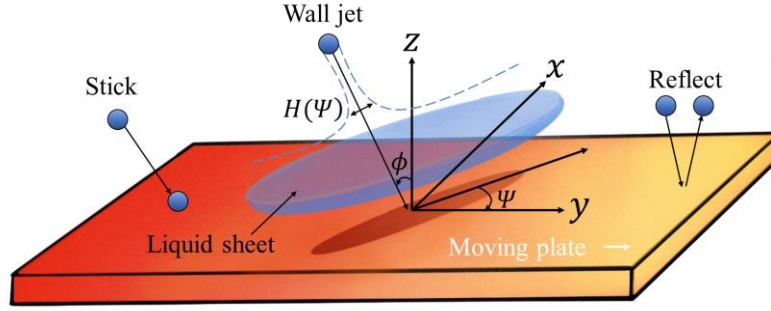
Figure 2-8. Illustration of the drop-wall impingement model.

The droplet loses all velocity components in the stick mode and stays on the surface until complete vaporization. In the reflect mode, the droplet leaves the surface after impingement with the direction of the vertical component of velocity inversed while the tangent velocity is unchanged. In the last mode, the droplet is assumed to glide on the surface after impingement in the manner of a liquid jet issued from the stagnation point. Under such an assumption, a group of gliding droplets can be viewed as the movement of a liquid sheet with a height of H above the vapor film. An empirical relation for H with regard to the impingement angle ϕ and the exit angle Ψ is given by [36]:

$$
H_{sheet} = H_\pi \exp\left[\zeta\left(1 - \frac{\Psi}{\pi}\right)\right]
$$

(116)

Where H_π is the height at $\Psi = \pi$. The parameter ζ can be determined from the mass and momentum conservation of the liquid sheet and can be related to the impingement angle ϕ by:

$$
\sin(\phi) = \frac{\exp(\zeta) + 1}{[\exp(\zeta) - 1]\left[1 + \left(\frac{\pi}{\zeta}\right)^2\right]}
$$

(117)

The exit angle is computed from the integration of Eq. (116) by interpreting the sheet height as the probability that a droplet leaves the impingement point at an angle between Ψ and $\Psi + \Delta\Psi$:

$$\Psi = -\frac{\pi}{\zeta}\ln\{1 - \gamma[1 - \exp(-\zeta)]\} \tag{118}$$

As the current study focuses on jet impingement cooling in steady-state industrial applications, the formation of the vapor film at the start of the jet impingement cooling process and the interaction between the vapor film and the impinging droplets are neglected the simulation. However, the effect of the vapor film is taken into account in the current study by considering partial heat transfer:

$$q''_{par} = \varepsilon_{eff} q''_{max} \tag{119}$$

Where ε_{eff} is the heat transfer effectiveness and q_{max} is the maximum possible heat flux that can be released from the complete vaporization of a droplet.

The maximum heat transfer happens in the nucleate boiling stage, where no vapor film exists on the surface. In this situation, when a spherical droplet impinges on the surface, it is assumed to deform into an equal-volume cylinder with a height of twice the distance between the droplet center and the hot surface for a short period of time, t_{cond}, as shown in Figure 2-9.
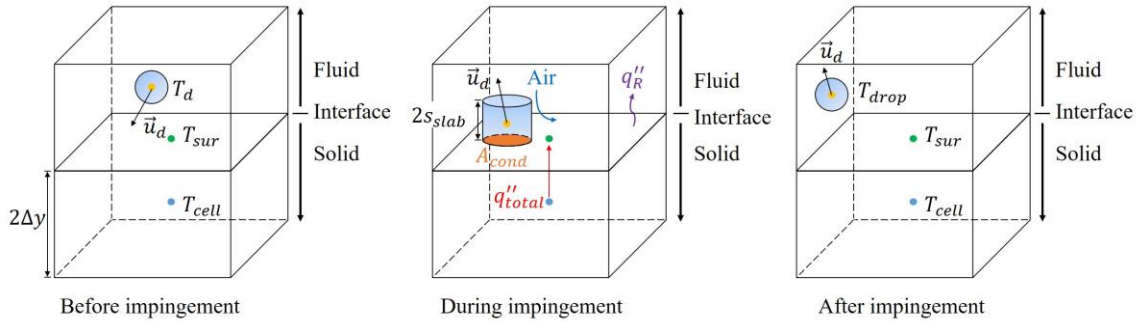
Figure 2-9. Illustration of the droplet-wall heat transfer model.

The deformed droplet and the surface undergo pure conduction through the effective contact area A_{cond}:

$$\frac{d}{dt}(m_d c_{p,d} T_d) = \frac{\lambda_d A_{cond}}{s}(T_{sur} - T_d) \tag{120}$$

Where effective contact area and the contact time are calculated from the following expressions, respectively [240, 241]:

$$A_{cond} = \frac{\pi}{8}(0.61 d_d \text{We}^{0.38})^2 \tag{121}$$

$$t_{cond} = \frac{\pi}{4}\sqrt{\frac{\rho_d d_d^3}{\sigma}} \tag{122}$$

The maximum heat flux then can be calculated by computing the enthalpy difference between vapor and liquid droplet:

$$q''_{max} = m_v\left[c_{p,d}T_d + c_{p,d}(T_{sat} - T_d) + h_{fg} + c_{p,v}(T_{sur} - T_{sat})\right] - m_d c_{p,d} T_d \tag{123}$$

Considering $m_v = m_{drop}$ due to mass conservation, Eq. (123) reduces to:

$$q''_{max} = m_d\left[c_{p,d}(T_{sat} - T_d) + h_{fg} + c_{p,v}(T_{sur} - T_{sat})\right] \tag{124}$$

In the presence of vapor film, the amount of heat flux absorbed by the droplet reduces due to the low thermal conductivity of water vapor compared to that of liquid water. The vapor film hovering above the surface acts as an insulation blanket. The actual heat flux is considered as a fraction of the maximum possible heat flux. The ratio of the actual heat flux and the maximum heat flux, ε_{eff}, is obtained from the following experiment-based empirical correlations [150]:

$$T_{sur} > T_{LF}: \qquad \varepsilon_{eff} = 3.771 \times 10^{-3}\text{We}^{0.691}\exp\left(-9.079 \times 10^{-4}\text{We}\right) \tag{125}$$

$$T_{sur} \leq T_{LF}: \qquad \varepsilon_{eff} = 9.844 \times 10^{-2}\text{We}^{0.3428} \tag{126}$$

Where T_{sur} is the slab surface temperature, T_{LF} is the Leidenfrost temperature, We is the droplet Weber number prior to impingement. Eq. (125) and Eq. (126) are applied to different heat transfer regimes. When $T_{sur} > T_{LF}$, heat transfer on the slab surface is in the film boiling regime. The

generated vapor film is steady on the slab surface and will prevent droplets from directly contacting the slab surface. As shown in Figure 2-10, the heat transfer effectiveness is less than 0.2 in the film boiling regime as the slab temperature decreases to below the Leidenfrost temperature, the film boiling regime changes to the transition boiling regime, which later shifts to the nucleate boiling regime. Because the superheat temperature decreases, the vapor layer collapses and becomes unstable. Without the blockage of the vapor layer, droplets can deposit on the slab surface while conducting heat transfer. The higher heat transfer effectiveness shown in Figure 2-10 acknowledges the drastic increase of heat flux due to the collapse of the vapor layer.
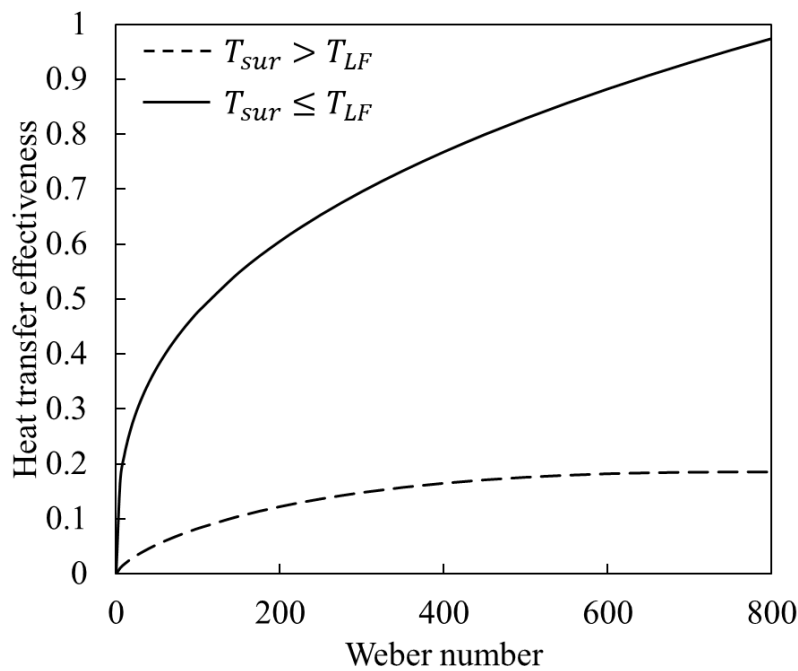
Figure 2-10. Heat transfer effectiveness as a function of droplet impinging Weber number.

Figure 2-10 also provides other insights into the mechanisms behind the change of heat transfer rate. The area enclosed by the two lines of heat transfer effectiveness indicates the potential improvement of spray cooling. As previously described, the difference between the two lines is the existence of the vapor layer. The low thermal conductivity of the vapor layer dominates the near-wall heat transfer when the slab surface temperature is high. To gain the additional heat transfer, methods that can break the vapor layer are encouraged. Increasing the spray flow rate to allow droplets to penetrate the vapor layer is one such method. Another interesting area on the plot is between the solid line and unity. This area represents the contact behavior of droplets. Although

droplets are not perfectly spherical during atomization, they still retain some curves on the surface. When droplets impinge onto the surface, they either break up into several child droplets or spread on the surface due to momentum conservation. Heat transfer between a droplet and the slab surface occurs when the droplet deforms and creates a sufficient contact area. As Eq. (120) and Eq. (121) state, the heat transfer rate is proportional to the contact area, which is a function of droplet Weber number. Thus, the area above the solid line in Figure 2-10 recognizes the limit of droplet deform upon impingement and the fact that the contact area is always smaller than the droplet surface area.

Eq. (125) and Eq. (126) are both incorporated into the impingement heat transfer model. A routine checks the droplet Weber number once the droplet is marked for impingement and calculates the corresponding heat transfer effectiveness. The criteria for selecting the heat transfer effectiveness are the local surface temperature and the Leidenfrost temperature. The local surface temperature varies on the slab surface, but it can be obtained from the last iteration of the continuous phase before the iteration of the discrete phase starts. The Leidenfrost temperature is another unknown, and it depends on the steel composition, surface condition, spray water flux, operating pressure, droplet size, and many others. Table 1-11 summarizes some of the correlations for predicting the Leidenfrost temperature in spray cooling applications. The data points are depicted in Figure 2-11. The values of the Leidenfrost temperature scatter over a wide range of temperatures, owning to different experiment conditions. Despite the wide range of the Leidenfrost temperature, some trends can still be interpreted from Figure 2-11. The Leidenfrost temperature strongly depends on the spray water flow rate and operating pressure, which affect the heat transfer by changing the impingement behavior and material properties of droplets. However, the influence of surface temperature is somewhat negligible. Because of the wide range of the Leidenfrost temperature, using a constant value as the transition criterion for the heat transfer effectiveness will result in considerable uncertainty. Upon examining the experiment conditions, the current study adopts the correlation developed by Hnizdil et al. to calculate the local Leidenfrost temperature at each droplet time step [145], because their experimental conditions were specifically designed for the typical secondary cooling process. The correlation is shown as follows:

$$T_{LF} = 351Q_w^{0.111}u_d^{0.174}D_{32}^{0.006} \tag{127}$$

Where Q_w is the spray water flux in l/m^2·s, u_d is the droplet mean velocity, and D_{32} is the Sauter mean diameter.
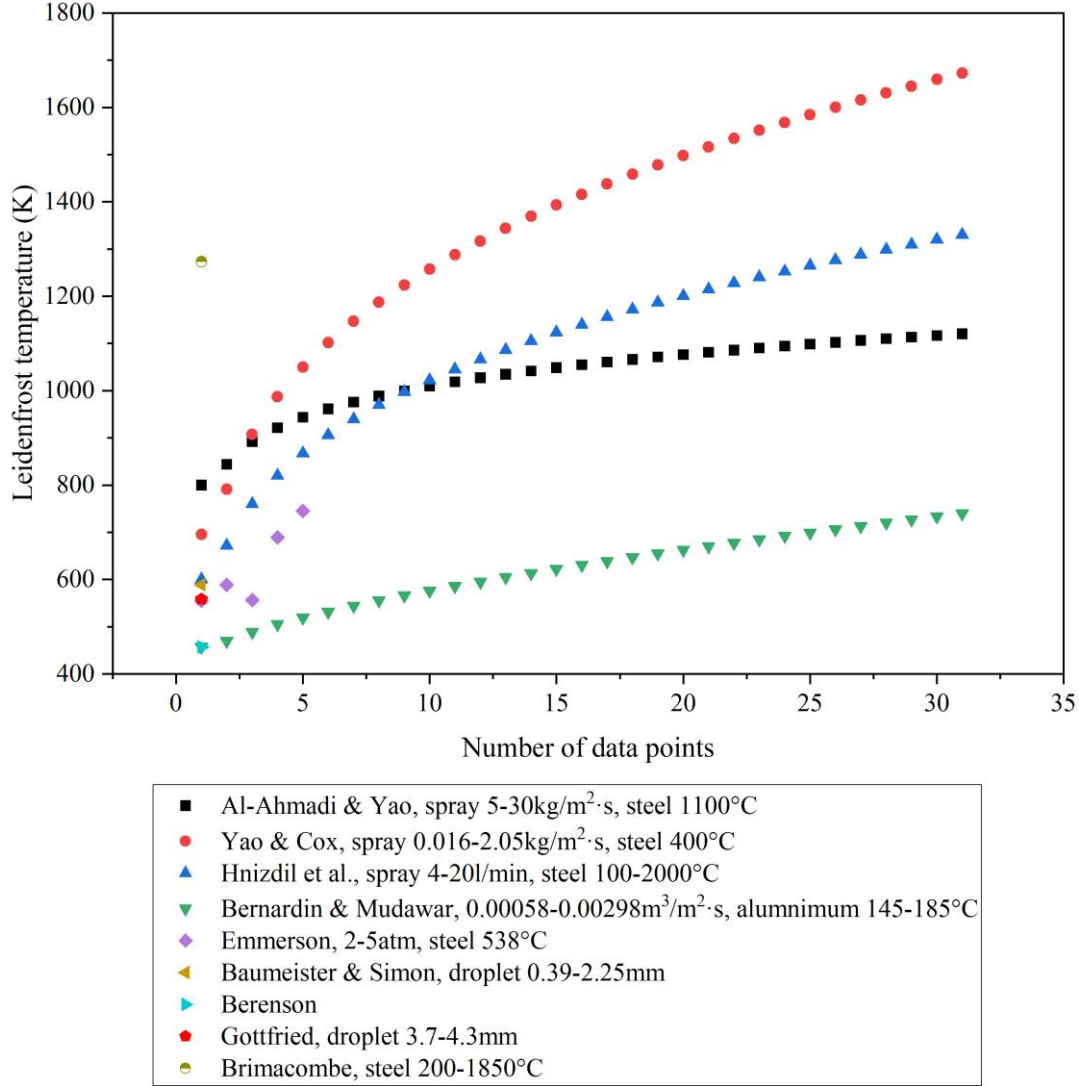
Figure 2-11. Leidenfrost temperature of steel obtained from open literature [143, 145, 146 , 148, 149, 151, 242, 243].

Once droplet temperature reaches the boiling point, a portion of the liquid droplet becomes water vapor, and the mass of the vapor is:

$$m_v = \frac{(\varepsilon_{eff} - 1)m_d c_{p,d}(T_{sat} - T_d) + \varepsilon_{eff} m_d h_{fg} + \varepsilon_{eff} m_d c_{p,v}(T_{sur} - T_{sat})}{h_{fg} + c_{p,v}(T_{sur} - T_{sat})} \tag{128}$$

A routine subtracts the computed vapor mass for each droplet after every impingement within one droplet time step. Droplet size also reduces due to mass transfer. The new droplet diameter can be found from the remaining droplet mass with the assumption that the droplet returns to spherical shape after the brief contact:

$$d_{d,new} = \left[\frac{6(m_d - m_v)}{\pi \rho_d}\right]^{1/3}$$

(129)

HTC on the hot surface due to jet impingement cooling and jet-induced convection is computed in the post-processing stage considering energy conservation, as shown in Figure 2-9. Between a fluid-type computational cell and its adjacent solid-type cell, heat transfers from the center of the solid cell to the solid-fluid interface by conduction and then dissipates into the environment through conduction to droplets, convection, and radiation. The heat flux across the solid-fluid interface is conserved. By applying Newton's law of cooling and the definition of HTC above, the total heat flux through the interface can be expressed as:

$$q''_{total} = \frac{\lambda_{steel}(T_{cell} - T_{sur})}{\Delta y} = \text{HTC}(T_{sur} - T_{drop}) + q''_R$$

(130)

Where T_{cell} is the temperature of the solid cell centroid. T_{face} is the temperature of the interface centroid. Δy is the distance from the solid cell centroid to the face centroid. Rearranging Eq. (130) can yield the following expression for HTC:

$$\text{HTC} = \frac{\lambda_{steel}(T_{cell} - T_{sur}) - \Delta y q''_R}{\Delta y (T_{sur} - T_{drop})}$$

(131)

Droplet evaporation ($T_d < T_{boil}$)

Droplet evaporation due to the heat exchange with the surroundings before boiling is determined by solving the following conservation equation of energy:

$$m_d c_{p,d} \frac{dT_d}{dt} = \pi d_d^2 h_{con}(T_\infty - T_d) + \frac{dm_d}{dt} h_{fg} + \pi d_d^2 \varepsilon_{st} \sigma_{SB}(T_R^4 - T_d^4) \tag{132}$$

Where m_d is the droplet mass, $c_{p,d}$ is the droplet specific heat, T_d is the droplet temperature, h_{con} is the convective heat transfer coefficient, T_∞ is the temperature of the gas phase, h_{fg} is the latent heat, ε_{st} is the droplet emissivity, σ_{SB} is the Stefan-Boltzmann constant, T_R is the radiation temperature, and it is defined as follows:

$$T_R = \left(\frac{G}{4\sigma_{SB}}\right)^{1/4} \tag{133}$$

Where G is the incident radiation and is defined as follows:

$$G = \int_{\Omega_{sol}=4\pi} I d\Omega_{sol} \tag{134}$$

Where I is the radiation intensity, Ω_{sol} is the solid angle.

In the meantime, liquid droplet vaporizes into water vapor which then diffuses into the surrounding gas phase due to the concentration difference at the droplet surface and the bulk fluid and the convection of the bulk flow. The rate of droplet mass change is calculated by using the following expression in each droplet time step [244, 245]:

$$\frac{dm_d}{dt} = \pi d_d^2 k_c \rho_a \ln(1 + B_m) \tag{135}$$

Where k_c is the mass transfer coefficient, B_m is the Spalding number.

The mass transfer coefficient shown in Eq. (135) can be obtained from the following Sherwood number correlation [246]:

$$\mathrm{Sh}_d = \frac{k_c d_d}{D_{i,m}} = 2.0 + 0.6\mathrm{Re}_d^{0.5}\mathrm{Sc}^{0.33} \tag{136}$$

Where $D_{i,m}$ is the diffusion coefficient of vapor in the gas phase, Re_d is the droplet Reynolds number, Sc is the Schmidt number and is defined as follows:

$$\mathrm{Sc} = \frac{\mu_v}{\rho_v D_{i,m}} \tag{137}$$

Where μ_v is the dynamic viscosity of vapor, ρ_v is the density of the vapor.

The Spalding number shown in Eq. (135) is defined as follows [244, 245]:

$$B_{\mathrm{m}} = \frac{Y_{i,s} - Y_{i,\infty}}{1 - Y_{i,s}} \tag{138}$$

Where $Y_{i,s}$ is the vapor mass fraction at the droplet surface, $Y_{i,\infty}$ is the vapor mass fraction in the gas phase.

The convective heat transfer coefficient shown in Eq. (132) can be obtained from the following modified Nu number [245]:

$$\mathrm{Nu}_d = \frac{h_{con} d_d}{\lambda_a} = 2.0 + 0.6\mathrm{Re}_d^{0.5}\mathrm{Pr}^{0.33} \tag{139}$$

Where λ_a is the thermal conductivity of the gas phase, Re_d is the droplet Reynolds number, Pr is the Prandtl number and is defined as follows:

$$\mathrm{Pr} = \frac{c_{p,a}\mu_a}{\lambda_a} \tag{140}$$

Where $c_{p,a}$ and μ_a are the specific heat and the dynamic viscosity of the gas phase.

Droplet boiling ($T_d = T_{boil}$)

When droplet temperature reaches the boiling temperature, Eq. (132) is modified to calculate the mass transfer rate of the droplet by assuming that the droplet temperature remains constant:

$$\frac{dm_d}{dt} h_{fg} = \pi d_d^2 h_{con}(T_\infty - T_d) + \pi d_d^2 \varepsilon_{st} \sigma_{SB}(T_R^4 - T_d^4) \tag{141}$$

Because droplet boils at constant temperature and it is assumed to be a perfect sphere throughout the boiling process, the droplet mass shown in Eq. (141) can be expressed as follows:

$$m_d = \frac{\pi d_d^3 \rho_d}{6} \tag{142}$$

Thus, the rate of mass change can be expressed as the rate of droplet diameter change:

$$\frac{dm_d}{dt} = \frac{d}{dt}\left(\frac{\pi d_d^3 \rho_d}{6}\right) = \frac{\pi \rho_d}{6}\frac{d(d_d^3)}{dt} = \frac{\pi \rho_d}{6} 3d_d^2 \frac{d(d_d)}{dt} = \frac{\pi d_d^2 \rho_d}{2}\frac{d(d_d)}{dt} \tag{143}$$

Replacing the rate of mass change in Eq. (132) with Eq. (143) and using the Nusselt number correlation for defined in Eq. (139) for the convective heat transfer coefficient shown in Eq. (141), yields the following boiling rate equation:

$$\frac{d(d_d)}{dt} = \frac{2}{\rho_d h_{fg}}\left[\frac{\lambda_a}{d_d}(2.0 + 0.6\mathrm{Re}_d^{0.5}\mathrm{Pr}^{0.33})(T_\infty - T_d) + \varepsilon_{st}\sigma_{SB}(T_R^4 - T_d^4)\right] \tag{144}$$

Two-way coupling between Eulerian and Lagrangian phases

The two-way coupling method accounts for the influences between the continuous phase and the discrete phase. The flow pattern of the continuous phase determines the solution of the discrete phase, and the presence of the discrete phase also imposes changes on the continuous phase. The influence of the continuous phase on the discrete phase is discussed in the previous sections. This section only focuses on the influence of the discrete phase on the continuous phase.

At the end of each droplet time step, the mass, momentum, and energy changes of the discrete phase due to evaporation, boiling, motion, and heat transfer are incorporated in the subsequent continuous phase calculations through source terms. The source term of mass in the continuous phase continuity equation is defined as follows:

$$S_{mass} = \frac{\dot{m}_{d,0} \Delta m_d}{m_{d,0} V_{cell}} \tag{145}$$

Where $\dot{m}_{d,0}$ is the initial mass flow rate of the droplet, $m_{d,0}$ is the initial mass of the droplet, Δm_d is the droplet mass change, V_{cell} is the volume of the cell where the droplet presents at the current time step. S_{mass} is added to Eq. (16) in the subsequent continuous phase calculations.

The source term of the continuous phase momentum equation is defined by examining the change in momentum of a droplet as it passes through each control volume:

$$S_{mom} = \left[\frac{3\mu_d C_D \text{Re}_D}{4\rho_d d_d^2} (\vec{u}_a - \vec{u}_d) + \frac{\vec{g}(\rho_d - \rho_a)}{\rho_d} \right] \frac{\dot{m}_d \Delta t}{V_{cell}} \tag{146}$$

Where the first and second terms in the square brackets on the right-hand side represent drag force and gravitational force, respectively. $\dot{m}_d$ is the mass flow rate of the droplets passing through the control volume, Δt is the droplet time step. S_{mom} is added to Eq. (17) in the subsequent continuous phase calculations.

The source term of the continuous phase energy equation is defined by examining the change in thermal energy of a droplet as it passes through each control volume:

$$S_{nrg} = \frac{\dot{m}_{d,0}}{m_{d,0} V_{cell}} \left[h_{lat}^0 (m_{d,o} - m_{d,in}) - m_{d,o} \int_{T^0}^{T_{d,o}} c_{p,d} dT + m_{d,in} \int_{T^0}^{T_{d,in}} c_{p,d} dT \right] \tag{147}$$

Where h_{lat}^0 is the latent heat at reference conditions, $m_{d,in}$ is the mass of the droplet entering the control volume, $m_{d,o}$ is the mass of the droplet leaving the control volume, $T_{d,in}$ is the temperature of the droplet entering the control volume, $T_{d,o}$ is the temperature of the droplet leaving the control volume. S_{nrg} is added to Eq. (43) in the subsequent continuous phase calculations.

The latent heat at reference conditions shown in Eq. (147) can be related to the boiling temperature as follows:

$$h_{lat}^0 = h_{lat} - \int_{T^0}^{T_{boil}} c_{p,v} dT + \int_{T^0}^{T_{boil}} c_{p,d} dT \tag{148}$$

Where h_{lat} is the latent heat at the boiling temperature, $c_{p,v}$ is the specific heat of vapor, $c_{p,d}$ is the specific heat of the droplet.

The iterative procedure for the Eulerian-Lagrangian multi-phase coupling is shown in Figure 2-12. The coupling between the continuous gas phase and the discrete phase is achieved by alternating calculations between the two. The governing equations for the gas phase are solved first using 400 steady-state iterations to establish a preliminary fluid field in the domain. Then, the droplet motion equation is solved together with the newly calculated gas velocity to find the position of the droplet at the end of a droplet time step. The changes of mass, momentum, and energy of the droplet are expressed as external source terms and incorporated into the conservation equations for the gas phase in the following steady-state iterations.
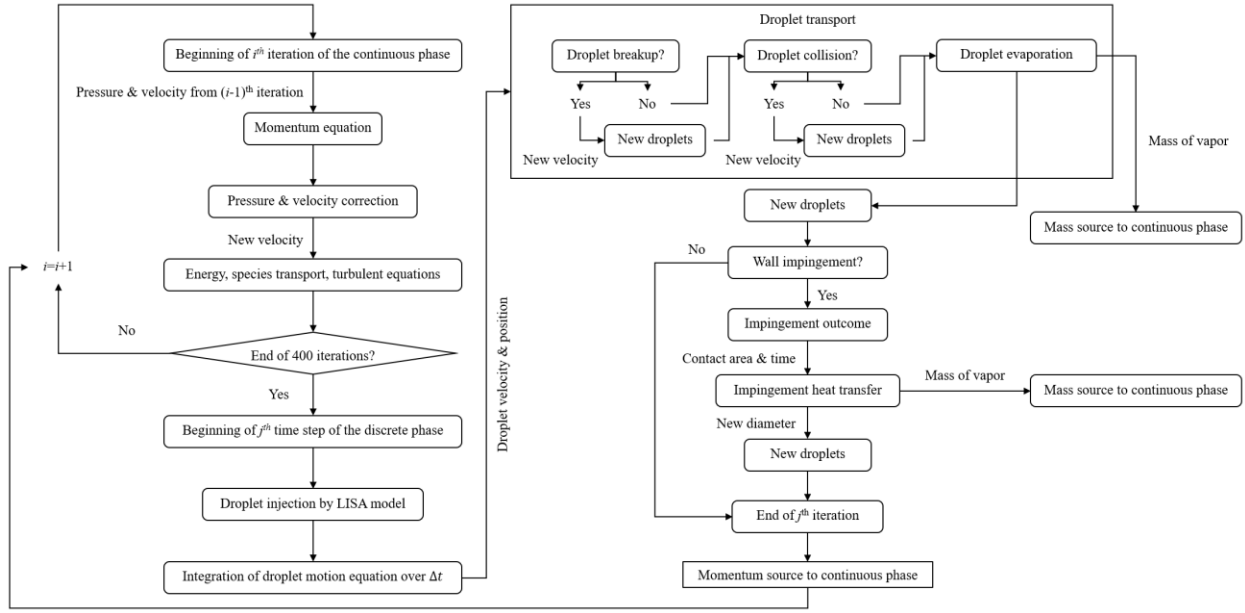
Figure 2-12. Iteration procedure for the Eulerian-Lagrangian multi-phase coupling.

2.1.3 Computational domain and boundary conditions

Computational domain

To simulate the heat transfer in the secondary cooling region, one must decide the size, location, and shape of the computational domain prior to any simulation. Ideally, a computational domain that includes the whole steel strand, rolls, and all the sprays is the best representation of a real casting machine. However, the total length of the secondary cooling region at a typical continuous casting machine is usually between 10m to 40m, whereas the average diameter of a water droplet is around 200μm. Besides the size difference, there are hundreds of spray nozzles installed in the secondary cooling, the quantity of the injected droplets every second is enormous. On the other hand, the control volumes in CFD simulations must have a comparable size to droplets in order to resolve detailed droplet-air interaction, droplet-droplet interaction, and droplet-wall interaction. Hence, a full-scale CFD simulation of a real casting machine with detailed spray simulation is not numerically feasible. In consideration of simulation efficiency, the simplified and sectioned computational domain is more practical. The sectioned domain only focuses on one spray between two adjacent rolls. One of the advantages of this approach is that the same computational domain can be used to simulate spray cooling at a different location in the secondary cooling region with a simple change of boundary conditions based on the interest of the study.

142

Hydraulic nozzle simulation

As shown in Figure 2-13, the current study considers a moving high-temperature S304 alloy steel plate cooled by a water jet issued from a flat-fan nozzle. The flat-fan nozzle is placed at a certain standoff distance above the cooling surface of the plate. The standoff distance for the baseline condition is 130mm, and it varies in the parametric study. The plate is 400 mm in length (y direction), 400 mm in width (x direction), and 30 mm in thickness (z direction) for single spray simulations. For simulations involve multiple sprays, the length, and width of the plate increase proportionally. The roll diameter and roll-to-roll distance, also referred to as roll pitch, also vary with the simulation condition. The values used in each simulation are given at the beginning of the corresponding results section. The plate is moving relative to the nozzle in the y direction during the cooling process.

Figure 2-13. Computational domain for hydraulic nozzle simulation.

As shown in Figure 2-3 (a), special treatment was made for the atomization process in the current study. It is well known that droplets are formed through two sequential breakup processes during atomization. First, the injected liquid exits the nozzle in a thin sheet form and breaks into multiple ligaments due to aerodynamic instabilities. Then, the unstable ligaments further break into spherical droplets. At the breakup length, L_b, the droplet formation process completes. The process

of sheet formation and breakup, ligament formation and breakup, and droplet formation are excluded from the current study to grain the overall computational efficiency. Owning to the fact that L_b is negligible compared to the spray distance, and the droplet size distribution at the breakup length has been well studied. A group of droplets is directly introduced into the domain at the inlet for all the simulations. Droplet size distribution at the injection location is predicted by the LISA model.

Another important aspect to mention is that the solidification of molten steel is neglected in the current study. An experiment has shown that the average solidified shell thickness at the beginning of the secondary cooling process is around 25mm, and the growth rate of the shell is estimated between 0.1mm/s to 0.4mm/s [247]. On the other hand, droplets travel at large velocities and reach a slab surface with 0.01s after injection. Since the scope of the spray cooling simulation is to investigate spray aerodynamics and droplet-slab impingement heat transfer, it is numerically convenient to exclude both the molten steel and the mushy region enclosed in the solidified shell. The steel slab in all the heat transfer simulations on the slab surface is represented by a 30mm thick solidified shell.

As for the roll contact, researchers have suggested different approaches to model the indentation mark on the slab surface. As shown in Figure 2-14, the center of the roll and the two contact points on the slab surface form an isosceles triangle. The two equal sides of the triangle are the radius of the roll, and the other side is the contact length, which is the horizontal distance between the two contact points. The angle between the two equal sides is the contact angle. Some researchers recommend a contact angle of 7° [7]. Others suggest a contact length equivalent to 10-20% of the roll diameter [10, 11]. From trigonometric relations, one can find the following constraint between the contact angle and the contact length:

$$L_{roll} = 2r_{roll} \sin\frac{\theta_{roll}}{2} \tag{149}$$

Where L_{roll} is the contact length, r_{roll} is the roll diameter, θ_{roll} is the contact angle.

Rearranging Eq. (149) and solving for θ_{roll}, yields:

$$\theta_{roll} = 2\sin^{-1}\left(\frac{L_{roll}}{2r_{roll}}\right) \tag{150}$$

Substituting the lower and upper limits of L_{roll} into Eq. (150), yields the range of the contact angle:

$$5.73° = 2\sin^{-1}\left(\frac{0.1r_{roll}}{2r_{roll}}\right) \leq \theta_{roll} \leq 2\sin^{-1}\left(\frac{0.2r_{roll}}{2r_{roll}}\right) = 11.48° \tag{151}$$

Based on the range shown in Eq. (151), a contact angle of $7°$ which is about the average is used in the current study to model the indentation marks on the slab surface.
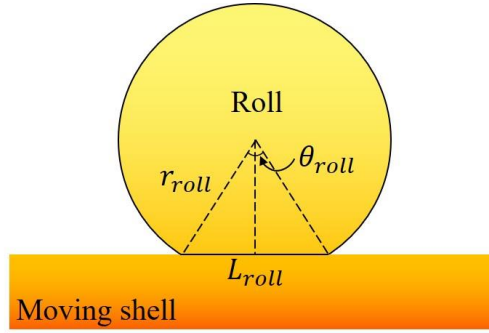
Figure 2-14. Illustration of the roll contact definition.

Air-mist nozzle simulation

Figure 2-15 (a) and (b) illustrate the computational domain for simulations with an air-mist nozzle. The simulation for each condition is consists of two separate simulations. The first simulation is conducted in the droplet formation region, including the entire nozzle and a gaseous region below the nozzle orifice. The dimension of the gas region in the first simulation is determined based on the calculation of the breakup length. A correlation derived from Arai and Hashimoto's experimental study on the disintegration of liquid sheets injected into a co-flowing air stream is used to estimate the range of the breakup length [248]. The correlation is expressed as a function of the liquid sheet thickness, gas Weber number, and liquid Reynolds number:

$$L_b = 0.123 t_{sht}^{0.5} \text{We}_a^{-0.5} \text{Re}_l^{0.6}$$ (152)

Where t_{sht} is the liquid sheet thickness, We_a is the Weber number of the air stream, Re_l is the Reynolds number of the liquid.

The liquid sheet thickness depends on both nozzle configuration and operating conditions. A study on the atomization of a liquid sheet by an impinging air stream by Fraser et al. has shown that the liquid sheet thickness varies from 30μm to 140μm at the presence of an air stream. Given that the water flow rate used in their experiment is about the average compared to that in the secondary cooling process, a value of 1000μm is set as the upper limit for the liquid sheet thickness when evaluating the breakup length. At the maximum liquid sheet thickness, the Weber number and Reynolds number shown in Eq. (152) are evaluated as follows, respectively:

$$\text{We}_a = \frac{t_{sht}\rho_a|\vec{u}_a|^2}{2\sigma} = \frac{0.001 \times 1.2 \times 20^2}{2 \times 0.0728} = 3.3$$ (153)

$$\text{Re}_l = \frac{t_{sht}\rho_l|\vec{u}_l|}{\mu_l} = \frac{0.001 \times 998.2 \times 20}{0.001} = 19964$$ (154)

Substituting the calculated values from Eq. (153) and Eq. (154) into Eq. (152) and converting the unit of the liquid sheet thickness to mm, the maximum breakup length can be estimated as follows:

$$L_b = 0.123 \times 1^{0.5} \times 3.3^{-0.5} \times 19964^{0.6} = 25.75mm$$ (155)

Thus, the liquid sheet breakup should complete within a distance of 25.75mm below the nozzle orifice. However, a value of 30mm is used in the current study as the height of the gas region in the first simulation to allow possible delays of the liquid sheet due to some other reasons. The length and the width of the gas region are set to the same value as the height. After the first simulation, the droplet distribution, including size, position, and velocity at the outlet of the gas region, is extracted and used as the inlet boundary condition for the second simulation. The computational domain for the second simulation is almost identical to the hydraulic nozzle

simulation, except the domain height is shorter. The height of the second simulation equals the difference between the standoff distance and the height of the first simulation, which equals 30mm.
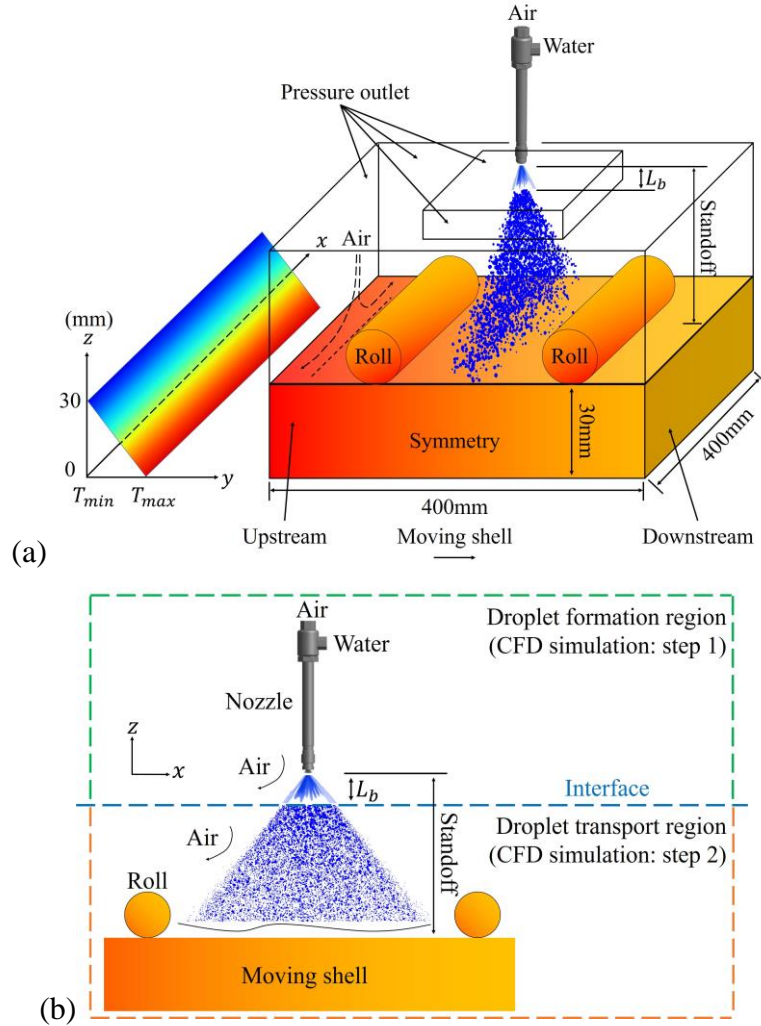
Figure 2-15. Computational domain for air-mist nozzle simulation: (a) isometric view, and (b) front view.

Boundary conditions

Boundary conditions become critical once the computational domain is chosen. Owing to the nature of the sectioned computational domain, some of the boundary surfaces used in the simulation are not physical boundaries. Measurements at such boundaries are not feasible. As shown in Figure 2-13 and Figure 2-15, there is at least one fluid region where heat transfer on the slab surface is investigated, and one solid region represents a 30mm thick solidified shell. For the

first simulation of the air-mist nozzle, the inlets for the compressed air and water are set as pressure inlet and mass flow inlet, respectively, to be consistent with the secondary cooling operation. All the side surfaces of the fluid region are set as pressure outlets, as flow through these surfaces can be adjusted according to the pressure distribution. The impingement surface is considered a conjugate heat transfer surface. In the numerical simulation, it is split into two identical and overlapping surfaces. During iterations, a conjugate heat transfer solver searches for a converged heat flux through both surfaces. The only boundary surface of the fluid region that requires special attention is the surface at the breakup length.

It is well known that turbulent jet is always associated with air entrainment due to the conservation of mass. Therefore, the wall type of boundary condition is not appropriate in this application. Both velocity inlet and pressure outlet boundary conditions can be applied to model the air entrainment effect in the simulation. The most intuitive method for the velocity inlet boundary condition is to assign a uniform velocity to the entire boundary surface, as shown in Figure 2-16 (a). It is also possible to use a non-uniform velocity profile at the boundary to account for the unevenly distributed air entrainment around the spray. Figure 2-16 (b) demonstrates a centric velocity profile on the boundary surface. Air velocity linearly decreases from the center of the injection axis, where the pressure is the lowest, and the air entrainment effect is the strongest.
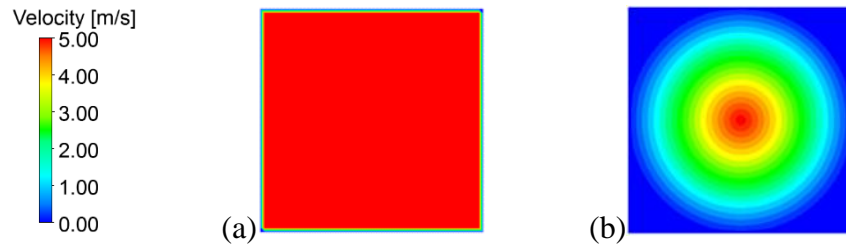
Figure 2-16. The velocity profile at the top surface: (a) uniform distribution, and (b) centric distribution.

Figure 2-17 shows the effect of the top boundary condition on the droplet distribution on the slab surface. In general, all three simulations predict similar droplet distribution in both the width direction and casting direction. This is not surprising since the spray conditions such as water flow rate and spray angle are identical in all the simulations. The results suggest that the spray conditions dominant the spray characteristics. Besides, the average injection velocity of droplets

148

is about 13m/s, which is more than twice the maximum air velocity given at the top surface. The boundary condition on the top surface does affect the droplet distribution at the beginning of the spray to a certain extent, as shown in Figure 2-17 (a), but the effect is limited in the upper region. Either one of the boundary conditions can be assigned to the top boundary surface without creating too much discrepancy. However, the velocity inlet condition can help establish a preliminary fluid field at the beginning of the calculation, accelerating the convergency. Therefore, the current study uses the uniform velocity as the inlet condition for the fluid region. The magnitude of the inlet velocity is set to 1.5m/s, the average air entrainment velocity based on the simulation with pressure outlet as the boundary condition for the top surface.
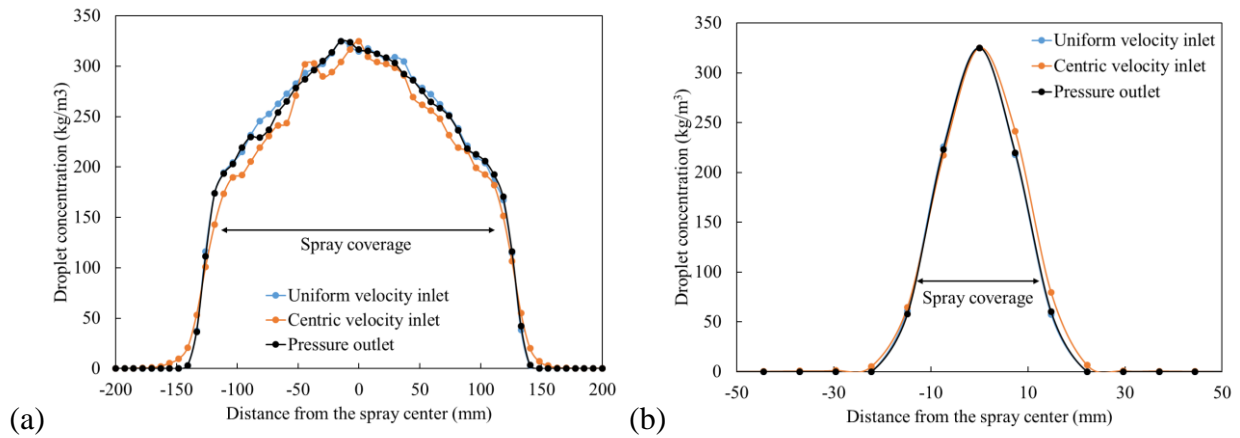
Figure 2-17. Droplet concentration on the slab surface: (a) in the width direction and (b) in the casting direction

The boundary conditions for the slab region are much more complicated. Two moving reference frames are applied to the slab region and the rolls to account for the translation and rotation effect, respectively. The side surfaces that are perpendicular to the casting direction are treated as symmetric planes since the computational domain is only a section of the whole steel slab. Physically, the conditions on the upstream surface of the slab in the casting direction are unknown prior to the simulation. Such information is also impossible to obtain from the actual operation. However, from the literature review [249] and a preliminary simulation, the temperature profile inside the semi-solidified shell in the secondary cooling satisfies the distribution shown in Figure 2-18. The temperature profile can be divided into two regions, one molten steel region where the temperature remains constant and one shell region where temperature decreases from the

maximum value in the molten steel region to the minimum at the surfaces. The rate of decrease is almost linear. Considering that the thickness of the solid region is 30mm below the surface, the temperature in the entire solid region should vary linearly through the thickness. Therefore, the current study uses a linear temperature distribution on the upstream surface, and the temperature change satisfies the linear equation shown in Figure 2-19. A fixed temperature is assigned to the bottom surface, and its magnitude is set to the maximum temperature on the upstream surface to ensure the consistency of the boundary conditions.
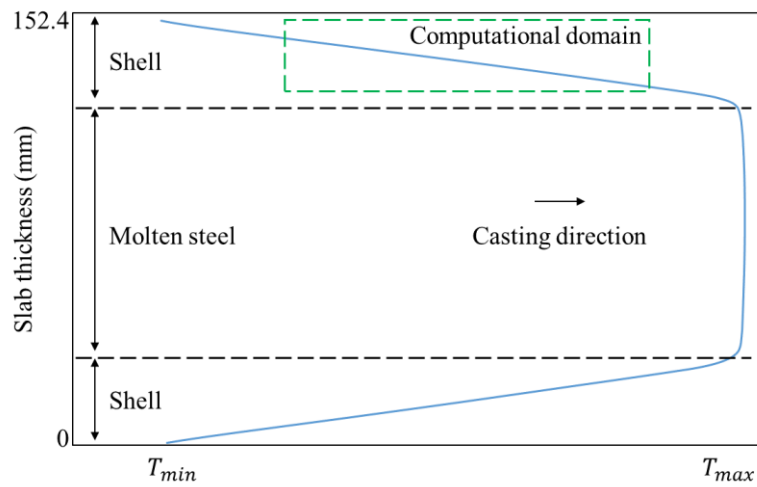
Figure 2-18. Temperature profile inside the semi-solidified steel slab.
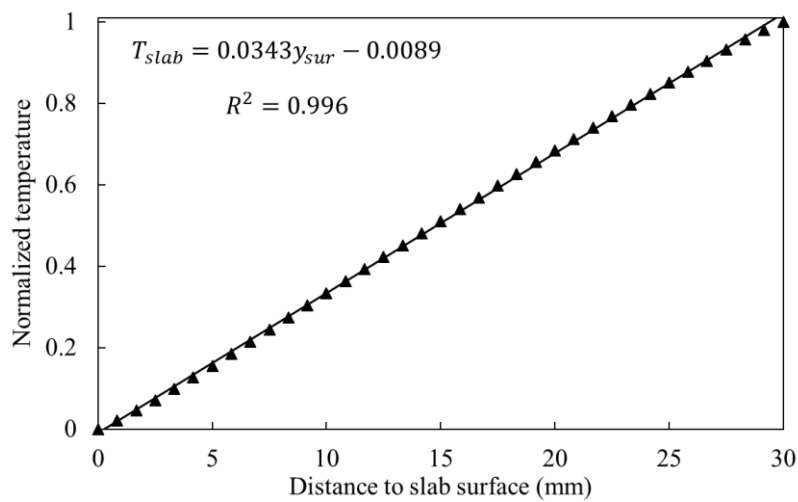
Figure 2-19. Shell temperature on the upstream surface as a function of shell thickness.

$$T_{slab} = 0.0343 y_{sur} - 0.0089$$

$$R^2 = 0.996$$

The downstream condition depends on the heat transfer within the solid region and the surface of the solid. The temperature on the downstream surface is constantly updating during the simulation. The initial temperature of the face centroid on the downstream surface of the solid region is set to that of the closest cell centroid. The temperature of the face centroid is constantly updating during the simulation according to the upstream conditions.

2.1.4 Grid independent study

Hydraulic nozzle simulation

Figure 2-20 shows the uneven spaced hexahedral mesh used in the computational domain. Most of the meshes are concentrated in the spray region and near the impingement surface, where air entrainment, droplet evaporation, droplet-wall impingement heat transfer, droplet boiling, wall jets exist. To obtain high-quality results for the flow and heat transfer in the wall boundary layer, a sensitivity study on the non-dimensional wall distance, y^+, is conducted and the results are shown in Figure 2-21. A value of y^+ equal to or less than 1 is recommended for resolving the wall jet flow in the near-wall region. Thus, $y^+ = 1$ is used as the criterion for the fined mesh in the current study.
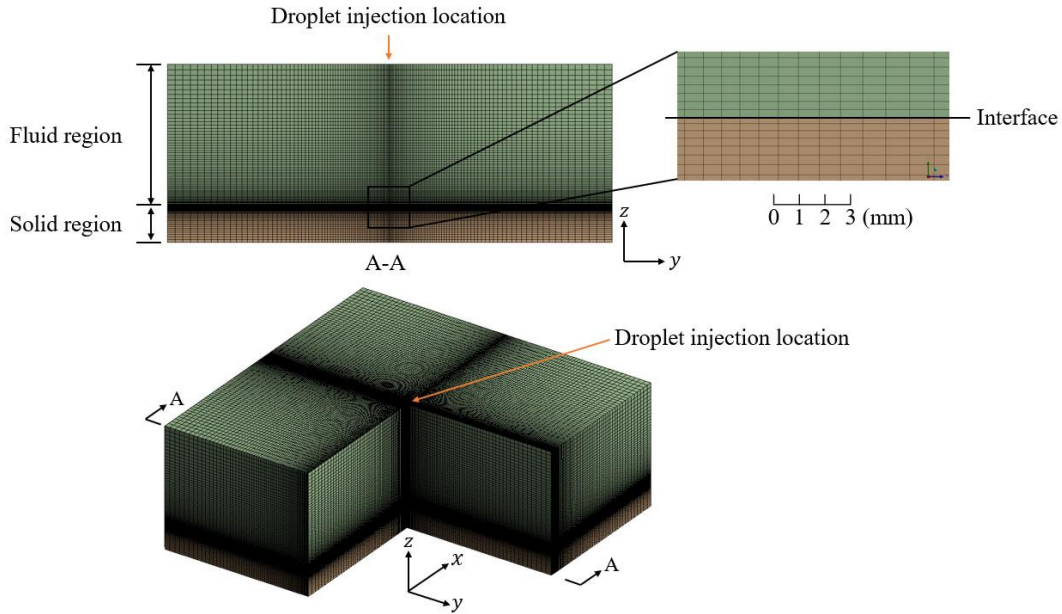
Figure 2-20. Uneven spaced hexahedral mesh applied to spray cooling simulations.
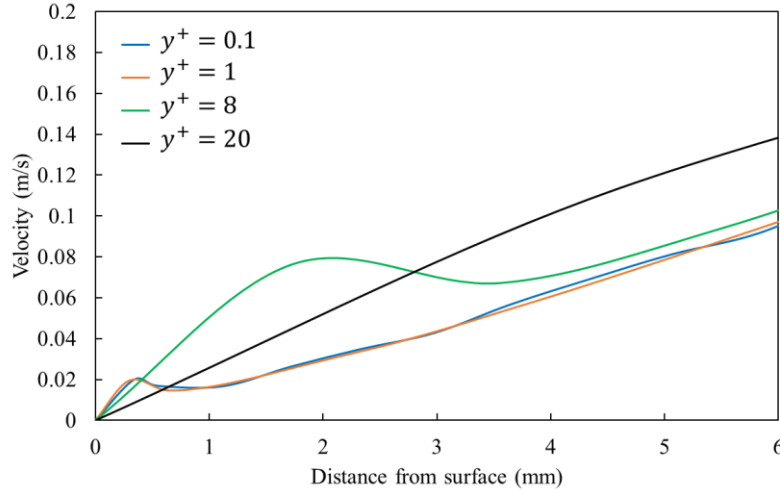
Figure 2-21. Air velocity in the vicinity of the slab surface with different y^+ values.

The mesh size in the roll region is biased toward the roll-slab contact area. Because the roll diameter varies in the current study, a universal mesh cell size would be insufficient for some roll diameters and excessive for others. Hence, the following ratio is used to determine the mesh cell size for different roll diameters:

$$\frac{N_{cell}}{L_{roll}} = \frac{cell\ quantities\ along\ contact\ length}{contact\ length} \tag{156}$$

Eq. (156) represents the number of mesh cells per unit contact length. The lower limit of this ratio is $\frac{1}{L_{roll}}$, where there is only one mesh cell across the contact length. The number of mesh cells must be sufficient to resolve the heat transfer between the roll and the slab and avoid any numerical error at the two contact points, two pinch points. As shown in Figure 2-22, all the mech cells around the pinch point in the fluid region converge to the pinch point. Such highly skewed control volume around the pinch point could result in non-physical solutions. The grid independent study for the ratio of $\frac{N_{cell}}{L_{roll}}$ is shown in Figure 2-23. The surface temperature distribution across a roll is depicted for five different ratios of $\frac{N_{cell}}{L_{roll}}$. The surface temperature converges when the ratio of $\frac{N_{cell}}{L_{roll}}$ increases to 0.715. Finer mesh beyond this ratio can only improve the results by 1%. However, because the mesh size in the contact region also affects the mesh around the pinch point, a ratio of 1.06 is used in the current study to ensure smooth transitions across the pinch points.

152
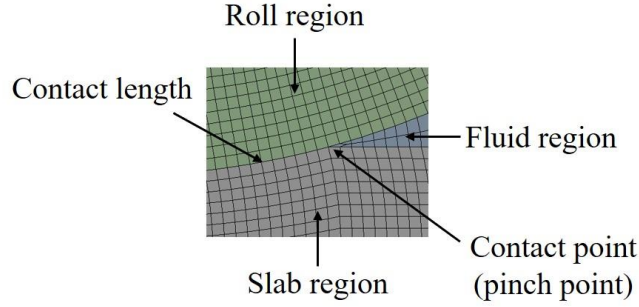
Figure 2-22. Enlarged view of mech cells around the pinch point.
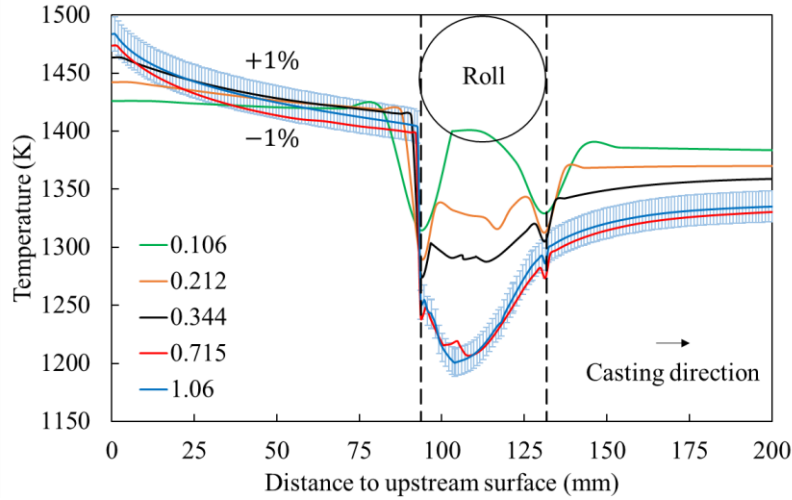
Figure 2-23. Surface temperature around roll contact at different ratios of $\frac{N_{cell}}{L_{roll}}$.

Air-mist nozzle simulation

The mesh size for the second step simulation of an air-mist nozzle is the same as that used for the hydraulic nozzle simulation. This section mainly focuses on the mesh size and quality in the first step simulation for an air-mist nozzle. Due to the intricate structures inside the nozzle, particularly in the upper region of the nozzle where air and water are supplied, the selection of mesh type and size significantly impacts the results. Figure 2-24 shows three different sets of mesh used for an air-mist nozzle. Figure 2-24 (a) and (b) are the tetrahedral-based meshes, and Figure 2-24 (c) is the polyhedral-based mesh. The minimum mesh size is set to 0.1mm, and the mesh is refined in both the fluid and near-wall regions. The total number of mesh cells for each mesh setup is

1626951, 12176445, 2269811, respectively. The polyhedral-based mesh can refine regions of interest without significantly increasing the total number of mesh cells. A similar refinement at the water inlet where the cross-section area is the minimum requires more than five times the amount used in the tetrahedral meshes. Therefore, the polyhedral-based mesh is used for the air-mist nozzle simulations in the current study.
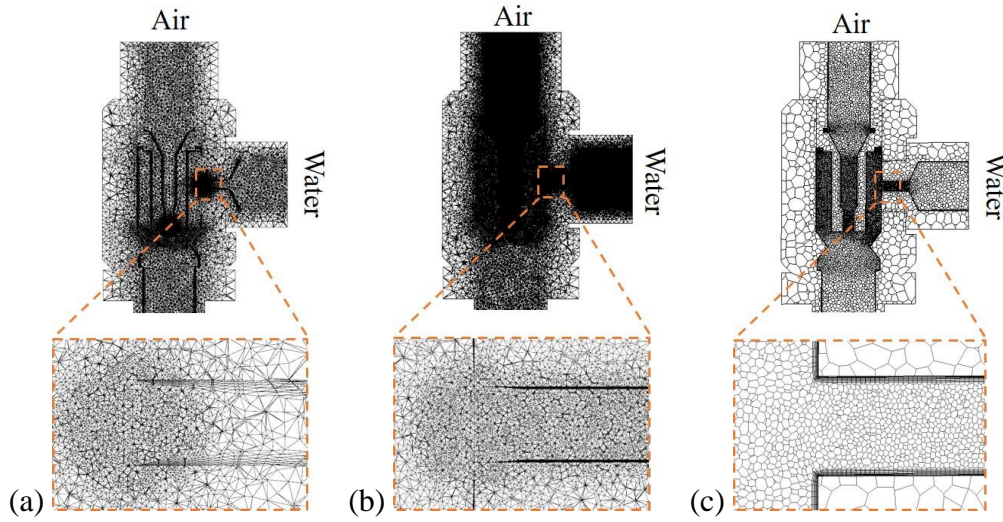
Figure 2-24. Cross-section view of the meshed region in the upper portion of an air-mist nozzle with: (a) coarse tetrahedral mesh, (b) refined tetrahedral mesh, and (c) polyhedral mesh.

Table 2-2 shows a grid independent study for the polyhedral-based mesh. 10 layers of boundary cells are applied to the near-wall regions in all three mesh setups. The only variable is the minimum mesh size, which reduces from 1mm to 0.1mm. The cell quantity proportionally increases to over two million from less than half a million. The average velocity at the nozzle orifice is selected to compute the difference between simulations. The average velocity converges to about 8.2m/s when the minimum mesh size reduces to 0.1mm. The relative difference also decreases to less than 1% with sufficient mesh refinement. Therefore, the polyhedral-based mesh with a minimum mesh size of 0.1mm is used for the first step simulation for the air-mist nozzle in the current study.

Table 2-2. Grid independent study for the polyhedral-based mesh.

Min. mesh (mm)	Cell quantity	y^+	Exit velocity (m/s)	Relative diff. (%)
1.0	376836	2.047	7.72	-
0.5	908387	2.051	8.27	6.65
0.1	2269811	2.199	8.22	0.61

Note:

- *Relative change is defined as follows:*

$$\% = 100\% \times \left| \frac{u_{curr} - u_{prev}}{u_{prev}} \right|$$

2.1.5 Numerical schemes

The second-order upwind scheme is applied to convection terms for the hydraulic nozzle simulation and the second step simulation of the air-mist nozzle. SIMPLE algorithm is used to couple velocity and pressure. Converged results can be reached after iteration proceeds alternatively between the continuous and discrete phases. Two hundred steady-state iterations in the continuous phase are conducted between two transient iterations in the discrete phase. The time step size for the discrete phase is set to 0.0005s.

For the first step simulation of the air-mist nozzle, the second-order upwind scheme is applied convection terms. The coupled scheme is used for the pressure-velocity coupling. The pseudo transient under-relaxation method is utilized for the steady-state calculation through the pseudo time step, which is defined as the minimum time scale in the computational domain [215]:

$$\Delta t_{pse} = \min(\Delta t_{conv}, \Delta t_P, \Delta t_v) \tag{157}$$

Where Δt_{conv} is the convective time scale, Δt_P is the dynamic time scale, Δt_v is the diffusion time scale. The four different time scales are defined as follows:

$$\Delta t_{conv} = \frac{0.3 L_{scale}}{\max{(u_{bc}, u_{domain})}} \tag{158}$$

$$\Delta t_P = \frac{0.3 L_{scale}}{u_{\Delta P}} \tag{159}$$

$$\Delta t_\nu = \frac{L_{scale}^2}{\nu} \tag{160}$$

Where L_{scale} is the representative length scale, u_{bc} is the maximum arithmetic average velocity at boundary faces, u_{domain} is the arithmetic average velocity in the computational domain, ν is the kinematic viscosity, $u_{\Delta P}$ is the velocity based on the pressure difference at open boundaries.

The representative length scale is defined as follows:

$$L_{scale} = \min\left[\sqrt[3]{V_{domain}}, \max\left(L_x, L_y, L_z\right)\right] \tag{161}$$

Where V_{domain} is the volume of the computational domain, L_x, L_y and L_z are the dimensions of the domain.

$u_{\Delta P}$ shown in Eq. (159) is defined as follows:

$$u_{\Delta P} = \sqrt{\frac{P_{bc,max} - P_{bc,min}}{\bar{\rho}_{domain}}} \tag{162}$$

Where $P_{bc,max}$ and $P_{bc,min}$ are the maximum and minimum pressure at the open boundaries, $\bar{\rho}_{domain}$ is the average density in the computational domain.

A typical converged result renders scaled mass residual of 10^{-3}, scaled energy residual of 10^{-6}, and scaled momentum and turbulence kinetic energy residuals of 10^{-4}. All the cases are developed based on the platform of the software package ANSYS Fluent 17.1.

2.1.6 Material properties

Gas phase

Air is treated as an isotropic single-phase multi-component gas in the simulation. The initial composition of air consists of 77wt% nitrogen and 23wt% oxygen. Once the vaporization of the droplet starts, a third component, water vapor, is added to the gas phase. The local density of air can be found either from the incompressible ideal gas law:

$$\rho_a = \frac{P_{op}}{R_{uni} T \sum_{i=1}^{N} \frac{Y_i}{M_{w,i}}}$$
(163)

Where P_{op} is the operating pressure and is equal to 101325Pa for the one atmospheric pressure, Y_i is the mass fraction of the ith component, $M_{w,i}$ is the molecular weight the ith component, R_{uni} is the universal gas constant and is equal to 8.314J/mol·K, T is the local temperature.

Or from the mass-weighted mixing law:

$$\rho_a = \frac{1}{\sum_{i=1}^{N} \frac{Y_i}{\rho_i}}$$
(164)

Where ρ_i is the molecular weight the ith component.

Figure 2-25 (a) shows the comparison of densities predicted by the ideal gas law and the mixing law against the data of dry air provided by Lienhard et al. [250]. The mixing law gives better predictions over the interested temperature range compared to the ideal gas law. The ideal gas assumption is not applicable to the secondary cooling process. Similarly, the thermal conductivity, specific heat, and viscosity of the gas mixture can also be found from the mass-weighted mixing law:

$$\lambda_a = \sum_{i=1}^{N} Y_i \lambda_i \tag{165}$$

$$c_{p,a} = \sum_{i=1}^{N} Y_i c_{p,i} \tag{166}$$

$$\mu_a = \sum_{i=1}^{N} Y_i \mu_i \tag{167}$$

Where λ_i is the thermal conductivity of the ith component, $c_{p,i}$ is the specific heat of the ith component, μ_i is the viscosity of the ith component.

The mixing law can accurately predict thermal conductivity and the specific heat, as shown in Figure 2-25 (b) and (c). However, the mixing law fails to give reasonable predictions for the viscosity. As shown in Figure 2-25 (d), the predictions by the mixing law are one order of magnitude larger than the actual viscosity, mostly due to the simplified gas components used in the current study. To maintain the current gas composition assumption while enhancing the property calculation, the following Sutherland law [251] and the power law [215] are recommended:

$$\mu_a = \mu_0 \left(\frac{T}{T_0}\right)^{3/2} \frac{T_0 + 110.56}{T + 110.56} \tag{168}$$

$$\mu_a = \mu_0 \left(\frac{T}{T_0}\right)^{2/3} \tag{169}$$

Where μ_0 is the viscosity at room temperature and pressure and is equal to 1.716×10^{-5}kg/m·s, T_0 is the reference temperature and is equal to 273K.

Figure 2-25 (d) compares the Sutherland law and the power law with the measured data. Both models can accurately predict the viscosity of the two-component gas mixture, especially near room temperature. The Sutherland law is slightly accurate than the power law, which can be viewed as another version of the Sutherland law.

In summary, the mass-weighted mixing law is used to predict the density, thermal conductivity, and specific heat of the gas mixture, and the Sutherland law shown in Eq. (168) is used to predict the viscosity. The properties of nitrogen and oxygen are based on the dataset provided by [250], the thermal conductivity and viscosity of water vapor are based on the study of Shmelkov et al. [252], the density of water vapor is calculated from the ideal gas law using one atmospheric pressure, and the specific heat of water vapor is extracted from [253]. The properties of these three materials are shown in Figure 2-26.
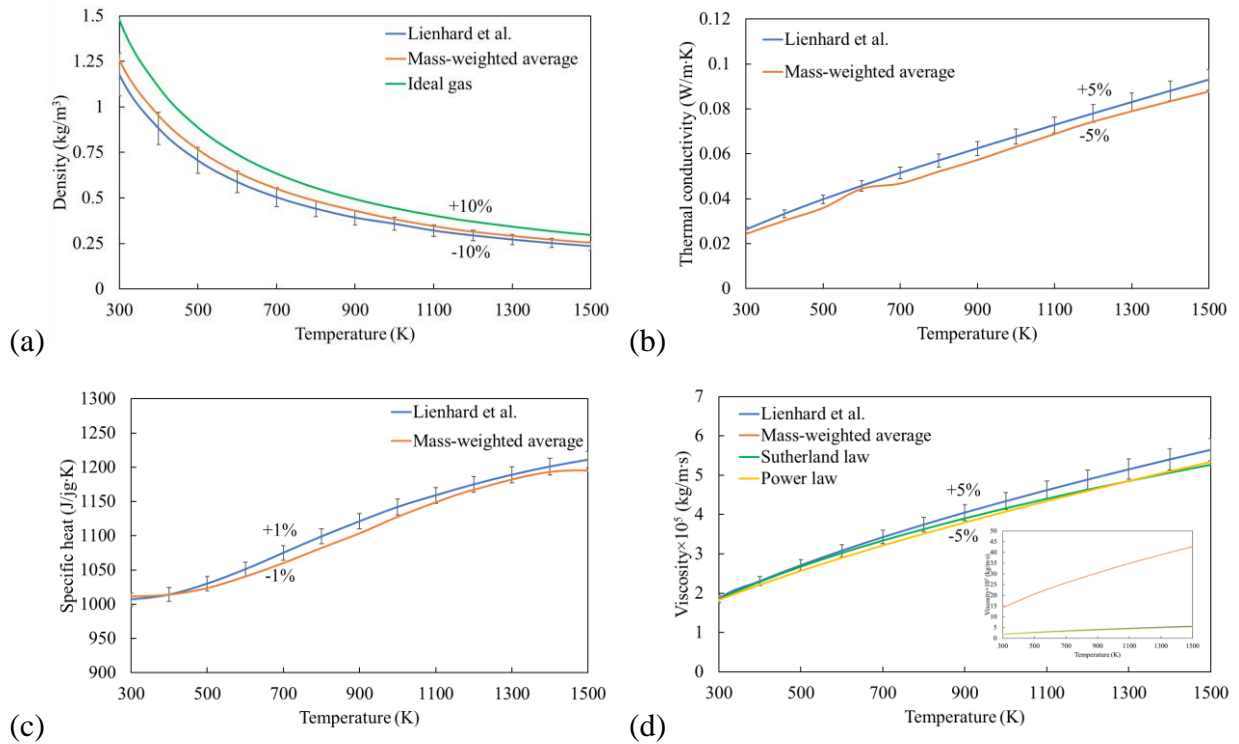
Figure 2-25. Comparisons of thermodynamic properties of air using different prediction models: (a) density, (b) thermal conductivity, (c) specific heat, and (d) viscosity.
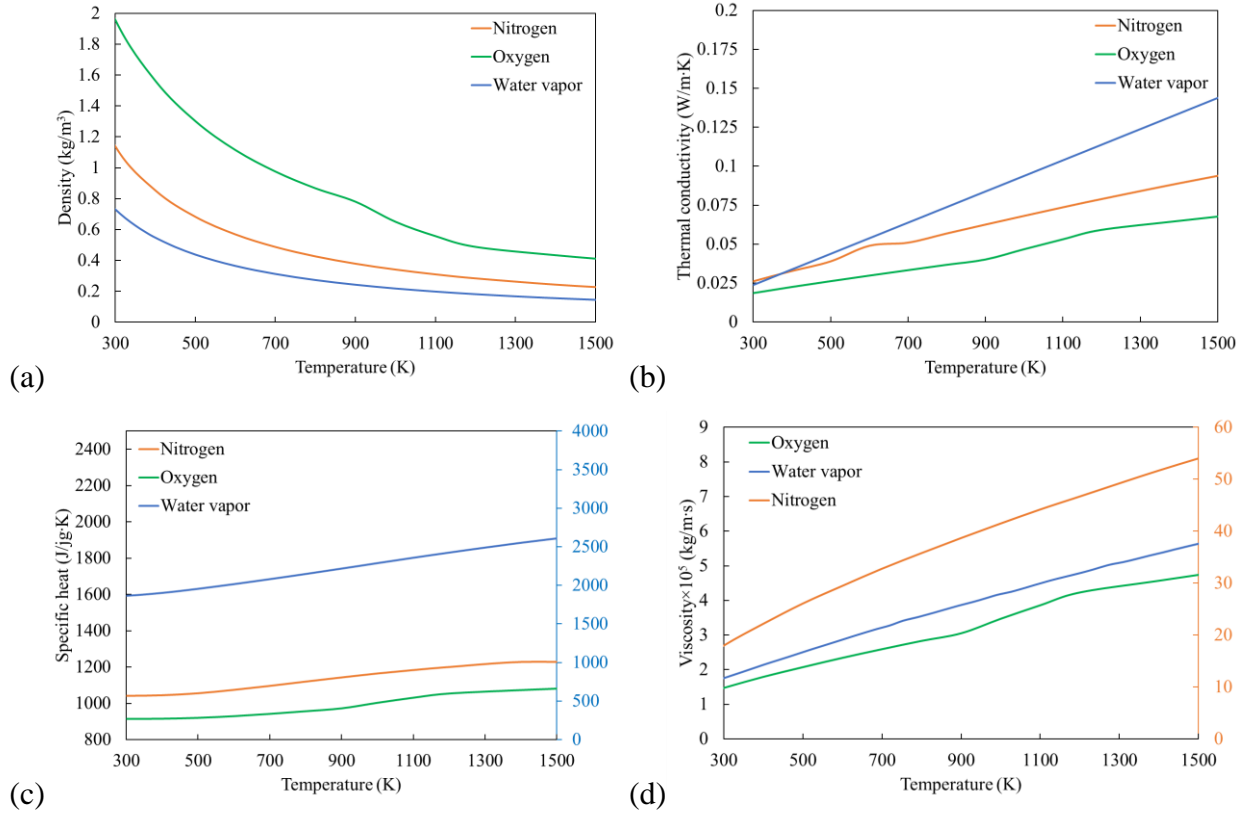
Figure 2-26. Thermodynamic properties of nitrogen, oxygen, and water vapor used in the current study: (a) density, (b) thermal conductivity, (c) specific heat, and (d) viscosity.

Water

Steel manufactures use the water from nearby water sources such as lakes and rivers, the exact composition of the cooling water varies widely from location to location and from day-to-day operation. However, there is little literature has linked the surface defects in secondary cooling with the water composition. Hence, the effect of other elements that may present in the cooling water is neglected, and the cooling water is assumed to be comprised of H_2O only. The properties of the cooling water are evaluated based on the local temperature in the domain. Figure 2-27 (a) to (e) shows the density, thermal conductivity, specific heat, viscosity, and water-air surface tension used in the current study [254]. Density and specific heat vary slightly before the boiling point, but both properties dramatically change near the boiling temperature. Thus, both properties are still considered temperature-dependent. The boiling temperature and the latent heat are considered constant and set to 373.15K and 2260kJ/kg, respectively.
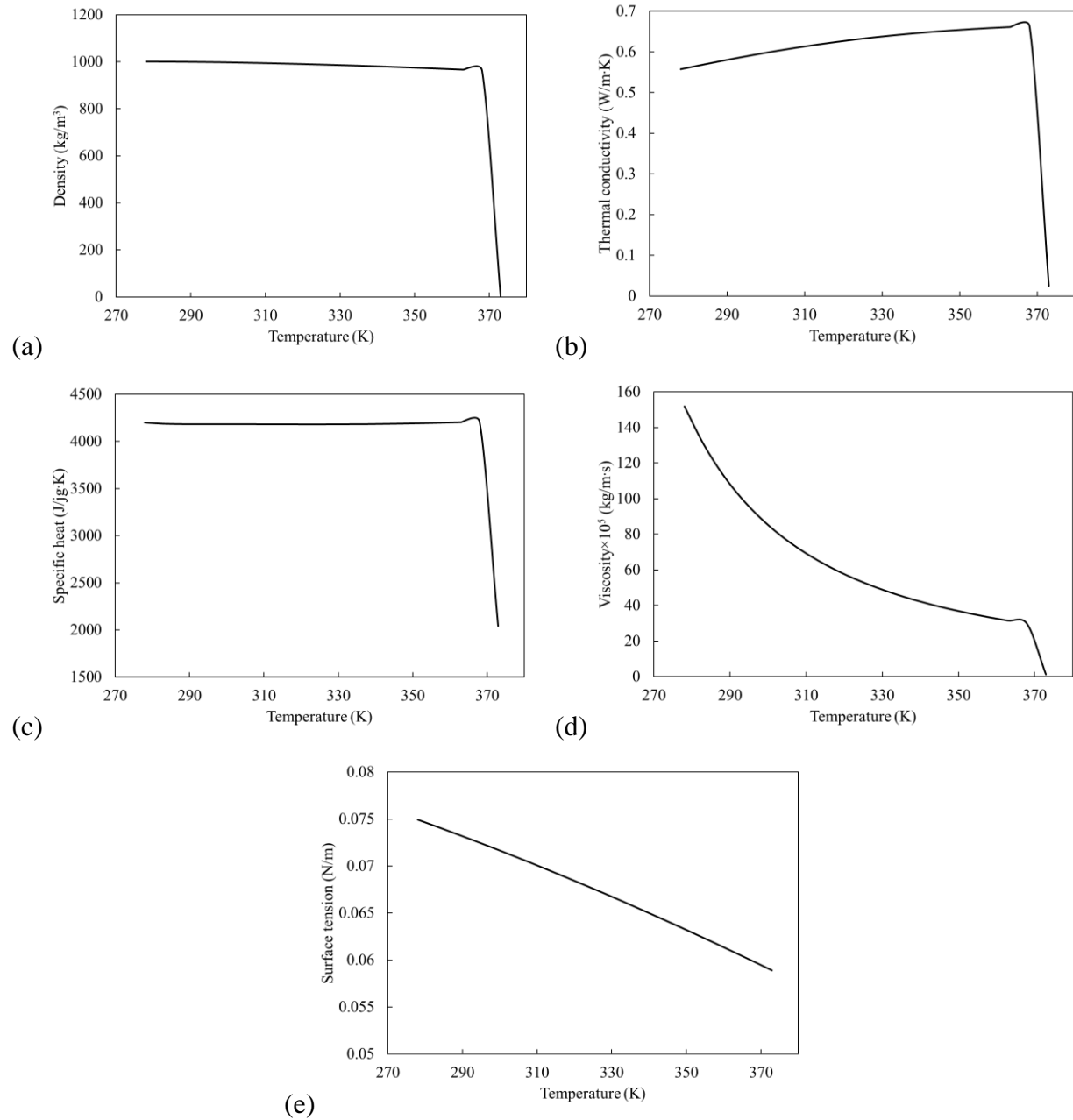
Figure 2-27. Thermodynamic properties of water liquid used in the current study: (a) density, (b) thermal conductivity, (c) specific heat, (d) viscosity, and (e) water-air surface tension.

Steel

A low carbon alloy steel obtained from an industrial collaborator is used in the current study. The steel properties are calculated by JMatPro, a thermo-mechanical calculation tool. The validation of JMatPro can be found elsewhere [256-259]. The composition of the steel is shown in section 2.2.6. For the simulation of heat transfer on steel slab surface, steel is treated as solid, and the

161

properties required in the simulation are density, thermal conductivity, and specific heat. Figure 2-28 shows the calculated density and thermal conductivity for the steel. The specific heat is derived by taking the slope of the enthalpy-temperature curve shown in Figure 2-41 (d):

$$c_{p,st} = \frac{\Delta h}{\Delta T} \tag{170}$$

Where Δh is the enthalpy difference over a small temperature range ΔT.

(a) (b)
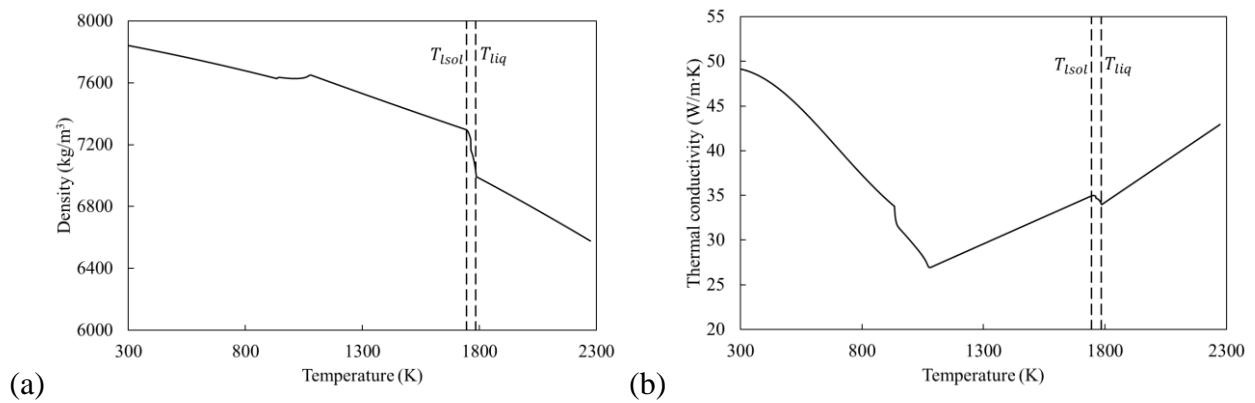
Figure 2-28. Thermodynamic properties of the steel used in the current study: (a) density, and (b) thermal conductivity.

Roll

Rolls are assumed to be made of creep-resistant low alloy steel X12Cr13 EN 1008-1-97 [180], which attains high mechanical properties such high impact strength and corrosion resistance after heat treatment. The thermodynamic properties of rolls are shown in Figure 2-29.
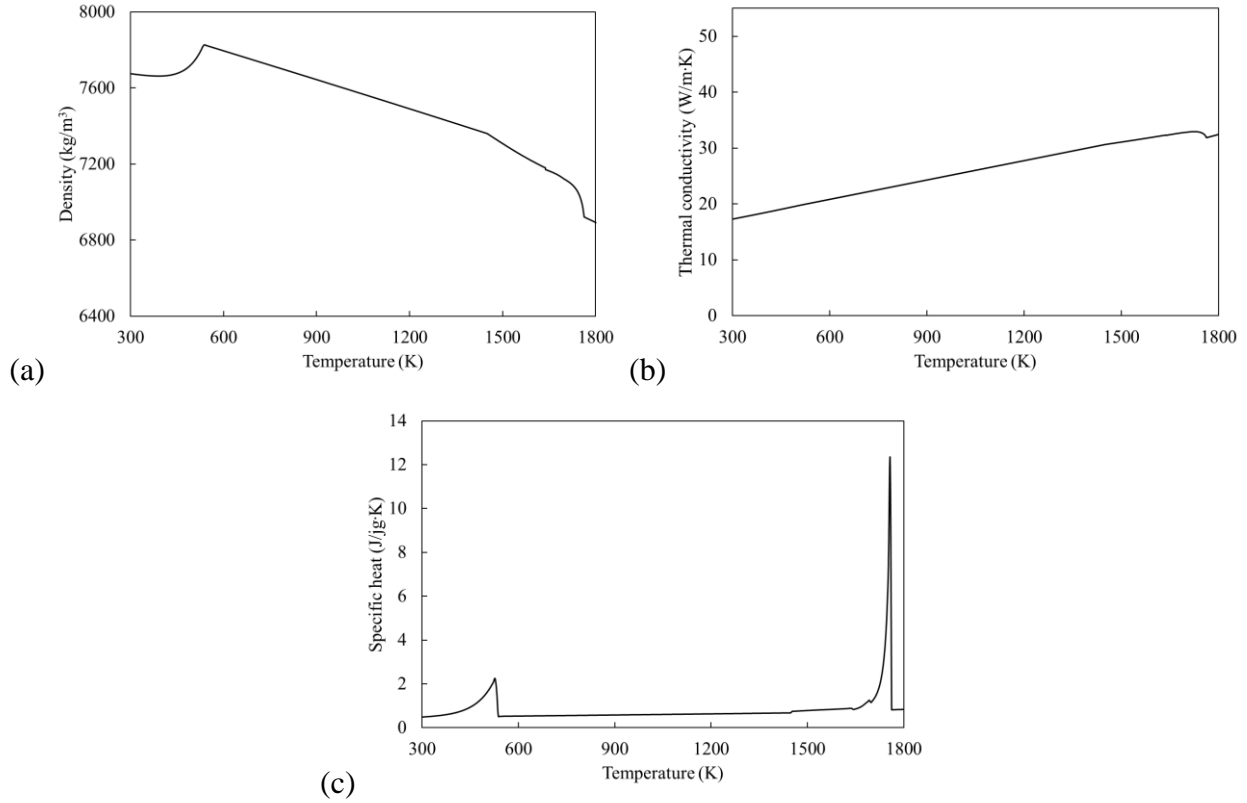
Figure 2-29. Thermodynamic properties of rolls used in the current study: (a) density, (b) thermal conductivity, and (c) specific heat.

2.2　Solidification in secondary cooling region

The Eulerian Volume-Of-Fraction model is applied to the current study to simulate the phase change and convection inside the semi-solidified steel slab. The molten steel and the solid steel are treated as two immiscible continuous phases. One set of conservation equations governs the fluid flow in the molten steel region, the mushy zone region, and the solid region. The results of the heat transfer on the steel slab surface are incorporated as the thermal boundary conditions in the current study.

2.2.1　Assumptions

In deriving the model, the following assumptions are made:

(1) The current study focuses on macroscopic modeling. The control volume is sufficiently small, and the phases are sufficiently intermixed. Both molten steel and solid are treated as chemically homogeneous and isotropic single-phase Newtonian fluids.

(2) There are no solid phase transitions within the solid region once solid is formed.

(3) Alloy elements are not considered in the current study, but their effects are taken into account through material properties.

(4) The microscopic crystal structure of the solid is not modeled in the current study. The presence of the crystals is treated as "viscous flow" when the crystal concentration is low and "porous medium" when its concentration is high.

(5) Under the first assumption, molten steel and solid present in the same control volume have the same properties determined by the cell temperature.

2.2.2 Governing equations

The transient Reynolds-averaged Navier-Stokes equations for mass, momentum, and energy are solved for the mixture of molten steel and solid. The Enthalpy-Porosity method is adopted in the current study to simulate the phase transfer and latent heat release phenomena involved during the solidification of molten steel [200-204].

Mass conservation

The equation for conservation of mass of an incompressible and isotropic Newtonian fluid can be written as follows:

$$\frac{\partial \rho_{st}}{\partial t} + \nabla \cdot (\rho_{st} \vec{u}_{st}) = 0 \tag{171}$$

Where ρ_{st} and $\vec{u}_{st}$ are the density and velocity of the liquid and solid mixture, respectively.

Momentum conservation

Steel alloys solidify over a range of temperatures. The lower and upper boundaries of the temperature range are donated as solidus and liquidus temperature, respectively. The two characteristic temperatures are a region filled with a mixture of liquid and solid, as shown in Figure 2-30. This region is referred to as the mushy zone. Inside the mushy zone, there are two sub-regions, i.e., free floating dendrite region and porous region. Liquid molten steel initially forms as smell solid particles, or equiaxed dendrites, which are advected in the liquid flow. Over time, these tiny particles grow and coalesce into columnar rigid solid structures. The microscopic dendritic nucleation and growth are not considered in the current study, but the presence of the mushy region is incorporated by modifying the momentum equation.
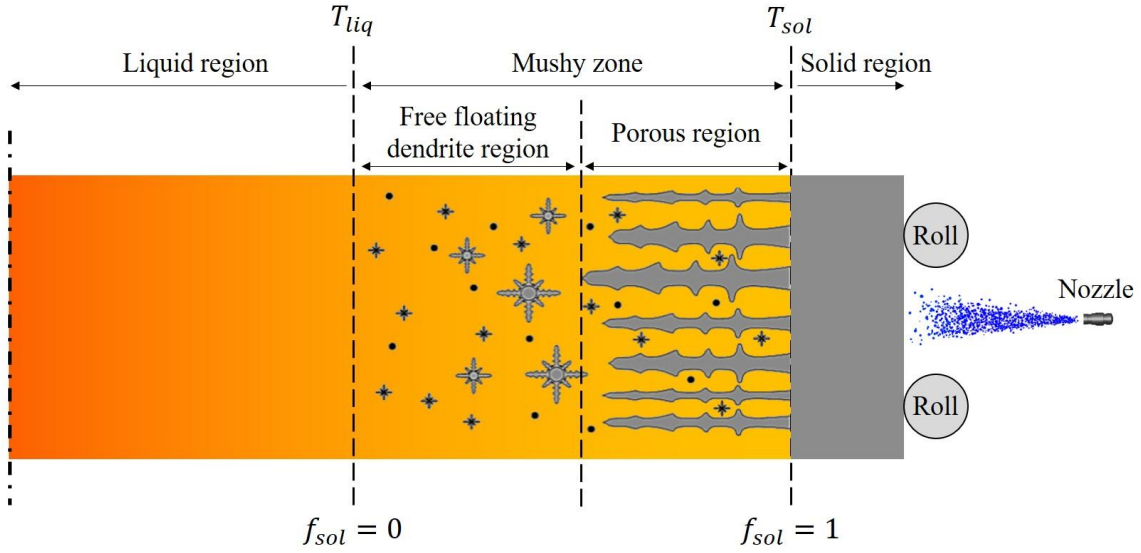
Figure 2-30. Illustration of the mushy zone.

A single momentum conservation equation is solved throughout the computational domain.

$$\frac{\partial}{\partial t}(\rho_{st}\vec{u}_{st}) + \nabla \cdot (\rho_{st}\vec{u}_{st}\vec{u}_{st}) = -\nabla P + \nabla\left[\mu_{eff}(\nabla\vec{u}_{st} + \nabla\vec{u}_{st}^{T})\right] + \rho_{st}\vec{g} + S_{por} \tag{172}$$

Where P is the pressure, μ_{eff} is the effective viscosity, and it changes the liquid viscosity in the free floating dendrite region, S_{por} is a momentum source term that takes effect in the porous region and is defined in Eq. (174).

In the free floating dendrite region, small crystals nucleate and grow in the molten steel. The solid fraction in this region is low, but the presence of the solid crystals does have some damping effect on the liquid. This effect is simulated by increase the liquid viscosity accordingly [260, 261]:

$$\mu_{eff} = \mu_{st} \left(\frac{A_{mushy}}{A_{mushy} - F_\mu f_{sol}} \right)^2 \tag{173}$$

Where μ_{st} is the viscosity of the mixture, F_μ is a switching function that ensures the correct damping model is applied to the corresponding mushy zone sub-region, A_{mushy} is a crystal constant, and a value of 0.5 is applied [261]. A more detailed discussion can be found in chapter 4. f_{sol} is the solid fraction and it depends on the local temperature and is one of the critical parameters in the solidification model. If complete diffusion to the equilibrium of all alloy elements is assumed, then the Lever rule model can be used to determine the solid fraction-temperature relation. However, the equilibrium assumption does not hold for a fast solidification process such as continuous casting. A more realistic model, the Scheil-Gulliver model, is used to calculate the solid fraction-temperature relation. Details about the model can be found elsewhere [262, 263]. The model assumes infinitely fast mixing in liquid, and no diffusion occurs in solid, and equilibrium exists on the liquid-solid interface. It is often recommended for rapid solidification processes [264].

In the porous region, closely packed columnar dendrites form a matrix of solid. This region is often treated as a porous medium, and the Carman-Kozeny relation is utilized to predict the flow resistance through a momentum source. [265]:

$$S_{por} = -\frac{\mu_{st}}{K_{per}} |\vec{u}_{st} - \vec{u}_{cast}| \tag{174}$$

Where $\vec{u}_{st}$ is the liquid velocity, $\vec{u}_{cast}$ is the velocity of the porous region, which is equal to the casting speed once the solid forms. The term on the right-hand side represents the viscous drag and is derived from Darcy's law. Eq. (174) shows the linear behavior of the pressure difference as a function of liquid velocity. At high liquid velocities, this relation becomes non-linear, and the quadratic Forchheimer term may be added to address the importance of the inertial effect. However, the Forchheimer term only becomes important at high Reynolds number (Re $\gg$ 10 [266], Re $\gg$ 1 [267], ReDa $\gg$ 1 [268]). For liquid flow in the secondary cooling region, the typical Reynolds number and Darcy number can be estimated as follows:

$$\text{Re} = \frac{\rho_{st}|\vec{u}_{st}|\sqrt{K_{per}}}{\mu_{st}} = \frac{7700 \times 0.0167 \times \sqrt{10^{-12}}}{5.5 \times 10^{-3}} = 0.02338 < 1 \tag{175}$$

$$\text{Da} = \frac{K_{per}}{\delta_{st}^2} = \frac{10^{-12}}{(50 \times 10^{-3})^2} = 4 \times 10^{-10} \tag{176}$$

$$\text{ReDa} = 9.352 \times 10^{-12} \leq 1 \tag{177}$$

Where $\vec{u}_{st}$ is the liquid velocity and is set to a value that is equivalent to 1m/min casting speed, K_{per} permeability and a value of 10^{-12} is adopted for the estimation [261], δ_{st} is the shell thickness and an average thickness of 50mm for a 200mm thick slab is used for the estimation.

Eq. (175) to Eq. (177) demonstrate that the Forchheimer term is not significant compared to the Darcy term. Only the Darcy term is included in Eq. (174) for predicting the flow resistance.

K_{per} shown in Eq. (174) is the permeability of the porous region, and it is defined as follows [261, 269-271]:

$$K_{per} = \frac{\lambda_{SDAS}^2}{180} \frac{(1 - f_{sol})^3}{f_{sol}^2} \frac{1}{(1 - F_\mu)} \tag{178}$$

Where λ_{SDAS} is the characteristic length, and it depends on the crystal shape. For spheres, the diameter of the sphere is recommended [272]. For slender cones, the characteristic length should be the base diameter [270]. For columnar dendrites, the secondary dendrite arm spacing is adopted

[273-275]. The secondary dendrite arm spacing has been closely related to thermal conditions and alloy content [276]. The following expression is used to estimate the secondary dendrite arm spacing in the current study [276]:

$$0 < C \leq 0.15wt\%: \qquad \lambda_{SDAS} = (169.1 - 720.9C)C_{cool}^{-0.4935} \qquad (179)$$

$$0.15wt\% < C: \qquad \lambda_{SDAS} = 143.9C_{cool}^{-0.3616}C^{(0.5501-1.996C)} \qquad (180)$$

Where C_{cool} is the cooling rate (°C/s). A more detailed discussion can be found in chapter 4.

The switching function shown in Eq. (173) and Eq. (178) has a smooth transition near the critical solid fraction where equiaxed grains start to agglomerate and form the columnar dendritic region. It is defined as follows: [261, 277]:

$$\text{Free floating region:} \qquad F_{\mu} = 0.5 - \frac{1}{\pi}\arctan[100(f_{sol} - f_c)] \qquad (181)$$

$$\text{Porous region:} \qquad F_p = 1 - F_{\mu} = 0.5 + \frac{1}{\pi}\arctan[100(f_{sol} - f_c)] \qquad (182)$$

Where f_c is the critical solid fraction, or packing fraction, and it separates the two mushy zone sub-regions. The value of the critical solid fraction is not explicitly known, and it depends on the material composition, microscopic structure of the solid, fluid flow conditions, and many other factors. Dantzig et al. suggest a range of 0.3-0.4 for rigid skeleton [272]. Baeckerud et al. reported a value of 0.27 for aluminum alloy A201 [278]. Vreeman et al. conducted a parametric study for aluminum copper and aluminum magnesium alloys and used a maximum of 0.3 [279]. Marsh recommended a range of 0.5-0.6 based on the study of lava and magma [280]. Oldenburg et al. applied a value of 0.5 when developed the switching function [261]. Kim et al. proposed a value of 0.525 by averaging various carbon steels used in continuous casting [281], adopted by the current study. A more detailed discussion can be found in chapter 4.

Turbulence model

The k-ω SST model is chosen for turbulence modeling due to its accuracy and computational efficiency. Eq. (19) and Eq. (20) are solved for obtaining k and ω with two additional source terms to account for the presence of the mushy zone:

$$S_k = -\frac{180\mu_{st}f_{sol}^2(1-F_\mu)k}{\lambda_{SDAS}^2(1-f_{sol})^3} \tag{183}$$

$$S_\omega = -\frac{180\mu_{st}f_{sol}^2(1-F_\mu)\omega}{\lambda_{SDAS}^2(1-f_{sol})^3} \tag{184}$$

Where k is the turbulence kinetic energy, ω is the turbulence dissipation rate.

Energy conservation

The Enthalpy-Porosity model applied in the current study does not track the liquid-solid interface explicitly. Instead, the model uses an enthalpy formulation to determine the solid distribution, which significantly reduces the computational time. The conservation of energy for both liquid and solid is written as follows:

$$\frac{\partial}{\partial t}\left(f_{liq}\rho_{liq}h_{liq}\right) + \nabla \cdot \left(f_{liq}\rho_{liq}h_{liq}\vec{u}_{liq}\right) = \nabla \cdot \left(k_{liq}\nabla T_{liq}\right) - S_{liq-sol} \tag{185}$$

$$\frac{\partial}{\partial t}(f_{sol}\rho_{sol}h_{sol}) + \nabla \cdot (f_{sol}\rho_{sol}h_{sol}\vec{u}_{sol}) = \nabla \cdot (k_{sol}\nabla T_{sol}) + S_{liq-sol} \tag{186}$$

Where liquid and solid are denoted by the subscript liq and sol, respectively. ρ is the density, h is the sensible enthalpy, $\vec{u}$ is the velocity, k is the thermal conductivity, T is the local temperature, $S_{liq-sol}$ is the energy exchange between liquid and solid. The liquid and solid fraction must satisfy the following constraint in each control volume:

$$f_{liq} + f_{sol} = 1 \tag{187}$$

The liquid enthalpy shown in Eq. (185) is calculated by:

$$h_{liq} = h_{sol} + h_{lat} \tag{188}$$

Where h_{lat} is the latent heat.

Because the control volume is constructed sufficiently small, it is reasonable to assume that both liquid and solid have the same material properties and temperature in the same control volume, such that:

$$\rho_{liq} = \rho_{sol} = \rho_{st} \tag{189}$$

$$T_{liq} = T_{sol} = T_{st} \tag{190}$$

And the liquid velocity and the solid velocity can be combined into a mixture velocity:

$$\vec{u}_{st} = f_{liq}\vec{u}_{liq} + f_{sol}\vec{u}_{sol} \tag{191}$$

Adding Eq. (185) to Eq. (186) and substituting Eq. (187)-(191) into the combined equation, yields the following expression:

$$\frac{\partial}{\partial t}(\rho_{st}h_{st}) + \nabla \cdot (\rho_{st}h_{st}\vec{u}_{st}) + \nabla \cdot \left(f_{liq}\rho_{st}h_{lat}\vec{u}_{liq}\right)$$

$$= \nabla \cdot (k_{st}\nabla T_{st}) + \frac{\partial}{\partial t}(f_{sol}\rho_{st}h_{lat}) \tag{192}$$

Where k_{st} is the average thermal conductivity and is equal to the arithmetic mean of k_{liq} and k_{sol}.

The third term on the left-hand side of Eq. (192) accounts for the convection of the latent heat. Solving f_{liq} and $\vec{u}_{liq}$ from Eq. (187) and Eq. (191), respectively, and substituting both terms into Eq. (192), yields:

$$\frac{\partial}{\partial t}(\rho_{st}h_{st}) + \nabla \cdot (\rho_{st}h_{st}\vec{u}_{st}) + \nabla \cdot (\rho_{st}h_{lat}\vec{u}_{st}) - \nabla \cdot (\rho_{st}h_{lat}f_{sol}\vec{u}_{sol})$$

$$= \nabla \cdot (k_{st}\nabla T_{st}) + \frac{\partial}{\partial t}(f_{sol}\rho_{st}h_{lat})$$

(193)

The third term on the left-hand side can be dropped based on Eq. (171). Thus, Eq. (193) becomes:

$$\frac{\partial}{\partial t}(\rho_{st}h_{st}) + \nabla \cdot (\rho_{st}h_{st}\vec{u}_{st})$$

$$= \nabla \cdot (k_{st}\nabla T_{st}) + \frac{\partial}{\partial t}(f_{sol}\rho_{st}h_{lat}) + \nabla \cdot (\rho_{st}h_{lat}f_{sol}\vec{u}_{sol})$$

(194)

Where $\vec{u}_{sol}$ is the solid velocity, and it equals the casting speed once the solid region forms.

The latent heat shown in Eq. (188), and Eq. (192)-(194) is adjusted in each control volume according to the local solid fraction [203]:

$$h_{lat} = \begin{bmatrix} h_{fg} & T_{liq} \leq T \\ h_{fg}(1 - f_s) & T_{sol} < T < T_{liq} \\ 0 & T \leq T_{sol} \end{bmatrix}$$

(195)

2.2.3   Computational domain and boundary conditions

Computational domain

Solidification coupled with single spray cooling

Figure 2-31 illustrates the computational domain used in the simulation of solidification coupled with single spray cooling. The domain is highlighted in orange color. The length and width of the domain are consistent with that of the heat transfer simulation shown in Figure 2-13, but the thickness of the domain increases to 200mm so that the domain can cover the entire slab region in the z direction. In this study, the slab region is cooled by two adjacent rolls and a water spray in between. It is worth mentioning that the size of the current computational domain is much larger than the actual slab region, which is cooled by one water spray. The extra space included in this study is to help minimize boundary effects. Besides, the effect of spray and rolls on solidification

can be better quantified using the current domain without concerning the cooling effect passed from the upstream. In addition, this domain is also used for model development and grid independent study.

The heat transfer on the slab surface is not included in the current simulation, but the effect of spray cooling and roll contact cooling is coupled by applying the HTC distribution on the slab surface as one of the boundary conditions. Details regarding the coupling methodology are discussed in the boundary conditions section. It is worth noting that this computational domain can be used to simulate different sections in the secondary cooling region with some modifications of roll diameter, roll gap spacing, spray standoff distance, spray flow rate, and the upstream conditions.
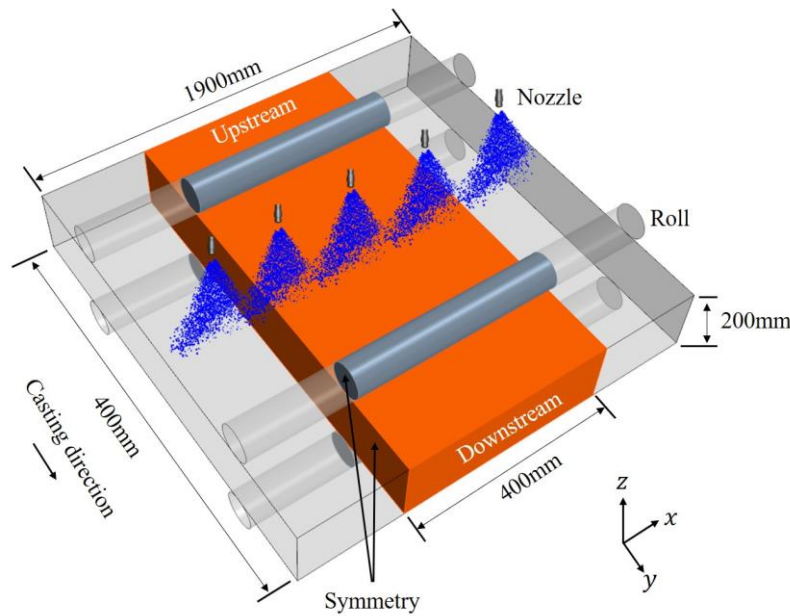
Figure 2-31. Computational domain for solidification simulation coupled with single spray cooling.

Solidification coupled with multi-spray cooling

In this study, a thin slab casting machine is utilized to demonstrate the application of the solidification model coupled with the aforementioned heat transfer on the slab surface model. Figure 2-32 shows the computational domain selected to study the initial solidification stage in continuous casting. Knowledge of the heat transfer rate on the slab surface and the solidification

rate inside the slab is pivotal for slab quality control because a sufficient cooling rate must be provided to maintain a proper solidification rate. Otherwise, defects or shell breakout incidents might occur. The initial solidification region includes the entire primary cooling region and the beginning of the secondary cooling region. To obtain more realistic fluid flow and temperature distributions from the primary cooling region rather than arbitrarily assuming the distributions, a separate fluid flow, solidification model were developed, and details about the model and the simulation results can be found elsewhere [282, 283]. The results at the end of the primary cooling region, i.e., the mold exit, are used as the inlet conditions in the current study.

As shown in Figure 2-32, there is a customized two-port SEN submerged into a rectangular mold which is followed by 9 rolls and 8 rows of water sprays. Each row contains 5 spray nozzles. The computational domain is extended to the entire slab width. The solidified shell, together with the enclosed molten steel, moves in the casting direction at a constant velocity. A contact angle of 7° between the rolls and the slab is assumed to include the depression effect on the slab surface [7]. Similarly, the heat transfer on the slab surface is conducted in a separate simulation, but the effect of spray cooling and roll contact cooling is coupled through the surface HTC distribution. Details regarding the coupling methodology are discussed in the boundary conditions section. Also, this computational domain can be used to simulate different sections in the secondary cooling region with some modifications of the boundary conditions.
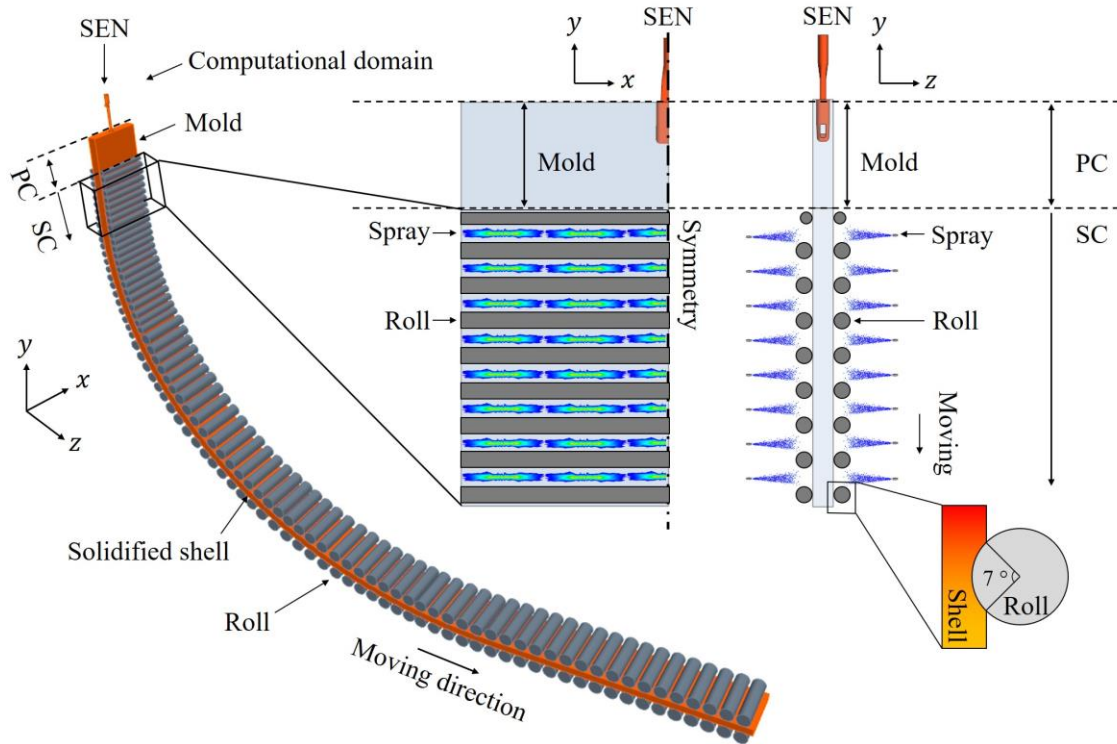
Figure 2-32. Computational domain for solidification simulation coupled with multi-spray cooling.

Boundary conditions

Solidification coupled with single spray cooling

As shown in Figure 2-31, the two faces of the computational domain perpendicular to the x direction are set as symmetric surfaces, indicating the domain is only one section of the slab. The two faces perpendicular to the y direction are referred to as the upstream and downstream surfaces, respectively. The initial temperature of the face centroid on the downstream surface is set to that of the closest cell centroid. The temperature of the face centroid is constantly updating during the simulation according to the upstream conditions. As for the upstream surface, both velocity and temperature conditions are assigned. Figure 2-33 (a) shows the velocity and temperature profiles applied to the upstream surface. The distribution of the two profiles is obtained at the mold exit from the primary cooling simulation, but the magnitude varies. If the domain is used to simulate the beginning of the secondary cooling region, then the two profiles extracted from the primary cooling simulation can be directly applied without any modification since the simulated region in the current model is physically connected with the primary cooling region. However, if the domain

174

is used to simulate any other locations in the secondary cooling region, then the magnitude of the profiles must be adjusted accordingly, but the distribution can be assumed unchanged. The two surfaces that are perpendicular to the *z* direction are cooled by water sprays and rolls, as well as the surrounding air. The effect of the heat transfer on the slab surface is coupled into the current study through HTC profiles, as shown in Figure 2-33 (b). The HTC values on these two surfaces, also known as the broad faces, reflect the cooling intensity on the slab surfaces and are kept constant throughout the simulation. The two broad faces are also treated as slip walls to reflect that the entire slab region is moving during the continuous casting process.
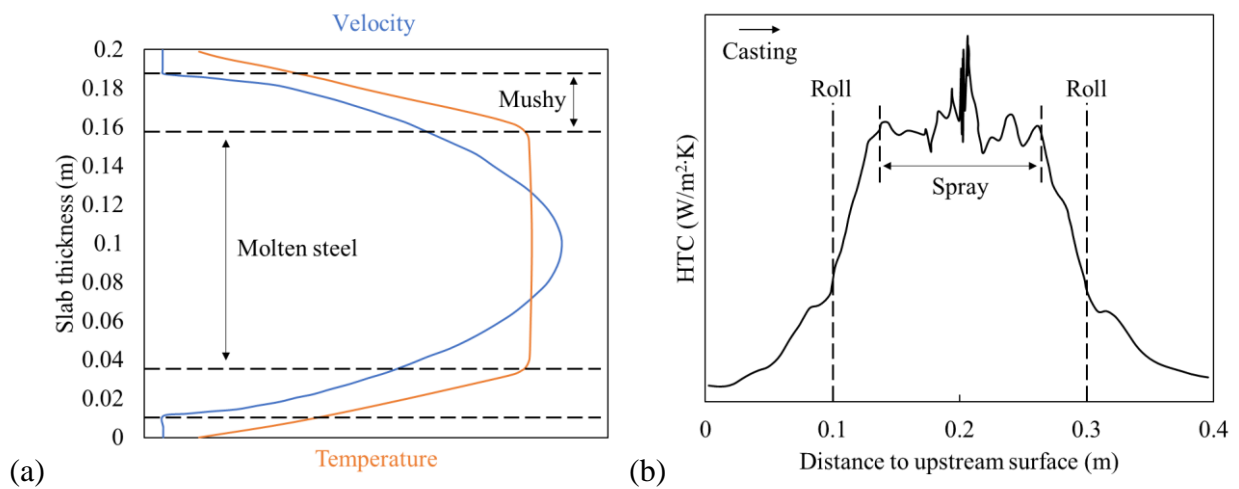
Figure 2-33. Side view of the boundary profiles at: (a) upstream surface, and (b) broad faces.

Solidification coupled with multi-spray cooling

The computational domain illustrated in Figure 2-32 involves many complex phenomena such as molten steel circulations in the mold, solidification, jet atomization, jet impingement heat transfer, and species transport. Also, the time scale and the length scale of jet impingement heat transfer are only a fraction compared to other macroscopic phenomena. One comprehensive three-dimensional numerical model covering every aspect in the initial solidification stage is still not available yet. To balance the efficiency and the accuracy of the simulation, the current study divides the simulation into three steps. Each step corresponds to one simulation, and a coupling procedure is developed to integrate all the simulations.

Figure 2-34 illustrates the domains and the coupling procedure. The first step simulation includes the SEN and the entire primary cooling region. An Eulerian-Eulerian approach is applied to simulate the circulation of the molten steel jets and the solidification of the molten steel against mold walls. The second step simulation includes a thin solidified shell, a pair of rolls, and 5 sprays between the rolls. 8 Eulerian-Lagrangian-based simulations are performed using this domain to obtain the heat transfer rate between a pair of rolls. Molten steel solidification is excluded from the step two simulation due to the significant time scale difference between the solidification and the spray cooling. The last step simulation considers the whole slab region below the mold, including 9 rolls and the effect of water sprays.

The results from the first and second step simulations are coupled with the last step simulation through boundary conditions. For instance, the volume fraction of solid, the velocity components of molten steel, and the temperature on the mold exit plane in the first step simulation are applied to the last step simulation as the inlet conditions. Similarly, the HTC profiles on the slab surface between rolls are used as the thermal boundary conditions in the last step simulation. Thus, with the information from the previous two simulations, the last simulation can resolve the solidification, turbulent molten steel flow, and the effect of heat transfer on the surface simultaneously in great detail.
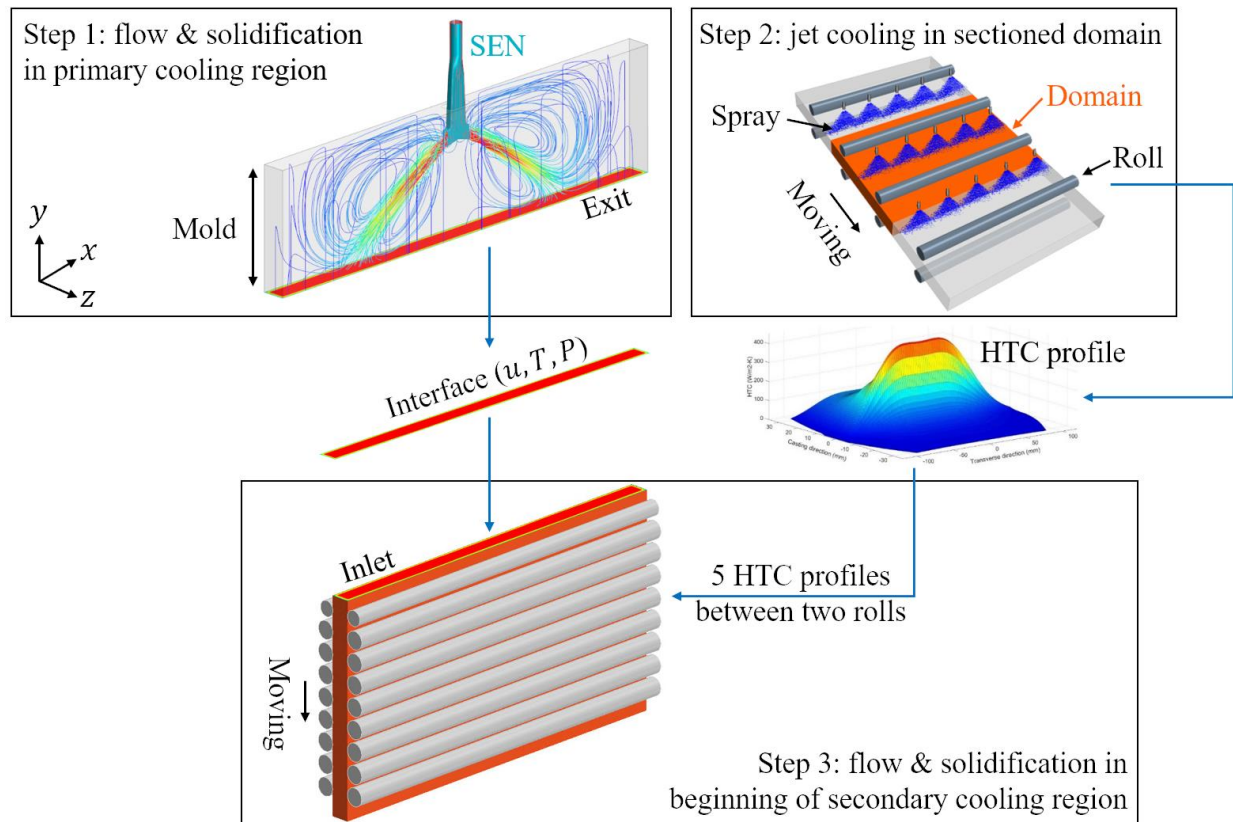
Figure 2-34. Three-step coupling simulation procedure for the simulation of initial solidification.

2.2.4 Grid independent study

The mesh size used for the solid region in the spray cooling simulation is not applicable for the solidification simulation. In the previous model, the smallest control volume is defined based on the characteristic length of a droplet. Usually, the diameter and the smallest mesh cell size are applied in the region where droplet impingement and heat transfer occur. While in the solidification simulation, the characteristic length is the dendrite arm spacing, and the finest mesh cell should be applied to the mushy zone and the solid region where velocity and temperature gradients are the highest. Therefore, it is critical to evaluate and optimize the mesh type and cell size. To achieve this purpose, three different mesh types and cell sizes are applied to the computational domain shown in Figure 2-31, and the results are summarized in Figure 2-35.
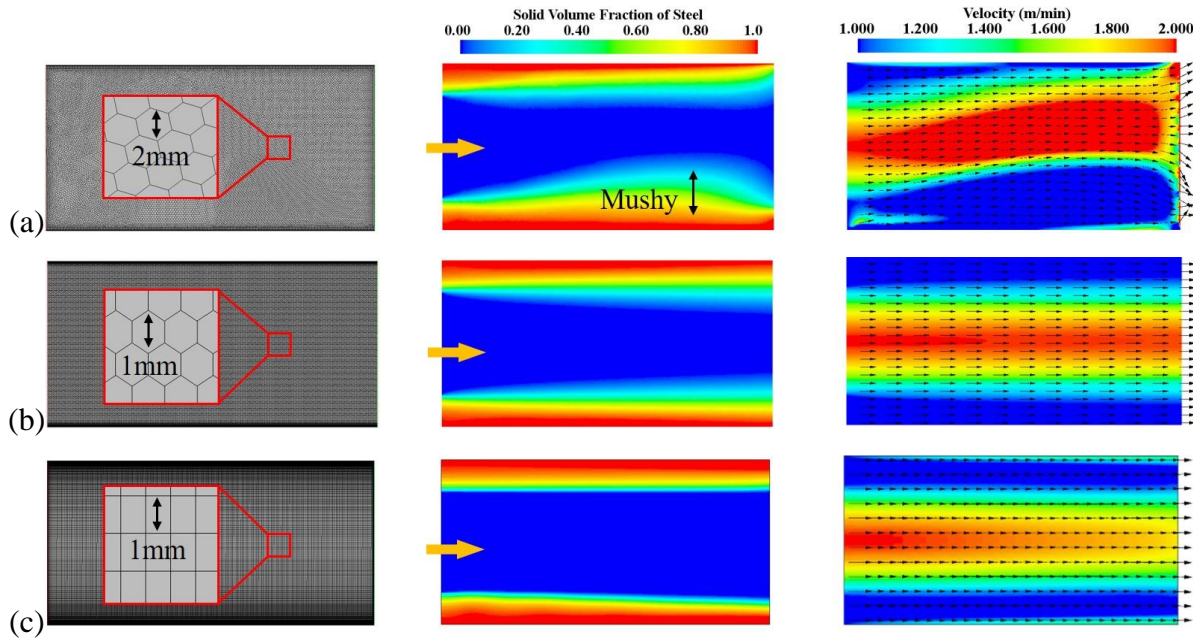
Figure 2-35. Grid independent study with: (a) 2mm polygon type of mesh, (b) 1mm polygon type of mesh, and (c) 1mm hexagon type of mesh.

Figure 2-35 shows the mesh distribution, solid volume fraction, and velocity distribution on a vertical cross-section of the slab, which is cooled by a water spray. Three different mesh and cell sizes, namely 2mm polygon type of mesh, 1mm polygon type of mesh, and 1mm hexagon type of mesh, are investigated in the current study. Based on the features of the solidification process in the secondary cooling region, where solid shell forms from the surfaces of the slab and grows towards the molten steel region in the center, a layer of 16 cells is applied to the shell region, and a uniform cell size of 1mm is used in the molten steel region.

The simulation with the largest cell size, 2mm polygon, predicts the thickest mushy zone, and the mushy zone on the bottom surface of the slab is much thicker than that on the top. The uneven growth of the solid shell on both surfaces imposes different resistances on the molten steel, which is lifted to some extent at the lower portion of the slab. Much more symmetric distributions of solid shell and fluid flow are observed using the refined polygon mesh and the hexagon mesh. Also, between the fine polygon mesh and the hexagon mesh, the mushy zone predicted by the hexagon mesh is much thinner, and the flow is able to expand to a broader region in the vertical direction due to less resistance. In general, the hexagon mesh has several advantages over the

polygon mesh in terms of accuracy, and the structured mesh is preferred in numerical studies of solidification, therefore, the hexagon type of mesh is selected for later simulations.

The issue of the total number of mesh cells in the computational domain arises in most 3-D solidification simulations. The previous studies have pointed out that fine cell size is required to capture the small increment of shell across the domain. On the other hand, the total number of mesh cells in the domain must be balanced to ensure the computational time is within a reasonable time period. For instance, if the 1mm hexagon mesh is applied to the simulation coupled with multiple sprays, the total number of mesh cells can easily exceed 20 million, which would require several weeks of computational time.

The adaptive mesh method is one method to balance the accuracy of the model and the computational time. The idea behind this method is straightforward that is to employ finer mesh cells in the region where the characteristic length is smaller. The procedure of the adaptive mesh method applied to the current study is shown in Figure 2-36. First, a preliminary simulation with the uniform coarse mesh cell of 10mm is conducted to obtain the general shell profile, including the location and thickness. Then, the coarse mesh is further refined based on the initial guess of the shell profile. The refinement mesh size is not universal across the shell thickness. In the current study, the mesh cell size inside the solid region where the solid fraction is larger than 0.9 is reduced to 50% of the previous size, and the one in the mushy zone where the solid fraction is between 0.1 and 0.9 is reduced by 75% compared to the last simulation. A new simulation with the refined mesh is then conducted, and the shell profile is compared with that from the previous simulation. If the difference in shell thickness between the two simulations is less than a pre-defined small number, usually 1%, then the process is stopped. Otherwise, the mesh refinement continues. It should be noted that the current mesh refinement procedure is recommended for simulations where the transition from the liquid region to the solid region is smooth, and there is no abrupt change during solidification. If the convection of the fluid flow becomes much intense such as the condition in the primary cooling region, where liquid jets impinge on the newly-formed thin shells periodically, a much more sophisticated refinement-coarsening adaptive mesh method is required. Such a method should dynamically refine the mesh cells in the mushy zone and coarsen those in

the liquid region according to the current flow condition. One example of this method can be found elsewhere [284].
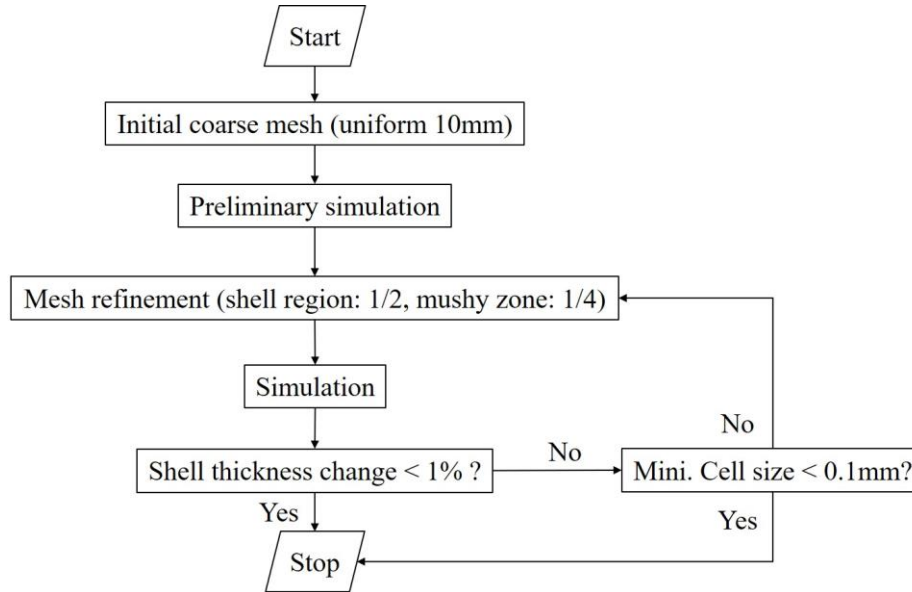
Figure 2-36. Flow chart of the adaptive mesh refinement procedure.

The effect of mesh refinement is shown in Figure 2-37. The hexagon type of mesh from the previous study is used to search for the optimum mesh cell size across the computational domain. A set of coarse mesh cell of 10mm is set to the domain before the preliminary simulation as the base cell size. The mesh cell is uniform across the domain. After the preliminary simulation, the adaptive mesh refinement routine is activated. Mesh cells in the mushy zone and the solid region are marked for refinement, and the cell sizes are reduced accordingly by the pre-defined ratios. The total number of the mesh cells after the first refinement increases by 450% to 324000. The mesh size is reduced from 10mm to 1.5mm in the mushy zone after 3 refinements, and the total number of mesh cells increases to more than 13 million. Such a drastic increase in the total number of mesh cells suggests that another stopping criterion should be considered during the refinement procedure. As shown in Figure 2-37, the distribution of solid fraction varies very little after 2 refinements. Hence, a maximum number of refinements, or the minimum mesh cell size, should be examined at the end of each refinement, and the procedure should be forced to stop when the stopping criterion is satisfied, even the change of the solidified shell is still larger than 1%. This stopping criterion is used to prevent computer memory overload by excessive mesh refinement.
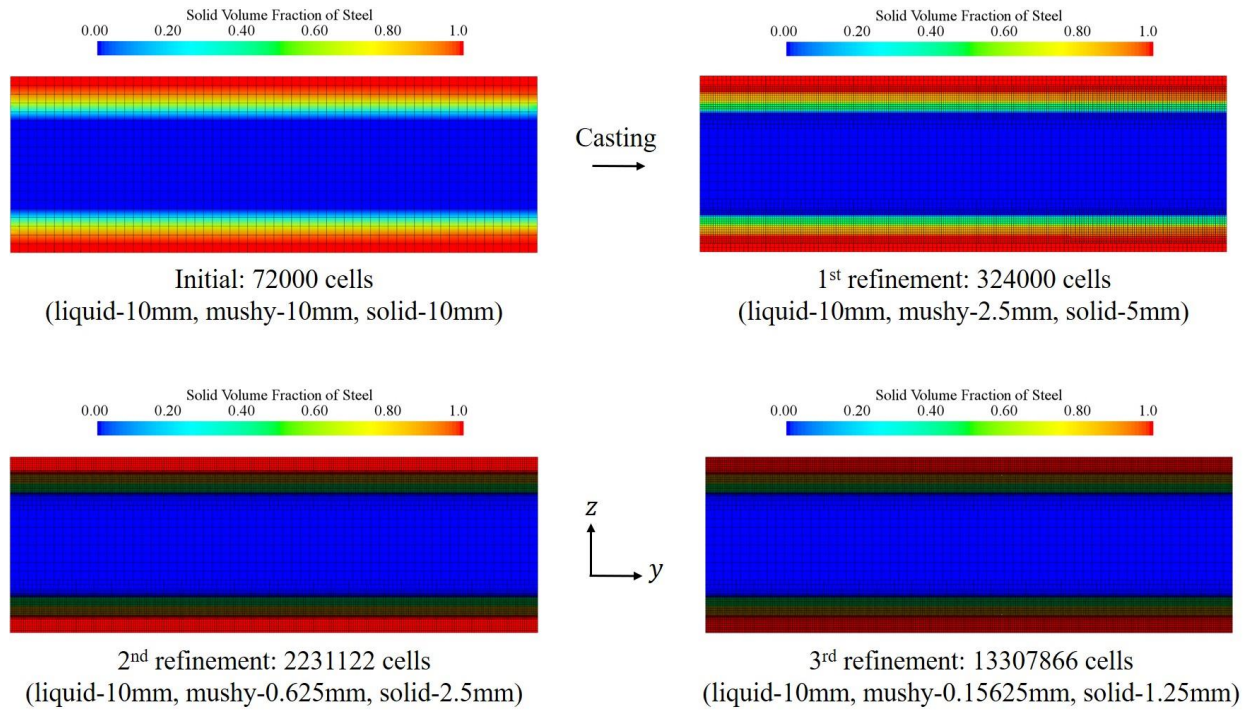
Figure 2-37. Mesh distribution on the central cross-section before and after each refinement.

The importance of the mesh refinement can be best seen from the shell thickness predictions. Figure 2-38 shows the solidified shell regions that grow from both the top and bottom surfaces of the slab toward the center. All the simulations with different mesh sizes can capture the increase of the solid shells due to the heat transfer on both surfaces of the slab. However, the increase of the solid shells in the preliminary simulation is somewhat abrupt compared to other simulations with mesh refinement. As the mesh size becomes finer, the mesh cell size in the mushy zone is of the same magnitude as the increment of the solidified shell. As a result, the shell growth becomes much smoother, and several increments of the shell thickness can be identified from the simulation.

Figure 2-39 evaluates the shell thickness along the centerline in the casting direction in both top and bottom shell regions. The preliminary simulation predicts the thinnest shell across the domain as expected since the mesh size is not fine enough to resolve the minimal shell growth. With the mesh refinement, shell thickness increases significantly until it reaches the grid-independent solution. Quantitatively speaking, the change of the shell thickness can be reduced to within 1%

after 3 refinements by using the current adaptive mesh method. Hence, the adaptive mesh method with maximum 3 refinements will be applied to future solidification simulations.
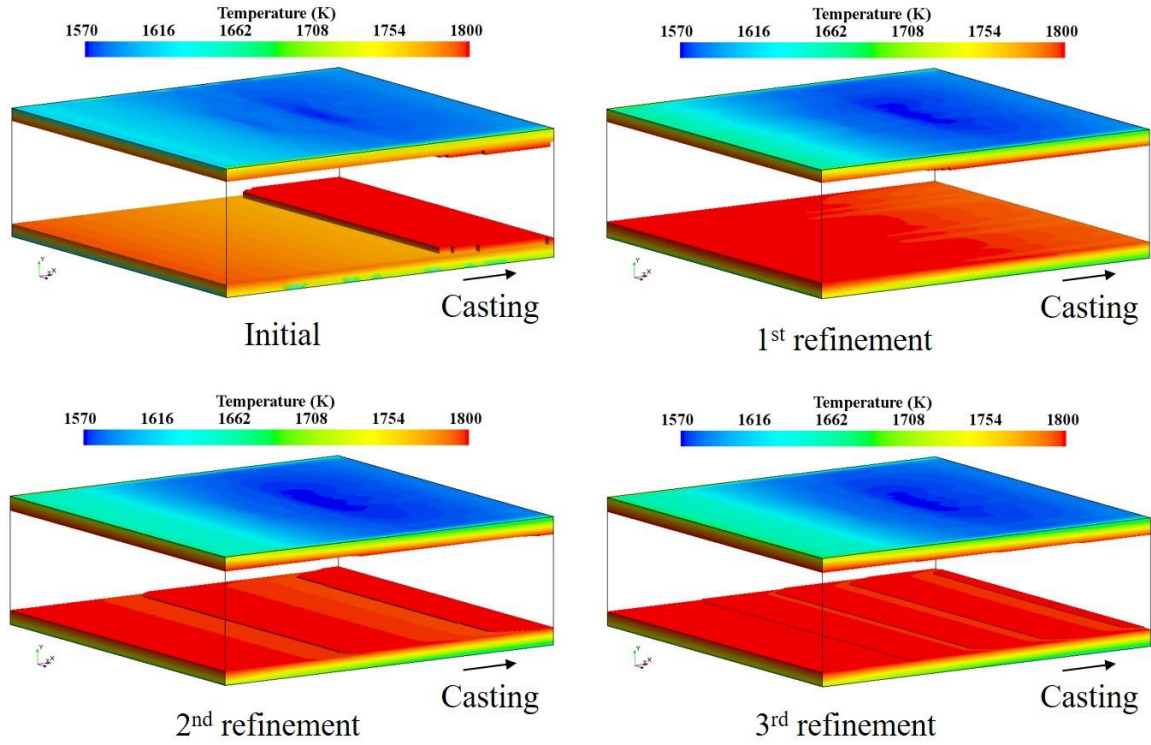
Figure 2-38. Solidified shells before and after each refinement.
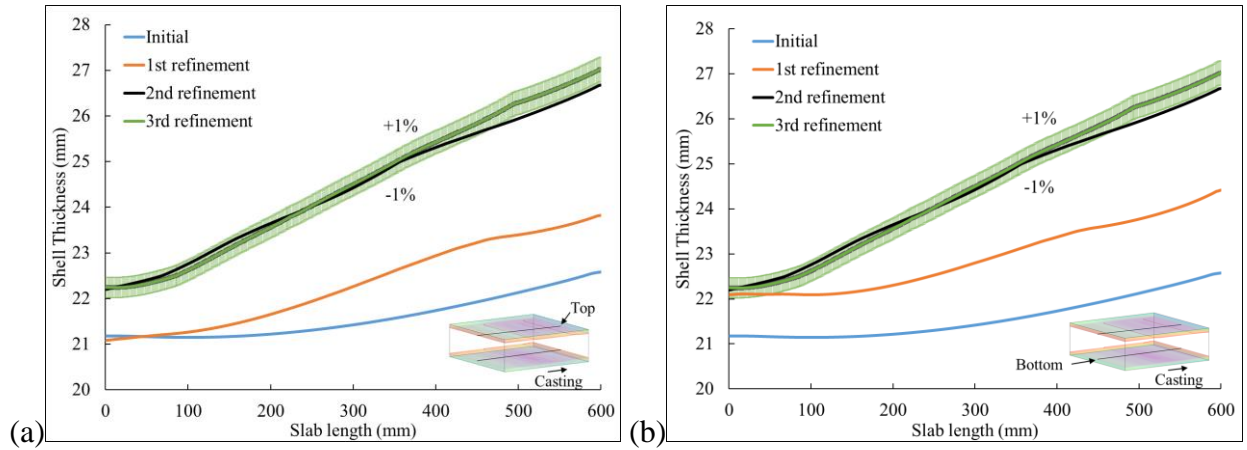
Figure 2-39. Comparisons of shell thickness before and after each refinement at: (a) top broad face, and (b) bottom broad face.

2.2.5 Numerical schemes

For all the solidification simulations, the second-order upwind scheme is applied to convection terms, and the first-order temporal discretization is used for time-related terms. The time step is set to 0.01s for all the simulations to resolve small shell increments. The SIMPLE algorithm is used to couple velocity and pressure. The adaptive mesh refinement procedure is integrated into the solver through a routine activated after a pre-defined time period. The time to call for a mesh refinement depends on the casting speed and the domain length. In general, the mesh cells are required to be adjusted after the incoming molten steel flows throughout the entire domain. The total number of mesh refinement is limited to 3 times unless the shell profile is converged first. If the shell profile does not converge after 3 mesh refinements, then the results in the last simulation will be used as the base simulation, and a new cycle of mesh refinement will be conducted. Converged results can be reached after the change of the shell thickness is within 1%. A typical converged result renders scaled mass residual of 10^{-3}, scaled energy residual of 10^{-6}, and scaled momentum and turbulence kinetic energy residuals of 10^{-4}. All the cases are developed based on the platform of the software package Star-CCM$^+$ 14.04.011.

2.2.6 Material properties

Solidification coupled with single spray cooling

A low carbon steel containing 0.05wt% carbon is used in the current study. The temperature-dependent material properties shown in Figure 2-40 were obtained from Dr. Pfeiler's dissertation [197]. Density, thermal conductivity, and dynamic viscosity were calculated by IDS, and the specific heat was provided by an industrial collaborator. The calculated liquidus and solidus temperatures are 1807K and 1789K, respectively. The latent heat of fusion is 243kJ/kg. Enthalpy is computed from the specific heat shown in Figure 2-40 (d).
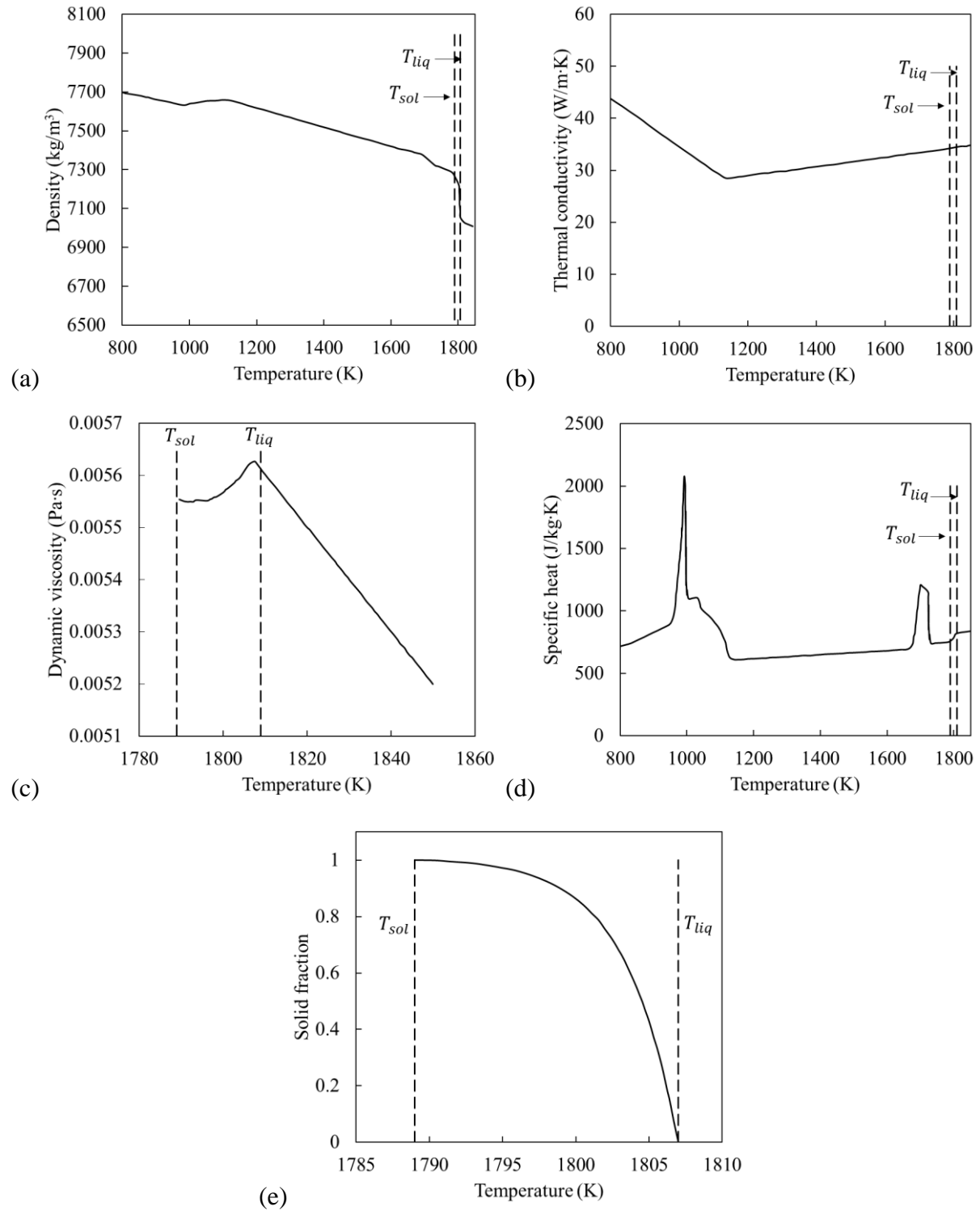
Figure 2-40. Thermodynamic properties of the steel used in the study of solidification coupled with a single spray: (a) density, (b) thermal conductivity, (c) dynamic viscosity, (d) specific heat, and (e) solid fraction [197].

Solidification coupled with multi-spray cooling

A low carbon alloy steel (0.2wt% C) obtained from an industrial collaborator is used in the current study. The steel properties are calculated by JMatPro and are shown in Figure 2-28 and Figure 2-41, respectively. The liquidus and solidus temperatures are obtained from the phase fraction diagram shown in Figure 2-41 (a). The liquidus temperature is defined as the point where delta ferrite appears, and the solidus temperature is defined as the point where liquid disappears. Even though the temperature in the secondary cooling region usually extends from 1800K to 1200K, the property calculation is carried out from 2300K to 300K to cover all the phase transition regions. As shown in Figure 2-28 (a), the shell shrinkage immediately takes place below the liquidus temperature due to the transition from liquid and delta ferrite to austenite. The effect of the phase transition is also visible on other property diagrams. Therefore, different phases are included in the material properties and are incorporated in the solidification simulations.
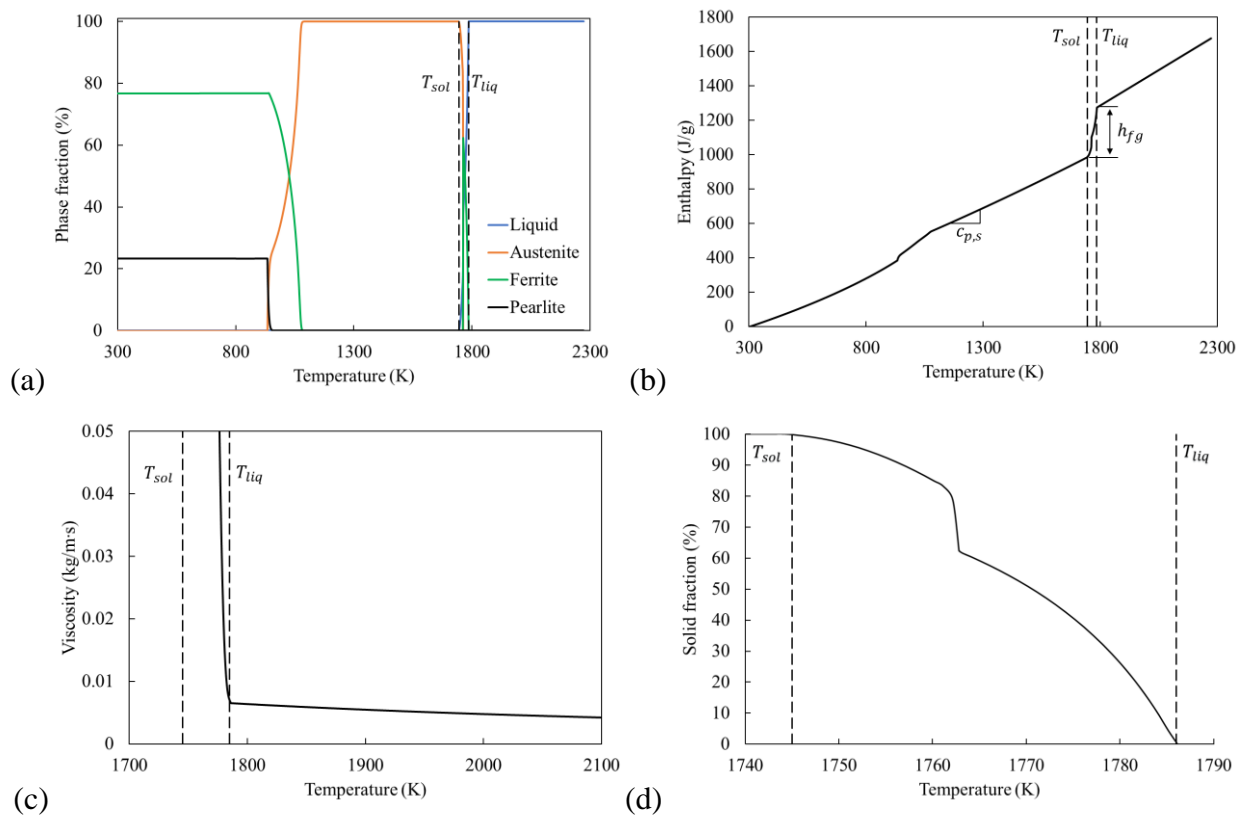
Figure 2-41. Thermodynamic properties of the steel used in the study of solidification coupled with multiple sprays: (a) phase fraction, (b) enthalpy, (c) viscosity, and (d) solid fraction.

185

3. RESULTS - HEAT TRANSFER ON STEEL SLAB SURFACE

3.1 Validations

3.1.1 Droplet size distribution

Hydraulic nozzle

Droplet size prediction prior to the impingement is crucial for determining the impingement outcome and the corresponding heat transfer rate. A Lechler 660.766 flat-fan hydraulic nozzle, which has an equivalent orifice diameter of 1.9mm and 90° spray angle with respect to the horizontal direction, was isothermally tested by an industrial collaborator using the VisiSize laser system, which is shown in Figure 3-1 (a). The nozzle was held 130 mm above the measurement plane to produce a full spray at the water flow rate of 11.36 L/min. Droplet size from the center to the edge of the spray was measured by the laser imaging system with a spatial increment of 20 mm. During the experiment, a pulsed light illuminated the screen, which was located 130mm below the exit of the nozzle. The short pulse froze the motion of the droplets, allowing blur-free visualization of droplet size and shape. Images from the digital camera were then transferred to a computer, and high-speed real-time particle sizing software analyzed the images obtained in order to build up the diameter distribution.
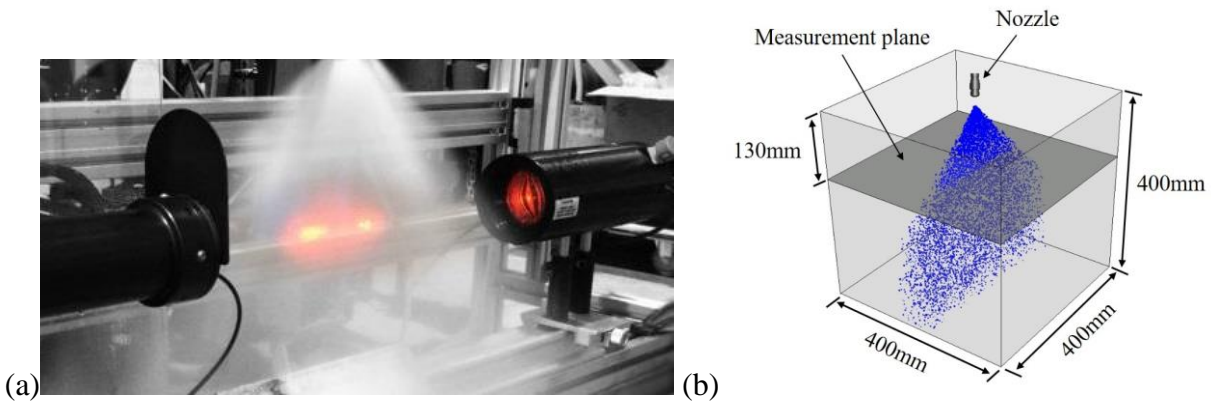
Figure 3-1. Droplet size distribution by: (a) experimental measurement [285], and (b) simulation.

As illustrated in Figure 3-1 (b), a cubic computational domain with sides of 400mm is used to simulate the spray process. The flat-fan nozzle is fixed at the top surface of the domain. The droplet

size distribution is measured on the plane that is 130mm below the nozzle orifice. All the boundary surfaces are set as pressure outlets to allow the surrounding air to flow freely through the boundary surfaces as the spray proceeds.

The measured average diameters from 0mm (spray center) to 120mm (spray edge) with the increment of 20mm are compared with the simulation, and the results are shown in Figure 3-2. The predictions by the current model show good agreement with the measurements. Droplet size shows an increasing trend from the center to the edge. Smaller droplets at the center of the spray are the result of much more frequent collisions and breakups, which are less potent near the edge of the spray where the droplet number density is lower. However, the model predicts smaller droplet diameters between 90mm and 110mm away from the center of the spray compared to the measurement, suggesting an over-prediction of droplet collision and breakup in this region. Due to the low droplet number density near the edge of the spray, the droplet-air interaction becomes the dominant mechanism for the breakup process. Because the current study treats droplets as rigid spherical bodies, the effect of surface tension is excluded from the simulation, thereby sacrificing some accuracy when such effect is no longer negligible. Nevertheless, water sprays in the secondary cooling region are designed to overlap with the adjacent ones, and the effect of droplet-air interaction is significantly reduced in the overlapping region.
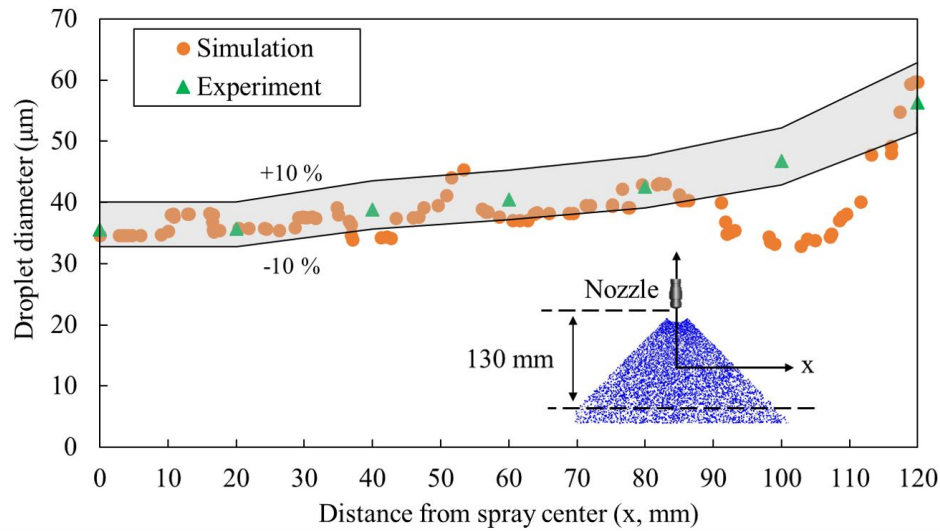
Figure 3-2. Validation of droplet size distribution.

Air-mist nozzle

The air-mist model is validated against the measurement for a Delevan Cool-Cast W19917-15 air-mist nozzle provided by an industrial collaborator. The measurement was conducted at the collaborator's facility. As shown in Figure 3-3, the nozzle was mounted on a moving device horizontally to avoid reflections of droplets from the ground through the measurement volume. A Phase Doppler Interferometry (PDI) was placed at a distance of 190mm from the nozzle orifice to measure the droplet size. During the measurement, the moving device carried the nozzle to different locations to allow the fixed PDI to measure the droplet size at different locations within the spray. At the end of the experiment, the point-based measurements were analyzed, and the volume-weighted average method was applied to produce representative droplet sizes.
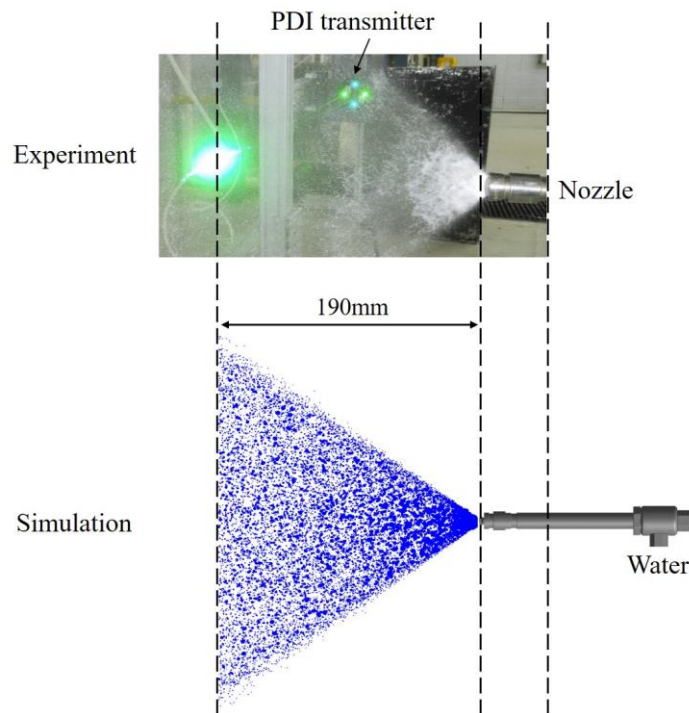
Figure 3-3. Illustration of droplet size measurement for an air-mist nozzle.

As illustrated in Figure 3-3, the same air-mist nozzle is simulated, and the orientation of the spray is also rotated to horizontal to match the setup in the experiment. The internal structure of the nozzle is included in the simulation to account for the water-air interaction. A cubic computational domain with sides of 200mm is used to model the spray outside of the nozzle. Because the

experiment was conducted at room temperature, it is assumed the atomization process is isothermal, and the reference temperature is set to 300K. The inlet for the compressed air is treated as a pressure inlet with a constant pressure of 30psi (206843Pa). The inlet for water is considered a velocity inlet with a constant flow rate of 4.5gpm (0.284L/s). All the surfaces of the cubic domain outside of the nozzle are set as pressure outlets to include the air entrainment phenomenon. The simulation is divided into two steps, as described in the methodology section. The first step simulation includes the entire nozzle and a 30mm region outside the nozzle. The second step simulation includes the rest of the domain. Once the second step simulation reaches the steady state, the droplet size distribution on the plane that is 190mm away from the nozzle orifice is analyzed and compared with the measurements.

Figure 3-4 shows the droplet size distribution on the monitor plane and the characteristic droplet diameters from the measurement. The predictions from the current model agree reasonably well with the volume-weighted average diameters from the experiment. Both the VOF-To-DPM model and the transition criteria are valid to predict the primary breakup process.
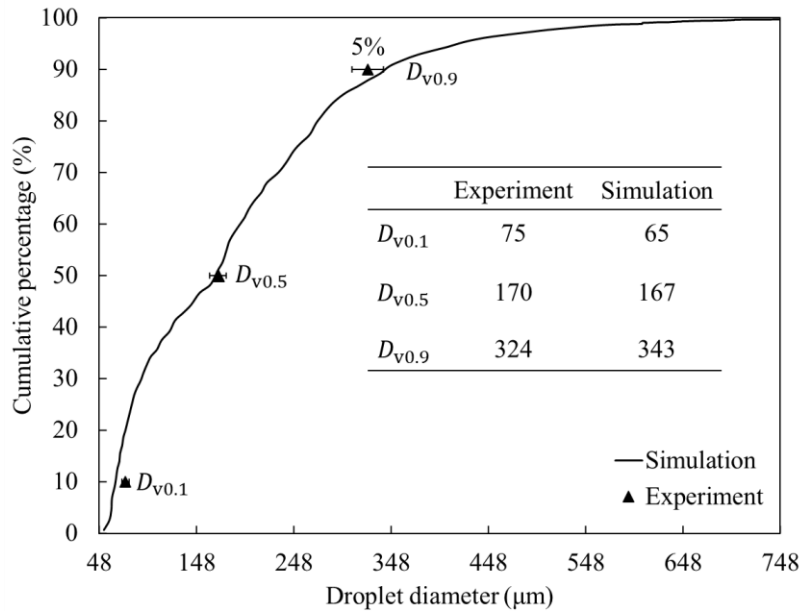
Figure 3-4. Droplet size distribution at 190mm from the air-mist nozzle.

Liquid jet in cross-flow

Another validation for the VOF-To-DPM model is against a benchmark experiment for a liquid jet in cross-flow [286]. The experiment carried out by Leong and Hautman has been used as a benchmark for validating numerical models of jet atomization. Figure 3-5 shows the computational domain of the simulation based on the numerical work of Xiaoyi et al. [287, 288]. A testing liquid was injected into a gas region from the bottom of the domain through a circular orifice with the diameter of d_0. Meantime, a stream of air at standard conditions was blown into the domain through a surface in front of the orifice. As the liquid jet "crosses" the fast-moving air stream, it was fragmented into strings of ligaments which further break into droplets. The size distribution of droplets generated from the primary breakup process was measured by a Phase Doppler Particle Analyzer (PDPA) downstream. The distance from the measurement location to the orifice is as far as $33d_0$ to avoid blurring imaging occurring in dense sprays. Adaptive mesh refinement is applied to the current study as recommended by Xiaoyi et al. The material properties and operating conditions used in the simulation are listed in Table 3-1.
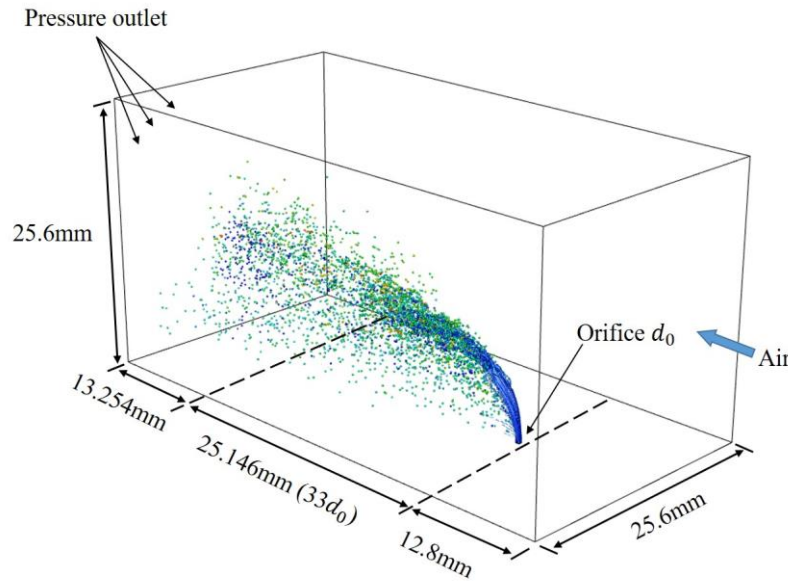
Figure 3-5. Computational domain for the cross-flow simulation.

Table 3-1. Material properties and operating conditions used in the cross-flow simulation.

Parameter	Value
Orifice diameter (mm)	0.762
Liquid mass flow rate (kg/h)	15.3
Liquid density (kg/m^3)	780
Liquid dynamic viscosity (kg/m·s)	0.0013
Liquid-air surface tension (N/m)	0.024
Liquid Reynolds number	3490
Liquid Weber number	180
Air velocity (m/s)	69
Liquid and air temperature (K)	300

An adaptive mesh method is also applied to the current study. The initial base mesh is set to 400µm universally throughout the computational domain. Meshes that satisfy the VOF-To-DPM transition criteria are refined up to 5 levels, where the minimum mesh size is 12.5µm. The minimum mesh size after 5 levels of refinement in the current study is half of that used in the work of Xiaoyi et al. According to their research if the minimum size is set to 25µm, then the transition from VOF ligaments to DPM droplets is only valid for ligaments that are larger than 25µm, below which are not considered for transition [287, 288]. Figure 3-6 shows the mesh distribution on the center cross-section plane after 5 levels of refinement. Finer meshes are seen in regions where the liquid core and ligaments present. The adaptive mesh routine checks the volume fraction of the liquid after each time step and refine or coarse the meshes if necessary. To help stabilize the solution, a time step of 10^{-7}s is used in the current study, and the droplet size distribution at 1.884ms is compared with the measurement and the prediction by Xiaoyi et al.
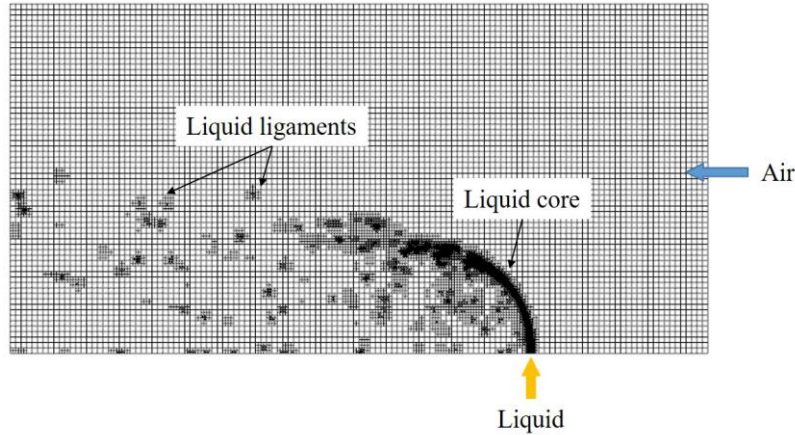
Figure 3-6. Mesh distribution on the center cross-section plane after 5 levels of refinement.

Figure 3-7 shows the simulation results of the liquid jet fragmented by the incoming airflow predicted by the VOF-To-DPM model. The deep blue iso-surface represents the regions where the volume fraction of liquid is larger than 0.1. The spheres surrounding the continuous liquid are the DPM droplets converted from the liquid. Wave disturbances grow on the liquid jet immediately after injection. The unstable jet core starts to break up into fragments at a distance of about $6d_0$. Most of the fragmented ligaments are carried downstream, where the qualified ligaments are converted to spherical droplets. Some ligaments detach from the liquid core at the early stage of the injection. Those ligaments grow from the periphery of the liquid core parallel to the airflow direction and extend further into the downstream. The breakup process of these ligaments is less catastrophic, and some of the ligaments stay cylindrical even after detaching from the liquid core. One of the enlarged views in Figure 3-7 shows such ligament. After detachment, both ends of the ligament form a near-sphere shape, which is very likely to be converted into DPM droplets.

Figure 3-8 shows the comparison of the droplet size distribution on the monitor plane with the data obtained from the literature. The predicted droplet diameter from Xiaoyi's simulation is shifted toward larger droplets by approximately 20μm due to insufficient mesh refinement [287]. By increasing the mesh refinement level to 5, the current study can capture the transition for droplets that are smaller than 25μm, thereby improving the accuracy of the simulation. This validation further demonstrates the importance of the mesh size for the VOF-To-DPM simulations.
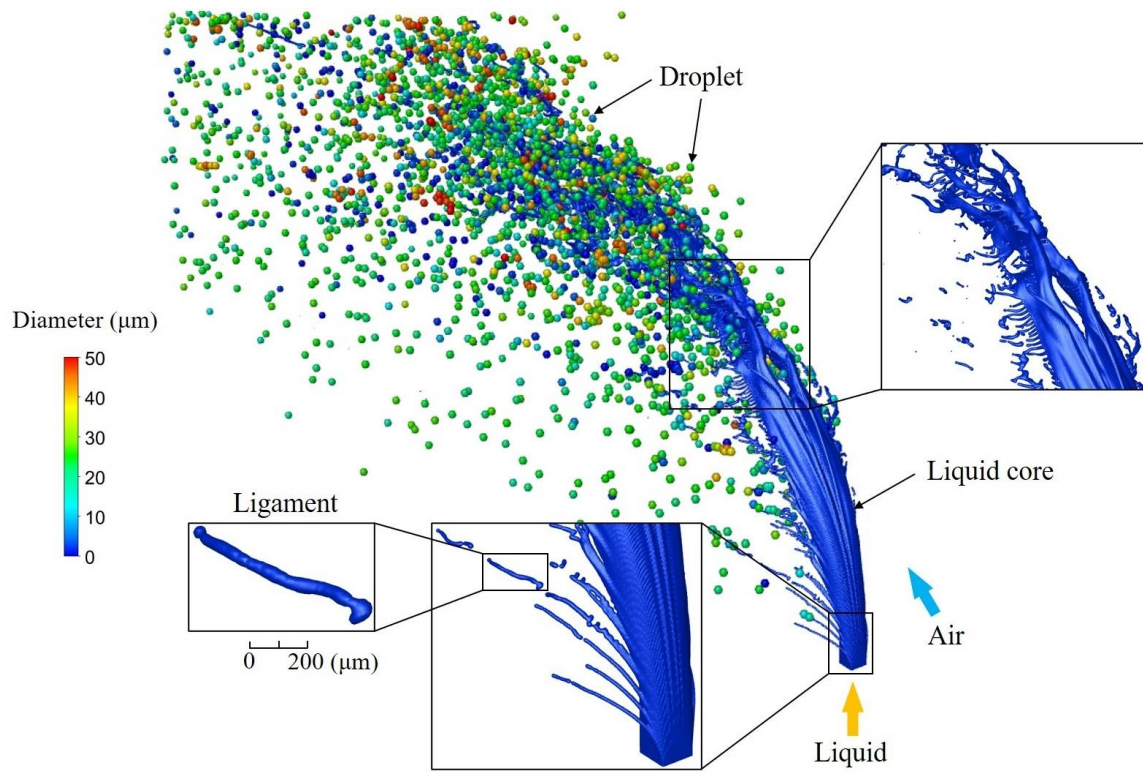
Figure 3-7. Liquid jet in cross-flow predicted by VOF-To-DPM model.
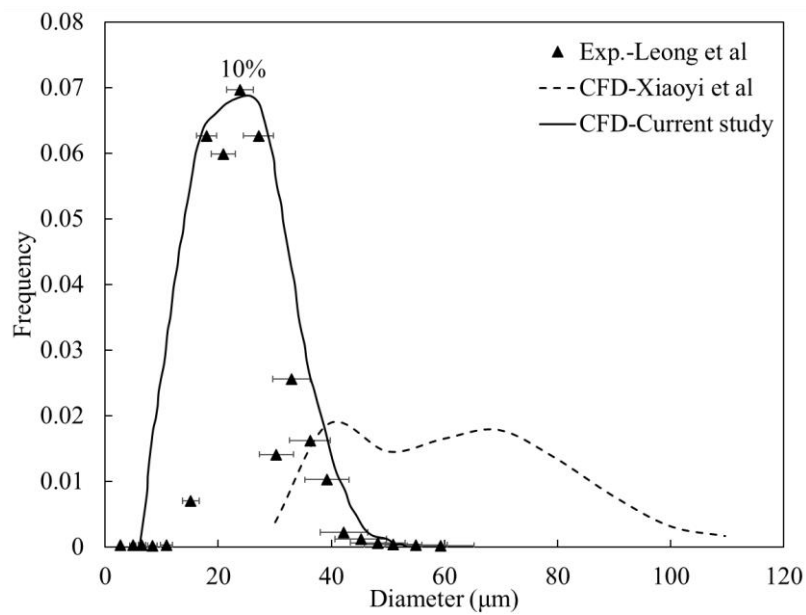
Figure 3-8. Comparison of the droplet size distribution for the cross-flow simulation.

3.1.2   Droplet impact pressure

Spray impact pressure measurement reflects the uniformity of spray on the impacted surface. The impact pressure is usually measured by a moving force sensor underneath a spray. Figure 3-9 illustrates the measurement process. During the measurement, the testing nozzle is placed above the sensor device and produces a spray throughout the measurement process. The sensor device first moves to the outside of the spray pattern and then traverses through the spray while taking measurements at predetermined intervals. The sensor device travels back and forth through the spray until the entire spray area has been covered, as shown in Figure 3-9 (b). The measuring forces detected by the sensor device are transformed into electric signals and stored in a computer. Finally, the impact pressure at each measurement location can be calculated based on the measuring forces and the known surface area at the tip of the sensor device.
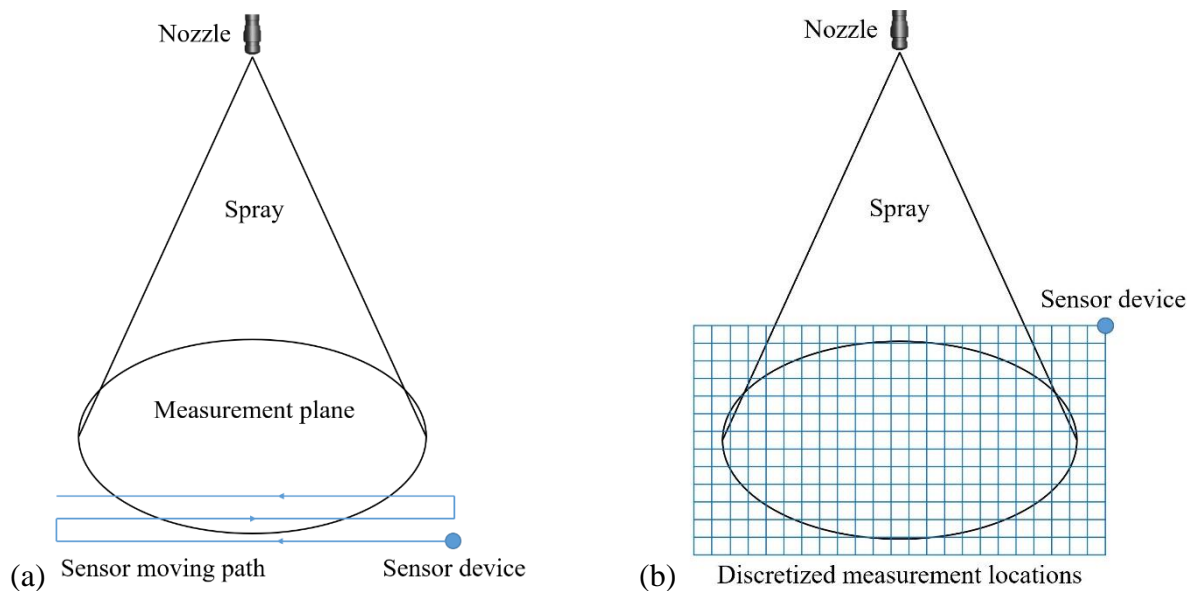
Figure 3-9. Illustration of the spray impact pressure measurement procedure at: (a) beginning, and (2) end of the measurement.

The measured impact pressures were obtained from ArcelorMittal Global R&D East Chicago Center [289]. The Lechler series 660.766.17 flat-fan dovetail nozzle was tested at the Low Impact Pressure Bench (LITB) during the experiment. The spray condition of 3gpm (0.1893L/s) at 70psi (482633Pa) is compared with the simulation. It should be noted that instead of modeling the sensor device, the current study calculates the impact pressure based on the following expression:

$$P_{impact} = \frac{C_d V_{cell} |\vec{u}_{vert}|}{A_{cell} t_{impact}} \qquad (196)$$

Where C_d is the droplet concentration in one control volume, V_{cell} and A_{cell} are the volume and face area of a control volume, respectively. $\vec{u}_{vert}$ is the vertical component of droplet velocity, and it resembles the normal impact in the measurement. t_{impact} is the nominal impact time, which is defined as when a droplet needs to pass the control volume.

Figure 3-10 shows the comparison of the impact pressure between the measurement and simulation. The simulated results show good agreement with the measured data throughout the spray region. The predictions and the measurements are linearly correlated with an R-squared value of 0.9928. In general, the measured pressure is slightly higher than the simulated one. One of the reasons is that droplets must reserve minimum kinetic energy in order to be detectable by the sensor device. Such minimum kinetic energy is determined by the precision of the sensor device. On the contrary, the impact pressure from the simulation is based on mass instead of force. According to Eq. (196), any droplet with non-zero mass and velocity will be included in the pressure calculation.
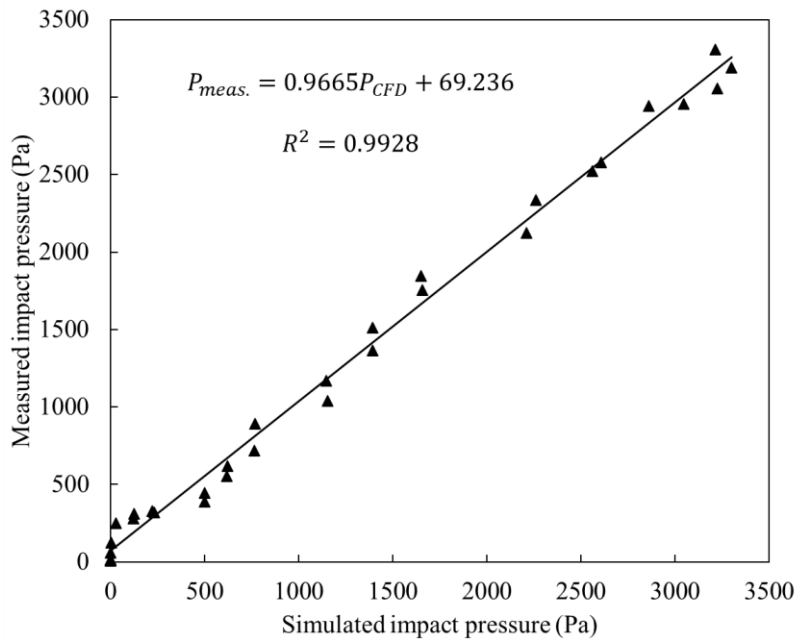
Figure 3-10. Comparison of the impact pressure between the measurement and simulation.

195

3.1.3 HTC distribution on the slab surface

The droplet-wall impingement heat transfer model is validated against the hot-plate experiment conducted at Brno University of Technology in collaboration with an industrial partner. Some of the experimental measurements can be found elsewhere [153, 176, 290-292]. The evaluation of the heat flux between droplets and the hot steel surface is of great interest to both academia and industry. Experimentally, the heat flux through the surface can be measured through either the steady-state or the transient method [137]. The sample is heated up to the target temperature in the steady-state method and maintained at that temperature while cooling by the liquid. The calculations of the wall heat flux involved are straightforward, but multiple experiments must measure the heat flux at different temperatures. On the other hand, in the transient method, only one experiment is necessary to obtain the cooling curve for a specific operating condition. Once the sample is heated up to the target temperature, the heating source is removed, and liquid spray is applied to continuously cool down the sample to the desired temperature. The wall heat flux is computed from the embedded thermocouples using the inversed heat conduction method. This method is more complicated and involves substantial calculation [293, 294], but it is closer to the industrial conditions and has been used extensively for most research studies.

The arrangement of the experimental stand is shown in Figure 3-11. During the experiment, a 600mm by 320mm by 20mm austenitic plate was preheated to 1250°C prior to the measurement and was fixed at a distance of 130mm above an upward-facing spray nozzle. All the plate surfaces were covered by insulation materials to reduce heat loss except the cooling surface. The nozzle was mounted on a trolley to move the nozzle during the experiment to simulate the continuous casting process. Cooling water was directly sprayed onto the plate surface when the trolley was moving in the positive direction, while the spray was reflected by a deflector when the trolley was moving in the opposite direction. A set of thermocouples embedded in the plate recorded temperatures at different locations throughout the experiment. Each thermocouple was placed 40 mm away from the adjacent ones. Both temperature inside the plate and the nozzle position were recorded during the experiment. The experiment was stopped when the plate temperature was below 500°C. The surface heat transfer coefficient and the heat flux through the surface are then calculated by a computer program using the inverse heat transfer method.
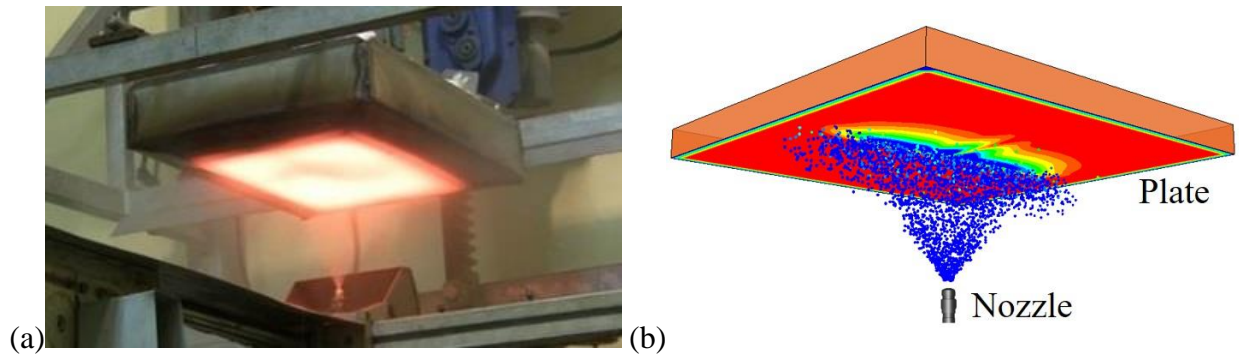
Figure 3-11. HTC distribution by: (a) experimental measurement [176], and (b) simulation.

Figure 3-12 shows the comparison of HTC on the plate surface with the measurements. Location A on the plate surface is right below the spray nozzle orifice, and location D is at the edge of the spray coverage. The average HTC values along the Y direction at each location are compared. In addition, the overall integrated HTC on the plate surface is also shown in Figure 3-12. There is a good agreement between the experimental data and the simulation results. The spray cooling peaks at locations A and B, where most of the droplets are concentrated. Small droplet size and the large surface-to-volume ratio at the center of the spray also contribute to the high heat transfer rate. In addition, droplets at the center have relatively smaller radial velocity components and can retain most of the momentum while traveling in the gas phase. In reality, it is very likely that those high-momentum droplets can penetrate the thin vapor film and contact the hot surface, resulting in an even higher heat transfer rate.

As shown in Figure 3-12, heat transfer rates at some locations are under-estimated compared to the measurements. One of the possible reasons is that the temperature of the specimen dropped below the Leidenfrost temperature near the end of the experiment, as the hot-plate experiment is designed to run a broad spectrum of temperature. The vapor layer in the vicinity of the plate surface disappears as the plate temperature decreases. As a result, the heat transfer rate increases drastically. Therefore, the average HTC from the experiment is higher than that from the simulation, which only takes film boiling into account. The current model is still valid for droplet-wall impingement heat transfer within the film boiling regime.
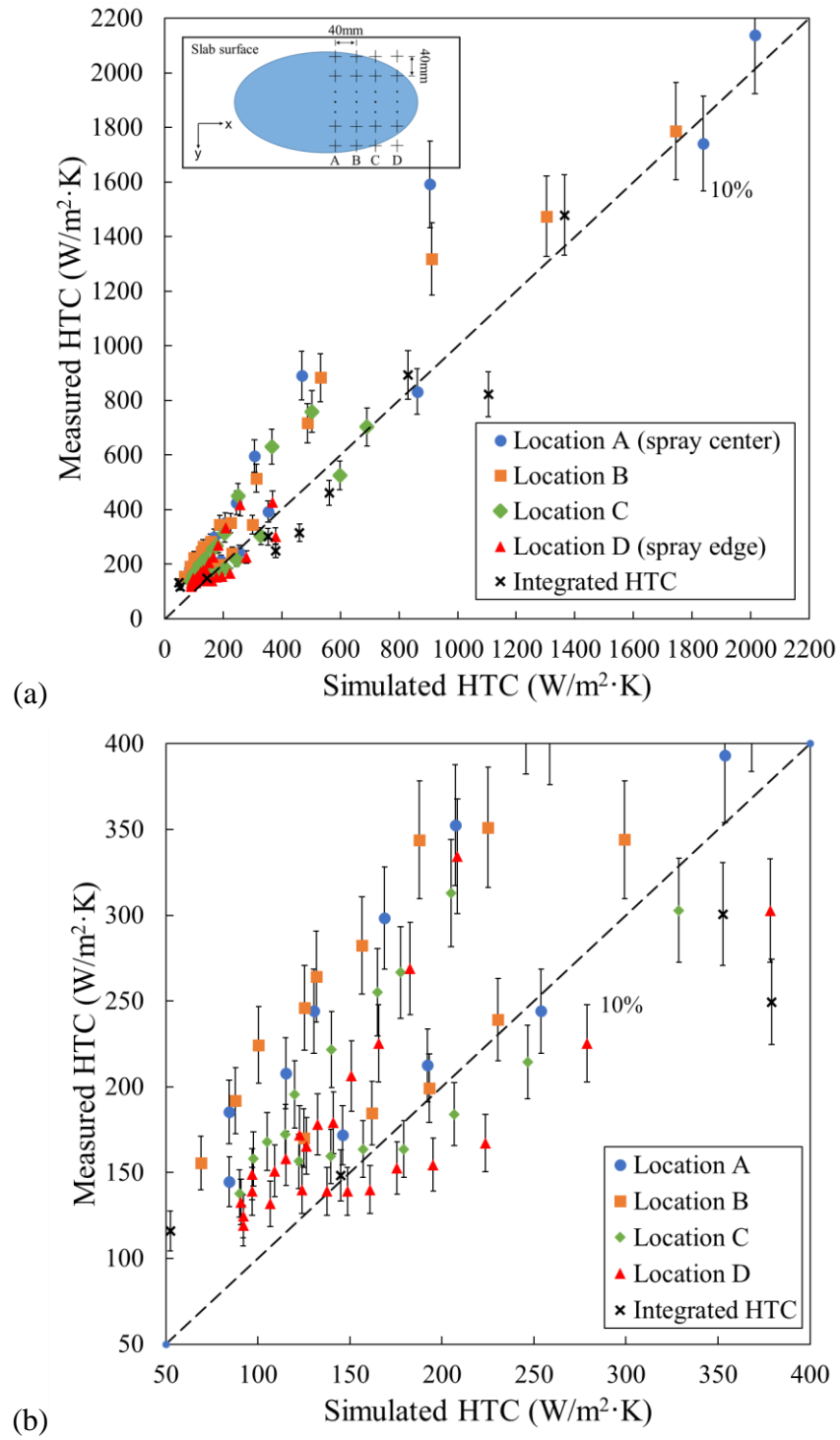
Figure 3-12. Comparison of HTC on the plate surface with the measurements: (a) the full range, and (b) enlarged view of the low HTC range.

3.2 Baseline

A Lechler 660.766 flat-fan hydraulic nozzle and a typical casting condition are investigated to establish the baseline condition. The water flow rate through the nozzle is 7L/min, and the spray standoff distance is 130mm. A 30mm thick and 400mm wide slab is placed below the nozzle. The reference frame of the slab region is moving at a constant velocity of 1m/min relative to the ground. The computational domain is shown in Figure 2-13, and the upstream boundary condition for the slab region is shown in Figure 2-18.

3.2.1 Droplet formation

Figure 3-13 shows the droplet distribution near the injection plane after the first droplet time step. The spray volume is outlined in the isometric view to illustrate the "flat-fan" shape. There is a total number of 39808 droplets generated. As described in the methodology section, droplets are randomly introduced into the computational domain from the injection plane. The location and the size of the plane are determined by the nozzle characteristics. Droplets are also assigned axial and radial velocities upon injection, as defined in Eq. (61) and Eq. (64).
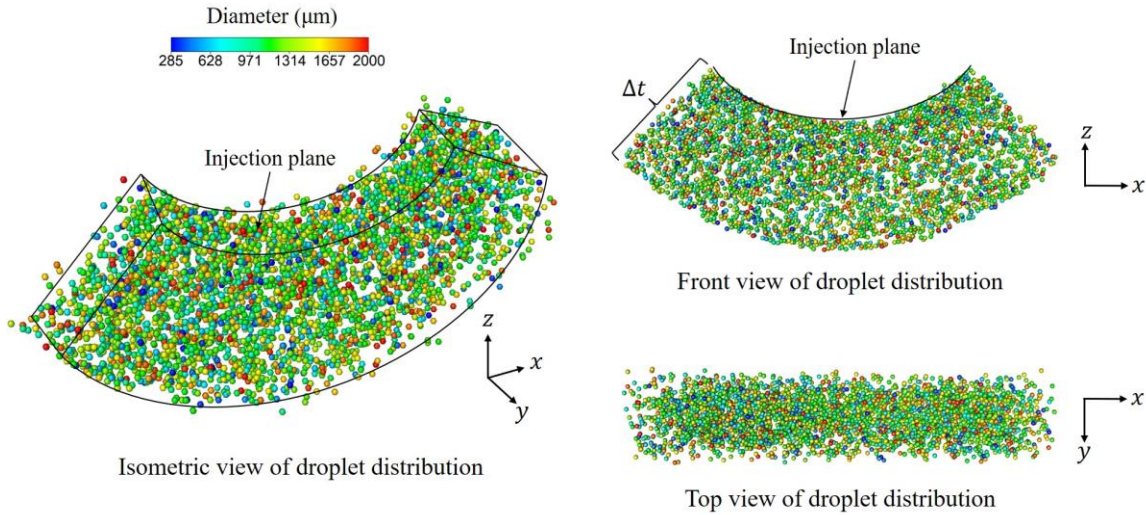
Figure 3-13. Droplet distribution near the injection plane.

Figure 3-14 summarizes the droplet size distribution near the injection plane after the first droplet time step. The Sauter mean diameter for this distribution is 1062.8μm. The initial droplet size is relatively large compared to that before impingement. However, these large droplets are prone to

break up while traveling through the air domain. Smaller droplets are expected prior to the droplet-wall impingement heat transfer.
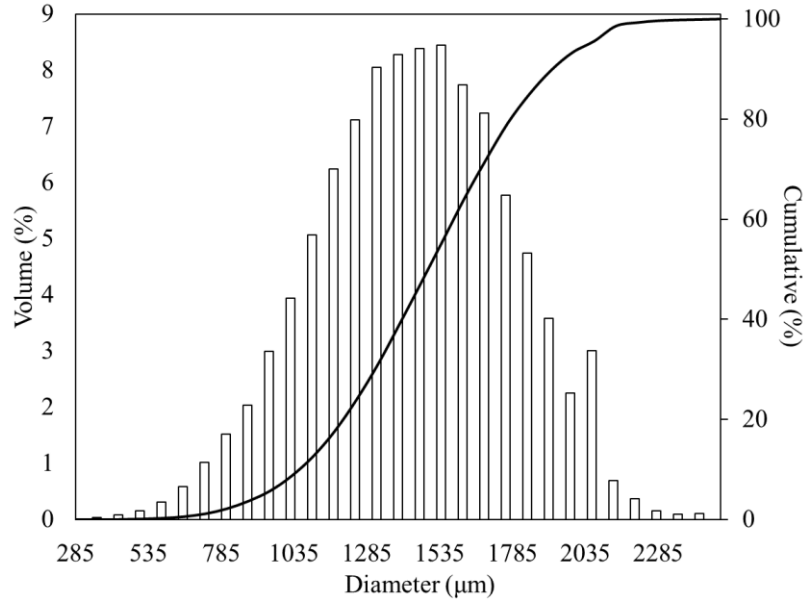
Figure 3-14. Droplet size distribution near the injection plane.

Figure 3-15 shows the droplet-air interaction during the injection. Prior to the injection, the air is uniformly distributed in the computational domain. After the first group of droplets is introduced, the surrounding air quickly forms a fan-shaped flow around the injected droplets. The interaction is due to the two-way coupling between droplet and air. The entrainment effect occurs further upstream from the droplet injection plane due to mass conservation, resulting in a much smaller angle of the fan-shaped airflow. Because of the difference in the fan angle, the spray region extends across the airflow boundary toward the end of the first droplet time step. Droplets within the airflow boundary where the velocity gradient is the highest are more likely to break up in the following time steps. It is also interesting to see that droplets with large diameters have a much higher Weber number, eventually leading to the break up downstream.
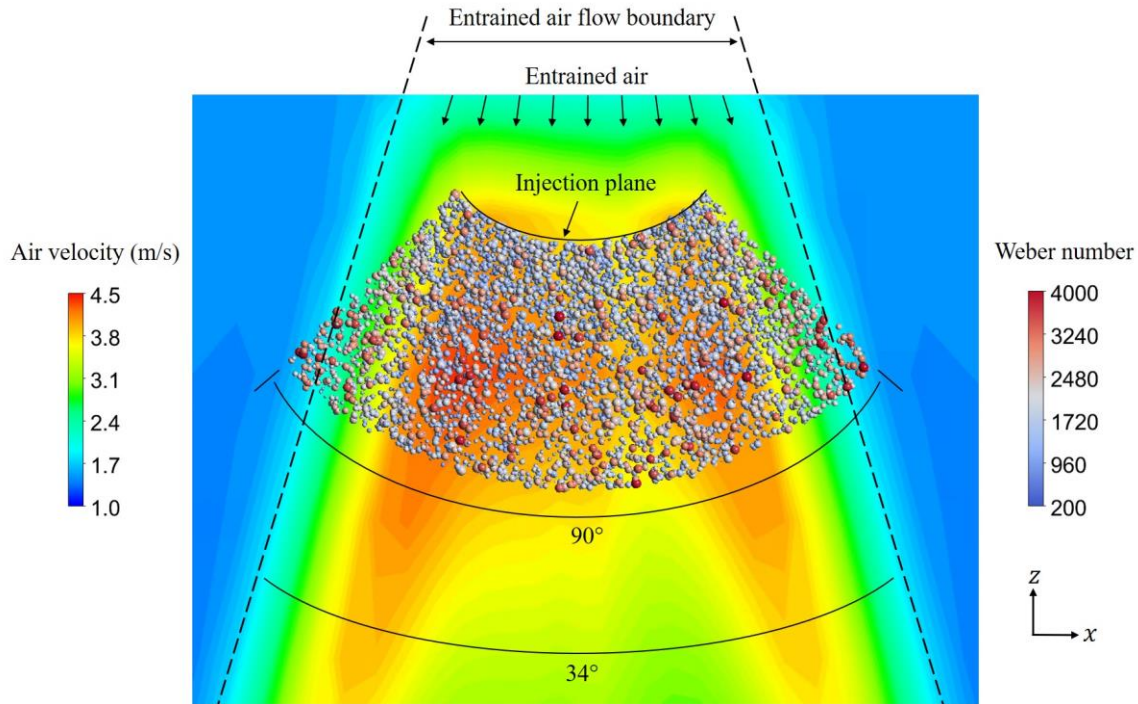
Figure 3-15. Droplet-air interaction upon injection.

Figure 3-16 shows the We and Re as a function of Oh after the first droplet time step. The calculation of the three dimensionless numbers is based on the work of Hsiang and Faeth [85]. The Oh number is less than 0.01, and the We number is between unity and 10. Accordingly, to the droplet breakup regime map summarized by Hsiang and Faeth, droplet deformation and breakup occurs at We>1. Droplets are believed to be in the oscillatory deformation mode, where approximately 20% of the droplet volume has deformed. The breakup occurs when the drag force overcomes the surface tension force. As the relative velocity between droplets and air continues to increase during the spray process, the breakup mode will continue to transition to much more severe regimes, as illustrated in Table 1-6.
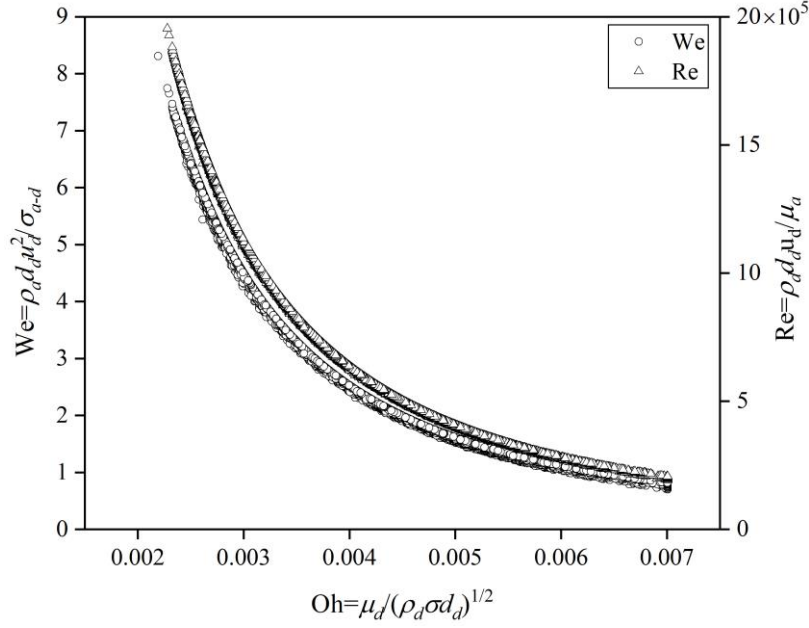
Figure 3-16. We and Re as a function of Oh upon droplet injection.

3.2.2 Droplet transport and dispersion

Figure 3-17 shows the transport and dispersion of droplets from injection to impingement. Because of the characteristics of the flat-fan nozzle, droplets issued from the nozzle disperse radially while traveling through the gas phase to form a fan-shaped spray. The angle of the fan shape varies very little during the transport and dispersion process. This indicates that the external forces imposed on droplets through two-way coupling are not strong enough to divert droplet trajectory, which is determined from the injection. The great inertial of the droplet is also seen in Figure 3-16. As expected, the droplet Weber number increases as the droplet travels further downstream. Droplet-air interaction, droplet-droplet interaction, and droplet breakup are the leading causes for such an increase. Under the current operating condition, droplets start to impinge on the slab surface at 0.01s after injection, as shown in Figure 3-17. Because of the fan-shaped spray pattern, droplets at the center of the spray impinge on the surface first and then followed by those on the edges. After 0.0155s, the full spray impinges on the surface.
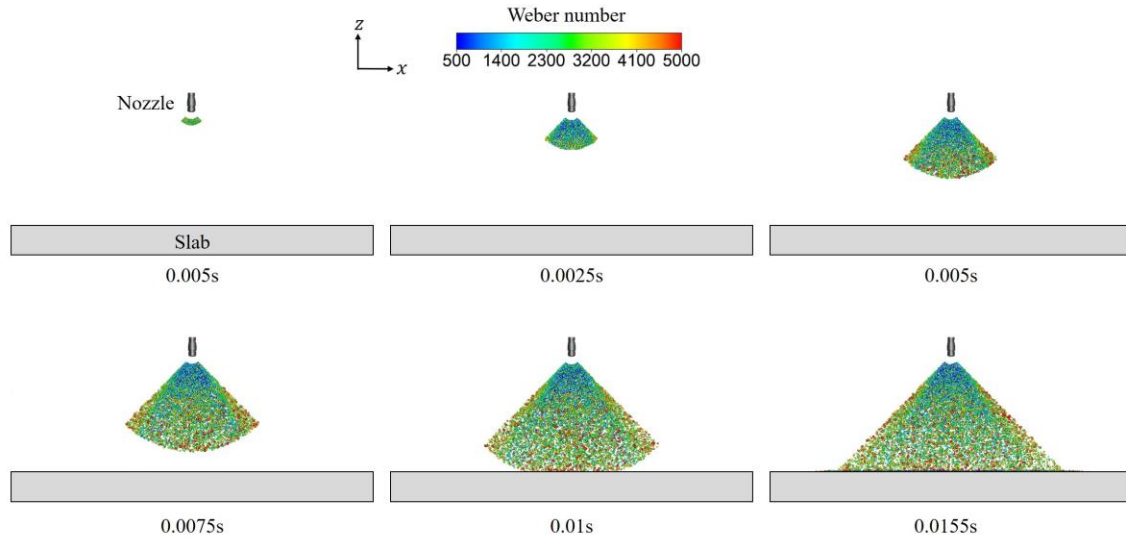
Figure 3-17. Droplet transport and dispersion from injection to impingement.

Figure 3-18 (a) and (b) demonstrate the droplet-air interaction in both the casting and slab width direction at 0.005s after injection. In both figures, the flow field of air is already established prior to droplet-wall impingement. This is because the continuous phase is solved in the steady-state, and the solution for the continuous phase has reached convergence before droplet injection. The established fluid flow of air will not change the final solution since the simulation is only stopped when the solutions for both continuous and discrete phases reach convergence. Besides, a well-established fluid field of the continuous phase can increase the overall stability of the simulation. Figure 3-18 shows that the dispersion of droplets happens in both the casting and slab width direction as the spray expands. The trajectories of droplets align with the motion of the high-velocity entrained air. The result is the decrease in the drag force. For droplets traveling along the boundary of the entrained air, it is possible that they can be carried away by the out-moving air stream if the droplet inertial is small. However, most of the droplets will continue to follow the fan-shape spray pattern until impingement.
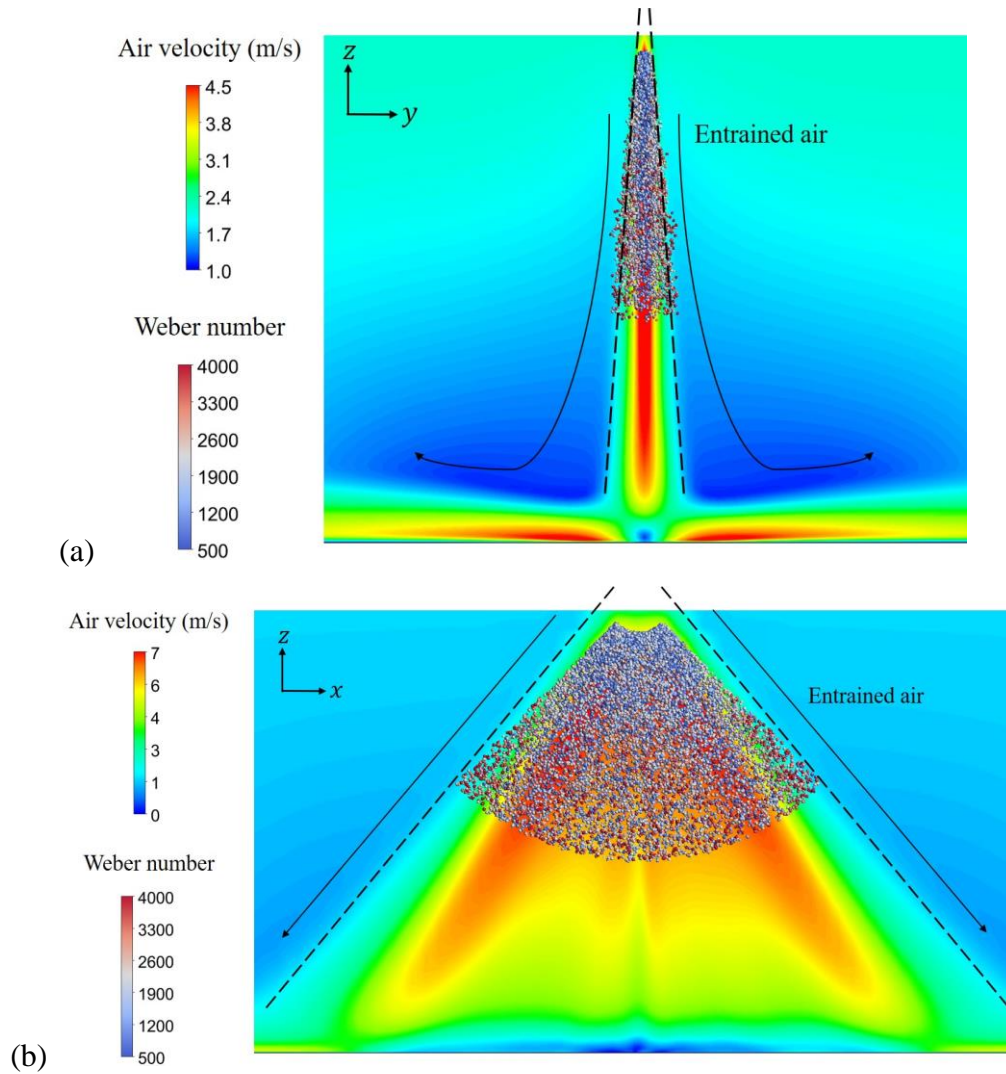
Figure 3-18. Droplet-air interaction during droplet transport and dispersion at: (a) casting direction, and (b) slab width direction.

Figure 3-19 compares the distribution of droplet number frequency at different locations above the slab surface. 130mm above the surface corresponds to the injection plane, and 1mm to the surface is the location prior to impingement. It is evident that droplet undergoes significant size changes immediately after injection, either through a breakup or through coalescence, or the combination of both. The effect of droplet-droplet interaction and droplet-air interaction becomes less dominant on droplet size as the spray approaches the surface. The drastic size change at the beginning of the spray is mostly due to the high droplet number density. With great inertial and small droplet-droplet distance, droplets near the nozzle orifice are more likely to undergo at least one size-change event, i.e., breakup and coalescence. The droplet number density decreases as the spray expands

in both the casting and slab width direction, thereby considerably lower the possibility of droplet-droplet interaction. Figure 3-19 also suggests that between the droplet-droplet interaction and the droplet-air interaction, the former plays a more critical role than the latter at a short standoff distance. If the standoff distance increases, the entrained air will interact with droplets more frequently and break up more droplets before impingement. The effect of the standoff distance and the droplet size will be discussed in the later section.
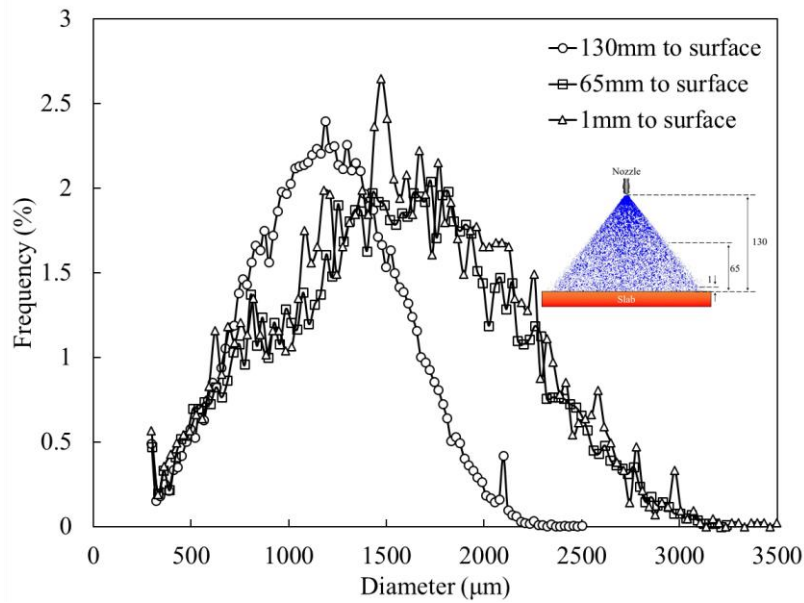
Figure 3-19. Droplet number frequency at different distances to slab surface.

3.2.3   Droplet-wall impingement

Both entrained air and water droplets impinge on the slab surface during the operation. Figure 3-20 shows the entrained airflow before and after impingement. Prior to impingement, the entrained airflow approaches the surface in a flat-fan shape, expanding much wider in the slab width direction. Upon impingement, air flow turns into several wall jets and flows parallel to the surface. In the slab width direction, as shown in Figure 3-20 (a), the two wall jets are separated by the entire width of the spray, and there is no distinct stagnation point in between. Because of the flat-fan shape, the incoming entrained airflow impinges on the surface at an angle ranging from 51.7° to 90° with respect to the slab surface. This is also the angle that the entrained airflow must turn in order to transfer to the wall jet. As shown in Figure 3-20 (a), the minimum turning angle is 51.7°

at the boundary of the spray region, and the angle increases to 90° at the center of the spray region. The smaller the turning angle, the smoother the transition to the wall jet.

In the casting direction, however, the transition to the wall jet must go through the stagnation point. As shown in Figure 3-20 (b), the expansion of the airflow in the casting direction is limited to a small region, and the entrained airflow approaches the surface at an angle of approximately 90°. As a result, the entrained airflow loses its axial velocity and splits into two wall jets at the stagnation point, where air velocity reaches the minimum and the static pressure increases to the maximum.
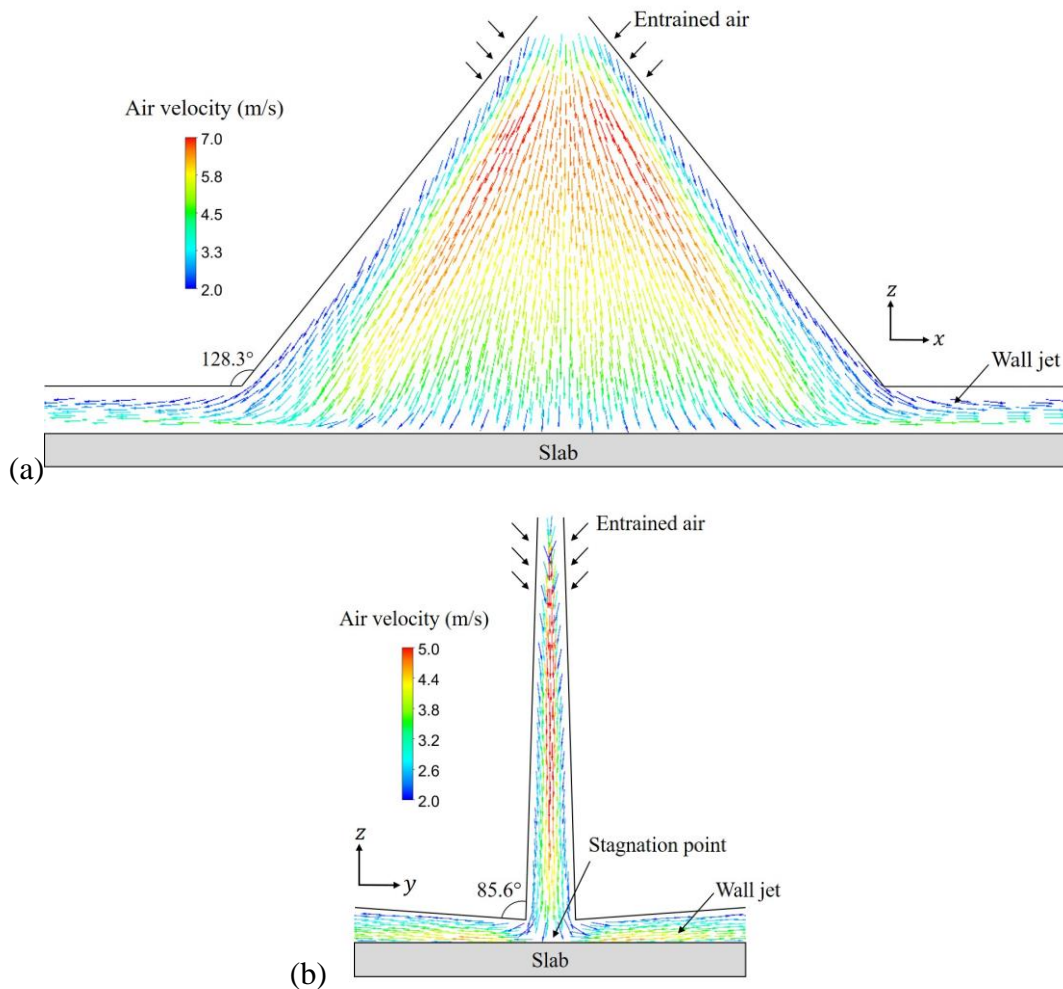
Figure 3-20. Air-wall impingement and wall jets on the surface at: (a) slab width direction, and (b) casting direction.

Figure 3-21 (a) indicates the formation and development of the wall jet in the slab width direction. The velocity profiles in the vicinity of the surface at 9 different locations are depicted in the plot. At the stagnation point (seen from the casting direction, also the spray center), the velocity of airflow drastically decreases from 4.3m/s at 20mm above the surface to zero on the surface. The wall jet starts to form at a distance of 0.4mm to the surface, and the magnitude of the wall jet continues to increase as it moves outward. The flow behavior at different locations within 60mm to the stagnation point is similar to some variations in velocity magnitude. Within this region, the incoming airflow interacts with the outgoing wall jet. This behavior starts to change at a distance of 80mm to the stagnation point. As the wall jet approaches the boundary of the spray region, the influence of the incoming flow decreases, and the wall jet dominants the near-wall flow condition. Beyond 100mm to the stagnation point, the wall jet fully develops, both in shape and magnitude. The influence region of the wall jet can reach 10mm above the surface, and the magnitude of the wall jet can increase to 4.7m/s, a value comparable to the incoming airflow inside the spray region. It is also interesting to see that once the wall jet reaches the maximum velocity at 100mm to the stagnation point, its velocity starts to decrease as the boundary layer expands. Similarly, in the casting direction shown in Figure 3-21 (b), the wall jet forms at the stagnation point and reaches the maximum velocity at a distance of 20mm to the stagnation point, but the boundary layer is thicker than that in the slab width direction.

(a)

(b)
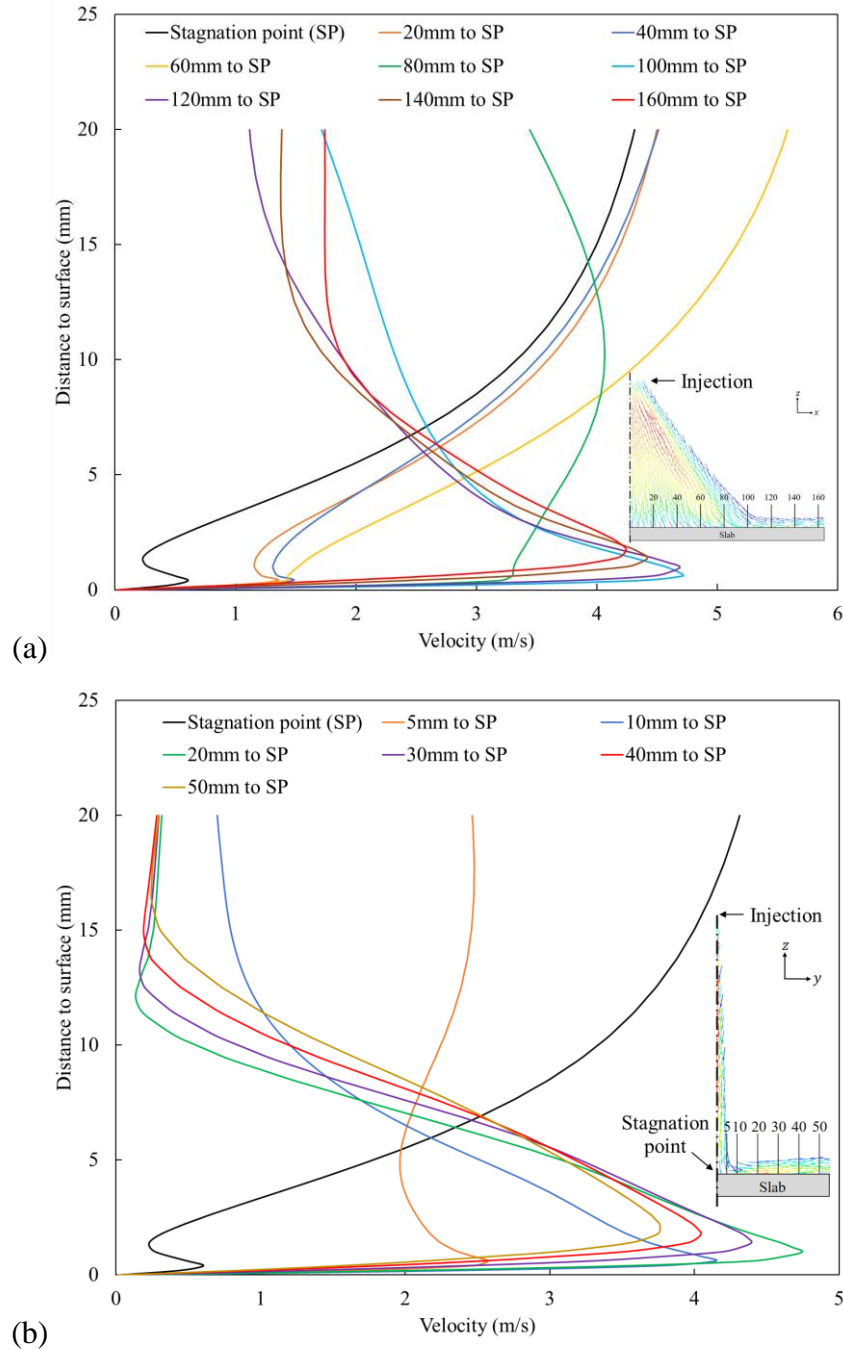
Figure 3-21. Wall jets of the impinging air at: (a) slab width direction, and (b) casting direction.

Once the droplet injection enters the steady-state, a distinct spray pattern will appear on the slab surface. The spray pattern is also known as spray coverage. It is the area on the slab surface where most of the droplets impinge and vaporize. Each type of nozzle can produce a unique spray pattern. The size of the pattern signals the influence region of a spray. Because most droplets concentrate

within the spray pattern, the heat transfer rate from spray cooling is also greater than anywhere else outside the pattern. In the current study, the spray pattern is represented by droplet concentration, and it is defined as:

$$C_d = \frac{m_d}{V_{cell}} \tag{197}$$

Where m_d is the total mass of droplets in a control volume, which has the volume of V_{cell}.

Figure 3-22 (a) and (b) show the spray pattern on the surface under the current operating conditions in terms of droplet concentration. Areas, where the droplet concentration is below 70kg/m^3, are blocked to highlight the spray pattern after impingement in Figure 3-22 (b). It is not surprising that the spray pattern stretches in the width direction of the slab and narrows in the casting direction, as the shape of the spray substantially dominates its shape. To some extent, the spray pattern can be seen as the projection of the spray on the slab surface with random distortions on the boundaries due to droplet splashes.

The spray pattern can also be used to interpret the movement of droplets on the surface. Figure 3-17 shows that droplets at the center of the spray impinge on the surface first, but the droplet concentration in the middle of the pattern shown in Figure 3-22 (b) is not the highest. This behavior suggests that droplets at the center of spray turn from vertical to horizontal after impingement. In fact, the center of a spray pattern is usually referred to as the stagnation point. Droplets split into two streams at the stagnation point and continue to move horizontally on the slab surface while boiling.
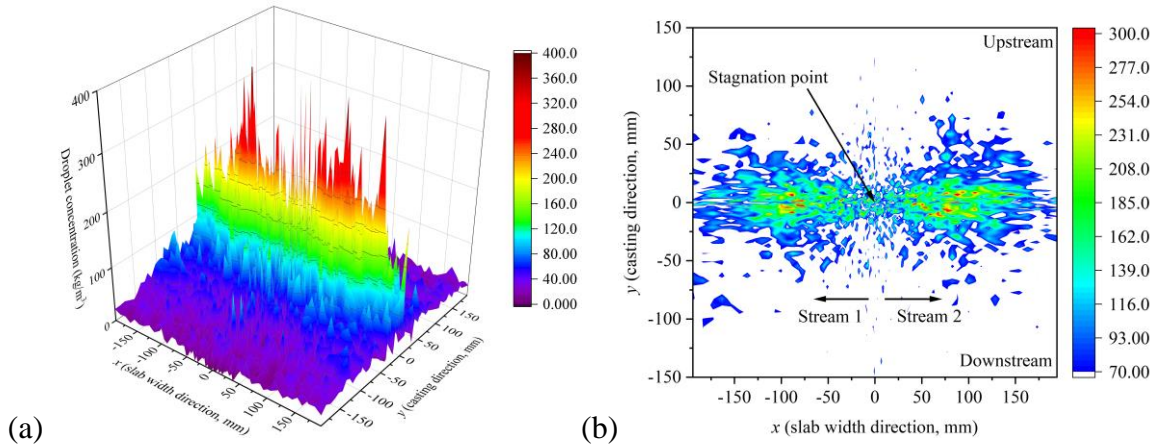
Figure 3-22. Droplet concentration on slab surface: (a) isometric view, and (b) top view.

3.2.4   Heat transfer and HTC distribution on the slab surface

Figure 3-23 shows the thermal boundary profiles in the near-wall region. Similar to the turbulent boundary layer shown in Figure 3-21, the thermal boundary layer in the casting direction is about twice thick as that in the slab width direction. Also, the thickness of the thermal boundary layer is affected by the incoming flow distribution prior to impingement heat transfer. As shown in Figure 3-23 (a), the thermal boundary layer decreases from the center to the boundary of the spray. This is mostly due to the intense conductive heat transfer between droplets and the slab. Outside of the spray region, the thermal boundary layer increases, together with the increase of the turbulent boundary layer. In the casting direction, the highest cooling rate is seen at the stagnation point. The thermal boundary layer monotonically increases as the distance to the stagnation point increases, suggesting a decrease of heat transfer rate in such direction.

(a)

(b)
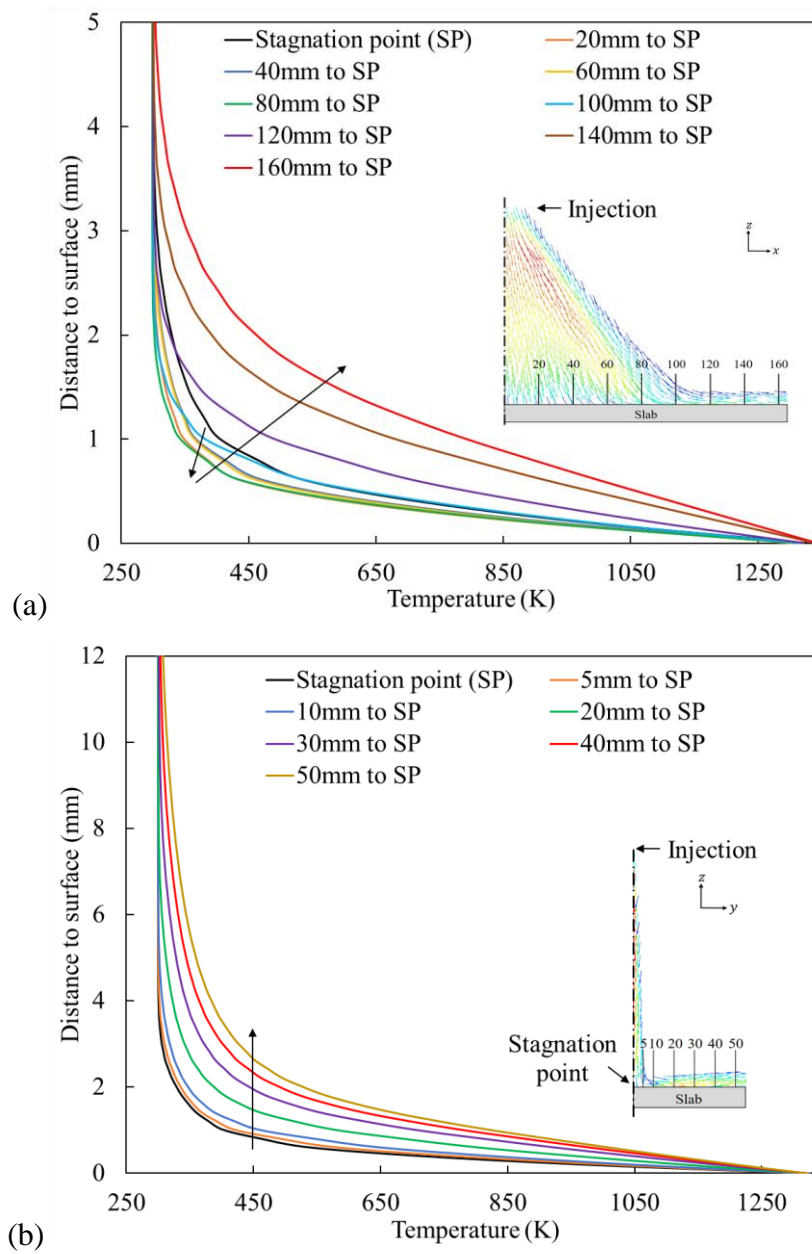
Figure 3-23. Thermal boundary profiles in the near-wall region at: (a) slab width direction, and (b) casting direction.

As shown in Figure 3-24 (a) and (b), slab temperature gradually decreases from the highest to the lowest in the casting direction. A visible low-temperature region forms on the slab surface as the slab passes the spray. The profile of the region aligns with the spray pattern, suggesting the dominant role of spray in determining the corresponding heat transfer. Outside the spray pattern, the slab loses energy through convection and radiation. Inside the spray pattern, additional heat

conduction to droplet and droplet boiling further cools down the hot slab. The effect of spray cooling can be quantified by surface HTC. The surface HTC is shown in Figure 3-24 (b). The HTC pattern is also stretched in the width direction of the slab, similar to the spray pattern. Within the HTC pattern, a higher heat transfer rate occurs at locations with higher droplet concentrations. More droplets available in the unit area means much more energy is required for droplet boiling, hence, higher heat transfer rate.
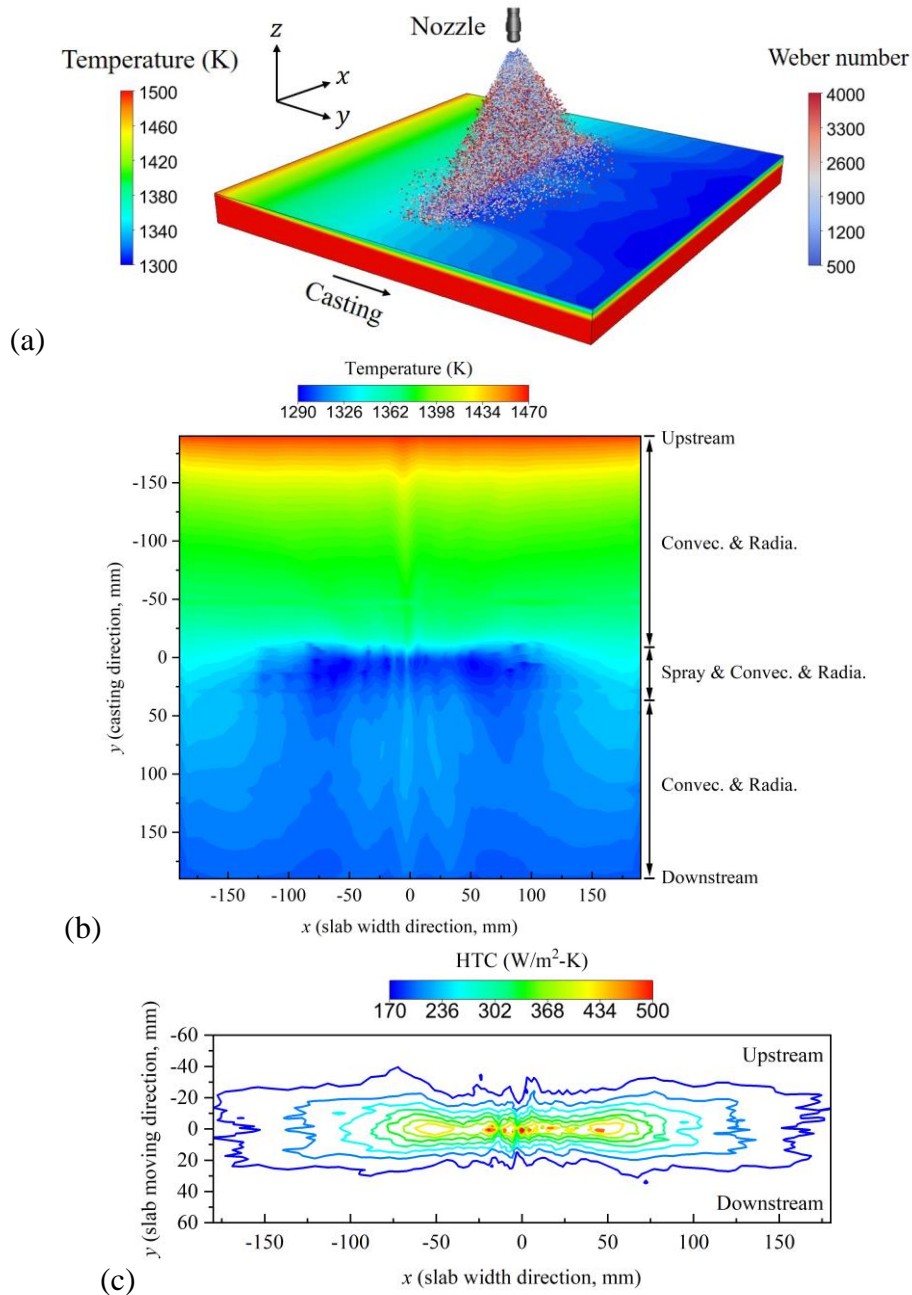
Figure 3-24. Heat transfer on slab surface: (a) isometric view of the spray and slab surface temperature, (b) top view of surface temperature, and (c) top view of surface HTC.

Figure 3-25 shows the temperature distribution inside the slab in both the slab width and casting directions. The upstream temperature of the slab region varies linearly from 1500K at the surface to 1700K at the bottom. To visualize the effect of surface heat transfer, including convection, radiation, and boiling, control volumes with temperatures lower than 1500K are cropped from Figure 3-25. The area of the cropped region indicates the influence of surface heat transfer. The temperature distribution inside the slab is much uniform in the slab width direction, whereas the temperature gradient gradually increases in the casting direction. The increase of the cropped area in the casting direction is due to the movement of the slab region. Because of the moving effect, every location on the slab surface is cooled continuously upstream to downstream. Thus, the cooling effect at the upstream is passed to the downstream, which is also shown in Figure 3-24 (a).
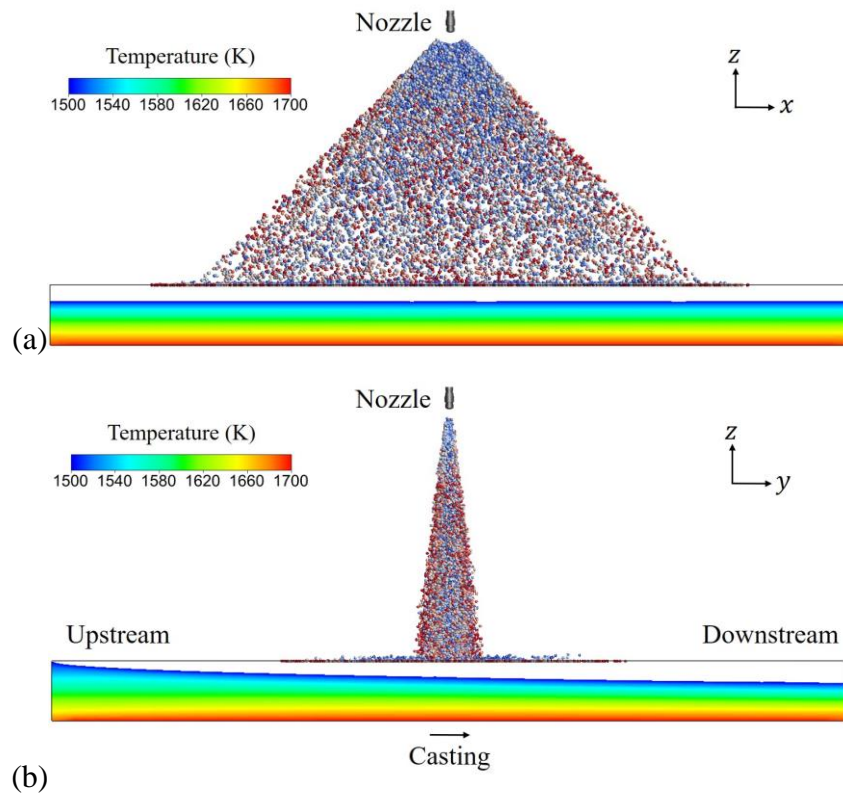
Figure 3-25. Slab internal temperature at: (a) slab width direction, and (b) casting direction.

Figure 3-26 compares the temperature change throughout the slab thickness at different locations inside the slab. In the slab width direction, the temperature variations are very similar, except within the first 2mm below the surface. The similarity indicates that the slab region is uniformly

cooled by the spray, which is desired in the secondary cooling operation. On the contrary, the temperature distributions in the casting direction vary significantly, as shown in Figure 3-26 (b). The shaded area represents the region affected by surface heat transfer, and it is bounded by the upstream and downstream temperatures. Because of the surface heat transfer and the moving effect, the 1500K isothermal surface is "compressed" from the surface to 11mm below the surface. This shows that the effect of surface heat transfer can penetrate up to 11mm inside the slab region. Compared to the entire slab thickness, this also affirms the assumption that the influence of surface heat transfer on solidification can be modeled through one-way coupling. From 11mm to 30mm, the temperature distribution inside the slab is dominated by the upstream boundary condition. The thickness of the region that is affected by the upstream boundary condition decreases from 30mm to 19mm, resulting in a much steeper temperature gradient downstream.
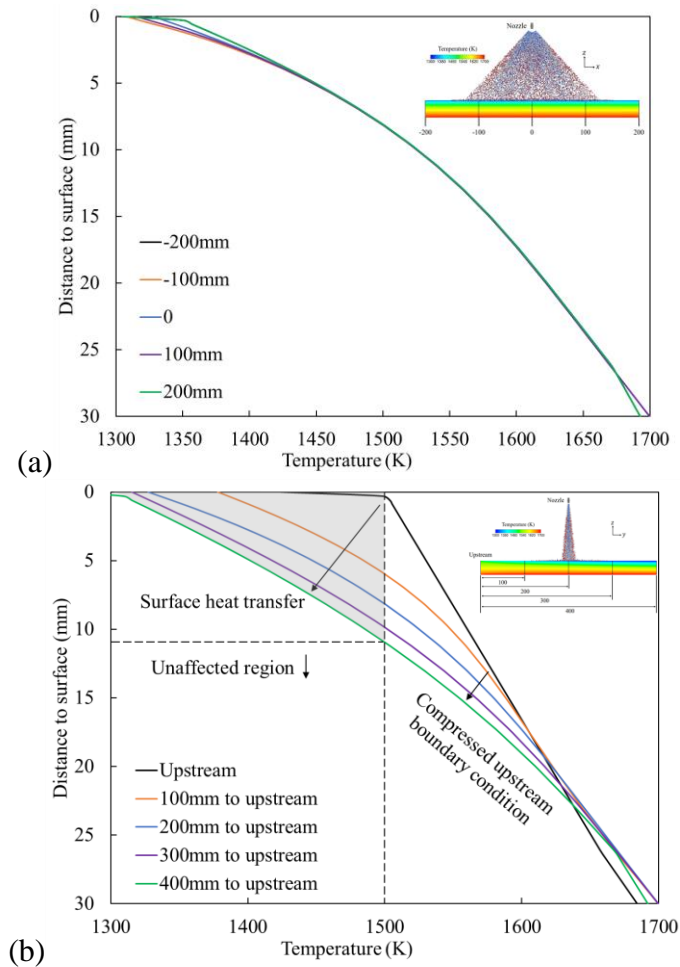
Figure 3-26. Slab internal temperature at different locations at: (a) slab width direction, and (b) casting direction.

214

3.2.5 Heat transfer intensity and uniformity

In the secondary cooling operation, a large cooling area and uniform cooling are desired to avoid residual stresses and strains. To quantify the cooling area, the efficiency of heat transfer, and the uniformity of cooling, the following three factors are proposed in the current study:

$$A_{spray} = \sum_{i=1}^{n} |A_i| \tag{198}$$

$$\text{HTC}_{avg} = \frac{1}{A_{spray}} \sum_{i=1}^{n} \text{HTC}_i |A_i| \tag{199}$$

$$\text{STD}_{spray} = \sqrt{\frac{1}{n}\sum_{i=1}^{n}\left(T_i - \frac{1}{n}\sum_{i=1}^{n} T_i\right)^2} \tag{200}$$

Where A_{spray} is the total spray-affected area on the slab surface. A_i and T_i are the area and temperature of the spray affected control volume. Figure 3-24 (a) and (b) demonstrate the typical spray cooling pattern on a moving slab surface. For a flat-fan type of nozzle, the majority of the impinging droplets are concentrated in an elliptical region. This region is narrow in the casting direction but stretches in the slab width direction. Correspondingly, the surface temperature in this area is lower due to the extra droplet-wall conduction other than convection and radiation. HTC_{avg} is the area-weighted average HTC in the spray affected area, and it indicates the overall intensity of jet impingement heat transfer over the spray coverage area. STD_{spray} is the standard deviation of surface temperature within the spray coverage area, and it measures the uniformity of jet impingement heat transfer.

The definition of the spray-affected area varies from literature to literature. Figure 3-27 shows the distribution of six candidate parameters on the slab surface. The outlined rectangular region in the middle is the projected spray area based on the spray standoff distance and the spray angles. The calculation of the sides of the projected spray area is similar to Eq. (72) and Eq. (73), but the breakup length is replaced by the spray standoff distance:

$$L_{spray} = 2H_{spray}tan\frac{\alpha_{spray}}{2} = 2 \times 130 \times tan\frac{90°}{2} = 260mm \tag{201}$$

$$w_{spray} = 2H_{spray}tan\frac{\beta_{spread}}{2} = 2 \times 130 \times tan\frac{12°}{2} = 27.33mm \tag{202}$$

As shown in Figure 3-27, each candidate parameter reaches either the minimum or the maximum within the projected spray area. All the parameters except the static pressure also have some influence outside of the projected spray area. According to the Bernoulli equation, the static pressure is transferred from the kinetic and potential energy of the flow. The high static pressure area is where the flow impinges on the surface and turns into wall jets. The fact that the projected spray area aligns perfectly with the high static pressure area suggests that droplet dispersion is mostly due to droplet inertial upon injection and the effect of droplet-air interaction is not the dominant mechanism for the dispersion. Therefore, most of the droplet-wall and air-wall impingement occur within the projected spray area, which only depends on the nozzle configurations.

After impingement, however, droplets are no longer confirmed in the projected spray area, as indicated by droplet concentration in Figure 3-27. A splash pattern forms after droplet-wall impingement. The pattern includes the entire projected spray area and some of its surrounding areas. Droplets that appear outside of the projected spray area are due to reflection from droplet-wall impingement and glide with the help of the outward moving airflow. In spite of the reflection and glide, the highest droplet concentration is still within the projected spray area. This type of spray impingement pattern then determines the heat transfer pattern on the surface. As illustrated by Nu, HTC, and surface heat flux, heat transfer rate reaches the maximum inside projected spray area, and the distribution of these parameters follows that of the spray and impingement patterns, which are narrow in the casting direction but are slender in the slab width direction. The influence of the spray gradually fades away from the projected spray area to the surrounding as droplet concentration decreases. The beam-like spray cooling effect outside of the projected spray area is another way to visualize the after-impingement trajectory of the droplet. The heat transfer rate also reaches the local maximum at the upstream, where the surface temperature is pre-defined as the thermal boundary condition and is set to 1500K. As indicated by the droplet concentration, droplets barely reach the upstream. Thus, the heat transfer mechanism near the upstream is dominated by

air convection and radiation. Since both the temperature of air and the surrounding is assumed to be 300K in the simulation, the temperature difference between the slab and the entrained, as well as the surrounding, is the highest near the upstream. Therefore, heat transfer is considerably promoted near the upstream.
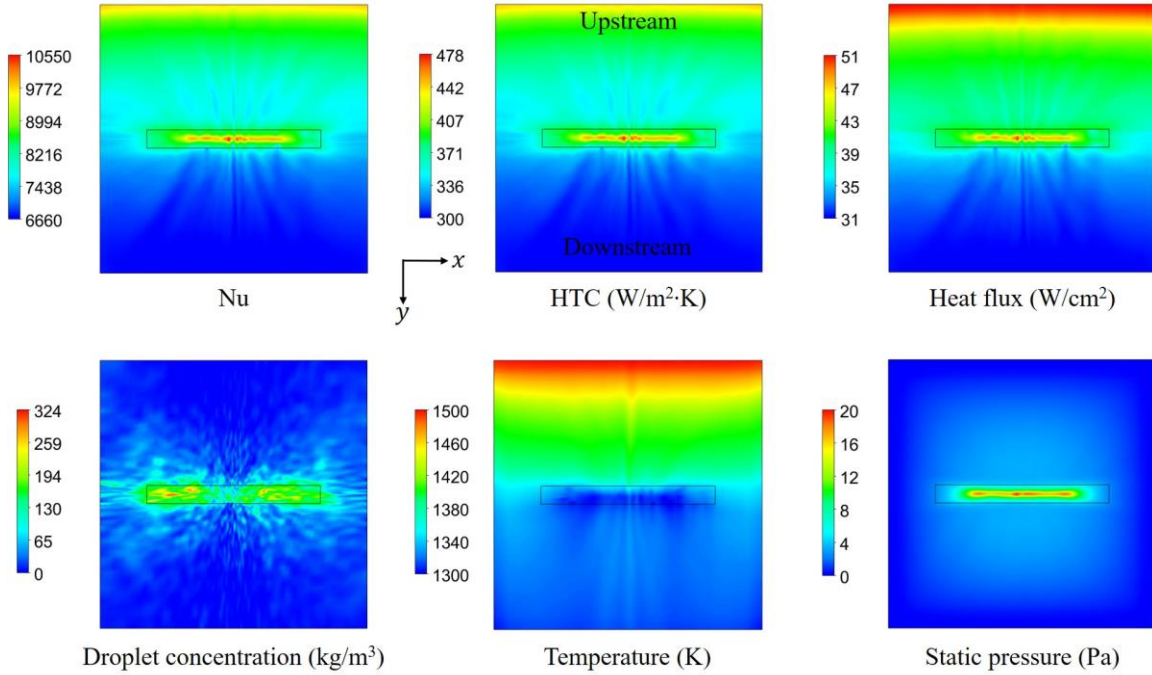
Figure 3-27. Top view of the spray cooling affected regions with respect to the projected spray area.

As the droplet-wall impingement heat transfer mainly occurs within the projected spray area and its periphery, the distribution of the aforementioned candidate parameters on the surface is cropped to highlight the spray-affected region. The threshold for each candidate parameter is found by adjusting the value so that the size of the cropped area is comparable to the projected spray area. Figure 3-28 compares the spray cooling pattern defined by different parameters. It is not surprising that the top three spray cooling patterns defined by Nu, HTC, and surface heat flux are similar to one another since they are related to each other by definition. The elliptical butterfly-shaped areas defined by these three parameters are centered in the middle of the projected spray area and extend slightly over the upper boundary. The pattern defined by the droplet concentration extends further outside the projected spray area due to droplet reflection and glide. The pattern is less symmetric than the top three patterns, and some of the areas at the center of the pattern are cropped by the

217

threshold. The pattern defined by temperature significantly differs from the others. The pattern is somewhat symmetric, but the region extends far beyond the projected spray area in both the slab width and casting direction. In the slab width direction, the pattern ends abruptly at the boundary of the computational domain. If the computational domain further increases in width, the pattern will continue to extend. In the casting direction, the pattern stretches further downstream and ends at a location 56mm away from the lower boundary of the projected spray area. The widespread pattern defined by temperature suggests that the surface temperature is affected by surface heat transfer and the conduction inside the slab region. The thermal diffusion below the surface passes the spray cooling effect far away from the projected spray area. The last pattern that is defined by the static pressure is restricted by the upper and lower boundaries of the projected spray area, and it is much closer to an ellipse. This pattern is shorter in the slab width direction compared to the other patterns. Because the static pressure is independent of the surface heat transfer phenomena, this pattern barely reflects the effect of thermal diffusion and droplet splash in the spray region.
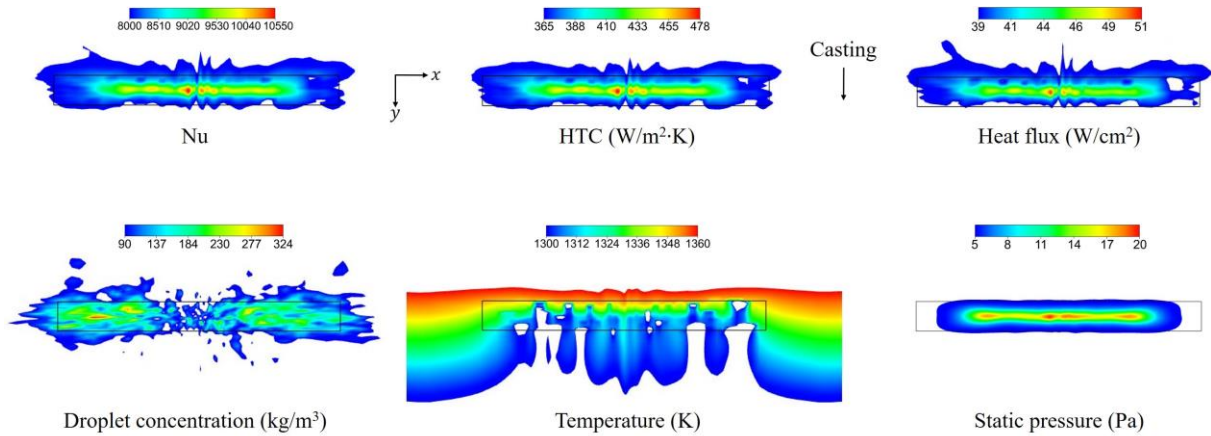
Figure 3-28. Spray cooling pattern by different definitions.

Table 3-2 summarizes the heat transfer intensity and uniformity in the spray-affected area shown in Figure 3-28. The values in the projected spray area are also given as references. The spray-affected areas defined by different parameters vary significantly in terms of the area, which is observed in Figure 3-28. As previously described, the patterns defined by Nu, HTC, and surface heat flux have comparable size and shape, and the areas are much larger than the projected spray area. The pattern defined by the droplet concentration is the second largest, mainly owning to droplet reflection and glide on the surface. The pattern defined by temperature has the largest area

due to the conduction inside the slab. The pattern will be much broader if the computational domain continues to expand. The pattern defined by the static pressure has the smallest area, and it is the only pattern that is smaller than the projected spray area.

On the other hand, the difference in HTC_{avg} and STD_{spray} between different patterns is insignificant. All the patterns suggest similar heat transfer intensity and uniformity. Among all the patterns, the one defined by temperature has the lowest HTC_{avg} and STD_{spray}. This is because those two parameters are area-weighted average values, and the area of the pattern is the largest compared to other patterns. Some of the non-spray-affected areas are also included in the calculation, thus, lowering the average values to a certain extent. With the information shown in Figure 3-28and Table 3-2, a pattern that can accurately represent both the impingement area and the spray cooled area is recommended. The patterns defined by Nu, HTC, and surface heat flux are all appropriate to represent the spray-affected area. However, since HTC is one of the primary indicators used in the secondary cooling operation and research, the pattern defined by HTC is selected to evaluate the heat transfer intensity and uniformity in the current study.

Table 3-2. Heat transfer intensity and uniformity in the spray-affected area defined by different parameters.

Parameter	Threshold	A_{spray} (cm^2)	HTC_{avg} (W/m^2·K)	STD_{spray} (K)
Nu	8000	109.40	384.25	9.71
HTC	365W/m^2·K	98.01	386.62	9.22
Heat flux	39W/cm^2	94.51	387.05	8.91
Droplet concentration	90kg/m^3	134.59	376.64	9.83
Temperature	1336K	314.58	355.57	7.91
Static pressure	5Pa	64.69	394.06	9.07
Projected spray area	NA	71.06	391.95	8.73

As shown in Table 3-2, the pattern defined by HTC, which is referred to as the spray cooling pattern in the later sections, is 38% larger than the projected spray area, suggesting that some of the impinged droplets can travel to regions outside of the projected spray area while boiling. The HTC_{avg} in the spray cooling pattern is slightly lower than that in the projected spray area. This is

because of the increase in the area. Similarly, STD_{spray} increases slightly compared to the reference value, indicating a larger temperature difference across the spray cooling pattern.

A well-performing spray should uniformly cool down a large surface area at a high heat transfer rate. Thus, both A_{spray} and HTC_{avg} should be as large as possible, and the STD_{spray} should be kept to a minimum. The optimum range for each parameter is not available from the literature. The current study adopts the values from the following analysis. The minimum value for A_{spray} should be equal to the projected spray area, which does not include the effect of droplet reflection and glide. The desired spray cooling should provide sufficient heat transfer at least within the projected spray area. The minimum value of HTC_{avg} varies considerably with the operating conditions. Figure 3-29 compares the lower limit of HTC from various sources. Due to the difference in nozzle type, spray water flow rate, and standoff distance, the minimum value of HTC ranges from 24W/m²·K to 430W/m²·K. Based on the definition of HTC shown in Eq. (130) for the continuous casting process, the calculation of HTC should include both the convection by the entrained air and the droplet-wall conduction. The minimum HTC in Figure 3-29 is 24W/m²·K, and it is calculated based on the modified Nozaki's equation shown in Table 1-12 [10]. The calculation uses a minimum spray flow rate of 8.33×10^{-3}L/m²·s, as indicated by the nozzle manufacture, and a temperature of 300K for the spray water. Although Nozaki's equation only includes two spray-related parameters, the effect of convection is included in the correlation. In fact, the contribution of air convection to the surface heat transfer is negligible compared to the droplet-wall conduction. A value of 8.7W/m²·K is recommended by Meng and Thomas [7] for the convective HTC. Nevertheless, a value of 24W/m²·K is used as the minimum HTC_{avg} for the spray-affected area in the current study to be consistent with the literature. As for STD_{spray}, the ideal minimum value is zero throughout the entire spray cooling pattern. The maximum value of STD_{spray} should be the one at which defects and crack occur. According to the definition shown in Eq. (200), STD_{spray} is a function of the temperature difference, which can be related to the thermal strain:

$$\varepsilon_{th} = \alpha_{th}(T_{sur} - T_{ref}) \tag{203}$$

220

Where α_{th} is the thermal linear expansion coefficient, T_{sur} is the local surface temperature, T_{ref} is the reference temperature. The thermal linear expansion coefficient is in the order of 10^{-5}. The average value for the steel composition used in the current study is $5.5 \times 10^{-5} 1/K$.

A critical strain for internal crack has been reported as a value between 0.2%-3.8% [295-298]. Based on this range, the minimum temperature difference to initiate the internal crack can be calculated by:

$$T_{sur} - T_{ref} = \frac{\varepsilon_{th}}{\alpha_{th}} = \frac{0.002}{5.5 \times 10^{-5}} = 36.36K \qquad (204)$$

To evaluate STD_{spray}, the current study assumes that T_{ref} equal to the average temperature of the spray cooling area. If the spray cooling area consists of n control volumes, and the temperature of the $(n$-$1)$ control volumes equal to T_{avg}. There is only 1 control volume where the temperature difference between that control volume and T_{avg} satisfies Eq. (206). Then, an internal crack is assumed to occur from that control volume. Although the actual average temperature for such a system is slightly larger than T_{avg}, but if n is sufficiently large, then the following relation must hold:

$$\lim_{n \to \infty} \left[\frac{(n-1)T_{avg} + T_i}{n} \right] = \lim_{n \to \infty} \left(T_{avg} - \frac{1}{n}T_{avg} + \frac{1}{n}T_i \right) = T_{avg} \qquad (205)$$

Where T_i is the temperature of the control volume where internal crack occurs.

Therefore, the minimum STD_{spray} when internal crack occurs is:

$$STD_{spray,crack} = \sqrt{\left(T_i - T_{avg} \right)^2} = 36.36K \qquad (206)$$

To avoid any internal crack, the maximum STD_{spray} that is allowed within the spray cooling pattern should be:

$$STD_{spray,max} < STD_{spray,crack} = 36.36K \qquad (207)$$

To summarize, the minimum value for A_{spray} should be equal to the projected spray area, which is set to 71.06cm^2 for a 90° flat-fan nozzle that operates at a standoff distance of 130mm. This value will change accordingly when the nozzle type and the standoff distance change, but the new value can be easily found by computing the sides from Eq. (201) and Eq. (202). The minimum HTC_{avg} is set to 24W/m^2·K for any area to be considered as spray affected. And the maximum STD_{spray} that is allowed within the spray cooling pattern to avoid any internal crack is 36.36K, which corresponds to 0.2% strain. Based on these requirements and the information listed in Table 3-2, the simulated nozzle under the baseline conditions has a relatively spray coverage area on the surface, and the spray can uniformly cool down the hot slab at a high heat transfer rate.
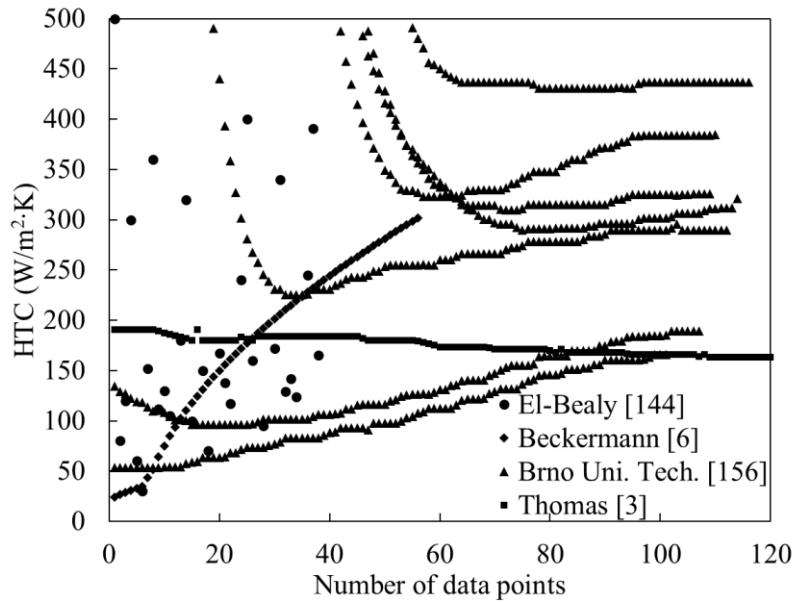
Figure 3-29. The lower limit of HTC from literature.

Figure 3-30 shows the percentage of wall heat flux through different heat transfer mechanisms within the spray-affected area. The heat transfer through convection is separated from the spray cooling effect for analysis. As shown in the plot, all three heat transfer mechanisms are expected within the spray cooling pattern, but the contribution to the overall heat transfer is different. Heat

transfer through spray cooling, i.e., droplet-wall conduction, is the dominant mechanism throughout the spray-affected area. The percentage of wall heat flux through spray cooling ranges from 70% to 76%, as shown in Figure 3-31. The contribution of spray cooling to the overall heat transfer within the spray-affected area reaches the maximum at the center of the cooling pattern. Radiation is the second largest source of heat transfer besides spray cooling. In general, the role of radiation becomes important when the slab temperature is higher than 1200K based on the Stefan-Boltzmann law. In the current study, radiation accounts for 22% to 28% of the total heat transfer within the spray-affected area. As shown in Figure 3-30, the highest radiation occurs at the upper boundary of the spray-affected area with respect to the casting direction. This is not surprised since the upstream surface temperature is higher, and the spray cooling only takes effect within the cooling pattern. The percentage of heat transfer by radiation decreases in the spray-affected area where spray cooling dominants the heat transfer. The role of radiation becomes important again near the lower boundary of the spray-affected area as the effect of spray cooling decreases. The effect of convection is the least important mechanism to the overall heat transfer. On average, the contribution of convection to the overall heat transfer is only 1.62%, and the highest percentage is 1.86%. As shown in Figure 3-18 and Figure 3-20, the maximum velocity of the entrained air is 5m/s, corresponding to a moderate Reynolds number of 1.4×10^5. The contribution of convection will increase if the spray flow rate, or the spray water pressure, increases. The increase will be even much higher for air-mist sprays, which utilize compressed air as one of the cooling fluids and can entrain a higher flow rate of air. Similarly, the contribution of convection decreases from the upstream to its minimum at the center of the spray-affected area and then resumes the increase downstream in the casting direction. The contribution from each heat transfer mechanism has laid the foundation for the optimization of the secondary cooling process. Overall, the effect of convection is negligible compared to the other heat transfer mechanisms. The effect of radiation and spray cooling is significant, but spray cooling prevails over radiation within the spray-affected area. Also, the optimization of radiation is limited, as indicated by the Stefan-Boltzmann law. Therefore, research and optimization of spray cooling is the key to increase the heat transfer intensity and uniformity for the secondary cooling process.
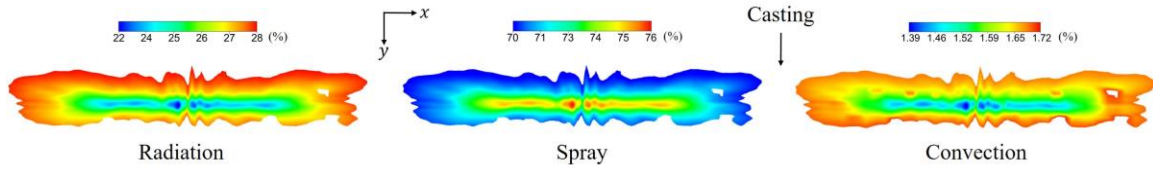
Figure 3-30. Percentage of wall heat flux through different heat transfer mechanisms within the spray-affected area.
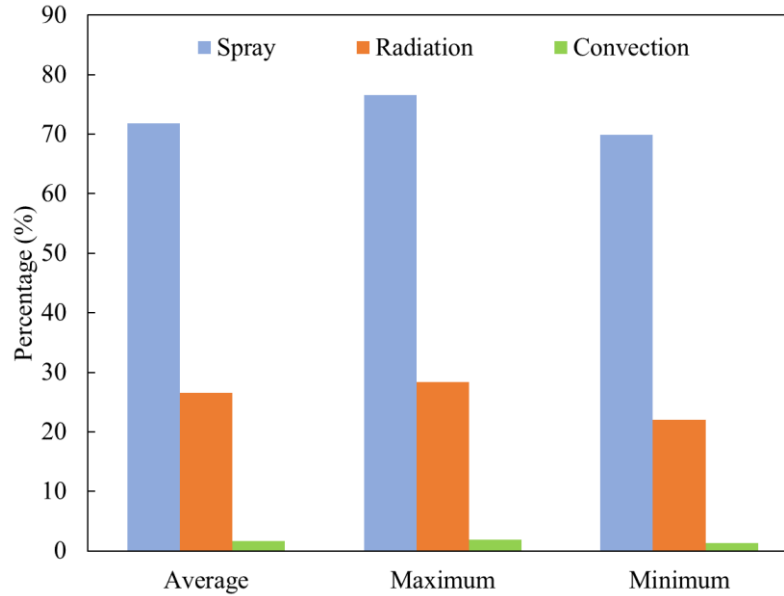
Figure 3-31. Ranges of percentage contribution to the overall heat transfer through different heat transfer mechanisms within the spray-affected area.

3.3   Parametric study

As mentioned previously, optimization of spray cooling is the key to increase the heat transfer intensity and uniformity for the secondary cooling process. The following sections will shift focus and evaluate the effect of nozzle configurations and operating conditions on the intensity and uniformity of heat transfer within the spray-affected area.

3.3.1   Effect of spray nozzle type

A Lechler 660.766 flat-fan hydraulic nozzle and a Delevan Cool-Cast W19917-15 air-mist nozzle are compared in this section to demonstrate the effect of droplet size on the heat transfer. As shown in Figure 3-19, the average droplet diameter prior to impingement is in the order of 1000μm. From

a droplet point of view, the amount of energy that a droplet can absorb from the slab can be found from Newton's cooling law:

$$\frac{dQ_d}{dt} = \text{HTC}(T_{sur} - T_d)A_d \tag{208}$$

Where Q_d is the total energy absorbed by the droplet, A_d is the surface area of the droplet, $(T_{sur} - T_d)$ is the temperature difference between the slab surface and the droplet.

The energy change of the droplet can also be expressed as follows:

$$\frac{dQ_d}{dt} = m_d c_{p,d} \frac{dT_d}{dt} \tag{209}$$

Where m_d is the droplet mass, $c_{p,d}$ is the specific heat of the droplet, T_d is the droplet temperature.

If radiation is neglected, Eq. (208) and Eq. (209) must be equal to meet the requirement of energy conservation:

$$\text{HTC}(T_{sur} - T_d)A_d = m_d c_{p,d} \frac{dT_d}{dt} \tag{210}$$

Rearranging Eq. (210) and solving for the temperature change, yields the following expression:

$$\frac{dT_d}{dt} = \frac{\text{HTC}(T_{sur} - T_d)A_d}{m_d c_{p,d}} = \frac{\text{HTC}(T_{sur} - T_d)}{\rho_d c_{p,d}} \frac{A_d}{V_d} \tag{211}$$

Where $\frac{A_d}{V_d}$ is the surface-to-volume ratio, and it can be replaced by droplet diameter through the following calculation:

$$\frac{A_d}{V_d} = \pi d_d^2 \frac{6}{\pi d_d^3} = \frac{6}{d_d} \tag{212}$$

Substituting Eq. (212) into Eq. (211), yields the following relation:

$$\frac{dT_d}{dt} = \frac{\text{HTC}(T_{sur} - T_d)}{\rho_d c_{p,d}} \frac{6}{d_d} \qquad (213)$$

Eq. (211) and Eq. (213) show that the temperature change rate of a droplet, which is equal to the rate of cooling of the slab, is linearly proportional to the surface-to-volume ratio but inversely proportional to the droplet diameter. A smaller droplet with a relatively large surface-to-volume ratio has a higher rate of temperature change, leading to a higher cooling rate. Even though the aforementioned calculations treat the droplet as a perfect sphere, the same principle is also valid for non-spherical droplets.

As demonstrated in the baseline simulation, there are two stages where droplet size is subject to change prior to impingement, and there are the droplet formation stage and the droplet transport stage. In the droplet formation stage, the size of a droplet mostly depends on the primary breakup process, which is related to the nozzle configuration, such as the internal nozzle structure, nozzle orifice area, spray angle, spray flow rate, and the number of fluids passing through the nozzle. All these factors will affect the primary breakup process, which determines the initial droplet size upon injection. In the droplet transport stage, droplet also changes in size through the secondary breakup and coalescence processes related to the droplet number density within a unit volume and the droplet-air interaction.

To promote droplet breakup in the aforementioned two stages, two-fluid nozzles, such as air-mist nozzles, are the most efficient method among many other techniques. In the droplet formation stage, the additional compressed air and the specially designed nozzle internal structures accelerate the primary breakup process and can lead to the generation of finer droplets. In the droplet transport stage, the well-mixed air-water mixture with high injection velocity entraps much more volumes of the surrounding gas phase, thereby significantly increasing the droplet-air interaction. Besides, air-mist nozzles are much flexible in terms of steel grade and slab size variation.

The simulation of the hydraulic nozzle is discussed in the baseline section. The simulation of the air-mist nozzle follows the two-step approach shown in Figure 2-15. The simulation conditions are the same as that of the baseline. The inlet for the compressed air is treated as a pressure inlet, and the pressure is set to 30psi (206843Pa) based on the operating condition provided by an industrial collaborator. The same threshold is used to crop the spray-affected area from the surface. The value of the threshold can be found in Table 3-2.

Figure 3-32 shows the droplet impingement pattern at the time of impingement. Due to the wide range of the droplet size, droplets are scaled to the same size in the figure but are colored differently based on their actual sizes. Regardless of the nozzle type, both patterns are slender in the slab width direction but narrow in the casting direction. This shows that the nozzle configurations such as orifice shape and spray angle play a pivotal role in the droplet distribution prior to impingement. The additional compressed air in the nozzle increases the instability of the liquid sheet upon injection, thus, resulting in much finer droplets from the primary breakup process. At the time of impingement, the average size of droplet issued from the air-mist nozzle is only 20% of that issued from the hydraulic nozzle. The advantage of finer droplets on heat transfer is shown in Figure 3-33. Due to the decrease of droplet diameter, or the increase of surface-to-volume ratio, heat transfer within the spray-affected area is significantly promoted. The maximum HTC increases by more than 370% when the droplet diameter decreases by 80%. Therefore, two-fluid nozzles are more suitable for conditions where a high heat transfer rate is required.
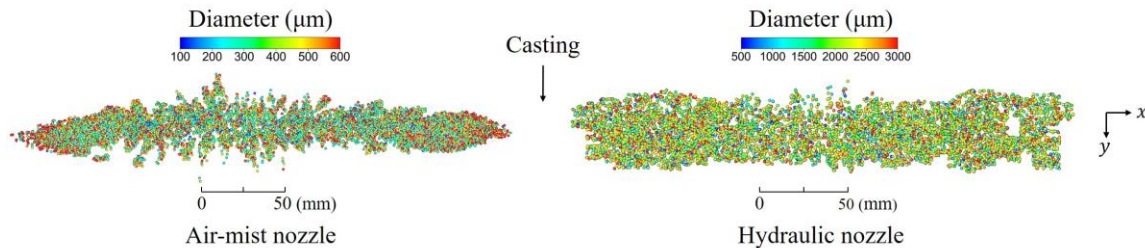
Figure 3-32. Droplet impingement pattern between hydraulic spray and air-mist spray.
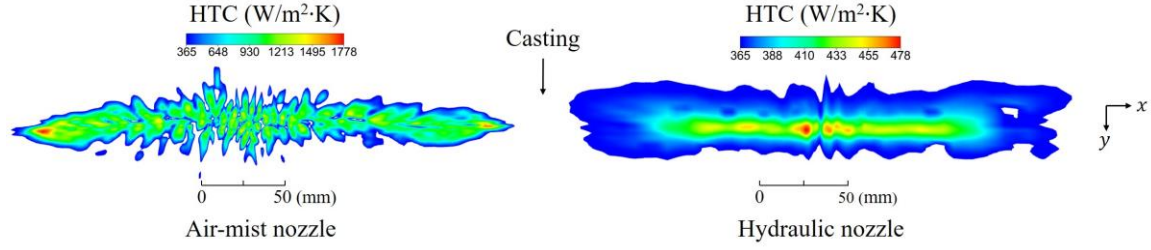
Figure 3-33. HTC distribution prior within the spray-affected area between hydraulic spray and air-mist spray.

Table 3-3 compares the droplet size distribution prior to impingement and the effect of spray cooling between the two nozzles. As shown in Figure 3-32, droplet size drastically reduces in the air-mist spray due to the intense air-water interaction and the resulting breakup processes. The average HTC has increased by more than threefold in the air-mist spray at the same water flow rate. However, there are several disadvantages of air-mist nozzles compared to hydraulic nozzles. The first disadvantage is the decrease of A_{spray}, as shown in Figure 3-32, Figure 3-33, and Table 3-3. The spray-affected area decreases by approximately 29% in the air-mist spray. The decrease of the spray-affected area is much evident in the casting direction. This indicates that droplet dispersion is limited in the casting direction, which is also related to the addition of compressed air. As shown in Table 3-3, the injection velocity from the air-mist nozzle has increased by 66%, thus, less time for droplets to fully disperse prior to impingement. In addition, finer droplets can reach the terminal velocity much faster, and the drifting droplets are much more likely to be carried away by the entrained airflow before contact with the surface. Detailed discussion on droplet size and critical velocity can be found in the effect of the standoff distance section. The second disadvantage is the increase of STD_{spray}, suggesting less uniform heat transfer throughout the spray affected area. As shown in Figure 3-32, the ratios of minimum and maximum droplet within the two patterns are very similar. Yet, the uniformity of heat transfer differs significantly. The different heat transfer rates between large and small droplets have a more significant impact on uniformity when all droplets are relatively small. On the other hand, if droplet size increases throughout the spray-affected area, the overall cooling rate decreases correspondingly, as indicated by Eq. (213).

It is worth mentioning that the two-fluid nozzles, in general, require additional investment compared to the single-fluid nozzles. The additional costs include more expensive nozzles, a secondary piping system for the additional fluid, and extra pumping power. However, all the additional costs can be justified if the slab quality is significantly improved. The selection of nozzle type is on a case-by-case basis, and the heat transfer rate is not the only influential factor. The decisive factors for the nozzle selection should be steel grade, casting conditions including casting speed and the slab dimensions, nozzle configurations such as standoff distance, spray angle, desired average HTC, the ratio of minimum and maximum flow rate, and the requirement of energy consumption.

Table 3-3. Droplet size distribution and the effect of spray cooling between hydraulic spray and air-mist spray.

Parameter	Hydraulic nozzle	Air-mist nozzle
Avg. injection velocity (m/s)	13.05 (droplet)	21.74 (air-water mixture)
$D_{v0.1}$ (μm)	868	65
$D_{v0.5}$ (μm)	1635	167
$D_{v0.9}$ (μm)	2370	343
A_{spray} (cm^2)	98.01	69.64
HTC_{avg} (W/m^2·K)	386.62	1271.98
STD_{spray} (K)	9.22	15.35

3.3.2   Effect of spray flow rate

Hydraulic nozzle

Spray flow rate is the most adjustable operating parameter in practice. The exact spray flow rate depends on the cooling application, as well as the desired temperature decrease. The spray flow rate must be high enough to provide sufficient heat transfer but low enough to avoid significant residual stresses and strains. The single-fluid hydraulic nozzle evaluated at the baseline condition is used in the current parametric study. Two new spray flow rates, i.e., 3.5L/min and 14L/min, are compared with the baseline.

Figure 3-34 and Figure 3-35 show the wall heat flux and the droplet number density within the spray-affected area at different spray flow rates. The increase of spray flow rate dramatically changes the droplet number density both during atomization and upon impingement. Since the nozzle type is fixed in all three simulations, the atomization regions are very similar between two different flow rates. However, the increased droplet number density at a higher flow rate will further promote droplet breakups and coalescences within the atomization region. After impingement, droplets tend to spread much further from the stagnation point, creating a wider spray-affected area on the slab surface with a much dense concentration, as shown in Table 3-4.
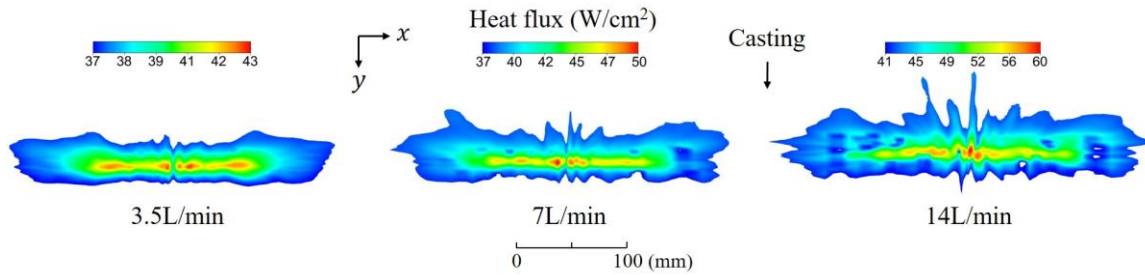
Figure 3-34. Wall heat flux within spray coverage at different spray flow rates.
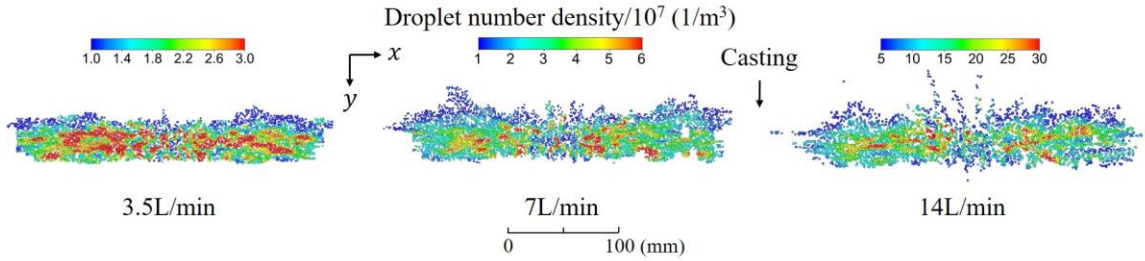
Figure 3-35. Droplet number density within spray coverage at different spray flow rates.

Table 3-4. Heat transfer intensity and uniformity at different spray flow rates.

Parameter	3L/min	7L/min	14L/min
A_{spray} (cm^2)	97.02	98.01	170.92
HTC$_{avg}$ (W/m^2·K)	363.13	386.62	444.18
STD$_{spray}$ (K)	5.24	9.22	24.55

The change of the surface condition at a high spray flow rate has a significant impact on the droplet-wall heat transfer as well. The most profound change is the increase of the total droplet-wall contact area due to the increase of the droplet number density. Heat conduction from the slab surface to the impinged droplets is intensified at large spray flow rate condition, as suggested by the increase of HTC_{avg} shown in Table 3-4. It is also possible that the droplet boiling regime might change to transition or even nucleate boiling at specific locations due to the increase of heat flux. If the wall superheat continues to decrease, the result is the collapse of the vapor film and the formation of a steady liquid film. On the other hand, although a large spray flow rate can produce a high heat transfer rate within the spray-affected area, it can also cause the non-uniform cooling issue. STD_{spray} shown in Table 3-4 increases by approximately 100% when doubling the spray flow rate, clearing indicating the severity of the non-uniformity inside the spray-affected area. Such high non-uniformity is the source of many defects and can lead to severe deformation of the slab. In addition, one constraint of a high spray flow rate is the extra investment in pumping systems. A good balance between sufficient heat transfer and cooling uniformity should always be the primary goal of the secondary cooling operations.

Air-mist nozzle

The flow rate through two-fluid nozzles will also impact the heat transfer on the slab surface. The same air-mist nozzle discussed in the spray nozzle type section is used to evaluate the influence of flow rate on the spray cooling performance. In the baseline simulation, the inlet for the compressed air is treated as a pressure inlet with a constant pressure of 30psi (206843Pa), and the inlet for water is considered a velocity inlet with a constant flow rate of 4.5gpm (0.284L/s). Because the condition from either inlet can affect the overall flow rate in the nozzle, the current study uses 4 different combinations of flow conditions to assess the effect of flow rate. The naming convention for each simulation is the combination of the flow conditions at the two inlets. For example, in the baseline condition, the inlet pressure of air is 30psi, and the flow rate of water is 4.5gpm, the name for this condition is shortened as "4.5gpm/30psi". Using this format, the 4 simulations that are discussed in this section are 4.5gpm/30psi, 4.5gpm/40psi, 6.5gpm/30psi, and 6.5gpm/40psi.

Figure 3-36 shows velocity distribution on the center cross-section of the nozzle and the liquid sheet attached to the nozzle orifice from the first step simulation. The compressed air is fed into

the nozzle through the inlet at the top, and water is supplied from the inlet at the right. The direction of the two fluids is perpendicular to each other. However, the two fluids are not mixing immediately after entering the nozzle to avoid possible blockage on either of the inlets. The compressed air is directly injected into the long mixing chamber, while water is intentionally led to swirling around on the airflow passage. The rotation of the water flow in the upper portion of the nozzle significantly improves the mixing between the two fluids once the water flow enters the mixing chamber. Through a series of varied cross-section areas, the velocity of both fluids decreases to below 10m/s, leading to the increase of the mixing time. Then, the well-mixed air-water mixture accelerates through another set of varied cross-section areas prior to injection. Upon injection, the mixture forms the signature liquid sheet, which subsequently breaks up into ligaments and droplets.
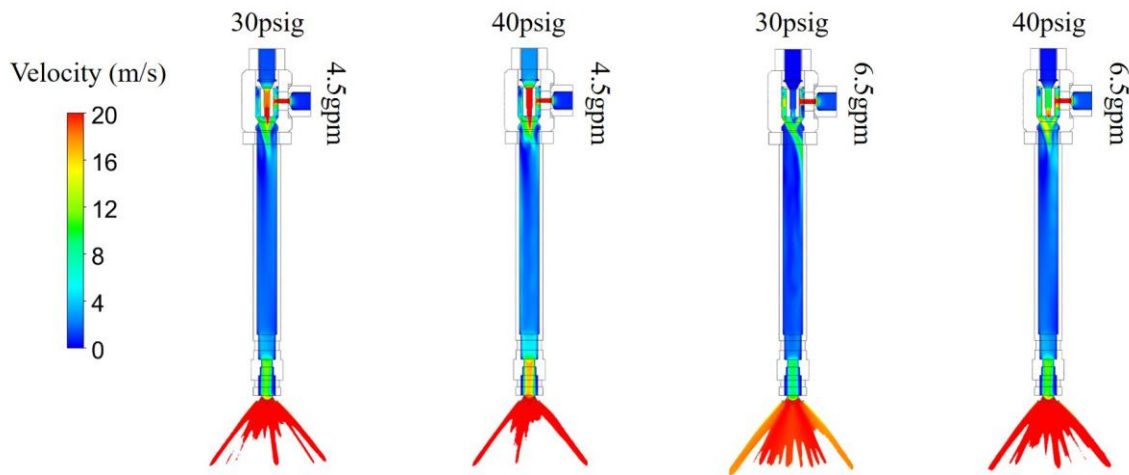
Figure 3-36. Velocity distribution on the center cross-section of the nozzle and the liquid sheet at different flow rates through the air-mist nozzle.

When the air injection pressure increases from 30psi to 40psi, the velocity of air increases correspondingly upon injection. In addition, the volume fraction of air in the mixture also increases, as shown in Figure 3-37. Since the volume fraction of water reduces, the volume of the resulting liquid sheet decreases. Another impact of the increase of air pressure is to accelerate the primary breakup process, as the reduced liquid sheet is less stable in a faster-moving fluid field. However, as shown in Table 3-5, because higher air pressure intensifies the primary breakup process, droplet size at the time of impingement decreases by more than 20%. As discussed in the

previous section, finer droplets can vaporize much faster than larger droplets, therefore, beneficial to the heat transfer on the slab surface. Similarly, higher HTC_{avg} is observed at higher air injection pressure, regardless of the water flow rate. It should also be noted that both A_{spray} and STD_{spray} decrease as the result of high air pressure. This shows that fine droplets with low terminal velocities are greatly affected by the high-velocity airflow. Some of the fine droplets are likely to be blown away from the slab surface without conducting heat transfer at all. Thus, there should be an upper limit for the air injection pressure at each flow rate of water to guarantee a sufficient spray-affected area on the slab surface.

On the contrary, the increase of water flow rate under the same air pressure significantly increases the volume fraction of water in the mixture. As shown in Figure 3-37, the volume of the liquid sheet increases and the breakup process is delayed to some extent. To overcome the increase of the consolidating forces such as surface tension and viscosity, higher air pressure is required to further increase the disruptive forces. For example, the primary breakup process is delayed under the 6.5gpm/30psi condition, and the final droplet size is approximately twice that under the 4.5gpm/30psi condition. Larger droplets are beneficial to the homogenization of slab surface temperature, but the heat transfer rate is compromised, as shown in Table 3-5. To recovery the heat transfer rate, the liquid sheet must be better atomized. Thus, the 6.5gpm/40psi condition comes into play. As shown in Figure 3-37, the breakup length is reduced under the high air pressure condition. Although the volume fraction of water decreases, the increase of the air pressure compensates for such a decrease. The better atomized fine droplets help recover some of the decreased heat transfer rates, as shown in Table 3-5. Interestingly, the increase of water flow from 6.4gpm to 4.5gpm is more than 40%, but the increase of air pressure from 30psi to 40psi is just over 30%. Thus, the average droplet size under the 6.5gpm/40psi condition is still larger than that under the 4.5gpm/40psi condition, therefore, resulting in a lower heat transfer rate. Such behavior suggests that the inlet flow conditions of two-fluid nozzles should be optimized together. If either one of the inlet conditions changes, the other should also be adjusted to maximize the overall performance.
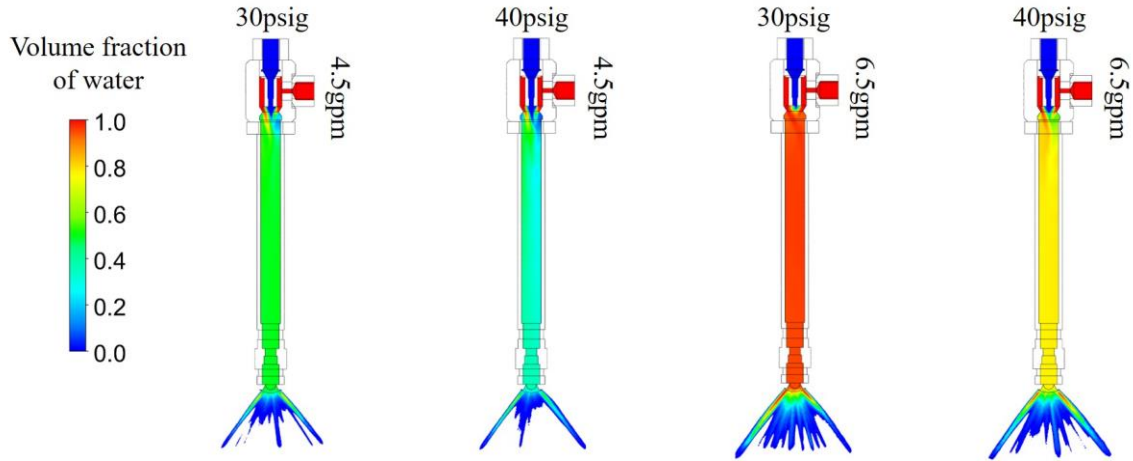
Figure 3-37. The volume fraction of water on the center cross-section of the nozzle and the liquid sheet at different flow rates through the air-mist nozzle.

Table 3-5. Droplet size distribution and the effect of spray cooling at different flow rates through the air-mist nozzle.

Parameter	4.5gpm/30psi	4.5gpm/40psi	6.5gpm/30psi	6.5gpm/40psi
$D_{v0.1}$ (µm)	65	50	119	92
$D_{v0.5}$ (µm)	167	124	305	229
$D_{v0.9}$ (µm)	343	314	781	583
A_{spray} (cm^2)	69.64	60.12	85.23	76.68
HTC$_{avg}$ (W/m^2·K)	1271.98	1286.11	1115.64	1281.51
STD$_{spray}$ (K)	15.35	17.03	11.56	17.86

3.3.3 Effect of standoff distance

Spray standoff distance is the vertical distance from the nozzle tip to the slab surface. In the baseline simulation, the standoff distance is set to 130mm, a relatively short distance in the secondary cooling practice. 5 different standoff distances are compared and evaluated against the baseline condition in this section. As indicated by Eq. (201) and Eq. (202), the projected spray area is linearly proportional to the standoff distance for the same nozzle. However, as shown in Figure 3-38, the actual spray-affected area does not increase correspondingly as expected. To highlight the relative size between the projected spray area and the spray affected area, the projected spray area is outlined and scaled to the same size between different standoff distances in Figure 3-38. A

234

scale bar is given below each spray cooling pattern for reference. In the baseline simulation, the size of the spray-affected area is 138% of the size of the projected spray area. Effective spray cooling is expected within the projected spray area where it should be. In addition, some of the spray-affected area further extends outside of the projected spray area due to droplet reflection and glide. Similar behaviors can also be observed at the standoff distance of 260mm. However, the spray-affected area separates into several smaller patches as the standoff distance continues to increase. A complete separation is seen after the standoff distance increases to 400mm. There are at least 4 patches that can be identified at a large standoff distance in Figure 3-38. The two larger patches at both ends of the spray-affected area are separated from the two smaller ones in the middle. After the standoff distance increases beyond 780mm, only scattered, spray-affected areas are observed on the slab surface. Also, the increase of the spray-affected area lags the increase of the projected spray area, showing less effective heat transfer at a high standoff distance.
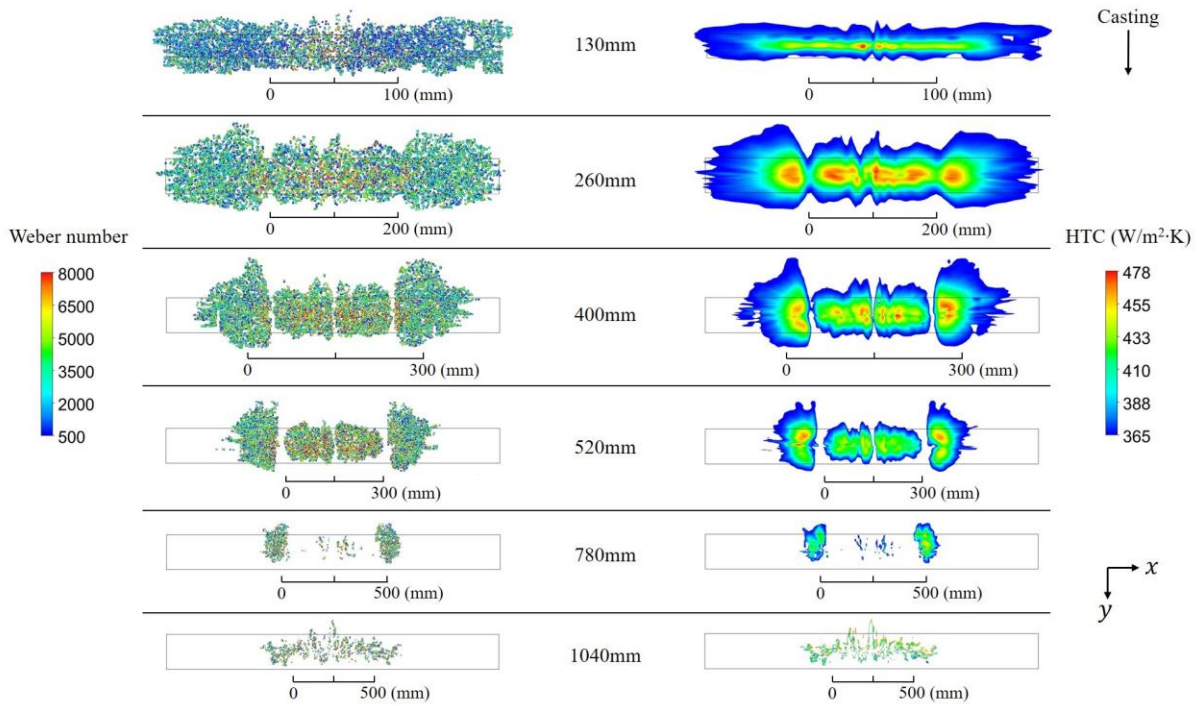
Figure 3-38. Droplet Weber number of spray cooling HTC distribution as a function of standoff distance.

Figure 3-39 compares the HTC_{avg} and the ratio of the spray-affected area and the projected spray area at different standoff distances. The decrease of HTC_{avg} is expected since the total mass flow

rate of water maintains constant throughout the simulations. The droplet number density decreases with the increase of standoff distance, as shown in Figure 3-38. Consequently, the HTC_{avg} within the spray pattern decreases. But interestingly, the ratio of the spray-affected area and the projected spray area increases briefly from 130mm to 260mm and then sharply decreases to less than 20% at the standoff distance of 1040mm. The increase of the spray affect area at the standoff distance of 260mm is mostly due to better atomization. The injected droplets still retain sufficient momentum to follow the projected trajectories while traveling through the gas phase. When the standoff distance increases, droplets must travel longer distances to reach the slab surface with the same inertial. Besides, droplet size consistently undergoes changes due to the secondary breakup process. As shown in Figure 3-40, the ratio of the droplet size prior to impingement and that upon injection decreases with the increase of the standoff distance. Because the nozzle type and the flow rate of water are fixed, the initial droplet size upon injection is the same for all the simulations. The decreasing size ratio indicates that the droplet-droplet and droplet-air interaction are constantly breaking up droplets during the spray process until the droplet size is small enough and the consolidating forces inside a droplet can overcome the disruptive forces imposing on the droplet.
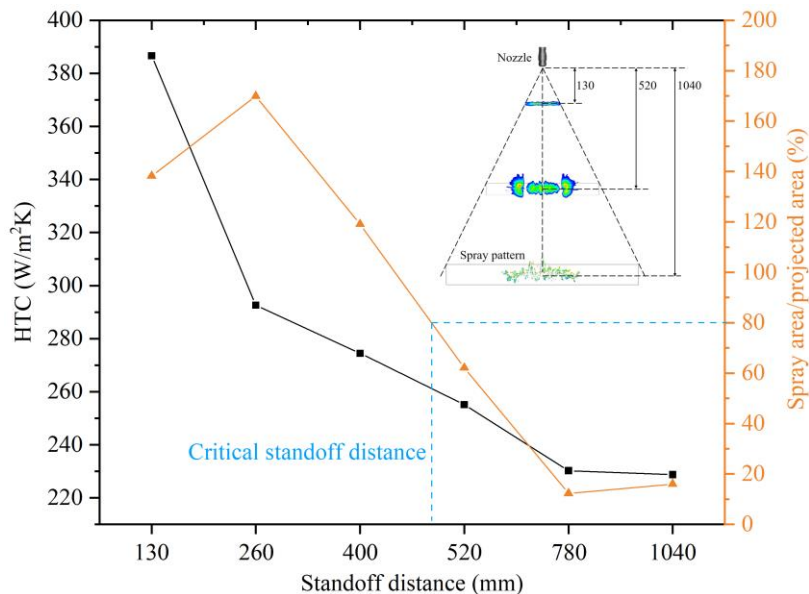
Figure 3-39. Effect of spray standoff distance on the heat transfer and spray affected area.
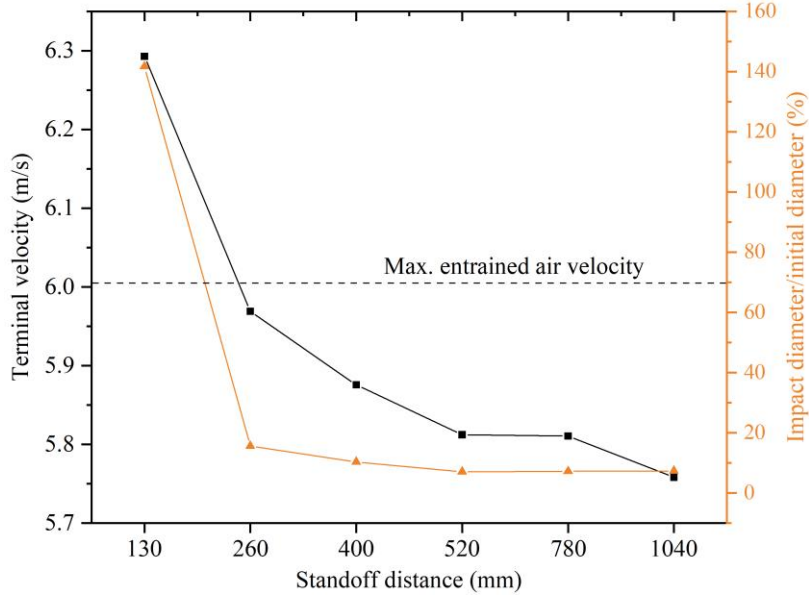
Figure 3-40. Effect of spray standoff distance on the droplet size and terminal velocity.

Although smaller droplets are desired in the secondary cooling practice, they are easily affected by other factors such as drag force and gravitational force. The drag force always acts in the opposite direction of the relative motion of a droplet, but the gravitational force plays a different role at different locations in the secondary cooling region. As shown in Figure 1-1, the slab is bent from the vertical position to the horizontal position, and water sprays are always facing perpendicularly to the slab surface. Also, both broad faces of the slab are cooled by water sprays. Thus, the direction of the gravitational force is perpendicular to the motion of droplets when the slab is in the vertical position, but it aligns with the motion of droplets in the horizontal position. The gravitational force only assists the motion of droplets when droplets move in the direction of gravity. Otherwise, it deaccelerates the moving droplets. Droplet encounters more resistance when both the gravitational force and the drag force impede its motion. The least resistance occurs when the gravitational force is against the drag force. Under such condition, without considering droplet inertial, the droplet terminal velocity can be found by equating the gravitational force with the drag force:

$$m_d g = \frac{\rho_a A_d C_d |\vec{u}_{ter}|^2}{2} \tag{214}$$

Where m_d is the droplet mass, ρ_a is the air density, A_d is the droplet frontal area, C_d is the drag coefficient, and it can be found from Eq. (93), $\vec{u}_{ter}$ is the terminal velocity of the droplet.

If a droplet is assumed to be spherical throughout its lifetime, then the droplet mass and the frontal area can be expressed by the droplet diameter:

$$m_d = \frac{\rho_d \pi d_d^3}{6} \tag{215}$$

$$A_d = \frac{\pi d_d^2}{4} \tag{216}$$

Substituting Eq. (215) and Eq. (216) into Eq. (214) and solving for the terminal velocity, yields,

$$|\vec{u}_{ter}| = \sqrt{\frac{4\rho_a g d_d}{3\rho_d C_d}} \tag{217}$$

Figure 3-40 shows the terminal velocity as a function of the standoff distance. The terminal velocity is calculated based on the surface mean diameter. As droplet size decreases at a longer standoff distance, the terminal velocity decreases accordingly. One of the disadvantages of the decreasing terminal velocity is the potential blown away by the entrained airflow. The magnitude of the entrained airflow is between 2m/s-6.1m/s. Once the terminal velocity of a droplet is less than the velocity of the surrounding air, the droplet is likely to be blown away by the outward moving air before reaching the slab surface and conducting heat transfer. The inertial from injection helps delay the time to reach the terminal velocity, but if the standoff distance is sufficiently long, droplets are still facing potential blown-away. When the gravitational force impedes the motion of a droplet, the droplet will deaccelerate first and reverse if the standoff distance is long. Under such conditions, the slab is not effectively cooled by the water spray.

A recent experimental study [299] has proven the existence of the critical standoff distance for each type of nozzle. It is the maximum allowable standoff distance to produce an effective cooling effect regardless of the mass flow rate of water. Within the critical standoff distance, it is

encouraged to increase the spray standoff distance to allow better atomization and a higher heat transfer rate. In addition, as the spray cooling coverage increases, the total number of nozzles required to cover the entire slab width reduces, which leads to considerable economic impact. The experimental study identified 500mm as the critical standoff distance for a flat-fan hydraulic nozzle, which is equivalent to an 80% area ratio in Figure 3-39. The critical standoff distance for air-mist nozzles is much shorter because the droplet size is already smaller than that from hydraulic nozzles. In general, spray nozzles should be installed at a distance such that it is shorter than the critical standoff distance but higher enough to allow droplets to sufficiently break up into smaller ones, and when a longer standoff distance is required due to various reasons, the water flow rate should be adjusted to ensure that droplets maintain sufficient momentum to overcome resistant forces during atomization.

3.3.4   Effect of spray direction

Spray direction describes the axial direction of a spray jet with respect to the direction of gravity. Figure 3-41 (a) illustrates three possible spray directions at a continuous caster. If the axial direction of a spray is the same as the gravitational direction, it is referred to as the top spray. The bottom spray has the exact opposite axial direction as the top spray. And the axial direction of a lateral spray is perpendicular to the gravitational direction. The reason to apply sprays from multiple directions during the continuous casting process is to assure a complete solidification of the steel slab before oxygen torches cut the slab into pieces. Failure to do so could result in a disastrous incident as molten steel may burst out during cutting. Another reason is to cool down the slab as uniformly as possible to minimize residual thermal stresses arisen from the temperature gradient inside the slab.

(a)

(b)
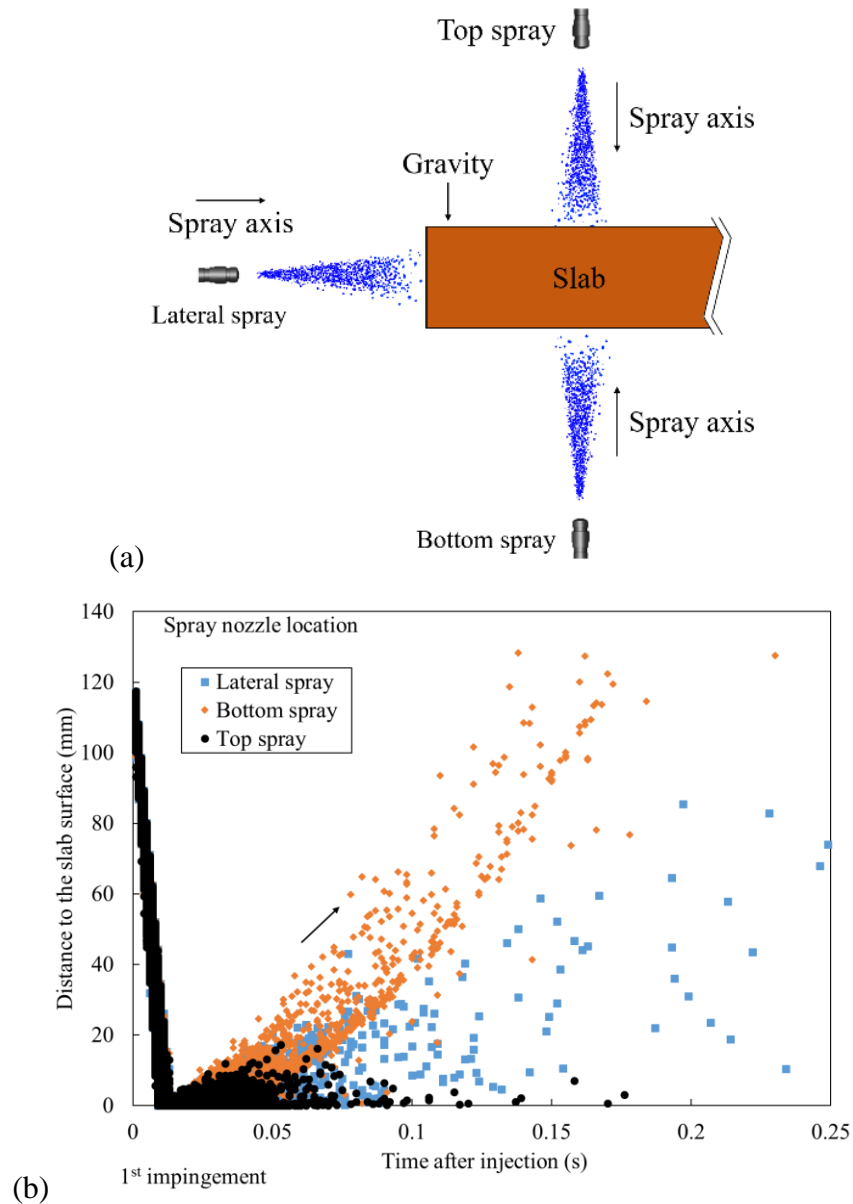
Figure 3-41. Effect of spray direction: (a) illustration of spray direction, and (b) droplet trajectories.

Yet, the cooling effect varies if the spray direction changes, even with the same spray standoff distance and water flow rate. As a matter of fact, gravity plays a vital role in determining the spray cooling effect. Figure 3-41 (b) compares droplet trajectories from three spray directions. For convenience, droplet trajectories from different spray directions are rotated so that the spray nozzle sits at 130 on the vertical axis, and the corresponding slab surface below the nozzle is represented by the origin. The horizontal axis indicates the lifetime of a droplet before it completely evaporates

240

or leaves the computational domain. Immediately after the injection, droplets approach and impinge on the slab surface within a very short period of time (less than 0.01s). The distance from droplet to slab surface is virtually linear to droplet lifetime. The direction of gravity has a very limited effect on droplet movement within this period.

However, the role of gravity becomes evident after the first impingement. Droplets injected from the top spray can hardly be reflected more than 20mm from the slab surface. Because the momentum retained in droplets after the first impingement is not enough to overcome such strong gravity. But the advantage of keeping droplets in the vicinity of the slab surface is that more droplets can absorb heat from the slab. On the contrary, almost no droplet can return to the slab surface after the first impingement in the case of bottom spray. Droplets fall off from the slab surface because of gravity. Heat transfer from slab to droplets only takes place for a brief contact moment. The last scenario, lateral spray, can be treated as the combination of the previous two. A portion of droplets stays close to the slab surface after the first impingement while the rest continue to move away from the slab surface without any impingement again.

The difference in the total residence time of droplets on the slab surface affects the heat transfer inevitably. The longer the residence time is, the higher the heat transfer rate will be. Figure 3-42 shows a smaller spray coverage and less cooling in the case of bottom spray compared to the top spray. The cooling effect in the lateral spray is somewhere in between. In practice, lateral sprays are only applied to the slab at the beginning of the secondary cooling region when the solidified shell is still relatively thin. The contribution of lateral sprays to the whole process is negligible compared to top sprays and bottom sprays. Insufficient cooling by bottom sprays shown in Figure 3-42 is also observed in casting operations, and it may induce potential crack issues if not appropriately addressed. One solution to compensate for the low heat transfer by bottom sprays is to increase the water flow rate while maintaining other operating parameters. Bottom sprays with an additional 10% to 15% of water can produce similar cooling effects to the top ones.

However, it is worth mentioning that the increase of cooling effect is at the sacrifice of compromising the uniformity of HTC, as evidently shown by the scattered spray patterns of B-3.60 (Bottom spray with 3.6L/min water flow rate) and B-3.75 (Bottom spray with 3.75L/min

water flow rate). This is because both the number of droplets and the momentum of droplets increase with the increase of water flow rate. More droplets in the spray means more heat transfer on the surface, and the result is a larger temperature difference across the spray. In addition, impinging droplets are reflecting further away from the spray pattern in order to create more space to accommodate the incoming droplets. It is also evident that the edges of the spray pattern become more oscillating with patches of satellite spray pattern around. The nature of the undulated boundary of the spray pattern is the chaotic behavior of droplet impingement. As indicated by previous research, non-uniform spray cooling is one of the leading causes of slab crack [300]. Thus, if the bottom sprays operate at an inadequately high flow rate, it is very likely that the crack issue will occur. To reduce the risk of crack, it is recommended to limit the maximum increase of water flow rate to 15% of the normal condition.
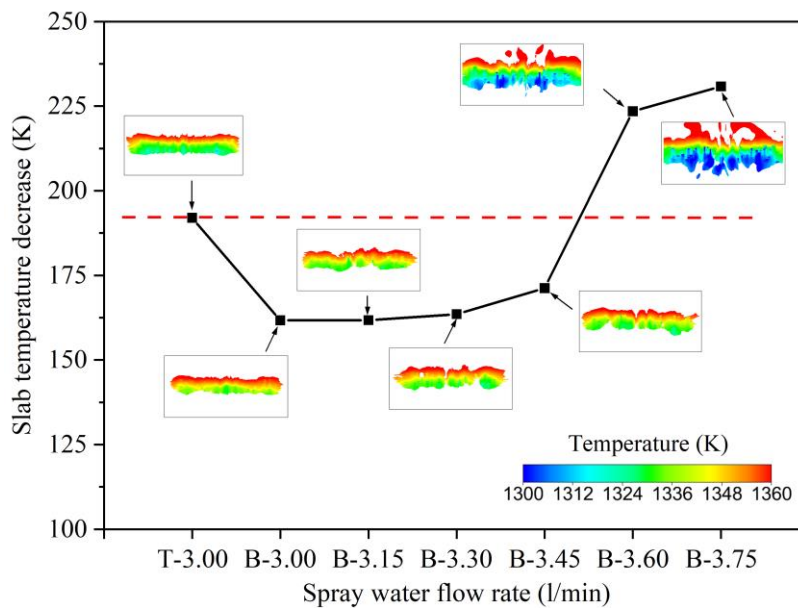
Figure 3-42. HTC pattern and spray cooling effect (T stands for "Top-spray" and B stands for "Bottom-spray").

3.3.5 Effect of casting speed

For high-productivity industrial applications, the cooling target must continuously move as it is cooled by stationary jets. Thus, the moving velocity is one of the most important operating parameters. It affects the heat transfer by changing the droplet distribution and residence time on the surface. Figure 3-43 shows the wall heat flux within the spray coverage at different moving

velocities. The butterfly-shaped cooling patterns are somewhat similar between two different moving velocities. All three patterns stretch in the slab width direction but contract in the casting direction. This proves that the cooling pattern is mostly determined by the spray characteristic, which is unique to every type of nozzle.

The effect of the plate moving velocity only becomes significant after impingement and in the plate moving direction. As shown in Figure 3-43, the width of the three spray coverages is comparable to each other, suggesting a very limited effect of the moving velocity in this direction. On the other hand, the length of the spray coverage in the casting direction decreases as the moving velocity increases. Such a phenomenon can be explained by the redistribution of the impinged droplets. Before impingement, the spatial distribution of droplets is the same in three simulations since the nozzle type and the spray flow rate is fixed. After impingement, the impinged droplets spread on the surface in both slab width and casting directions. While the moving velocity has little effect on the spread of droplets in the width direction, it dramatically affects the spread of droplets in the negative casting direction, which is opposite to the plate moving direction. The friction between droplets and the moving plate prevents droplets from spreading in the negative casting direction and pulls droplets toward the positive casting direction, thereby resulting in compressed spray coverage.
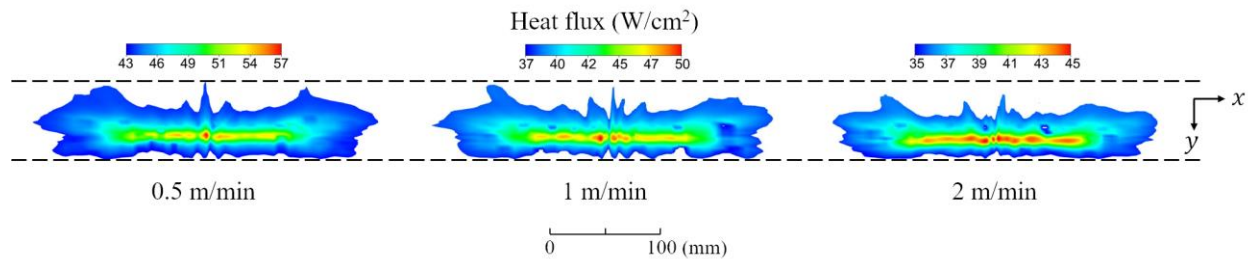
Figure 3-43. Wall heat flux within spray coverage at different plate moving velocities.

As shown in Table 3-6, A_{spray} decreases as the moving velocity increases, mostly owning to the redistribution of the impinged droplets in the moving direction. HTC_{avg} also reduces at high moving velocities. This is because the impinged droplets in the plate moving direction have less opportunity to stay in contact with the hot surface and conduct heat transfer, as shown in Figure 3-44. Another consequence of the droplet redistribution is the non-uniform heat transfer, indicating

by the large STD_{spray} at high moving velocities. When droplets in the plate moving direction are compressed in a small area, both the droplet number density and the heat transfer rate increase in that area. However, the droplet number density must decrease at other locations because of mass conservation, therefore, leading to a lower heat transfer rate. The result is the large temperature gradient across the spray coverage and non-uniform cooling. In practice, the moving velocity is usually adjusted based on the measured surface temperature. Whenever a higher heat transfer rate is required, the moving velocity can be gradually reduced until the desired cooling condition is reached.

Table 3-6. Heat transfer intensity and uniformity at different casting speeds.

Casting speed (m/min)	A_{spray} (cm^2)	HTC_{avg} (W/m^2·K)	STD_{spray} (K)
0.5	143.21	424.14	8.95
1	98.01	386.62	9.22
2	95.22	378.45	11.71
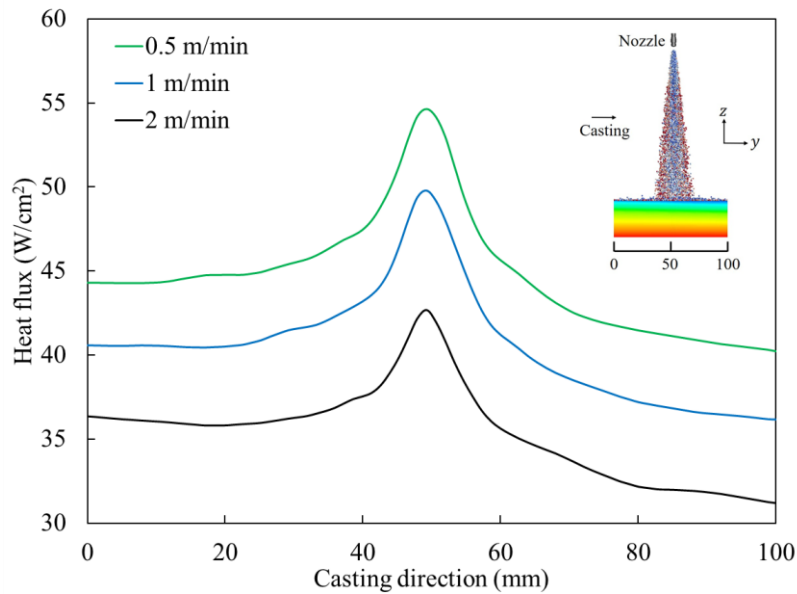
Figure 3-44. Wall heat flux distribution in the plate moving direction at different moving velocities.

3.3.6   Effect of nozzle-to-nozzle distance

Nozzle-to-nozzle distance becomes critical when multiple jets are required to cool down a large piece of the hot object. Because the jet also expands in the radial direction as it approaches the hot surface axially, there might be a region where two adjacent jets overlap and interact, as shown in Figure 3-45. In the field of jet impingement heat transfer, the overlap of two adjacent jets and its effect on heat transfer is closely related to the ratio of the nozzle-to-nozzle distance, which is donated to D in the current study, and the spray distance, H. The spray distance, which is also referred to as the standoff distance, is the distance from the nozzle exit to the stagnation point on the hot surface. The spray coverage area enlarges as H increases but the heat transfer rate decreases until a critical spray distance is reached, beyond which the jet impingement cooling effect is barely noticeable [301]. However, to highlight the role of the nozzle-to-nozzle distance in jet impingement heat transfer, the spray distance remains constant in the current study, but the ratio of the two is still used for discussion in order to be consistent with other research studies. Since the spray angle used in the current study is 90°, the spray distance equals about half of the spray coverage length in the x direction. The two adjacent jets are considered to be completely separate when the ratio of D/H is larger than 2. Thus, the three simulations investigated in the current study, i.e., $D/H = 0.5$, $D/H = 1$, and $D/H = 2$, correspond to the substantial overlap, the moderate overlap, and separation of the two jets.
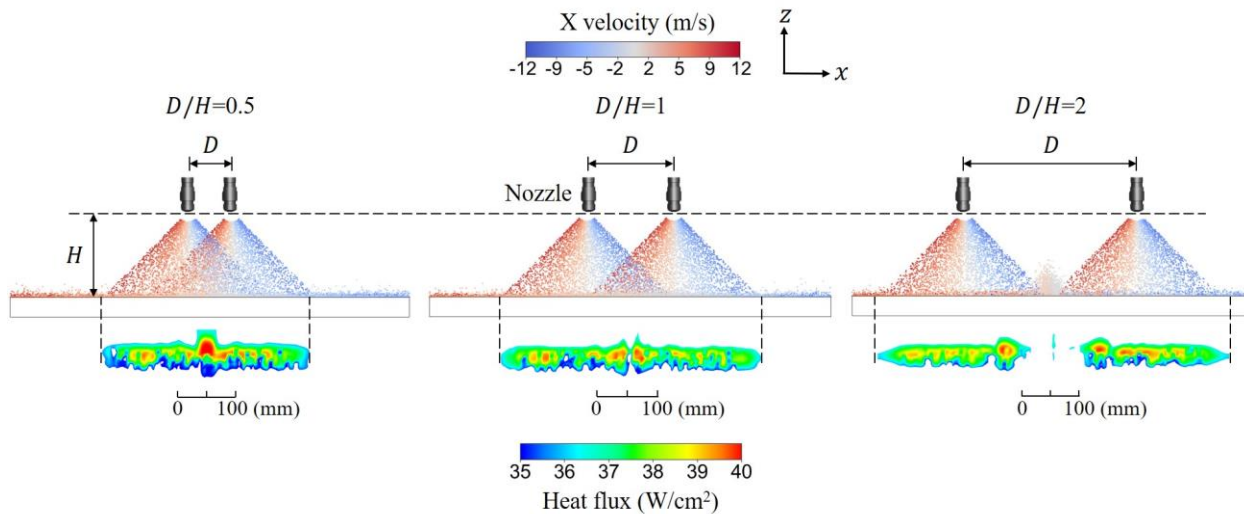
Figure 3-45. Wall heat flux within spray coverage at different D/H ratios.

245

As shown in Figure 3-45, the ratio of D/H determines the interaction of the two adjacent jets. The two jets start to overlap when $D/H < 2$ and the overlap region continues to increase as D/H approaches to zero, a condition where the two jets overlap entirely. Because both jets expand radially during atomization, droplets originated from different jets in the overlap region have the opposite radial velocity. The result is the neutralization of the radial velocity component. Another change in the overlap region is the droplet number density. As the overlap region grows, there are almost twice as many droplets in the overlap region outside the region. The net effect on heat transfer is the increase of HTC in the overlap region. Interestingly, the overlap of the atomization region does not guarantee the overlap of the spray coverages on the hot surface. The two spray coverages are still distinguishable even when $1 < D/H < 2$, where the two jets already overlap during atomization, as shown in Figure 3-45. The emergence of the two spray coverages happens when $D/H < 1$. The net cooling effect on the hot surface by the two overlap jets behaves as a single jet. Such effect is more distinct at $D/H = 0.5$ where the highest heat flux is seen at the center of the overlap region, and the heat flux gradually decreases along with the wall jet directions, similar to the spray pattern produced by a single jet. Meantime, the enhanced cooling in the overlap region further increases the non-uniformity within the spray coverage, as shown in Table 3-7. STD_{spray} increases as the ratio of D/H decreases, which imposes a lower limit for the nozzle-to-nozzle distance.

However, the behaviors of jet impingement heat transfer are entirely different when $D/H \geq 2$. As shown in Figure 3-45, under such conditions, there are no interactions between the two adjacent jets prior to impingement. After impingement, on the other hand, the wall-jet flows from the two jets moving in the opposite directions collide somewhere between the two jets on the hot surface, resulting in another local stagnation region. The combined wall jets and the entrained gas flow turn away from the surface and form a "fountain" shape, as shown in Figure 3-45 and Figure 3-46. A cluster of droplets is raised from the surface and trapped in the fountain. The rest of the droplets changes the moving direction from x to y, forming two new wall jets as if they were injected from the stagnation point sitting in the middle of the fountain. Because of the fountain effect, the local cooling condition considerably alters. The collision of the droplets from the two wall jets counterbalances the increase of the droplet number density in the fountain. In addition, some of the droplets are entrained in the fountain and are raised above the surface, thereby losing the

opportunity to absorb heat from the hot surface. The overall effect is the increase of A_{spray} due to the completely separation of the two spray coverages and the decrease of HTC in the fountain. The turbulent gas flow after the fountain forms merely offsets the loss of droplet boiling. The reduced heat transfer rate can also be visualized in Figure 3-46 (b), where the plate below the fountain is slightly hotter than that covered by jets. Yet less overlap of the two jets improves the cooling uniformity, as indicated by STD_{spray} in Table 3-7. In practice, $D/H = 2$ should be considered as the upper limit to avoid the onset of the fountain effect, which is detrimental to the heat transfer.
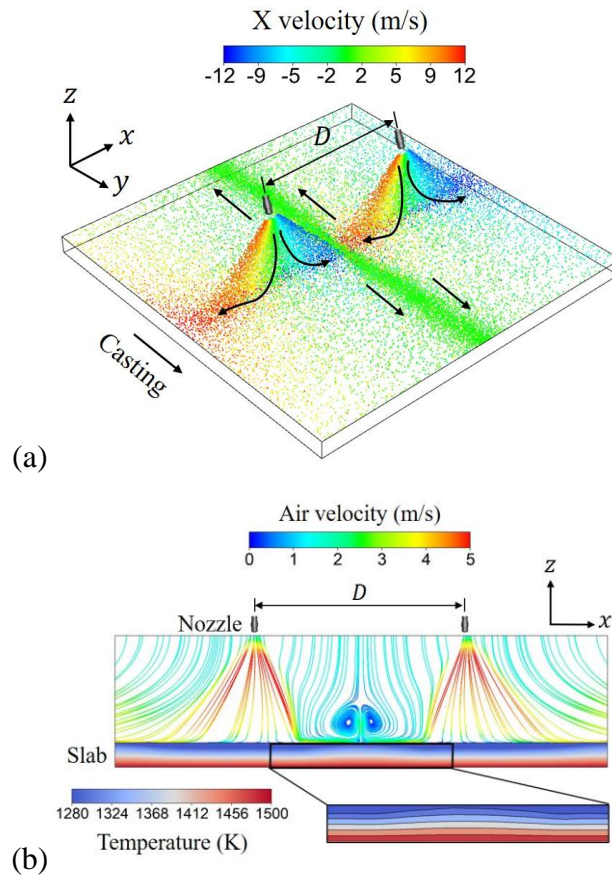
Figure 3-46. Fountain effect at $D/H = 2$: (a) droplet distribution on the moving hot surface, and (b) gas streamlines and plate inner temperature.

Table 3-7 . Heat transfer intensity and uniformity at different nozzle-to-nozzle distances.

D/H	A_{spray} (cm²)	HTC_{avg} (W/m²·K)	STD_{spray} (K)
0.5	150.86	359.37	20.75
1	149.87	360.46	17.77
2	175.12	360.52	14.88

For any arbitrary spray angle, Figure 3-47 illustrates the relationship between the spray overlapping length and the ratio of D/H. The spray overlapping length can be calculated based on following the trigonometric relations:

$$\delta_{ovlp} = 2Htan\frac{\alpha_{spray}}{2} - D \tag{218}$$

Where δ_{ovlp} is the overlapping spray length, α_{spray} is the full spray angle.
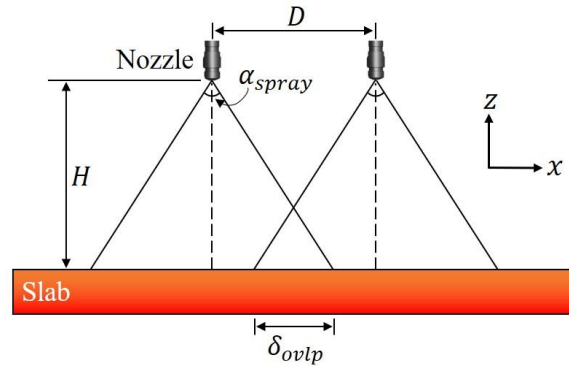
Figure 3-47. Illustration of the overlapping spray length of two sprays with an arbitrary spray angle (not to scale).

The ratio of D/H can be derived from the range of δ_{ovlp}. As previously described, δ_{ovlp} is a positive number in the case where the two adjacent sprays overlap. Thus, the lower limit for δ_{ovlp} should be zero. The upper limit for δ_{ovlp} should be half of the spray coverage length in the slab width direction. Theoretically, the upper limit for δ_{ovlp} is the spray coverage length of a single spray in the slab width direction. However, as shown in Figure 3-45, the cooling effect from two overlapping sprays with $D/H = 0.5$ is indistinguishable from that of a single spray. Further

overlapping of the two sprays will drastically increase STD_{spray}, which counterbalances the increase of the heat transfer rate. Hence, the value of δ_{ovlp} should be restricted to the following range to produce effectively spray cooling:

$$0 \leq \delta_{ovlp} \leq H tan \frac{\alpha_{spray}}{2} \tag{219}$$

Substituting the expression for δ_{ovlp} shown in Eq. (218), yields:

$$0 \leq 2H tan \frac{\alpha_{spray}}{2} - D \leq H tan \frac{\alpha_{spray}}{2} \tag{220}$$

Rearranging Eq. (220) and solving for D/H, yields:

$$tan \frac{\alpha_{spray}}{2} \leq \frac{D}{H} \leq 2 tan \frac{\alpha_{spray}}{2} \tag{221}$$

The shaded area in Figure 3-48 defines the optimum ratio of D/H for different spray angles.
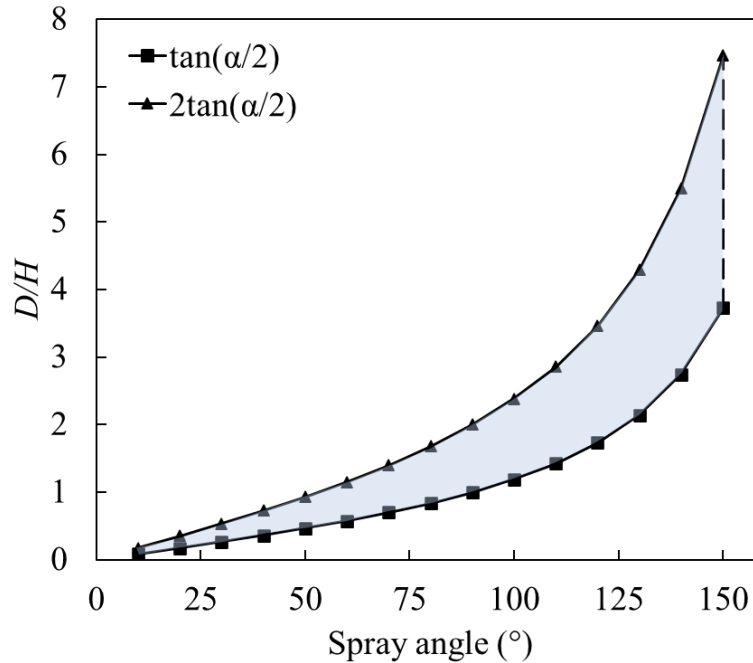
Figure 3-48. The optimum ratio of D/H for different spray angles.

3.3.7 Effect of row-to-row distance

The distance between adjacent rows of spray nozzles is another parameter that needs to be carefully considered during the design stage of the continuous casting machine. In practice, there is a roll placed in between the adjacent rows of sprays. One of the reasons is to avoid droplet accumulations between rows of sprays. Figure 3-49 demonstrates the effect of row-to-row distance if there is no roll placed in between. To exclude the effect from other parameters, only one spray is considered in each row. The two adjacent rows are separated by 100mm and 200mm, respectively. Both nozzles at the different rows operate at the baseline condition. As shown in Figure 3-49, all sprays can be identified under the current conditions. No interaction or collision of the two sprays is observed, implying that even the shorter row distance is wide enough for both sprays to completely expand in the casting direction. Unlike the favorable overlapping of two adjacent sprays in the same row, the overlapping of two sprays from different rows is not preferred during the operation. In addition, a belt of water droplets forms on the slab surface between the two sprays in both conditions. The belt itself is the result of droplet accumulation on the slab surface. As shown in Figure 3-49 (b), after droplets impinge onto the slab surface, they are reflected from the spray region to other locations on the surface. In the region between the two sprays, droplets generated

from different sprays eventually meet at the center between the two sprays. Because more droplets come from the two sprays, the previously accumulated droplets are pushed to move outward in the slab width direction. The width of the droplet belt is comparable in both conditions, but it takes approximately twice the time for droplets to reach the belt from the spray impingement area at a wider row-to-row distance.
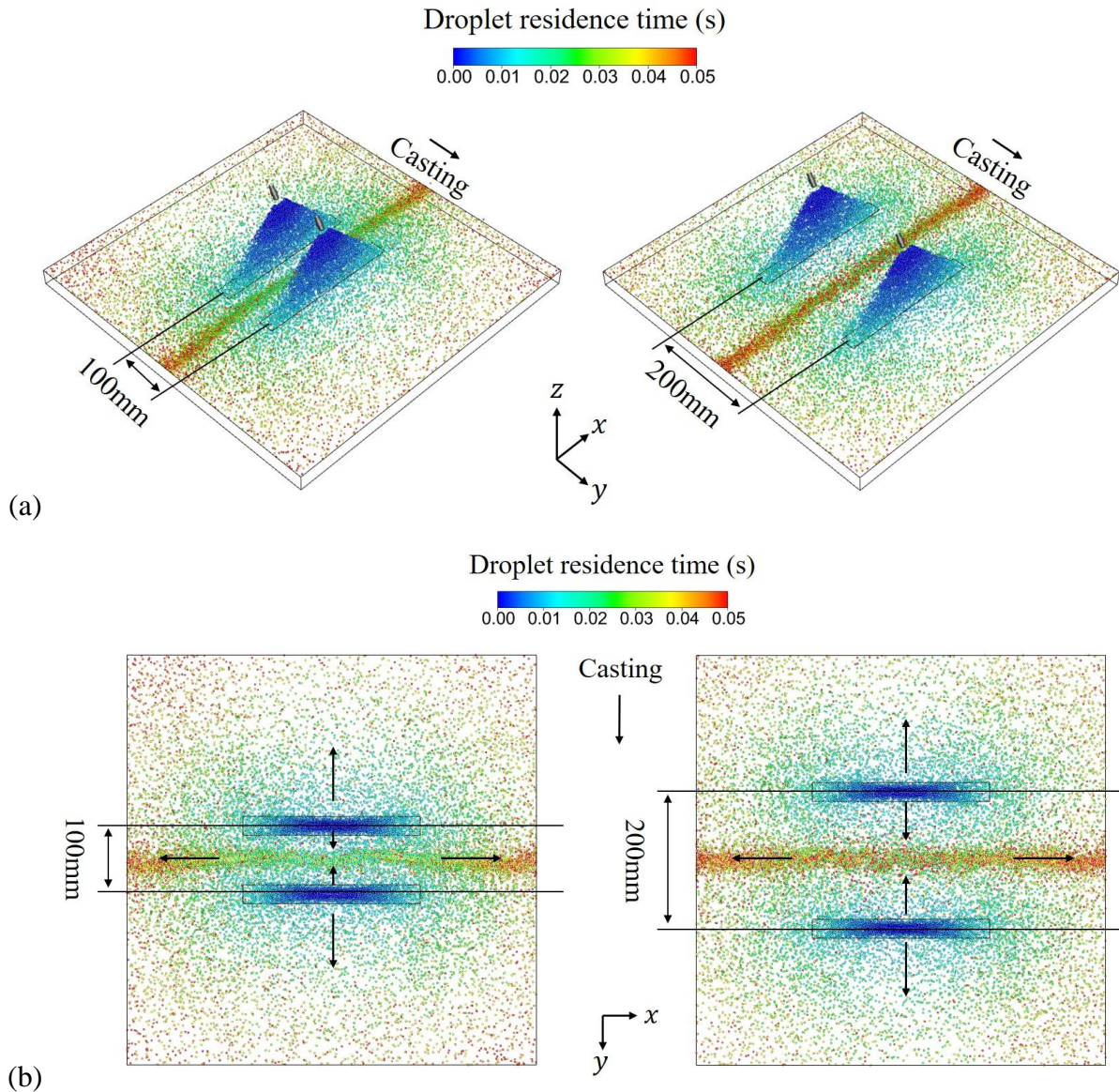
Figure 3-49. Droplet distribution at different row-to-row distances: (a) isometric view, and (b) top view.

The cooling effect on the surface significantly differs from the baseline condition, where the row-to-row distance is equivalent to infinite. Due to the existence of the belt in between the two sprays, the heat transfer also increases at such a location, as shown in Figure 3-50. The two squares on the surface represent the projected spray areas, and they are used as a reference for comparisons. The highest heat flux is observed in the vicinity of the upstream, which is due to the highest temperature difference between the surface and the surrounding. Along the casting direction, a high heat transfer rate occurs at the location of the projected spray area as expected, but there are also two distinguishing features that appear during the heat transfer process compared to the baseline condition. First, a strip of high heat transfer region forms between the two sprays, corresponding to the aforementioned droplet belt. This belt acts as a single cooling source if the row-to-row distance is sufficiently wide. If the row-to-row distance decreases, the belt will interfere with the expanding sprays. Droplets are forced to redistribute on the surface without continuously moving outward. Under such conditions, several cooling strips can form in between the two sprays, as shown in Figure 3-50. Second, the spray cooling patterns deform from that in the baseline condition, as shown in Figure 3-51. In the current study, both ends of the spray cooling pattern bend in the direction away from its adjacent row. This is mostly due to the moving belt in between the two sprays. As shown in Figure 3-50, once the belt forms at the center of the surface, it is pushed outward in the slab width direction by the incoming droplets from the two sprays. While it is moving, it also expands in other directions and interferes with the droplets at the edge of the spray-affected area. Thus, droplets near the edge of the spray-affected area are pushed to create more space for the moving belt. As shown in Figure 3-51, the blank space between the two bent spray-affected areas indicates the moving behavior of the belt. At a short row-to-row distance, the bending effect is much evident as the droplet number density and momentum are both higher.
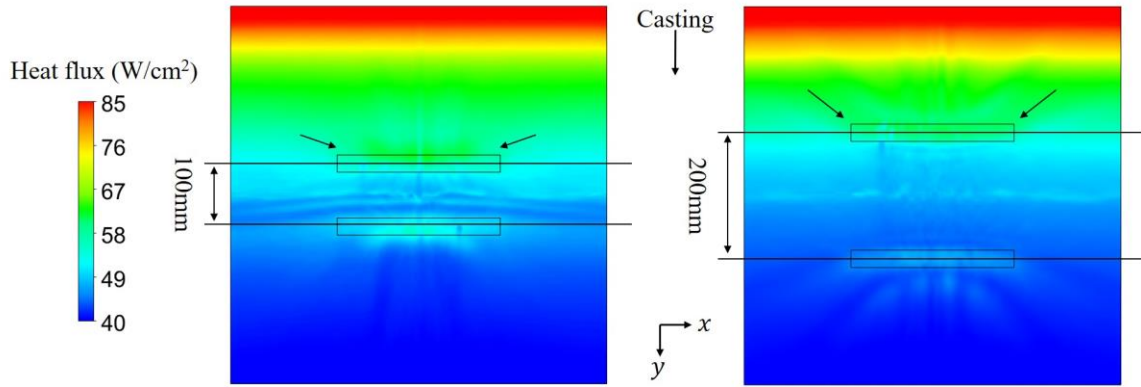
Figure 3-50. Heat flux distribution on the slab surface at different row-to-row distances.
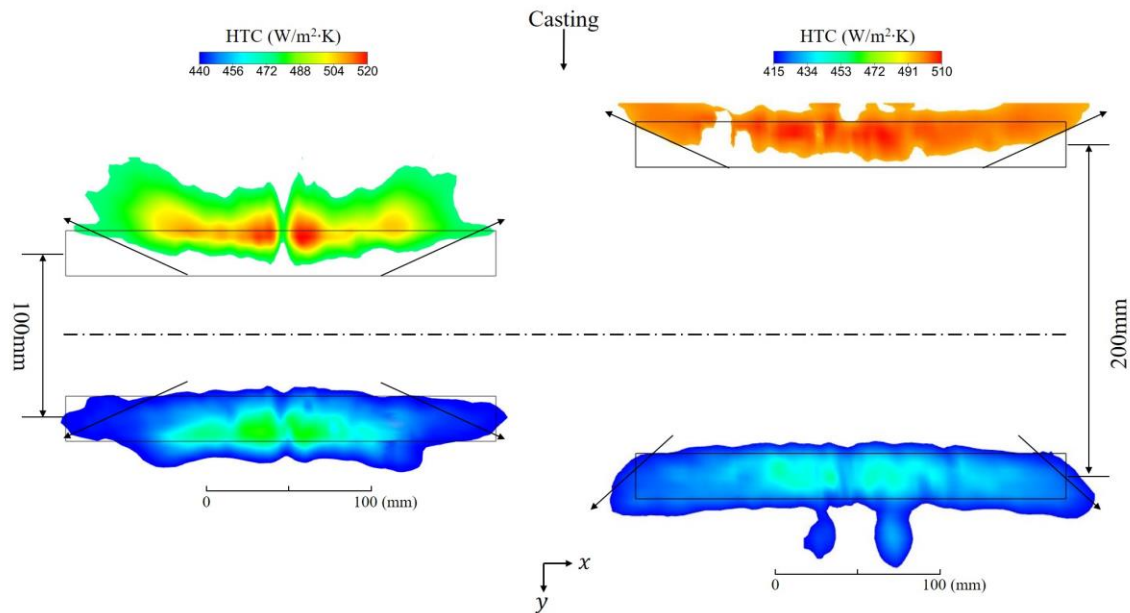
Figure 3-51. HTC distribution on the slab surface at different row-to-row distances.

Table 3-8 summarizes the heat transfer intensity and uniformity at different row-to-row distances. It is interesting that both heat transfer intensity and uniformity are different in the adjacent two sprays. The spray-affected area is always wider the downstream, regardless of the row-to-row distance. Because of the expansion of the droplet belt, some of the droplets moving in the slab width direction are pushed to the casting direction, thus, increasing the spray-affected area downstream. At the upstream, heat transfer is much more intense and non-uniform, as indicated by HTC_{avg} and STD_{spray} in Table 3-8. At shorter row-to-row distance, the difference in heat

transfer between the upstream spray and the downstream spray is smaller, implying a higher overall heat transfer rate. Nevertheless, the spray cooling performance of each spray in the two simulations varies from location to location despite the same spray conditions. Besides, the droplet belt between the two adjacent rows can interfere with the spray cooling process, further deviating the spray cooling effect from the baseline condition. Therefore, rolls are necessary to be placed in between the two adjacent rows to prevent interference from the droplet belt. From the heat transfer point of view, a shorter row-to-row distance is preferred at locations where a higher heat transfer rate is required, but the distance should be sufficiently wide to install a roll in between the rows.

Table 3-8. Heat transfer intensity and uniformity at different row-to-row distances.

Row-to-row distance (mm)	A_{spray} (cm^2)	HTC$_{avg}$ (W/m^2·K)	STD$_{spray}$ (K)
100 (upstream spray)	96.36	485.59	9.74
100 (downstream spray)	95.57	454.16	7.89
200 (upstream spray)	63.91	496.09	8.36
200 (downstream spray)	117.34	431.99	6.73

3.3.8 Effect of arrangement of nozzles

The effect of nozzle-to-nozzle distance and row-to-row distance on the surface heat transfer is discussed separately in the previous sections. This section evaluates the combined effect of both parameters. As shown in Figure 3-52, two different arrangements of nozzles are compared in the current study. In both arrangements, the ratio of D/H is set to 1.15, which indicates moderate overlapping between the two adjacent sprays in the same row. The row-to-row distance is set to 100mm to ensure sufficient cooling between rows. Although both the nozzle-to-nozzle distance and the row-to-row distance are fixed, there are still two different arrangements of nozzles in between rows, which are the rectangular arrangement and the staggered arrangement. In the rectangular arrangement, the sprays in different rows are perfectly aligned in the casting direction, thus, forming a rectangular shape if the corresponding edges of the sprays in two different rows are connected. In the staggered arrangement, nozzles in different rows are staggered in the casting direction. In the current study, three rows of sprays are considered, and there are two sprays in each row, except the second row in the staggered arrangement, which requires three sprays to form

the staggered pattern. The operating conditions are the same for all the nozzles in both arrangements. In addition, the computational domain is extended to 600mm in both the casting and slab width directions. A projected spray area is also created for each spray as a reference. However, due to the overlapping between the two sprays in the same row, the calculated projected spray areas also overlap. Thus, the two overlapping projected spray areas are treated as one area that includes both overlapping sprays in the current study.
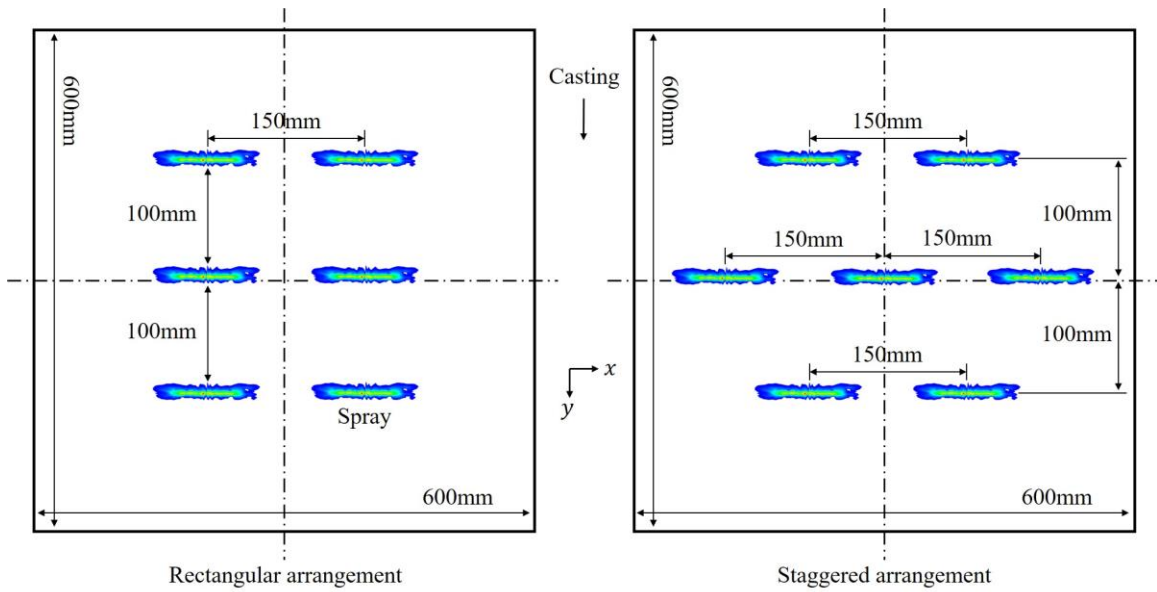
Figure 3-52. Illustration of two arrangements of nozzles.

Figure 3-53 shows the droplet distribution at different arrangements of nozzles. Similarly, a strip of accumulated droplets is observed between every two adjacent rows in the slab width direction. Droplets from different sprays accumulate in the middle between the adjacent rows and move outward in the slab width direction. Two strips of droplets are seen in both simulations, as shown in Figure 3-53 (b). Interestingly, strips of droplets also present in the casting direction, which is not seen in the previous study of row-to-row distance. These strips of droplets originate from the overlapping region between the two adjacent sprays in the same row and move away from the sprays. This outward moving effect is evident between the first row and the upstream, or between the third and downstream. Between the adjacent rows, because the outward moving droplets generated from different rows are heading in different directions, droplets merge into a cluster and hover between the rows. A larger cluster of droplets is observed in the rectangular arrangement

compared to that in the staggered arrangement, as shown in Figure 3-53 (b). In the staggered arrangement, droplets generated from the middle spray in the second row push the cluster toward the adjacent tows and create low droplet number density regions on both sides of the spray in the *y* direction. In addition, the two outward moving strips of droplets are also pushed further toward the adjacent tows, which are the first and the third rows, considerably changing the landscape on the surface.

(a)

(b)
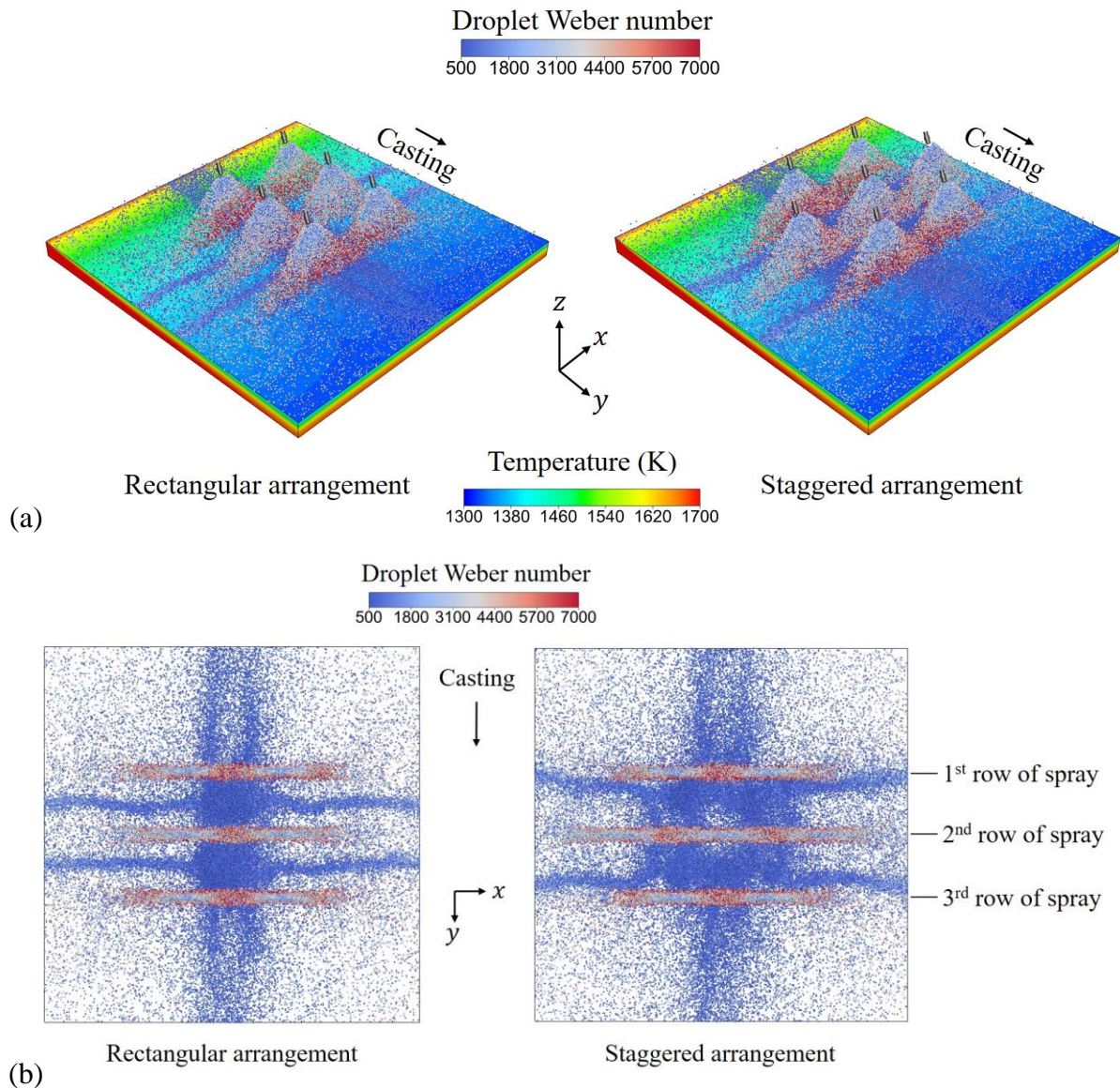
Figure 3-53. Droplet distribution at different arrangements of nozzles: (a) isometric view, and (b) top view.

Because of different droplet distributions on the surface, the surface heat transfer in the staggered arrangement also changes accordingly. Figure 3-54 shows the HTC patterns in both arrangements. The threshold value is adjusted for each row to create a pattern that is comparable to the size of the projected spray area. In both arrangements, the spray patterns at the second row are less affected by the presence of droplet strips, and distinct overlapping patterns can be seen in the overlapping area. HTC patterns at first and the third rows are significantly affected by the presence of droplet strips. The HTC patterns at the first row extend throughout the entire width of the computational domain, whereas the HTC patterns at the third row can barely cover the entire projected spray area. The spray-affected areas summarized in Table 3-9 also show this decreasing trend of HTC patterns in the casting direction. HTC_{avg} also decreases in the casting direction as the result of slab moving effect and droplet distribution, and less uniform cooling at the first row, as STD_{spray} is more than twice that of the other two rows.
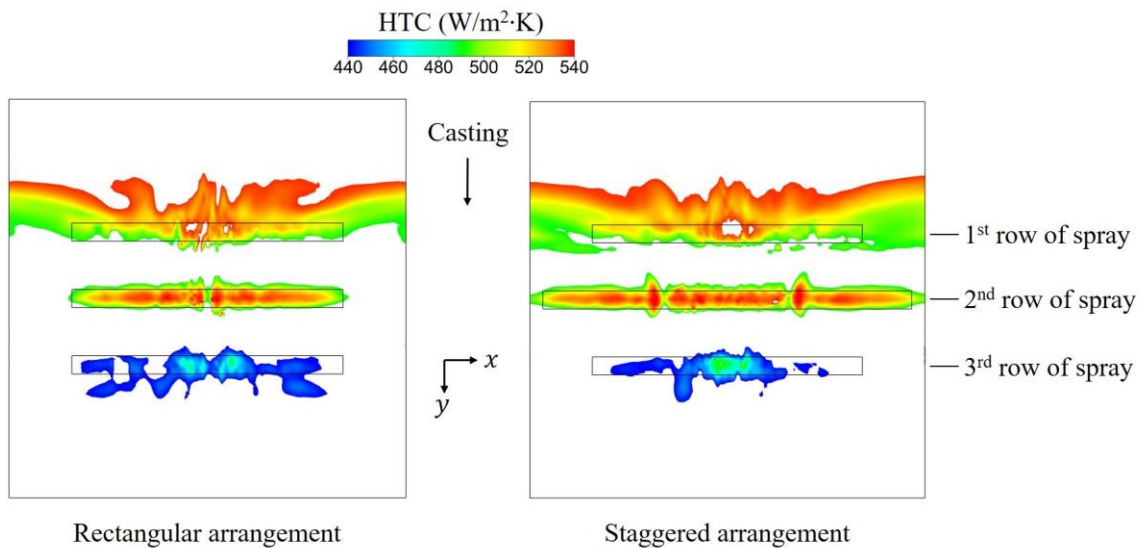
Figure 3-54. HTC distribution on the slab surface at different arrangements of nozzles.

257

Table 3-9. Heat transfer intensity and uniformity at different arrangements of nozzles.

Row-to-row distance (mm)	A_{spray} (cm^2)	HTC$_{avg}$ (W/m^2·K)	STD$_{spray}$ (K)
Rectangular (1st row)	436.14	515.29	19.41
Rectangular (2nd row)	151.32	511.74	8.59
Rectangular (3rd row)	137.33	452.26	7.48
Staggered (1st row)	523.87	513.00	19.26
Staggered (2nd row)	224.39	512.51	8.85
Staggered (3rd row)	126.78	454.38	9.12

Figure 3-55 compares the surface temperatures of the two arrangements. The surface temperature at the second row is the lowest in both arrangements, which suggests much intense cooling at such a location. As shown in Table 3-9, HTC$_{avg}$ at the second row is slightly lower than that at the first row, but the high spray cooling rate at the first row is applied over a much wider spray area and with much less uniformity. Besides, due to the limited number of sprays simulated in the current study, the cooling effect at first and the third row is underestimated to a certain extend. Before the first and after the third row, the slab is not sufficiently cooled by any sprays. Heat conduction inside the slab helps recover the slab temperature at these locations. Thus, the spray cooling effect at the second row is much more realistic compared to that at the other rows.
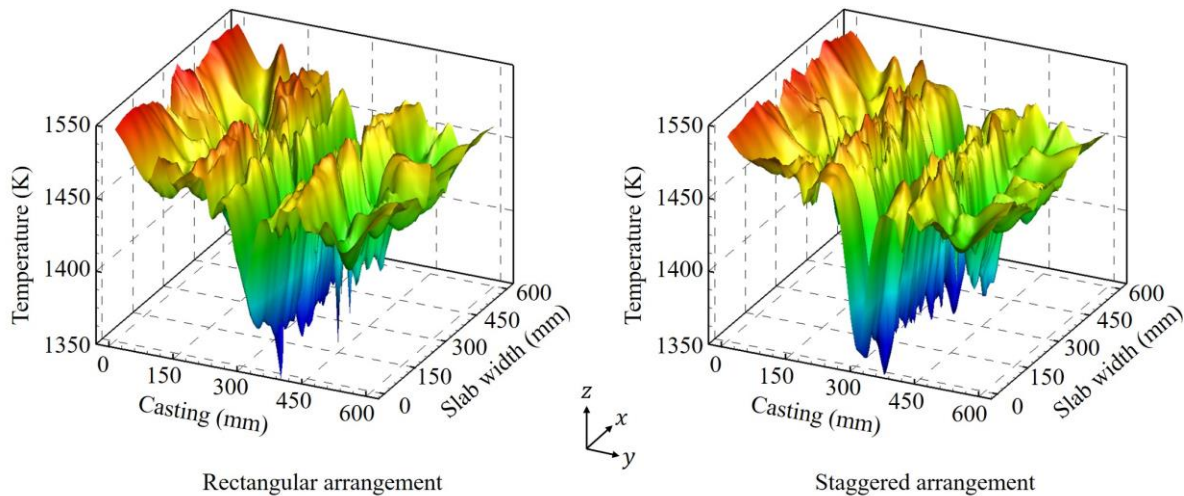
Figure 3-55. Slab surface temperature at different arrangements of nozzles.

Figure 3-56 visualizes the surface temperature difference between the two arrangements. First, the surface temperatures from the two arrangements are overlapped based on the spatial coordinates. Then, the surface temperature in each control volume of the staggered arrangement is subtracted from the rectangular arrangement. Finally, the difference between the two temperatures is plotted in Figure 3-56. As shown in the figure, the temperature difference before the first row and after the third row is zero, implying the same heat transfer rate. Because the radiation and convection conditions are the same in both arrangements, such behavior is evident. The non-zero temperature difference occurs within the spray-affected area and between rows of sprays. Since the temperature difference is always positive, the surface temperature of the rectangular arrangement is higher than that of the staggered arrangement, which indicates sufficient spray cooling in the staggered arrangement. The highest temperature difference occurs downstream of the second row. This is also the location where the nozzle arrangement is different. As shown in Figure 3-53 (b), the middle spray at the second row helps break the hovering droplets and reduce stagnation regions where heat transfer is compromised. However, such a mechanism is not observed in the rectangular arrangement. Although the temperature difference between the two arrangements is less significant if rolls are placed in between rows of sprays as discussed in the previous section, the staggered arrangement is still recommended for intense and uniform spray cooling practice because it offers the chance to cool down the regions that may not be sufficiently cooled by previous rows.
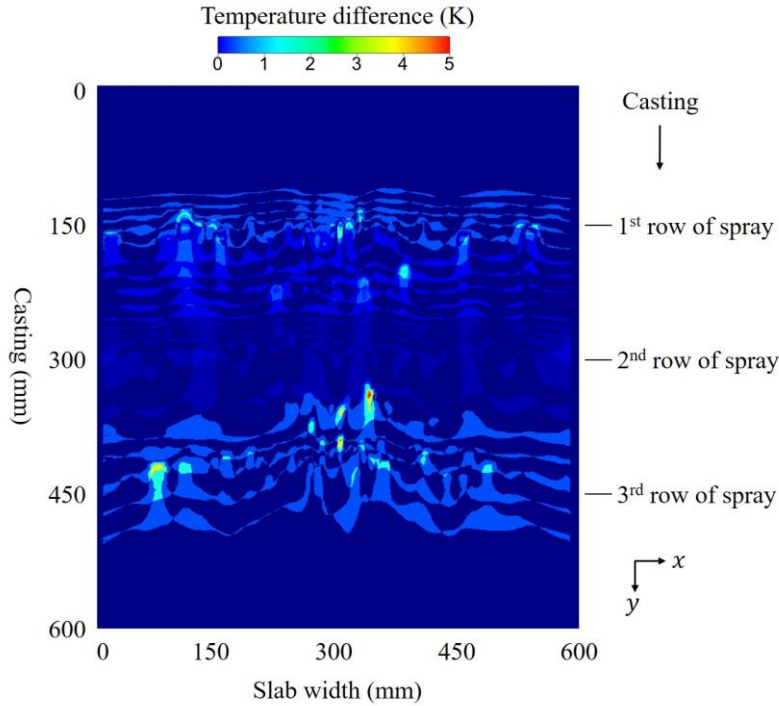
Figure 3-56. Slab surface temperature difference at different arrangements of nozzles.

3.3.9 Effect of roll and roll pitch

Rolls, also referred to as rollers, support the newly-formed solid shell and prevent any undesired bending or bulging of the slab in the secondary cooling region. The roll diameter and the roll pitch, which is the distance between the center of the two adjacent rolls, are varied accordingly based on the estimated shell thickness and the desired bending curvature of the slab. In addition to the aforementioned functions, rolls also conduct heat with the moving slab during operation. A measurement by Xia et al. has shown that the heat transfer by roll contact accounts for 10% of the total heat transfer on the slab surface [12]. Besides, as previously described, sprays are substantially affected by the adjacent sprays from different rows if there is no roll installed in the middle. This section evaluates the effect of roll presence and the roll pitch on the droplet distribution and the heat transfer. Figure 3-57 illustrates the computational domain and the definition of roll pitch. The roll diameter is set to 70mm in the current study. Three values of D_{roll} are compared and they are 90mm, 130mm, and 170mm. The ratios of roll diameter and roll pitch are 0.78, 0.54, and 0.41, respectively.
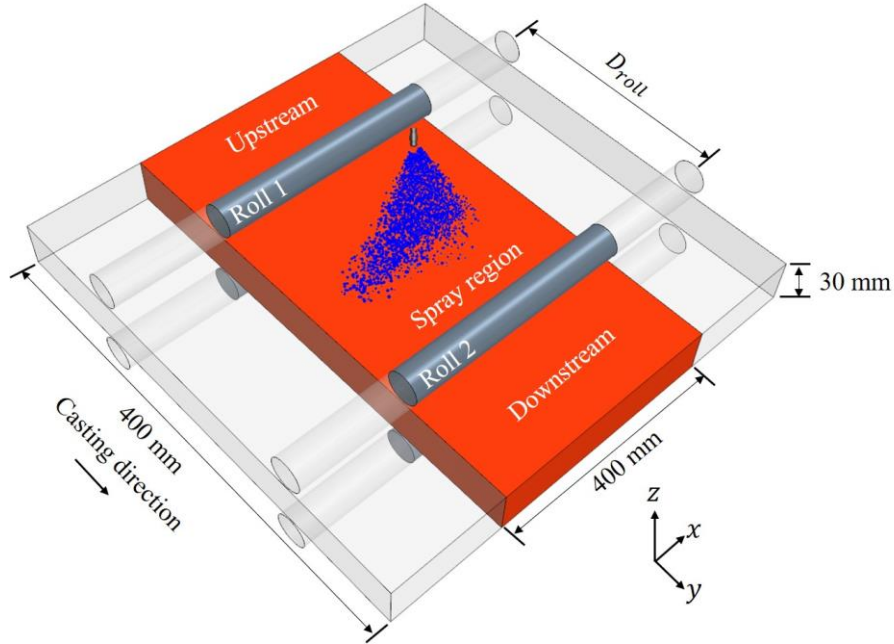
Figure 3-57. Illustration of roll pitch (computational domain is highlighted in orange and is not to scale).

The effect of roll presence is shown in Figure 3-58. The baseline simulation is referred to as "spray cooling without rolls" in the figure, opposite to the simulation of "spray cooling with rolls". In the baseline simulation, droplets can reflect, spread, or glide on the slab surface without any constraints from any object. This condition is equivalent to infinite roll pitch. Detailed results regarding the droplet behavior and the heat transfer are discussed in the previous sections. Under the baseline condition, the entire surface of the slab is covered by water droplets but with different concentrations, depending on the location on the surface. Higher droplet concentration is expected in the spray-affected area. Droplet concentration gradually decreases in both the casting and slab width directions. Most of the droplets are seen in the slab width direction in and around the spray affect area, which is determined by nozzle characteristics. However, when a pair of rolls are placed on the slab surface, all the droplets are confined in the space between rolls. Droplet movement in the casting direction is blocked by the roll contact, which results in a strip of droplets forming along the line of the roll contact, as shown in Figure 3-58. Eventually, droplet distribution is compressed in the casting direction. Because the current simulation only includes one spray in between a pair of rolls, only one strip of droplets is seen at one side of each roll. If more sprays are considered, as it is in the secondary cooling process, droplet accumulation is expected on both

sides of the roll contact. Although rolls are rotating during the operation, no droplet is seen to be attached to the roll surface and transported to the other side of the slab.
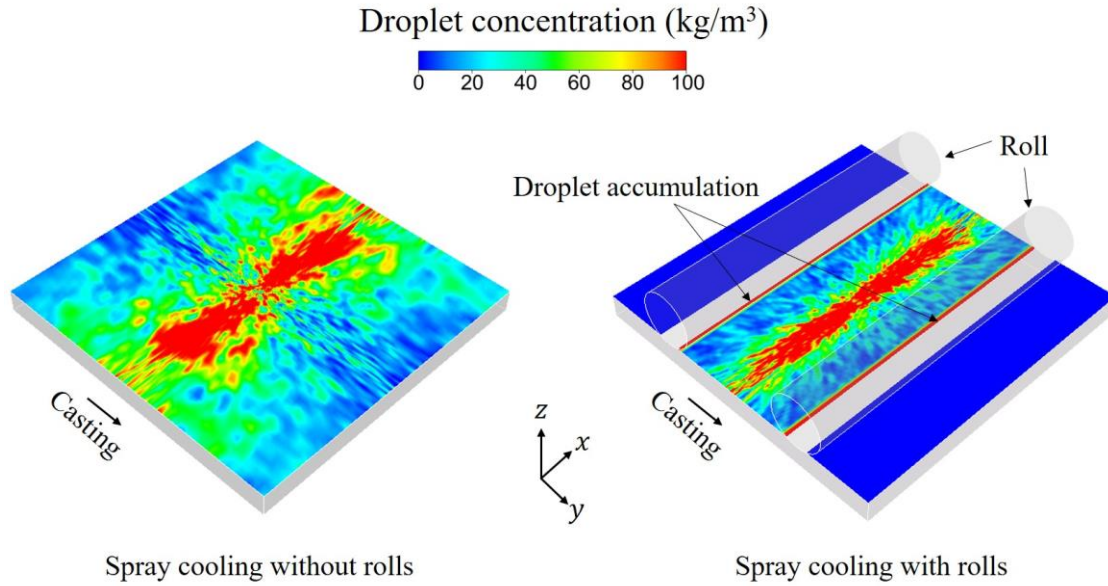
Figure 3-58. Water droplet distribution on the slab surface with and without rolls.

Table 3-10 compares the heat transfer intensity and uniformity with and without rolls. Both A_{spray} and HTC_{avg} increase when a roll is placed on each side of the spray. A_{spray} increases by approximately 18% and HTC_{avg} increases by 4%. The increase of both the spray-affected area and heat transfer intensity is due to the change of droplet distribution on the surface. As shown in Figure 3-58, droplets are confined between the rolls instead of spreading on the entire slab surface. As a result, the concentrated droplets further promote heat transfer. Another advantage of confined spray is the increase of heat transfer uniformity. STD_{spray} decreases by 46% compared to the baseline simulation, as the droplet distribution becomes more uniform in the cooling area.

Table 3-10. Heat transfer intensity and uniformity with and without rolls.

	A_{spray} (cm^2)	HTC_{avg} (W/m^2·K)	STD_{spray} (K)
Without rolls	98.01	386.62	9.22
With rolls	116.63	403.18	4.97

Figure 3-59 shows the energy flow for the spray cooling simulation with rolls. As illustrated in Figure 3-57, the slab surface can be divided into three sections relative to the location of the spray and the casting direction. The two rolls are referred to as "Roll 1" and "Roll 2" along the casting direction. The area from the upstream surface to roll 1 is simplified as "Upstream". Similarly, the area from roll 2 to the downstream surface is named "Downstream". The surface in between roll 1 and roll 2 and is cooled by the spray is the "Spray region". Inside the slab region, heat is supplied from the upstream surface and leaves the slab region through the downstream surface and the top surface, consisting of the three sections. The energy that passes through the top surface is considered as the total energy supply to the heat transfer on the surface. The percentage of energy flow by each heat transfer mechanism is compared with the total energy supply. At "Upstream" and "Downstream", heat is released from the slab surface to the surroundings through both radiation and convection. The naming convention for each heat transfer mechanism starts with the name of the section, followed by the heat transfer mechanism. For example, heat transfer by radiation at "Upstream" is simplified to "Upstream by radiation". Similarly, radiation and convection are the main heat transfer mechanisms on the surface of roll. There is also a portion of the energy stored in the roll and is used to increase the internal temperature of the roll. For instance, the increase of the internal energy of roll 1 is referred to as "Roll 1 by storage". In the spray region, spray cooling is used as the third heat transfer mechanism other than radiation and convection. The amount of energy released to droplets is labeled as "Spray region by spray".
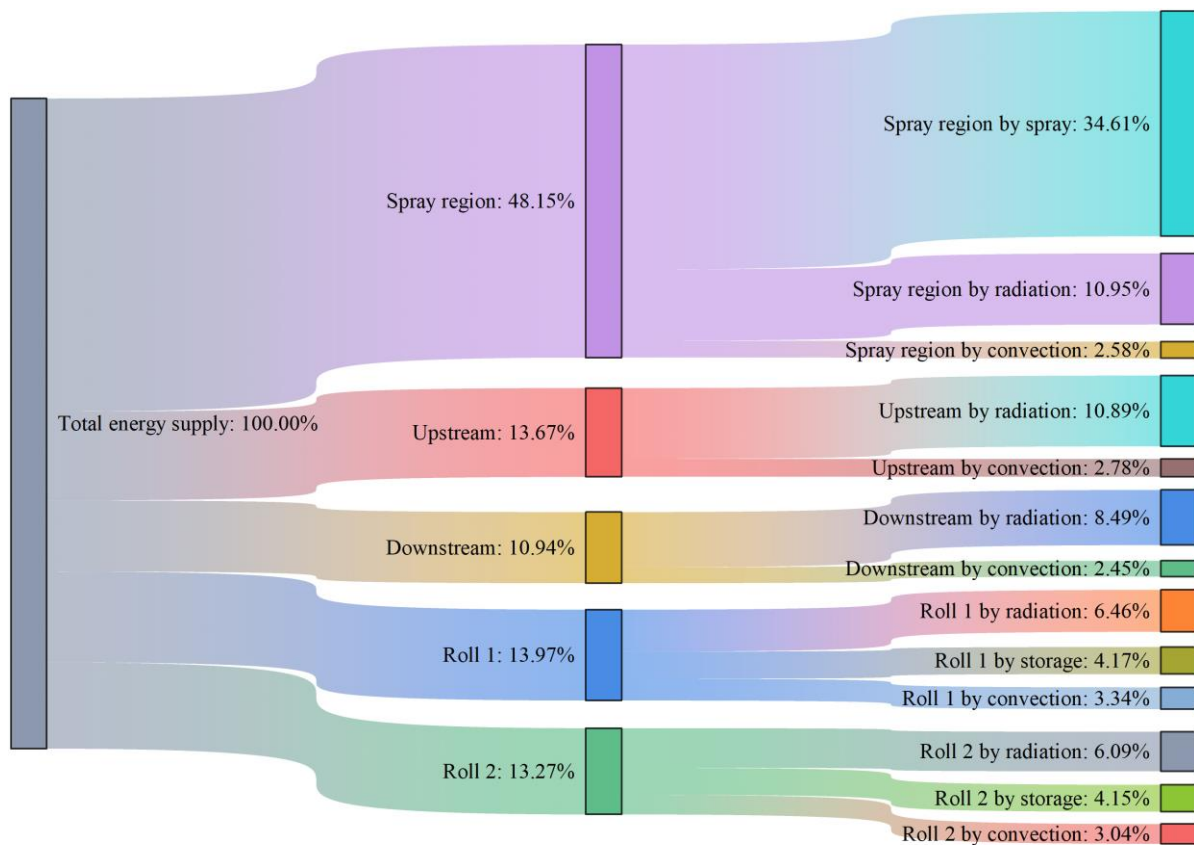
Figure 3-59. Energy flow diagram for spray cooling with rolls.

As shown in Figure 3-59, approximately half of the energy released from the slab is through the spray region, primarily due to the effect of spray cooling. The rest of the energy leaves the slab region somewhat evenly through the upstream and downstream surfaces, as well as the pair of rolls. The amount of energy released from the upstream surface and roll 1 is slightly higher because the hot slab is yet to be cooled significantly. On the upstream surface, radiation is the primary heat transfer mechanism compared to convection, which only accounts for 2.78% of the total energy supplied. Similar heat transfer mechanisms are also seen downstream. Heat transfer by radiation is more than three times that of convection. This trend is also consistent in the spray region. However, nearly 72% of energy through the spray region is absorbed by water droplets. This demonstrates the significance of spray cooling among all the heat transfer mechanisms in the secondary cooling process. On average, about 13.62% of the energy is transferred to the roll through the roll contact area. About 70% of the absorbed energy is further released to the

surroundings through the surface of the roll by radiation and convection. The rest 30% of the absorbed energy, is stored in the roll to increase its internal energy.

It is also worth noting that the temperature distribution inside the roll is not uniform. It is affected by both the rotation of roll and the movement of the slab. Figure 3-60 shows the temperature distribution on a cross-section of the roll and the temperature change after a full rotation of the roll. To better describe the temperature change, the contact point from the roll center to the slab surface is defined as 0°. As indicated by the white arrow, the slab moves toward the right, and the roll rotates counter-clockwise. Heat is transferred from the slab region to the roll through the contact area. Thus, the highest temperature occurs around 0°. As the roll rotates, the absorbed energy dissipates, and the temperature inside the roll continuously decreases from 3.5° to 356.5°. On the surface of the roll, 70% of the absorbed energy is released to the surroundings by radiation and convection. This is the reason why temperature decreases radially from 3.5° to 356.5°. The lowest temperature occurs at 356.5° before the roll contacts with the slab again. This process repeats as the roll starts another rotation.
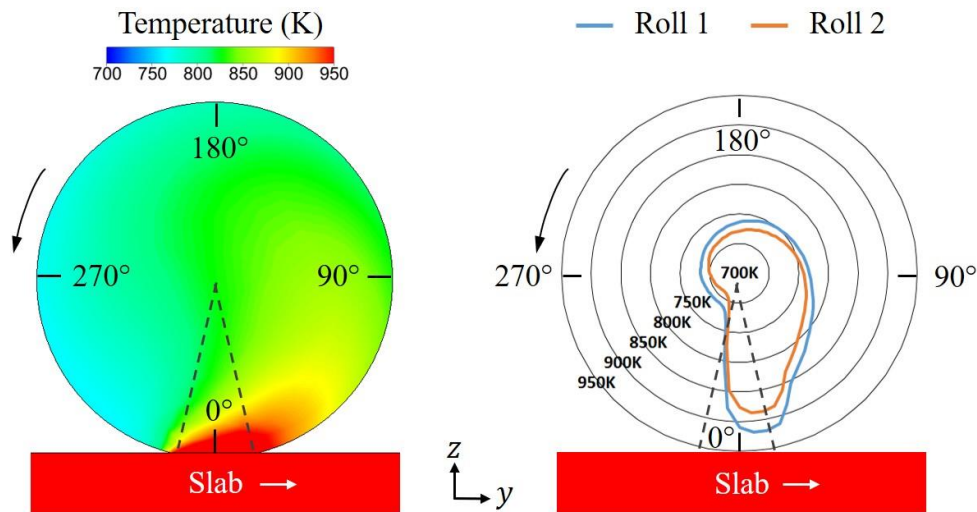
Figure 3-60. Temperature distribution inside the roll in the casting direction.

As shown in Figure 3-59, the amount of energy transferred to roll 1 is slightly higher than that transferred to roll 2. Figure 3-60 also compares the surface temperature of roll 1 and roll 2. To better visualize the temperature distribution relative to the rotation degree, the cartesian

265

coordinates are converted into polar coordinates in the plot. A sharp increase of the surface temperature is observed in both rolls at 356.5° where the roll contact heat transfer begins. The temperature plateaus at 0°, and the increase ends at 3.5° where the roll contact heat transfer completes. The surface temperature of roll 1 at 3.5° is slightly higher than that of roll 2, as indicated in Figure 3-59. Between 3.5° to 356.5°, both rolls release energy to their surroundings by radiation and convection. The rate of heat transfer on both rolls is comparable, as suggested by the similar rate of temperature change in Figure 3-60.

Figure 3-61 shows the effect of roll pitch on the entrained air distribution. Unlike the wall jet flow shown in Figure 3-20, the development of the entrained air after impingement on the slab surface is restricted by the presence of rolls. The restricted airflow circulates in the region between the roll and the spray. The size of the circulations is affected by the roll pitch. A smaller roll pitch provides limited space for the airflow to developed after impingement with the slab. The wall jet flows upward on the roll surface shortly after issuing from the stagnation point. However, the strong entrainment effect drags the climbing flow back into the spray. As the roll pitch increases, the wall jet is able to develop for a longer distance before climbing up the roll surface. In addition, as the circulation is further away from the spray, the entrainment effect is much less, and the up-climbing flow can across the roll surface and reach the other side of the roll. The crossing effect is observed when the ratio of roll diameter and the roll pitch is larger than 0.54. As shown in Figure 3-62, when the ratio is less than 0.54, there is a low wall shear stress area on the roll surface. This is the location where the up-climbing flow is dragged back into the spray. This low wall shear stress area ends at the top of the roll surface when the surrounding airflow is no longer affected by the spray. The area of the low wall shear stress region decreases as the roll pitch increases, and it disappears when the ratio is larger than 0.54, where no flow separation is observed.

Figure 3-62 also shows that the roll pitch can barely affect the atomization process, but it significantly changes the distribution of water droplets on the surface after the impingement. Droplets are confined in a much smaller region when the roll pitch is small. As shown in Figure 3-58, some droplets accumulate at the roll contact location and form a belt along the roll surface. On the other hand, the heat transfer is enhanced at the small roll pitch due to the increase of droplet concentration and the decrease of A_{spray}. Consequently, the heat transfer uniformity decreases.

Therefore, a small roll pitch is recommended for the region where intense cooling is required, such as the beginning of the secondary cooling process. The roll pitch can be gradually increased along the casting direction with the decrease of slab temperature and heat transfer intensity.
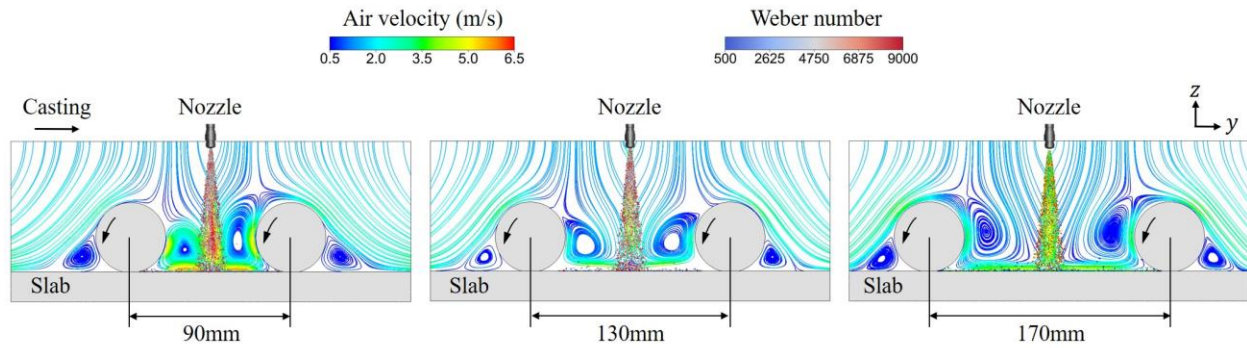
Figure 3-61. The effect of roll pitch on the entrained air distribution.
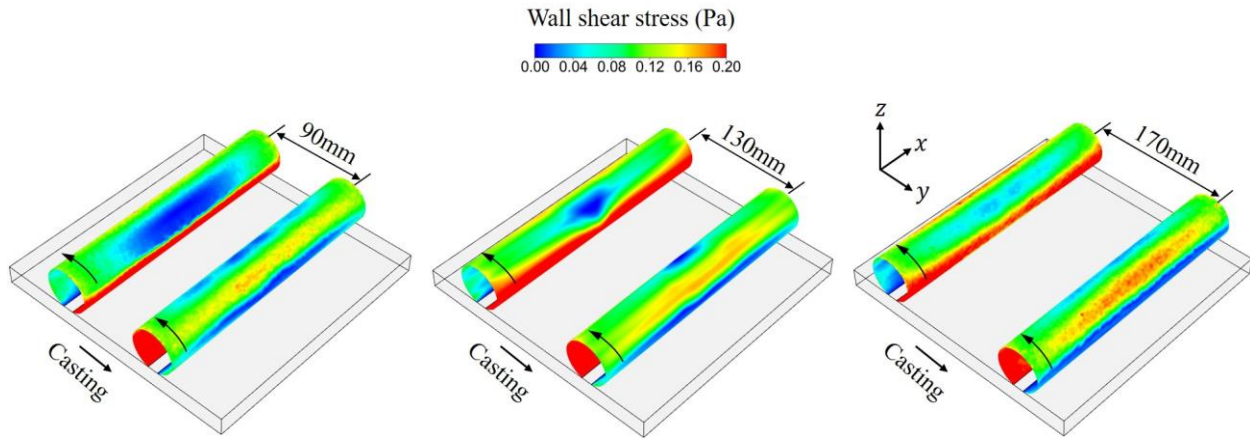
Figure 3-62. Wall shear stress on the roll surfaces.

Table 3-11. Heat transfer intensity and uniformity at different roll pitches.

Roll pitch (mm)	A_{spray} (cm^2)	HTC$_{avg}$ (W/m^2·K)	STD$_{spray}$ (K)
90	85.93	452.65	5.27
130	96.93	423.81	5.01
170	116.63	403.18	4.97

3.3.10 Effect of spray angle

The spray angle and dispersion angle of a spray determine the size of the spray region and the boundaries of the corresponding impingement pattern on the target surface. The definition of the two angles is shown in Figure 2-4. Both angles are considered as the characteristics of a nozzle and are designed by nozzle manufactures. For a flat-fan nozzle used in the secondary cooling process, the spray angle is measured in the slab width direction, whereas the spread angle is measured in the casting direction. In general, only the spray angle of flat-fan nozzles is provided by nozzle manufactures as one of the selection criteria for different applications. The degree of the spray angle varies from 20° to 120°. In comparison, the information regarding the spread angle is not always accessible. In the baseline simulation, the spray angle is set to 90° based on the information provided by the nozzle manufacture. The spread angle is determined from an experiment by an industrial collaborator and is set to 12°.

Figure 3-63 shows the effect of spray angle and spread angle on droplet concentration at the time of impingement. As predicted by Eq. (201) and Eq. (202), the dimension of the spray-affected area on the slab surface increases as the two angles increase. Besides the increase of the spray-affected area, the spray region in the gas phase also widens at large spray angles. Because the water flow rate is constant, the same amount of water droplets is distributed into a much wider region, therefore, lowering the droplet concentration within the spray-affected area. The impact of spray angle is much significant than that of spread angle. As shown in Figure 3-63 (a), the length of the spray affect area in the slab width direction increases by approximately 200% once the spray angle increases from 60° to 120°. As suggested by Eq. (201), the theoretical increase should be precisely 200% when the spray angle is doubled if droplet dispersion is neglected. On the other hand, the increase of spray-affected area is less than 50%, even when the increase of the spread angle is 100%. This also implies that most droplets are distributed in the slab width direction, and the size of the spray region is mainly determined by the spray angle. It is possible for droplets to disperse in the casting direction due to droplet-droplet and droplet-air interactions, but the number of the dispersed droplets in such direction is limited. In addition, it is reasonable to distribute most of the droplets in the slab width direction in secondary cooling applications since the heat transfer in the slab width direction is preferred. In the casting direction, however, any area on the slab is cooled

by multiple water sprays as the slab moves. Hence, the coverage of each spray in the casting direction is not required to be as wide as that in the slab width direction.

(a)

(b)
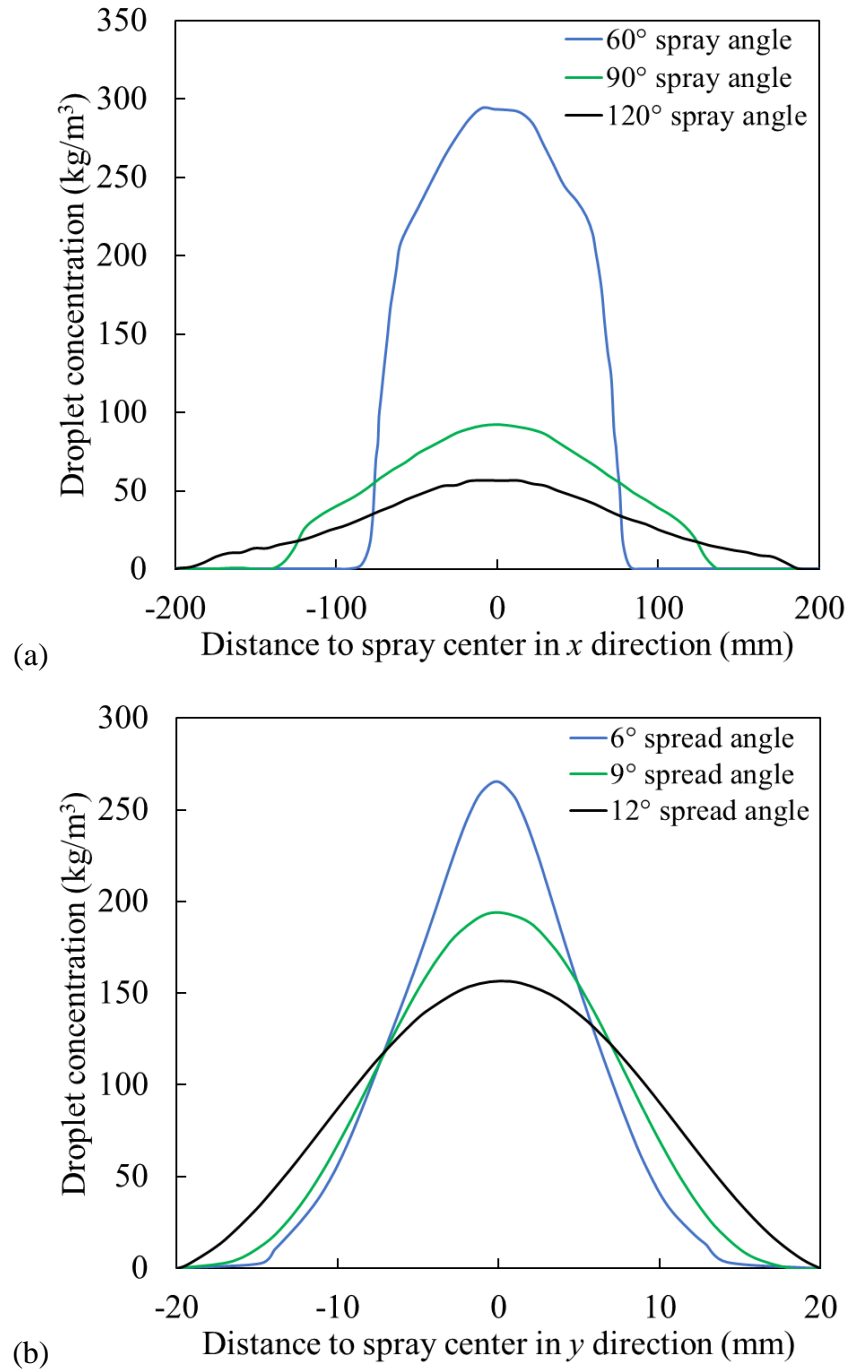
Figure 3-63. Effect of (a) spray angle, and (b) spread angle on droplet concentration on the slab surface.

Figure 3-64 compares the heat transfer within the spray-affected area at different spray angles. As shown in the figure, the coverage of the spray-affected area and the heat transfer rate have a strong dependence on the spray angle. As indicated by Figure 3-63 (a), the overall spray coverage in the slab width direction reduces to less than 200mm at a spray angle of 60°. As the spray angle increases, the spray-affected area expands in the slab width direction and reaches 400mm when the spray angle increases to 120°. A similar effect is seen on A_{spray} in Table 3-12. While the spray-affected area is expanding, the droplet concentration increases within the area by more than 80% compared to that at 60° spray angle. Consequently, with fewer droplets available for heat transfer at a large spray angle, the heat transfer rate significantly reduces. As shown in Table 3-12, HTC_{avg} decreases by 55% when spray angle increases from 60° to 120°. The drastic change of heat transfer due to the change of droplet distribution also demonstrates the dominant effect of droplet centration on the spray cooling process. However, similar to previous sections, the dilute droplet distribution helps alleviate the non-uniformity during the heat transfer process. STD_{spray} decreases by 64% when the spray angle is doubled, which noticeably reduces the potential of crack due to the significant temperature difference inside the slab.
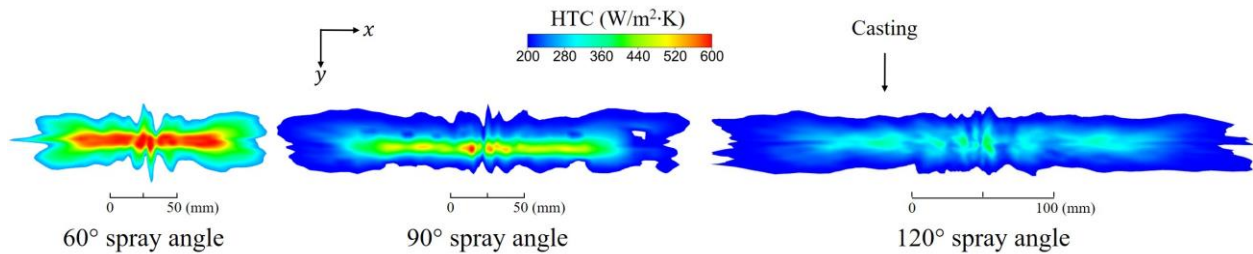
Figure 3-64. Effect of spray angle on HTC pattern.

Table 3-12. Heat transfer intensity and uniformity at different spray angles.

Spray angle (°)	A_{spray} (cm^2)	HTC_{avg} (W/m^2·K)	STD_{spray} (K)
60	59.65	500.34	15.27
90	98.01	386.62	9.22
120	132.79	221.97	5.55

3.3.11 Effect of spray water temperature

The effect of spray water temperature on the heat transfer intensity is indecisive in the published works. Bhatt et al. have concluded from an experiment that with the enhancement of water temperature, the heat removal rate increases due to the increase of the latent heat extraction time and droplet-wall contact area [302]. However, Zhang et al. conducted a heat transfer simulation for the secondary cooling process and found that the slab surface temperature decreases by 40°C when the spray water temperature decreases from 45°C to 25°C [303]. A study by Cai and Wu shows that the heat transfer rate decreases by 5% with the spray water temperature increases by 10°C [304]. A similar trend was also observed by Pohanka et al., who experimentally measured the heat transfer coefficient as a function of spray water temperature and found the average heat transfer coefficient decreases by 13.3% when the spray water temperature increases from 20°C to 50°C [305]. This trend was also acknowledged and incorporated into the HTC correlation developed by Nozaki et al. [165] and its variations by other researchers [10, 11, 164].

In the spray evaporative cooling process, the sprayed droplet removes the energy from the slab through two sequential processes, which are sensible heat removal and latent heat removal. Because water is injected as a liquid, the initial temperature of a droplet must be lower than 100°C under the atmospheric pressure. Thus, the evaporative cooling process always starts with the sensible heat removal until the droplet temperature reaches the boiling point, after which the latent heat removal begins. The amount of energy transferred to the droplet due to sensible heat removal can be calculated by:

$$Q_{sen} = m_d c_{p,d}(T_{sat} - T_d) \tag{222}$$

Where Q_{sen} is the amount of energy due to sensible heat removal, m_d is the droplet mass, $c_{p,d}$ is the droplet specific heat, T_{sat} is the saturation temperature, and T_d is the droplet temperature.

While the amount of energy transferred to the droplet due to latent heat removal is:

$$Q_{lat} = m_d h_{fg} \tag{223}$$

Where Q_{lat} is the amount of energy due to sensible heat removal, and h_{fg} is the latent heat of vaporization.

Under 1 atmosphere pressure, T_{sat} is 373K and T_d is smaller than 373K. Thus, Q_{lat} differs from Q_{sen} by at least one order of magnitude. This is also the reason why evaporative cooling is preferred in order to attain the maximum heat transfer rate. However, due to the Leidenfrost effect, the heat transfer process within the spray-affected area is dominated by film boiling. Therefore, obtaining the techniques to break the barrier of the vapor layer that prevents droplets from direct contacting with the hot surface has been the major challenge for the application of evaporative cooling.

Bhatt et al. have identified two methods to reach the maximum latent heat removal rate for evaporative cooling applications: high renewal rate of droplets and low residence time [305]. Both methods are designed to break the vapor film and to prevent it from accumulating on the surface. The lower limit for the high renewal rate of droplets is set to 2kg/m²·s in the literature, but the range of low residence time is not defined. Once both requirements are satisfied, the heat transfer will be dominated by latent heat removal. Hence, the heat transfer rate increases with the increase of spray water temperature since droplets can evaporate much faster at higher spray temperatures.

The lower limit of the renewal rate of droplets within the cooling area can be converted into the spray flow rate by:

$$Q_{water} = \frac{2kg}{m^2 s} \times \frac{98.01 m^2}{10^4} \times \frac{1m^3}{998.2 kg} \times \frac{1000L}{1m^3} \times \frac{60s}{min} = 1.18 L/min \qquad (224)$$

Most of the sprays used in the secondary cooling process satisfy the minimum spray flow rate condition shown in Eq. (224). However, satisfying this condition alone will not guarantee the maximum latent heat removal. The high renewal rate allows high momentum droplets to reach the slab surface, but the latent heat removal rate can still below if the residence time is short. The theoretical maximum time for droplet-wall impingement heat transfer is equal to the amount of time for the slab to pass the spray-affected area in the casting direction:

$$t_{spray} = 27.33 \times 10^{-3}m \times \frac{1min}{1m} \times \frac{60s}{1min} = 1.64s \tag{225}$$

Where the theoretical dimension of the spray affect area in the casting direction is obtained from Eq. (202).

As shown in Figure 2-9, the droplet-wall impingement heat transfer occurs between two sequential reflections, and the contact time for the heat conduction can be estimated by Eq. (122):

$$t_{cond} = \frac{\pi}{4}\sqrt{\frac{\rho_d d_d^3}{\sigma_{a-d}}} = \frac{\pi}{4}\sqrt{\frac{998.2 \times 0.0015^3}{0.0719404}} = 5.37ms \tag{226}$$

Although $t_{cond} \ll t_{spray}$, droplets are highly dynamic during the impingement process and will leave the spray-affected area within a relatively short period of time due to reflection and the high renewal rate of droplets. Figure 3-65 compares the distribution and magnitude of HTC for different spray water temperatures. The projected spray area is outlined as a reference, and the dimensions are calculated based on Eq. (201) and Eq. (202). Minor variations are observed in terms of the distribution and magnitude of HTC at different spray water temperatures. A similar trend is also observed in Table 3-13. The short total contact time between the droplet and the surface indicates that sensible heat removal also plays an essential part in the spray cooling process. As the spray water temperature increases, the amount of sensible heat removal reduces, and the latent heat removal does not counterbalance that decrease. Therefore, the heat transfer rate decreases. If the latent heat removal time further increases, such as the condition in the experiment conducted by Bhatt et al., the heat transfer rate will be significantly improved at higher spray water temperature.
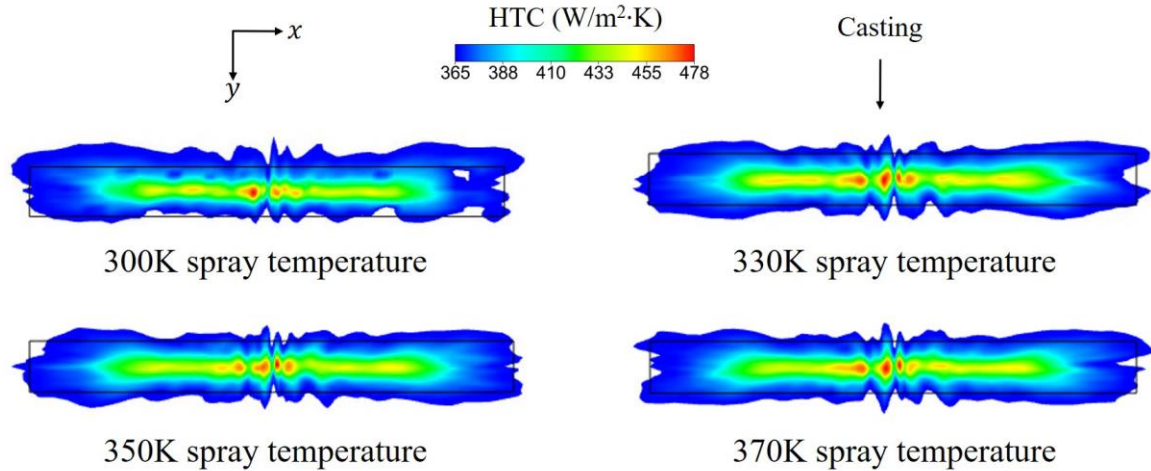
Figure 3-65. Effect of spray temperature on HTC pattern.

Table 3-13. Heat transfer intensity and uniformity at different spray water temperatures.

Spray temperature (K)	A_{spray} (cm^2)	HTC_{avg} (W/m^2·K)	STD_{spray} (K)
300	98.01	386.62	9.22
330	97.30	382.43	8.65
350	96.54	380.64	8.51
370	96.86	377.65	8.38

3.3.12 Effect of slab surface temperature

The slab surface temperature is constantly changing throughout the secondary cooling process. Figure 3-66 shows the typical boiling curve during and after the continuous casting process. The desired surface temperature in the secondary cooling region is between 900°C and 1200°C [19]. As indicated in the figure, droplet boiling during most of the secondary cooling process is in the film boiling regime. The surface temperature is higher than the Leidenfrost temperature until near the end of the process. In the film boiling regime, the heat flux through the slab surface reaches the minimum and varies very little during the secondary cooling process. In Figure 3-66, the Leifenfrost temperature is identified as 1000°C. When the slab surface temperature decreases to below the Leifenfrost temperature, the heat flux significantly increases to the maximum, referred to as the Critical Heat Flux (CHF), as the filing boiling regime shifts to the transition boiling regime. The exact value of the Leifenfrost temperature depends on the local spray conditions. As

shown in Table 1-11 and Figure 2-11, the Leifenfrost temperature varies in a wide temperature range, and it is lower than 1200K in most of the published research. Hence, film boiling is the dominant heat transfer mechanism during the secondary cooling process, and it is the only heat transfer mechanism for specific steel grades and spray cooling practices.
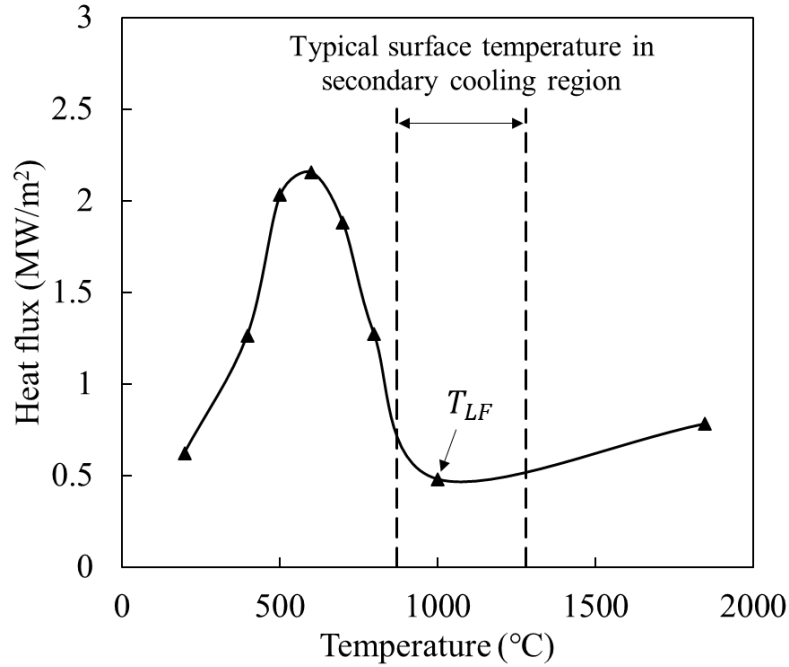
Figure 3-66. Typical boiling curve and the surface temperature range in continuous casting of steel [19, 243, 303].

The current study uses Eq. (127) to evaluate the local Leifenfrost temperature and use the predicted temperature as the criterion to determine the expression for the heat transfer effectiveness. Figure 3-67 shows the Local Leidenfrost temperature on the slab surface under the baseline condition. The projected spray area in the middle of the slab is outlined to indicate the spray impingement location. As shown in Eq. (127), the Leifenfrost temperature is a function of spray flux, droplet velocity, and droplet Sauter mean diameter, all of which are determined by the spray condition. Thus, even though the slab surface temperature varies, the Leifenfrost temperature depends on the local spray condition. This is why the distribution of the Leifenfrost temperature is similar to that of the droplet concentration shown in Figure 3-27. The highest Leifenfrost temperature occurs at the locations where the droplet concentration is also the highest. The calculated Leifenfrost temperature is much lower than 1000°C. This implies that for the baseline spray cooling condition,

275

the surface heat transfer is only determined by filing boiling throughout the entire secondary cooling region. In fact, as shown in Figure 3-68, the maximum Leidenfrost temperature at the highest possible spray flow rate is just above 1300K, which is still lower than the slab surface temperature in most of the secondary cooling operations.
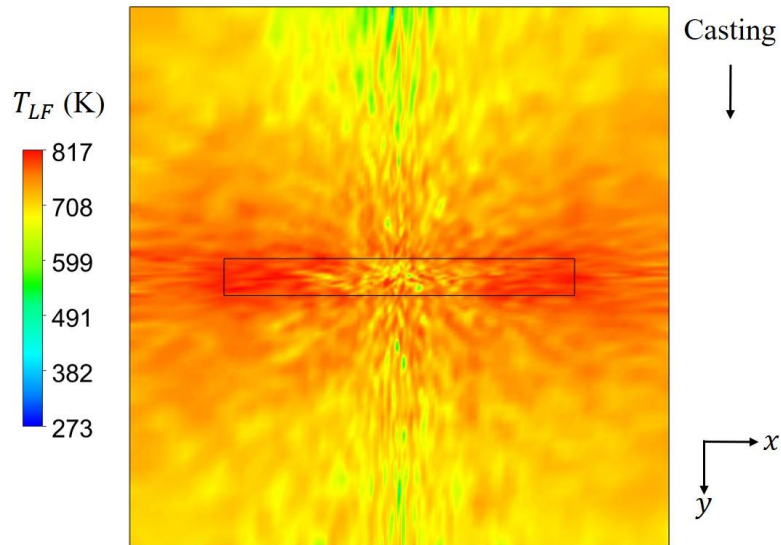
Figure 3-67. Local Leidenfrost temperature on the slab surface under the baseline condition.
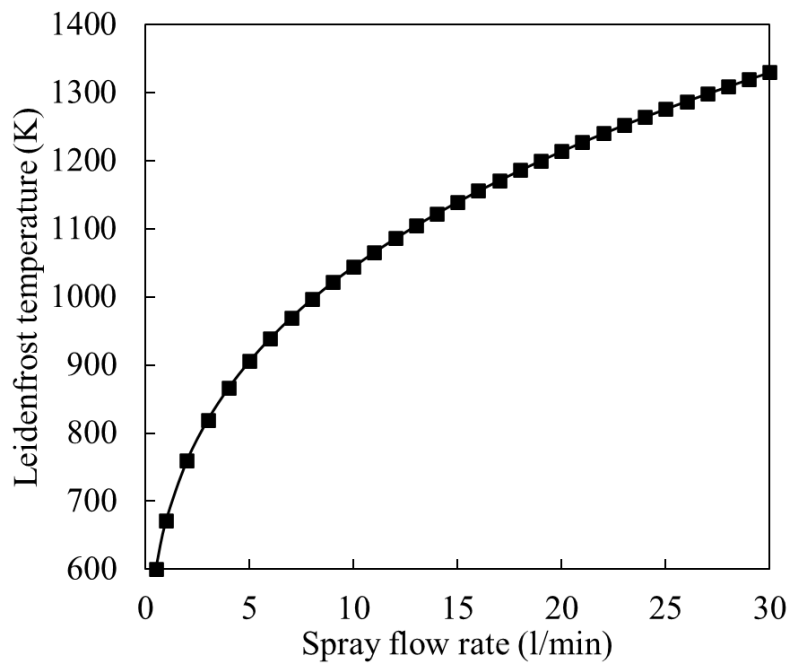
Figure 3-68. Local Leidenfrost temperature as a function of the spray flow rate [145].

Figure 3-69 shows the heat transfer effectiveness on the slab surface when $T_{sur} > T_{LF}$. The highest heat transfer effectiveness is seen within the spray area, but the magnitude is lower than 0.2, which shows the dominant effect of the vapor layer in film boiling heat transfer. High heat transfer effectiveness occurs when the droplet Weber number is large such that droplets have sufficient momentum to penetrate the existing vapor layer and absorb heat directly from the slab. Similar to the Leidenfrost temperature, the heat transfer effectiveness is also independent of the surface temperature in the film boiling regime. It is determined when the nozzle configuration and spray condition are decided.
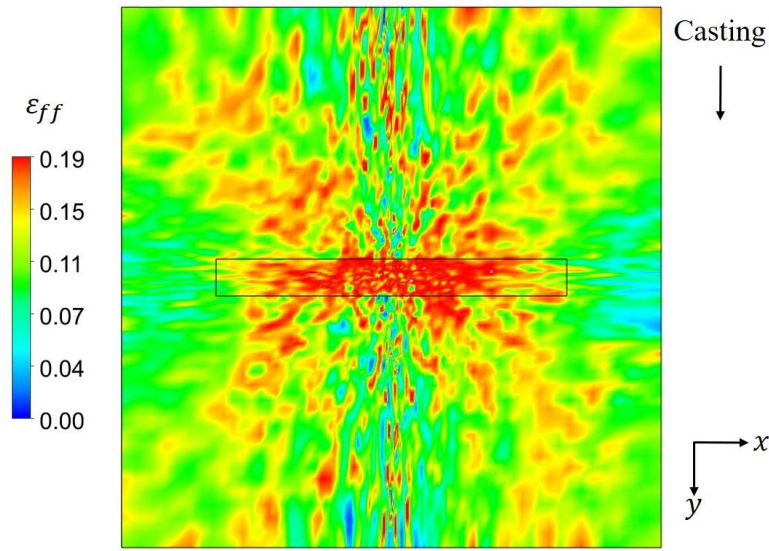
Figure 3-69. Heat transfer effectiveness on the slab surface when $T_{sur} > T_{LF}$.

Figure 3-70 shows the HTC distribution within the spray-affected area at different slab surface temperatures. The temperature on the upstream surface of the computational domain is scaled to different values based on the distribution shown in Figure 2-19. The spray condition is fixed for different surface temperatures and is the same as the baseline condition. As demonstrated in Figure 3-67, Figure 3-68, and Figure 3-69, both the local Leidenfrost temperature and the heat transfer effectiveness are independent of the surface temperature under the current spray condition. Thus, the spray cooling effect varies only a little between different surface temperatures in terms of the shape and size of the spray-affected area and the distribution and magnitude of HTC. As a result, the heat transfer intensity and uniformity within the spray-affected area also show the little dependency of the surface temperature, as shown in Table 3-14.
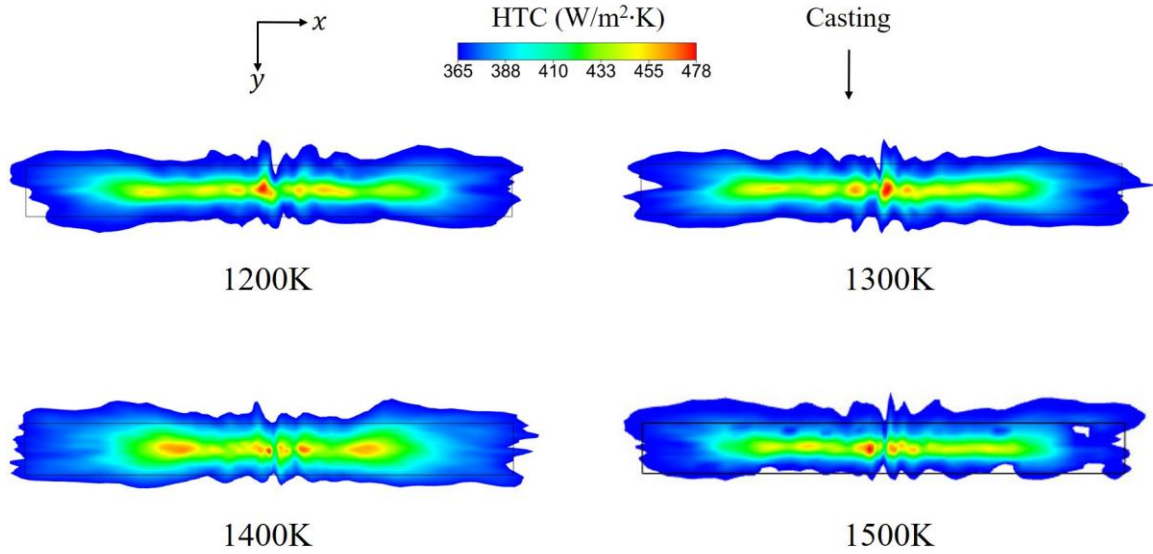
Figure 3-70. Effect of slab surface temperature on HTC pattern.

Table 3-14. Heat transfer intensity and uniformity at different slab surface temperatures.

Surface temperature (K)	A_{spray} (cm^2)	HTC$_{avg}$ (W/m^2·K)	STD$_{spray}$ (K)
1200	99.81	390.35	9.87
1300	96.93	388.39	9.29
1400	102.83	388.33	9.95
1500	98.01	386.62	9.22

Although the calculated Leidenfrost temperature is significantly lower than the slab surface temperature under the current spray condition, it is still worth mentioning the heat transfer behavior near and below the Leidenfrost temperature. As shown in Figure 3-67, the highest local Leidenfrost temperature is 817K under the current spray condition. To demonstrate the change of boiling regimes, the minimum temperature on the upstream surface is adjusted to 825K, and the Leidenfrost temperature is fixed to 817K. Figure 3-71 shows the HTC and the surface temperature from the simulation. At the initial cooling stage, the slab surface temperature is higher than the Leidenfrost temperature. The heat transfer effectiveness is calculated based on Eq. (125). The heat transfer rate at this stage is low due to the effect of the vapor blanket. As the slab surface temperature approaches the Leidenfrost temperature, the HTC noticeably increases. Once the slab surface temperature decreases to below the Leidenfrost temperature, a shape increase of the HTC

is observed in Figure 3-71, as the film boiling regime shifts to the transition regime. Eq. (126) is used to evaluate the heat transfer effectiveness, which also significantly increases, as shown in Figure 2-10. The increase of the HTC is more than four times after the boiling regime changes. As the slab surface temperature continues to decrease, the HTC slightly increases. Since the heat transfer is no longer dominated by the vapor layer, some dependency on slab surface temperature is expected.
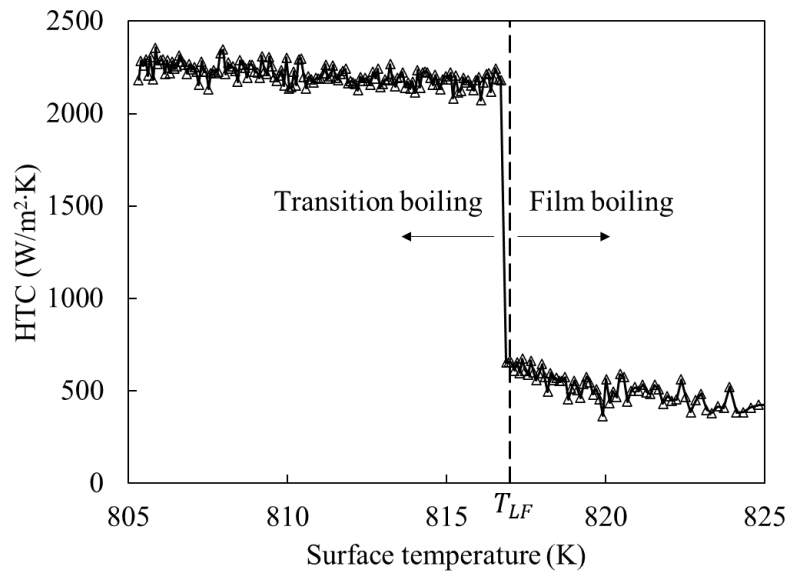
Figure 3-71. Increase of HTC as the surface temperature across the Leidenfrost temperature.

3.3.13 Effect of spray cooling on the narrow face

In the continuous casting of steel, the narrow faces are conditionally spray cooled. If the spray cooling on the broad faces is unable to provide a sufficient heat transfer rate to the solidification process, then the narrow faces should also be spray cooled. For example, if the size ratio of the broad face and narrow face is small, such as billet, both broad faces and narrow faces require spray cooling. If the size ratio is sufficiently large, but the superheat is high, or the casting speed is fast, then the narrow faces at the beginning of the secondary cooling region are spray cooled. Figure 3-72 compares the entrained air velocity distribution with and without narrow face spray cooling. In the case without narrow face spray cooling, the entrained airflow from the top broad face meets the airflow from the bottom broad face somewhere near the narrow face. The two flows merge as one and separate as two wall jets after impinging on the narrow face. Then, the two wall jets

circulate back to the merging point, and two circulations form near the narrow face. The pair of air circulations disappears when a water spray is introduced to cool the narrow face. As shown in Figure 3-72, the presence of the narrow face spray completely changes the distribution of the entrained airflow around the narrow face. The entrained air flows by the narrow face spray and by the broad face sprays form two fast-moving streams, which then impinge on the edges of the narrow face. The impinged stream splits into two wall jets at the edge, and two small circulations form at the boundary of the sprays.
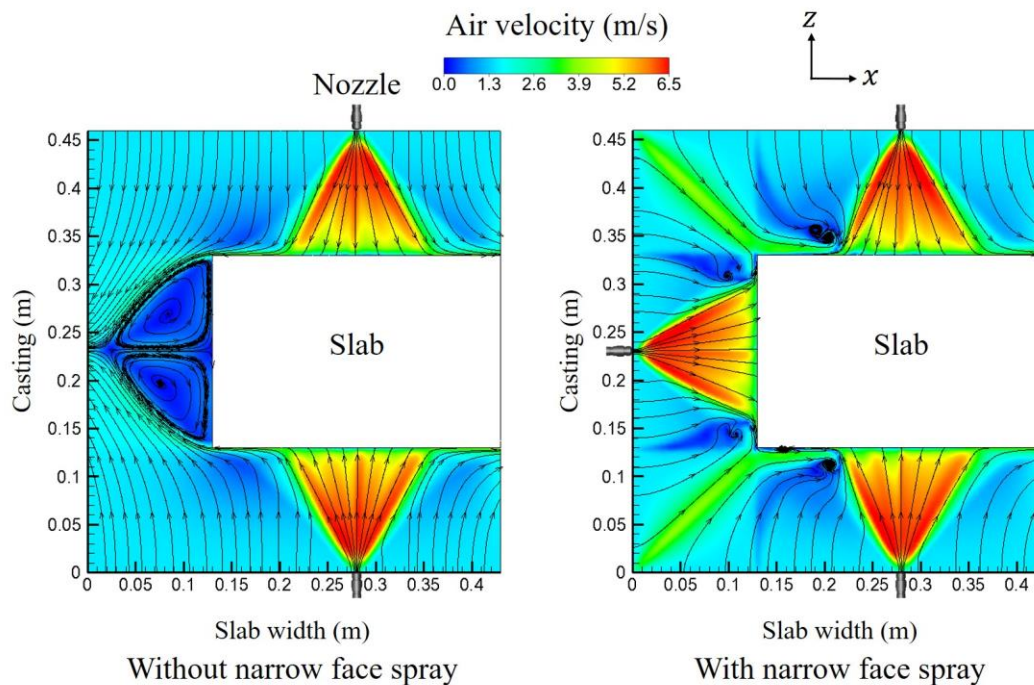
Figure 3-72. Entrained air velocity distribution with and without narrow face spray cooling.

Figure 3-73 shows the droplet distribution and the slab surface temperature in the cases with and without narrow face spray cooling. The behaviors of the droplet are discussed in detail in the section on spray direction. Droplets issued from the top broad surface have the advantage of longer residence time on the slab surface, whereas those issued from the bottom broad face have only one droplet-wall impingement before falling off from the surface, thereby leading to 15% less heat transfer. Droplets issued from the narrow spray, which is also referred to as the lateral spray in the previous section, are likely to attach to the surface for a longer time compared to that in the bottom spray. Thus, moderate heat transfer is seen from the lateral spray. Similarly, in the case without

the narrow face spray, the two sprays on the top and bottom broad faces behave as the top and bottom sprays, and there is no interaction between the two sprays. The narrow face is cooled by both radiation and air convection. The lowest surface temperature occurs at the boundaries between the narrow face and the broad faces. This region is subject to two-dimensional heat transfer, therefore, has the highest heat transfer rate. Two-dimensional heat transfer indicates that heat is extracted from both lateral and horizontal directions at the corner. Due to this effect, the temperature at corners is lower than that on the surface, referred to as the over-cooling effect. With the narrow face spray, aside from the change of the entrained air distribution, droplets from the narrow face spray can also interact with the broad face sprays. The intensified heat transfer on the narrow face furthers decreases the slab surface temperature, and the extent of the over-cooling effect at the edge also increases.
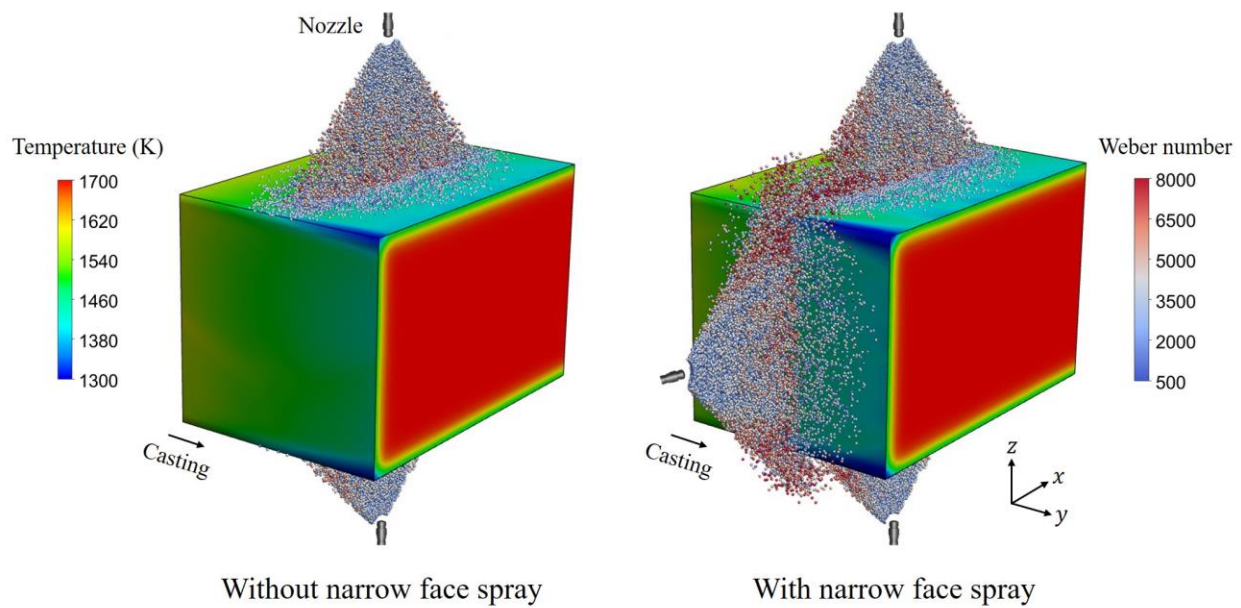
Figure 3-73. Comparison of droplet distribution with and without narrow face spray cooling.

The over-cooling effect on the edges in the case with the narrow face spray can be better visualized in Figure 3-74. The low-temperature region near the edge further extends to the upstream due to the additional heat removal on the narrow face. Figure 3-75 compares the temperature at a simple line locates on one of the edges to quantify the over-cooling effect on the edges. The effect of narrow face spray cooling becomes more important as the temperature difference widens between

the two scenarios. The highest temperature difference occurs downstream and is more than 20K. The difference between the solid and dashed lines is mainly due to the narrow face spray cooling and some contribution from the intensified air convection. Thus, the shaded area between the two lines represents the net effect of spray cooling on the narrow face.
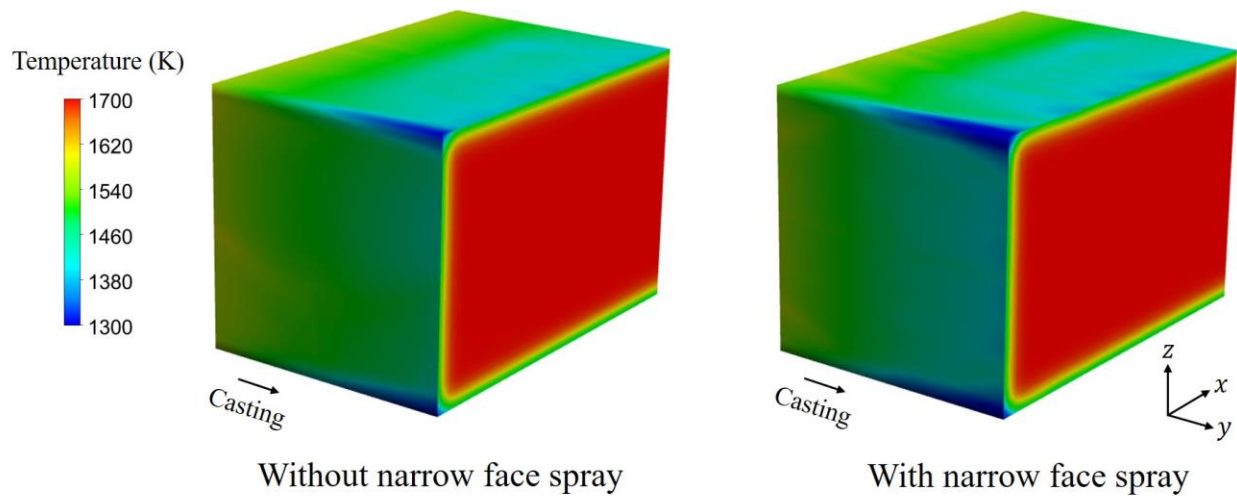
Figure 3-74. Comparison of slab surface temperature distribution with and without narrow face spray cooling.
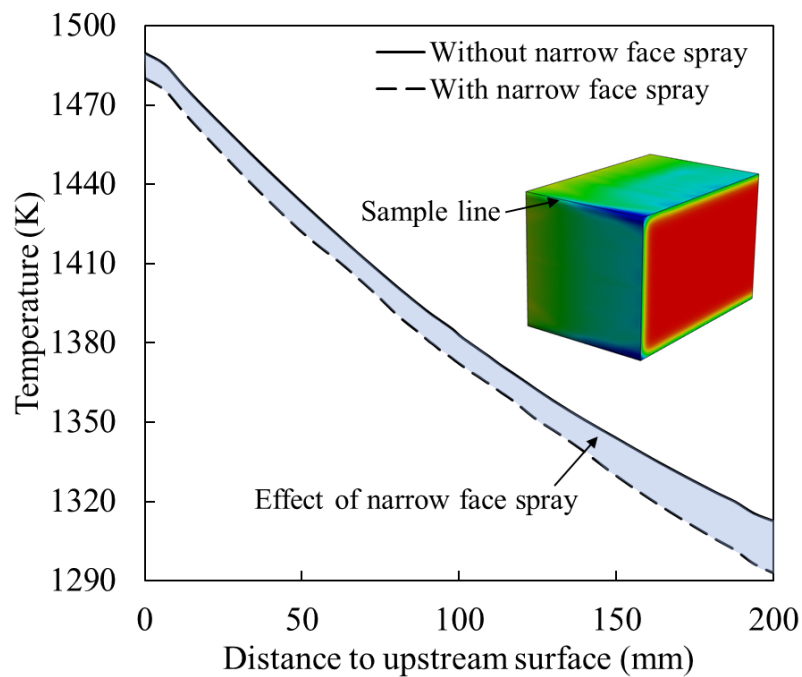
Figure 3-75. Comparison of slab surface temperature along the sample line.

Figure 3-76 shows the temperature difference on the narrow face between the two scenarios. The non-negative values indicate the higher surface temperature in the case without narrow face spray. Higher temperature difference occurs downstream near the two edges due to the two-dimensional heat transfer effect. Interestingly, the temperature difference near the top broad face is even higher than that near the bottom broad face. This is because the spray direction on the top broad face aligns with the direction of gravity and the droplet residence time increases on the top broad face. Thus, more energy is extracted from the top broad face. At the upstream, the temperature difference is moderate, and it is caused by different distributions of the entrained airflow. In summary, the additional narrow face spray cooling can help decrease the surface temperature by about 10K, but the intensified over-cooling effect at the edges of the slab must be carefully evaluated. Uncontrolled edge over-cooling can lead to considerable residual thermal stress, which can eventually contribute to surface defects such ad corner crack.
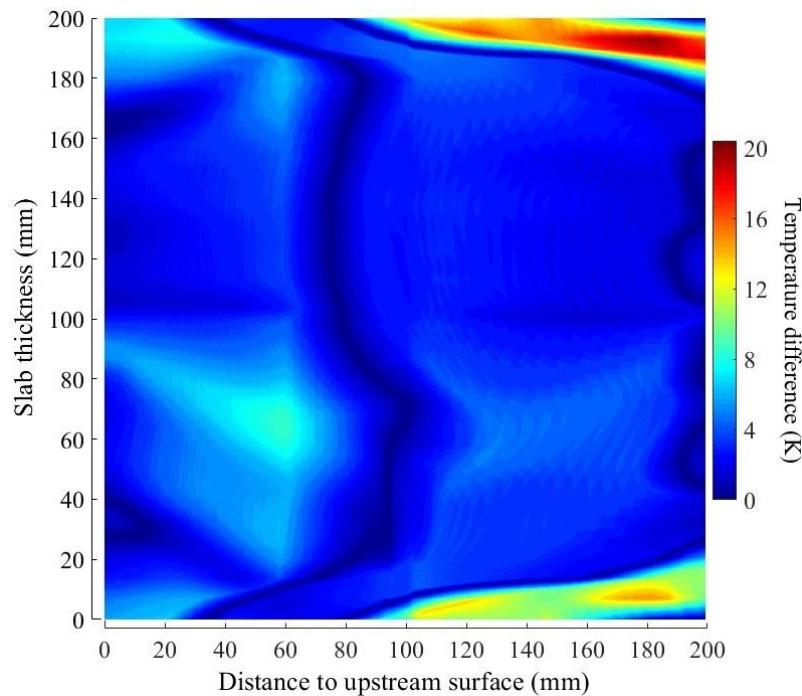
Figure 3-76. The temperature difference on the narrow face between the two cooling operations.

3.4   HTC correlation

Previous parametric studies are helpful for fundamental research and the development of casting control strategies. However, each simulation requires hundreds of computing hours to reach

convergence using 40 to 80 CPUs. To meet the requirement of real-time online casting control, the high-fidelity three-dimensional simulations are converted into a simplified mathematic expression which correlates with nine of the most important operating parameters.

3.4.1   Numerical approach

Figure 3-77 illustrates the development process of HTC correlations using the numerical approach. This approach consists of three stages, which are the numerical simulation stage, the data analysis stage, and the Graphic User Interface (GUI) development stage. Before the numerical simulation stage, a pool of operating conditions is generated based on the suggestions from several industrial collaborators. The operating conditions are further categorized into different groups based on the control parameter. For instance, if the determining factor in one operation condition is the spray flow rate, this condition is labeled as "spray flow rate condition x". The advantage of categorizing the operating conditions is to better analyze the effect of each determining factor on the overall heat transfer rate. Once all the operating conditions are determined, the numerical simulation stage starts. A high-fidelity baseline CFD model is required at the beginning of this stage. This includes model verification and results validation. The high-fidelity model should contain the essential physics during the secondary cooling process, such as atomization, droplet breakup, droplet collision, air entrainment, droplet-steel impingement heat transfer, and steel slab cooling. The second step is to build an HTC database through parametric study with the help of high-performance computing. Each identified operating condition is modeled in this step. Next, in the data analysis stage, the distribution of HTC within the spray-affected area on the slab surface is decomposed into two normalized universal distribution functions. In contrast, the magnitude of HTC is lumped into a characteristic value, which later is correlated with the most representative operating parameters through regression analysis or curve fitting. Finally, a user-friendly graphic interface based on Unity® 3D platform provides the input windows for users to type in the desired operating condition and reconstructs the local HTC values based on the pre-defined correlation and the distribution functions. The predicted HTC values are stored in the versatile comma-separated values (csv) format, which can be directly applied to solidification calculations. The proposed numerical methodology should benefit the steel industry by expediting the development process of HTC correlations and can further improve the accuracy of the existing casting control systems.
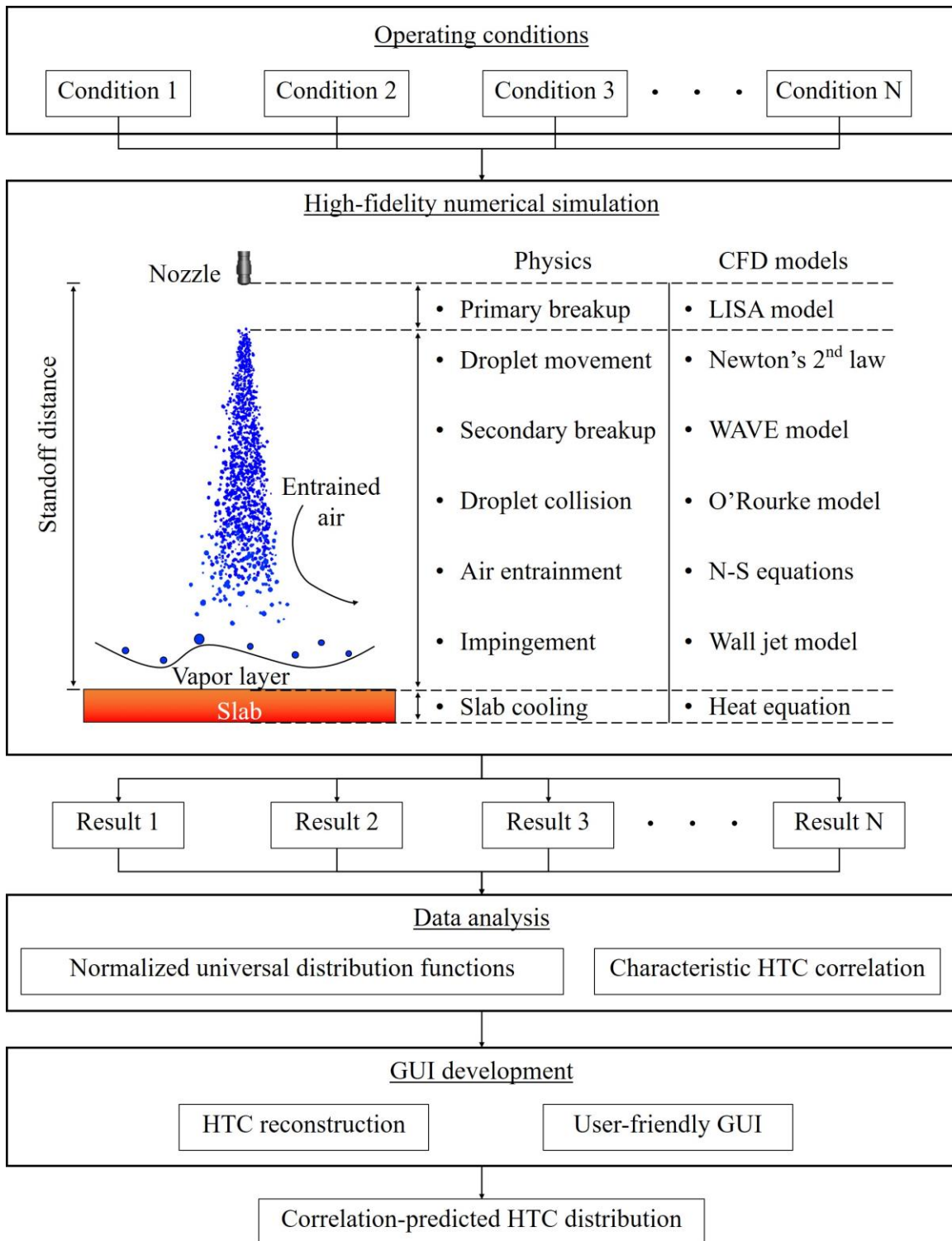
Figure 3-77. Numerical approach for the HTC correlation and user interface development.

3.4.2 Operating conditions

Nine casting operating parameters are identified as contributing factors to determining HTC values, and they are spray water flow rate, nozzle-to-nozzle distance, standoff distance, spray water temperature, casting speed, the distance between adjacent spray rows, spray angle, spray direction, and air spray pressure. From a mathematic point of view, each contributing factor should be tested for at least several values in order to be representative in the final HTC correlations. Table 3-15 summarizes all the contributing factors and their corresponding ranges applied in the current study. It is noteworthy that the unit of each factor is converted in accordance with the plant operation. Furthermore, slab surface temperature is excluded from the parametric study for two reasons: (1) slab surface temperature is above the Leidenfrost temperature throughout most of the secondary cooling region. Under such conditions, heat extraction during spray cooling is dominated by the vapor film boiling mechanism. The change of HTC with slab surface temperature is negligible, as shown in the slab surface temperature section. (2) slab surface temperature is one of the to-be-determined parameters during solidification calculation, which depends on the predicted HTC as the thermal boundary condition.

Table 3-15. Summary of contributing factors applied in the HTC correlations.

Contributing factor	Symbol	Range
Spray water flow rate (L/min)	Q_w	3.5-15
Nozzle-to-nozzle distance (mm)	D_{noz}	65-650
Standoff distance (mm)	H_{sp}	65-260
Spray water temperature (K)	T_{sp}	300-372
Casting speed (m/min)	V_{cs}	0.5-5
Distance between adjacent spray rows (mm)	D_{row}	10-650
Spray angle (degree)	θ_{sp}	45-120
Spray direction (-)	η_{sp}	0.85-1
Air spray pressure (psi)	P_a	0-40

Note:

- D_{nozzle} and D_{row} are set to zero for the single spray to exclude the effects from other sprays.

- Three distinct values are assigned to the spray direction, i.e., 0.85, 0.925, and 1, to represent the bottom spray, the lateral spray, and the top spray, respectively. The bottom spray is assumed to be 15% less effective than the top spray, as measured by Bolle and Moureau [137]. The lateral spray is assumed to be 92.5% as effective as the top spray.

3.4.3 HTC distributions

The temperature and HTC distributions on the slab surface by a single flat-fan nozzle under a typical casting condition (Q_w =7L/min, $D_{noz} = D_{row}$ =650mm, H_{sp} =130mm, T_{sp} =300K, V_{cs}=1m/min, θ_{sp}=90°, η=1, P_a=0) are shown in Figure 3-24 (b) and (c). However, as shown in Figure 3-24 (c), within the butterfly-shaped profile, the HTC peaks near the stagnation point where droplet momentum is the highest and decreases in both the casting and slab width directions. In other words, even the nine operating parameters are determined, the exact value of HTC also depends on the location on the slab surface. Thus, the local HTC is a function of the nine operating parameters and the two spatial coordinates. Mathematically, it is possible to correlate the local HTC with eleven parameters, but it is more convenient to compute the two spatial coordinates together with the local HTC value instead of requesting the spatial coordinates from users. The calculation of the two spatial coordinates is discussed in the HTC reconstruction section in detail.

In addition, as shown in the previous parametric study section, different operating conditions produce similar HTC profiles on the slab surface. Despite the differences in the operating condition, the characteristics of the flat-fan nozzles used in these simulations are quite similar. Thus, the corresponding spray impingement pattern and heat transfer pattern are also similar. Since all the CFD-predicted HTC profiles have similar distributions in space, it is much more convenient to use two normalized universal distribution functions to represent the distribution of HTC in both the casting (y direction) and slab width direction (x direction) for all the operating conditions. Figure 3-78 demonstrates the normalized HTC distributions in the casting and slab width directions. It is worth mentioning that the two normalized universal distribution functions discussed in the current study can be applied to other flat-fan type of nozzles, as the effect of the spray angle is considered in the development process. However, the current method can also be applied to other types of nozzles, but with some modifications to the expressions of the distribution functions.
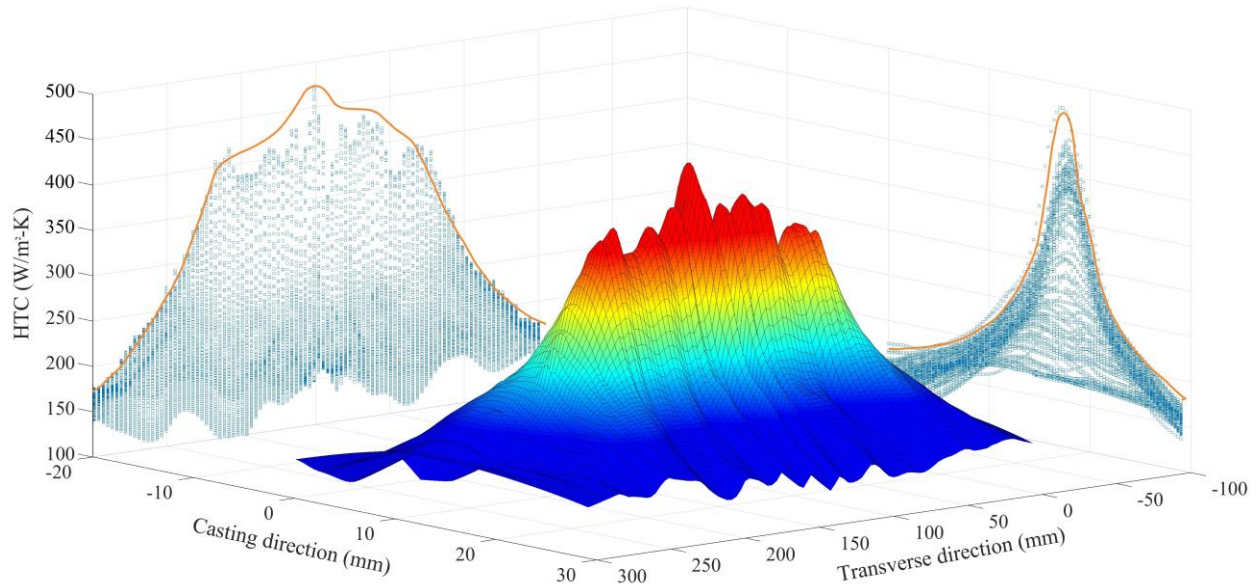
Figure 3-78.Normalized HTC distributions in the casting and slab width directions.

Figure 3-79 illustrates the process of "disintegration and reconstruction" of the two-dimensional HTC distribution. The overall process consists of three stages. Stage 1 and stage 2 are completed during the development process, and stage 3 is programmed in the GUI and takes place whenever a prediction by the correlation is required. In stage 1 and stage 2, any two-dimensional CFD predicted HTC distribution could be disintegrated into two parts, which are the normalized universal distribution functions and a lumped representative HTC value. The two distribution functions are found by projecting all the HTC patterns to both the casting and slab width directions and curve fitting the projected data points, as shown in Figure 3-78. The lumped HTC values from all the operating conditions are correlated with the nine operating parameters through regression analysis. Thus, the two-dimensional HTC distribution is disintegrated into three mathematical expressions. Last, in the reconstruction stage, the GUI assembles the three mathematic and exports the predicted HTC values based on the inputs from users.
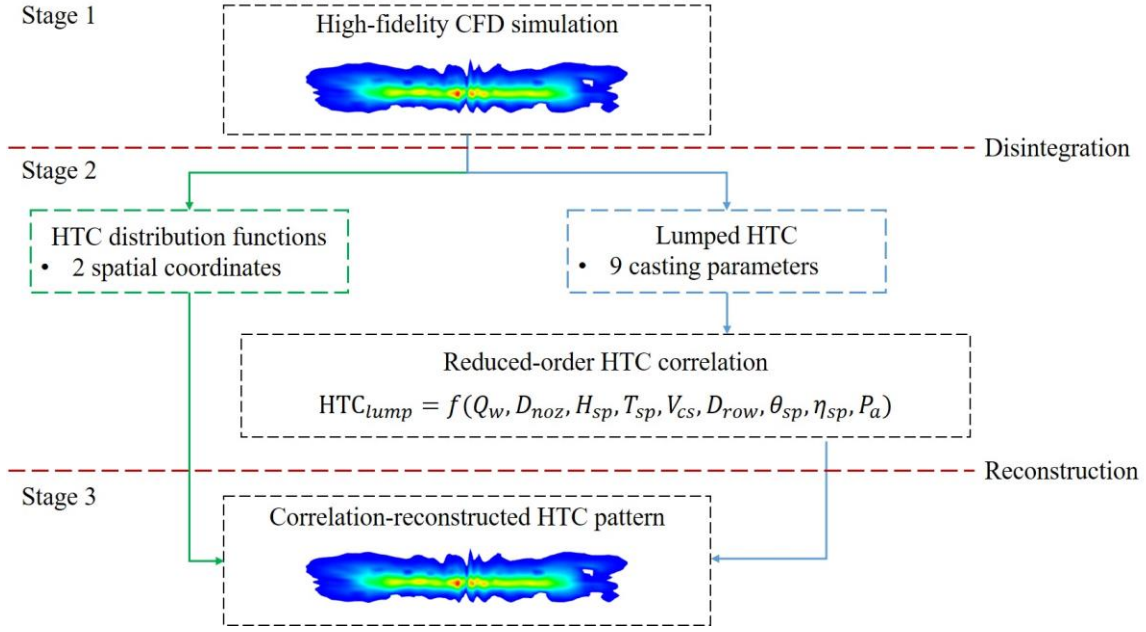
Figure 3-79. Disintegration and reconstruction of the two-dimensional HTC distribution.

In stage 2, the two spatial coordinates, together with the corresponding HTC value, at any given point in a CFD-predicted HTC profile are normalized to values between zero to unity based on the following definitions:

$$X_{norm,i} = \frac{X_i - \min(X_1, X_2, \cdots, X_n)}{\max(X_1, X_2, \cdots, X_n) - \min(X_1, X_2, \cdots, X_n)} \tag{227}$$

$$Y_{norm,j} = \frac{Y_j - \min(Y_1, Y_2, \cdots, Y_m)}{\max(Y_1, Y_2, \cdots, Y_m) - \min(Y_1, Y_2, \cdots, Y_m)} \tag{228}$$

$$HTC_{norm-x,i} = \frac{HTC_i - \min(HTC_1, HTC_2, \cdots, HTC_n)}{\max(HTC_1, HTC_2, \cdots, HTC_n) - \min(HTC_1, HTC_2, \cdots, HTC_n)} \tag{229}$$

$$HTC_{norm-y,j} = \frac{HTC_j - \min(HTC_1, HTC_2, \cdots, HTC_m)}{\max(HTC_1, HTC_2, \cdots, HTC_m) - \min(HTC_1, HTC_2, \cdots, HTC_m)} \tag{230}$$

The two normalized universal distribution functions shown in Figure 3-78 can be treated as the projections of the two-dimensional HTC pattern. The expression of the two normalized universal distribution functions can be obtained through curve fitting:

$$f(X_{norm,i}) = 0.2645 \sin(0.6426X_{norm,i} - 0.1679)$$
$$+ 0.9131 \sin(3.411X_{norm,i} - 0.03306)$$
$$+ 0.07107 \sin(25.91X_{norm,i} + 1.393)$$
$$+ 0.009289 \sin(34.21X_{norm,i} - 2.974)$$
$$+ 0.0117 \sin(68.73X_{norm,i} + 1.896)$$
$$+ 0.01235 \sin(58.79X_{norm,i} + 0.9767)$$

(231)

$$f(Y_{norm,i}) = 0.5564\exp\left[-\left(\frac{Y_{norm,i} - 0.6499}{0.09418}\right)^2\right]$$
$$- 0.02968\exp\left[-\left(\frac{Y_{norm,i} - 0.7191}{0.01933}\right)^2\right]$$
$$+ 0.08142\exp\left[-\left(\frac{Y_{norm,i} - 0.2788}{0.1721}\right)^2\right]$$
$$+ 0.4706\exp\left[-\left(\frac{Y_{norm,i} - 0.6144}{0.2372}\right)^2\right]$$

(232)

Figure 3-80 shows the normalized universal distribution functions in the slab width and casting directions. The two curves fitted functions server as the boundary of the CFD-predicted data points.
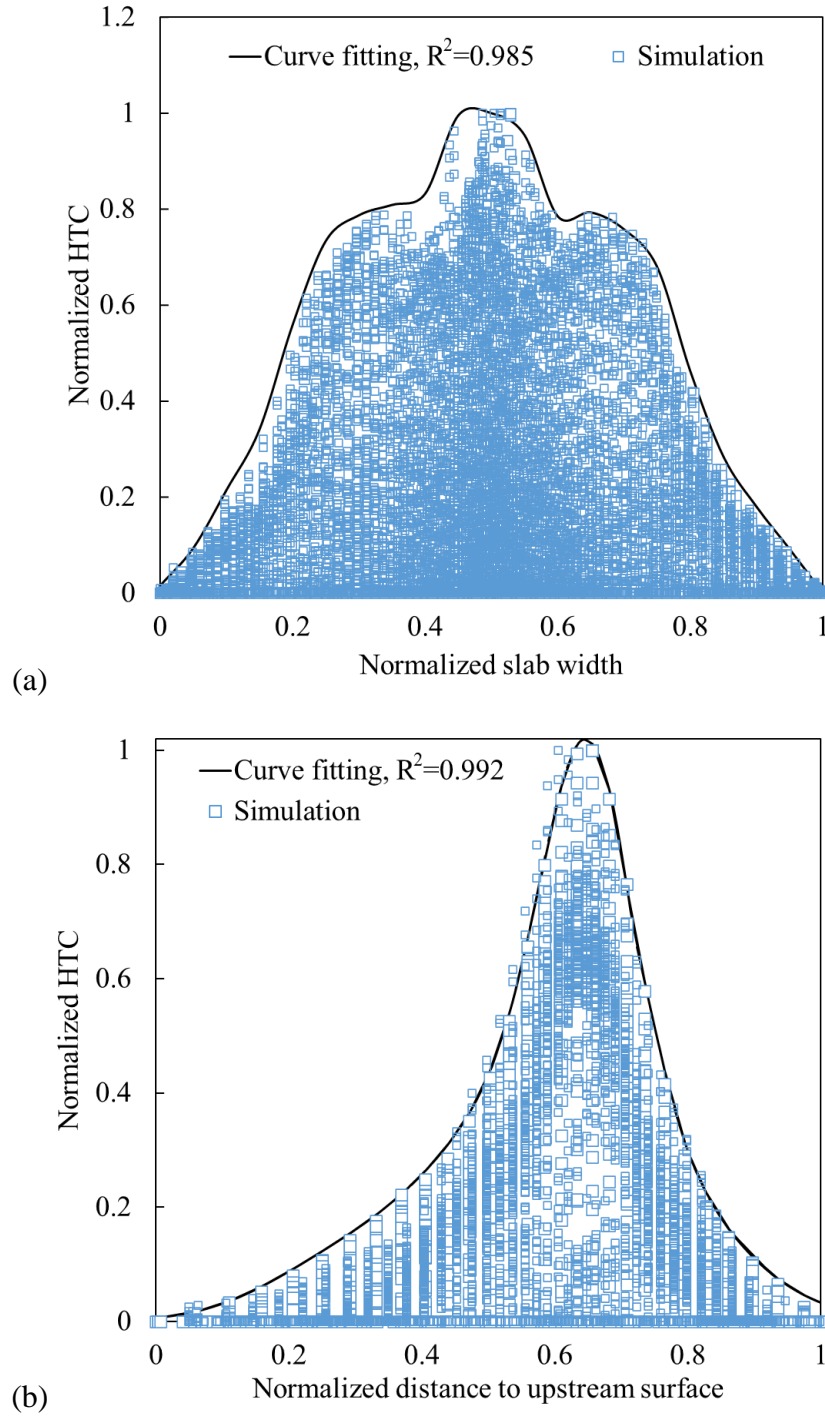
Figure 3-80. Normalized universal distribution functions in: (a) slab width direction, and (b) casting direction.

The two normalized universal distribution functions shown in Eq. (231) and Eq. (232) are based on the simulations for single spray scenarios. However, the same distribution functions can also

be applied to multiple overlapping sprays. As shown in Figure 3-45, the overlapping effect has a limited impact on the water droplet distribution in the casting direction. The primary effect of the spray overlapping is to increase the heat transfer rate in the overlapping area in the slab width direction. Figure 3-81 shows the CFD-predicted data points from an overlapping spray simulation with $D/H = 1.15$ and the normalized universal distribution function in the slab direction. The single spray-based distribution function reasonably outlines the distribution of the CFD-predicted data points. The highest heat transfer rate occurs in the middle of the normalized slab width, which corresponds to the heat transfer in the overlapping area. The single spray-based distribution function overpredicts the normalized heat transfer rate between the nozzle and the center of the overlapping area. The accuracy of the distribution function increases from the nozzle location to the edge of the spray.
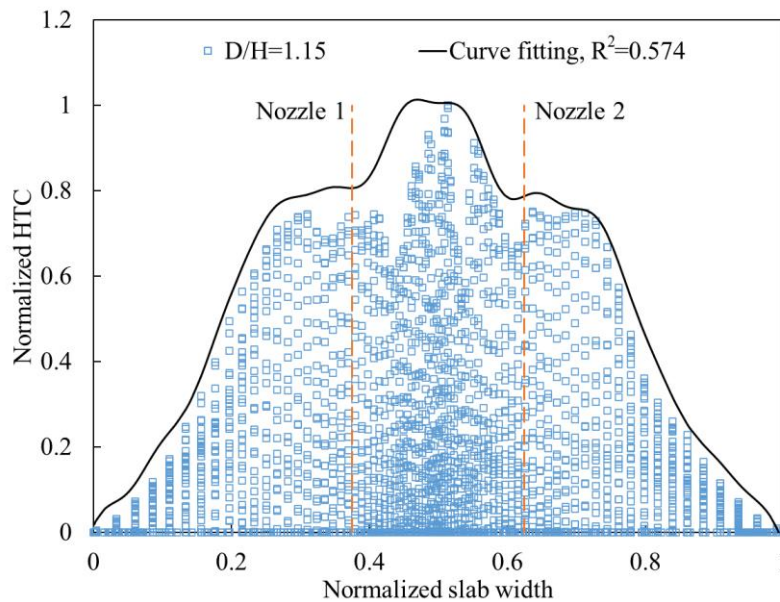
Figure 3-81. The normalized universal distribution function in the slab direction and the HTC data points from an overlapping spray simulation with $D/H = 1.15$.

3.4.4 Correlation of the lumped HTC

In the field of heat transfer, HTC correlations are usually expressed in non-dimensional forms in order to reveal the governing physical parameters explicitly. While the non-dimensional correlations are widely adopted by academia, they are somewhat obscure for caster operators. In practice, HTC is expressed in dimensional forms and is a function of measurable operating

parameters. The current study follows this convention, and all the correlations are expressed in dimensional forms. HTC is a localized parameter, and its value varies in both casting direction and transverse direction. However, with the assumption that the HTC distributions from different operating conditions satisfy the same normalized universal distribution function, the HTC distribution under any given operating condition can be reconstructed based on the two universal distribution functions and an operating condition-dependent characteristic HTC. Such characteristic HTC is independent of particular coordinates, and it is a unique lumped value for any given condition. The current study adopts the following definition to calculate the characteristic value of HTC for any specific condition:

$$HTC_{lump} = HTC_{max} - HTC_{ref} \tag{233}$$

Where HTC_{max} is the maximum HTC within the spray-affected area. HTC_{ref} is a reference HTC, and it will be added back to the predicted HTC. Because the two normalized universal distribution functions range from zero to unity, the predicted HTC will be forced to be zero when one of the distribution functions equals zero. The existence of HTC_{ref} helps avoid such non-physical predictions. HTC_{ref} is defined as follows in the current study:

$$HTC_{ref} = \min \left(HTC_{1,max}, HTC_{2,max}, \cdots, HTC_{n,max} \right) \tag{234}$$

Where $HTC_{n,max}$ is the maximum HTC within the spray-affected area in the nth condition.

The final form of the correlation should be mathematically simple. Otherwise, it will require a significant amount of time for calculation and result in delaying the casting control. The simplest type of regression analysis is linear regression. The most straightforward application of the linear regression in the current study is to solve for the coefficients in the following multivariable linear regression correlation:

$$HTC_{lump} = A_0 + A_1 Q_w + A_2 D_{noz} + A_3 H_{sp} + A_4 T_{sp} + A_5 V_{cs} + A_6 D_{row} + A_7 \theta_{sp} \tag{235}$$
$$+ A_8 \eta_{sp} + A_9 P_a$$

The coefficients in Eq. (235) is obtained from OriginLab, and the final form of the multivariable linear regression-based correlation is shown as follows:

$$\text{HTC}_{lump} = 170.8182 + 6.76988Q_w + 0.00676D_{noz} - 0.05131H_{sp} - 0.11645T_{sp} \quad (236)$$
$$+ 71.38408V_{cs} - 0.24248D_{row} - 1.46264\theta_{sp} + 88.92064\eta_{sp}$$
$$+ 5.89801P_a, R^2 = 0.63$$

Figure 3-82 compares the CFD-predicted HTC values and the correlation-predicted HTC values. The multivariable linear correlation predictes reasonale HTCs compared with the CFD simulations. In addition, the multivariable linear correlation only involves two basic mathematic operations, which are multiplication and addition. Such a feature should accelerate the overall calculation speed, thereby enabling near real-time casting control.
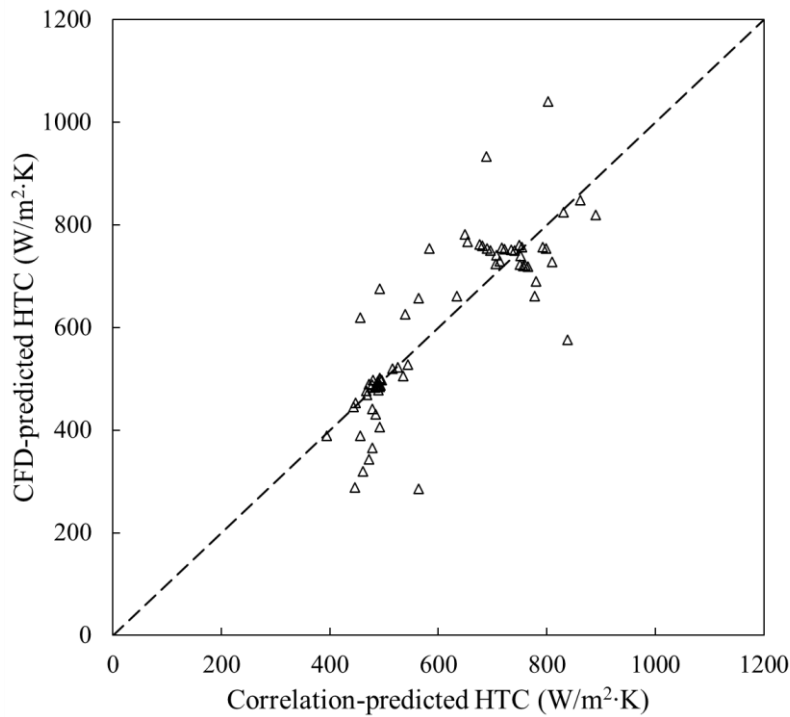
Figure 3-82. Comparison between CFD-predicted HTC and correlation-predicted HTC.

Figure 3-83 shows the comparison of HTC predicted by the multivariable linear correlation and the correlations from open literature. Due to the wide range of the experimental conditions, the

HTC values predicted by the literature correlations scatter from less than 100 to more than 20000. It is important to note that all the literature correlations contain fewer variables compared to the current study. Thus, for the operating parameters that are not considered in the literature correlations, they are assumed to be constants and equal to the values that are used in the baseline condition. There are also variables regarded as necessary in the literature correlations but are excluded from the current study. For example, the correlation developed by Klinzing et al. [168] considers the effect of slab surface temperature, and both Fujimoto et al. and Hernández-Bocanegra treat D_{30} as one of the determining parameters for HTC [169, 171]. This is the reason that the multivariable linear correlation developed in the current study predicts the same HTC values under some conditions. However, as discussed in the parametric study section, each parameter included in the multivariable linear correlation has a considerable impact on heat transfer. Therefore, it is of great importance to consider the effect of these parameters when evaluating HTC.
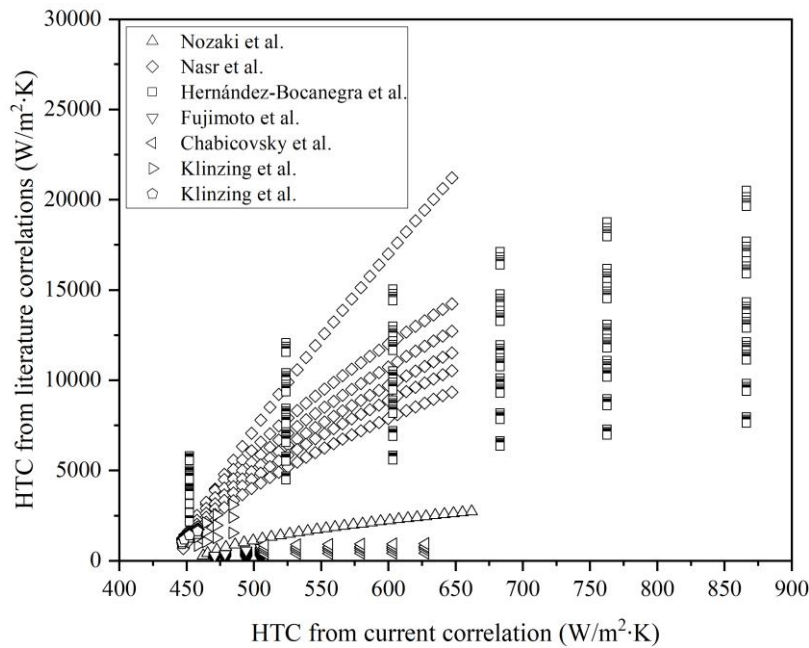
Figure 3-83. Comparison of the predicted HTC with data from open literature.

3.4.5 HTC reconstruction and GUI

The two-dimensional HTC distribution is reconstructed during the application. The reconstruction process consists of three steps, which are defining the projected spray affected area, computing the

lumped HTC, and generating the HTC distribution. The spray-affected area is excluded from the normalized universal distribution functions, but it should be considered in the reconstruction stage. For any specific operating condition, the projected spray-affected area on the steel surface can be calculated based on standoff distance, spray angle, and spread angle, as shown in Figure 3-84.
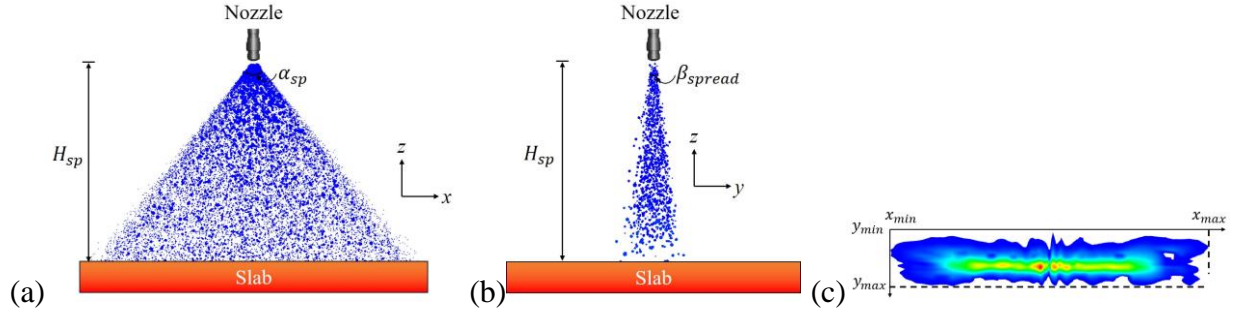
Figure 3-84. Illustration of projected spray-affected area on steel surface in: (a) casting direction, (b) slab width direction, and (c) top view (not to scale).

The boundaries of the projected spray affected area, as shown in Figure 3-84 (c), can be found from trigonometric relations and are defined as follows:

$$X_{min} = 0 \tag{237}$$

$$X_{max} = 2H_{sp} \tan\left(\frac{\alpha_{sp}}{2}\right) \tag{238}$$

$$Y_{min} = 0 \tag{239}$$

$$Y_{max} = 2H_{sp} \tan\left(\frac{\beta_{spread}}{2}\right) \tag{240}$$

The lumped HTC is calculated based on Eq. (236) with the nine pre-determined operating parameters. Finally, the local HTC value at any given point (X_i, Y_j), within the spray-affected area can be computed based on Eq. (231), Eq. (232), and Eq. (236):

$$\text{HTC}_{local,i} = f(X_{norm,i})f(Y_{norm,i})\text{HTC}_{lump} + \text{HTC}_{ref} \tag{241}$$

With the user-defined spatial increments in both directions, a two-dimensional HTC distribution can be generated. Figure 3-85 shows the comparison of the CFD-predicted HTC distribution and

the correlation-predicted HTC distribution. The HTC distribution obtained from the CFD simulation has random fluctuations on the slab surface compared to the smooth distribution predicted by correlation. This is because the high-fidelity CFD simulation is able to capture complex phenomena during droplet-steel impingement heat transfer, such as droplet reflection and sliding droplet on the steel surface. The reconstructed low order HTC distribution excludes some of these detailed local effects to gain computational efficiency. However, the correlation-predicted HTC distribution includes the spatial variations within the spray-affected area, similar to that in the CFD simulation.

(a)
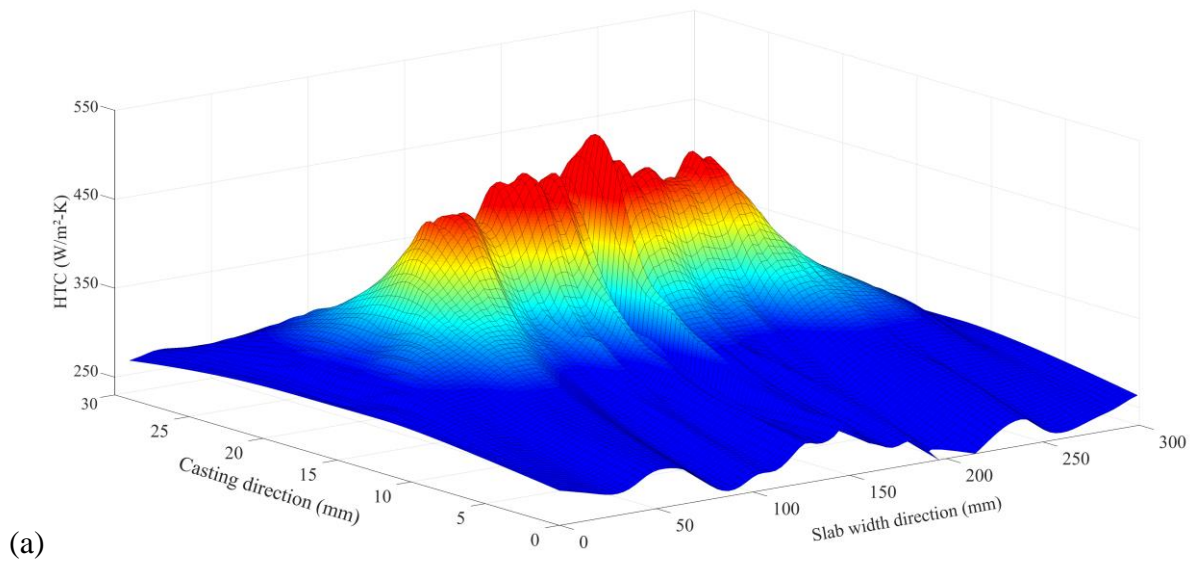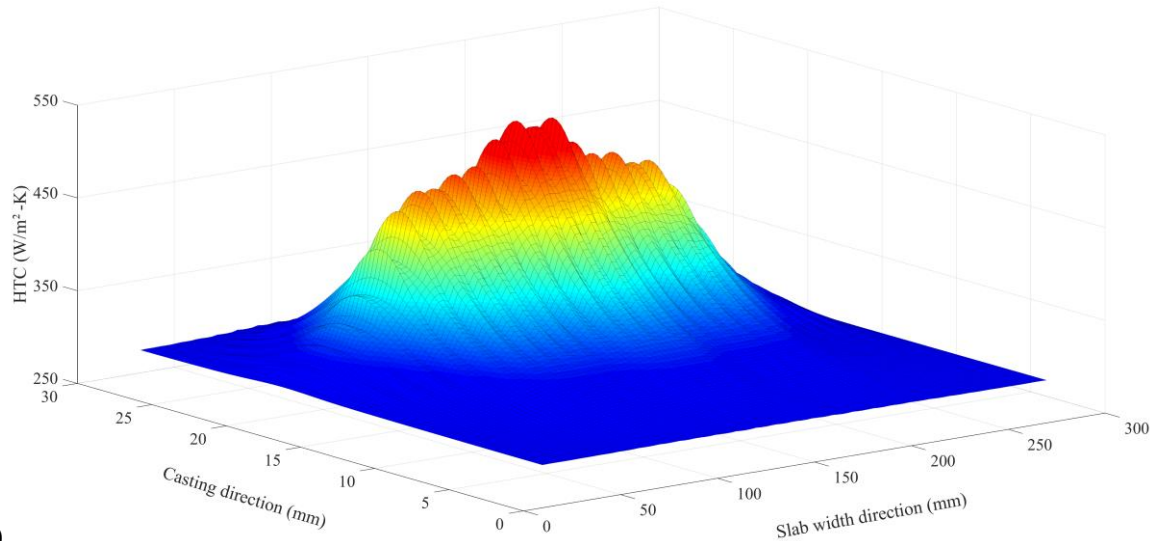
(b)

Figure 3-85. Comparison of the HTC distribution between: (a) CFD-prediction, and (b) correlation-prediction.

The correlation along with the reconstruction procedure developed in the current study can be programmed in new casting control systems as a subroutine. Alternatively, a GUI was created as a complementary component for the existing control systems. Figure 3-86 shows the interface of the beta version. The interface illustrates the definition of HTC coverage to eliminate confusion and ambiguities. The input buttons allow users to type the values of the eight operating parameters and the increments in the two directions. An on-demand hidden window contains the detailed definition of each input parameter. The program executes when users click on the "Generate" button and creates a spreadsheet in versatile comma-separated values (csv) format, which includes the particular coordinates and the corresponding local HTC values within the HTC coverage. The spreadsheet can be conveniently imported into the existing control system as the boundary condition for solidification calculation. Future versions of the HTC GUI will focus on producing massive HTC predictions by allowing users to import a matrix of operating conditions instead of typing the numbers manually.
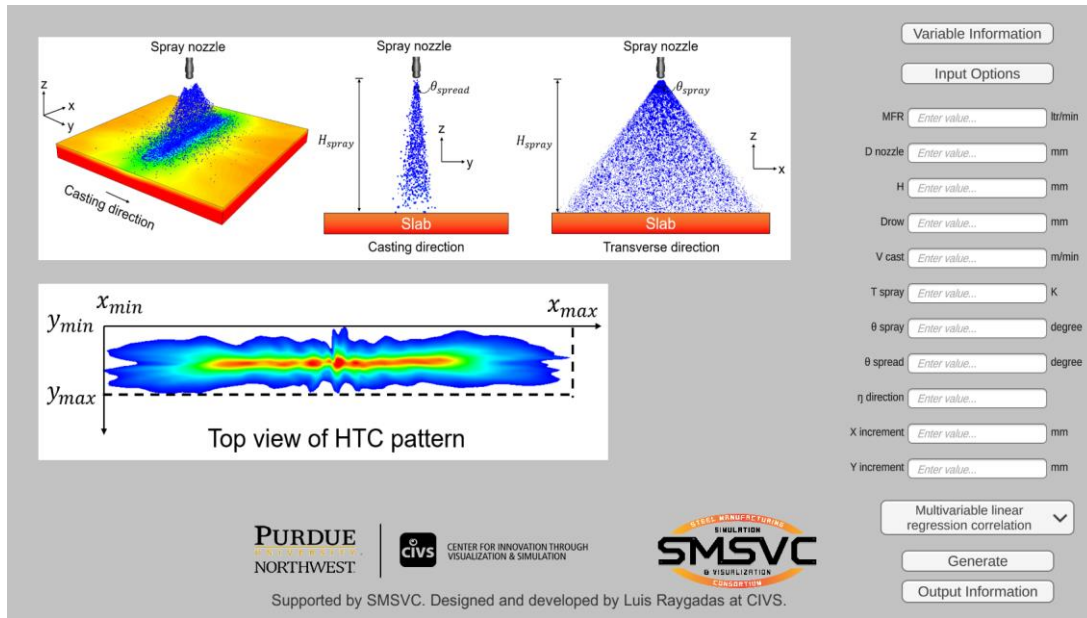
Figure 3-86. Graphic User Interface for HTC prediction.

3.4.6 Potential applications

Aforementioned HTC correlations, together with the GUI, should benefit the steel industry from at least the following aspects:

(1) accelerating the development process of HTC correlations for new nozzle configurations and operating conditions. For example, spray cooling technology is consistently evolving as the nozzle manufacturers advance spray nozzle designs. New spray characteristics, i.e., finer water droplet size, shorter liquid sheet breakup length, multi-phase spray, etc., must be considered in HTC correlations. The current numerical approach should significantly reduce the amount of time to develop new correlations whenever spray characteristics change. Moreover, the demand for new types of steel products is increasing steadily. Each type of steel requires a particular spray cooling strategy, including nozzle type (hydraulic or air-mist), nozzle layout, and spray intensity (spray flow rate and standoff distance). The current high-performance computer-aided numerical method will be helpful in designing a new cooling strategy in a timely manner.

(2) realizing on-site real-time dynamic spray cooling control. One of the primary goals of developing HTC correlations is to enable real-time control during continuous casting. The HTC

299

correlations proposed in this study and the user-friendly interface will allow instant generation of HTC values in both casting and transverse directions. When this prediction process is automated and integrated with the solidification prediction module and control module, the prediction and dynamic control process can be completed near real-time.

(3) supporting spray nozzle selection during the caster design stage. The current HTC GUI was built for both off-line and on-line applications. When applied off-line, the HTC GUI can be used for "what if" scenarios and provide HTC values for different nozzle arrangements and operating conditions. Engineers can select the optimum nozzle type and cooling strategy for a specific caster based on the predicted HTC values. (4) Troubleshooting malfunctioning nozzles. The previous HTC correlations were developed based on ideal operating conditions. Thus, they can be used to identify nozzles that deviate from design conditions. For example, clogged nozzles due to inclusion deposition will produce different spray patterns on the slab surface, therefore, generate a different cooling profile. Operators can compare the predicted temperature profile with the measured one and pinpoint the malfunctioning nozzle where the temperature difference is significant (beyond tolerance).

4. RESULTS – SOLIDIFICATION IN SECONDARY COOLING REGION

4.1 Solidification coupled with single spray cooling

4.1.1 Validations

Shell thickness in a stationary thin solidifying body

The analytical solution of temperature in an unconstrained solidifying body derived by Weiner and Boley and the corresponding simulation developed by Koric and Thomas are compared with the current model [249, 306]. Although the work conducted by Weiner and Boley oversimplifies the complex physical phenomena of solidification, it has become a useful benchmark problem for the verification of numerical models.

The problem considered here is an idealization of the early stage of solidification of a metal casting in a stationary mold, as shown in Figure 4-1. Initially, the metal and the mold walls are kept at the same temperature. At time zero, the temperature of the mold wall suddenly decreases to a lower temperature which is lower than the solidification temperature, so that solidification begins immediately. The computational domain is a small thin slice body in the mold. One end of the thin body is against the mold wall, and the other end extends into the molten steel region. The temperature on the end that attaches to the wall is set to constant, and it equals the temperature of the mold wall. All the other sides of the thin body are assumed to be adiabatic walls, and heat transfer is not permitted during solidification. Thus, the heat flux only flows from the liquid to the mold wall. Such assumptions convert the three-dimensional heat transfer problem to a relatively simple one-dimensional heat transfer problem. Since the dimensions of the thin body are negligible compared to that of the mold, the aforementioned simplifications are reasonable.

To avoid the calculation for the mushy zone, Weiner and Boley assumed that there is zero superheat in the molten steel. Thus, the liquidus temperature equals the solidus temperature, and both are set to 1494.35°C in the simulation. All the material properties of the metal are assumed to be constant during solidification and are listed in Table 4-1. The length of the computational domain in the y direction is set to 30mm, as suggested by Koric and Thomas [137]. The width in

the x direction has little impact on the final results due to the adiabatic wall assumption, and it is set to 5mm in the simulation.
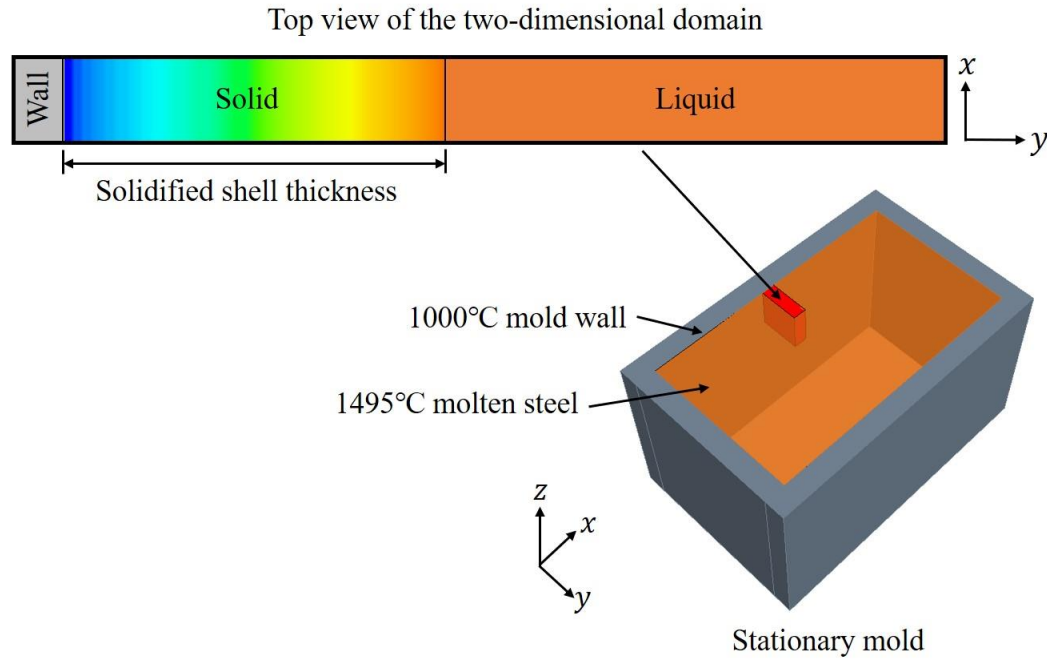
Figure 4-1. Illustration of the simplified two-dimensional stationary thin solidifying body.

Table 4-1. Material properties of the solidifying metal.

Parameter	Value
Conductivity (W/m·K)	33
Specific heat (J/kg·K)	661
Density (kg/m³)	7500
Liquidus temperature (°C)	1494.35
Solidus temperature (°C)	1494.35
Initial temperature (°C)	1495
Latent heat (J/kg·K)	272000
Viscosity (Pa·s)	6.667×10^{-9}

Figure 4-2 compares the temperature distribution within the solidifying body at 1s, 5s, 10s, 20s, and 40s. The cold mold wall locates at 0mm on the horizontal axis, whereas the molten steel is at

locations where the temperature is equal to 1495°C. Temperature decreases almost linearly from the liquid-solid interface to the cold mold wall as heat passes through the solidifying body. Because both the mold wall and the molten steel are kept at constant temperatures, the solidifying body will continuously grow from the cold mold wall toward the molten steel. The temperature distribution predicted by the current study matches reasonably well with the analytical calculation, as well as the numerical work by Koric and Thomas.
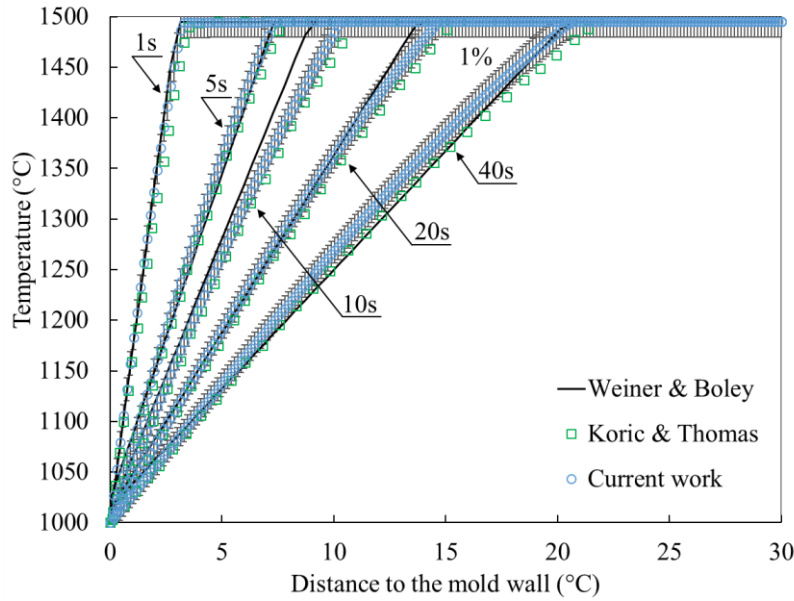
Figure 4-2. Temperature distribution in the solidifying body at different times.

Shell thickness in a moving thin solidifying body

Based on the work of Weiner and Boley, Koric and Thomas further advanced numerical models to simulate the solidification process in a moving thin slice [249]. The computational domain is shown in Figure 4-3. The thin solidifying body is still a two-dimensional slice in a large stationary mold. To simulate the effect of continuous casting, the thermal boundary condition at the mold wall is changed to the following time-dependent heat flux from the constant temperature:

$$q''_{mold} = \frac{6.5 \times 10^6}{\sqrt{t+1}}$$

(242)

During the simulation, the heat flux varies with the advancement of the simulation time as if the thin body were moving along the casting direction. In addition, the previous pure metal is also changed to a multicomponent low carbon steel. The elements are listed in Table 4-2 based on the work of Li and Thomas [307]. The phase fraction was calculated by the lever rule, and all the material properties were computed based on the weight-averaged method. The calculated liquidus temperature and solidus temperature are 1411.79°C and 1500.72°C, respectively. Detailed information regarding the material property can be found elsewhere [249, 307].

Top view of the two-dimensional domain
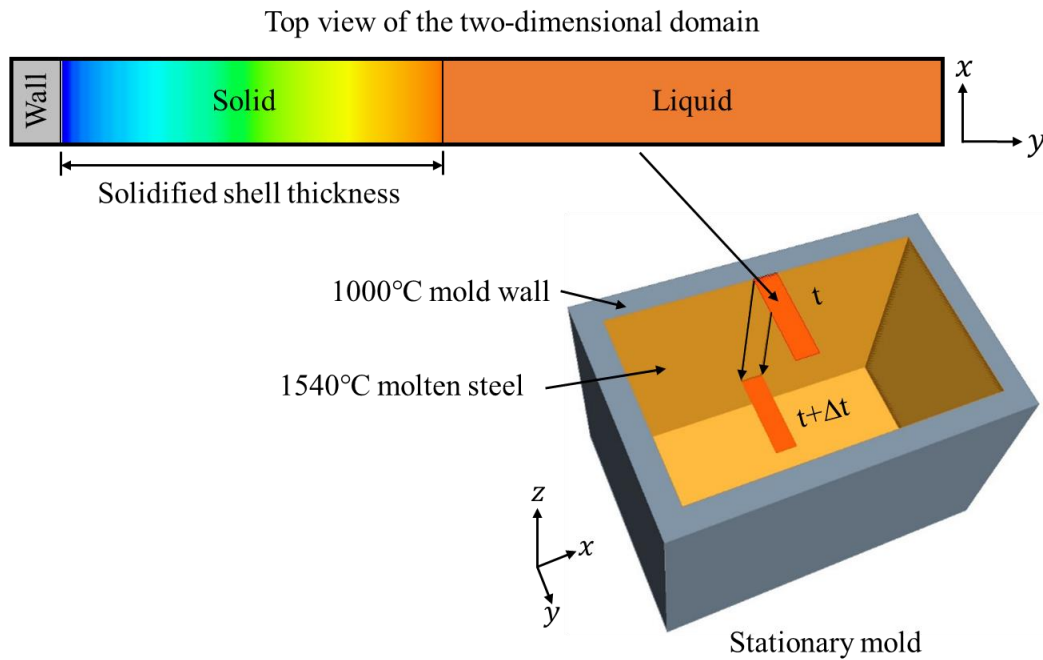
Figure 4-3. Illustration of the simplified two-dimensional moving thin solidifying body.

Table 4-2. Steel composition used in the moving thin solidifying body simulation.

Element	wt%
Fe	97.843%
C	0.27%
Mn	1.52%
Si	0.34%
P	0.012%
S	0.015%

Figure 4-4 compares the temperature in the moving solidifying body at different times after the solidification process starts. The temperature within the solidified body and the liquid region matches well with the predictions by Koric and Thomas. The temperature in the mushy zone predicted by the current work is slightly higher than in the literature. Due to the lack of information regarding the numerical model, the current work adopts some of the model constants from other literature, as discussed in chapter 2. Nevertheless, the current predictions still show good agreement with the literature. The overall average difference and maximum difference between the current work and the literature are 0.96% and 4.55%, respectively.
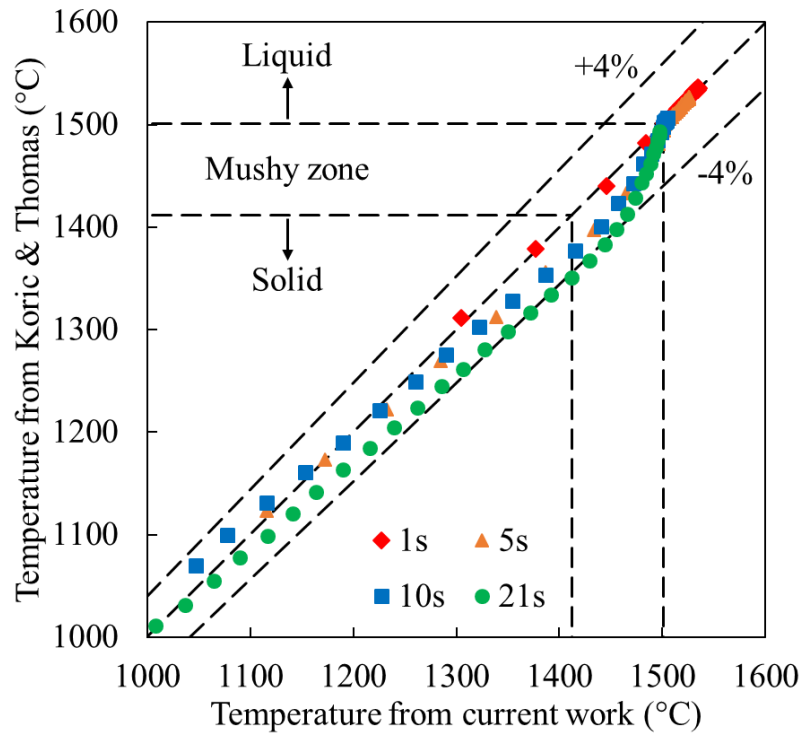
Figure 4-4. Comparison of temperature in the moving thin solidifying body.

4.1.2   Baseline

Fluid flow distribution

Figure 4-5 shows the flow velocity variations throughout the slab thickness and at different locations in the casting direction. As described in Figure 2-33 (a), a 20mm thick solidified region is assumed upstream, where the temperature is adjusted to between 1500K and 1818K. The

velocity of the solidified region is set to the casting speed, which equals 1m/min (0.01667m/s). The molten steel between the top and bottom solidified regions is assumed to satisfy a parabolic-shaped velocity distribution based on previous studies [282, 283]. Thus, the liquid-solid interface at the upstream is assumed to be sharp. As shown in Figure 4-5, the velocity distribution varies slightly in the casting direction. The parabolic-shaped velocity distribution is observed at both the middle and downstream. The velocity magnitude in the molten steel decreases to some extent. In contrast, the velocity magnitude increases in the solid region. In addition, the velocity transition from liquid to solid becomes much smoother downstream. Such behavior indicates the existence of the mushy zone, and the liquid-solid transition happens over a certain distance instead of on a plane. Because the flow resistance in the mushy zone is lower than that in the solid region, the bulk liquid expands into the mushy zone, thereby increasing the velocity in the mushy zone and lowering the velocity in the liquid region due to the conservation of momentum.
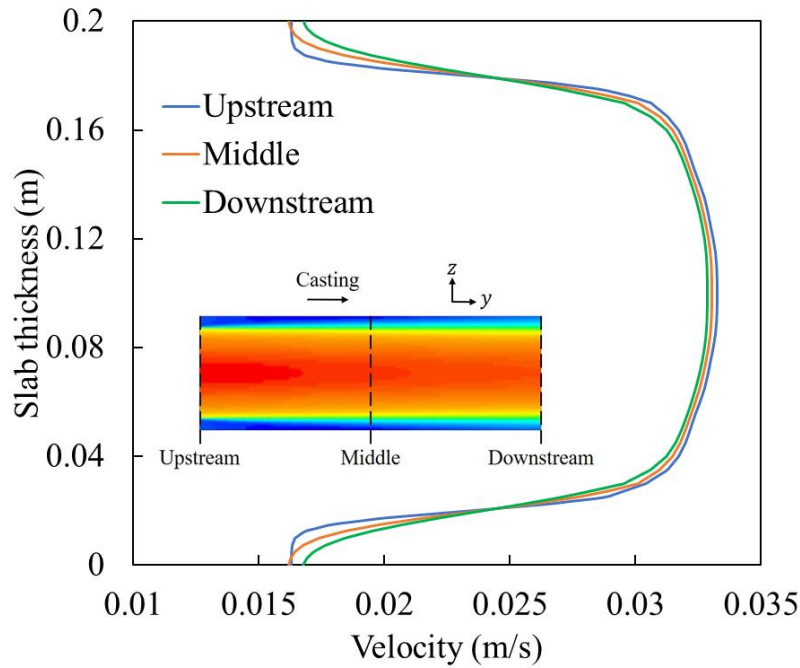
Figure 4-5. Velocity distribution throughout the slab thickness at different locations in the casting direction.

Figure 4-6 shows the Re number distribution within the slab. The characteristic length is set to the length of the control volume when evaluating the Re number. Two isolines where the solid fraction equals 0.1 and 0.9 are plotted as the boundary of the mushy zone for reference. The definition of

the solid front varies from the solid fraction 0.75 to 0.9 in previous numerical studies, and the solid fraction of 0.9 is acknowledged as the best representation of the solid region [197, 295, 308-311]. The maximum Re number occurs at the center of the liquid region, where the liquid is unaffected by the heat transfer on the slab surfaces. The Re number decreases from the center of the slab to the surface in the same direction of heat transfer. The average Re number in the mushy zone is 56.4, and it further decreases to 28.7 in the solid region. The low Re number throughout the mushy zone also justifies the insignificance of Forchheimer's term, as discussed in chapter 2. In addition, because the entire solidified region still moves in the casting direction at casting speed, and the simulated slab segment is located at the beginning of the secondary cooling region where the dynamic viscosity is relatively low, the Re number maintains non-zero values in the solid region instead of zero. If the upstream boundary condition changes to a much lower temperature profile, the Re number in the solid region will further decrease until it reaches zero.
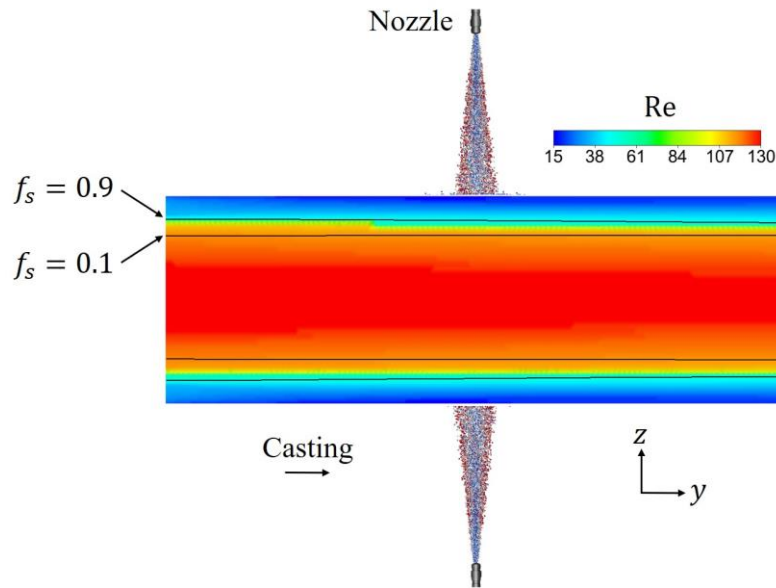
Figure 4-6. Re number distribution within the slab.

Figure 4-7 shows the dynamic viscosity variation throughout the mushy zone. As shown in Figure 2-30, the mushy zone consists of two subregions, which are the free floating dendrite region and the porous region. The presence of the dendrites in the free floating dendrite region is modeled by increasing the flow viscosity, as indicated in Eq. (173). As shown in Figure 4-7, the dynamic viscosity model takes effect between the liquid front and the critical solid fraction, which is

approximately 14mm wide, as shown in Figure 4-8. The increase of the viscosity is much smoother at lower solid fractions, and it drastically decreases to zero approaching the critical solid fraction, where the porous medium model takes effect.
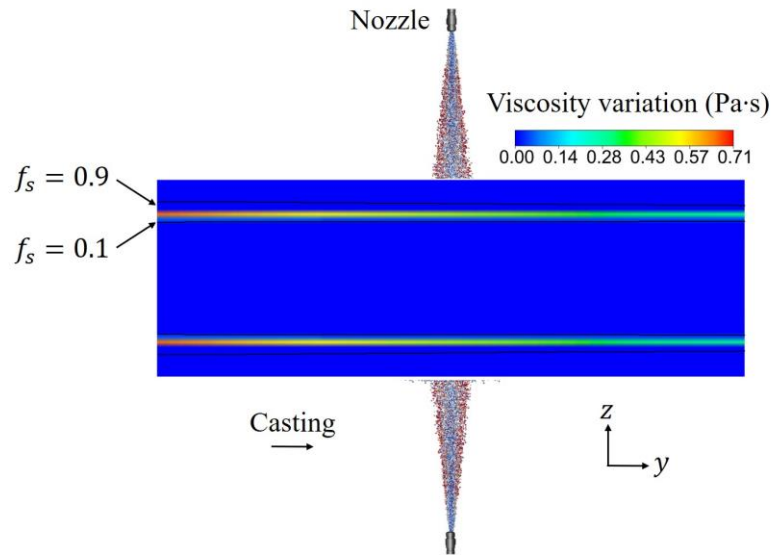
Figure 4-7. Dynamic viscosity variation throughout the mushy zone.
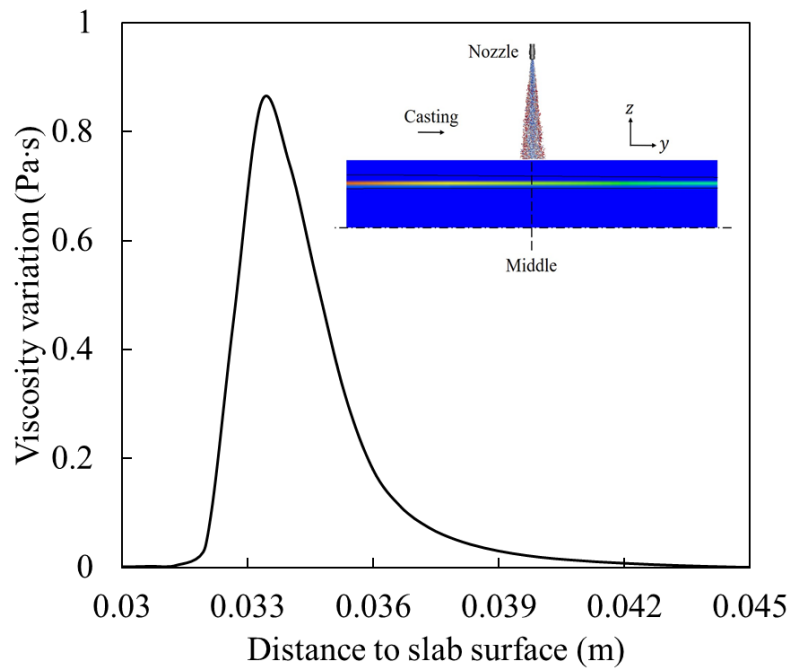
Figure 4-8. Dynamic viscosity variation below the spray affected area.

Figure 4-9 shows the porous zone resistance in the porous region. The resistance force only becomes significant when the solid fraction is larger than the critical solid fraction. The significant resistance force indicates the presence of the columnar dendrites where the liquid flow is further damped by the closely packed dendrites. The porous region extends from the critical solid fraction to the solid region with a solid fraction of unity, at which the resistance decreases to zero as solid is impermeable to the flow.
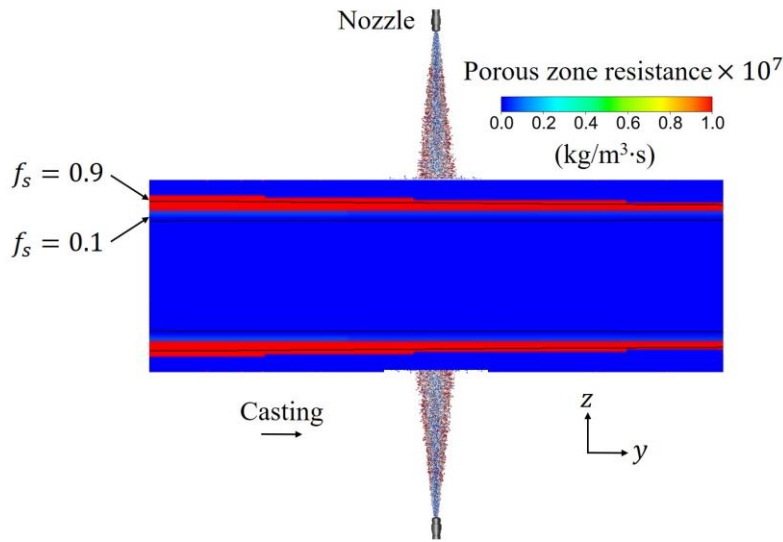
Figure 4-9. Porous zone resistance throughout the mushy zone.

Temperature distribution

Figure 4-10 shows the temperature distribution within the slab in the casting direction. The molten steel at the center of the slab maintains the 11K superheat throughout the computational domain and is unaffected by the heat transfer on the slab surfaces. The effect of spray cooling has a more significant impact within the solid region where the solid fraction is above 0.9. The temperature gradient within the solid region significantly increases after the slab passes the spray due to heat conduction. In contrast, the temperature distribution in the slab width direction is much uniform, as shown in Figure 4-11. Although the heat transfer rate is higher at the center of the spray, as described in chapter 3, the effect of spray cooling on the temperature distribution inside the slab is limited to the region near the surface. The effect of spray cooling is barely distinguishable in the mushy zone and the liquid region.
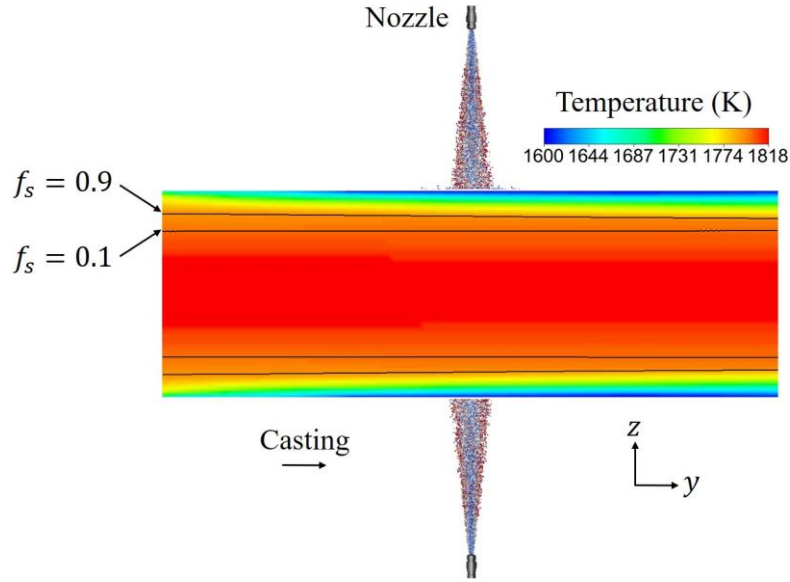
Figure 4-10. Temperature distribution within the slab in the casting direction.
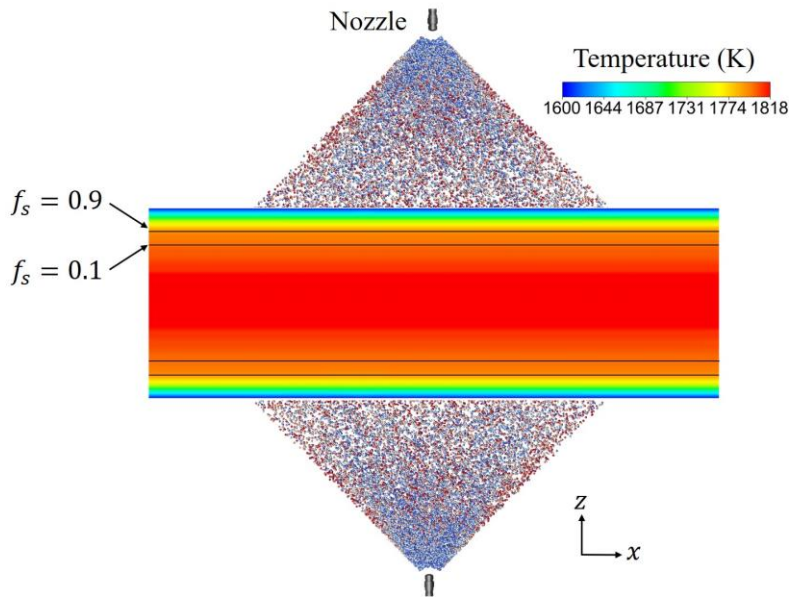
Figure 4-11. Temperature distribution within the slab in the slab width direction.

Figure 4-12 shows the temperature distribution throughout the slab thickness at different locations in the casting direction. As shown in Figure 4-10, the temperature of the molten steel maintains a reasonably flat shape throughout the computational domain, whereas the temperature gradient in the solid region increases due to the spray cooling effect on the surfaces. The transition from the steep temperature distribution within the mushy zone to the flat distribution in the liquid region

slightly shifts toward the center of the slab as the slab is cooled by the two sprays on the surfaces. The temperature gradient within the mushy zone and the solid region is approximately linearly as the result of pure heat conduction through these regions.
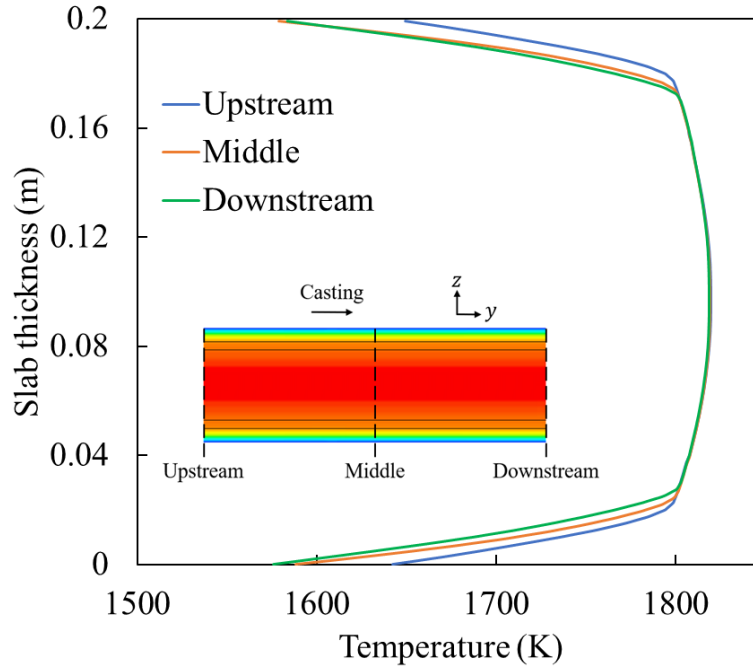
Figure 4-12. Temperature distribution throughout the slab thickness at different locations in the casting direction.

As discussed previously, one of the primary goals of modern continuous casting is to produce high-quality defect-free steel products. An optimum cooling rate in the secondary cooling region is desired to minimize residual thermal stresses and strains within the solidified slab. Insufficient cooling rate will lead to bulging or even breakout incidents, whereas overcooling can result in excessive residual stresses and strains. The theoretical minimum cooling rate can be defined as follows:

$$C_{cool} = \frac{\Delta T_{sup} + T_{liq} - T_{sol}}{L_{ML}/V_{ca}} \tag{243}$$

Where ΔT_{sup} is the superheat, L_{ML} is the metallurgical length of the steel slab where solidification completes. The numerator in Eq. (243) represents the minimum amount of heat that must be

removed from the secondary cooling process. It corresponds to a state that the entire slab is just cooled down to the solidus temperature. The denominator in Eq. (243) defines the total cooling time. L_{ML} is usually controlled to be shorter than the length of the casting machine, but for the purpose of theoretical evaluation, it is assumed to equal to the length of the casting machine, which varies from 10m (a thin slab casting machine) to 25m (a regular slab casting machine). The casting speed used in Eq. (243) is the average speed over a normal casting period. Thus, the theoretical minimum cooling rate for a 25m long regular slab casting machine which operates under the current condition is:

$$C_{cool} = \frac{11K + 1807K - 1789K}{25m/(1m/min)} = 0.019K/s \tag{244}$$

The maximum cooling rate can be derived based on Eq. (204), which defines the maximum temperature decrease in the slab without initiating internal crack. For the purpose of efficient cooling, the maximum temperature decrease should occur when the slab passes each spray. Therefore, the maximum cooling rate can be defined as follows:

$$C_{cool} = \frac{T_{sur} - T_{ref}}{w_{spray}/V_{ca}} \tag{245}$$

Where $T_{sur} - T_{ref}$ is the minimum temperature difference to initiate the internal crack, and it is defined in Eq. (204), w_{spray} is the width of the spray affect area in the casting direction, and it is defined in Eq. (202). When a slab is cooled under the current spray condition, the maximum cooling rate can be calculated as follows:

$$C_{cool} = \frac{36.36K}{27.33mm/(1m/min)} = 22.17K/s \tag{246}$$

Figure 4-13 shows the cooling rate variation within the slab in the casting direction. Similarly, the bulk liquid region at the center of the slab is barely affected by the spray cooling on the surfaces. Thus, the cooling rate in the liquid region is zero. In the vicinity of the liquid-mushy zone interface, a small temperature gradient occurs, and the cooling rate starts to increase as solid free floating

dendrites appear in the liquid. The average cooling rate throughout the mushy zone and the solid region is 0.415K/s and 2.73K/s, respectively. The highest cooling rate in the slab is 6.43K/s, and it occurs on the surface of the slab. The solidified region maintains a relatively high cooling rate during and after spray cooling due to the large temperature gradient. From the point of slab quality, the current cooling rate is moderate compared to the maximum safe cooling rate, and it should sufficiently cool down the slab without inducing any thermal-related defects.
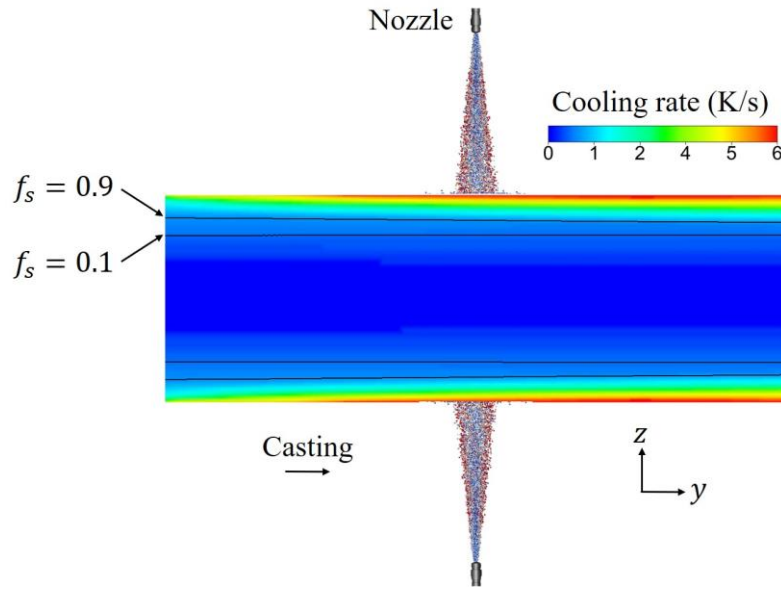
Figure 4-13. Cooling rate variation within the slab in the casting direction.

Shell growth

Figure 4-14 and Figure 4-15 compare the shell growth in both the casting and slab width directions. The shell thickness is only considered in the solid region where the solid fraction is greater than 0.9. The areas with lower solid fractions are blocked in the plots. The initial shell thickness at the upstream is assumed based on the temperature distribution. Under the current cooling condition and temperature distribution, the solidified shell grows mainly in the casting direction, and the net growth of the solidified shell throughout the computational domain is 4.41mm. The shell thickness is much uniform in the slab width direction. Interestingly, the variation of the shell thickness in the casting direction is much smoother than that of the surface temperature, as described in chapter 3. Even at the spray cooling location, where the heat transfer rate on the surface is the highest, there is no drastic increase in the shell thickness. This behavior suggests that the influence of the

313

heat transfer on the slab surface can only reach the near-surface region within the slab, beyond which the effect of intense heat transfer on the surface diffuses to different directions through heat conduction which tends to minimize the temperature difference within the slab.
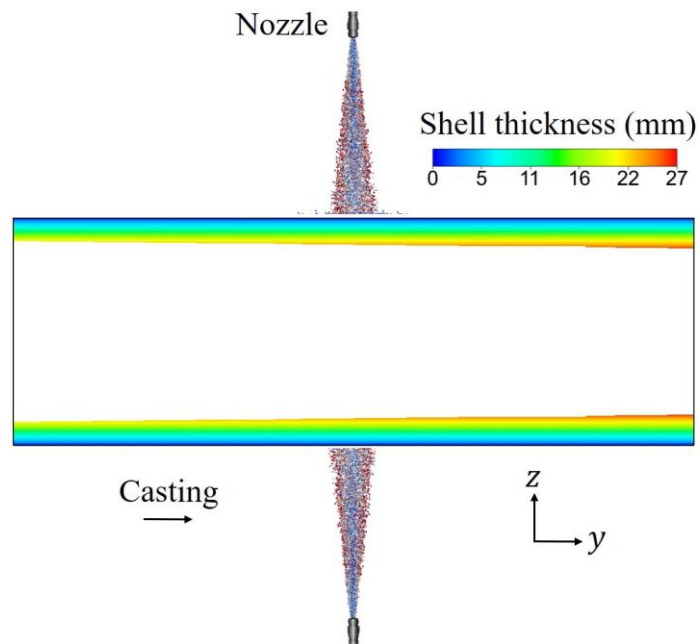
Figure 4-14. Shell thickness in the solid region in the casting direction.
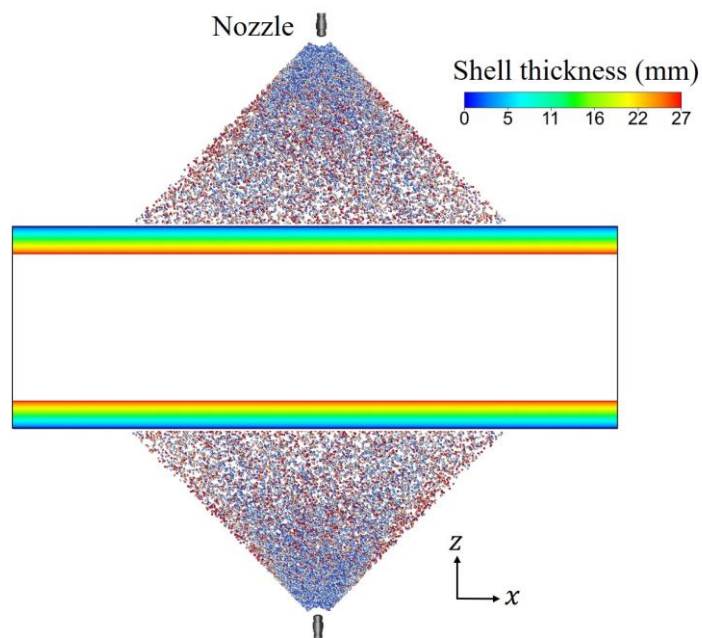
Figure 4-15. Shell thickness in the solid region in the slab width direction.

Figure 4-16 compares the shell thickness and the shell growth rate in both the casting and slab width directions. The color black represents the shell thickness, and the blue color stands for the shell growth rate. The solid line shows the condition in the casting direction, and the dashed line indicates the condition in the slab width direction. In the casting direction, the shell growth rate increases from zero at the upstream surface to 0.18mm/s at the downstream surface. The shell growth rate reaches the maximum slightly downstream of the spray cooling, locates at half-length of the computational domain. Further downstream of the spray cooling, the shell growth rate slightly decreases but still maintains a relatively high value due to the heat conduction within the solidified region. On the contrary, both the shell thickness and the shell growth rate barely vary in the slab width direction, as the conditions of heat conduction and convection are similar throughout the slab width direction, except for the regions near the narrow faces.
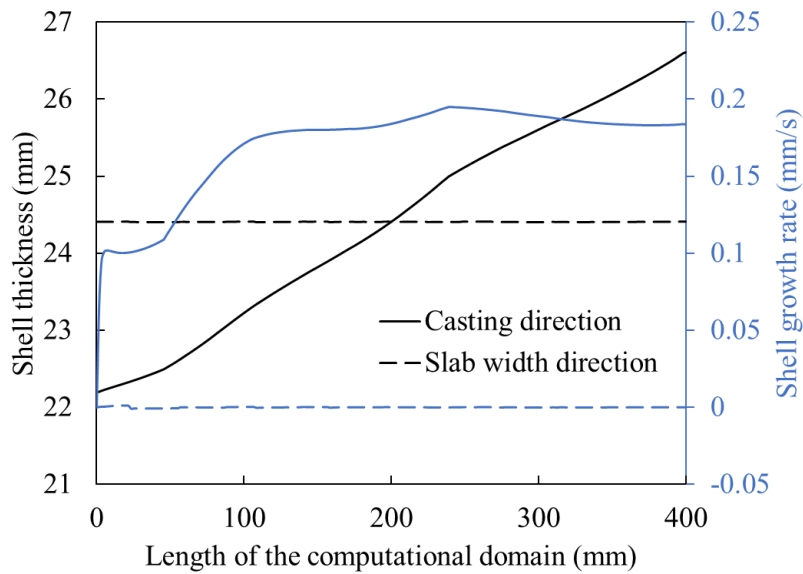
Figure 4-16. Solidified shell thickness and shell growth rate in both the casting and slab width directions.

The average shell growth rate in the casting direction is 0.17mm/s. If the water sprays at every row in the secondary cooling region can produce the same cooling condition, the total length for a slab of 200mm thickness to completely solidifies can be estimated as follows:

$$L_{ML} = \frac{100mm}{0.17mm/s} \times \frac{1m}{min} \times \frac{1min}{60s} = 9.8m \tag{247}$$

Eq. (247) indicates the minimum metallurgical length for the current casting conditions. However, the spray cooling condition varies in the casting direction, and it continuously decreases as less heat transfer rate is required downstream. Thus, the actual metallurgical length is longer than the estimated one, and it is usually between 20m to 40m for a slab of 200mm thickness.

Figure 4-17 shows the secondary dendrite arm spacing throughout the slab thickness at different locations in the casting direction. As shown in Eq. (179) and Eq. (180), the secondary dendrite arm spacing can be correlated with the carbon content and the local cooling rate, and it affects the permeability in the porous region. The variation of the secondary dendrite arm spacing occurs in the mushy zone and the solid region. The maximum secondary dendrite arm spacing is 387μm at the liquid-mushy zone interface, and it decreases to around 50μm near the surface. The secondary dendrite arm spacing also decreases in the casting direction, as the growing dendrites pack more closely in the solidified region.
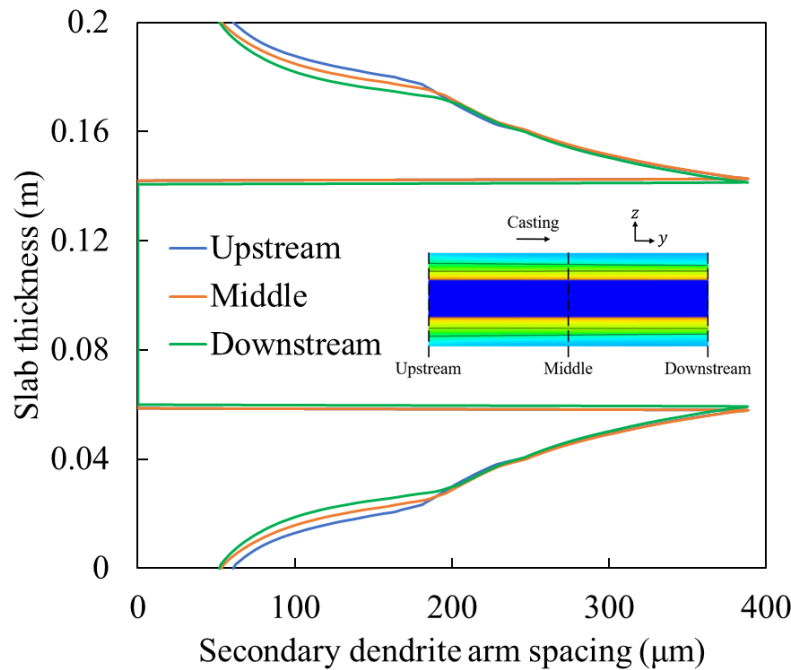
Figure 4-17. Secondary dendrite arm spacing throughout the slab thickness at different locations in the casting direction.

4.1.3   Parametric study

Effect of secondary dendrite arm spacing

As shown in Figure 2-30, the effect of secondary dendrite arm spacing is significant in the porous region and negligible in the free floating dendrite region. In the porous region, secondary dendrite arm spacing is considered the characteristic length of the closely packed solidified dendrites. It affects the field flow distribution between dendrites through resistance forces. The size of secondary dendrite arm spacing can be correlated with the local cooling rate and carbon content, as summarized in Eq. (179) and Eq. (180). Figure 4-18 compares the secondary dendrite arm spacing at several cooling rates and carbon contents based on Eq. (179) and Eq. (180). At a low cooling rate such as 0.0001K/s, the dependency on carbon content is indistinguishable. Because of the low cooling rate, the size of a single dendrite is larger than that in faster cooling, therefore, wider spacing between the adjacent secondary branches on a dendrite. As the cooling rate increases, the dependency on carbon content starts to reveal. In molten steel with higher carbon content, the solubility difference of carbon between the solid phase and the liquid phase is larger. Thus, relatively larger dendrites with wider secondary dendrite arm spacing form.
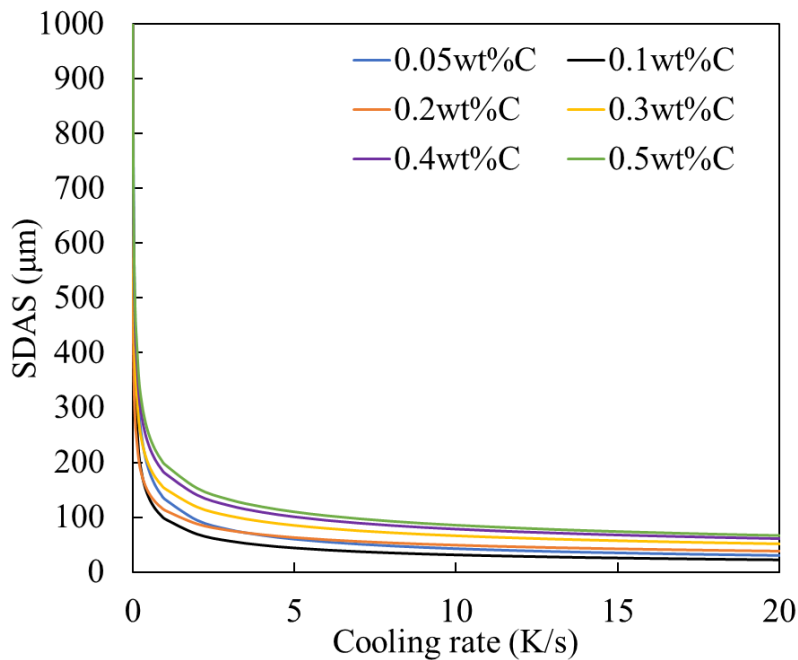
Figure 4-18. Secondary dendrite arm spacing as a function of the local cooling rate and carbon content based on the work of Won and Thomas [276].

In terms of fluid flow and heat transfer, the direct effect of secondary dendrite arm spacing is to increase the permeability of the porous zone, as indicated in Eq. (178). The permeability, in turn, affects the flow resistance, which is shown in Eq. (174). Substituting the expression for permeability into Eq. (174), yields:

$$S_{por} = -\frac{180\mu_{st}f_{sol}^2(1 - F_\mu)}{\lambda_{SDAS}^2(1 - f_{sol})^3}|\vec{u}_{st} - \vec{u}_{cast}| \tag{248}$$

Eq. (248) shows the inverse dependency of the flow resistance force on the square of secondary dendrite arm spacing. As the secondary dendrite arm spacing increases, there is more space between dendrites for the liquid flow to penetrate, and less resistance force imposes on the liquid flow. Figure 4-19 compares the porous zone flow resistance force at different secondary dendrite arm spacings. To isolate the effect of secondary dendrite arm spacing on flow resistance, three simulations with different fixed secondary dendrite arm spacings were carried out. According to Figure 4-18, the secondary dendrite arm spacing ranges from 10μm to 1000μm at a carbon content of 0.05wt%. Thus, the secondary dendrite arm spacing is set to 10μm, 100μm, and 1000μm in the three simulations, respectively.
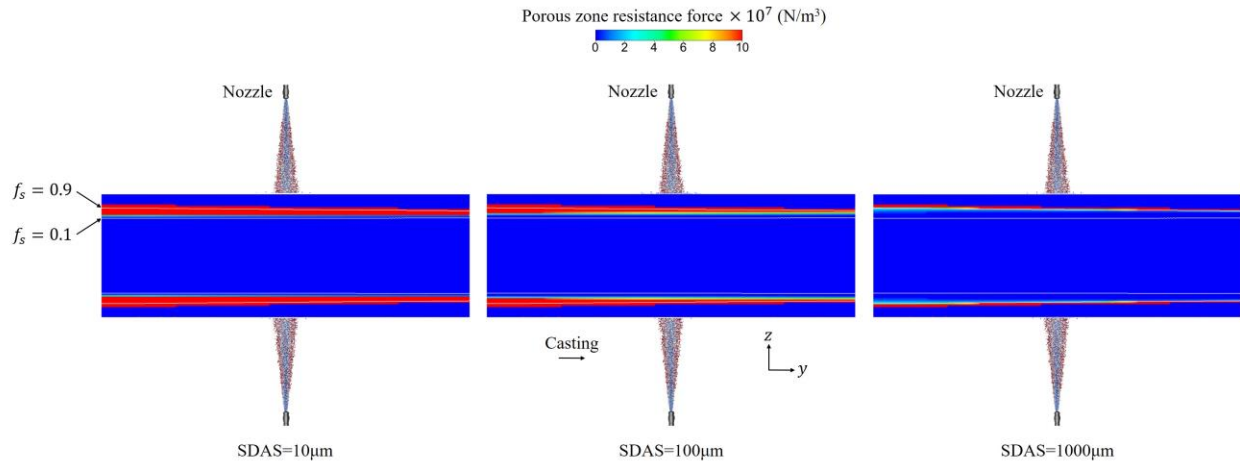
Figure 4-19. Comparison of porous zone flow resistance force at different secondary dendrite arm spacings.

As shown in Eq. (248), the flow resistance approach infinity when the solid fraction increases to unity. Physically, this condition implies that the solid region is impermeable to the liquid flow. In

the mushy zone, where the flow resistance becomes effective, the magnitude of the flow resistance drastically increases as the solid fraction increases. At lower secondary dendrite arm spacing, the solidified dendrites pack much closer to each other. Thus, the liquid experiences much higher resistance over a wider range of the mushy zone. As the secondary dendrite arm spacing increases from 10μm to 1000μm, the flow resistance decreases by four orders of magnitude. With less flow resistance in the mushy zone, the liquid flow penetrates further into the semi-solidified region. Thus, the region of high flow resistance narrows as the secondary dendrite arm spacing increases, as shown in Figure 4-19.

However, as shown in Figure 4-20, the net effect of different secondary dendrite arm spacings on the shell thickness is negligible. Although the flow resistance decreases by four orders of magnitude as the secondary dendrite arm spacing increases from the minimum to the maximum possible size under the current condition, the lowest flow resistance force in the mushy zone is still in the order of million, which is sufficiently large for the liquid flow. Because the flow resistance shapely increases to a large number beyond the critical solid fraction, the solidification process becomes insensitive to the secondary dendrite arm spacing in the solid region.
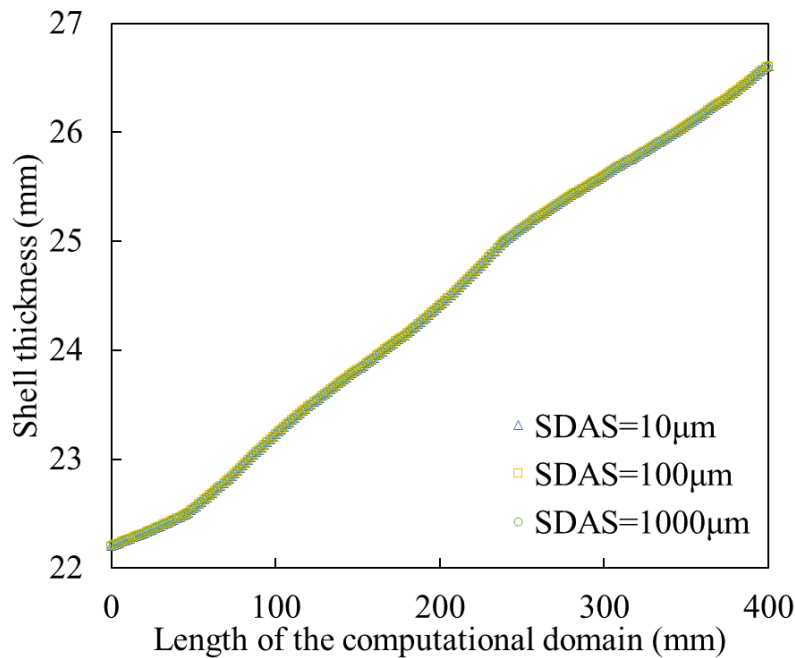
Figure 4-20. Comparison of shell thickness at different secondary dendrite arm spacings.

Effect of critical solid fraction

The critical solid fraction given in Eq. (181), and Eq. (189) determines the onset of the transition between the free floating dendrite region and the porous region. Physically, this parameter indicates the boundary between the equiaxed dendrites and the columnar dendrites. The early study on the critical solid fraction, also referred to as the packing fraction, was based on packed beds and rigid skeleton. The reported value of critical solid fraction scatters over a wide range. Dantzig et al. suggest a range of 0.3-0.4 for rigid skeleton [272]. Baeckerud et al. reported a value of 0.27 for aluminum alloy A201 [278]. Vreeman et al. conducted a parametric study for aluminum copper and aluminum magnesium alloys and used a maximum of 0.3 [279]. Marsh recommended a range of 0.5-0.6 based on the study of lava and magma [280]. Oldenburg et al. applied a value of 0.5 when developed the switching function [261]. Kim et al. proposed a value of 0.525 by averaging various carbon steels used in continuous casting [281]. As shown in Figure 4-21, the effect of the critical solid fraction is to shift the switching functions either toward the liquid or toward the solid.
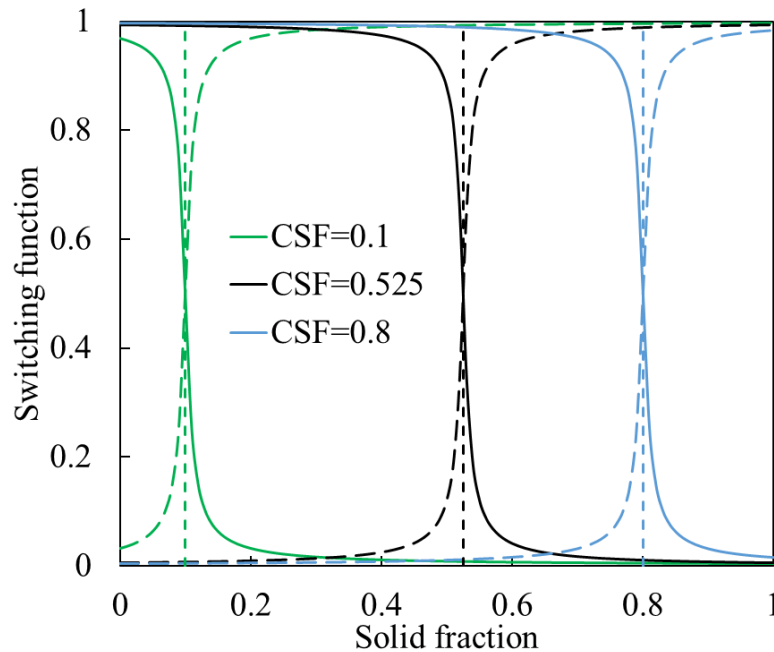
Figure 4-21. Switching function between the free floating dendrite region and the porous region at different critical solid fractions.

As the critical solid fraction shifts, the model governing the flow resistance in specific region changes. For example, when the critical solid fraction increases from 0.27 to 0.525, the flow

resistance in the region between the two critical values is determined by the free floating dendrite model instead of the porous model. On the contrary, if the critical solid fraction increases, the flow resistance model in the overlapping region changes to the porous model. Figure 4-22 shows the solid fraction throughout the mushy zone and solid region at different critical solid fractions. As the critical solid fraction increases from 0.27 to 0.525, the flow resistance model of a 3mm wide region changes to the porous model. The flow resistance calculation in the rest of the domain is unaffected by the change of the critical solid fraction.
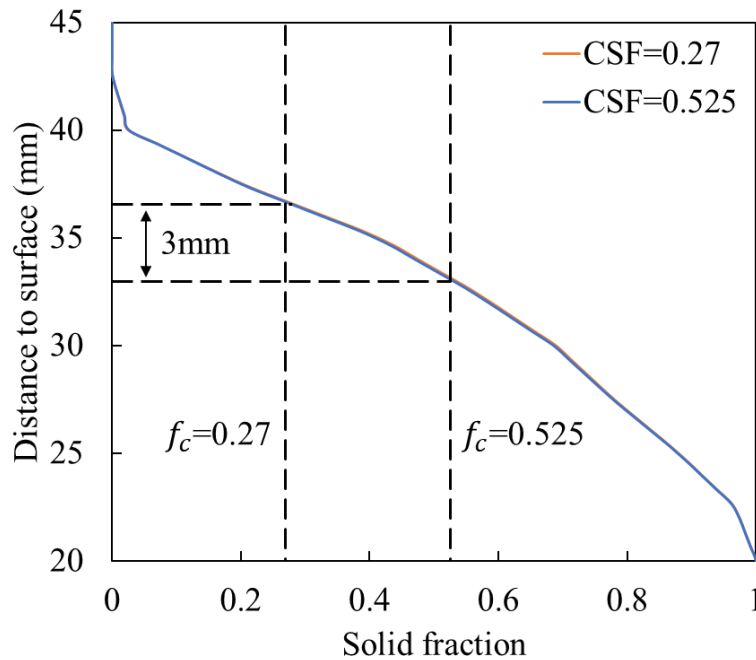
Figure 4-22. Solid fraction throughout the mushy zone and the solid region at different critical solid fractions.

However, as shown in Figure 4-22 and Figure 4-23, the convection and solidification process is barely affected by the change of the critical solid fraction. The difference in shell thickness is within 1%. This is because the affected region is only 3mm, and it is negligible compared to the thickness of the mushy zone and solid region. In addition, even though the flow resistance mode in the 3mm region is switched to the free floating dendrite model as the critical solid fraction increases, the effective viscosity is still sufficiently large to provide the necessary resistance. Therefore, the predicted shell thicknesses are comparable. It is worth mentioning that as the critical solid fraction continues to increase, the flow condition in most of the mushy zone region will be

governed by the free floating dendrite model. The simulations with the critical solid fraction of 0.7 and 0.8 failed to converge, which suggests that the free floating dendrite model is suitable for the low solid fraction regions. If this model is applied to a high solid fraction region, where dendrites form a fixed network and closed pack together, the result will not reflect the actual solidification process. In addition, numerical instabilities will rise when the critical solid fraction approaches unity.
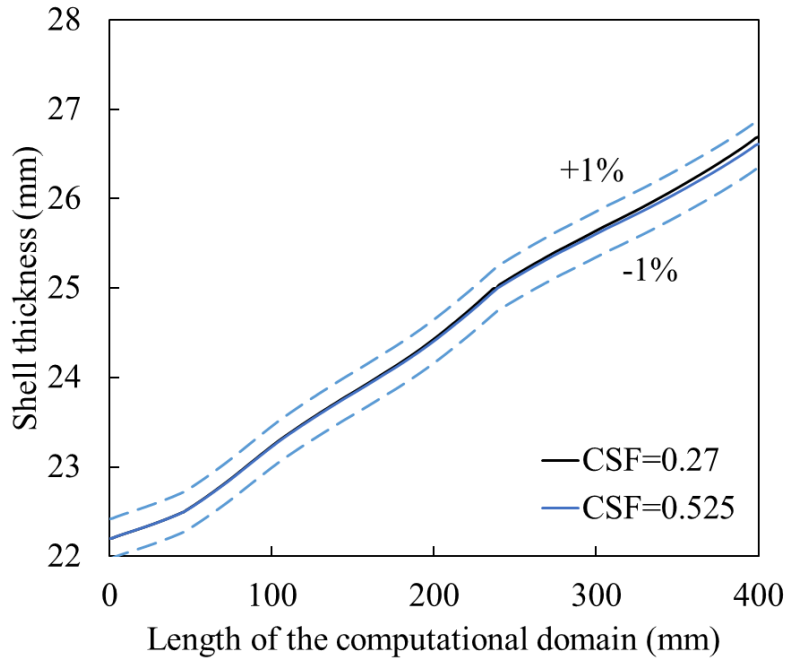
Figure 4-23. Comparison of shell thickness at the critical solid fraction of 0.27 and 0.525.

Effect of crystal constant

The crystal constant defined in Eq. (173) is a model coefficient that physically depends on the aspect ratio and surface roughness of the crystal. In the model proposed by Metzner [260], it is treated as a constant, and a value of 0.5 is recommended [261]. Mathematically, the crystal constant can be considered as a fine-tuning coefficient to obtain the optimum effective viscosity. Eq. (173) can be rearranged as the ratio of effective viscosity and dynamic viscosity:

$$\frac{\mu_{eff}}{\mu_{st}} = \left(1 - \frac{F_\mu f_{sol}}{A_{mushy}}\right)^{-2} \tag{249}$$

322

Eq. (249) indicates the effectiveness of the free floating dendrite model at different solid fractions, which should be activated at the solid fraction between zero and the critical solid fraction. As shown in Figure 4-24, the ratio of $\frac{\mu_{eff}}{\mu_{st}}$ significantly varies as the crystal constant changes. Under the baseline condition with the critical solid fraction of 0.525, a value of 0.5 produces the most reasonable viscosity increase, where the ratio of $\frac{\mu_{eff}}{\mu_{st}}$ approach unity at lower solid fraction and significantly increases to approximately 120 near the critical solid fraction and then rapidly reduces to unity again beyond the critical solid fraction. At other values of the crystal constant, the viscosity increase is either too small to be effective or too large to stop the flow unexpectedly.
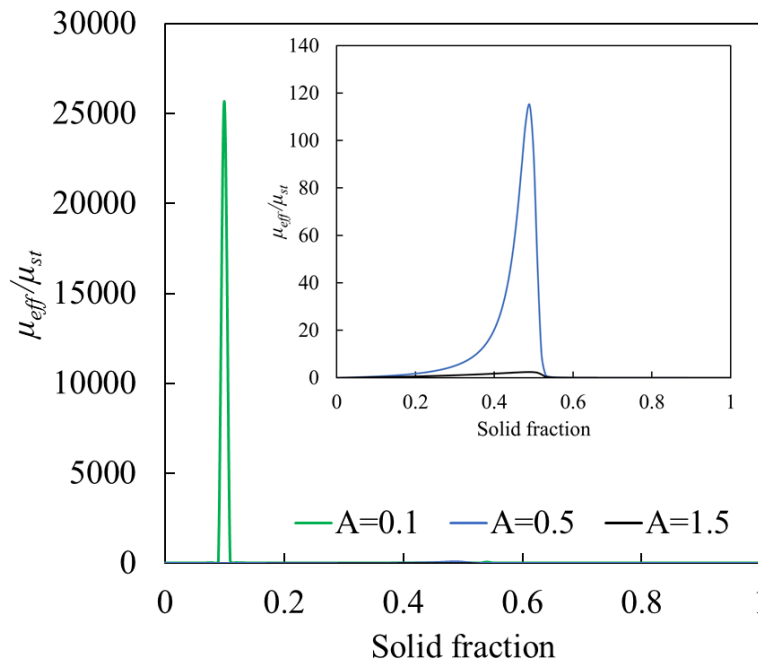
Figure 4-24. The ratio of effective viscosity and dynamic viscosity as a function of the solid fraction at different crystal constants.

Figure 4-25 compares the temperature distribution in the casting direction at different crystal constants. The temperature distribution between the crystal constant of 0.5 and 1.5 is barely noticeable, even though the ratio of $\frac{\mu_{eff}}{\mu_{st}}$ is only slightly above unity at the critical solid fraction. Consequently, the sluggish effect in the free floating dendrite region significantly decreases, and the liquid flow can penetrate further into the mushy zone. However, the temperature distribution

shown in Figure 4-25 and the shell thickness shown in Figure 4-26 suggests that the free floating dendrite region is too thin under the current condition to be of great importance to the convection and solidification process. The average thickness of the free floating dendrite region in the current simulation is 6mm, which is about 18% of the porous region. However, it is not encouraged to discard the free floating dendrite model and only use the porous model for the entire semi-solid and solid region without examining the relative importance of the two models. The selection of the mushy zone model depends on the steel composition, cooling rate, dendrite morphology, relative thickness of the mushy zone, and many other factors, which makes the selection process highly case-dependent.
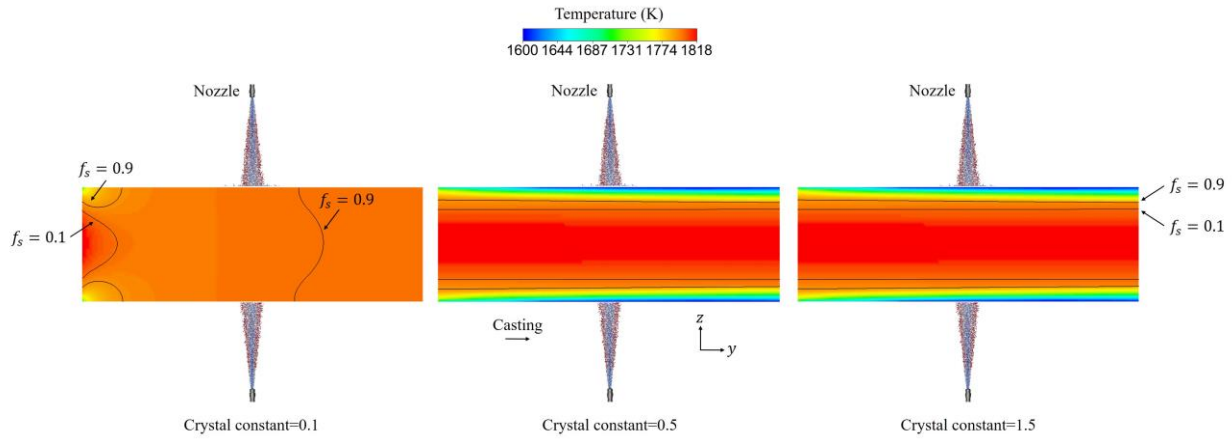
Figure 4-25. Comparison of temperature distribution at different crystal constants.

On the other hand, the solidification process completely changes at the lower crystal constantly. As shown in Figure 4-25, the high-temperature region is confined near the upstream surface, and the pre-defined low-temperature region only occurs at the corner of the upstream surface. Such fluid flow and heat transfer conditions have nothing in common with the baseline condition. Due to the change in flow and heat transfer, the solidification behavior significantly differs, as shown in Figure 4-27. When the crystal constant decreases from the baseline condition, the ratio of $\frac{\mu_{eff}}{\mu_{st}}$ drastically increases to more than 25000 at the solid fraction of 0.1, as shown in Figure 4-24. The unrealistic increase of viscosity at a low solid fraction leads to an unreasonably high resistance near the upstream surface. The pre-defined high momentum at the upstream surface rapidly dissipates through the high viscosity fluid in the computational domain. This is the reason that a

parabolic shape of void forms near the upstream surface. Similarly, the pre-defined subcooling condition at the corners leads to the formation of two half-cylindrical solid regions. Because of the high viscosity, the upstream flow only penetrates 16mm into the computational domain. However, the fixed thermal boundary condition at the upstream surface continues to supply heat to the fluid in the rest of the computational domain through heat conduction. The temperature and solid fraction profiles gradually flatten in the casting direction as energy dissipates in the domain.
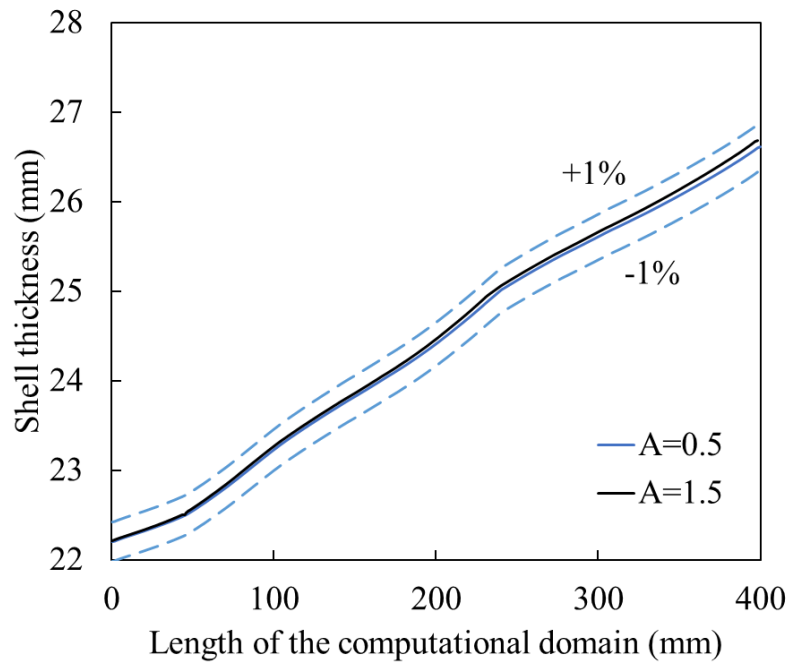
Figure 4-26. Comparison of shell thickness at the crystal constant of 0.5 and 1.5.
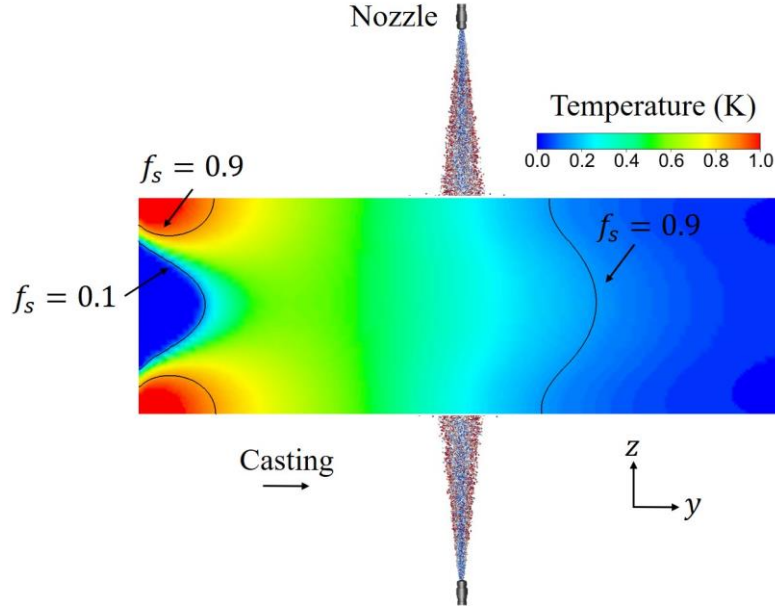
Figure 4-27. Solid fraction distribution in the casting direction at a crystal constant of 0.1.

The undesired convection and solidification process at low crystal constants has led to the need for a minimum crystal constant at which the increase of the effective viscosity is still within a reasonable range. From the physical meaning of the free floating dendrite model, the effective viscosity should always be larger than the dynamic viscosity in order to numerically produce a sluggish effect to represent the presence of free floating dendrites. Therefore, the ratio of $\frac{\mu_{eff}}{\mu_{st}}$ must be larger than or at least equal to unity throughout the free floating dendrite region:

$$\frac{\mu_{eff}}{\mu_{st}} = \left(1 - \frac{F_\mu f_{sol}}{A_{mushy,mini}}\right)^{-2} \geq 1 \tag{250}$$

Rearranging Eq. (250) and solving for $A_{mushy,mini}$, yields:

$$A_{mushy,mini} \geq \frac{F_\mu f_{sol}}{2} \tag{251}$$

Figure 4-28 shows the minimum crystal constant as a function of the solid fraction at different critical solid fractions. The distribution of the minimum crystal constant follows that of the relative

viscosity, which increases almost linearly from the liquid-mushy zone interface to the point near the critical solid fraction and drastically decreases to less than 0.01 beyond the critical solid fraction. In addition, the minimum crystal constant also depends on the value of the critical solid fraction, which determines the end of the linear increase of the minimum crystal constant. At higher critical solid fraction, the minimum crystal constant maintains a steady increase as most of the mushy zone is treated as the free floating dendrite region. It is worth mentioning that the minimum crystal constant defined in Eq. (251) is the optimum value and should not be considered the basis for model calibration. It is more of a numerical criterion that forces the free floating dendrite model to constantly increase the liquid viscosity instead of decreasing. As discussed previously, the ratio of $\frac{\mu_{eff}}{\mu_{st}}$ increases significantly by several orders of magnitude as the crystal constant approaches the minimum value. Thus, to avoid numerical instability, the optimum value should be higher than the minimum value but maintains relatively low to produce sufficient effective viscosity in the free floating dendrite region.
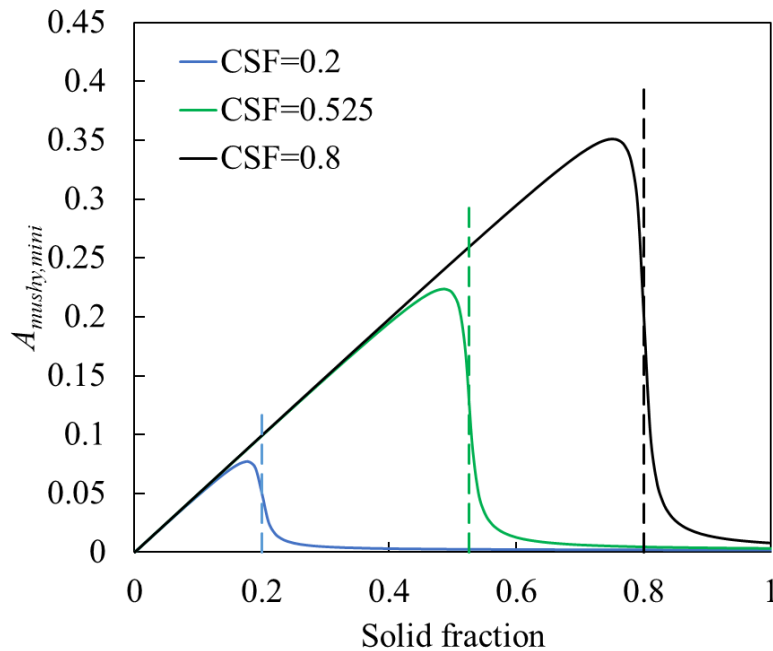
Figure 4-28. The minimum value of crystal constant as a function of the solid fraction at different critical solid fractions.

Effect of switching function constant

The switching function given in Eq. (181) and Eq. (182) is used to switch between flow resistance models based on the local solidification condition. As described in Figure 2-30, in the early stage of solidification, equiaxed dendrites nucleate in the supercooled liquid and move together with the liquid. Since the relative velocity between the two phases is small, the effect of drag force can be treated as the increase of the liquid viscosity. In the later stage of solidification, a fixed columnar dendrite network forms near the surface, and the relative motion between the two-phase becomes more important. In addition, the liquid flow also moves between interdendritic regions, which further increases the flow resistance. As acknowledged in previous studies, the interdendritic flow is governed by Darcy's law [312-316]. Since then, different methods have been proposed to combine the two flow resistance models into one continuum models [269, 271, 317].

Oldenburg and Spera proposed a hybrid model and used switching functions to transition between the models [261]. The model was later improved by Chang and Stefanescu [277]. The switching function, F_μ, and its conjugate, F_p, were artificially selected to ensure a smooth transition. The constant coefficient before the solid fraction is the switching function constant. However, the origin of this constant was not documented in the research work of Oldenburg and Spera. A value of 100 was adopted by the two authors and the following researchers. Figure 4-29 illustrates the change of the switching function at different solid fractions while the switching constant ranges from 1 to 500. Although the transition between the two switching functions takes place at the critical solid fraction, the effect of the switching constant on the transition process is independent of the critical solid fraction. The only effect of critical solid fractions is to shift the entire figure by a specific value. To isolate the effect of the switching constant, the critical solid fraction is set to 0.525 in the current study.

As shown in Figure 4-29, the switching function for the free floating dendrite region is represented by solid lines, whereas its counterpart for the porous region is shown by dashed lines. The smoothness of the transition is controlled by the switching constant when the switching constant is less than 100. A smaller switching constant in this range corresponds to the long transition between the free floating dendrite region and the porous region. The interface between the two regions expands and penetrates both regions. The two regions become indistinguishable when the

switching constant reduces to zero, at which the entire domain is filled with well-mixed equiaxed and columnar dendrites. This is inconsistent with the existing observations. In the range of 80 to 120, the transition is insensitive to the switching constant. The switching between the two regions is rapid near the critical solid fraction, and the interface between the two regions is relatively thin. Beyond the value of 200, the increase of the switching constant further decreases the smoothness of the transition, which becomes rapid and steep near the critical solid fraction. Such behavior will result in a very thin interface between the two regions.
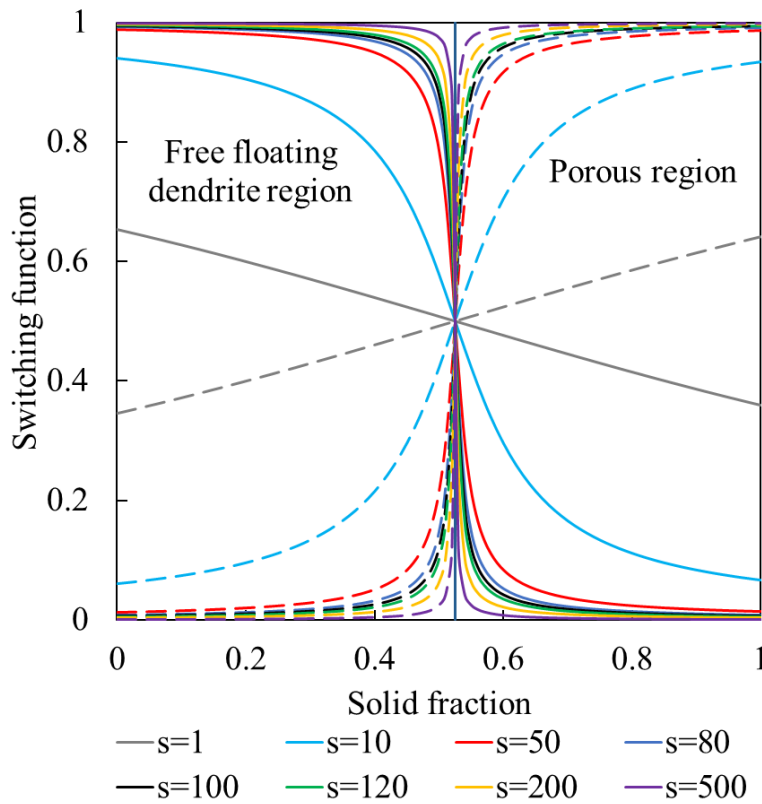
Figure 4-29. Switching function as a function of the solid fraction at different switching constants.

Figure 4-30 compares the velocity distribution from the spray cooling location on the surface to the liquid region in the slab at different switching constants. The liquid region ends at approximately 30mm from the surface, within which the flow velocity dramatically decreases to the casting speed. The difference in velocity distribution is indistinguishable when the switching constant is larger than 100. Although the value of the switching function differs by 0.1 as the

switching constant increases from 100 to 500, as shown in Figure 4-29, and the ratio of $\frac{\mu_{eff}}{\mu_{st}}$ increases by one order of magnitude as shown in Figure 4-31, such deviation is still negligible during the convection and solidification process. This is because the effect of switching constant on the flow viscosity is only noticeable when the solid fraction is in the range of 0.42 to 0.525. Even within this range, the damping effect from viscosity on the liquid flow is also indistinguishable despite the large difference in the ratio of $\frac{\mu_{eff}}{\mu_{st}}$, since the largest effective viscosity is already 86 times of the largest dynamic viscosity.
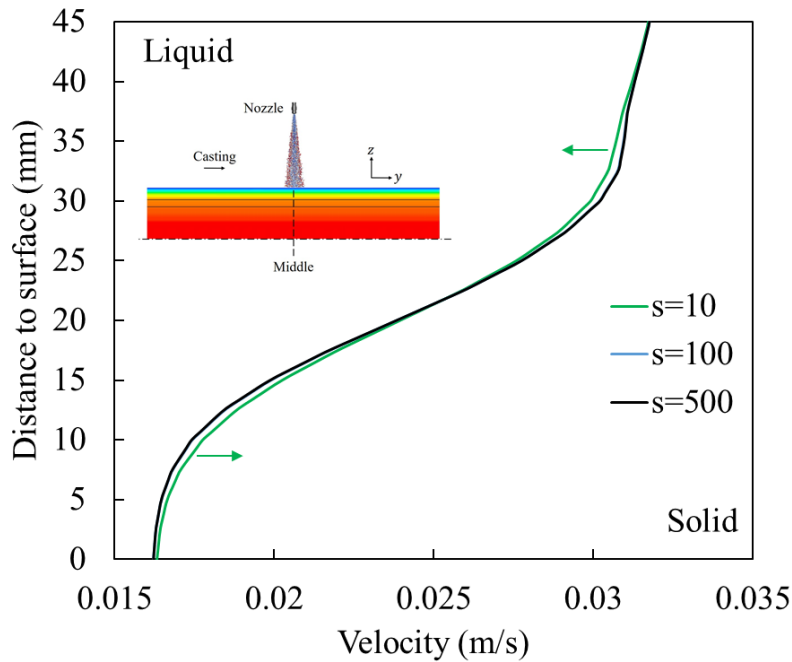
Figure 4-30. Comparison of velocity distribution at different switching constants.

When the switching constant decreases to 10, a well-mixed region is assumed between the free floating dendrite region and the porous region. The net effect of this mixing behavior is different in different regions. As shown in Figure 4-29 and Figure 4-30, as the transition becomes much smoother, the porous permeability model is activated early during the solidification process. Thus, the liquid flow also experiences significant porous resistance forces early in the domain. As a result, the velocity magnitude of the liquid flow is damped to some extent. On the contrary, the effect of porous resistance force is lowered beyond the critical solid fraction, and the lowered portion is replaced by the extension of the free floating dendrite model. The overall effect is the reduction of

the flow resistance. Therefore, the flow velocity in the mushy zone slightly increases, as shown in Figure 4-30.
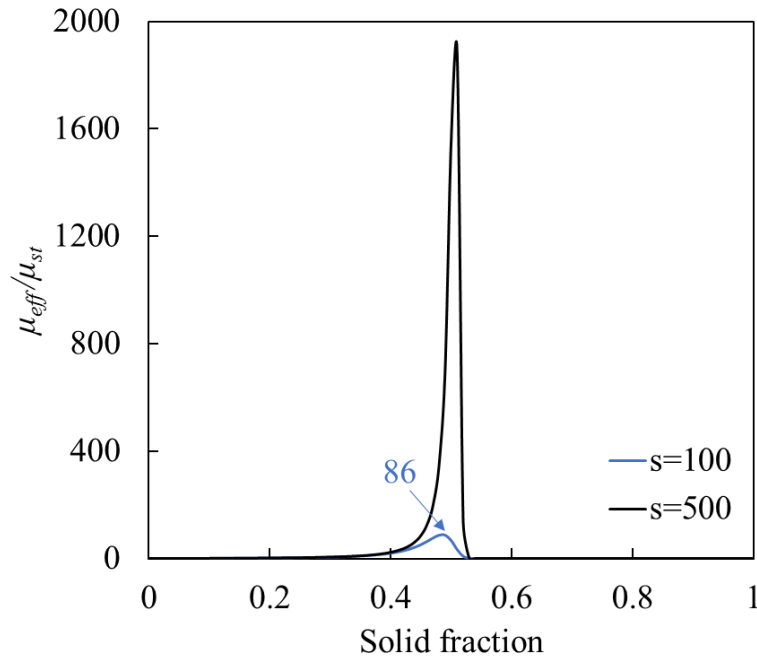
Figure 4-31. The ratio of effective viscosity and dynamic viscosity as a function of the solid fraction at different switching constants.

Figure 4-32 compares the shell thickness at different switching constants. Similarly, the shell thickness is virtually identical as the switching constant increases from 100 to 500. However, when the switching constant decrease to 10, the shell thickness also decreases by approximately 1%. The reason for the shell thickness reduction is primarily due to the change of the flow resistance. As shown in Figure 4-30, the flow resistance slightly increases at low solid fractions, and the flow velocity decreases by some extent in response to such an increase. Yet, the magnitude of the flow velocity is still higher than that in the mushy zone and solid region. Thus, no additional solidification occurs in the liquid region. In the meantime, the flow resistance decreases in the porous region, which allows the liquid flow to penetrate interdendritic regions as the liquid flow deliveries superheat to its surrounding, temperature in the mushy zone increases. Therefore, less solid forms as the switching constant decreases. Figure 4-32 compares the shell thickness from the solid front to the liquid front at different switching constants. The difference in the solid fraction is more evident in the porous region near the solid front, where the flow resistance should be sufficiently large to completely stop the liquid flow. With the aforementioned information, a

proper switching constant should be equal to at least 80 to ensure rapid transition at the critical solid fraction. The convection and solidification process is insensitive to the switching constant as it increases beyond 80.
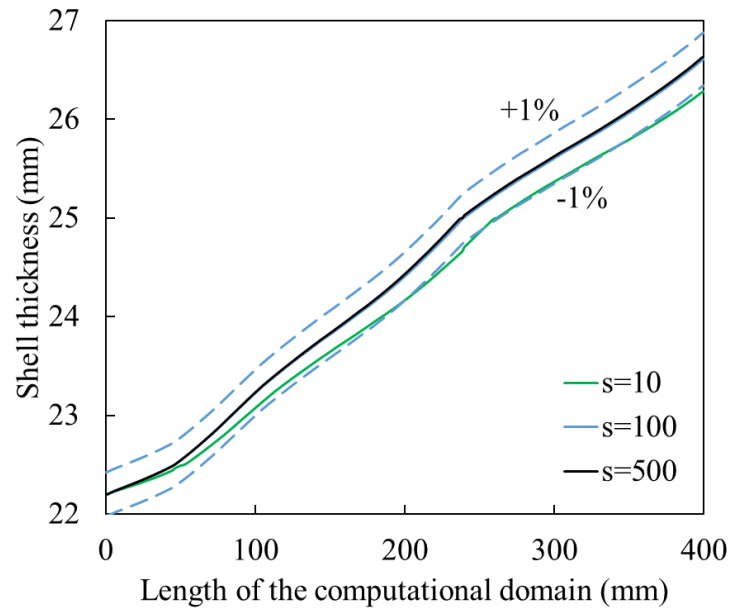
Figure 4-32. Comparison of shell thickness at different switching constants.
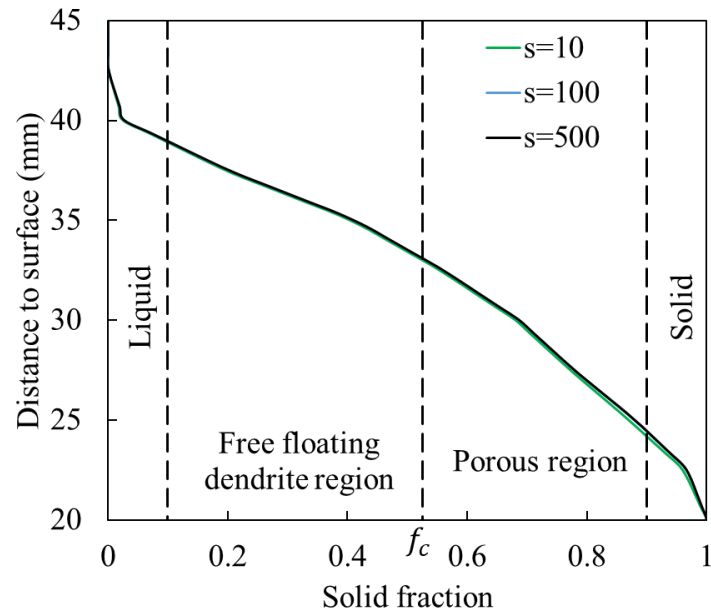
Figure 4-33. Solid fraction throughout the mushy zone and solid region at different switching constants.

Effect of cooling rate

As discussed in chapter 3, several factors can affect the heat transfer on the slab surface. Some key factors include spray nozzle type, spray flow rate, standoff distance, casting speed, spray angle, nozzle-to-nozzle distance, nozzle arrangement, and a few others. The effect of nozzle-to-nozzle distance and nozzle arrangement on the solidification process will be discussed in the later multi-spray section. The net effect of the rest factors on the heat transfer process is to either change the spray-affected area or change the HTC within the spray-affected area. However, variations of the spray-affected area can be treated as the change of the HTC on the surface. For example, when the standoff distance increases, the spray-affected area expands in both casting and slab width directions, and HTC_{avg} within the spray-affected area decreases. If the slab is only cooled by one spray, then the change of the standoff distance affects both the spray-affected area and the HTC on the surface. Yet, during the actual secondary cooling process, the slab is cooled by multiple sprays in the slab width direction. If the spray-affected area of each nozzle increases, the total cooling length is still equal to the width of the slab. Overall, the only difference when the standoff distance increases are the decrease of HTC on the surface. The variation of the spray-affected area in the casting direction has a similar effect on the overall heat transfer rate. Therefore, to better understand the fundamental changes of the solidification process under different spray cooling conditions, it is necessary to examine the change of HTC on the surface. Furthermore, the current study converts the HTC to heat flux through the surface to include the effect of surface temperature, which significantly affects the temperature gradient within the slab.

Figure 4-34 summarizes the maximum and minimum heat flux through slab surface under different spray cooling conditions from the study of heat transfer on the slab surface. From the investigated operating conditions, the minimum heat flux through slab surface is about 5W/cm^2, whereas the maximum heat flux is around 125W/cm^2. In the baseline condition, the average heat flux within the spray-affected area is approximately 55W/cm^2. To compare the effect of different heat fluxes on the convection and solidification process within the slab, three heat fluxes, which are 5W/cm^2, 55W/cm^2, and 125W/cm^2, are considered in the current study. The corresponding heat flux distribution from the study of surface heat transfer is applied to the current simulation as the thermal boundary condition.
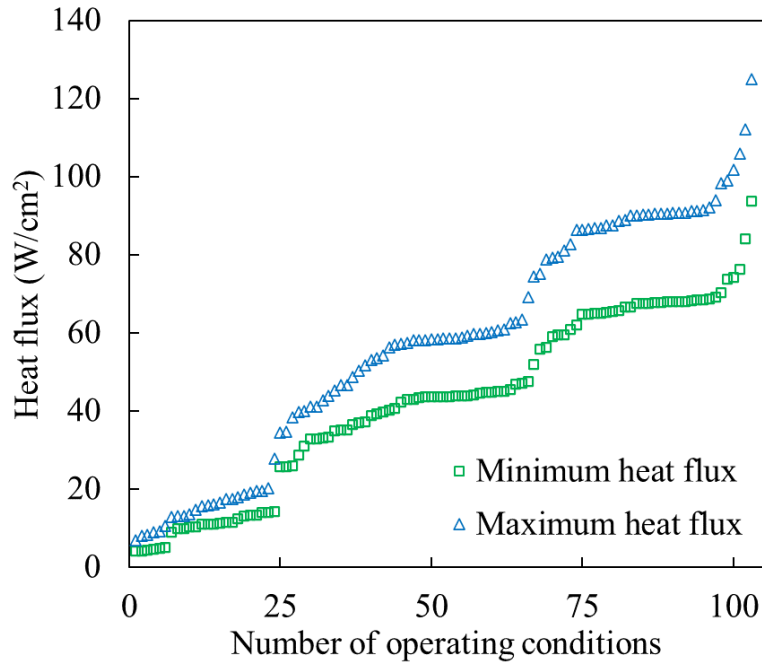
Figure 4-34. Heat flux through slab surface under different spray cooling conditions.

Figure 4-35 compares the Re number distribution in the casting direction at the three heat fluxes. The average Re number and other critical parameters during the convection and solidification process are summarized in Table 4-3. The Re number of the liquid flow and in the mushy zone is insensitive to the heat transfer on the surface. More noticeable changes are observed in the solidified shell. The Re number decreases in the solid region as the heat transfer rate increases on the surface, which also leads to the increase of the cooling rate throughout the solid region, as shown in Figure 4-36.
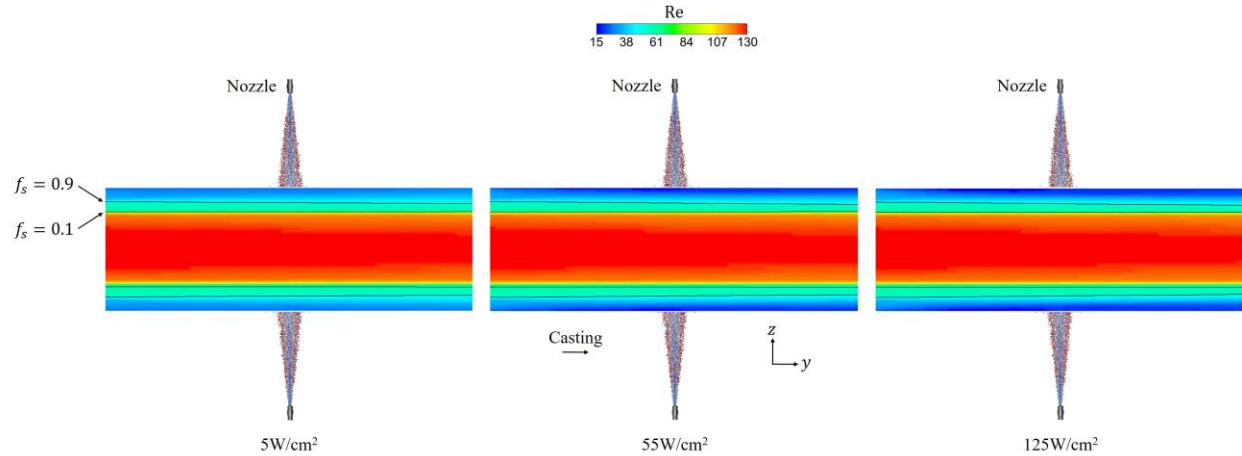
Figure 4-35. Comparison of the Re number in the casting direction at different heat fluxes due to surface spray cooling.
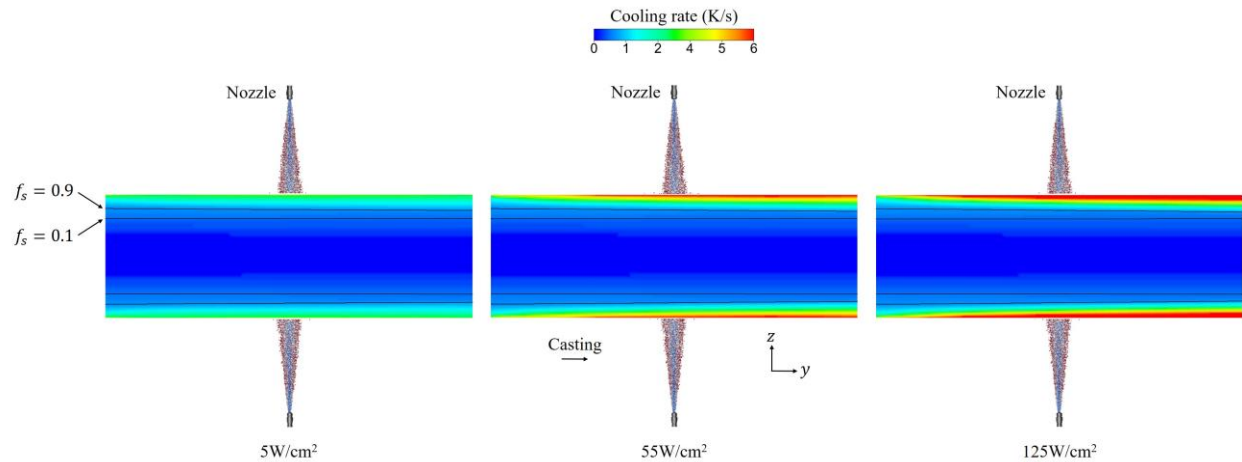
Figure 4-36. Comparison of cooling rate variation within the slab at different heat fluxes due to surface spray cooling.

As shown in Figure 4-37 and Table 4-3, the average temperature in the liquid region and mushy zone is relatively constant regardless of the spray cooling condition on the surface. The significant impact of the heat transfer rate on the surface is on the slab surface temperature. Higher heat flux, which corresponds to intensified spray cooling conditions such as short standoff distance, higher spray flow rate, narrow spray angle, and two-fluid spray, can result in much lower surface temperature. While the average temperature in the mushy zone maintains relatively constant, the lower surface temperature can cause a much steeper temperature gradient across the solid region, which is the inverse of the slope in Figure 4-37. The temperature difference gradually decreases

from the surface to the liquid front, and the three temperature profiles in Figure 4-37 converges to the same point in the liquid region. Under the current operating condition, the effect of surface heat transfer disappears at approximately 25mm below the surface. Further downstream in the secondary cooling region, where the solidified shell is much thicker, the influence of the spray cooling can penetrate deeper in the slab but with a much lower temperature gradient.
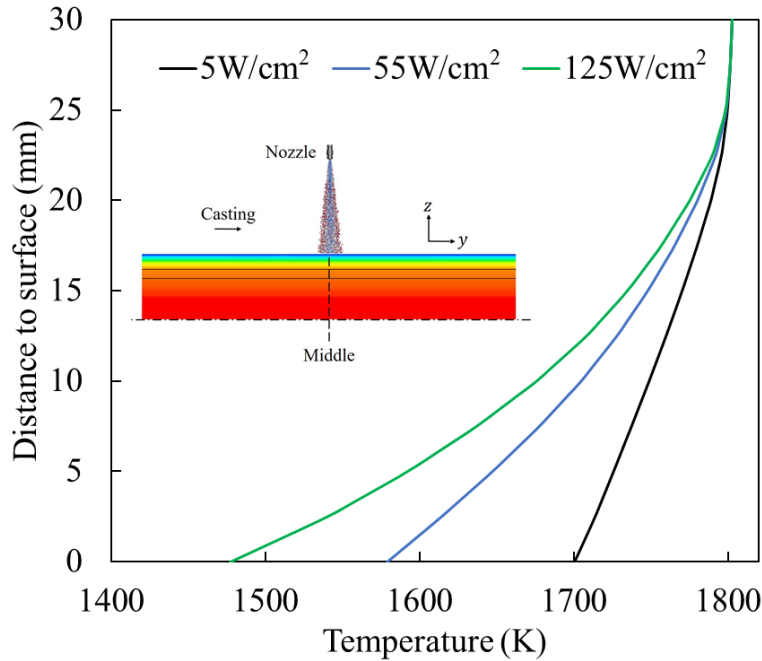
Figure 4-37. The temperature throughout the mushy zone and the solid region at different heat fluxes due to surface spray cooling.

Figure 4-38 shows the effect of surface temperature or cooling rate is significant to the solidification process. Within 80mm to the upstream surface, the difference in shell thickness is negligible. The boundary condition on the upstream surface still dominates the initial shell growth, and the surface heat transfer rate is also low without spray cooling. As the semi-solidified slab continues to move in the casting direction, the shell thickness curves diverge and increase at different rates. Compared to the baseline condition, the shell thickness at lower surface heat flux decreases by a maximum 5% at the downstream surface, whereas the shell thickness increases by about 3% at the exact location if the surface heat flux doubles. The location where the shell thickness differs from the baseline is upstream of the spray cooling location. According to the study of surface heat transfer, the spray-affected area extends about 27.33mm in the casting

direction. Yet, the effect of spray cooling already becomes important in the upstream of the spray cooling due to heat conduction within the solid region. As shown in Figure 4-39, the shell growth rate exhibits a much stronger dependence on the surface heat flux. The difference from the baseline condition is as high as 30% in the low heat flux simulation. If the current spray cooling conditions are applied to all the nozzles at a continuous caster, the metallurgical length will differ to a great extent. This is the reason that spray cooling control is one of the most effective methods to adjust the metallurgical length during the continuous casting operation.
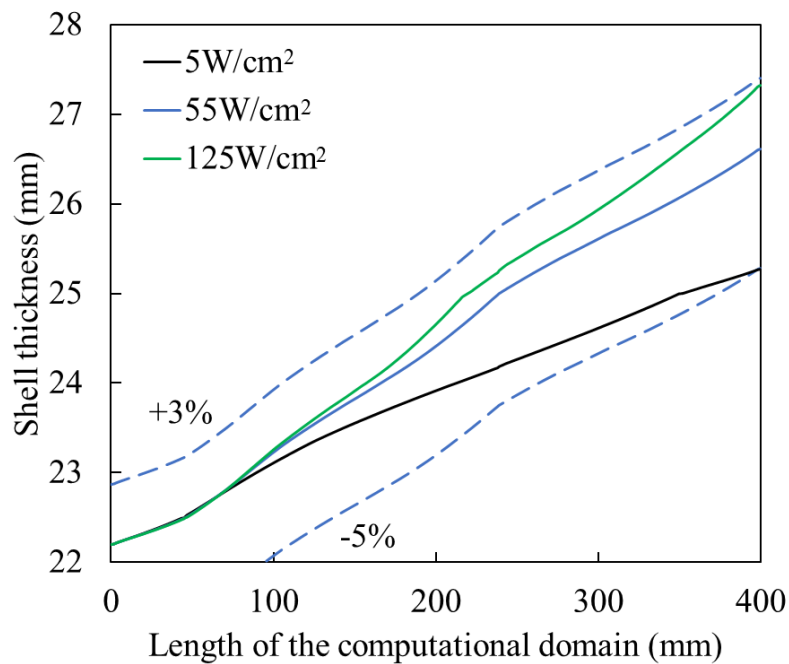
Figure 4-38. Comparison of shell thickness at different heat fluxes due to surface spray cooling.
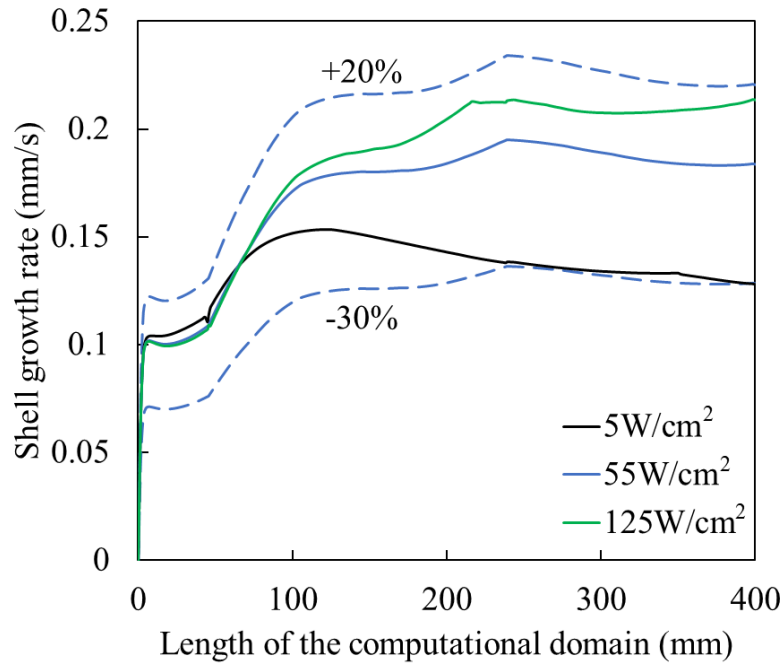
Figure 4-39. Comparison of shell growth rate in the casting direction at different heat fluxes due to surface spray cooling.

Table 4-3. Summary of the key parameters during the convection and solidification process at different heat fluxes.

Parameter		5W/cm²	55W/cm²	125W/cm²
Average Re number	Liquid	122.5	122.3	122.3
	Mushy	56.2	56.4	56.5
	Solid	31.6	28.7	27.8
Average temperature (K)	Liquid	1814.9	1814.9	1814.9
	Mushy	1802.9	1803.1	1803.1
	Solid	1756.8	1719.4	1694.2
Average cooling rate (K/s)	Liquid	0.0935	0.0933	0.0932
	Mushy	0.418	0.415	0.413
	Solid	1.70	2.73	3.44
Shell thickness increase (mm)		3.07	4.41	5.12
Average shell growth rate (mm/s)		0.135	0.169	0.182

Effect of rolls

As discussed in chapter 3, the effect of rolls on the surface heat transfer is to increase the total heat transfer through roll contact heat conduction in addition to restricting droplet distribution, as shown in Figure 3-58. On average, about 13.62% of the total energy through the slab surface is transferred to the roll. To investigate the effect of roll on solidification within the slab, two rolls with a diameter of 70mm are considered on each side of the broad face. The indentation on the slab surface caused by rolls is assumed to be 0.5mm, corresponding to a 7° contact angle. The two rolls are placed 50mm from the spray upstream and downstream, respectively. The heat transfer behavior between the slab and rolls within the rolls can be found in chapter 3.

The effect of the presence of rolls on solidification is shown in Figure 4-40. Compared to the baseline simulation, the initial shell thickness is thinner when a roll is placed between the spray and the upstream surface. This is because the gliding droplets toward the upstream surface are blocked by the presence of the roll. The increased heat transfer due to roll contact does not entirely compensate for the loss of droplet boiling heat transfer in this region. Thus, the net effect is the reduction of shell thickness upstream of the spray.

Once the slab passes the upstream roll and enters the inter-roll region where droplets are confined, the cooling rate noticeably increases across the solid region, as shown in Figure 4-41. When the slab reaches the downstream surface, the cooling rate in most of the solid regions has increased to more than 6K/s. While in the baseline simulation, only the near-surface region is cooled at such a high cooling rate. As a result, the shell thickness with the presence of rolls surpasses that in the baseline simulation. By the time when the moving slab reaches the downstream surface, the difference in shell thickness between the two simulations increases to more than 1.5%. Hence, the presence of rolls has two effects on the surface heat transfer and solidification process. One is to increase the total heat transfer by about 13%, and the other, which is more important, is to increase the heat transfer in the inter-roll region by confining the reflected droplets between rolls.
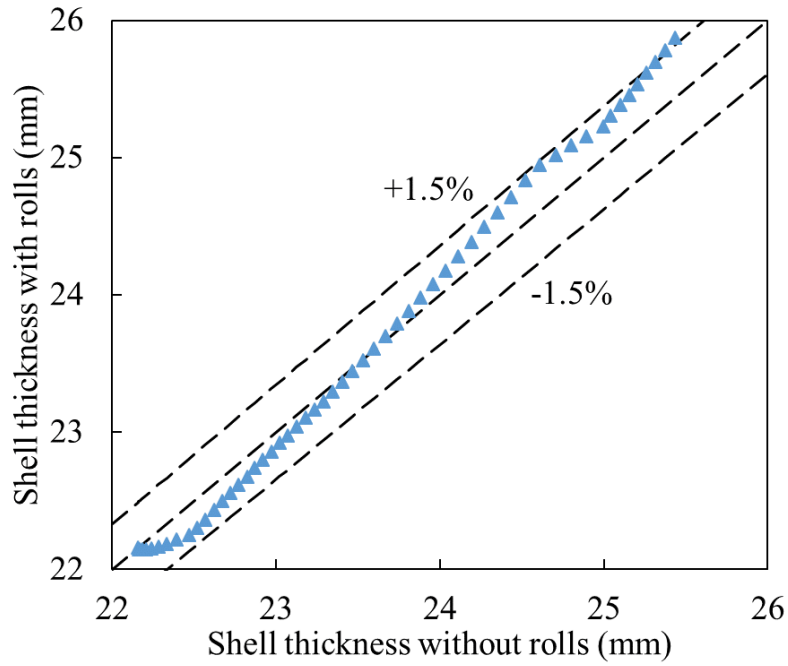
Figure 4-40. Comparison of shell thickness with and without rolls.
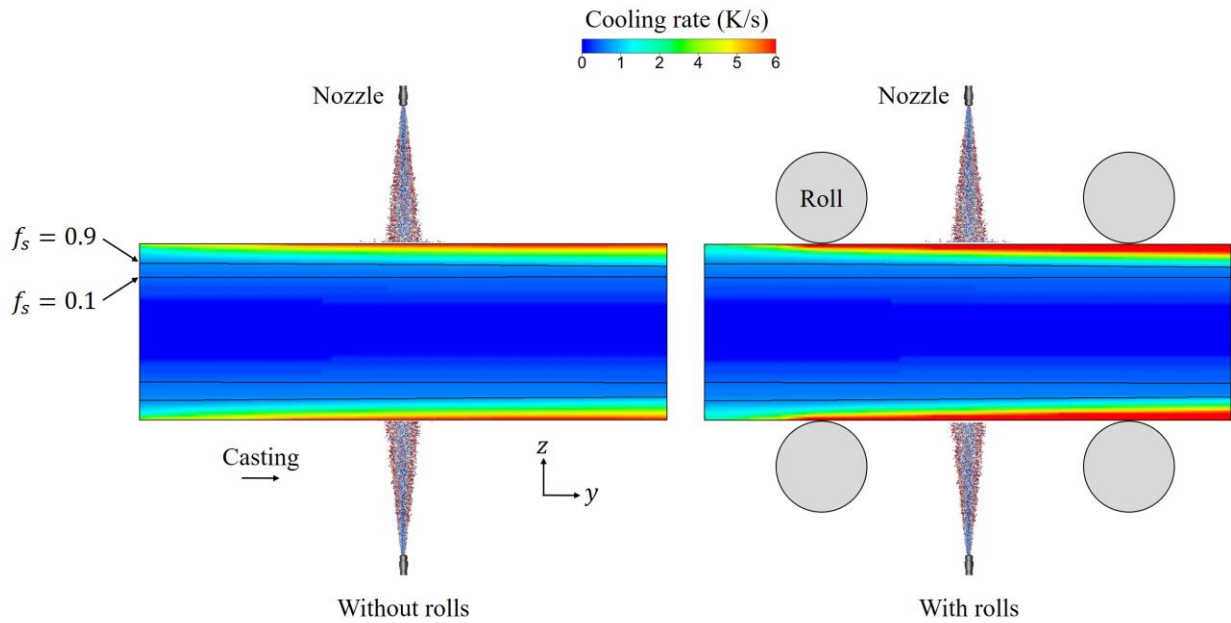
Figure 4-41. Comparison of cooling rate variation within the slab with and without rolls.

Solidification coupled with HTC correlation prediction

In section 3.4, a methodology that reduces the high-fidelity CFD simulations to mathematically simple expressions has been presented, together with the two-dimensional spatial reconstruction technique. The reconstructed two-dimensional HTC distribution is compared with that from the CFD simulation in Figure 3-85. The same HTC distributions are coupled with the solidification model, and the comparison of shell thickness is shown in Figure 4-42. The two shell thicknesses show a strong correlation with each other, and the difference is within 1%. As shown in Figure 3-82, the correlation predicted HTC differs from the CFD simulation predicted HTC to some extent under certain operating conditions, primarily due to the multi-variable nature embedded in the correlation. However, the impact of such difference in HTC on the surface decreases within the slab as temperature variation rapidly dissipates in the solid region through heat conduction. Thus, the difference in shell thickness at the solid front, which is more than 22mm below the surface, reduces to less than 1%. If the correlation predicted HTC is applied to the later stage of solidification where the solid region is close to half of the slab thickness, the difference in the surface heat transfer would further decrease.

$$\delta_{st,spray}=0.9983\delta_{st,\mathrm{HTC}}+0.0873$$
$$R^2=0.9989$$
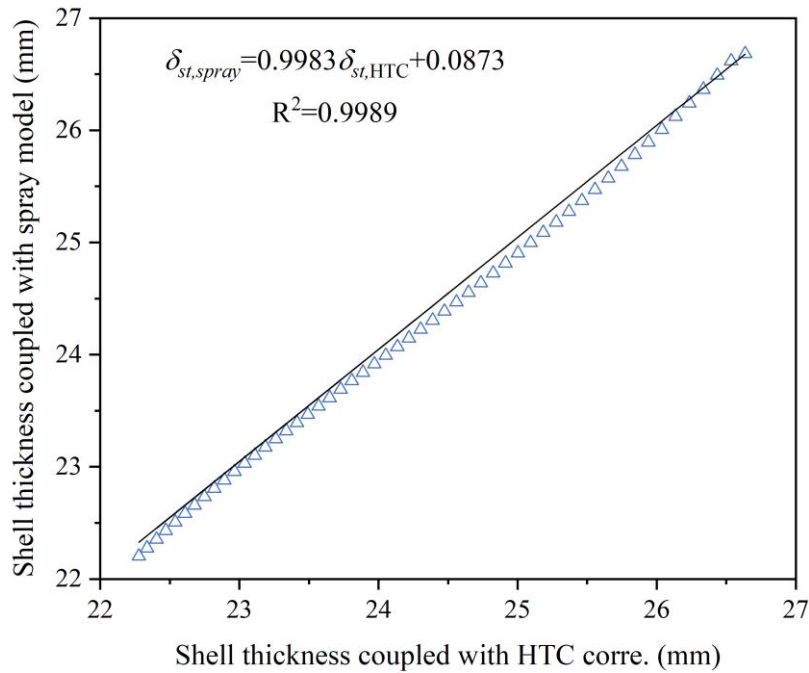
Figure 4-42. Comparison of predicted shell thickness from solidification simulations coupled with spray cooling model and with HTC correlation.

4.2 Solidification coupled with multi-spray cooling

4.2.1 Investigation of solidification in a slab segment

Effect of nozzle-to-nozzle distance

The previous sections have discussed the effect of a single spray on the convection and solidification process in the slab region. However, as shown in chapter 3, the interaction of the adjacent sprays in the slab width direction also plays a vital role in determining the heat transfer intensity and uniformity on the slab surface. The effect of this interaction can be quantified by the ratio of D/H. The optimum range of D/H is given in Eq. (221) and illustrated in Figure 3-48. For a 90° flat-fan nozzle, the recommended range of D/H is between 0.5 and 2. In this section, the effect of different ratios of D/H on solidification will be investigated. Three values of D/H are considered in the current study, which are 0.5, 1, and 2. The three ratios correspond to the scenario of substantial overlap, moderate overlap, and separation of two adjacent sprays.

The droplet distribution and heat transfer on the slab surface are discussed in chapter 3, and the influence on the spray-affected area is shown in Figure 3-45. At $D/H = 0.5$, the spray affected areas from the two adjacent sprays are indistinguishable and merge as one area. At $1 < D/H < 2$, the two spray affected areas overlap to some extent but can still be recognized as two separate areas. Once the D/H increases to 2 and beyond, the two adjacent sprays no longer interact with each other, and the two spray-affected areas are divided by a "fountain", where droplets are raised by the circulating flows local stagnation region. The difference in the surface heat transfer also affects the solidification process within the slab.

Figure 4-43 shows the cooling rate profiles at different depths inside the slab from the surface. The origin is fixed on the surface, and the distance to the surface is represented by negative numbers. The cooling rate profiles vary accordingly with the temperature variation on the surface. At $D/H = 0.5$, higher cooling rate is observed in the middle of the slab where the two adjacent sprays impinge and act as a single spray, as shown in Figure 4-43 (a). The fluctuations of the cooling profile at 0.1mm below the surface reflect the spray-affected area, and the effect of the two sprays are indistinguishable. Deeper into the solid region, the variations of the cooling rate gradually disappear as the heat conduction in the solid region tends to homogenize the temperature

distribution in the slab width direction. The variations vanish at 3mm below the surface except at the center of the slab. The two adjacent sprays overlap at the center of the slab, where droplet concentration reaches the maximum. Thus, the highest cooling rate occurs at such a location. The higher cooling rate at the center of the slab is still visible at 8mm below the surface. The effect of surface heat transfer and the overlap of the two adjacent sprays completely disappear at 10mm below the surface. In most secondary cooling operations, the initial shell thickness at the mode exit is between 20mm to 40mm. 10mm below the surface only accounts for less than half of the shell thickness. Hence, the surface heat transfer condition mainly affects the near-surface region, beyond which the effect of surface heat transfer is virtually uniformly distributed to the entire solid region through heat conduction. This thermal homogenization process also ensures that the fluctuations of heat transfer on the surface have a minimum impact on dendrite formation. Otherwise, a considerable variation of the final dendritic structure will undermine the slab quality.

At $D/H = 1$, wider fluctuations are seen in the near-surface cooling rate profile as the spray-affected area increases. Under the current condition, the two adjacent sprays have moderate overlap at the center of the slab. However, the highest cooling rate does not occur at the slab center because the two sprays are competing instead of merging as one spray, as shown in Figure 3-45. This is the reason that the cooling rate suddenly decreases at the slab center. The fluctuations of cooling rate within each spray-affected area rapidly disappear at 3mm below the surface. The more considerable variation in the middle continues to penetrate the solid region, and the effect is still noticeable at 10mm below the surface, as shown in Figure 4-43 (b). When the ratio of D/H increases to 2 and beyond, the spray-affected area expands to the entire slab surface, but most variations vanish at 3mm below the surface. At the center of the slab, the "fountain" effect causes a visible decrease of the cooling rate, which is still detectable at 10mm below the surface, as shown in Figure 4-43 (c). To avoid thermal stress and strain-related defects in the final products, localized temperature variation deep in the solid region should be prevented. Nevertheless, the variations of cooling rate in the slab width direction have little impact on the shell growth in the casting direction, as shown in Figure 4-44. The shell thickness profiles at different nozzle-to-nozzle distances are almost identical since the overlap effect does not change the spray and heat transfer behaviors in the casting direction.
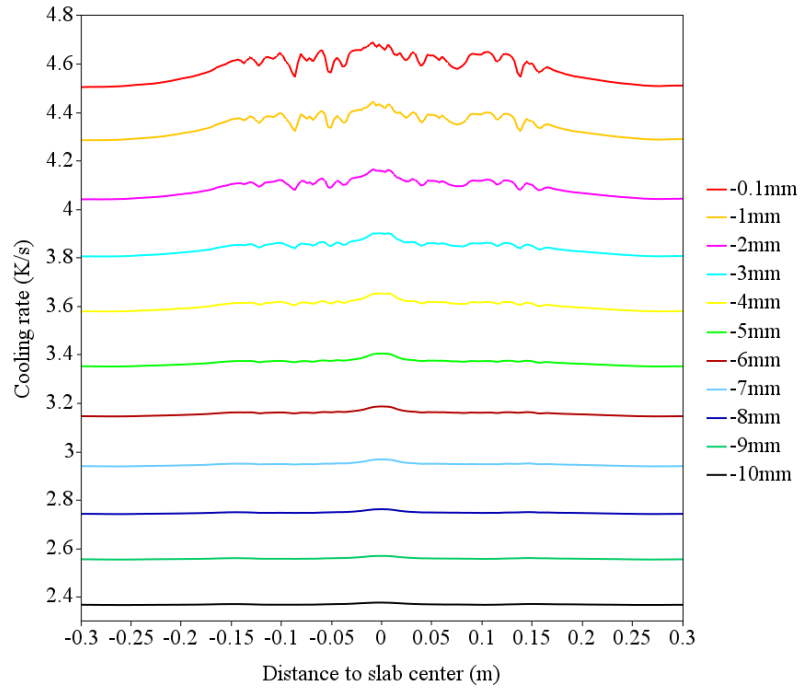
(a)
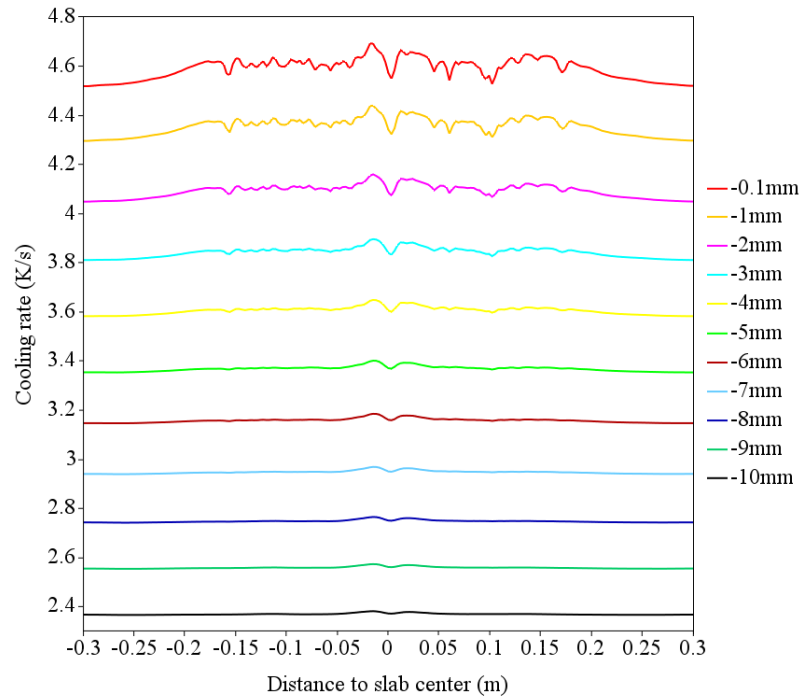
(b)

Figure 4-43. Comparison of cooling rate variation in the slab width direction at different depths inside the slab and different ratios of D/H: (a) $D/H = 0.5$, (b) $D/H = 1$, and (c) $D/H = 2$.

Figure 4-43 continued

(c)
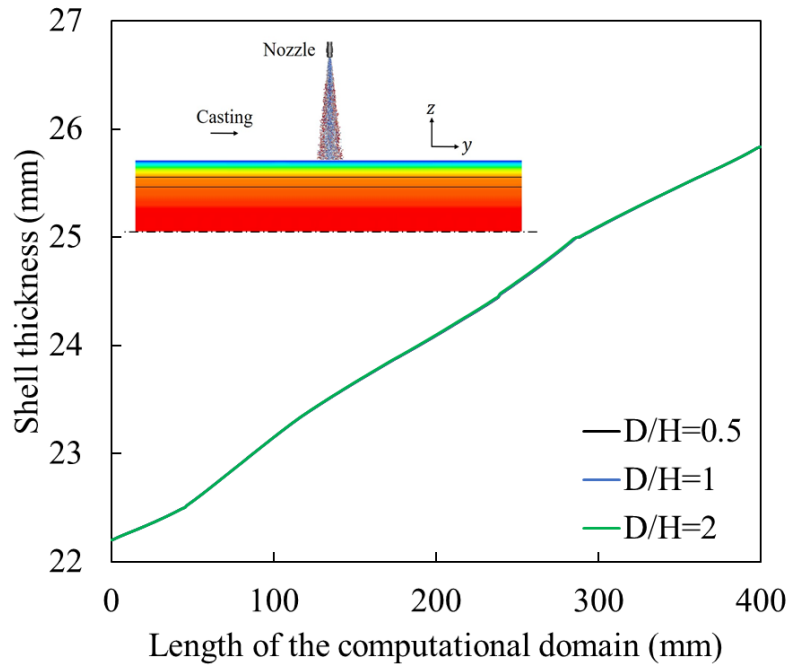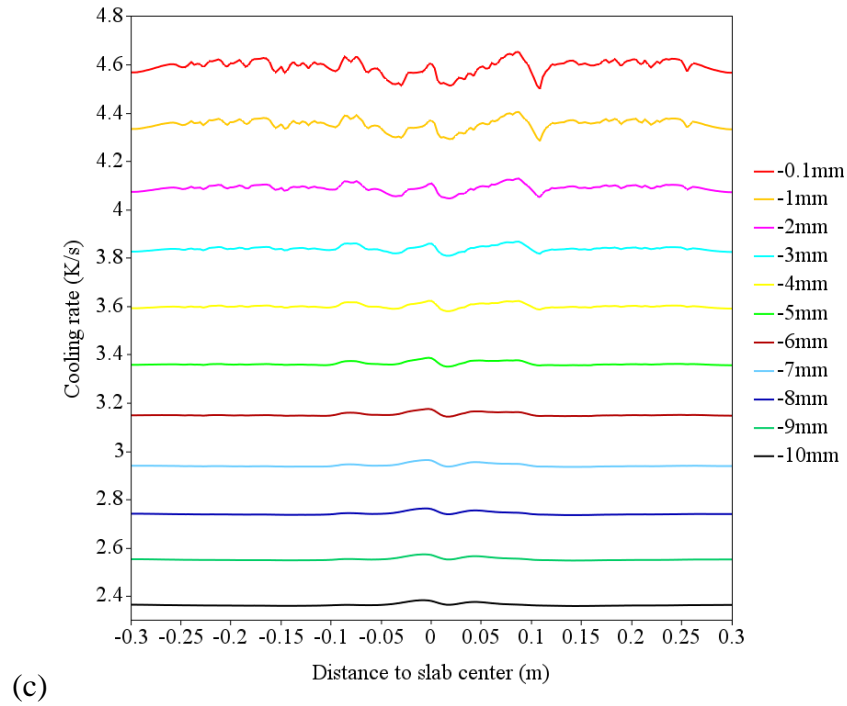
Figure 4-44. Comparison of shell thickness in the casting direction at different ratios of D/H.

Effect of arrangement of nozzles

As discussed in chapter 3, the spatial arrangement of nozzles at the same row and between the adjacent rows significantly affects the uniformity of heat transfer on the slab surface. Two of the widely adopted nozzle arrangements are investigated in the previous chapter using the spray cooling model. The staggered arrangement is recommended for intense and uniform spray cooling practice. In the current section, the effect of the nozzle arrangement on the heat transfer and solidification process within the slab will be evaluated. Six sampling locations within the slab are selected for comparison. The relative position of the sampling locations is shown in Figure 4-45. There are three sampling locations in both the casting and slab width directions, respectively. The sampling locations in the slab width direction, which are W1, W2, and W3, pass through the three rows of sprays in both arrangements. The sampling location C1 and C3 pass through the sprays at the first and third row in the casting direction in both arrangements. The sampling location C2 only passes through the spray overlap regions in the rectangular arrangement but passes the middle spray at the second row in the staggered arrangement.
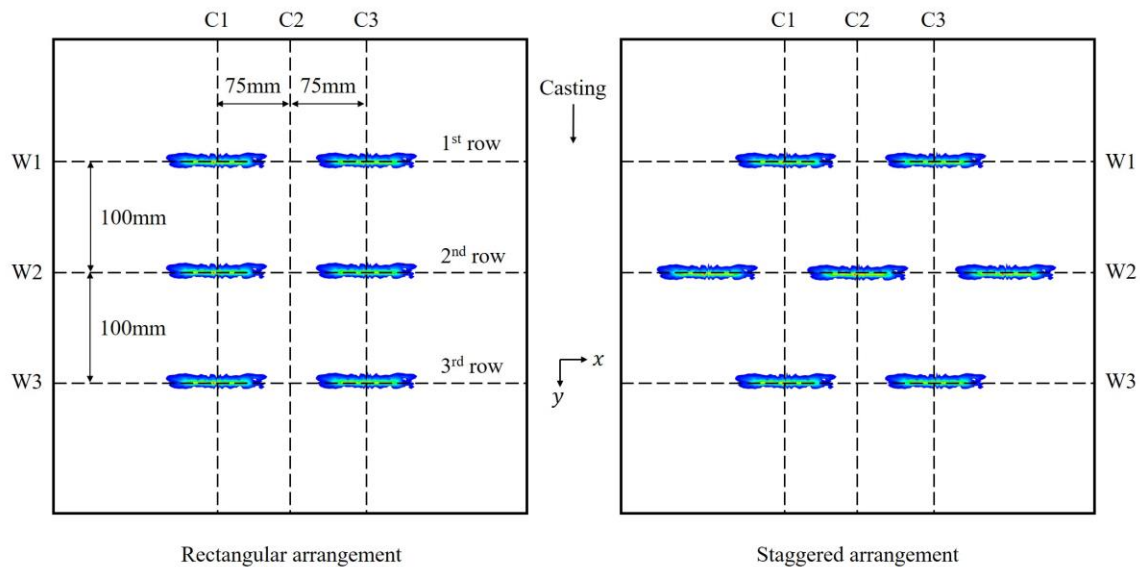
Figure 4-45. Top view of the sampling locations relative to nozzles in both arrangements (C and W stand for casting and width, respectively).

Figure 4-46 compares the cooling rate profile at different distances below the slab surface at the sampling locations of W1, W2, and W3. The arrow in the plot represents the center of a spray. As

346

shown in Figure 4-46 (a), when the high-temperature slab enters the first row of spray cooling, the effect of surface heat transfer can barely penetrate beyond 2mm below the surface regardless of the nozzle arrangement. This is because the first row of spray in the current study is assumed to be the first row in the secondary cooling region. At the sampling location of W1, the hot slab is only cooled by half of the spray in the casting direction. In addition, the nozzle arrangement at the first row is identical in both arrangements. Thus, the difference between spray cooling and other heat transfer mechanisms is yet to be evident.

Once the slab passes the second row, the difference in nozzle arrangement becomes more significant, as shown in Figure 4-46 (b). In the second row, the effect of spray cooling already dominates the surface heat transfer. Thus, the cooling profile becomes more sensitive to the arrangement of nozzles. In the rectangular arrangement, the two sprays are placed 150mm from each other, and the spray overlap occurs at the center of the slab, where a higher cooling rate is observed due to the increase of droplet concentration. The overlap effect extends at least 10mm below the surface before it disappears through heat conduction in the solid region. In the staggered arrangement, with the additional spray in the middle of the second row, the variation of cooling rate in the spray overlap region is suppressed. The three sprays act as a single spray and provide uniform cooling to the spray-affected area. As shown in Figure 4-46 (b), because the current study only considers three sprays at the second row, there are moderate fluctuations at the edge of the two side sprays. This behavior will be eliminated during the actual secondary cooling process when the entire slab width is covered by sprays. Nevertheless, the fluctuations at the edge of the sprays only propagate to 5mm below the surface.

At the third row of spray, similar cooling profiles are seen in the rectangular arrangement since the arrangement of nozzles there is identical to the first and second row. The effect of spray overlap on the surface also propagates to more than 10mm below the surface. While in the staggered arrangement, the variation of cooling rate is insignificant, and the effect of surface heat transfer rapidly disappears at 2mm below the surface. This again proves that the staggered arrangement decreases the temperature nonuniformity in the slab width direction. In terms of shell growth in the casting direction, as shown in Figure 4-47, the difference between the two arrangements is negligible since the surface heat transfer mainly affects the near-surface region.

347
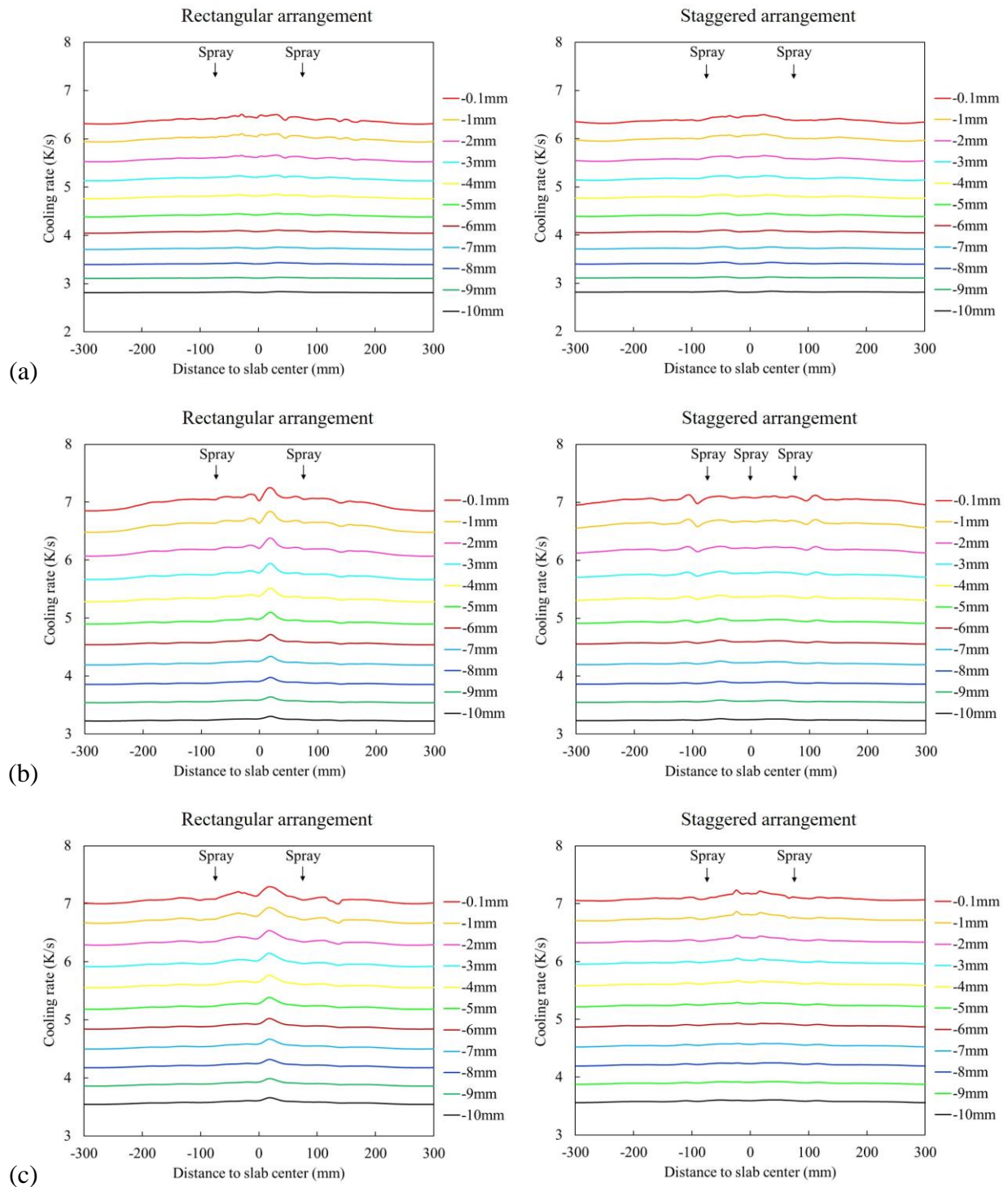
Figure 4-46. Comparison of cooling rate variation in the slab width direction at different depths inside the slab between the two nozzle arrangements and at: (a) W1, (b) W2, and (c) W3.
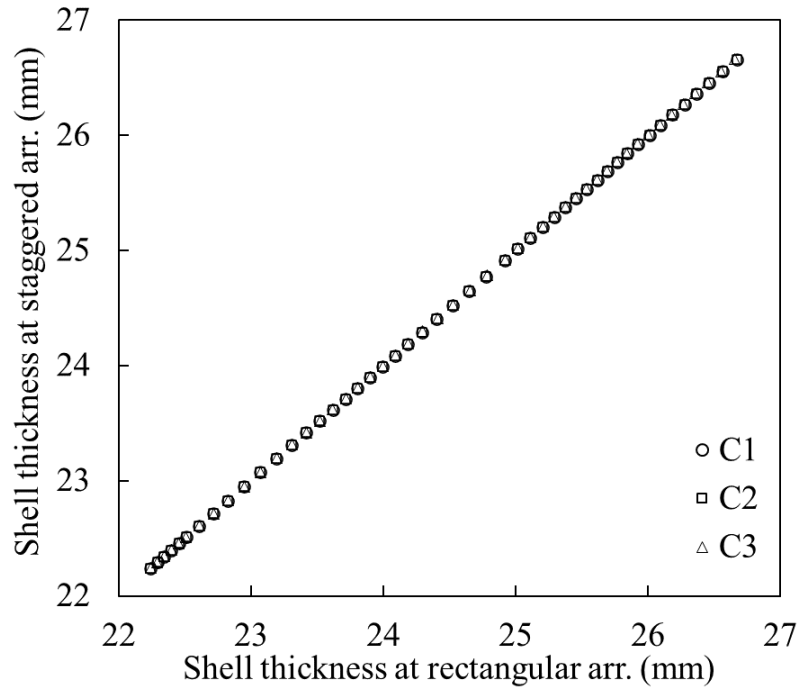
Figure 4-47. Comparison of shell thickness in the casting direction at different locations between the two nozzle arrangements.

4.2.2 Investigation of solidification in a thin slab

The configuration and the operation of the water sprays are pivotal for the quality of the solidified slab, as both undercooling and overcooling are undesired. Knowledge of jet impingement heat transfer with the moving slab and the sequential solidification is essential to optimize the casting operation, especial for the initial solidification stage where sufficient cooling rate must be provided to maintain a proper solidification rate; otherwise, breakout incident might occur. The current study utilizes a thin slab casting machine to demonstrate the application of the aforementioned surface heat transfer model and solidification model, together with the coupling procedure. The computational domains, boundary conditions, and coupling procedure are shown in Figure 2-32 and Figure 2-34. The typical operating conditions are summarized in Table 4-4. Certain parameters such as roll diameter, casting speed, and spray conditions vary slightly at different locations in the secondary cooling region and are considered as proprietary information. Hence, these parameters are given in ranges instead of exact values. The results of fluid flow and solidification in the primary cooling region can be found elsewhere [282, 283]. This section only focuses on fluid flow and solidification in the secondary cooling region.

Table 4-4. Summary of operating conditions at the thin slab casting machine.

Parameter	Value (range)
Ratio of slab width and thickness	20.25
Mold height (m)	0.8
Computational domain length (m)	2.5
Casting speed (m/s)	0.00833-0.0333
Superheat (K)	18-30
Roll diameter (m)	0.145-0.175
Roll pitch (m)	0.0875
Spray flow rate (kg/s)	0.179-0.222
Spray angle (°)	90-120
D/H	0.82-2.08
Air pressure (kPa)	310-330
HTC_{avg} (W/m²·K)	286-802

Fluid flow distribution

Figure 4-48 shows the fluid flow distribution on the center cross-section plane in the mold and slab. The results in the primary cooling region are obtained from the step 1 simulation, and the flow distribution in the secondary cooling region is calculated from the step 3 simulation. Because the investigated thin slab casting machine is equipped with a bifurcated SEN, the typical "double roll" pattern is observed in the primary cooling region. The concept of "roll" in the primary cooling region referrers to flow circulation. In the double roll mode, the molten steel jet issuing from one of the SEN ports splits into two streams upon impinging on the narrow face. One stream circulates along with the mold powder layer and returns to the SEN, forming the upper roll. The other stream, on the other hand, continues to travel downwards along the solidifying shell surface and returns to the center of the mold, forming the lower roll. Because the jet can impinge on the newly formed thin shell, the jet angle and the flow rate are both key research topics in the field of mold flow optimization. Otherwise, improper jet impingement will remelt the thin shell and can even lead to a breakout incident.

Under the current operating condition, the jet impingement occurs slightly above the mold exit. Thus, the lower roll further penetrates the secondary cooling region. As shown in Figure 4-48, the impact of the mold flow circulations can extend to 2m below the meniscus, which is equivalent to 1.2m below the mold exit. Within the penetration depth, the flow condition at the beginning of the secondary cooling region is still dominated by the flow characteristics in the primary cooling region. As the molten steel cools down, the slurry effect becomes more critical, and it slows down the liquid flow to some extent. In addition, flow resistance increases as the solidified region grow into the liquid region. Therefore, the circulation effect is considerably damped, and the liquid flow only maintains the velocity in the casting direction after the penetration depth.
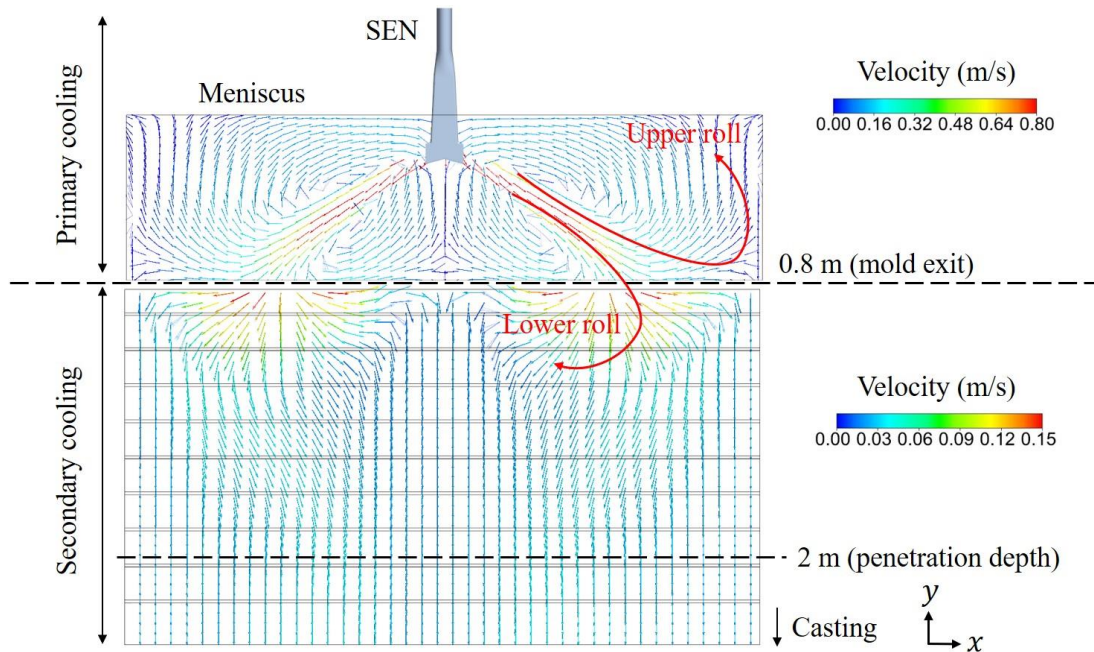
Figure 4-48. Front view of fluid flow distribution during initial solidification.

Figure 4-49 shows the Re number distribution on the center cross-section plane of the slab at the beginning of the secondary cooling region. The highest Re number occurs at the mold exit where the two lower rolls enter the secondary cooling region, after which a portion of the lower roll with higher velocity returns to the mold and the rest with lower velocity moves downward in the casting direction, as shown in Figure 4-49 (a). In the slab thickness direction, the solidified shell occupies some liquid regions, and the flow area reduces in the casting direction as solidification continues.

Due to the decrease of flow area, the liquid flow accelerates, and the Re number increases to more than 150 at the end of the current domain, as shown in Figure 4-49 (b).
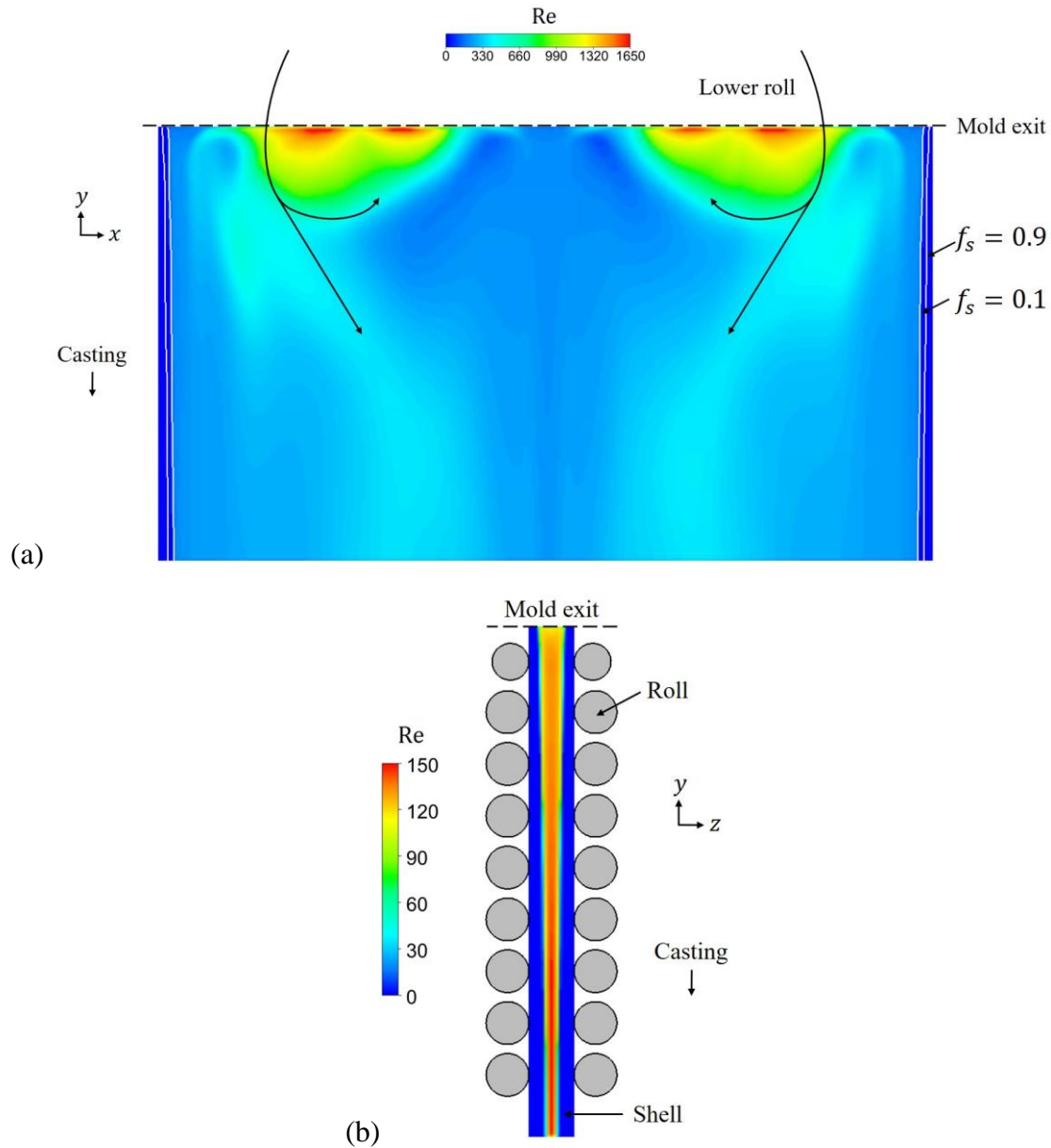
Figure 4-49. Re number distribution within the slab during initial solidification from: (a) front view, and (b) side view.

Figure 4-53 shows the sampling locations at eight different locations. Six sampling locations are on the center cross-section plane in the slab width direction, and the rest two sampling locations are on the center cross-section plane in the slab thickness direction. As shown in Figure 4-51, in

the slab width direction, the Re number peaks near the quarter of the broad face and rapidly reduces to 0.07 in the solid region. The magnitude of the Re number quickly reduces by more than 50% between the upstream and the middle sampling locations. In the lower portion of the domain, the variation of the Re number is insignificant compared to that in the upper portion of the domain. In the casting direction, the Re number at the center of the broad face maintains a relatively low value because flow velocity reduces as the two opposite moving lower rolls emerge at the center of the slab. In addition, the variation of the Re number at the center is negligible. On the other hand, at the quarter of the broad face, the Re number drastically reduces to approximately 250 from 1350 within 400mm below the mold exit, as shown in Figure 4-52. This is also the deepest potion where the returning lower roll can reach the secondary cooling region. The Re number slightly increases to 350 at about 800mm below the mold exit as the downward moving flow originating from the lower roll passes through the quarter of the broad face at half of the domain height. In the slab thickness direction, the profile of the Re number transitions from the flat distribution at the upstream to the parabolic distribution at the downstream, as shown in Figure 4-53. In the upper portion of the domain, the profile of the Re number decreases in the slab thickness direction and increases in magnitude in the casting direction as the flow area reduces. While in the lower portion of the domain, both the magnitude and spread of the Re number decrease as the liquid flow experiences more resistance from expanding mushy zone.
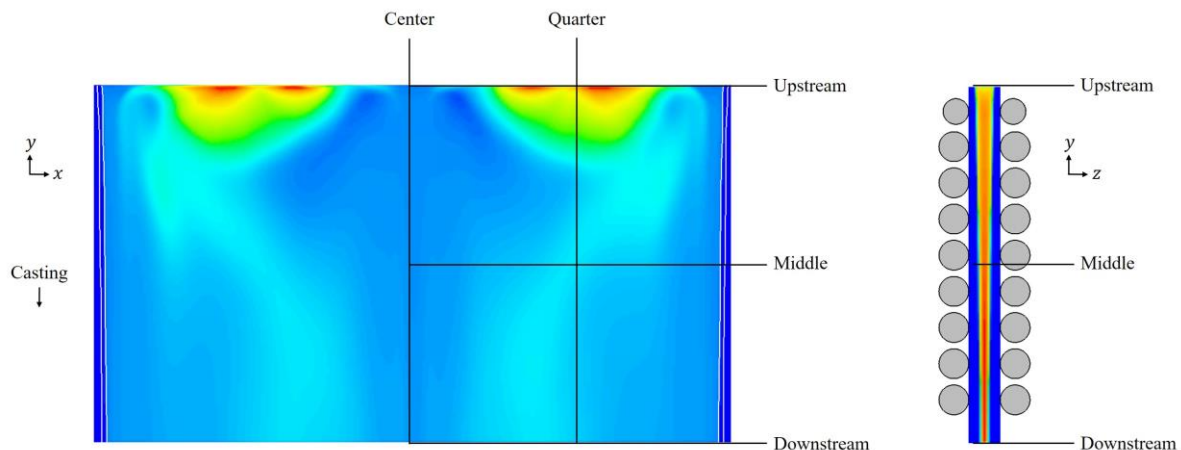
Figure 4-50. Illustration of the sampling locations at the beginning of the secondary cooling region.
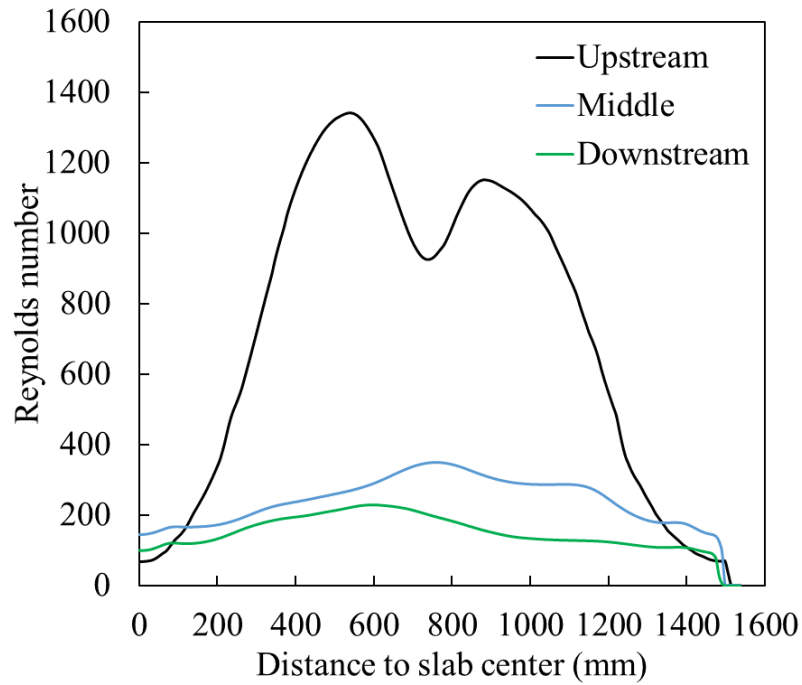
Figure 4-51. Re number variation in the slab width direction at the beginning of the secondary cooling region.
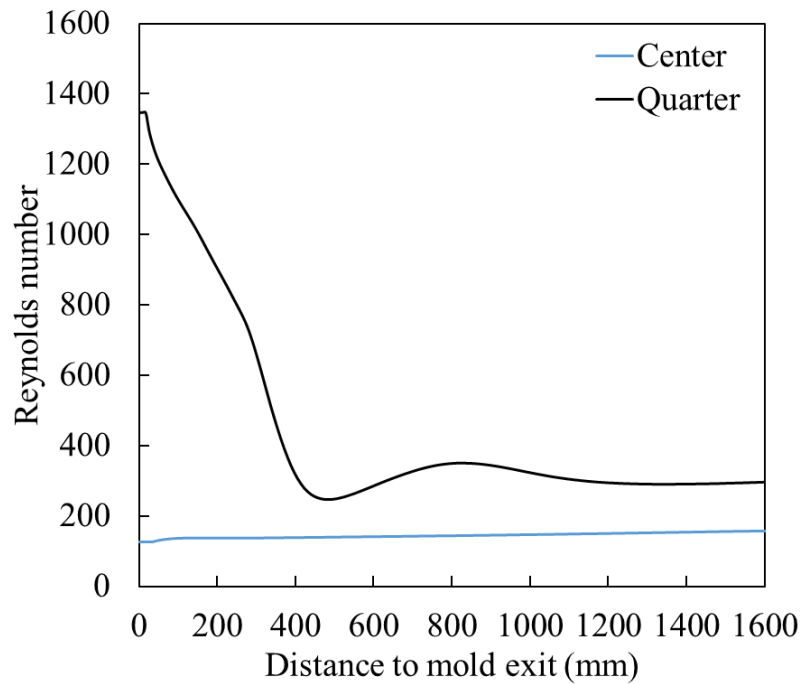
Figure 4-52. Re number variation in the casting direction at the beginning of the secondary cooling region.

(d)
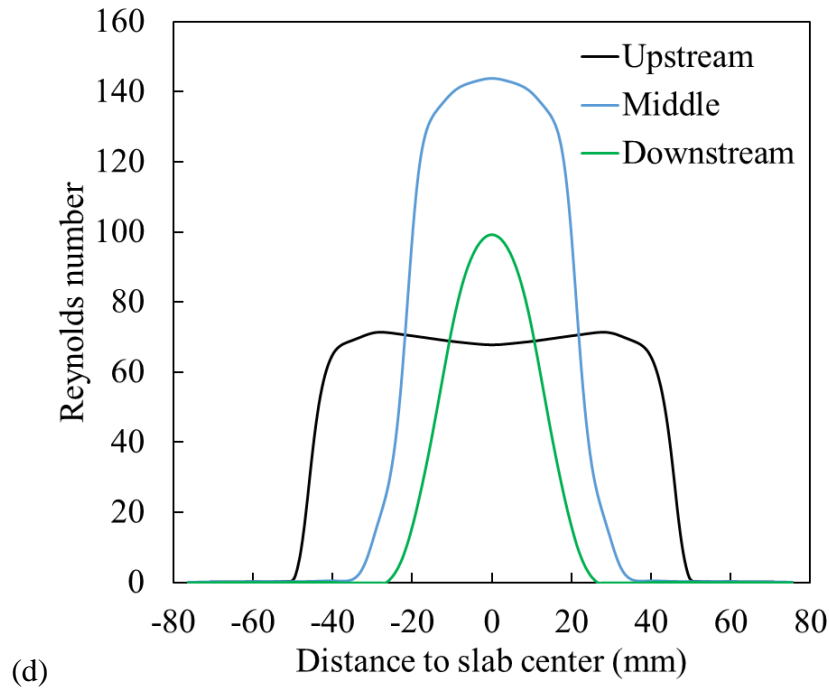
Figure 4-53. Re number variation in the slab thickness direction at the beginning of the secondary cooling region.

Temperature distribution and shell growth

Figure 4-54 visualizes the combined results from step 1 and step 3 simulations. The streamlines represent the movement of the molten steel in the mold. The high-momentum molten steel jet penetrates deeply into the mold upon injection from the SEN. The jet splits into two streams of flow near the mold exit, forming a large circulation in the upper mold region and a small circulation in the lower region. The half-cut colored region stands for the solidified shell. It is defined as the region where the volume fraction of solid is larger than 0.9. The two enlarged figures depict the growth of the shell during the initial solidification stage. The solidified shell starts to form near the meniscus with a thickness less than 2 mm. The shell thickness continues to grow as the slab moves in the casting direction. At the end of the initial solidification region, the shell thickness increases to approximately 35 mm. A large surface temperature gradient is observed in the primary cooling region, as intense heat transfer is required to ensure a sufficient solidification rate. The surface temperature in the secondary cooling region is much more uniform. Slight temperature variation is seen at approximately a quarter of the broad face due to the presence of the high-velocity high-temperature stream splitting from the lower roll, as shown in Figure 4-50.
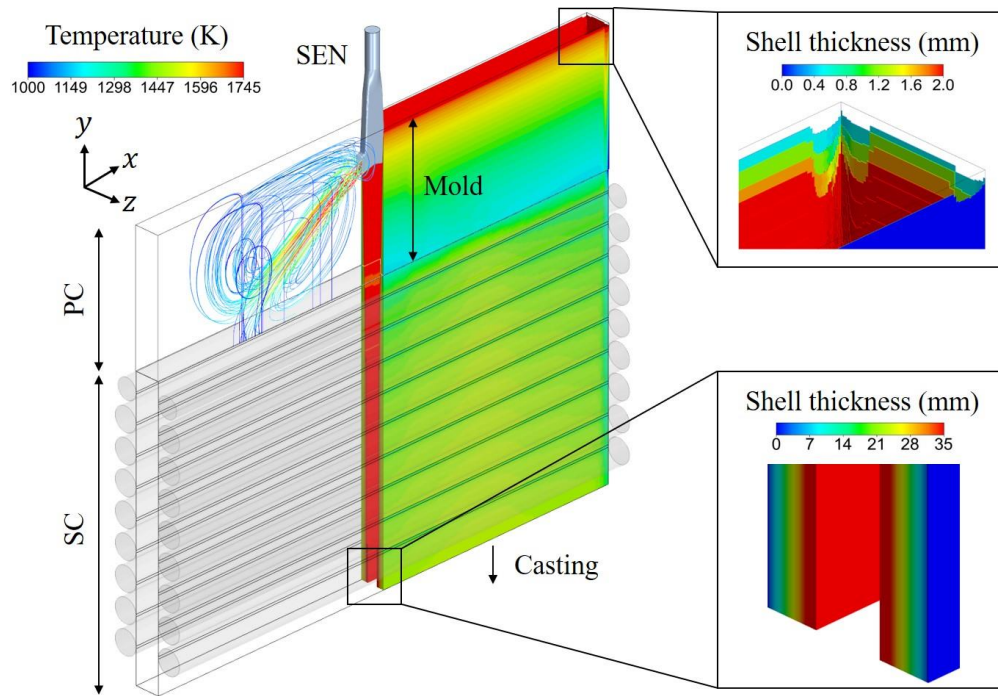
Figure 4-54. Combined results of the initial solidification featuring on the molten steel jet in the mold and shell growth.

Figure 4-55 shows the cooling rate variation on the center cross-section planes in both the slab width direction and the slab thickness direction. The highest cooling rate occurs on the surface of the slab where spray cooling takes place. The magnitude of the cooling rate rapidly decreases from the surface of the slab to the liquid region. As shown in Figure 4-56, the average cooling rate in the liquid region is 0.135K/s, which is approximately 10% of that in the solid region. In the casting direction, as shown in Figure 4-57, the cooling rate varies insignificantly at the center of the slab, whereas it increases from 0.121K/s to 0.135K/s at the quarter of the broad face within 600mm below the mold exit, as the influence of the lower roll disappears. In the slab thickness direction, as shown in Figure 4-58, the change of the cooling rate is the highest at the upstream since the heat transfer rate in the primary cooling region is much higher than that in the secondary cooling region. In addition, the shell thickness is relatively thin at the beginning of the secondary cooling region. Similar to the variation of the Re number, the variation of the cooling rate mostly takes place in the upper region of the current domain, where the lower roll dominates the flow condition. Beyond the penetration depth of the lower roll, the variation of the cooling rate throughout the solid region

becomes less steep, and the high cooling rate region expands to the slab center as the solidified shell grows in thickness.
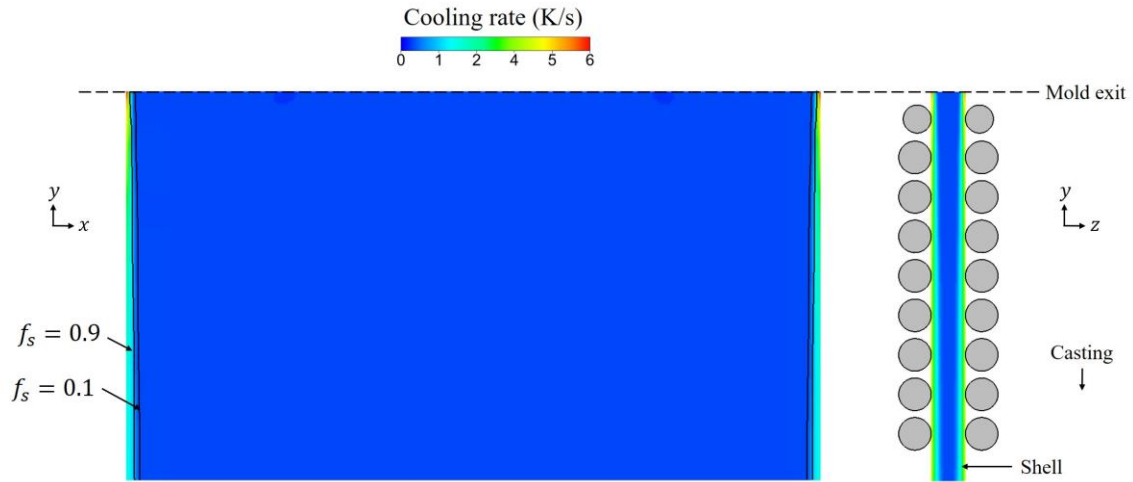
Figure 4-55. Front view and side view of the cooling rate variation at the beginning of the secondary cooling region.
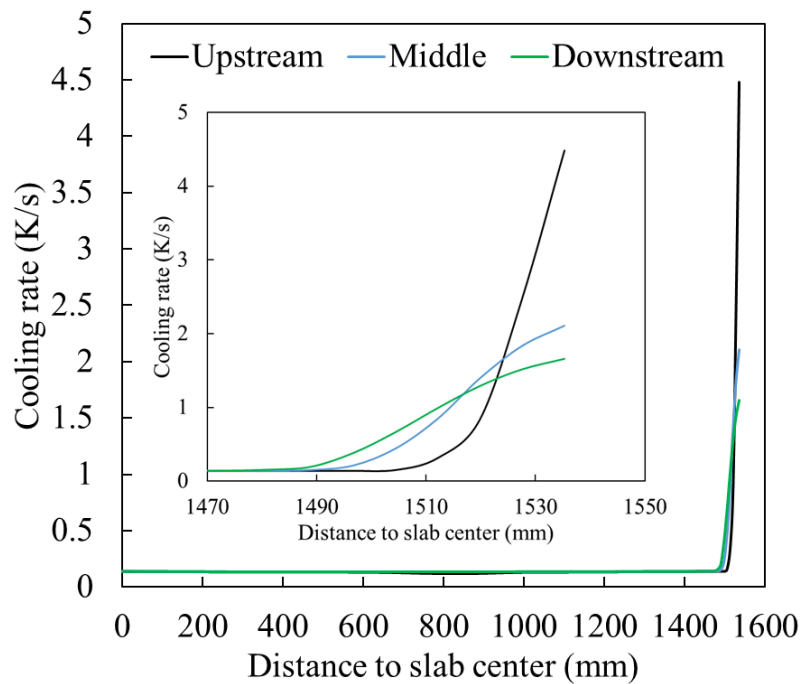
Figure 4-56. Cooling rate variation in the slab width direction at the beginning of the secondary cooling region.
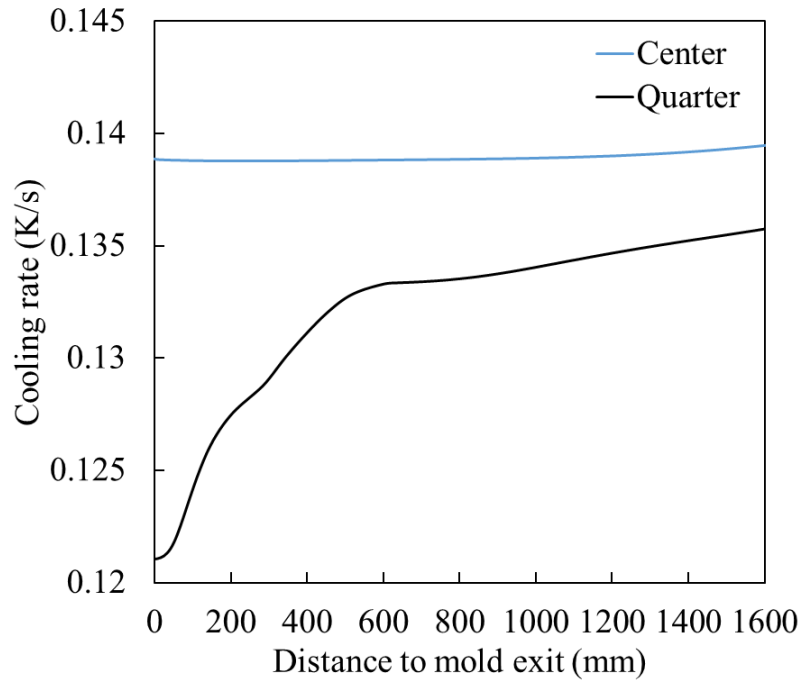
Figure 4-57. Cooling rate variation in the casting direction at the beginning of the secondary cooling region.
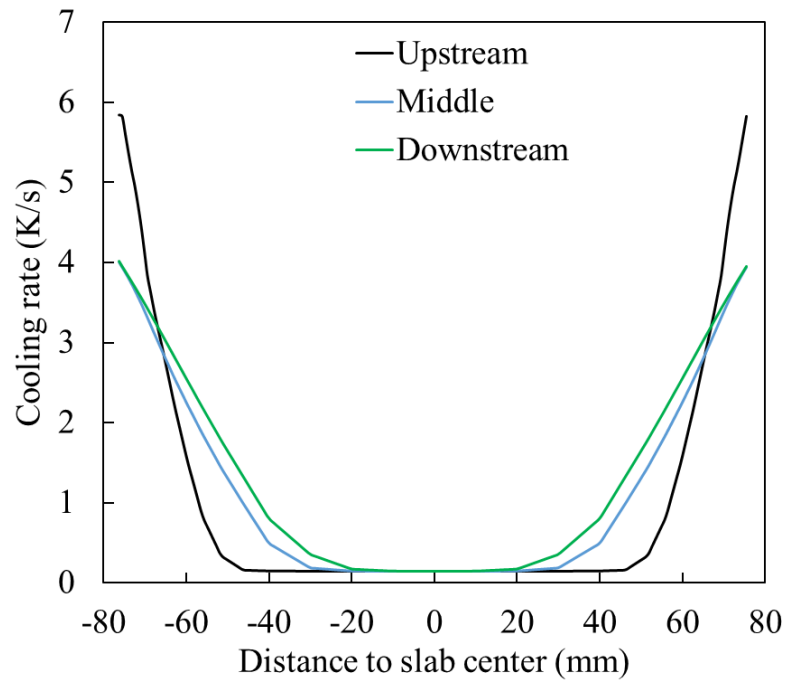
Figure 4-58. Cooling rate variation in the slab thickness direction at the beginning of the secondary cooling region.

Figure 4-59 shows the cooling rate variation at the corner of the slab at the beginning of the secondary cooling region. Due to the two-dimensional heat transfer effect, the cooling rate at the corner of the slab is much higher than other locations on the surface. In the casting direction, the cooling rate decreases from 9K/s at the mold exit to about 5K/s at the end of the current domain, with periodic peaks between where spray cooling takes effect. The cooling rate drastically decreases between the mold exit and the first spray cooling location. The heat transfer mechanism transitions from heat conduction in the primary cooling region to radiation and convection at the beginning of the secondary cooling region. The variation of the cooling rate enters a steady state at 600mm below the mold exit.
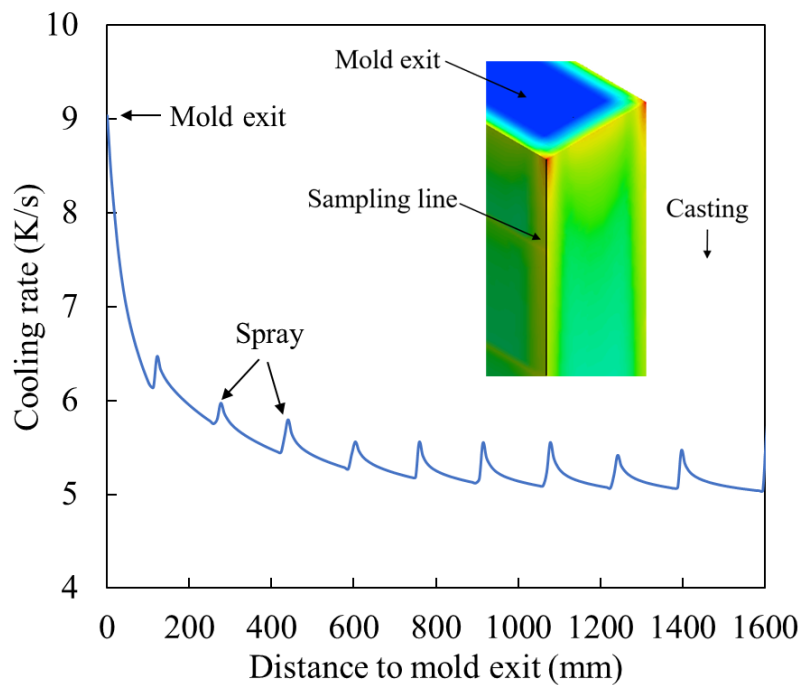
Figure 4-59. Cooling rate variation at the corner of the slab at the beginning of the secondary cooling region.

Figure 4-60 compares the standard temperature variation on the slab surfaces and throughout the shell region. "BF spray 1" stands for the first row of spray on the broad face, whereas "NF" is the abbreviation of the narrow face, which is cooled by radiation and natural convection. The name "Shell" represents the solidified shell region in the current domain. The standard temperature variation at the mold exit is more than 100K due to the transition of the heat transfer mechanism

and the difference in heat transfer rate in different regions. Once the slab enters the spray cooling region, the temperature standard variation decreases to 55K at the first row of spray cooling, and it continues to decrease after the slab passes each row of spray. At the end of the eighth row of spray, the temperature standard variation decreases to 38K. Meantime, the temperature standard variation increases to 172K on the narrow face. As discussed in chapter 3, most of the narrow face area is cooled by radiation and convection, whereas the edge is also cooled by the heat transfer on the broad face. Hence, the temperature difference between the edge and the rest of the narrow face is considerably significant. On average, the temperature standard variation throughout the solid region is 163K. This is because the solid front within the slab maintains the solidus temperature during solidification while the surface is cooled by different heat transfer mechanisms.
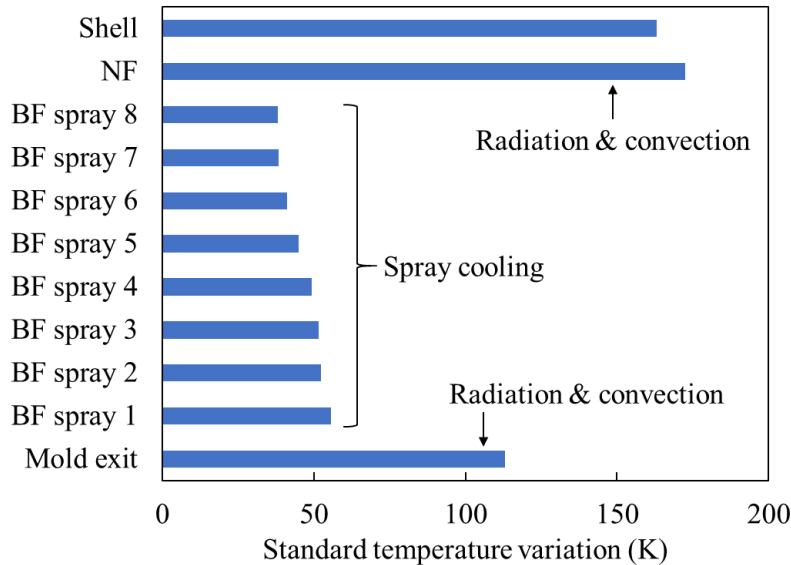
Figure 4-60. Comparison of standard temperature variation on the slab surfaces and throughout the shell region.

Figure 4-61 shows the solidified shell profile at 0.82 m from the mold center on one of the broad faces of the slab. The molten steel solidifies at an average rate of 25 mm/m in the mold until the shell thickness plateaus at 0.6 m below the top of the mold. This is also where the molten steel jet impinges on the narrow face, and the upper and lower rolls form. The high-temperature jet continues to transfer heat to the previous solidified shell, therefore, remelts some of the shells. The shell growth resumes below the mold as water sprays provide sufficient heat transfer on the slab surface. The average solidification rate in the spray region is 11.76 mm/m.
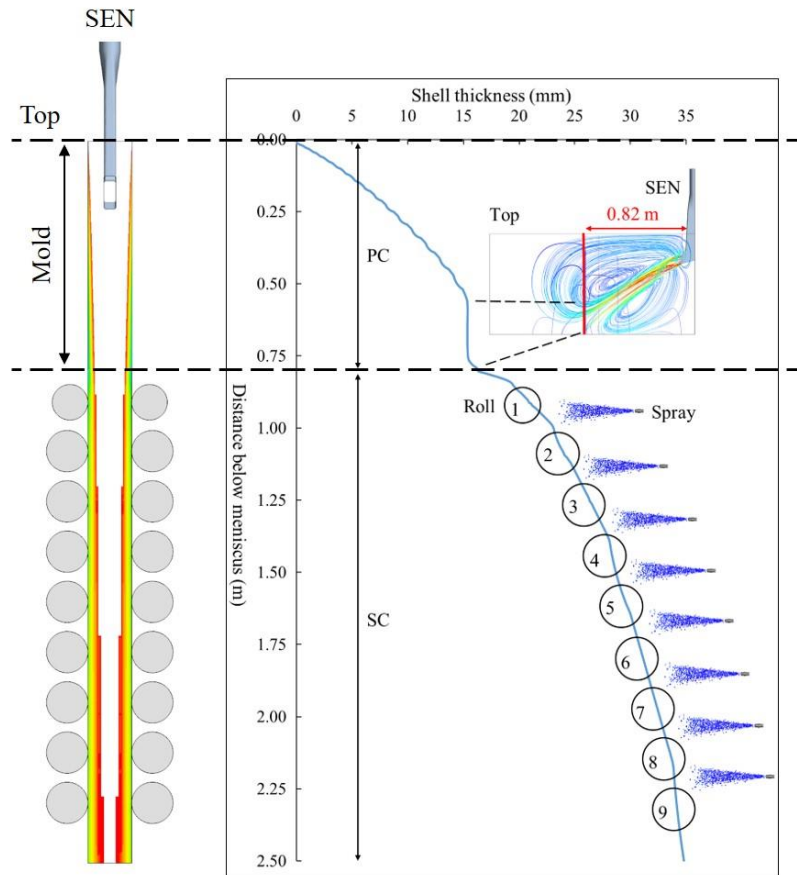
Figure 4-61. Side view of the shell profile on broad faces from the meniscus to the end of the initial solidification stage.

Validation of shell thickness

In this section, the simulated shell thickness is compared with the measurements obtained from a breakout incident. As shown in Figure 4-62, the breakout incident started during the early solidification stage in the upper mold region. The cause of the breakout was identified as the result of insufficient lubrication between the solidified shell and the mold wall. At the breakout location, the improper lubricated solidified shell stuck on the mold wall, which led to the local shell thinning effect. Within a short period of time, the thinning effect propagated to the entire broad face. However, the breakout incident did not occur until the thinning shell left the primary cooling region because the shell was still supported by the mold walls. Upon leaving the primary cooling region, the unsupported shell cannot provide sufficient force to contain the enclosed molten steel. Thus, the molten steel burst from the shell at the thinning location, and the breakout occurred. Figure 4-63 illustrates the casting speed and superheat change during the breakout incident. The local

361

thinning effect took place before time zero. The effect of the shell thinning was detected by thermocouples at time zero, and the sticker alarm went off as it is designed. Within the first 40s, the operator started to diagnose the cause of the alarm and responded by decreasing the casting speed. It was expected that shell thickness could increase at the lower casting speed, and the thickened shell can compensate for the local thinning effect. Later, the superheat was doubled to adjust the shell growth rate. However, the efforts made were insufficient to eliminate the breakout incident, which eventually took place at 143s after the sticker alarm went off.
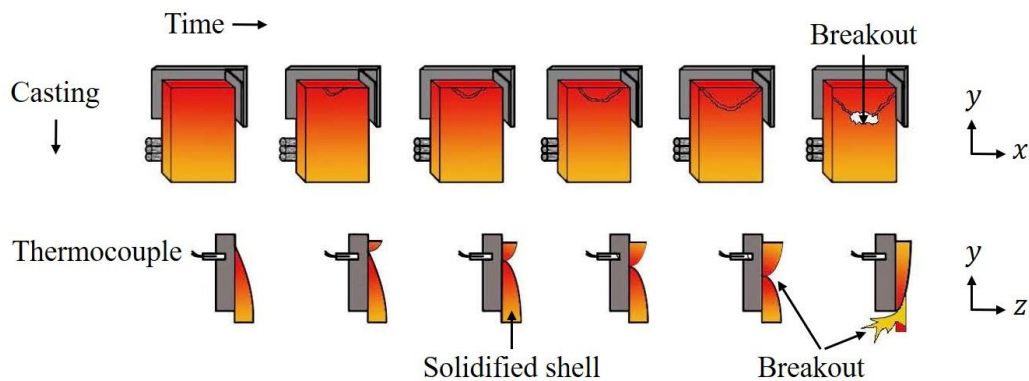
Figure 4-62. Illustration of the occurrence of a sticking-type breakout.
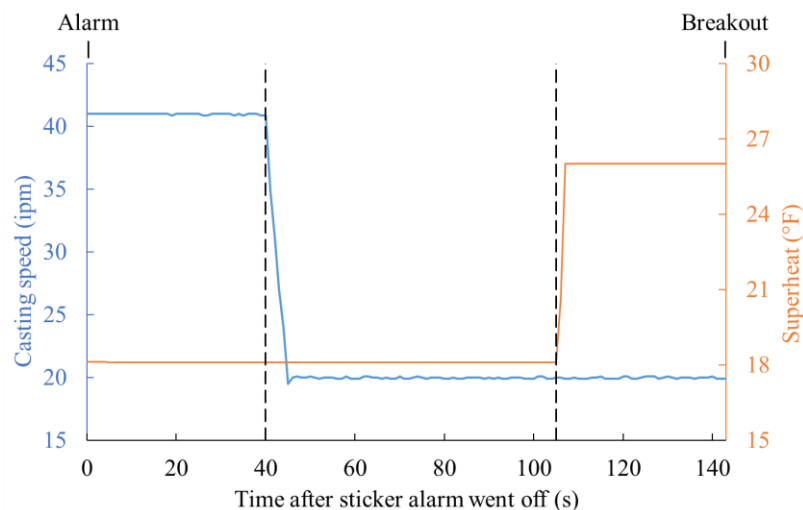
Figure 4-63. Casting speed and superheat change during the breakout incident.

After the molten steel drained, the solidified shell was covered, and a series of measurements were conducted at two different locations on the broad faces. The two locations are referred to as

location A and location B in the current study, which are 720.2mm and 822.3mm away from the center of the slab, respectively. Measurements were taken at 5mm intervals in the casting direction at both locations. The top 81mm of the recovery shell was excluded from the measurement due to the irregular casting condition prior to the breakout incident. The comparison between the measurements and the simulated shell thickness is shown in Figure 4-64. The predicted shell thickness is in good agreement with the measured values at both locations. Smooth shell growth is observed in both measurement and simulation in the upper region of the mold. In the lower portion of the mold, the measured shell thickness fluctuates, and the percentage difference increases to more than 5% at some locations. One of the major reasons for such variation is the change of the casting conditions during the breakout incident. As shown in Figure 4-63, the changes were implemented instantaneously, and the drastic change in the operating conditions, such as casting speed, has a significant impact on the solidification process. On the other hand, the current study assumes that the casting condition enters another steady state after the change of superheat completes. Thus, the simulated shell thickness steadily increases at both locations. Nevertheless, the numerical models, together with the coupling procedure, predict accurate shell thickness in the initial solidification region. Such comprehensive models will continue to benefit the industry by serving as a trouble-shooting tool and offering optimized operating conditions.
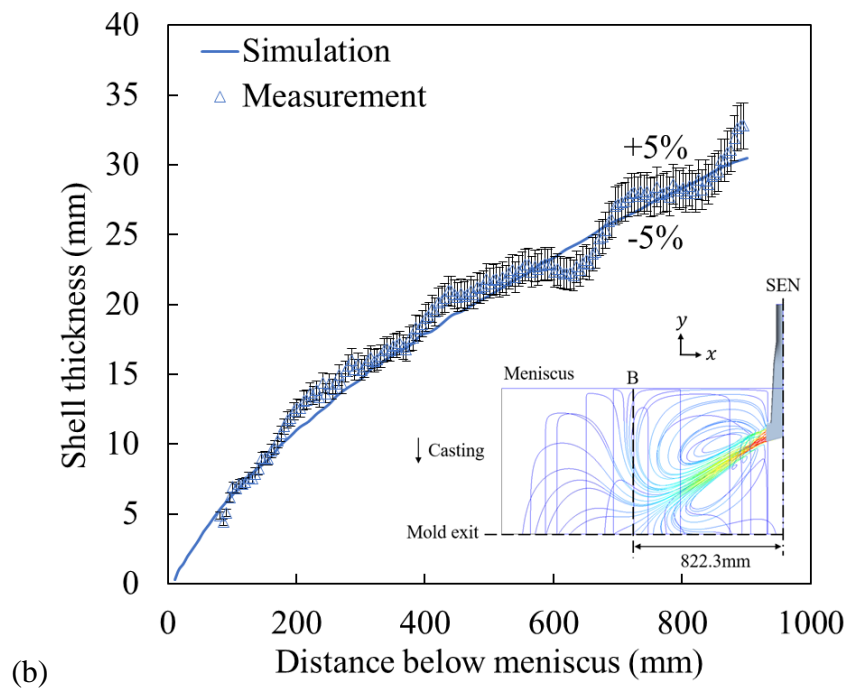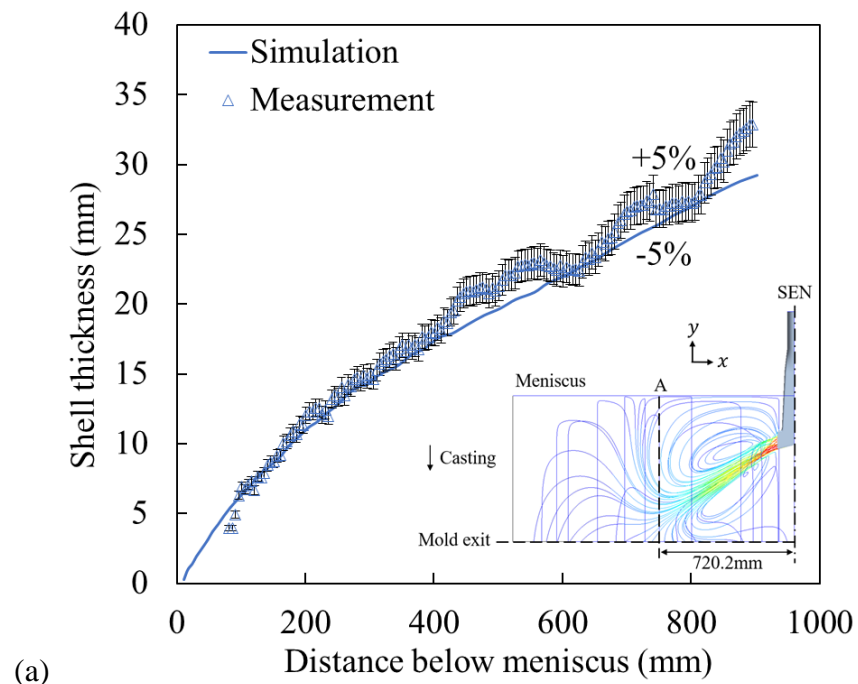
Figure 4-64. Comparison of shell thickness with measurements at: (a) location A, and (b) location B.

Sensitivity of the input of material properties

Figure 4-65 demonstrates the sensitivity of material properties on solidification prediction. In the previous sections, temperature-dependent material properties shown in Figure 2-28 and Figure 2-41 are considered in the simulations. Each of the material properties varies significantly during the continuous casting process. However, this section presents a simulation with constant material properties to quantify the sensitivity of material properties on solidification prediction. The constant material properties are set as the arithmetic mean over the temperature range of 1000K to 1820K. The constant material properties used in the current simulation are summarized in Table 4-5. Enthalpy is computed from specific heat based on Eq. (170). The computational domain and boundary conditions are identical to the thin slab simulation.

The comparison of the predicted shell thickness and the measured values are shown in Figure 4-65. The impact of material properties is significant on solidification prediction. The average percentage difference between the measured and simulated shell thickness at location A and location B is 49.88% and 31.13%, respectively. The predicted shell is much thinner compared to the measurements and the baseline simulation with temperature-dependent material properties. As shown in chapter 2, the material properties are involved in the calculation of mass, momentum, turbulence, and energy equations. Thus, variations in the material properties directly affect the distributions of flow and temperature, which consequently influence the shell thickness. Table 4-6 summarizes the sensitivity of temperature-dependent material property on solidification simulation. Specific heat and dynamic viscosity have a more significant impact compared to other properties, as they are critical parameters of the enthalpy-porosity model.

Table 4-5. Summary of constant material properties.

Material property	Value
Density (kg/m^3)	7450.49
Thermal conductivity (W/m·K)	31.04
Specific heat (J/kg·K)	753.20
Dynamic viscosity (Pa·s)	0.679
Liquidus temperature (K)	1785
Solidus temperature (K)	1745
Latent heat (J)	276440
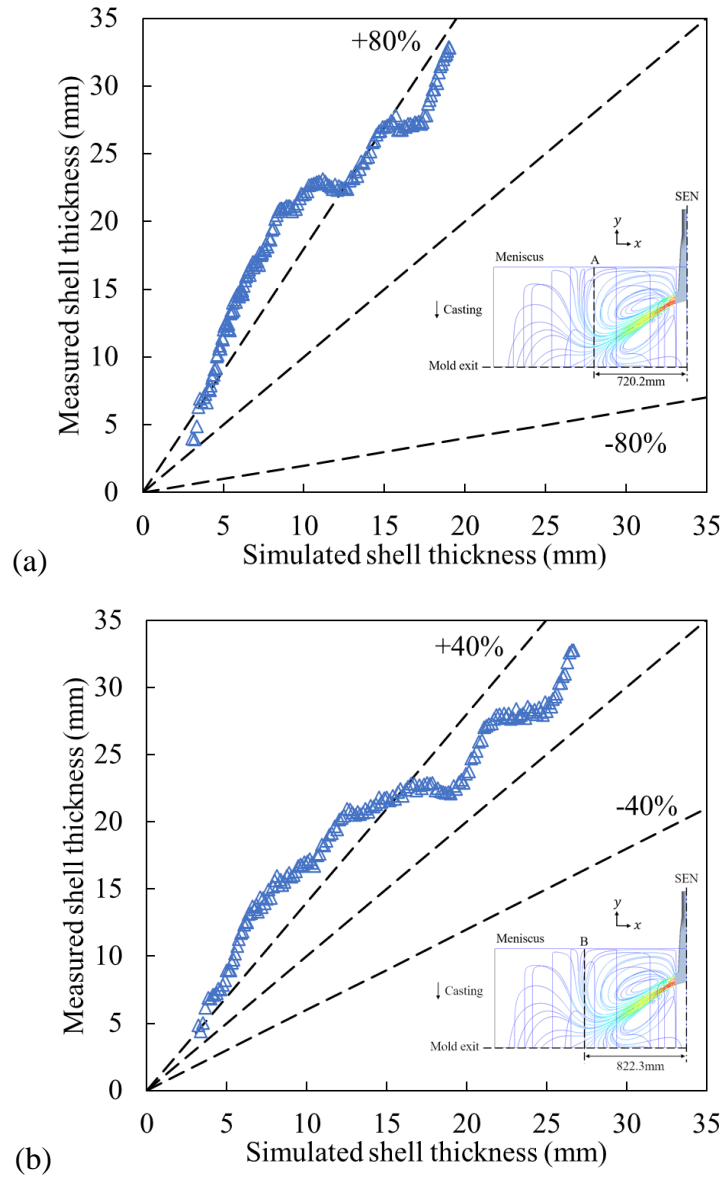
Figure 4-65. Comparison of shell thickness with measurements with constant material properties at: (a) location A, and (b) location B.

Table 4-6. Summary of sensitivity of the input of the temperature-dependent material property on solidification simulation.

Material property	Variation from constant properties	
	Location A	Location B
Temperature dependent density	13.51%	13.39%
Temperature-dependent thermal conductivity	7.12%	2.53%
Temperature-dependent specific heat	44.09%	64.83%
Temperature dependent dynamic viscosity	-41.15%	-23.90%
Linear solid fraction curve (lever rule)	-8.00%	-5.99%

5. CONCLUSIONS AND OUTLOOK

5.1 Conclusions

Secondary cooling is a delicate process because the cooling rate of water spray directly affects the slab surface and internal quality. Efficient and uniform heat removal during secondary cooling is critical to enhancing steel strength. Because insufficient cooling will lead to slab surface bulging or even breakout, whereas excessive cooling will result in cracks and other defects due to significant residual thermal stresses and strains, any slab which does not meet the required quality will be downgraded or scrapped, and remelted. Inefficiencies and production faults represent enormous energy and financial burden. In order to remain competitive and continuously produce high-quality and high-strength steel, the spray cooling parameters must be carefully selected to provide sufficient and uniform heat transfer across the slab. With the advancement of HPC, CFD has become a powerful tool to gain insights into complex fluid flow and heat transfer problems. Yet, few successful numerical models for the heat transfer phenomena during secondary cooling have been reported, mainly owing to the complex phenomena involved. Therefore, the current study presented two three-dimensional continuum numerical models for the transport of mass, momentum, and energy during the secondary cooling process.

The first model features the simulation of water spray impingement heat and mass transfer on the surface of a moving slab with the consideration of atomization, droplet dispersion, droplet-air interaction, droplet-droplet interaction, droplet-wall impingement, the effect of vapor film, and droplet boiling. The model has been validated against five benchmark experiments in terms of droplet size prior to impingement, droplet impingement pressure, and HTC on the slab surface. The validated model has been applied to a series of numerical simulations to investigate the effects of spray nozzle type, spray flow rate, standoff distance, spray direction, casting speed, nozzle-to-nozzle distance, row-to-row distance, arrangement of nozzles, roll and roll pitch, spray angle, spray water temperature, slab surface temperature, and spray cooling on the narrow face. The major research findings of the study on the heat transfer on the slab surface are summarized as follows:

(1) A flat-fan type of nozzle was used to demonstrate the model capability. During the atomization process, the droplet size is relatively large. However, these large droplets are prone to break up while traveling through the air domain. Smaller droplets are expected prior to the droplet-wall impingement heat transfer.

(2) The droplet-droplet interaction plays a more critical role than the droplet-air interaction at a short standoff distance, but both effects become less dominant on droplet size as droplets approach the surface. At a spray flow rate of 7L/min and a standoff distance of 130mm, droplets start to impinge on the slab surface at 0.01s after injection, and the full spray impinges after 0.0155s.

(3) A distinct spray pattern appears on the slab surface upon droplet-wall impingement. Each type of nozzle can produce a unique spray pattern. The size of the pattern signals the influence region of a spray. The spray pattern of a flat-fan type of nozzle stretches in the slab width direction but is narrow in the casting direction, forming an elliptical butterfly-shaped pattern.

(4) The profile of the heat transfer region aligns with the spray pattern, suggesting the dominant role of spray in determining the heat transfer on the slab surface. Outside the spray pattern, the slab loses energy through convection and radiation. While inside the spray pattern, additional heat conduction to droplet and droplet boiling further cools down the hot slab. Six candidate parameters were proposed as thresholds to determine the spray cooling region, but the patterns defined by Nu, HTC, and surface heat flux are more appropriate to represent the spray-affected area. However, since HTC is one of the primary indicators used in the secondary cooling operation and research, the pattern defined by HTC was selected to evaluate the heat transfer intensity and uniformity.

(5) During the secondary cooling process, uniform cooling within a large cooling area is desired. A_{spray}, HTC_{avg}, and STD_{spray} were proposed to quantify the cooling area, the efficiency of heat transfer, and the uniformity of cooling. A_{spray} is the total spray-affected area on the slab surface. The minimum value for A_{spray} should be equal to the projected spray area, which is set to 71.06cm^2 for a 90° flat-fan nozzle that operates at a standoff distance of 130mm. HTC_{avg} is the area-weighted average HTC in the spray-affected area, and it indicates the overall intensity of jet impingement heat transfer over the spray coverage area. A value of 24W/m^2·K is used as the

minimum HTC_{avg} based on the modified Nozaki's equation. STD_{spray} is the standard deviation of surface temperature within the spray coverage area, and it measures the uniformity of impingement heat transfer. The maximum STD_{spray} that is allowed within the spray cooling pattern to avoid any internal crack is 36.36K, which corresponds to 0.2% strain.

(6) The effect of surface heat transfer can penetrate up to 11mm inside the slab region. Compared to the entire slab thickness, this also affirms the assumption that the influence of surface heat transfer on solidification can be modeled through one-way coupling.

(7) Heat transfer through spray cooling is the dominant mechanism throughout the spray-affected area. It accounts for 70% to 76% of the total wall heat flux through the spray-affected area. Radiation is the second largest source of heat transfer besides the spray cooling, and it accounts for 22% to 28% of the total heat transfer within the spray-affected area. The role of radiation becomes important again near the lower boundary of the spray-affected area as the effect of spray cooling decreases. The effect of convection is the least important mechanism to the overall heat transfer. On average, the contribution of convection only accounts for 1.62% of the overall heat transfer.

(8) Two-fluid nozzles such as air-mist nozzles have emerged in modern continuous casting. Droplet size drastically reduces the air-mist spray due to the intense air-water interaction and the resulting breakup processes. Due to the decrease of droplet diameter, or the increase of surface-to-volume ratio, heat transfer within the spray-affected area is significantly promoted. The maximum HTC increases by more than 370% when the droplet diameter decreases by 80%. The average HTC has increased by more than threefold in the air-mist spray at the same water flow rate. However, A_{spray} decreases by approximately 29% in the air-mist spray. The decrease is much evident in the casting direction, which is related to the addition of compressed air. In addition, STD_{spray} increases in the air-mist spray, suggesting less uniform heat transfer throughout the spray-affected area. It is worth mentioning that the two-fluid nozzles require additional investments such as more expensive nozzles, a secondary piping system for the additional fluid, and extra pumping power. Thus, the selection of nozzle type is on a case-by-case basis, and the heat transfer rate is not the only influential factor. Factors for the nozzle selection include steel

grade, casting conditions, nozzle configurations, desired average HTC, and the requirement of energy consumption.

(9) The increase of spray water flow rate significantly increases the droplet number density, expanding the spray coverage area A_{spray}. Heat conduction from the hot surface to the impinged droplets is intensified at a large spray flow rate. The boiling regime might change to transition or even nucleate boiling at specific locations due to the increase of heat flux. On the other hand, a large spray flow rate can also cause non-uniform cooling.

(10) The increase of air pressure accelerates the primary breakup process, as the reduced liquid sheet is less stable in a faster-moving fluid field. Droplet size at the time of impingement decreases by more than 20%, thereby beneficial to the heat transfer on the slab surface. Both A_{spray} and STD_{spray} decrease as the result of high air pressure. This shows that fine droplets with low terminal velocities are greatly affected by the high-velocity airflow. Some of the fine droplets are likely to be blown away from the slab surface without conducting heat transfer at all. Thus, there should be an upper limit for the air injection pressure at each flow rate of water to guarantee a sufficient spray-affected area on the slab surface.

(11) The simulation results verified the existence of the critical standoff distance for each type of nozzle. It is the maximum allowable spray distance to produce effective cooling. The standoff distance can affect the secondary cooling process by damping or generating turbulence. If the nozzle is placed close to the surface, vortices along the jet axis will not have sufficient distance to develop and merge with the jet core, and the jet will impinge on the solid surface with almost uniform velocity distribution undissipated kinetic energy. The longer the standoff distance is, the higher the turbulent intensity will be. However, heat transfer is more uniform throughout the entire slab surface in the case of a longer standoff distance due to the sufficient dispersion of droplets horizontally. In practice, it is encouraged to increase the spray standoff distance to maximize the spray coverage as long as the nozzle operates within the critical standoff distance and the target slab temperature is met. The critical standoff distance for air-mist nozzles is much shorter because the droplet size is already smaller than that from hydraulic nozzles.

(12) Effect of spray direction. Droplets from different spray directions follow almost identical trajectories to the slab surface during the atomization process due to high injection velocity. Within a short period of time, the effect of gravity hardly affects the path of the droplet. However, once droplets impact the slab surface, the direction of gravity plays a significant role in terms of the impact outcome. The cooling effect is extensively promoted when the spray direction is aligned with the direction of gravity but compromises when droplets are sprayed against gravity. In the Top spray, most of the droplets eventually stick on the slab surface until they completely evaporate. In the Bottom spray and the Lateral spray, droplets continue to move away from the slab instead of re-impacting on the slab surface after the first impingement. The spray direction affects the impingement heat transfer changing the residence time of droplet on slab surface, rather than altering the injection path of the droplet, and HTC on slab surface in the Top spray is larger than that from the other two sprays. One solution to compensate for the insufficient heat transfer by lateral sprays and bottom sprays is to add an additional 10%-15% of water while maintaining other operating parameters.

(13) The effect of the plate moving velocity only becomes significant after impingement and in the plate moving direction. Both A_{spray} and HTC_{avg} decrease as the moving velocity increases due to the redistribution of the impinged droplets in the moving direction. But STD_{spray} increases at high moving velocities, indicating much severer non-uniform heat transfer under such conditions.

(14) The effect of nozzle-to-nozzle distance can be represented by the ratio of D/H. At a $90°$ spray angle, the ratio should be constrained at the range of 0.5-2 to ensure a proper overlap of the two adjacent jets. HTC increases in the overlap area but with the sacrifice of decreasing A_{spray} and increasing STD_{spray}. Jet cooling at $D/H \geq 2$ should be avoided. Otherwise, the heat transfer will decline in between the jets due to the fountain effect.

(15) Unlike the favorable overlapping of two adjacent sprays in the same row, the overlapping of two sprays from different rows is not preferred during the operation. The spray-affected area is always wider the downstream, regardless of the row-to-row distance. Because of the expansion of the droplet belt, some of the droplets moving in the slab width direction are pushed to the casting

direction, thus, increasing the spray-affected area downstream. At the upstream, heat transfer is much more intense and non-uniform. At a shorter row-to-row distance, the difference in heat transfer between the upstream spray and the downstream spray is smaller, implying a higher overall heat transfer rate. Besides, the droplet belt between the two adjacent rows can interfere with the spray cooling process, further deviating the spray cooling effect from the baseline condition. Therefore, rolls are necessary to be placed in between the two adjacent rows to prevent interference from the droplet belt.

(16) Much more sufficient spray cooling was observed in the staggered arrangement of nozzles, where the middle spray at the second row helps break the hovering droplets and reduce stagnation regions where heat transfer is compromised. Although the temperature difference between the two arrangements is less significant if rolls are placed between rows of sprays, the staggered arrangement is still recommended for intense and uniform spray cooling practice because it offers the chance to cool down the regions that may not be sufficiently cooled by previous rows.

(17) When a roll is placed on each side of a spray, A_{spray} increases by approximately 18% and HTC_{avg} increases by 4% due to the change of droplet distribution on the surface. Droplets are confined in between the rolls instead of spreading on the entire slab surface. As a result, the concentrated droplets further promote heat transfer. STD_{spray} decreases by 46% compared to the baseline simulation as the droplet distribution becomes more uniform in the cooling area. The energy flow diagram has shown that approximately half of the energy released from the slab is through the spray region, primarily due to spray cooling. On average, about 13.62% of the energy is transferred to the roll through the roll contact area. About 70% of the absorbed energy is further released to the surroundings through the surface of the roll by radiation and convection. The rest 30% of the absorbed energy is stored in the roll to increase its internal energy. In addition, the temperature distribution inside the roll is not uniform. The highest temperature occurs around 0°. As the roll rotates, the absorbed energy dissipates, and the temperature inside the roll continuously decreases from 3.5° to 356.5°. The lowest temperature occurs at 356.5° before the roll contacts with the slab again. This process repeats as the roll starts another rotation.

(18) The roll pitch can barely affect the atomization process, but it significantly changes the distribution of water droplets on the surface after the impingement. Droplets are confined in a much smaller region when the roll pitch is small. Some of the droplets accumulate at the roll contact location and form a belt along the roll surface. On the other hand, the heat transfer is enhanced at the small roll pitch due to the increase of droplet concentration and the decrease of A_{spray}. Consequently, the heat transfer uniformity decreases. Therefore, a small roll pitch is recommended for the region where intense cooling is required, such as the beginning of the secondary cooling process. The roll pitch can be gradually increased along the casting direction with the decrease of slab temperature and heat transfer intensity.

(19) The coverage of the spray-affected area and the heat transfer rate have a strong dependence on the spray angle. The impact of spray angle is much significant than that of spread angle. The length of the spray affects the area in the slab width direction increases by approximately 200% once the spray angle increases from 60° to 120°. On the other hand, the increase of spray-affected area is less than 50% even when the increase of the spread angle is 100%, which implies that major of the droplets are distributed in the slab width direction, and the size of the spray region is mainly determined by the spray angle. HTC_{avg} decreases by 55% when the spray angle increases from 60° to 120°. However, STD_{spray} decreases by 64% when the spray angle is doubled.

(20) Little variations are observed in terms of the distribution and magnitude of HTC at different spray water temperatures. The short total contact time between the droplet and the surface indicates that sensible heat removal also plays an essential part in the spray cooling process. As the spray water temperature increases, the amount of sensible heat removal reduces, and the latent heat removal does not counterbalance that decrease. Therefore, the heat transfer rate decreases. If the time for the latent heat removal further increases, the heat transfer rate will be significantly improved at higher spray water temperature.

(21) The current study adopted the correlation developed by Hnizdil et al. to evaluate the local Leidenfrost temperature at each droplet time step. The highest local Leidenfrost temperature is 817K under the current spray condition, implying that the surface heat transfer is only determined by filing boiling throughout the entire secondary cooling region. Similarly, the heat transfer

effectiveness is also independent of the surface temperature in the film boiling regime. It is determined when the nozzle configuration and spray condition are decided. As the slab surface temperature approaches the Leidenfrost temperature, the HTC noticeably increases. Once the slab surface temperature decreases to below the Leidenfrost temperature, the increase of the HTC is more than four times as the film boiling regime shifts to the transition regime.

(22) Spray cooling on the narrow face is required if the size ratio of the broad face and narrow face is small, or a sufficient large cooling rate is desired at the beginning of the secondary cooling region. With the narrow face spray, aside from the change of the entrained air distribution, droplets from the narrow face spray can also interact with the broad face sprays. The intensified heat transfer on the narrow face furthers decreases the slab surface temperature by about 10K, and the extent of the over-cooling effect at the edge also increases, which must be carefully evaluated. Uncontrolled edge over-cooling can lead to significant residual thermal stress, eventually contributing to surface defects such ad corner crack.

(23) A three-step numerical approach has been developed to generate HTC correlations, which can be expressed as a function of several essential operating parameters. The approach consists of the high-fidelity numerical simulation step, the data analysis step, and the GUI development step. High-fidelity numerical simulations with the aid of HPC were used to create the HTC database. The two-dimensional HTC distribution from each simulation was decomposed into two normalized universal distribution functions and a lumped characteristic HTC in the data analysis step. Last, a GUI was developed to reconstruct the two-dimensional HTC distribution during application. The calculated HTC distribution is stored in the versatile comma-separated values (csv) format, and it can be directly applied as a boundary condition to on-site off-line/on-line solidification calculation at steel mills.

In the second numerical model, the existing volume-averaged Enthalpy-Porosity method has been extended to include the slurry effect at low solid fractions through a switching function. The effect of surface heat transfer, including spray cooling, was incorporated through the use of HTC distribution on the slab surface as the thermal boundary condition. The model has been validated against the analytical solution for a stationary thin solidifying body and the simulation for a moving

thin solidifying body. The effects of secondary dendrite arm spacing, critical solid fraction, crystal constant, switching function constant, cooling rate, rolls, nozzle-to-nozzle distance, and arrangement of nozzles have been evaluated using the validated model. In addition, the model, along with the three-step coupling procedure, has been applied to simulate the initial solidification process in continuous casting. The prediction is in good agreement with the measured shell thickness, which was obtained from a breakout incident. The major research findings of the study of heat transfer and solidification inside the slab are summarized as follows:

(1) Inside the semi-solidified slab, the maximum Re number occurs at the center of the slab, where the liquid is unaffected by the heat transfer on the slab surfaces. The average Re number in the mushy zone is 56.4, and it further decreases to 28.7 in the solid region. The low Re number throughout the mushy zone justifies the insignificance of Forchheimer's term in the momentum equation.

(2) The temperature gradient within the solid region significantly increases after the slab passes the spray due to heat conduction. In contrast, the temperature distribution in the slab width direction is much uniform. The effect of spray cooling on the temperature distribution inside the slab is limited to the region near the surface, beyond which the effect of surface heat transfer dissipates through heat conduction which tends to minimize the temperature difference within the slab. The highest cooling rate is 6.43K/s, and it occurs on the surface of the slab. The average cooling rate throughout the mushy zone and the solid region is 0.415K/s and 2.73K/s.

(3) The solidified shell grows mainly in the casting direction, and the net growth of the solidified shell throughout the computational domain is 4.41mm at an average rate of 0.17mm/s. The shell growth rate reaches the maximum slightly downstream of the spray cooling. At further downstream of the spray cooling, the shell growth rate slightly decreases but still maintains a relatively high value due to the heat conduction within the solidified region. On the contrary, both the shell thickness and the shell growth rate barely vary in the slab width direction.

(4) The flow resistance force in the porous region is inversely dependent on the square of secondary dendrite arm spacing. The variation of the secondary dendrite arm spacing mainly occurs in the

mushy zone and the solid region. The maximum secondary dendrite arm spacing is 387μm at the liquid-mushy zone interface, and it decreases to around 50μm near the surface. As the secondary dendrite arm spacing increases from 10μm to 1000μm, the flow resistance decreases by four orders of magnitude. However, the net effect of different secondary dendrite arm spacings on the shell thickness is negligible because even the lowest flow resistance force in the mushy zone is still in the order of million, which is sufficiently large to stop the liquid flow in the porous region.

(5) The critical solid fraction indicates the boundary between the equiaxed dendrites and the columnar dendrites. The effect of the critical solid fraction is to shift the switching functions either toward the liquid or toward the solid. Consequently, the model governing the flow resistance in the shifted region changes. Yet, the solidification process is barely affected by the change of the critical solid fraction. The difference in shell thickness is within 1%. The simulations with the critical solid fraction of 0.7 and 0.8 failed to converge, suggesting that the free floating dendrite model is more suitable for the low solid fraction regions. If this model is applied to a high solid fraction region, where dendrites form a fixed network and closed pack together, the result will not reflect the actual solidification process. In addition, numerical instabilities will rise when the critical solid fraction approaches unity.

(6) The crystal constant is a function of the aspect ratio and surface roughness of the crystal. It can be treated as a fine-tuning coefficient to obtain the optimum effective viscosity. The ratio of $\frac{\mu_{eff}}{\mu_{st}}$ significantly varies as the crystal constant changes. At the critical solid fraction of 0.525, a value of 0.5 for crystal constant produces the most reasonable viscosity increase. The temperature distribution between the crystal constant of 0.5 and 1.5 is barely noticeable. When the crystal constant decreases from 0.5 to 0.1, the ratio of $\frac{\mu_{eff}}{\mu_{st}}$ drastically increases to more than 25000, which imposes an unrealistic sluggish effect in the free floating dendrite region and completely stops the liquid flow in the vicinity of the upstream surface. To avoid any unrealistic flow condition, the crystal constant should be larger than a lower limit, which is equal to $\frac{F_\mu f_{sol}}{2}$.

(7) The smoothness of the transition between the free floating dendrite region and the porous region is controlled by the switching constant when the switching constant is less than 100. Smaller

switching constant in this range corresponds to long transition and considerable damping effect on the liquid flow. The two mushy zone regions become indistinguishable when the switching constant reduces to zero. In the range of 80 to 120, the transition is insensitive to the switching constant. Beyond the value of 200, the increase of the switching constant further decreases the smoothness of the transition, which becomes rapid and steep near the critical solid fraction. The shell thickness is virtually identical as the switching constant increases from 100 to 500. However, when the switching constant decrease to 10, the shell thickness also decreases by approximately 1%. A minimum value of 80 is recommended to ensure a rapid and smooth transition at the critical solid fraction.

(8) The Re number decreases in the solid region as the heat transfer rate increases on the surface. The average temperature in the liquid region and mushy zone is fairly constant regardless of the spray cooling condition on the surface. The effect of surface heat transfer disappears at approximately 25mm below the surface. Further downstream in the secondary cooling region, where the solidified shell is much thicker, the influence of the spray cooling can penetrate deeper in the slab but with a much lower temperature gradient. The shell thickness decreases by a maximum 5% at the downstream surface as the surface heat flux decreases from $55W/cm^2$ to $5W/cm^2$, whereas the shell thickness increases by about 3% at the exact location if the surface heat flux increases from $55W/cm^2$ to $125W/cm^2$.

(9) The initial shell thickness is thinner when a roll is placed in front of a spray in the casting direction. Because the reflected droplets are blocked by the presence of the roll. The increased heat transfer due to roll contact does not entirely compensate for the loss of droplet boiling heat transfer in this region. Once the slab enters the inter-roll region where droplets are confined, the cooling rate noticeably increases across the solid region. When the slab reaches the downstream surface, the cooling rate in most of the solid regions has increased to more than 6K/s, and the shell thickness has increased by more than 1.5%.

(10) A reconstructed two-dimensional HTC distribution predicted by the HTC correlation has been coupled with the solidification model to demonstrate the availability of the correlations in assisting the high-fidelity three-dimensional solidification simulations. The simulated shell thickness by

coupling with the reconstructed HTC profile only differs from the CFD simulation predicted HTC by less than 1%.

(11) The shell thickness profiles at different nozzle-to-nozzle distances are almost identical since the overlap effect does not change the spray and heat transfer behaviors in the casting direction. The effect of nozzle-to-nozzle distance has a more significant impact on the slab width direction. At $D/H = 0.5$, the highest cooling rate is observed in the middle of the slab, where the two adjacent sprays impinge and act as a single spray. The effect of surface heat transfer and the overlap of the two adjacent sprays completely disappear at 10mm below the surface. At $D/H = 1$, the two adjacent sprays have moderate overlap at the center of the slab, and the effect of surface heat transfer is still noticeable at 10mm below the surface. When the ratio of D/H increases to 2 and beyond, most of the variations of cooling rate vanish at 3mm below the surface, except for the "fountain" effect, which is still detectable at 10mm below the surface.

(12) The cooling profile is also sensitive to the arrangement of nozzles. In the rectangular arrangement, the overlap effect of the adjacent sprays extends at least 10mm below the surface before it disappears through heat conduction in the solid region. In the staggered arrangement, with the additional spray in the middle of the second row, the variation of cooling rate in the spray overlap region is suppressed. The three sprays act as a single spray and provide uniform cooling to the spray-affected area. In terms of shell growth, the difference between the two arrangements is negligible since the surface heat transfer mainly affects the near-surface region.

(13) A thin slab casting machine has been used to demonstrate the application of the surface heat transfer model, the solidification model, and the coupling procedure. The coupled models have been applied to simulate the initial solidification stage, where a sufficient cooling rate must be provided to maintain a proper solidification rate. Otherwise, a breakout incident might occur. Because the investigated thin slab casting machine is equipped with a bifurcated SEN, the typical "double roll" pattern is observed in the primary cooling region. The impact of the mold flow circulations can extend to 2m below the meniscus. Within the penetration depth, the flow condition at the beginning of the secondary cooling region is still dominated by the flow characteristics in the primary cooling region.

(14) During the initial solidification stage, the solidified shell starts to form near the meniscus with a thickness less than 2 mm. The shell thickness continues to grow as the slab moves in the casting direction. At the end of the initial solidification region, the shell thickness increases to approximately 35 mm. The average solidification rate in the mold and the spray region is 25 mm/m and 11.76 mm/m, respectively. The average cooling rate in the liquid region is 0.135K/s, which is approximately 10% of that in the solid region. Due to the two-dimensional heat transfer effect, the cooling rate at the corner of the slab is much higher than other locations on the surface. In the casting direction, the cooling rate at the corner decreases from 9K/s at the mold exit to about 5K/s at the end of the current domain, with periodic peaks in between where spray cooling takes effect. The standard temperature variation at the mold exit is more than 100K. Once the slab enters the spray cooling region, the temperature standard variation decreases to 55K at the first row of spray cooling, and it decreases to 38K at the end of the initial solidification region. The temperature standard variation is 172K on the naturally cooled narrow face.

(15) The impact of material properties is significant on solidification prediction. Variations in the material properties directly affect the distributions of flow and temperature, which consequently influence the shell thickness. The average percentage difference between the measured and simulated shell thickness with constant material properties at location A and location B is 49.88% and 31.13%, respectively. Among all the thermodynamic material properties, specific heat and dynamic viscosity have a more significant impact compared to other properties, as they are critical parameters of the enthalpy-porosity model.

5.2   Outlook

Future research on the secondary cooling process includes the following aspects:

(1) The current study assumes that the entire secondary cooling region can be divided into a series of rectangular sections, and similar sections can be modeled by the same computational domain with minor modifications of the boundary conditions. The current models can be further advanced by considering the curvature of the bending section and extending the computational domain to simulate a larger region. One of the significant challenges of including the bending section is

meshing. As discussed in chapter 2, biased fine mesh is desired at the spray impingement heat transfer location and the liquid-mushy zone interface. Curved computational domains will skew the mesh, adding another complexity to the numerical simulations. Besides, extending the computational domain to model a larger portion, if not the entire section, of the secondary cooling region will need a significant increase of computational power. The efficiency of the simulations should be balanced with the accuracy of the results.

(2) The current study treats the semi-solidified slab as a smooth and flat moving plate. This assumption excludes oscillation marks and any other surface defects from the simulations. Further study can explore the effect of oscillation marks on the surface heat transfer.

(3) The current solidification model assumes that both liquid steel and solid are chemically homogeneous and isotropic, and the material properties are only a function of the local temperature. Solute diffusion and advection are not included in the current model. It is well recognized that the transport of solute leads to macrosegregation, which cannot be removed by subsequent processing. Future research should include such an effect in the solidification model in order to provide more comprehensive predictions for the secondary cooling process.

(4) Future research can further enhance the current macroscopic solidification model by incorporating it with microscopic models. For example, the secondary dendrite arm spacing has been demonstrated as one of the essential parameters in the permeability model, and it is closely related to the local cooling rate and carbon content. Further study can utilize numerical methods such as the phase-field method to predict the secondary dendrite arm spacing for different operating conditions. The predictions from the microscopic simulations can be used as input conditions in the macroscopic simulations.

(5) Further research can replace the regression-based HTC correlations with the machine learning-powered Reduced Order Models (ROMs) for online real-time casting control. As machine learning, artificial intelligence, big data mining, and digital twin have emerged as the core of industrial 4.0 initiatives, and future research can take advantage of these technologies and develop high-fidelity implicit ROMs. One of the advantages of implementing machine learning is to increase the number

of input parameters from a few to hundreds, even thousands. Once the ROMs are integrated with other technologies such as big data mining and digital twin, the accuracy of the casting control will further be improved.

REFERENCES

[1] U.S. Energy Information Administration. (n.d.). *Manufacturing Energy Consumption Survey (MECS)*. https://www.eia.gov/consumption/manufacturing/data/2014/index.php?view=data

[2] U.S. Department of the Interior, U.S. Geological Survey. (2019). *Mineral Commodity Summaries 2019*. https://www.usgs.gov/centers/nmic/mineral-commodity-summaries

[3] Association of Iron and Steel Technology. (2019). 2019 AIST Electric Arc Furnace Roundup. *Iron & Steel Technology*, January 2019, 128-151.

[4] U.S. Department of Transportation the Pipeline and Hazardous Materials Safety Administration. *Incident Statistics*. https://portal.phmsa.dot.gov/analytics/saw.dll?PortalPages

[5] Thomas, B. G. (2004). Continuous Casting (metallurgy). *Yearbook of Science and Technology*. New York, NY: McGraw-Hill.

[6] *From steel to semi-finished products*. (2018, June 21). Tec-science. Retrieved from https://www.tec-science.com/material-science/steel-making/steel-semi-finished-products-continuous-ingot-casting/

[7] Meng, Y. A., & Thomas, B. G. (2003). Heat-transfer and solidification model of continuous slab casting: CON1D. *Metallurgical and Materials Transactions B*, *34*(5), 685-705.

[8] Lechler, Inc. USA. (n.d.). *Flat fan nozzles*. Lechlerusa. https://www.lechlerusa.com/en/products/product-by-type/flat-fan-nozzles

[9] Lechler, Inc. USA. (n.d.). *Twin-fluid nozzles for secondary cooling in continuous casting processes*. Lechlerusa. https://www.lechlerusa.com/en/products/product-by-market/metals/nozzles-for-secondary-cooling/twin-fluid-nozzles-for-secondary-cooling

[10] Hardin, R. A., Liu, K., Beckermann, C., & Kapoor, A. (2003). A transient simulation and dynamic spray cooling control model for continuous steel casting. *Metallurgical and Materials Transactions B*, *34*(3), 297-306.

[11] Mosayebidorcheh, S., & Gorji-Bandpy, M. (2017). Solidification and thermal performance analysis of the low carbon steel during the continuous casting process. *Journal of Advanced Materials and Processing*, *5*(3), 3-11.

[12]   Xia, G., Schiefermuller, A. (2010). The influence of support rollers of continuous casting machines on heat transfer and on stress-strain of slabs in secondary cooling. *Steel Research International*, *81*(8), 652-659.

[13]   Shiro, N. (1984). The maximum and minimum values of the heat Q transmitted from metal to boiling water under atmospheric pressure. *International Journal of Heat and Mass Transfer*, *27*(7), 959-970.

[14]   Agrawal, C. (2019). Surface quenching by jet impingement-a review. *Steel Research International*, *90*(1), 1800285.

[15]   Mozumder, A. K., Monde, M., & Woodfield, P. L. (2005). Delay of wetting propagation during jet impingement quenching for a high temperature surface. *International Journal of Heat and Mass Transfer*, *48*(25-26), 5395-5407.

[16]   Weigand, B., & Spring, S. (2011). Multiple jet impingement-a review. *Heat Transfer Research*, *42*(2), 101-142.

[17]   Ma, H., Silaen, A. K., & Zhou, C., Q. (2020). Numerical development of heat transfer coefficient correlation for spray cooling in continuous casting. *Frontiers in Materials*, *7*, 397.

[18]   Glaser, H. (1962). Untersuchungen an schlitz-und mehrdüsenanordnungen bei der trocknung feuchter oberflächen durch warmluftstrahlen. *Chemie Ingenieur Technik*, *34*(3), 200-207.

[19]   Sengupta, J., Thomas, B. G., & Wells, M. A. (2005). The use of water cooling during the continuous casting of steel and aluminum alloys. *Metallurgical and Materials Transactions A*, *36*(1), 187-204.

[20]   Zuckerman, N., & Lior, N. (2006). Jet impingement heat transfer: physics, correlations, and numerical modeling. *Advances in Heat Transfer*, *39*, 565-631.

[21]   Viskanta, R. (1993). Heat transfer to impinging isothermal gas and flame jets. *Experimental Thermal and Fluid Science*, *6*(2), 111-134.

[22]   Martin, H. (1977). Heat and mass transfer between impinging gas jets and solid surfaces. *Advances in Heat Transfer*, *13*, 1-60.

[23]   Maurel, S., & Solliec, C. (2001). A turbulent plane jet impinging nearby and far from a flat plate. *Experiments in Fluids*, *31*(6), 687-696.

[24]   Mugele, R. A., & Evans, H. D. (1951). Droplet size distribution in sprays. *Industrial & Engineering Chemistry*, *43*(6), 1317-1324.

[25]   Rayleigh, L. (1878). On the instability of jets. *Proceedings of the London Mathematical Society*, *1*(1), 4-13. London Mathematical Society.

[26]   Weber, C. (1931). Disintegration of liquid jets. *Journal of Applied Mathematics and Mechanics*, *11*(2), 136-159.

[27]   Ohnesorge, W. (1936). The formation of drops by nozzles and the breakup of liquid jets. *Journal of Applied Mathematics and Mechanics*, *16*(6), 355-358.

[28]   Zeoli, N., Tabbara, H., & Gu, S. (2011). CFD modeling of primary breakup during metal powder atomization. *Chemical Engineering Science*, *66*(24), 6498-6504.

[29]   Altimira, M., Rivas, A., Anton, R., Sanchez Larraona, G., & Ramos, J. C. (2007,). Fan-spray atomizers analysis through mathematical modeling. *Proceedings of the 21ˢᵗ ILASS-Europe Meeting*. Institute for Liquid Atomization and Spray Systems.

[30]   Koutsakis, K., Gu, S., & Vardelle, A. (2013). Three dimensional CFD simulation of liquid copper break up for the liquid precursor spraying. *Surface and Coatings Technology*, *220*, 214-218.

[31]   Kalata, W., Brown, K., O'Donnell, S., & Schick, R. J. (2014). Transfer efficiency for an oil spray application. *Proceedings of the 26ᵗʰ ILASS Americas Annual Conference on Liquid Atomization and Spray Systems*. Institute for Liquid Atomization and Spray Systems-Aemericas.

[32]   Alkhedhair, A., Jahn, I., Gurgenci, H., Guan, Z., He, S., & Lu, Y. (2016). Numerical simulation of water spray in natural draft dry cooling towers with a new nozzle representation approach. *Applied Thermal Engineering*, *98*, 924-935.

[33]   Senecal, P. K., Schmidt, D. P., Nouar, I., Rutland, C. J., Reitz, R. D., & Corradini, M. L. (1999). Modeling high-speed viscous liquid sheet atomization. *International Journal of Multiphase Flow*, *25*(6-7), 1073-1097.

[34]   Fung, M. C., Inthavong, K., Yang, W., & Tu, J. (2012). CFD modeling of spray atomization for a nasal spray device. *Aerosol Science and Technology*, *46*(11), 1219-1226.

[35]   Nijdam, J. J., Guo, B., Fletcher, D. F., & Langrish, T. A. (2006). Lagrangian and Eulerian models for simulating turbulent dispersion and coalescence of droplets within a spray. *Applied Mathematical Modelling*, *30*(11), 1196-1211.

[36]   Naber, J. D., & Reitz, R. D. (1988). Modeling engine spray/wall impingement. *SAE Transactions*, 118-140.

[37]   Lefebvre, A. H., & McDonell, V. G. (2017). *Atomization and sprays* (2nd ed.). Cleveland, OH: CRC press.

[38]   Bhatia, J. C., Domnick, J., Durst, F., & Tropea, C. (1988). Phase-Doppler-anemometry and the log-hyperbolic distribution applied to liquid sprays. *Particle & Particle Systems Characterization*, *5*(4), 153-164.

[39]   Xu, T. H., Durst, F., & Tropea, C. (1993). The three-parameter log-hyperbolic distribution and its application to particle sizing. *Atomization and Sprays*, *3*(1).

[40]   Babinsky, E., & Sojka, P. E. (2002). Modeling drop size distributions. *Progress in Energy and Combustion Science*, *28*(4), 303-329.

[41]   Rosin, P., & Rammler, E. (1933). Laws governing the fineness of a powdered coal. *Journal of the Institute of Fuel*, *7*.

[42]   König, G., Anders, K., & Frohn, A. (1986). A new light-scattering technique to measure the diameter of periodically generated moving droplets. *Journal of Aerosol Science*, *17*(2), 157-167.

[43]   Damaschke, N., Kalantari, D., Roisman, I. V., & Tropea, C. (2005). Characterization of spray transport and spray/wall interactions using the IPI technique. *Proceedings of the 20th ILASS- Europe Meeting*, 379-384. Institute for Liquid Atomization and Spray Systems.

[44]   Kawaguchi, T., Kobayashi, T., & Maeda, M. (2002). Measurement of spray flow by an improved interferometric laser imaging droplet sizing (ILIDS) system. In R. J. Adrian (Ed.), C. Tropea (Ed.). *Laser Techniques for Fluid Mechanics* (209-220). Heidelberg, Berlin: Springer.

[45]   Glover, A. R., Skippon, S. M., & Boyle, R. D. (1995). Interferometric laser imaging for droplet sizing: a method for droplet-size measurement in sparse spray systems. *Applied Optics*, *34*(36), 8409-8421.

[46]   Albrecht, H. E., Damaschke, N., Borys, M., & Tropea, C. (2013). *Laser Doppler and phase Doppler measurement techniques*. Heidelberg, Berlin: Springer.

[47]   Damaschke, N., Nobach, H., Nonn, T. I., Semidetnov, N., & Tropea, C. (2005). Multi-dimensional particle sizing techniques. *Experiments in Fluids*, *39*(2), 336-350.

[48]   Hernández-Bocanegra, C. A., Minchaca-Mojica, J. I., Acosta-González, F. A., Zhou, X., & Thomas, B. G. (2013). Measurement of heat flux in dense air-mist cooling: Part II-The influence of mist characteristics on steady-state heat transfer. *Experimental Thermal and Fluid science*, *44*, 161-173.

[49]   Presser, C., Papadopoulos, G., & Widmann, J. F. (2006). PIV measurements of water mist transport in a homogeneous turbulent flow past an obstacle. *Fire Safety Journal*, *41*(8), 580-604.

[50]   Sheppard, D. T., & Lueptow, R. M. (2005). Characterization of fire sprinkler sprays using particle image velocimetry. *Atomization and Sprays*, *15*(3).

[51]   Popper, J., Abuaf, N., & Hetsroni, G. (1974). Velocity measurements in a two-phase turbulent jet. *International Journal of Multiphase Flow*, *1*(5), 715-726.

[52]   Yanta, W. (1973, July). Measurements of aerosol size distributions with a laser Doppler velocimeter/LDV. *Proceedings of the 6th Fluid and Plasma Dynamics Conference*, 705. American Institute of Aeronautics and Astronautics.

[53]   Zalay, A. D., Bouse, L. F., Carlton, J. B., Crookshank, H. R., Eberle, W. R., Howie, R. E., & Shrider, K. R. (1980). Measurement of airborne spray with a laser Doppler velocimeter. *Transactions of the ASAE*, *23*(3), 548-0552.

[54]   Zhang, Y. Z., Wen, Z., Zhao, Z. W., Huang, J., Wu, W. F., & Li, B. W. (2019). Velocity characteristics of air-mist jet during secondary cooling of continuous casting using PIV and LDV. *ISIJ International*, *59*(6), 1072-1080.

[55]   Bauckhage, K., & Flögel, H. H. H. (1985, July). Simultaneous measurement of droplet size and velocity in nozzle sprays. *Proceedings of the 2nd International Symposium on Applications of Laser Anemometry to Fluid Mechanics*. Center for Alicated Thermodynamics and Fluid Mechanics at the Technical University of Lisbon.

[56]   Saffman, M. (1984). Simultaneous measurement of size, concentration and velocity of spherical particles by a laser Doppler method. *Laser Anemometry in Fluid Mechanics-II*, 85-104.

[57]   Bachalo, W. D., & Houser, M. J. (1984). Phase/Doppler spray analyzer for simultaneous measurements of drop size and velocity distributions. *Optical Engineering*, *23*(5), 235583.

[58]   Husted, B. P., Petersson, P., Lund, I., & Holmstedt, G. (2009). Comparison of PIV and PDA droplet velocity measurement techniques on two high-pressure water mist nozzles. *Fire Safety Journal*, *44*(8), 1030-1045.

[59]   Schnars, U., & Jueptner, W. (2005). *Digital holography: Digital hologram recording, numerical reconstruction, and related techniques*. Heidelberg, Berlin: Springer.

[60]   Guildenbecher, D. R., Engvall, L., Gao, J., Grasser, T. W., Reu, P. L., & Chen, J. (2014). Digital in-line holography to quantify secondary droplets from the impact of a single drop on a thin film. *Experiments in Fluids*, *55*(3), 1670.

[61]   Guildenbecher, D. R., Gao, J., Reu, P. L., & Chen, J. (2013). Digital holography simulations and experiments to quantify the accuracy of 3D particle location and 2D sizing using a proposed hybrid method. *Applied Optics*, *52*(16), 3790-3801.

[62]   Polat, S., Huang, B., Mujumdar, A. S., & Douglas, W. J. M. (1989). Numerical flow and heat transfer under impinging jets: a review. *Annual Review of Heat Transfer*, 2.

[63]   Hofmann, H. M., Kaiser, R., Kind, M., & Martin, H. (2007). Calculations of steady and pulsating impinging jets-an assessment of 13 widely used turbulence models. *Numerical Heat Transfer, Part B: Fundamentals*, *51*(6), 565-583.

[64]   Jiang, X., Siamas, G. A., Jagus, K., & Karayiannis, T. G. (2010). Physical modelling and advanced simulations of gas-liquid two-phase jet flows in atomization and sprays. *Progress in Energy and Combustion Science*, *36*(2), 131-167.

[65]   Gao, S., & Voke, P. R. (1995). Large-eddy simulation of turbulent heat transport in enclosed impinging jets. *International Journal of Heat and Fluid Flow*, *16*(5), 349-356.

[66]   Beaubert, F., & Viazzo, S. (2002). Large eddy simulation of a plane impinging jet. *Comptes Rendus Mécanique*, *330*(12), 803-810.

[67]   Hällqvist, T. (2003). *Numerical study of impinging jets with heat transfer*. [Doctoral dissertation, KTH Royal Institute of Technology]. Google Scholar.

[68]   Olsson, M., & Fuchs, L. (1998). Large eddy simulations of a forced semiconfined circular impinging jet. *Physics of Fluids*, *10*(2), 476-486.

[69]   Launder, B. E., & Spalding, D. B. (1972). *Lectures in mathematical models of turbulence*. Academic Press.

[70]   Craft, T. J., Graham, L. J. W., & Launder, B. E. (1993). Impinging jet studies for turbulence model assessment-II. An examination of the performance of four turbulence models. *International Journal of Heat and Mass Transfer*, *36*(10), 2685-2697.

[71]   Yakhot, V., & Orszag, S. A. (1986). Renormalization group analysis of turbulence. I. Basic theory. *Journal of Scientific Computing*, *1*(1), 3-51.

[72]   Shih, T. H., Liou, W. W., Shabbir, A., Yang, Z., & Zhu, J. (1995). A new *k-ε* eddy viscosity model for high reynolds number turbulent flows. *Computers & Fluids*, *24*(3), 227-238.

[73]   Heck, U., Fritsching, U., & Bauckhage, K. (2001). Fluid flow and heat transfer in gas jet quenching of a cylinder. *International Journal of Numerical Methods for Heat & Fluid Flow*, *11*(1), 36-49.

[74]   Wilcox, D. C. (1998). *Turbulence modeling for CFD* (pp. 172-180). La Canada, CA: DCW industries.

[75]   Heyerichs, K., & Pollard, A. (1996). Heat transfer in separated and impinging turbulent flows. *International Journal of Heat and Mass Transfer*, *39*(12), 2385-2400.

[76]   Menter, F. (1993, July). Zonal two equation *k-ω* turbulence models for aerodynamic flows. *Proceedings of the 23rd Fluid Dynamics, Plasmadynamics, and Lasers Conference*. American Institute of Aeronautics and Astronautics.

[77]   Lane, W. R. (1951). Shatter of drops in streams of air. *Industrial & Engineering Chemistry*, *43*(6), 1312-1317.

[78]   Hinze, J. O. (1955). Fundamentals of the hydrodynamic mechanism of splitting in dispersion processes. *AIChE Journal*, *1*(3), 289-295.

[79]   Hsiang, L. P., & Faeth, G. M. (1995). Drop deformation and breakup due to shock wave and steady disturbances. *International Journal of Multiphase Flow*, *21*(4), 545-560.

[80]   Kennedy, J. B., & Roberts, J. (1990). Rain ingestion in a gas turbine engine. *Proceedings of the 4th ILASS Meeting* (p. 154). Institute for Liquid Atomization and Spray Systems.

[81]   Nicholls, J. A., & Ranger, A. A. (1969). Aerodynamic shattering of liquid drops. *AIAA Journal*, *7*(2), 285-290.

[82]   AVCO Systems Division Wilmington. (1970). *A study of drop breakup behind strong shocks with applications to flight* (No. AVSD-0110-70-RR). Wilmington, MA: Reinecke, W. G., & Waldman, G. D.

[83]   Liu, Z., & Reitz, R. D. (1997). An analysis of the distortion and breakup mechanisms of high speed liquid drops. *International Journal of Multiphase Flow*, *23*(4), 631-650.

[84]   Krzeczkowski, S. A. (1980). Measurement of liquid droplet disintegration mechanisms. *International Journal of multiphase flow*, *6*(3), 227-239.

[85]   Pilch, M., & Erdman, C. A. (1987). Use of breakup time data and velocity history data to predict the maximum size of stable fragments for acceleration-induced breakup of a liquid drop. *International Journal of Multiphase Flow*, *13*(6), 741-757.

[86]   Hsiang, L. P., & Faeth, G. M. (1992). Near-limit drop deformation and secondary breakup. *International Journal of Multiphase Flow*, *18*(5), 635-652.

[87]   Hsiang, L. P., & Faeth, G. M. (1993). Drop properties after secondary breakup. *International Journal of Multiphase Flow*, *19*(5), 721-735.

[88]   Wierzba, A. (1990). Deformation and breakup of liquid drops in a gas stream at nearly critical Weber numbers. *Experiments in Fluids*, *9*(1-2), 59-64.

[89]   Omidvar, A., & Khaleghi, H. (2012). An analytical approach for calculation of critical weber number of droplet breakup in turbulent gaseous flows. *Arabian Journal for Science and Engineering*, *37*(8), 2311-2321.

[90]   Flock, A. K., Guildenbecher, D. R., Chen, J., Sojka, P. E., & Bauer, H. J. (2012). Experimental statistics of droplet trajectory and air flow during aerodynamic fragmentation of liquid drops. *International Journal of Multiphase Flow*, *47*, 37-49.

[91]   Liu, A. B., Mather, D., & Reitz, R. D. (1993). Modeling the effects of drop drag and breakup on fuel sprays. *SAE Transactions*, 83-95.

[92]   Taylor, G. I. (1963). The shape and acceleration of a drop in a high speed air stream. *The Scientific Papers of GI Taylor*, *3*, 457-464.

[93]   O'Rourke, P. J., & Amsden, A. A. (1987). *The TAB method for numerical calculation of spray droplet breakup* (No. 872089). *SAE Technical Paper*.

[94]   Reitz, R. (1987). Modeling atomization processes in high-pressure vaporizing sprays. *Atomization and Spray Technology*, *3*(4), 309-337.

[95]   Reitz, R. D., & Bracco, F. V. (1986). Mechanisms of Breakup of Round Liquid Jets. In N. Cheremisnoff (Ed.), *The Encyclopedia of Fluid Mechanics* (pp. 223-249). Washington, D.C.: Department of Energy.

[96]   Reitz, R. D., & Bracco, F. V. (1982). Mechanism of atomization of a liquid jet. *Physics of Fluids*, *25*(10), 1730-1742.

[97]   Beale, J. C., & Reitz, R. D. (1999). Modeling spray atomization with the Kelvin-Helmholtz/Rayleigh-Taylor hybrid model. *Atomization and Sprays*, *9*(6).

[98]   Patterson, M. A., & Reitz, R. D. (1998). Modeling the effects of fuel spray characteristics on diesel engine combustion and emission. *SAE Transactions*, 27-43.

[99]   Apte, S. V., Gorokhovski, M., & Moin, P. (2003). LES of atomizing spray with stochastic modeling of secondary breakup. *International Journal of Multiphase Flow*, *29*(9), 1503-1522.

[100]   Tanner, F. X. (1997). Liquid jet atomization and droplet breakup modeling of non-evaporating diesel fuel sprays. *SAE Transactions*, 127-140.

[101]   Ibrahim, E. A., Yang, H. Q., & Przekwas, A. J. (1993). Modeling of spray droplets deformation and breakup. *Journal of Propulsion and Power*, *9*(4), 651-654.

[102]   Chryssakis, C., & Assanis, D. N. (2008). A unified fuel spray breakup model for internal combustion engine applications. *Atomization and Sprays*, *18*(5).

[103]   Chryssakis, C. A., Assanis, D. N., & Tanner, F. X. (2011). Atomization models. In Nasser A. Editor, *Handbook of Atomization and Sprays* (215-231). Springer, Boston, MA.

[104]   Park, J. Y., & Blair, L. M. (1975). The effect of coalescence on drop size distribution in an agitated liquid-liquid dispersion. *Chemical Engineering Science*, *30*(9), 1057-1064.

[105]   Shah, P. S., Fan, L. T., Kao, I. C., & Erickson, L. E. (1972). Modeling of growth processes with two liquid phases: a review of drop phenomena, mixing, and growth. *Advances in Applied Microbiology*, *15*, 367-414.

[106]   Ashgriz, N., & Givi, P. (1987). Binary collision dynamics of fuel droplets. *International Journal of Heat and Fluid Flow*, *8*(3), 205-210.

[107]   Jiang, Y. J., Umemura, A., & Law, C. K. (1992). An experimental investigation on the collision behaviour of hydrocarbon droplets. *Journal of Fluid Mechanics*, *234*, 171-190.

[108]   Qian, J., & Law, C. K. (1997). Regimes of coalescence and separation in droplet collision. *Journal of Fluid Mechanics*, *331*, 59-80.

[109]   Brenn, G., & Kolobaric, V. (2006). Satellite droplet formation by unstable binary drop collisions. *Physics of Fluids*, *18*(8), 087101.

[110]   Gotaas, C., Havelka, P., Jakobsen, H. A., Svendsen, H. F., Hase, M., Roth, N., & Weigand, B. (2007). Effect of viscosity on droplet-droplet collision outcome: Experimental study and numerical comparison. *Physics of Fluids*, *19*(10), 102106.

[111]   Kurt, O., Fritsching, U., & Schulte, G. (2007, September). Binary collisions of droplets with fluid and suspension particles. *Proceedings of the 21st ILASS Meeting*, 10-12. Institute for Liquid Atomization and Spray Systems.

[112]   Kuschel, M., & Sommerfeld, M. (2013). Investigation of droplet collisions for solutions with different solids content. *Experiments in Fluids*, *54*(2), 1440.

[113]   Estrade, J. P., Carentz, H., Lavergne, G., & Biscos, Y. (1999). Experimental investigation of dynamic binary collision of ethanol droplets–a model for droplet coalescence and bouncing. *International Journal of Heat and Fluid Flow*, *20*(5), 486-491.

[114]   Bush, J. W., & Hasha, A. E. (2004). On the collision of laminar jets: fluid chains and fishbones. *Journal of Fluid Mechanics*, *511*, 285-310.

[115]   Wadhwa, N., Vlachos, P., & Jung, S. (2013). Noncoalescence in the oblique collision of fluid jets. *Physical Review Letters*, *110*(12), 124502.

[116]   Finotello, G., Kooiman, R. F., Padding, J. T., Buist, K. A., Jongsma, A., Innings, F., & Kuipers, J. A. M. (2018). The dynamics of milk droplet–droplet collisions. *Experiments in Fluids*, *59*(1), 17.

[117]   Ashgriz, N., & Poo, J. Y. (1990). Coalescence and separation in binary collisions of liquid drops. *Journal of Fluid Mechanics*, *221*, 183-204.

[118]   Los Alamos National Laboratory. (1981). *Collective drop effects on vaporizing liquid sprays* (No. LA-9069-T). Los Alamos, NM: O'Rourke, P. J.

[119]   Rioboo, R., Tropea, C., & Marengo, M. (2001). Outcomes from a drop impact on solid surfaces. *Atomization and Sprays*, *11*(2), 155-165.

[120]   Yarin, A. L. (2006). Drop impact dynamics: splashing, spreading, receding, bouncing…. *Annual Review of Fluid Mechanics*, *38*, 159-192.

[121]   Ogawa, H., Matsui, Y., Kimura, S., & Kawashima, J. I. (1997). Three-dimensional computation of in-cylinder flow and combustion characteristics in diesel engines-Effect of wall impingement models of fuel droplet behavior on combustion characteristics. *JSAE Review*, *18*(2), 95-99.

[122] Kuniyoshi, H., Tanabe, H., Sato, G. T., & Fujimoto, H. (1980). Investigation on the characteristics of diesel fuel spray. *SAE Transactions*, 2998-3014.

[123] Werlberger, P., & Cartellieri, W. P. (1987). Fuel injection and combustion phenomena in a high speed DI diesel engine observed by means of endoscopic high speed photography. *SAE Transactions*, 27-37.

[124] Grover, R. O., & Assanis, D. N. (2001, July). A spray wall impingement model based upon conservation principles ((fs-3) fuel sprays 3-modeling). *Proceedings of the 5th International Symposium on Diagnostics and Modeling of Combustion in Internal Combustion Engines*, *75*. The Japan Society of Mechanical Engineers.

[125] Bai, C., & Gosman, A. D. (1995). Development of methodology for spray impingement simulation. *SAE Transactions*, 550-568.

[126] Kalantari, D. (2013). Evaluation of some of the existing models for droplet and spray/wall interactions. *Fluid Dynamics & Materials Processing*, *92*, 169-182.

[127] Werner, S. R., Jones, J. R., Paterson, A. H., Archer, R. H., & Pearce, D. L. (2007). Air-suspension coating in the food industry: Part II-micro-level process approach. *Powder Technology*, *171*(1), 34-45.

[128] Mahulkar, A. V., Marin, G. B., & Heynderickx, G. J. (2015). Droplet-wall interaction upon impingement of heavy hydrocarbon droplets on a heated wall. *Chemical Engineering Science*, *130*, 275-289.

[129] Lee, S. Y., & Ryu, S. U. (2006). Recent progress of spray-wall interaction research. *Journal of Mechanical Science and Technology*, *20*(8), 1101-1117.

[130] Šikalo, Š., Tropea, C., & Ganić, E. N. (2005). Impact of droplets onto inclined surfaces. *Journal of Colloid and Interface Science*, *286*(2), 661-669.

[131] Stanton, D. W., & Rutland, C. J. (1996). Modeling fuel film formation and wall interaction in diesel engines. *SAE Transactions*, 808-824.

[132] Bai, C. X., Rusche, H., & Gosman, A. D. (2002). Modeling of gasoline spray impingement. *Atomization and Sprays*, *12*(1-3).

[133] Yoon, S. S., & DesJardin, P. E. (2006). Modelling spray impingement using linear stability theories for droplet shattering. *International Journal for Numerical Methods in Fluids*, *50*(4), 469-489.

[134] Mundo, C. H. R., Sommerfeld, M., & Tropea, C. (1995). Droplet-wall collisions: experimental studies of the deformation and breakup process. *International Journal of Multiphase Flow*, *21*(2), 151-173.

[135] Cossali, G. E., Coghe, A. L. D. O., & Marengo, M. (1997). The impact of a single drop on a wetted solid surface. *Experiments in Fluids*, *22*(6), 463-472.

[136] Fukumoto, M., Nishioka, E., & Nishiyama, T. (2002). New criterion for splashing in flattening of thermal sprayed particles onto flat substrate surface. *Surface and Coatings Technology*, *161*(2-3), 103-110.

[137] Bolle, L., & Moureau, J. (2016). Theory and application on spray cooling of hot surfaces. *Multiphase Science and Technology*, *28*(4), 321-417.

[138] Wang, H., Yu, W., & Cai, Q. (2012). Experimental study of heat transfer coefficient on hot steel plate during water jet impingement cooling. *Journal of Materials Processing Technology*, *212*(9), 1825-1831.

[139] Wang, B., Lin, D., Xie, Q., Wang, Z., & Wang, G. (2016). Heat transfer characteristics during jet impingement on a high-temperature plate surface. *Applied Thermal Engineering*, *100*, 902-910.

[140] Wachters, L. H. J., Bonne, H., & Van Nouhuis, H. J. (1966). The heat transfer from a hot horizontal plate to sessile water drops in the spherodial state. *Chemical Engineering Science*, *21*(10), 923-936.

[141] Toda, S., & Uchida, H. (1973). Study of liquid film cooling with evaporation and boiling. *Transactions of JSME*, *2*, 44-62.

[142] Moreaux, F., Chevrier, J. C., & Beck, C. (1978). Caracteristiques et cohtrole par miniordinateur de refroidissements par pulverisation. *Proceedings of the 6th International Heat Transfer Conference*, 101-105. International Heat Transfer Conference Digital Library.

[143] Bernardin, J. D., & Mudawar, I. (1999). The Leidenfrost point: experimental study and assessment of existing models. *Journal of Heat Transfer*, *121*(4), 894-903.

[144] Raudensky, M., & Horsky, J. (2005). Secondary cooling in continuous casting and Leidenfrost temperature effects. *Ironmaking & Steelmaking*, *32*(2), 159-164.

[145] Hnizdil, M., Kominek, J., Lee, T. W., Raudensky, M., Carnogurska, M., & Chabicovsky, M. (2020). Prediction of Leidenfrost Temperature in Spray Cooling for Continuous Casting and Heat Treatment Processes. *Metals*, *10*(11), 1551.

[146]   Baumeister, K. J., & Simon, F. F. (1973). Leidenfrost temperature-its correlation for liquid metals, cryogens, hydrocarbons, and water. *Journal of Heat Transfer*, *95*(2), 166-173.

[147]   Bernardin, J. D., & Mudawar, I. (2004). A Leidenfrost point model for impinging droplets and sprays. *Journal of Heat Transfer*, *126*(2), 272-278.

[148]   Al-Ahmadi, H. M., & Yao, S. C. (2008). Spray cooling of high temperature metals using high mass flux industrial nozzles. *Experimental Heat Transfer*, *21*(1), 38-54.

[149]   Yao, S. C., & Cox, T. L. (2002). A general heat transfer correlation for impacting water sprays on high-temperature surfaces. *Experimental heat transfer*, *15*(4), 207-219.

[150]   Issa, R. J. (2004). *Numerical modeling of the dynamics and heat transfer of impacting sprays for a wide range of pressures* [Doctoral dissertation, University of Pittsburgh]. University of Pittsburgh.

[151]   Berenson, P. J. (1961). Film-boiling heat transfer from a horizontal surface. *Journal of Heat Transfer*, *83*(3), 351-356.

[152]   Thomas, B. G., & Ho, B. (1996). Spread sheet model of continuous casting. *Journal of Manufacturing Science and Engineering*, *118*(1), 37-44.

[153]   Blazek, K., Moravec, R., Zheng, K., Lowry, M., & Yin, H. (2013). Dynamic Simulation of Slab Centerline Behavior of the Continuous Casting Process during Large Speed Transitions and Their Effects on Slab Internal Quality. *Proceedings of the 5th International STEELSIM Conference*. The Austrian Society for Metallurgy and Materials.

[154]   Petrus, B., Zheng, K., Zhou, X., Thomas, B. G., & Bentsman, J. (2011). Real-time, model-based spray-cooling control system for steel continuous casting. *Metallurgical and Materials Transactions B*, *42*(1), 87-103.

[155]   Laitinen, E., & Neittaanmäki, P. (1988). On numerical simulation of the continuous casting process. *Journal of Engineering Mathematics*, *22*(4), 335-354.

[156]   Thomas, B. G., Behera, A. K., Bentsman, J., Zheng, K., Vapalahti, S., Petrus, B., Castillejos, A. H., & Acosta, F. A. (2006). Online dynamic control of cooling in continuous casting of thin steel slabs. *Proceedings of NSF Grant Conference*. National Science Foundation.

[157]   Zheng, K., Petrus, B., Thomas, B. G., & Bentsman, J. (2007). Design and implementation of a real-time spray cooling control system for continuous casting of thin steel slabs. *Proceedings of AISTech-Iron and Steel Technology Conference 2007*, (12 pages). AIST Digital Library.

[158] Słota, D. (2009). Identification of the cooling condition in 2-D and 3-D continuous casting processes. *Numerical Heat Transfer, Part B: Fundamentals*, *55*(2), 155-176.

[159] El-Bealy, M. O. (2011). Air-water mist and homogeneity degree of spray cooling zones for improving quality in continuous casting of steel. *Steel Research International*, *82*(10), 1187-1206.

[160] Ji, C., Luo, S., Zhu, M., & Sahai, Y. (2014). Uneven solidification during wide-thick slab continuous casting process and its influence on soft reduction zone. *ISIJ international*, *54*(1), 103-111.

[161] Zhao, Y., Chen, D. F., Long, M. J., Shen, J. L., & Qin, R. S. (2014). Two-dimensional heat transfer model for secondary cooling of continuously cast beam blanks. *Ironmaking & Steelmaking*, *41*(5), 377-386.

[162] Kavička, F., Dobrovská, J., Štětina, J., Stránský, K., Katolický, J., Sekanina, B., Heger, J., & Francová, H. (2016). *Numerical models of solidification and their application in metal and ceramic technology*. Brno, Czech Republic.

[163] Chen, Z. (2016). *Study of spray-cooling control for maintaining metallurgical length or surface temperature during speed drop for steel continuous casting* [Doctoral dissertation, University of Illinois at Urbana-Champaign]. Illinois Digital Environment for Access to Learning and Scholarship.

[164] Hardin, R. A., & Beckermann, C. (2018, May). Heat transfer and solidification modeling of continuous steel slab casting. *Proceedings of AISTech-Iron and Steel Technology Conference 2018*. AIST Digital Library.

[165] Nozaki, T., Matsuno, J. I., Murata, K., Ooi, H., & Kodama, M. (1978). A secondary cooling pattern for preventing surface cracks of continuous casting slab. *ISIJ International*, *18*(6), 330-338.

[166] Brimacombe, J. K., Agarwal, P. K., Baptista, L. A., Hibbins, S., & Prabhakar, B. (1980). Spray cooling in the continuous casting of steel. *Continuous Casting*, *2*, 109-123.

[167] Hardin, R. A., Shen, H., & Beckermann, C. (2000, August). Heat transfer modeling of continuous steel slab caster using realistic spray patterns. *Proceedings of Modelling of Casting, Welding and Advanced Solidification Processes IX*, 729-736. The Minerals, Metals & Materials Society.

[168] Klinzing, W. P., Rozzi, J. C., & Mudawar, I. (1992). Film and transition boiling correlations for quenching of hot surfaces with water sprays. *Journal of Heat Treating*, *9*(2), 91-103.

[169] Fujimoto, H., Hatta, N., Asakawa, H., & Hashimoto, T. (1997). Predictable modelling of heat transfer coefficient between spraying water and a hot surface above the Leidenfrost temperature. *ISIJ international*, *37*(5), 492-497.

[170] Nasr, G. G., Yule, A. J., & Bendig, L. (2013). *Industrial sprays and atomization: design, analysis and applications*. Berlin/Heidelberg, Germany: Springer Science & Business Media.

[171] Hernández-Bocanegra, C. A., Minchaca-Mojica, J. I., Acosta-González, F. A., Zhou, X., & Thomas, B. G. (2013). Measurement of heat flux in dense air-mist cooling: Part II-The influence of mist characteristics on steady-state heat transfer. *Experimental Thermal and Fluid Science*, *44*, 161-173.

[172] Chabicovsky, M., Kotrbacek, P., Bellerova, H., Kominek, J., & Raudensky, M. (2020). *Spray cooling heat transfer above Leidenfrost temperature*. *Metals*, *10*(9), 1270.

[173] Long, M., Chen, H., Chen, D., Yu, S., Liang, B., & Duan, H. (2018). A combined hybrid 3-D/2-D model for flow and solidification prediction during slab continuous casting. *Metals*, *8*(3), 182.

[174] Touloulian, Y. S., Powell, R. W., Ho, C. Y., & Klemens, P. B. (1972). *Thermophysical Properties of Matter*. New York, NY: IFI/Plenum.

[175] Morales, R. D., Lopez, A. G., & Olivares, I. M. (1990). Heat transfer analysis during water spray cooling of steel rods. *ISIJ International*, *30*(1), 48-57.

[176] Horsky, J., Raudensky, M., & Tseng, A. A. (2005). Heat transfer study of secondary cooling in continuous casting. *Proceedings of AISTech-Iron and Steel Technology Conference 2005*, *2*, 141-148. AIST Digital Library.

[177] Chen, Z., Bentsman, J., Thomas, B. G., & Mastsui, A. (2017). Study of spray-cooling control for maintaining metallurgical length during speed drop in steel continuous casting. *Proceedings of AISTech-Iron and Steel Technology Conference 2017*. AIST Digital Library.

[178] Lan, Y. (2000). *FEM analysis of bulging between rolls in continuous casting*. [Master's thesis, University of Illinois at Urbana-Champaign]. Continuous Casting Consortium.

[179] El-Bealy, M. O. (2013). Spray cooling pattern and microthermomechanical rigidity criterion for improving inner quality in continuously cast steel slabs. *Ironmaking & Steelmaking*, *40*(3), 167-188.

[180] Viňáš, J., Brezinová, J., & Guzanová, A. (2013) Analysis of the quality renovated continuous steel casting roller. *Sadhana*, *38*(3), 477-490.

[181] Bhattacharya, A. K., & Sambasivam, D. (2009). Optimization of oscillation parameters in continuous casting process of steel manufacturing: Genetic Algorithms versus Differential Evolution. In Wellington Pinheirp dos Santos Editor, *Evolutionary Computation* (77-102). In-Teh.

[182] Mazumdar, S., & Ray, S. K. (2001). Solidification control in continuous casting of steel. *Sadhana*, *26*(1-2), 179-198.

[183] Bolender, T., & Cappel, J. (2004). Continuous casting without secondary spray water cooling. *Steel Grips*, *2*(2), 1-6.

[184] Thomas, B. G., & Stone, D. (1998). *Measurement of temperature, solidification, and microstructure in a continuous cast thin slab*. Retrieved from CiteSeer[X].

[185] Thomas, B. G., O'Malley, R., Shi, T., Meng, Y., Creech, D., & Stone, D. (2000). Validation of fluid flow and solidification simulation of a continuous thin-slab caster. *Proceedings of Modeling of Casting, Welding, and Advanced Solidification Processes IX*, *20*, 25. Shaker Verlag GmbH.

[186] Wu, M., Vakhrushev, A., Karimi-Sibaki, E., Kharicha, A., & Ludwig, A. (2014). Advanced process simulation of solidification and melting. *BHM Berg-und Hüttenmännische Monatshefte*, *159*(1), 30-40.

[187] Ludwig, A., & Mogeritsch, J. (2016). Compact seaweed growth of peritectic phase on confined, flat properitectic dendrites. *Journal of Crystal Growth*, *455*, 99-104.

[188] Ludwig, A., Kharicha, A., Hölzl, C., Domitner, J., Wu, M., & Pusztai, T. (2014). 3D Lattice Boltzmann flow simulations through dendritic mushy zones. *Engineering Analysis with Boundary Elements*, *45*, 29-35.

[189] Ahmadein, M., Wu, M., & Ludwig, A. (2015). Analysis of macrosegregation formation and columnar-to-equiaxed transition during solidification of Al-4 wt.% Cu ingot using a 5-phase model. *Journal of crystal growth*, *417*, 65-74.

[190] Boettinger, W. J., Coriell, S. R., Greer, A. L., Karma, A., Kurz, W., Rappaz, M., & Trivedi, R. (2000). Solidification microstructures: recent developments, future directions. *Acta Materialia*, *48*(1), 43-70.

[191] Krane, M. J. M., Johnson, D. R., & Raghavan, S. (2009). The development of a cellular automaton-finite volume model for dendritic growth. *Applied Mathematical Modelling*, *33*(5), 2234-2247.

[192] Schiff, J. L. (2011). *Cellular automata: a discrete view of the world*. Hoboken, NJ: Wiley.

[193] Zaeem, M. A., Yin, H., & Felicelli, S. D. (2012). Comparison of cellular automaton and phase field models to simulate dendrite growth in hexagonal crystals. *Journal of Materials Science & Technology*, *28*(2), 137-146.

[194] Jeong, J. H., Goldenfeld, N., & Dantzig, J. A. (2001). Phase field model for three-dimensional dendritic growth with fluid flow. *Physical Review E*, *64*(4), 041602.

[195] Karma, A., & Rappel, W. J. (1996). Numerical simulation of three-dimensional dendritic growth. *Physical Review Letters*, *77*(19), 4050.

[196] Karma, A., & Rappel, W. J. (1999). Phase-field model of dendritic side branching with thermal noise. *Physical Review E*, *60*(4), 3614.

[197] Pfeiler, C. (2008). *Modeling of turbulent particle/gas dispersion in the mold region and particle entrapment into the solid shell of a steel continuous caster* [Doctoral dissertation; University of Leoben]. ResearchGate.

[198] Pfeiler, C., Wu, M., & Ludwig, A. (2005). Influence of argon gas bubbles and non-metallic inclusions on the flow behavior in steel continuous casting. *Materials Science and Engineering: A*, *413*, 115-120.

[199] Pfeiler, C., Thomas, B. G., Wu, M., Ludwig, A., & Kharicha, A. (2008). Solidification and particle entrapment during continuous casting of steel. *Steel Research International*, *79*(8), 599-607.

[200] Voller, V., Markatos, N., & Cross, M. (1985). Techniques for accounting for the moving interface in convection/diffusion phase change. In R.W. Lewis & K. Morgan (Eds.), *Unknown Book Title* (pp. 595-609). Swansea, U. K.: Pineridge Press.

[201]   Voller, V. R., Markatos, N. C., & Cross, M. (1986). Solidification in convection-diffusion. In N. C. Markatos, M. Cross, D. G. Tatchell, & N. Rhodes (Eds.), *Numerical simulation of fluid flow and heat/mass transfer processes* (pp. 425-432). Berlin, Germany: Springer.

[202]   Voller, V. R., Cross, M., & Markatos, N. C. (1987). An enthalpy method for convection/diffusion phase change. *International Journal for Numerical Methods in Engineering*, *24*(1), 271-284.

[203]   Voller, V. R., & Prakash, C. (1987). A fixed grid numerical modelling methodology for convection-diffusion mushy region phase-change problems. *International Journal of Heat and Mass Transfer*, *30*(8), 1709-1719.

[204]   Voller, V. R., Brent, A. D., & Prakash, C. (1989). The modelling of heat, mass and solute transport in solidification systems. *International Journal of Heat and Mass Transfer*, *32*(9), 1719-1731.

[205]   Morgan, K. (1981). A numerical analysis of freezing and melting with convection. *Computer Methods in Applied Mechanics and Engineering*, *28*(3), 275-284.

[206]   Gartling, D. K. (1978). Finite element analysis of convective heat transfer problems with change of phase. *International Nuclear Information System*, *9*(24).

[207]   Liu, X. F., Zhang, J. Y., Du, W. D., Zhai, Q. J., & Li, Q. (2007). Analysis of flow field and temperature distribution in compact strip production casting process. *Ironmaking & Steelmaking*, *34*(6), 491-500.

[208]   Wu, M., Vakhrushev, A., Nummer, G., Pfeiler, C., Kharicha, A., & Ludwig, A. (2010). Importance of melt flow in solidifying mushy zone. *The Open Conservation Biology Journal*, *2*(1), 16-23.

[209]   Vakhrushev, A., Ludwig, A., Wu, M., Tang, Y., Nitzl, G., Hackl, G., & Vakhrushev, A. (2011). Modeling of heat transfer and solidification processes in thin slab caster. *Proceedings of European Conference on Continuous Casting*. AIM Associazione Italiana di Metallurgia.

[210]   Vakhrushev, A., Wu, M., Ludwig, A., Tang, Y., Hackl, G., & Nitzl, G. (2012). Modeling of the flow-solidification interaction in thin slab casting. *Proceedings of IOP Conference Series: Materials Science and Engineering*, *33*(1), 012014. IOP Publishing.

[211]   Garcia-Hernandez, S., de Jesús Barreto, J., Morales, R. D., & Arcos-Gutierrez, H. (2013). Numerical simulation of heat transfer and steel shell growth in a curved slab mold. *ISIJ International*, *53*(5), 809-817.

[212] Niu, R., Li, B., Liu, Z., & Li, X. (2017, August). Numerical investigation on effect of strip addition on solidification behavior in bloom continuous casting. *Proceedings of the 7th International STEELSIM Conference*. The Austrian Society for Metallurgy and Materials.

[213] Tang, L., Yao, M., Wang, X., & Zhang, X. (2012). Non-uniform thermal behavior and shell growth within mould for wide and thick slab continuous casting. *Steel Research International*, *83*(12), 1203-1213.

[214] Hofmann, H. M., Kaiser, R., Kind, M., & Martin, H. (2007). Calculations of steady and pulsating impinging jets-an assessment of 13 widely used turbulence models. *Numerical Heat Transfer, Part B: Fundamentals*, *51*(6), 565-583.

[215] ANSYS, Inc Ansys® Fluent 2020R1. (n.d.). *Help System: Theory Guide*. https://ansyshelp.ansys.com/account/secured?returnurl=/Views/Secured/corp/v211/en/flu_th/flu_th.html

[216] Cussler, E. L., & Cussler, E. L. (2009). *Diffusion: mass transfer in fluid systems*. Cambridge university press.

[217] Yimer, I., Campbell, I., & Jiang, L. Y. (2002). Estimation of the turbulent Schmidt number from experimental profiles of axial velocity and concentration for high-Reynolds-number jet flows. *Canadian Aeronautics and Space Journal*, *48*(3), 195-200.

[218] Tominaga, Y., & Stathopoulos, T. (2007). Turbulent Schmidt numbers for CFD analysis with various types of flow field. *Atmospheric Environment*, *41*(37), 8091-8099.

[219] Kuo, K. K. (2005). *Principles of combustion* (2nd ed.). New Jersey, NJ: John Wiley & Sons, Inc.

[220] Bailly, C., & Comte-Bellot, G. (2015). *Turbulence*. Berlin, Germany: Springer.

[221] Yakhot, V., Orszag, S. A., & Yakhot, A. (1987). Heat transfer in turbulent fluids-I. Pipe flow. *International Journal of Heat and Mass Transfer*, *30*(1), 15-22.

[222] Chua, L. P., & Antonia, R. A. (1990). Turbulent Prandtl number in a circular jet. *International Journal of Heat and Mass Transfer*, *33*(2), 331-339.

[223] Siegel, R. H. J. R., & Howell, J. R. (1992). *Thermal radiation heat transfer*. Washington DC: Hemisphere Pub. Corp.

[224] Han, Z., Parrish, S. E., Farrell, P. V., & Reitz, R. D. (1997). Modeling atomization processes of pressure-swirl hollow-cone fuel sprays. *Atomization and Sprays*, *7*(6), 663-684.

[225] Post, S. L., & Hewitt, A. J. (2018). Flat-fan spray atomization model. *Transactions of the ASABE*, *61*(4), 1249-1256.

[226] Altimira, M., Rivas, A., Larraona, G. S., Anton, R., & Ramos, J. C. (2009). Characterization of fan spray atomizers through numerical simulation. *International Journal of Heat and Fluid Flow*, *30*(2), 339-355.

[227] Sayinci, B. (2015). Effect of strainer type, spray pressure, and orifice size on the discharge coefficient of standard flat-fan nozzles. *Turkish Journal of Agriculture and Forestry*, *39*(5), 692-704.

[228] Lichtarowicz, A., Duggins, R. K., & Markland, E. (1965). Discharge coefficients for incompressible non-cavitating flow through long orifices. *Journal of Mechanical Engineering Science*, *7*(2), 210-219.

[229] Dombrowski, N., & Hooper, P. C. (1962). The effect of ambient density on drop formation in sprays. *Chemical Engineering Science*, *17*(4), 291-305.

[230] Schmidt, D. P., Corradini, M. L., Rutland, C.J. (1999). A two-dimensional, non-equilibrium model of flashing nozzle flow. *Proceedings of the 3rd ASME/JSME Joint Fluids Engineering Conference*. American Society of Mechanical Engineers.

[231] Tomar, G., Fuster, D., Zaleski, S., & Popinet, S. (2010). Multiscale simulations of primary atomization. *Computers & Fluids*, *39*(10), 1864-1874.

[232] Adeniyi, A., Morvan, H., & Simmons, K. A. (2017). A coupled Euler-Lagrange CFD modelling of droplets-to-film. *The Aeronautical Journal*, *121*(1246), 1897-1918.

[233] Brackbill, J. U., Kothe, D. B., & Zemach, C. (1992). A continuum method for modeling surface tension. *Journal of Computational Physics*, *100*(2), 335-354.

[234] Sami, M. (2018, February 28). Ansys fluent 19 speeds up CFD spray simulations. Ansys Blog. https://www.ansys.com/blog/fluent-19-speeds-cfd-spray-simulations.

[235] Pal, B. (2019). *Numerical investigation of spray formation in air-blast atomizers: numerical study of air-blast atomization using a hybrid volume of fluid/discrete phase solver* [Doctoral dissertation, Delft University of Technology]. Google Scholar.

[236] Li, J., & Kawano, H. (1995). Simulating water-drop movement from noncircular sprinkler nozzles. *Journal of Irrigation and Drainage Engineering*, *121*(2), 152-158.

[237] Gosman, A. D., & Loannides, E. (1983). Aspects of computer simulation of liquid-fueled combustors. *Journal of Energy*, *7*(6), 482-490.

[238]   Shuen, J. S., Chen, L. D., & Faeth, G. M. (1983). Evaluation of a stochastic model of particle dispersion in a turbulent round jet. *AIChE Journal*, *29*(1), 167-170.

[239]   Bernardin, J. D., & Mudawar, I. (1999). The Leidenfrost point: experimental study and assessment of existing models. *Journal of Heat Transfer*, *121*(4), 894-903.

[240]   Birkhold, F. (2007). Selektive katalytische reduktion von stickoxiden in kraftfahrzeugen: Untersuchung der einspritzung von harnstoffwasserlösung [Doctoral dissertation, Universität Karlsruhe]. Google Scholar.

[241]   Akao, F., Araki, K., Mori, S., & Moriyama, A. (1980). Deformation behaviors of a liquid droplet impinging onto hot metal surface. *ISIJ International*, *20*(11), 737-743.

[242]   Emmerson, G. S. (1975). The effect of pressure and surface material on the Leidenfrost point of discrete drops of water. *International Journal of Heat and Mass Transfer*, *18*(3), 381-386.

[243]   Brimacombe, J. K., Samarasekera, I. V., & Lait, J. E. (1984). *Continuous casting: heat flow, solidification and crack formation*. Warrendale, PA: Iron & Steel Society of AIME.

[244]   Miller, R. S., Harstad, K., & Bellan, J. (1998). Evaluation of equilibrium and non-equilibrium evaporation models for many-droplet gas-liquid flow simulations. *International Journal of Multiphase Flow*, *24*(6), 1025-1055.

[245]   Sazhin, S. S. (2006). Advanced models of fuel droplet heating and evaporation. *Progress in Energy and Combustion Science*, *32*(2), 162-214.

[246]   Ranz, W. E., & Marshall, W. R. (1952). Evaporation from drops, Part I and Part II. *Chemical Engineering Progress*, *48*(3), 141-146.

[247]   Tang, L., Yao, M., Wang, X., & Zhang, X. (2012). Non-uniform thermal behavior and shell growth within mould for wide and thick slab continuous casting. *Steel Research International*, *83*(12), 1203-1213.

[248]   Arai, T., & Hashimoto, H. (1985). Disintegration of a thin liquid sheet in a concurrent gas stream. *Proceedings of the 3rd international conference on liquid atomization and spray systems*. Institute for Liquid Atomization and Spray Systems.

[249]   Koric, S., & Thomas, B. G. (2006). Efficient thermo-mechanical model for solidification processes. *International Journal for Numerical Methods in Engineering*, *66*(12), 1955-1989.

[250]   Lienhard, I. V., & John, H. (2005). *A heat transfer textbook*. Phlogiston press.

[251]   Sutherland, W. (1893). LII. The viscosity of gases and molecular force. *The London, Edinburgh, and Dublin Philosophical Magazine and Journal of Science*, *36*(223), 507-531.

[252]   Shmelkov, Y., & Samujlov, E. (2012). Comparison of numerical simulation results for transport and thermodynamic properties of the solid fuels combustion products with experimental data. *Proceedings of EPJ Web of Conferences*. EDP Sciences.

[253]   Engineering ToolBox, (2005). *Water Vapor-Specific Heat*. https://www.engineeringtoolbox.com/water-vapor-d_979.html.

[254]   Dinçer, İ., & Zamfirescu, C. (2016). *Drying phenomena: theory and applications*. New Jersey, NJ: John Wiley & Sons.

[255]   Datt, P. (2011). Latent heat of vaporization/condensation. *Encyclopedia of snow, ice and glaciers*, 703-703.

[256]   Guo, Z., Saunders, N., Miodownik, A. P., & Schillé, J. P. (2005). Modelling of materials properties and behaviour critical to casting simulation. *Materials Science and Engineering: A*, *413*, 465-469.

[257]   Guo, Z., Saunders, N., Miodownik, P., & Schillé, J. P. (2008). Modeling material properties of lead-free solder alloys. *Journal of Electronic Materials*, *37*(1), 23-31.

[258]   Saunders, N., Guo, U. K. Z., Li, X., Miodownik, A. P., & Schillé, J. P. (2003). Using JMatPro to model materials properties and behavior. *JOM*, *55*(12), 60-65.

[259]   Guo, Z., Saunders, N., Schillé, J. P., & Miodownik, A. P. (2009). Material properties for process simulation. *Materials Science and Engineering: A*, *499*(1-2), 7-13.

[260]   Metzner, A. B. (1985). Rheology of suspensions in polymeric liquids. *Journal of Rheology*, *29*(6), 739-775.

[261]   Oldenburg, C. M., & Spera, F. J. (1992). Hybrid model for solidification and convection. *Numerical Heat Transfer, Part B Fundamentals*, *21*(2), 217-229.

[262]   Gulliver, G. H. (1913). The quantitative effect of rapid cooling upon the constitution of binary alloys. *Journal of the Institute of Metals*, *9*(1), 120-157.

[263]   Scheil, E. (1942). Bemerkungen zur schichtkristallbildung. *Zeitschrift für Metallkunde*, *34*(3), 70-72.

[264]   Sarreal, J. A., & Abbaschian, G. J. (1986). The effect of solidification rate on microsegregation. *Metallurgical Transactions A*, *17*(11), 2063-2073.

[265]   Carman, P. C. (1937). Fluid flow through granular beds. *Transactions of the Institution of Chemical Engineers*, *15*, 150-166.

[266]   De Schampheleire, S., De Kerpel, K., Ameel, B., De Jaeger, P., Bagci, O., & De Paepe, M. (2016). A discussion on the interpretation of the darcy equation in case of open-cell metal foam based on numerical simulations. *Materials*, *9*(6), 409.

[267]   Krane, M. J. M. (1998). *Transport phenomena during the solidification of binary and ternary metal alloys*. [Doctoral dissertation, Purdue University]. ProQuest.

[268]   Krane, M. J. M., & Incropera, F. P. (1996). A scaling analysis of the unidirectional solidification of a binary alloy. *International Journal of Heat and Mass Transfer*, *39*(17), 3567-3579.

[269]   Plotkowski, A., & Krane, M. J. M. (2017). The discrete nature of grain attachment models in simulations of equiaxed solidification. *Applied Mathematical Modelling*, *47*, 31-44.

[270]   Beckermann, C., & Viskanta, R. (1988). Double-diffusive convection during dendritic solidification of a binary mixture. *PhysicoChemical Hydrodynamics*, *10*(2), 195-213.

[271]   Vreeman, C. J., Krane, M. J. M., & Incropera, F. P. (2000). The effect of free-floating dendrites and convection on macrosegregation in direct chill cast aluminum alloys: Part I: model development. *International Journal of Heat and Mass Transfer*, *43*(5), 677-686.

[272]   Dantzig, J. A., & Rappaz, M. (2016). *Solidification: Revised & Expanded*. Lausanne, Switzerland: EPFL press.

[273]   Coleman, J., & Krane, M. J. M. (2020). Influence of liquid metal feeding on the flow and macrosegregation in DC casting. *Materials Science and Technology*, *36*(4), 393-402.

[274]   Feng, Y., Založnik, M., Thomas, B., & Phillion, A. (2019, May). A 3D discrete-element model for simulating liquid feeding during dendritic solidification of steel. *Proceedings of IOP Conference Series: Materials Science and Engineering*, *529*(1), 012031. IOP Publishing Ltd.

[275]   Feng, Y., Založnik, M., Thomas, B. G., & Phillion, A. B. (2020). Meso-scale simulation of liquid feeding in an equiaxed dendritic mushy zone. *Materialia*, *9*, 100612.

[276]   Won, Y. M., & Thomas, B. G. (2001). Simple model of microsegregation during solidification of steels. *Metallurgical and Materials Transactions A*, *32*(7), 1755-1767.

[277]   Chang, S., & Stefanescu, D. M. (1996). A model for macrosegregation and its application to Al-Cu castings. *Metallurgical and Materials Transactions A*, *27*(9), 2708-2721.

[278]   Bäckerud, L., Chai, G., & Tamminen, J. (1992). *Solidification Characteristics of Aluminum Alloys 2*. Schaumburg, IL: American Foundry Society.

[279]   Vreeman, C. J., & Incropera, F. P. (2000). The effect of free-floating dendrites and convection on macrosegregation in direct chill cast aluminum alloys: Part II: Predictions for Al-Cu and Al-Mg alloys. *International Journal of Heat and Mass Transfer*, *43*(5), 687-704.

[280]   Marsh, B. D. (1981). On the crystallinity, probability of occurrence, and rheology of lava and magma. *Contributions to Mineralogy and Petrology*, *78*(1), 85-98.

[281]   Kim, K. H., Oh, K. H., & Lee, D. N. (1996). Mechanical behavior of carbon steels during continuous casting. *Scripta Materialia*, *34*(2), 301-307.

[282]   Zhou, X., Moore, M. T., Ma, H., Silaen, A. K., & Zhou, C. Q. (2019). Adaptive mesh refinement of the solidification front in continuous caster simulations. *Proceedings of the ASME 2019 International Mechanical Engineering Congress & Exposition (IMECE 2019)*, 59452, V008T09A052. ASME Digital Collection.

[283]   Resa, J., Moore, M., Zhou, X., Ma, H., Silaen, A. K., & Zhou, C. Q. (2020). Analysis of Solidification and Thermal-Mechanical Behaviors in Continuous Casting. *Proceedings of the 149th TMS Annual Meeting & Exhibition,* 1175-1187. Berlin, Germany: Springer.

[284]   Moore, M. T. (2019). *Numerical simulation of a continuous caster* [Master thesis, Purdue University]. Purdue University.

[285]   Oxford Lasers. (n.d.). *Droplet size and velocity*. https://www.oxfordlasers.com/laser-imaging/industrial-nozzles

[286]   Leong, M. Y., & Hautman, D. J. (2002). Near-field spray characterization of a liquid fuel jet injected into a crossflow. *Proceedings of the 15th Annual Conference on Liquid Atomization and Spray Systems*. Institute for Liquid Atomization and Spray Systems.

[287]   Li, X., Arienti, M., Soteriou, M., & Sussman, M. (2010). Towards an efficient, high-fidelity methodology for liquid jet atomization computations. *Proceedings of the 48th AIAA Aerospace Sciences Meeting Including the New Horizons Forum and Aerospace Exposition*. Aerospace Research Central.

[288]   Li, X., Soteriou, M., Arienti, M., & Sussman, M. (2011). High-fidelity simulation of atomization and evaporation in a liquid jet in cross-flow. *Proceedings of the 49th AIAA aerospace sciences meeting including the new horizons forum and aerospace exposition*. Aerospace Research Central.

[289] Penno, M., Yin, H., Moravec, R., & Blazek, K. (2012). Measurement of spray cooling nozzle impact pressure footprints and its applications in continuous casting. *Iron and Steel Technology*, *9*(7), 67.

[290] Moravec, R., Blazek, K., Horsky, J., Graham, C., Fiegle, S., Dombovic, T., & Kaurich, T. (2011). Coupling of solidification model and heat transfer coefficients to have valuable tool for slab surface temperatures prediction. *Proceedings of the 7th METEC InSteelCon,* 1-9. Stahlinstitut VDEh.

[291] Horský, J., & Raudenský, M. (2005). Measurement of heat transfer characteristics of secondary cooling in continuous casting. *Proceedings of the 14th Conference on Metallurgy and Materials METAL*, 1-8. TANGER Ltd.

[292] Raudensky, M., Stetina, J., Horsky, J., Mauder, T., & Klimes, L. (2017). Optimization of cooling in nozzle overlapping area of continuous casting by using experiments and mathematical models. *Proceedings of the 9th European Continuous Casting Conference & Exhibition*, 781-790. Austrian Society for Metallurgy and Material.

[293] Prevodnosti, P. I. T. (2016). Estimation of the number of forward time steps for the sequential Beck approach used for solving inverse heat-conduction problems. *Materiali in Tehnologije*, *50*(2), 207-210.

[294] Kvapil, J., Pohanka, M., & Horský, J. (2015). Estimation of the thermal contact conductance from unsteady temperature measurements. *Materiali in Tehnologije*, *49*(2), 219-222.

[295] Hu, W., Zhang, Y., Yuan, G., Zhang, X., & Wang, G. (2019). Hot temperature mechanical behavior of high-permeability 6.5 wt% Si electrical steel in a mushy zone. *Steel Research International*, *90*(9), 1900105.

[296] Yamanaka, A., Nakajima, K., & Okamura, K. (1995). Critical strain for internal crack formation in continuous casting. *Ironmaking & Steelmaking*, *22*(6), 508-512.

[297] Okamura, K., & Kawashima, H. (1989). Three-dimensional elasto-plastic and creep analysis of bulging in continuously cast slabs. *Tetsu-to-Hagane*, *75*(10), 1905-1912.

[298] Kristiansson, J. O. (1984). Thermomechanical behavior of the solidifying shell within continuous-casting billet molds-a numerical approach. *Journal of Thermal Stresses*, *7*(3-4), 209-226.

[299]   Blazek, K., & Moravec, R. (2019). The effect of standoff distance on the cooling efficiency of air mist and hydraulic nozzles. *Proceedings of AISTech-Iron and Steel Technology Conference 2019*. AIST Digital Library.

[300]   Ji, C., Cai, Z. Z., Wang, W. L., Zhu, M. Y., & Sahai, Y. (2014). Effect of transverse distribution of secondary cooling water on corner cracks in wide thick slab continuous casting process. *Ironmaking & Steelmaking*, *41*(5), 360-368.

[301]   Ma, H., Silaen, A. A., & Zhou, C. Q. (2021). Simulation of spray cooling on hot steel slabs in continuous casting. *Journal of Thermal Science and Engineering Applications*, *13*(1). 011004.

[302]   Bhatt, N. H., Chouhan, D., Pati, A. R., Varshney, P., Das, L., Kumar, A., ... & Mohapatra, S. S. (2017). Role of water temperature in case of high mass flux spray cooling of a hot AISI 304 steel plate at different initial surface temperatures. *Experimental Heat Transfer*, *30*(5), 369-392.

[303]   Zhang, J., Chen, D., Wang, S., & Long, M. (2011). Compensation control model of superheat and cooling water temperature for secondary cooling of continuous casting. *Steel Research International*, *82*(3), 213-221.

[304]   Cai, K., & Wu, Y. (1983). Mathematical model for heat transfer in solidification of continuously cast slabs. *Acta Metallrugica Sinica*, *20*(3), B146.

[305]   Pohanka, M., Votavova, H., Raudensky, M., Hwang, J. Y., You, J. W., & Lee, S. H. (2018). The effect of water temperature on cooling during high pressure water descaling. *Thermal Science*, *22*(6 Part B), 2965-2971.

[306]   Weiner, J. H., & Boley, B. A. (1963). Elasto-plastic thermal stresses in a solidifying body. *Journal of the Mechanics and Physics of Solids*, *11*(3), 145-154.

[307]   Li, C., & Thomas, B. G. (2004). Thermomechanical finite-element model of shell behavior in continuous casting of steel. *Metallurgical and Materials transactions B*, *35*(6), 1151-1172.

[308]   Park, J. K., Thomas, B. G., & Samarasekera, I. V. (2002). Analysis of thermomechanical behaviour in billet casting with different mould corner radii. *Ironmaking & Steelmaking*, *29*(5), 359-375.

[309]   Won, Y. M., Yeo, T. J., Seol, D. J., & Oh, K. H. (2000). A new criterion for internal crack formation in continuously cast steels. *Metallurgical and Materials Transactions B*, *31*(4), 779-794.

[310] Jonšta, Z., Hernas, A., & Mazanec, K. (1998). Contribution to mechanical metallurgy behaviour of steel during continuous casting. *Journal of Materials Processing Technology*, *78*(1-3), 90-94.

[311] Kim, K. H., Yeo, T. J., Oh, K. H., & Lee, D. N. (1996). Effect of carbon and sulfur in continuously cast strand on longitudinal surface cracks. *ISIJ international*, *36*(3), 284-289.

[312] Mehrabian, R., Keane, M., & Flemings, M. C. (1970). Interdendritic fluid flow and macrosegregation; influence of gravity. *Metallurgical and Materials Transactions B*, *1*(5), 1209-1220.

[313] Chang, S., & Stefanescu, D. M. (1996). A model for macrosegregation and its application to Al-Cu castings. *Metallurgical and Materials Transactions A*, *27*(9), 2708-2721.

[314] Fujii, T., Poirier, D. R., & Flemings, M. C. (1979). Macrosegregation in a multicomponent low alloy steel. *Metallurgical Transactions B*, *10*(3), 331-339.

[315] Ridder, S. D., Kou, S., & Mehrabian, R. (1981). Effect of fluid flow on macrosegregation in axi-symmetric ingots. *Metallurgical Transactions B*, *12*(3), 435-447.

[316] Maples, A. L., & Poirier, D. R. (1984). Convection in the two-phase zone of solidifying alloys. *Metallurgical Transactions B*, *15*(1), 163-172.

[317] Bennon, W. D., & Incropera, F. P. (1987). A continuum model for momentum, heat and species transport in binary solid-liquid phase change systems-I. Model formulation. *International Journal of Heat and Mass Transfer*, *30*(10), 2161-2170.

VITA

Haibo Ma was born in Zhaotong, Yunnan Province, China, in 1991 to a pair of young parents, who unfortunately drifted apart several years later. He grew up in that small and undeveloped city with a naive dream lingering throughout his childhood: "to become a scientist.". Following his childish fantasy, he enrolled at Central South University in Changsha, Hunan Province, China, in the fall of 2010. After four eventful years, he received a bachelor's degree in Thermal Energy and Dynamic Engineering in June 2014. In the same year, he accepted a postgraduate recommendation from Central South University and enrolled in the School of Energy Science and Engineering. He worked as a graduate research assistant at the Center of Thermal Equipment Simulation and Visualization, directed by Professor Ping Zhou at Central South University. Just when he thought he would spend the next three years on one master thesis, he came upon a chance to earn another master's degree at Purdue University Northwest through a dual-degree program. He arrived in the United States in January 2015 without even knowing that he had just ended an era and started a completely different chapter in his life. He was hired as a quarter-time student worker the next day and began his six-year-long journey at the Center for Innovation through Visualization and Simulation (CIVS) at Purdue University Northwest while still in the wake of jet lag. Through numerous ups and downs, he managed to complete both master's degrees in 2017. He received his Master of Science in Dynamic Engineering and Engineering Thermophysics from Central South University in May 2017 with a thesis titled "Evaluation of flow behavior in copper electro-refining cell with difference inlet arrangements.". Later in August, he received his Master of Science in Mechanical Engineering from Purdue University Northwest with a thesis titled "Numerical analysis of raceway formation and combustion in a blast furnace with pulverized coal injection.". Shortly after graduation, he entered the doctoral program in the School of Mechanical Engineering at Purdue University in West Lafayette in the fall of 2017. He is expecting his Doctor of Philosophy in August 2021.

PUBLICATIONS

Ma, H., Silaen, A. K., & Zhou, C. Q. (2021). Simulation of spray cooling on hot steel slabs in continuous casting. *Journal of Thermal Science and Engineering Applications*, *13*(1), 011004 (12 pages).

Ma, H., Silaen, A. K., & Zhou, C. Q (2020). Numerical development of heat transfer coefficient correlation for spray cooling in continuous casting. *Frontiers in Materials*, *7*, 397 (18 pages).

Ma, H., Lee, J., Tang, K., Liu, R., Lowry, M., Silaen, A. K., & Zhou, C. Q. (2019). Modeling of spray cooling with a moving steel slab during the continuous casting process. *Steel Research International*, *90*(4), 1800393 (8 pages).

Zhou, P, Ma, H., Xie, Z., Yan, H. J., & Zhou, C. Q. (2017). Evaluation of flow behavior in copper electro-refining cell with different inlet arrangements. *Transactions of Nonferrous Metals Society of China*, *27*(10), 2282-2290.

Anisiuba, V. E., Ma, H., Silaen, A., & Zhou, C. Q. (2021). Modeling of Air-Mist Spray in Continuous Casting of Steel. *Proceedings of AISTech-Iron and Steel Technology Conference 2021*, (12 pages). AIST Digital Library.

Ma, H., Ma, S., Moss, R., Fisher, M., Silaen, A. K., & Zhou, C. Q. (2020). CFD analysis and optimization on an insertion electromagnetic flowmeter. *Proceedings of the ASME 2020 International Mechanical Engineering Congress & Exposition (IMECE 2020)*, 84539, V006T06A029 (11 pages). ASME Digital Collection.

Mosquera Salazar, E. A., Ma, H., Liu, R., Silaen, A., & Zhou, C. Q. (2020). Numerical model development for air-mist spray in steel secondary cooling process using the VOF-to-DPM multiphase transition model. *Proceedings of AISTech-Iron and Steel Technology Conference 2020*, (7 pages). AIST Digital Library.

Moore, M. T., Resa, J., Zhou, X., Ma, H., Silaen, A. K., & Zhou, C. Q. (2020). Analysis of a continuous caster simulation with adaptive mesh refinement along the solidification front. *Proceedings of AISTech-Iron and Steel Technology Conference 2020* (12 pages). AIST Digital Library.

Ma, H., Silaen, A. K., & Zhou, C. Q. (2019). Study on numerical simulation strategy for spray cooling during continuous casting of steel. *Proceedings of the 8th International STEELSIM Conference*, 394-410. The Austrian Society for Metallurgy and Materials.

Ma, H., Liu, R., Lowry, M., Silaen, A. K., & Zhou, C. Q. (2019). Numerical investigation of spray cooling at various operation conditions during continuous casting operation. *Proceedings of AISTech-Iron and Steel Technology Conference 2019*, 1425-1440. AIST Digital Library.

Zhou, X., Moore, M., Resa, J., Ma, H., Silaen, A. K., & Zhou, C. Q. (2019). Adaptive mesh refinement of the solidification front in simulations of a continuous caster. *Proceedings of the ASME 2019 International Mechanical Engineering Congress & Exposition (IMECE 2019)*, 8, V008T09A052 (10 pages). ASME Digital Collection.

Zheng, D., Ma, H., Silaen, A. K., & Zhou, C. Q. (2019). CFD analysis of reversed installation on flow measurements by a plate orifice. *Proceedings of the ASME 2019 International Mechanical Engineering Congress & Exposition (IMECE 2019)*, 7, V007T08A054 (6 pages). ASME Digital Collection.

Ma, H., Lee, J., Liu, R., Lowry, M., Silaen, A. K., & Zhou, C. Q. (2018). Numerical analysis of heat transfer for jet impingement on a hot steel plate during secondary cooling. *Proceedings of the 16th International Heat Transfer Conference*, 6423-6430 (8 pages). International Heat Transfer Conference Digital Library.

Ma, H., Tang, K., Liu, R., Lowry, M., Silaen, A. K., & Zhou, C. Q. (2018). Numerical modeling of water impingement and heat transfer with solid slabs during secondary cooling in a continuous

caster. *Proceedings of the ASME 2018 International Mechanical Engineering Congress & Exposition (IMECE 2018)*, 8A, V08AT10A010 (9 pages). ASME Digital Collection.

Wang, H. & Ma, H. (2017). Production practice of copper electrolysis with parallel flow technology. *China Nonferrous Metallurgy*, 46(4), 7-11.

Tang, K., Zhou, P., Ma, H., Zhang, J., Li, J., & Zhou, C. Q. (2017). The development of virtual KIVCET furnace based on the Unity3D. *International Electronic Elements*, 25(7), 10-14.

Ma, H., Okosun, T., Silaen, A. K., Wu, B., Tang, G., & Zhou, C. Q. (2016). Numerical analysis of raceway combustion under different operating conditions in blast furnace. *Proceedings of the Materials Science & Technology 2016 (MS&T 2016)*, 8 pages. ASM Conference Proceedings.

Ma, H., Chen, X., Hwang, H., Pratt, M., Mulligan, R. J., Wu, B., Tang, G., & Zhou, C. Q. (2016). CFD modeling of a ladle with top stirring lance. *Proceedings of CFD Modeling and Simulation in Materials Processing*, 169-177. TMS Member Library.

Ma, H., Sun, H., Li, X., Shang, S., Song, Q., & Bai, H. (2013). Optimum control for thermal engineering parameters of the organic heat carrier in the waste heat recovery. *Energy Conservation*, 32(10), 23-27.

Shang, S., Bai, H., Sun, H., Ma, H., & Li, X. (2013). A study on the heat transfer process influenced by the coking of heat transfer oil in the waste heat recovery pipeline. *Energy Conservation*, 32(5), 70-72.